Development of Satellite Interferometry Methods for Volcanic Surveillance



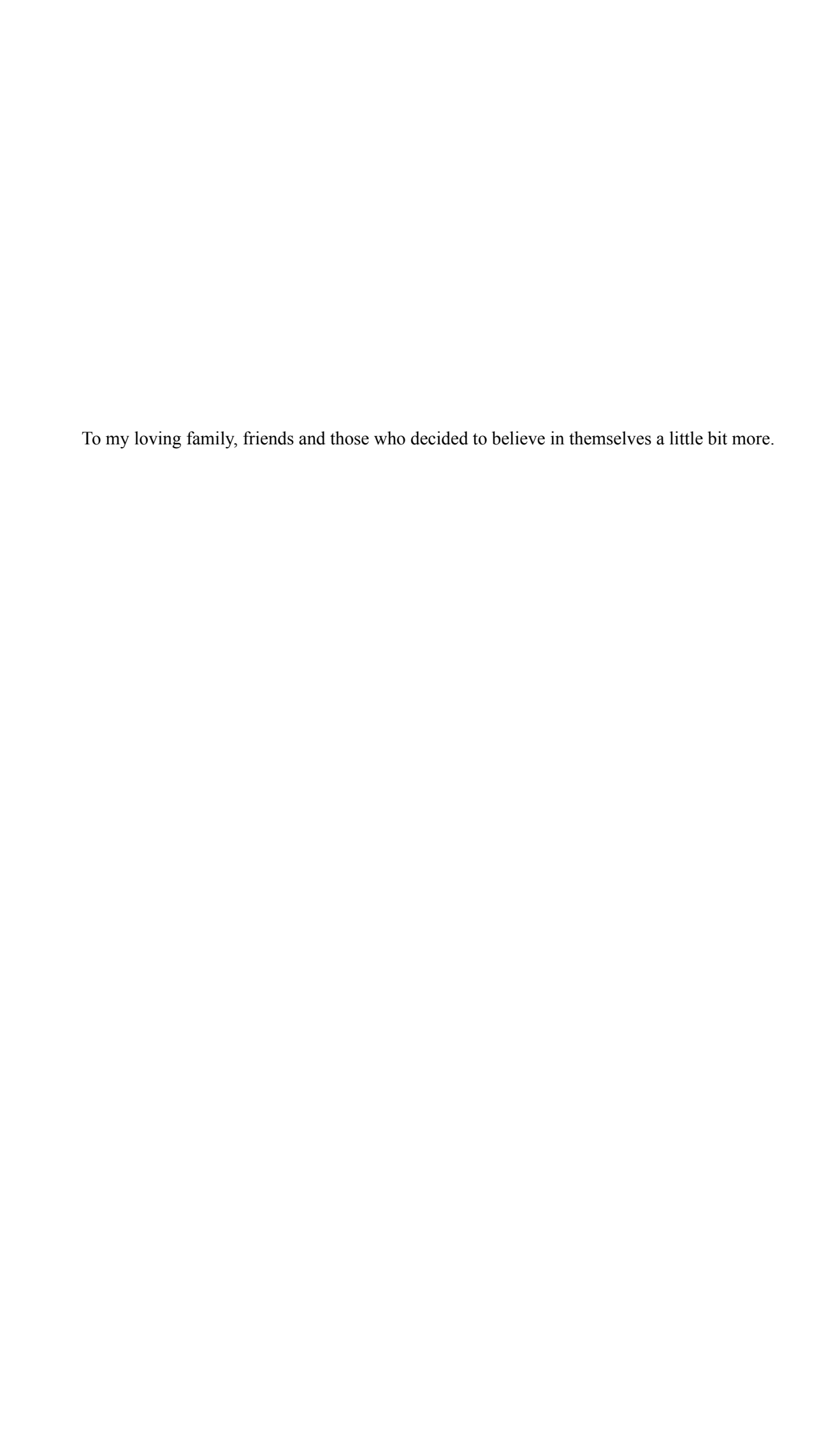
Monika Przeor

Director: Dr. Luca D'Auria and Dr. Susi Pepe

Tutor: Dr. Juan Pedro Díaz González

Faculty of Physics University of La Laguna

This dissertation is submitted for the degree of *Doctor in Industrial, Computer and Environmental Engineering*



Declaration

I hereby declare that except where specific reference is made to the work of others, the contents of this dissertation are original and have not been submitted in whole or in part for consideration for any other degree or qualification in this, or any other university. This dissertation is my own work and contains nothing which is the outcome of work done in collaboration with others, except as specified in the text and Acknowledgements. This dissertation contains fewer than 65,000 words including appendices, bibliography, footnotes, tables and equations and has fewer than 150 figures.

Monika Przeor June 2024

Acknowledgements

Hay personas que, por el simple hecho de estar a tu lado, hacen que los malos momentos sean un poco más llevaderos. Su sola presencia ha sido mi fuerza durante los años de mi doctorado. En este momento, quiero detenerme y dedicarles un agradecimiento especial a ellos: familiares y amigos que estuvieron conmigo en los momentos difíciles, llenos de obstáculos y complicaciones, pero también a aquellos que compartieron conmigo las alegrías, risas y felicidad.

Primero de todo, mis más profundos agradecimientos a mis padres, quienes me enseñaron que no hay cosas imposibles, solo aquellas que requieren un poco más de tiempo para conseguir. Su empatía, apoyo y paciencia son incalculables. Gracias por enseñarme a seguir con mis objetivos y a no rendirme. Gracias por mostrarme que las limitaciones no existen, que somos nosotros mismos quienes las establecemos. Junto a ellos, también agradezco a mis hermanas. Tener dos amigas para toda la vida me da fuerzas y seguridad. Puedo precipitarme con la certeza de que, si me caigo, ellas estarán ahí para ayudarme a levantarme. Gracias por estar siempre a mi lado, apoyarme y escucharme.

Un lugar muy especial en estos agradecimientos es para mi querido marido, Iván. Él es mi roca, mi fuerza y mi motivación para superarme cada día. Me ayuda a afrontar las adversidades con calma y optimismo, siempre encontrando el lado positivo de las cosas. Me considero muy afortunada de poder compartir los proyectos de la vida con él y saber que siempre puedo contar con su apoyo. Gracias por su paciencia, amor y ayuda en todos los niveles que he necesitado a lo largo de estos años.

Mis agradecimientos también están dirigidos a mis directores de tesis. Una mención especial para Luca, quien no solo ha sido mi director de tesis, sino que también se ha convertido en un amigo. Su conocimiento y calidad humana lo hacen inigualable. Es un ejemplo a seguir, y me llena de orgullo haber sido su doctoranda.

A lo largo de los años de doctorado, también he ganado amigos y he reforzado amistades existentes. Su presencia ilumina mis días, haciendo que, aunque llueva, siempre vea el sol. Gracias por acompañarme en este viaje y por creer en mí.

Abstract

This thesis focuses on satellite radar data analysis methods applied to volcanic surveillance. The importance of this study lies in the application of Differential Interferometric Synthetic Aperture Radar with a Small Baseline Subset (DInSAR-SBAS) to improve the prediction of potential volcanic events in the future and to understand the processes taking place in the volcanic areas of interest. A highly successful geodetic method, such as satellite radar interferometry, allows the creation of interferograms and time series showing the behaviours of each analysed data pixel over time. In this thesis, we applied the statistical tool to the time series results, named Independent Component Analysis (ICA), to eliminate potential noise sources and uncover hidden deformation patterns in the complex signals. Employing the ICA statistical tool to the DInSAR SBAS dataset is the most innovative aspect of this thesis. Finally, the deformation data undergo mathematical inversion to modelise the source parameters that create the observed anomalies. We applied the aforementioned method to study three volcanically active areas on Hawaii, La Palma, and Tenerife islands. The results show that conducting such studies can help understand the volcanic processes that could occur in the future, providing an advantage to society living and sharing space with volcanoes. The selected areas were chosen to monitor volcanoes in areas with high potential for volcanic events. In the case of Hawaii, the importance of applying the ICA to the DInSAR SBAS dataset allowed the recognition of the deformation patterns of two volcanoes on the island that interact in opposite ways. This study helped to understand volcanic processes that had been the objective of scientific debate for more than 100 years. In the case of La Palma, the study focused on imaging the magmatic path in the crust that was followed in the pre-eruptive phase of the eruption of Tajogaite and during its first days. Finally, Tenerife island showcases the high background activity of the Teide volcano. The aim of studying this area was to understand the source and the processes that took place during the seismic crisis of 2004-2005. The outcomes of those studies shed light on the effectiveness of the applied methods to active volcanoes, enabling the understanding of geodetic processes and the prediction of future volcanic activity.

Publications

Thesis Publications

- **Przeor, M.**, D'Auria, L., Pepe, S., Tizzani, P., and Cabrera-Pérez, I. (2022). Elastic interaction between Mauna Loa and Kīlauea evidenced by independent component analysis. Scientific Reports, 12(1), 19863.
- **Przeor, M.**, Castaldo, R., D'Auria, L., Pepe, A., Pepe, S., Sagiya, T., Solaro, G., Tizzani, P., Barrancos J., and Pérez, N. (2024). Geodetic imaging of magma ascent through a bent and twisted dike during the Tajogaite eruption of 2021 (La Palma, Canary Islands). Scientific Reports, 14(1), 212.
- Przeor, M., D'Auria, L., Pepe, S., Tizzani, P., Barone, A., Vitale, A., Pérez, N. and Castaldo, R. (2024). Independent Component Analysis and Finite element modelling of the 2004-2005 ground deformation in Tenerife (Canary Islands). Front. Earth Sci. Sec. Solid Earth Geophysics. Volume 12 2024; doi: 10.3389/feart.2024.1412827

Other Publications

- D'Auria, L., Koulakov, I., Prudencio, J., Cabrera-Pérez, I., Ibáñez, J. M., Barrancos, J., Martínez van Dorth, D., D. Padilla, G., Przeor, M., Ortega, V., Hernández, P. and Peréz, N. M. (2022).
 Rapid magma ascent beneath La Palma revealed by seismic tomography. Scientific Reports, 12(1), 17654.
- Cabrera-Pérez, I., D'Auria, L., Soubestre, J., Przeor, M., Barrancos, J., García-Hernández, R., Ibáñez, J., Koulakov, I., Martínez van Dorth, D., Ortega, V., Padilla, G., Sagiya, T. and Pérez, N. (2023). Spatio-temporal velocity variations observed during the pre-eruptive episode of La Palma 2021 eruption inferred from ambient noise interferometry. Scientific Reports, 13(1), 12039.
- Cabrera-Pérez, I., D'Auria, L., Soubestre, J., Martínez van Dorth, D., Cervigón-Tomico, G., Martín-Lorenzo, A., Przeor, M., García-Hernández, R., Padilla, G., Barrancos, J., Padrón, E. and Pérez, N. M. (2023). Estudios de tomografía de ruido sísmico para la exploración geotérmica en Canarias. Boletin Geologico y Minero, 134(3).
- Cabrera-Pérez, I., Soubestre, J., D'Auria, L., Barrancos, J., Martín-Lorenzo, A., van Dorth, D. M., Padilla, G., Przeor, M. and Pérez, N. M. (2023). Geothermal and structural features of La Palma island (Canary Islands) imaged by ambient noise tomography. Scientific Reports, 13(1), 12892.
- Cabrera-Pérez, I., Soubestre, J., D'Auria, L., Przeor, M., García, R., Barrancos, J., Padilla, G., Pérez, N. and Prudencio, J. (2024). Ambient noise tomography of El Hierro island (Canary Islands). Frontiers in Earth Science, 11, 1326634.

Contents

Li	st of l	Figures	XV
1	Intr	oduction	1
	1.1	Remote Sensing on active volcanoes	1
	1.2	Motivation	
2	Volc	cano Geodesy and Remote Sensing	5
	2.1	Volcano geodesy	5
	2.2	Active sensors for Remote Sensing	6
	2.3	Global Navigation Satellite System GNSS	7
	2.4	Interferometric Synthetic Aperture Radar InSAR	8
3	Inte	rferogram phase processing	15
	3.1	Interferogram generation	15
	3.2	Adaptive filter and coherence generation	18
	3.3	Phase unwrapping	19
	3.4	Refinement and re-flattening	20
	3.5	Phase to height conversion and geocoding	21
	3.6	Phase to displacement conversion and geocoding	22
4	Inte	rferometric Stacking SBAS	25
	4.1	Connection graphs	25
	4.2	Interferometric Process	26
	4.3	Inversion: First Step	27
	4.4	Inversion: Second Step	28
	4.5	Geocoding	30
5	Inde	ependent Component Analysis (ICA)	33
	5.1	Independent Component Analysis	33
	5.2	ICA for SBAS DInSAR dataset	3/1

xii Contents

6	Volc	ano De	formation Source Models	37
	6.1	Analyt	tical volcano deformation source models	37
		6.1.1	Mogi point pressure source	38
		6.1.2	McTigue finite spherical model	39
		6.1.3	Okada dike-like model	40
		6.1.4	Sill-like model	41
	6.2	Nume	rical volcano deformation source models	43
7	Inve	erse Mo	delling	45
	7.1	Linear	inverse modelling	46
	7.2	Nonlin	near inverse modelling	47
8	Elas	stic inter	raction between Mauna Loa and Kīlauea evidenced by independent compon-	
	ent a	analysis		49
	8.1	Introdu	uction	49
	8.2	Result	s	52
	8.3	Discus	ssion	56
	8.4	Metho	ds	62
		8.4.1	DInSAR SBAS time series	62
		8.4.2	Independent component analysis (ICA) of DInSAR SBAS time series	63
		8.4.3	Nonlinear inverse modelling	64
		8.4.4	GPS data	64
		8.4.5	Numerical modelling of the stress and strain fields	65
9	Geo	detic im	naging of magma ascent through a bent and twisted dike during the Tajogaite	;
	erup	otion of	2021 (La Palma, Canary Islands)	69
	9.1	Introdu	uction	69
	9.2	Result	s	71
		9.2.1	Preliminary non-linear inversion and dike geometry	71
		9.2.2	Geodetic imaging	72
	9.3	Discus	ssion	78
	9.4	Data a	nd Methods	82
		9.4.1	Data and processing of GNSS time series	82
		9.4.2	DInSAR Sentinel-1 data and processing	83
		9.4.3	Non-linear inversion for the shallow dike geometry	84
		9.4.4	Geodetic imaging	87
10	Inde	ependen	nt Component Analysis and Finite element modelling of the 2004-2005 ground	
	defo	rmatio	n in Tenerife (Canary Islands)	89
	10.1	Introd	uction	89

Contents

	10.2	Data and Methods	92
		10.2.1 SBAS DInSAR time series	92
		10.2.2 Independent Component Analysis (ICA) of SBAS DInSAR time series	93
		10.2.3 Non-linear source modeling through the Finite Element Modeling	93
	10.3	Results	94
		10.3.1 SBAS DInSAR time series	94
		10.3.2 Application of the ICA to the DInSAR dataset	94
		10.3.3 Non-linear optimization in Finite Element Modeling	96
	10.4	Discussion and Conclusion	96
11	Conc	clusions	103
	11.1	Conclusions for Elastic interaction between Mauna Loa and Kīlauea evidenced by ICA	103
	11.2	Conclusions for Geodetic Imaging of magma ascent of the Tajogaite eruption of 2021	104
	11.3	Independent component analysis and finite element modelling of the 2004-2005	
		ground deformation in Tenerife (Canary islands)	104
	11.4	General conclusions	105
Re	feren	ces	107
Аp	pendi	ix A Supplementary material for: Elastic interaction between Mauna Loa and	
	Kīla	uea evidenced by ICA	115
Аp	pendi	ix B Supplementary material for: Geodetic imaging of magma ascent through a	
	bent	and twisted dike during the Tajogaite eruption of 2021 (La Palma, Canary Islands	131
Ap	pendi	ix C Thesis Publications	147
Ap	pendi	ix D Other Publications	187

List of Figures

1.1	Ancient Serapeo marketplace. Photography taken in 2023	2
2.1	GNSS stations in La Palma operated by Involcan.	9
2.2	N-S, E-W and U-D components of GNSS station ARID in La Palma between the 6th	
	of September and 16th of October of 2021. Green vertical line represents the day of	1.0
	the beginning of the eruption of Tajogaite.	10
2.3	Electromagnetic spectrum.	11
2.4	Schematic visualisation of satellite sending and receiving electromagnetic waves in	
	reference time t_0 and the following pulse of the radar in time t_1	12
3.1	Two radar images of the study area. The left one is the master file acquired on the	
	02nd of September, while the image on the right is the slave radar image acquired	
	on the 14th of September of 2021. Note that the radar images are represented in the	
	geometry of the SAR data acquisition; the georeferentiation is done in the later step	16
3.2	Initial interferogram ϕ_1 - ϕ_2 of two SAR images of the same area and similar ac-	
	quisition geometries. The resulting interferogram contains the fringes created by the	
	ground deformation previous to the eruption of Tajogaite, orbital differences, topo-	
	graphy, atmospheric perturbances and noise. The interferogram is not georeferenced.	17
3.3	Synthetic interferogram (left) and Digital Elevation Model (DEM) (right) used to	
	remove the topographic effects on the interferogram.	17
3.4	Differential interferogram as a product of topographic and orbital effects removed.	
	The fringes are between $-\pi$ and π . The interferogram is not georeferenced	18
3.5	The estimated coherence (left) and the filtered interferogram (right). The images are	
	not georeferenced	19
3.6	Unwrapped phase.The image is not georeferenced.	20
3.7	Wrapped (left) and unwrapped (right) interferograms after refinement and re-flattening.	21
3.8	Precision (left) and resolution (right) images. The images are georeferenced. Units	
	of measurements are expressed in meters [m]	22
3.9	Georeferenced Slant range displacement in [m]	23

xvi List of Figures

4.1 4.2	Spatial (left) and temporal (right) connection graphs	26
	of 2021. The images are not georeferenced.	27
4.3	Displacement velocity $[mm/yr]$ resulted of the First Inversion of SBAS processing.	28
4.4	Re-flattened and re-filtered wrapped interferogram (left) and unwrapped (right)	29
4.5	Mean displacement velocity in $[mm/yr]$ after atmospheric corrections. The image is not georeferenced.	29
4.6	Cumulative LOS dispalcement for the 26th of September of 2021 in [mm]	31
5.1 5.2	Comparison between the PCA and ICA distribution of the features after [21] Application of ICA and PCA to the mixed signal. The a) represents three independent functions combined into a mixed signals b). The c) represents the decomposed signal into three independent components, and the d) represents the decomposition into three	34
	principal components	35
6.1	Synthetic horizontal and vertical displacement for point pressure source [3]	38
6.2	Synthetic horizontal and vertical displacement for point pressure source	39
6.36.4	Synthetic horizontal and vertical displacement for finite rectangular dislocation model. Synthetic horizontal and vertical displacement 2D representation for finite rectangu-	40
6.5	lar dike-like dislocation model	41
6.6	dislocation model	42
6.7	lar dislocation model	42
	elled with the tetrahedral mesh	44
7.1	An interaction of the Nelder-Mear method over two-dimensional space showing points after [39]	48
8.1	Main geologic and seismicity map of Mauna Loa and Kīlauea [41]	50
8.2	LOS deformation cumulative maps. (A), (B), (C): ENVISAT 093 orbit; (D), (E), (F): ENVISAT 343 orbit; (G), (H), (I): ENVISAT 472 orbit; (J), (K), (L): ENVISAT 200 orbit (see Table S2 for track details). Column 1 shows the LOS cumulative displacement DInSAR map; columns 2 and 3 represent the first and second components resulting from applying the ICA decomposition algorithm. The black crosses indicate the points used for extracting the time series shown in Fig. 8.3, while black dots	
	are the reference points used for the DInSAR SBAS processing.	54

List of Figures xvii

8.3	LOS displacement time series of Mauna Loa and Kīlauea summits. (A), (C), (E),	
	(G): time series for LOS displacement of Mauna Loa; (B), (D), (F), (H): time series	
	for Kīlauea volcano. Time series of LOS data are shown with continuous black lines;	
	time series of the first component of ICA are indicated with the dashed black lines,	
	while the dotted black lines report the time series of the second component of ICA.	
	Vertical lines mark major volcanic episodes and the date of the beginning of the GPS	
	dataset: (A) Mother's Day flow, which began erupting from Pu'u 'Ō'ō on 12th May	
	2003; (B) small bench collapse on 30th July 2006; (C) Father's Day eruption on 17th	
	June 2007; (D) explosion on 19th March 2008; (E) the second half of 2008 which	
	represent the time interval where the GPS measurements are available; (F) active	
	vent within Halema'uma'u crater in January 2009	55
8.4	LOS deformation cumulative maps. (A), (B), (C): ENVISAT 093 orbit; (D), (E),	
	(F): ENVISAT 343 orbit; (G), (H), (I): ENVISAT 472 orbit; (J), (K), (L): ENVISAT	
	200 orbit (see Table S2 for track details). Column 1 shows the LOS cumulative dis-	
	placement DInSAR map; columns 2 and 3 represent the first and second components	
	resulting from applying the ICA decomposition algorithm. The black crosses indic-	
	ate the points used for extracting the time series shown in Fig. 3, while black dots	
	are the reference points used for the DInSAR SBAS processing	57
8.5	Inverse modelling of the Kīlauea ground deformation source for four selected tracks:	
	(A), (B), (C): ENVISAT 093 orbit; D, E, F: ENVISAT 343 orbit; G, H, I: ENVISAT	
	472 orbit; J, K, L: ENVISAT 200 orbit, respectively. Column 1 represents the first	
	component (ICA1) encompassing a radius of 11 km from Halema'uma'u Crater.	
	Column 2 represents the Mogi analytical model as a result of the inverse modelling.	
	Column 3 shows the residuals of the inverse modelling and the observed data	58
8.6	Inverse modelling of the Kīlauea ground deformation source for four selected tracks:	
	(A), (B), (C): ENVISAT 093 orbit; (D), (E), (F): ENVISAT 343 orbit; (G), (H), (I):	
	ENVISAT 472 orbit; (J), (K), (L): ENVISAT 200 orbit, respectively. Column 1 rep-	
	resents the first component (ICA2) encompassing a radius of 15 km from Halema'uma'u	
	Crater. Column 2 represents the inverse model. Column 3 shows the residuals	60

xviii List of Figures

8.7	3D numerical modelling of strain fields. (A) The Digital Elevation Model of Hawai'i Island, with the red line representing the trace (A-A'), used in panels (C–E). (B)	
	tridimensional representation of the modelled ground deformation sources of Mauna	
	Loa and Kīlauea volcanoes. The sources are numbered according to Table A.14 in the	
	supplementary material. (1) the Mauna Loa dike-shaped source from ICA1; (2) the	
	Kīlauea Mogi-like source from ICA1; (3) the Kīlauea sill-shaped source from ICA2.	
	Storage areas and topography are exaggerated in size for clarity. (C) the volumetric	
	strain field represented along the A-A' trace due to an overpressure applied to the	
	Mauna Loa dike-like source. (D) volumetric strain field along the A-A' trace due to	
	an overpressure applied to the Kīlauea Mogi-like source. (E) volumetric strain field	
	along the A-A' trace due to an overpressure applied to the $K\bar{\imath}$ lauea sill-like source	61
8.8	Areal strain time series for Mauna Loa GPS stations. The labels are triplets of GPS	
	stations surrounding the summit cone of Moku□ āweoweo Caldera (see Figure S2	
	for locations). The y-axis on the right shows the aerial strain scale in µstrain, the	
	dimension of the vertical axis is 5 µstrain, Time series colours are alternated in black	
	and red	66
8.9	Areal strain time series for Kīlauea GPS stations. The labels are triplets of GPS	
	stations surrounding the summit cone of Halema□uma□u Crater (see Figure S2 for	
	the locations). The y-axis on the right shows the aerial strain scale in µstrain, the	
	dimension of the vertical axis is 10 µstrain, being marked by ticks. Note that the	
	axis scale in this figure is different from that of Figure 8.8. Time series colours are	
	alternated in black and red	67
8.10	3D numerical modelling of stress fields. (A) The Digital Elevation Model of Hawai'i	
	Island, with the red line representing the trace (A-A'), used in panels (C-E). (B) tri-	
	dimensional representation of the modelled ground deformation sources of Mauna	
	Loa and Kīlauea volcanoes. The sources are numbered according to Table S1 in the	
	supplementary material. 1) the Mauna Loa dike-shaped source from ICA1; 2) the	
	Kīlauea Mogi-like source from ICA1; 3) the Kīlauea sill-shaped source from ICA2.	
	Storage areas and topography are exaggerated in size for clarity. (C) stress field	
	represented along the A-A' trace due to an overpressure applied to the Mauna Loa	
	dike-like source. (D) stress field along the A-A' trace due to an overpressure ap-	
	plied to the Kīlauea Mogi-like source. (E) stress field along the A-A' trace due to an	
	overpressure applied to the Kīlauea sill-like source	68
9.1	The geological map and the GNSS permanent stations location of La Palma. The	
	lower right-hand side panel shows the location of the island of La Palma (in red)	
	within the Canaries. The legend explains the meaning of the colour shades on the	
	map and the GNSS station. The NW-SE alignment of the effusive fissure of the	
	2021 eruption is represented by the red line (A–A')	70

List of Figures xix

9.2	Tridimensional representation of the dike geometry and the topography of La Palma	
	island. Panel A is a view from S.W., while B is from W. Earthquake hypocenters are	72
0.2	represented as cyan circles. The axes are represented in meters (m).	73
9.3	Distribution of absolute and differential dike opening for the 8th (ascending orbit) and	
	Sept. 10th 2021 (descending orbit). Grey dots represent the projection on the dike	
	of all the seismic events located between Sept. 11th and 28th. The seismic events	
	colour in the images of Sept. 8th is represented with dark grey in order to highlight	
	the total of earthquakes produced in the analysed period. Orange stars indicate the	74
0.4	future location of the main eruptive vent	74
9.4	Distribution of absolute and differential dike opening for the 14th (ascending orbit) and Sept. 16th 2021 (descending orbit). Grey dots represent the projection on the dike	
	of all the seismic events located between Sept. 11th and 28th, while green dots rep-	
	resent seismic events that occurred between two successive images. Blue ellipsoids	
	and black squares represent, respectively, the features in the dike opening function	
	and the clusters of seismic events discussed in the text. Orange stars indicate the	
	future location of the main eruptive vent	75
9.5	Distribution of absolute and differential dike opening for the 20th (ascending orbit)	
	and Sept. 22nd, 2021 (descending orbit). The volcano symbol indicates the position	
	of the main eruptive vent	76
9.6	Distribution of absolute and differential dike opening for the 26th (ascending orbit)	
	and Sept. 28th, 2021 (descending orbit). The meaning of the symbols is the same as	
	in Fig. 9.5	77
9.7	Schematic model of the plumbing system dynamics for key dates. Orange stars rep-	
	resent the location of the future site of the volcanic vent in the days preceding the	
	eruption. The symbols of the volcano represent the location of the actual volcanic	
	vent. Yellow arrows represent the magma ascent directions, while the green arrow	
	indicates the incipient collapse of the magma reservoir. The blue dashed lines rep-	
0.0		80
9.8	Solutions of some GNSS permanent stations solutions. Blue, red, and black hori-	
	zontal lines show the E–W, N–S, and U–D components of deformation, respectively.	
	The vertical red dotted line marks the day the eruption began, while the green dotted	
	vertical line marks the day when the first significant deformation was recorded at	0.5
0.0	stations MOLU and FUEN	85
9.9	DInSAR deformation maps for La Palma in pre-and (A and C panel) and early-eruptive (B and D panel) phases. (A and B) represent the ascending orbit, while (C	
	and D) represent the descending one. Black crosses show the location of the eruptive	
	vents	86
		00

List of Figures

10.1	Geological map of Tenerife after Barrera et al. [77]. The legend explains the meaning	
	of the color shades on the map. The three SVCs are marked with the tanned yellow	
	square with the SVCs' names included. The rim of the caldera is shown with the black	
	line with the triangles. Black triangles represent the volcanoes Pico Viejo, Teide, and	
	Montaña Blanca. A dashed black line represents the three rifts	91
10.2	Optimized source parameters.	94
10.3	The 2003 – 2005 SBAS-DInSAR mean velocity map represented in Line-Of-Sight	
	(cm/year). The gray circle shows the area of interest, where the ICA decomposi-	
	tion is applied, while the three gray squares represent the zones of the local negative	
	deformation, discussed by Fernández et al. [109]	95
10.4	Four independent component maps (A-D) extracted by ICA within the selected area	
	of a 9 km radius from the summit of the Teide volcano. The amplitude of the ground	
	deformation pattern components is normalized	97
10.5	ICA components and their respective energy.	98
10.6	Modelling result: (A) data, (B) model, and (C) residuals for the inverse modeling of	
	the first component of the ICA decomposition, respectively. TThe amplitude of the	
	ground deformation pattern components is normalized	98
10.7	Three-dimensional model of the retrieved source, responsible of 2004-2005 the ground	
	deformation. (A) map of Tenerife island, with the yellow box indicating the zoom of	
	Las Cañadas region. (B) Las Cañadas region, featuring the N-S (A-A') and E-W (B-	
	B') profiles employed to represent the vertical sections of topography and the source.	
	(C-D) the N-S and E-W sections of the topography in Las Cañadas and the ground	
	deformation modeled source, while (E-F) show the enlarged views of panels (C-D)	100
A.1	Areal strain time series for Mauna Loa GPS stations. The labels are triplets of GPS	
	stations surrounding the summit cone of Moku□ āweoweo Caldera (see Figure S2	
	for locations). The y-axis on the right shows the aerial strain scale in µstrain, the	
	dimension of the vertical axis is 5 µstrain, Time series colours are alternated in black	
	and red	116
A.2	Areal strain time series for Kīlauea GPS stations. The labels are triplets of GPS	
	stations surrounding the summit cone of Halema□uma□u Crater (see Figure S2 for	
	the locations). The y-axis on the right shows the aerial strain scale in µstrain, the	
	dimension of the vertical axis is 10 µstrain, being marked by ticks. Note that the	
	axis scale in this figure is different from that of Figure S1. Time series colours are	
	alternated in black and red	117

List of Figures xxi

A.3	Location of satellite tracks and GPS stations. The lower map shows Hawai'i Island.
	The blue rectangle shows the GPS study area of Mauna Loa, while the red rectangle
	represents the area of Kīlauea GPS stations. Green rectangles mark ENVISAT satel-
	lite data tracks along ascending (093) and descending orbits (343, 472, and 200). The
	upper maps show Mauna Loa and Kīlauea summits, respectively, with blue triangles
	representing the GPS stations of Mauna Loa and red triangles, GPS stations of Kīlauea. 118
A.4	Location of additional ENVISAT satellite tracks. Purple rectangles mark the tracks of
	ENVISAT satellite along descending orbits with swaths varying from I3 to I6 (26.0°
	to 42.8°); orange rectangles mark the tracks of ENVISAT satellite along ascending
	orbits with swaths varying from I2 to I4 (19.2° to 36.3°)
A.5	LOS deformation maps of Mauna Loa. A,B,C: ENVISAT 136 (IS3) orbit; D,E,F:
	ENVISAT 365 (IS2) orbit; G,H,I: ENVISAT 408 (IS4) orbit (see table S4 for track
	details). Column 1 shows raw data; columns 2 and 3 represent respectively the first
	and the second component resulting from applying the ICA decomposition algorithm.
	Black crosses: see figure 2 for description, while black dots are the reference points
	used to the SBAS-LOS performance
A.6	LOS deformation maps of Kīlauea. A,B,C: ENVISAT 114 (IS5) orbit; D,E,F: EN-
	VISAT 429 (IS3) orbit; G,H,I: ENVISAT 114 (IS6) orbit (see table S1 for track de-
	tails). Column 1 shows raw data; columns 2 and 3 represent respectively the first and
	the second component resulting from applying the ICA decomposition algorithm.
	Black crosses: see figure 2 for description, while black dots are the reference points
	used to the SBAS-LOS performance
A.7	Mauna Loa GPS station triples used for computing the areal strain time series. Blue
	triangles represent the GPS stations on Mauna Loa summit Caldera. Every triplet of
	stations is bordered by black lines and filled by a green grid
A.8	Kīlauea GPS station triples used for computing the areal strain time series. Red tri-
	angles represent the GPS stations in Kīlauea summit Caldera. Every triplet of stations
	is bordered by black lines and filled by a green grid
A.9	LOS deformation cumulative maps, first and second component of ICA decomposi-
	tion of ENVISAT 093 orbit for four different intervals. A, D, G, J: LOS cumulative
	displacement DInSAR map; B, E, H, J (column 2) and C, F, I, L: (column 3) repres-
	ent respectively the first and the second component resulting from applying the ICA
	decomposition algorithm. The black crosses indicate the points used for extracting
	the time series shown in figure 4, while black dots are the reference points used for
	the DInSAR SBAS processing

xxii List of Figures

A.10	LOS deformation cumulative maps, first and second component of ICA decomposi-	
	tion of ENVISAT 343 orbit for four different intervals. A, D, G, J: LOS cumulative	
	displacement DInSAR map; B, E, H, J (column 2) and C, F, I, L: (column 3) repres-	
	ent respectively the first and the second component resulting from applying the ICA	
	decomposition algorithm. The black crosses indicate the points used for extracting	
	the time series shown in figure 4, while black dots are the reference points used for	
	the DInSAR SBAS processing.	125
A 11	LOS deformation cumulative maps, first and second component of ICA decomposi-	1-0
	tion of ENVISAT 472 orbit for four different intervals. A, D, G, J: LOS cumulative	
	displacement DInSAR map; B, E, H, J (column 2) and C, F, I, L: (column 3) repres-	
	ent respectively the first and the second component resulting from applying the ICA	
	decomposition algorithm. The black crosses indicate the points used for extracting	
	the time series shown in figure 4, while black dots are the reference points used for	
	the DInSAR SBAS processing	126
Δ 12	LOS deformation cumulative maps, first and second component of ICA decomposi-	120
A.12	tion of ENVISAT 200 orbit for four different intervals. A, D, G, J: LOS cumulative	
	displacement DInSAR map; B, E, H, J (column 2) and C, F, I, L: (column 3) repres-	
	ent respectively the first and the second component resulting from applying the ICA	
	decomposition algorithm. The black crosses indicate the points used for extracting	
	the time series shown in figure 8.4, while black dots are the reference points used for	125
A 12	the DInSAR SBAS processing	12/
A.13	3D numerical modelling of stress fields. (A) The Digital Elevation Model of Hawai'i	
	Island, with the red line representing the trace (A-A'), used in panels (C-E). (B) tri-	
	dimensional representation of the modelled ground deformation sources of Mauna	
	Loa and Kīlauea volcanoes. The sources are numbered according to Table S1 in the	
	supplementary material. 1) the Mauna Loa dike-shaped source from ICA1; 2) the	
	Kīlauea Mogi-like source from ICA1; 3) the Kīlauea sill-shaped source from ICA2.	
	Storage areas and topography are exaggerated in size for clarity. (C) stress field	
	represented along the A-A' trace due to an overpressure applied to the Mauna Loa	
	dike-like source. (D) stress field along the A-A' trace due to an overpressure ap-	
	plied to the Kīlauea Mogi-like source. (E) stress field along the A-A' trace due to an	
	overpressure applied to the Kīlauea sill-like source.	128
A.14	Parameters of modelled sources of ground deformation. The results are the mean	
	value and standard deviation of the modelled parameters of separated inversions of	
	each track	129
A.15	Inventory of the four analysed ENVISAT satellite data tracks in the 2003-2010 period,	
	covering both volcanoes	129
A.16	Percentage of energy of every component of decomposition for each track	129

List of Figures xxiii

A.17	Inventory of the 6 analyzed and discarded tracks of ENVISAT satellite data in 2003-2010 period
B.1	Data, model, and residuals for the source of the ground deformation on La Palma (columns 1, 2, and 3, respectively) for each data acquisition date of the ascending orbit. 132
B.2	Data, model, and residuals for the source of the ground deformation on La Palma (columns 1, 2, and 3, respectively) for each of the data acquisition dates of the des-
B.3	cending orbit
B.4	model while the right-hand side panel shows the retrieved model
B.5	model while the right-hand side panel shows the retrieved model
B.6	true model while the right-hand side panel shows the retrieved model
B.7	model while the right-hand side panel shows the retrieved model
B.8	hand side panel)
B.9	hand side panel)
B.10	hand side panel)
	hand side panel)
	point represents the daily data solution while each x-symbol represents the synthetic model solution. Red, blue, and green colors represent the vertical, N-S, and E-W
D 12	components, respectively
	January to November 2021
B.13	LOS-projected mean displacement velocity maps for the descending orbit tracks from January to November 2021
B.14	Horizontal cumulative displacement of GNSS station ARID. We represent the cumulative horizontal displacement from the 12th to the 28th of September 2021. Each point represents a daily solution. The red point marks the beginning of the time series.
	We annotated relevant dates as discussed in the text
B.15	SAR datasets' key parameters for data acquired in this study

Chapter 1

Introduction

1.1 Remote Sensing on active volcanoes

Volcanic phenomena demonstrate the powerful forces of nature and present potential challenges for nearby populations. They can impact the environment, affect cities and communities, and have consequences for the atmosphere. They also act as creators of new lands and suppliers of minerals, fertilising areas affected by their deposits. The consequences of volcanic activity are so significant that their importance in society cannot be overlooked.

In the past, society could notice some volcanic anomalies by meticulously observing volcanoes. In the case of one of the most hazardous volcanic areas in Europe, the Phlegraean Fields in Italy, specifically in the town of Pozzuoli adjacent to Naples, the volcanic anomalies observed in the past constitute one of the most important examples of manifestations of volcano deformation. The observation of ground deformation fluctuations was possible due to changes in the shoreline level in the ancient Serapeo marketplace, constructed in the first century BCE [1] (see Fig. 1.1). During its history, it experienced ups and downs in the shoreline, obligating the citizens to construct a second level of columns as the first one sank below sea level.

The most noticeable episode of deformation in the Serapeo was observed before the eruption of Monte Nuovo in 1538, where the ground uplift was up to 12 meters and strongly accelerated (about 4-5 meters) in the days preceding the eruption. During these days, the shoreline moved backwards approximately 400 meters [2].

While the eruption of Monte Nuovo could be detected in time due to the strong volcanic manifestations that enabled residents to move away from areas with great volcanic activity, not all volcanoes send clear messages about their imminent eruption. The advancements in science have facilitated the application of crucial volcano monitoring tools for predicting eruptions. These techniques can be applied in regions with high volcanic risk, difficult access, or a lack of resources for volcanic surveillance. Using detailed scientific techniques, including precise ground deformation measurements and other geophysical methods, allows us to obtain an accurate image of the volcano's state. Various disciplines and methods exist to quantify outliers from the background activity of the volcano. How2 Introduction



Figure 1.1 Ancient Serapeo marketplace. Photography taken in 2023.

ever, some of these methods are still new and innovative. A highly modern and accurate approach to studying volcanoes is remote sensing, which allows the detection of volcanic unrest and temperature changes on the surface, quantifies the gas emissions in the atmosphere, etc. Also, applying remote sensing methods allows the collection of millimetre-precise ground deformation measurements. Observing the deformation of a volcano from space aids in understanding the volcano's behaviour before, during, and after an eruption. The information obtained from the sensors used in satellites constitutes a set of very powerful tools whose quantity of data is barely harnessed.

The geodetic data analysis method involves employing a technique known as Differential Satellite Interferometry (DInSAR). Its approach is primarily based on comparing the phases of electromagnetic waves by overlaying images of backscattered waves (radiograms) from the same satellite radar in the area of interest. The products of such overlays are interferograms, images depicting the phase variation of waves between two radar images. Interferograms illustrate the phase difference between two superimposed images, allowing the identification of areas affected by ground deformation.

Obtaining interferograms from a study area enables the analysis of the prevailing geophysical and geological conditions. Additionally, analysing deformation in a specific area can indicate the state of the volcano and help us understand the endogenous or exogenous factors that can cause changes in its behaviour. Ground deformation can be caused by the magmatic reservoirs in the crust when new inputs of magma occur, magma cooling in the crust, changes in the hydrothermal system due to pore pressure changes, variations in gas saturations in the subsurface, or even thermal expansion. However, on the surface, we can also detect landslides and movements in the flanks of volcanic edifices, the growth of volcanic domes, water withdrawal, etc. All these ground deformation changes are visible through the processing of SAR data.

1.2 Motivation 3

1.2 Motivation

This thesis originated from an interest in conducting a detailed investigation of ground deformation on volcanic islands. It aimed to image the magmatic or hydrothermal sources that drive volcanic activity and contribute to the observed ground deformation. The study mainly focused on the active volcanic islands of La Palma and Tenerife in the Canary Islands and Hawaii Island. Although these volcanic areas have been well-studied, there has been a lack of investigation into the sources of ground deformations and the mechanisms contributing to the observed behaviours in the areas of interest.

The first objective of this thesis is to analyse satellite interferometry data. We used this method because it provides a broad dataset over time and covers extensive areas of study. These data can also be used to apply inverse modelling to identify the causative sources of the observed ground deformation.

This achievement has been reached through two approaches: first, through the application of novel methods in the Python programming language, and second, by utilising existing computer programs that facilitate obtaining raw satellite radar data and performing the desired processing. Secondly, the preprocessed SAR dataset was analysed using statistical tools to obtain clearer data on the ground deformation. Finally, a non-linear inversion of the ground deformation dataset was applied with the aim of obtaining the characteristics of the source causing the observed ground movement.

These processing steps were applied to three different volcanic complexes. In the case of Hawaii Island, the focus was primarily on obtaining information about the interaction between two volcanoes, Mauna Loa and Kilauea (Chapter 8). The study on the elastic interaction of two volcanoes on Hawaii Island enabled the understanding of the scenery and forces responsible for the peculiar behaviour of both volcanoes. While the hypothesis of the interaction between Mauna Loa and Kilauea had already been proposed, this study provided insights into the specific causes behind their particular behaviour.

For La Palma Island, the main objective was to image the spatio-temporal ascent of magma preceding the eruption and during its initial days (Chapter 9). The ground deformation on La Palma was observed during the pre-eruptive episode of the Tajogaite eruption in 2021. However, this study focused on analysing the deformation, identifying the source responsible for the volcanic activity, and imaging the kinematic movement toward the surface of the magma. This kind of study had not been done before in La Palma, and this research allowed for a detailed understanding of the magmatic behaviour preceding the Tajogaite eruption.

Tenerife Island was studied to uncover the hidden volcanic processes occurring in the dormant volcano (Chapter 10). Ground deformation had been observed in the past, but the source responsible for the deformation had never been modelled. This work made it possible to understand better the internal processes that occurred during the crisis of 2004-2005 in Tenerife.

The eruption of Tajogaite in 2021 emphasised the importance of monitoring the islands' volcanoes for both the scientific community and the Canarian society. On a personal level, it made me realise the crucial importance of this study in enhancing our understanding of the processes occurring on the islands. It highlighted how even subtle changes in the volcanic system can impact volcanic dynamics

4 Introduction

and how such research plays a vital role in forecasting scenarios before and during an eruption. In this meaning, the thesis aimed to understand the processes occurring in the mentioned volcanoes and shed light on potential future eruptions.

Chapter 2

Volcano Geodesy and Remote Sensing

2.1 Volcano geodesy

Geodesy is a branch of Earth sciences that studies and quantifies the size and geometry of the Earth. The origin of geodesy can be associated with the early assertions of Pythagoras, who claimed that the Earth is a sphere. Later, Aristotle declared that the Earth was spherical. A highly significant contribution to geodesy came from Eratosthenes (276-195 BCE), who calculated the Earth's circumference, estimating its curvature and, consequently, its size [1].

Geodesy began to gain greater importance with the development of more precise mathematics and cartographic tools. However, it was only in the 20th century that new high precision instruments were developed, and geodetic reference systems could be established.

One sub-branch of geodesy is volcanic geodesy, which focuses on quantifying ground displacement in volcanic areas. While studying the Kilauea volcano, Thomas A. Jaggar discovered that the summits of active volcanoes experience surface uplifts and descents due to changes in magma reservoirs [1]. However, one cannot discuss volcanic geodesy without mentioning one of the pioneering scientists in this subfield. Kiyoo Mogi, in 1958, made a fundamental contribution to this field [3]. As a pioneer, Mogi attributed surface movements to changes in subsurface pressure. He applied these studies to two volcanoes of great importance in the field of volcanology, Sakurajima (Japan) and Kilauea (United States). His point source inflation model, known as the "Mogi model," has been widely used to interpret ground deformation data associated with volcanic activity.

Volcano geodesy gained even more significance when its methods were applied during the eruption of Mount St. Helens in 1980. During the two-month dome formation, observing how the volcano's surface deformed due to internal processes in the volcanic edifice was possible. These observations were made possible through Electronic Distance Measurement (EDM) and theodolites. These geodetic methods allowed the observation of dome construction and, subsequently, its collapse, resulting in the north flank landslide of the volcano [1].

Along with the early application of geodetic tools in volcanoes, a new way of observing volcanic movements from space emerged. In the 1950s, experiments with radar sensors were conducted.

However, the use of radar in volcanic studies became possible with the launch of a satellite equipped with Synthetic Aperture Radar (SAR), such as the European Remote Sensing Satellite-1 (ERS-1) in 1991 [1].

For military purposes, the United States developed a highly precise cartographic navigation tool known as the Global Positioning System (GPS), which was developed in the 1970s and became operational for civilian uses in the 1980s [1]. In the late XX century, its highly precise cartographic advantages were applied to studying volcanic areas.

Implementing radars on satellites allowed for the development of a powerful tool for quantifying ground deformation. Satellite Radar Interferometry (InSAR) became today's most powerful tool in volcano geodesy.

Nowadays, volcano monitoring technology is undergoing significant development, largely driven by the launches of satellites equipped with highly precise sensors, such as the prominent Sentinel constellation from the Copernicus program of the European Space Agency (ESA). These satellites offer advanced Earth observation capabilities, providing detailed data and more frequent coverage, revolutionising our ability to understand and anticipate volcanic activity.

2.2 Active sensors for Remote Sensing

Remote sensing is a modern and valuable tool for obtaining the physical characteristics of an area through detecting reflected radiation from a distance. Two types of remote sensing sensors are distinguished by their ability to either passively receive signals or actively emit and calculate the time it takes for the backscattered signal to be received.

Passive sensors utilise naturally emitted radiation to gather information and observe an object of interest. Its range of observations includes radiometers and spectrometers that operate with different wavelengths. Passive sensors receive waves from the visible spectrum, infrared, and some ranges of the microwave spectrum.

Active sensors emit electromagnetic signals and measure the time it takes for the return signal to be received. The changes experienced by the emitted signal and the backscattered signal are measured, providing information about the changes undergone by the object of study. These sensors operate within the microwave spectrum, allowing them to function both during the day and at night, regardless of cloud cover.

A radar is an example of an active remote sensing sensor that operates with an electromagnetic signal. The antenna on board the satellite or airborne platform emits a series of pulses in the microwave spectrum and receives the backscattered pulses from the target. Analysing the backscattered signal allows one to reconstruct a 2D image of the reflecting surface.

2.3 Global Navigation Satellite System GNSS

Global Navigation Satellite System (GNSS) refers to the combination of constellations belonging to the United States, Russia, Europe, and others. Initially, the United States developed the global navigation system, called the Navigation Satellite Time and Ranging Global Positioning System (NAVSTAR GPS). Nowadays, the term GPS is commonly used and recognised. Russia (formerly the Soviet Union) has developed a similar navigation system called GLONASS. Finally, the European Space Agency (ESA) launched a satellite constellation named Galileo. All three constellations operate in the L-band microwave frequency. Each constellation has slight differences from the others [1].

In the case of NAVSTAR GPS, there are 30 satellites orbiting in 6 circular orbits at an altitude of 20,200 km. GPS transmits positioning signals on two frequencies in the L-band. L1 operates at a frequency of 1575.42 MHz, with a wavelength of 19 cm. The L2 band operates at a frequency of 1227.6 MHz with a wavelength of 24.4 cm. Satellite information is transmitted using a Pseudo-Random Noise (PRN) code with the corresponding identification for each satellite [1].

GLONASS also has 30 satellites orbiting in 3 orbits at an altitude of 19,100 km. The L1 band operates in the frequency range from 1602.5625 to 1615.5 MHz, while L2 operates in the frequency range from 1246.4375 to 1256.5 MHz. Satellite data is transmitted using the same PRN code and different frequencies for each satellite within the mentioned ranges [1].

Finally, Galileo has 30 satellites in 3 orbits operating at an altitude of 23,616 km. The L1 band transmits data at a frequency of 1575.42 MHz. This frequency band is unified with the L1 of the GPS constellation, allowing for data sharing without overlapping or interrupting the GPS data signal. The more precise L5 band operates at a frequency of 1176.45 MHz [1].

Each satellite broadcasts the signal of its position at every moment, along with highly accurate (absolute) time information, satellite details, ionospheric conditions, etc. This information receives GNSS receivers. The receivers collect data from all satellites visible at the precise moment and calculate the distance between the receiver and the satellites sending data at that time. Assuming the exact position of the satellites is known, the distance between at least four satellites and the receiver is calculated. This way, the location of the receiver is known with great precision. The more satellites the receiver captures, the higher the accuracy of the location calculation. The receiver's position is obtained with three spatial coordinates (latitude, longitude, and altitude) [1].

Observing the receiver's position variation over time allows for visualising the ground displacement in the vertical and horizontal axes with millimetric precision. With the aim of obtaining precise information about the position, the absolute or relative mode of GNSS positioning can be employed. Absolute positioning is based on obtaining the location of GNSS stations (receivers and antennas) with respect to the global reference coordinate system (e.g., World Geodetic System 1984, WGS84). This way, the exact and absolute position of the station is known according to the global reference system [1].

However, for volcanic surveillance purposes, the relative positioning mode is often used when dealing with local or regional networks with a large number of GNSS stations in a limited area [1]. In this way, the position of each station in the network is obtained with respect to the absolute position of a reference station. This reference station is assumed to be stable or not included within the deformation zone. The GNSS station network is installed continuously (cGNSS), saving position and time data according to the configured sampling frequency.

In the case of stations installed in the Canary Islands, belonging to the Instituto Volcanológico de Canarias (INVOLCAN) and collaborators such as the University of Nagoya and Grafcan, the stations are part of the Red Geodésica Canaria. The stations record data every 30 seconds and send a Receiver Independent Exchange Format (RINEX) file each day. An example of a Canarian geodetic network installed on the island of La Palma is included in Figure 2.1.

The RINEX files from each station are analysed using the free software Gamit/Globk [4]. These files are preprocessed with Gamit to correct errors and apply atmospheric and clock corrections. The first estimation of GNSS station positions is obtained by calculating the baseline between network stations. Subsequently, with the Globk software, satellite orbits, clocks, the receiver clock, and the plate tectonics corrections are estimated. Following this, station positions are adjusted to the reference station. The displacement of the reference station is estimated to achieve greater precision in the GNSS stations of interest. The final step involves obtaining the relative positions of stations in the N-S, E-W, and vertical axes. Figure 2.2 provides an example of such results, illustrating the deformation experienced by one of the GNSS stations during the volcanic crisis in La Palma in 2021.

For the purposes of this thesis, the GNSS dataset was used as complementary information to the SAR data.

2.4 Interferometric Synthetic Aperture Radar InSAR

Satellite Radar Interferometry is based on using electromagnetic waves emitted from antennas integrated onboard the satellites. This utilisation of electromagnetic waves from antennas is known as Radio Detection and Ranging (RADAR). Electromagnetic waves work in the microwave spectrum, encompassing between 300 MHz and 300 GHz [1] (Figure 2.3). The antenna sends pulses of electromagnetic waves toward the Earth's surface with a fixed and established wavelength. The signal reaches the surface and reflects in all directions due to objects on Earth along the path between the antenna and the surface, and a small part of the signal returns to the satellite. The arrival time of the electromagnetic wave return is calculated, obtaining an image of the surface (Figure 2.4). The imaged result of the reflected waves from the surface is called a radiogram.

The principles of Interferometric Synthetic Aperture Radar are explained in the following. The same satellite scans the same area on different days (Figure 2.4). The superposition of radiograms allows obtaining the phase difference ($\Delta \phi$) between two SAR images. The phase change of the wave between one radiogram and another provides information about the variation in the distance travelled by the wave and, consequently, about the displacement (ΔR) along the satellite's Slant Range (SR)

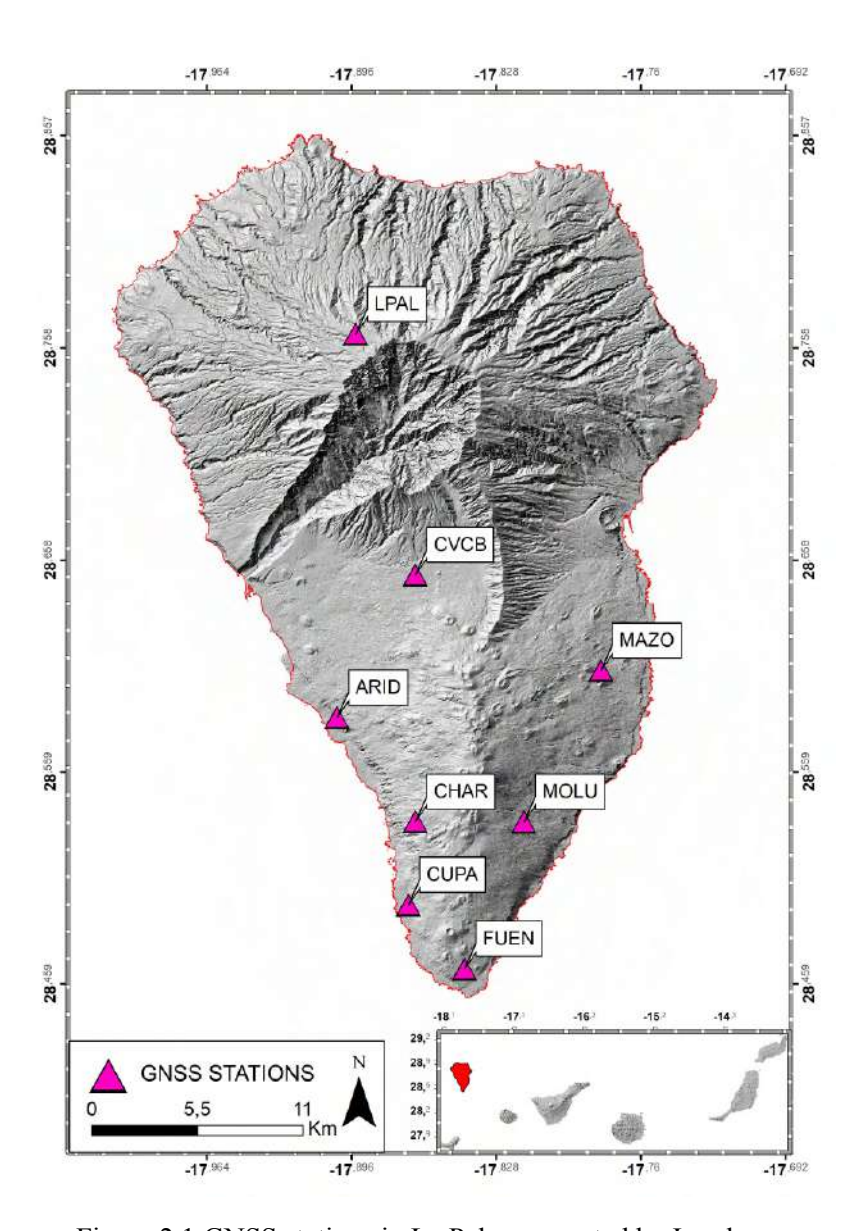


Figure 2.1 GNSS stations in La Palma operated by Involcan.

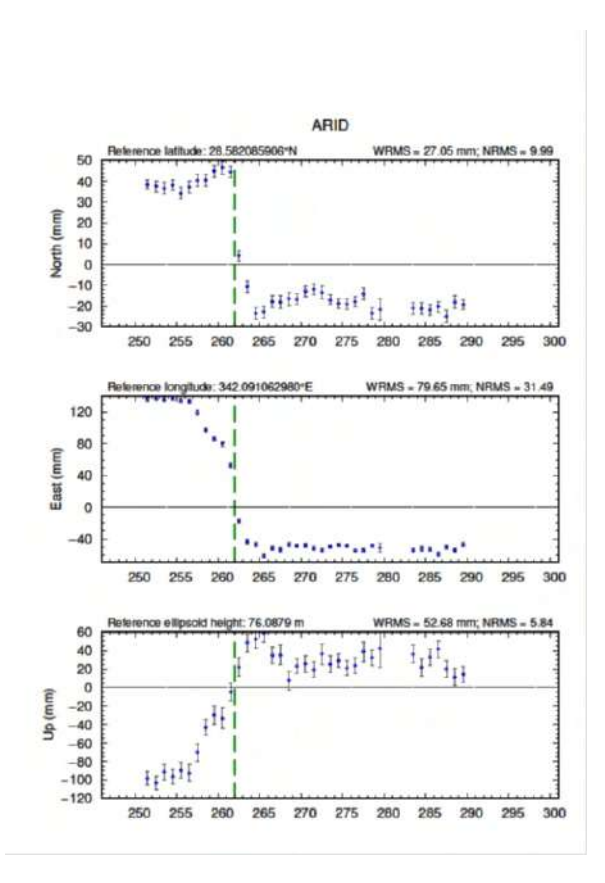


Figure 2.2 N-S, E-W and U-D components of GNSS station ARID in La Palma between the 6th of September and 16th of October of 2021. Green vertical line represents the day of the beginning of the eruption of Tajogaite.

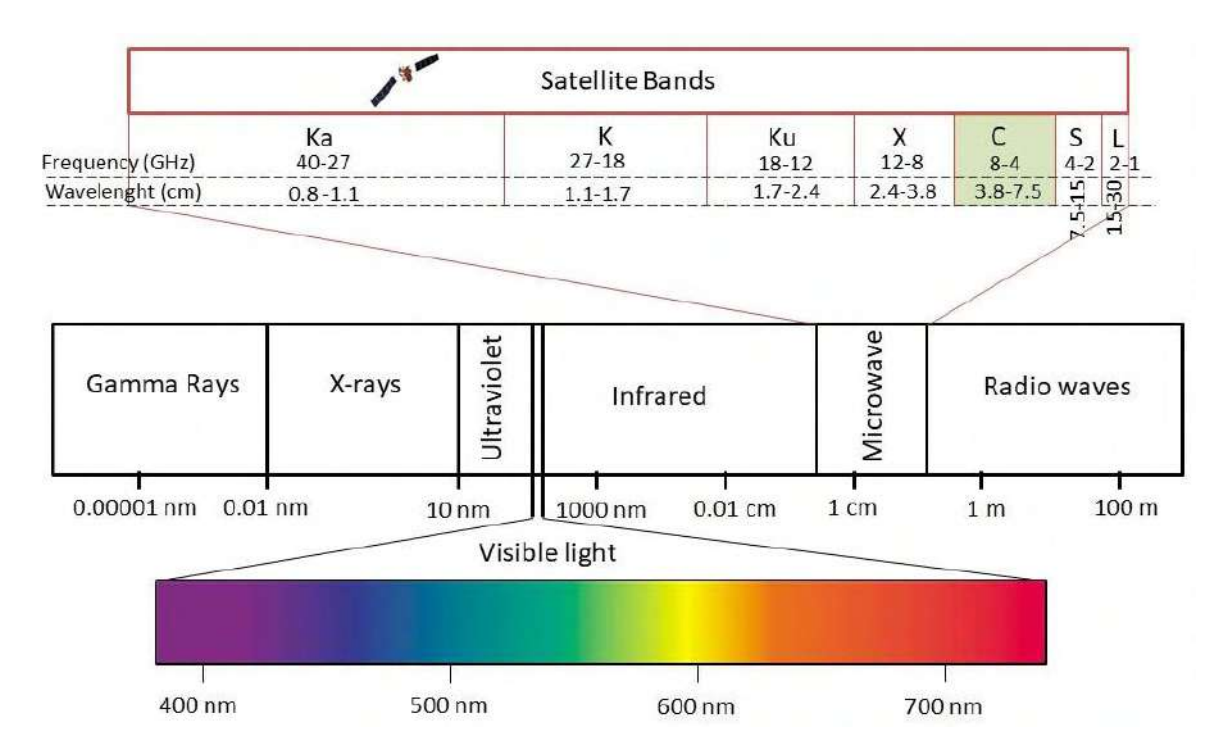


Figure 2.3 Electromagnetic spectrum.

direction from the sensor to the target. The range and azimuth directions of the satellite, as well as the processing methods of the raw data, condition the resolution of the SAR images [1]. The phase difference between two SAR images is used to create an interferogram.

This technique is a valuable tool in the scientific field, especially in volcano geodesy. The precision of the obtained displacement images depends on the wavelength used by the satellite. However, as the wavelength decreases, the precision with which details of the deformation can be obtained increases. Since electromagnetic waves bounce back and change direction when impacting a rough surface and are vulnerable to ionospheric and atmospheric conditions, it is necessary to strike a balance between the desired image precision and the ability to avoid obstacles that prevent the wave from reaching the target.

The microwaves can be affected by objects such as vegetation cover, particles in the ionosphere, and atmospheric effects in the troposphere, among others; it is essential to use different satellites for different purposes. The band selection and, consequently, the satellite providing these data are crucial for analysing deformations in volcanoes. Sensors working with the C-band wavelength range are often preferred to obtain optimal displacement data in volcanic environments. This spectrum range has wavelengths of approximately 5.6 cm, allowing it to overcome small obstacles and efficiently reach the surface. Moreover, this wavelength band is remarkably accurate, enabling the acquisition of millimetric precision images of ground displacements.

Regarding volcanic environments, the C-band offers extensive possibilities. The advantages of this type of wavelength are that the waves can penetrate the atmosphere (although subsequent pro-

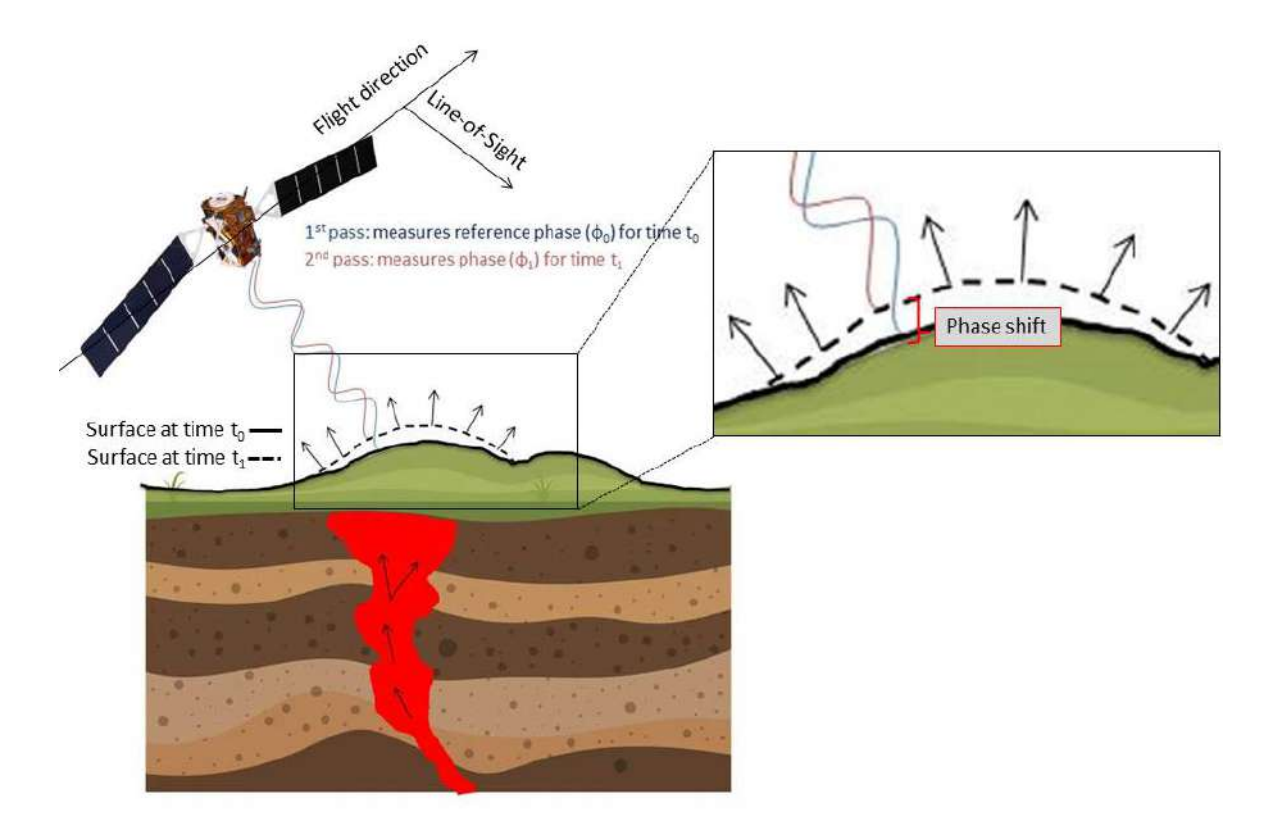


Figure 2.4 Schematic visualisation of satellite sending and receiving electromagnetic waves in reference time t_0 and the following pulse of the radar in time t_1 .

cessing is required to eliminate their effects). This allows the images of ground deformation to be obtained, providing good spatial resolution. Therefore, the Envisat and Sentinel-1 satellites have been selected to fulfil the objectives of this thesis. The Envisat data were available from 2002 until 2012, and the Sentinel-1 started to acquire the data in 2014 and is still active [1].

Satellite interferometry provides various products, among which interferograms, cumulative deformation maps, displacement maps, coherence maps, etc., stand out. The most essential product is the interferogram. These images depict the phase difference of electromagnetic waves between two SAR images. Interferograms can be wrapped or unwrapped depending on their processing and how they represent the wave phase difference. Wrapped interferograms show interference fringes, where each fringe in the interferogram represents the displacement of an area equivalent to half the wavelength. These fringes show changes in the phase of the electromagnetic waves backscattered on the Earth's surface.

Each fringe represents a phase change of 2π (in radians). Phase wrapping occurs when the limit of $\pm\pi$ radians is exceeded, which can introduce ambiguities in interpretation. However, this type of interferogram is highly optimal for visualising deformation patterns. Unwrapped interferograms are used to avoid ambiguities and errors in quantitative interpretation. Unwrapping the phases provides more precise displacement values.

Moving beyond interferogram complexities, the process of acquiring and overlaying multiple SAR images leads to a distinct product known as Differential Synthetic Aperture Radar Interferometry am(DInSAR). It involves a temporal series of SAR data that generates cumulative and displacement maps between the radar sensor and the Earth's surface. Analysing a large amount of SAR data is mostly archived by applying the Small BAseline Subset algorithm (SBAS), which allows the analysis of even small deformations over big areas with a large amount of data. This thesis offers a step-by-step explanation of the InSAR (Chapter 3) and the DInSAR SBAS (Chapter 4) processing.

Chapter 3

Interferogram phase processing

In this chapter, the complete processing of InSAR is detailed. Each subsection outlines an essential step in data processing to obtain the final product of the interferogram where the noise, orbital and topographic effects are removed, and the final product is georeferenced. To aid in comprehending each processing step, the chapter includes figures illustrating each stage.

The InSAR processing focused on La Palma island on two sampling days in ascending orbits. One was on the 02nd of September, nine days before the beginning of the seismic crisis in La Palma, and the other was six days before the eruption's onset, on the 14th of September 2021, when the magmatic intrusion had already begun.

The processing outlined herein can be easily achieved using platforms that facilitate InSAR generation, such as Earth Console by ESA (formerly G-POD [5]), which was utilised to archive Envisat satellite data (Chapter 8 and 10). This chapter discusses the processing of Sentinel-1 data using © sarmap SA 2022, SARscape 5.6.2.1 software. The help manual processes of SARscape were followed to comprehend each step of processing [6].

3.1 Interferogram generation

The first step of interferogram generation is described in the following. This step aims to obtain the distance between each point at the surface and the satellite.

Two radar images were acquired in the same area in two different sampling periods and located in slightly different sensor positions to obtain the interferogram. The radar image of the 02nd of September of 2021 is considered the master or primary file, while the 14th of September is the slave or secondary file (Fig. 3.1).

As the raw SAR data contain the information of the amplitude (A) and the phase (ϕ) of the backscattered microwave (echo), it is necessary to subtract the phase information of both radar images. Two radar images with the same acquisition geometry are superposed during this step, called co-registration [7, 6].

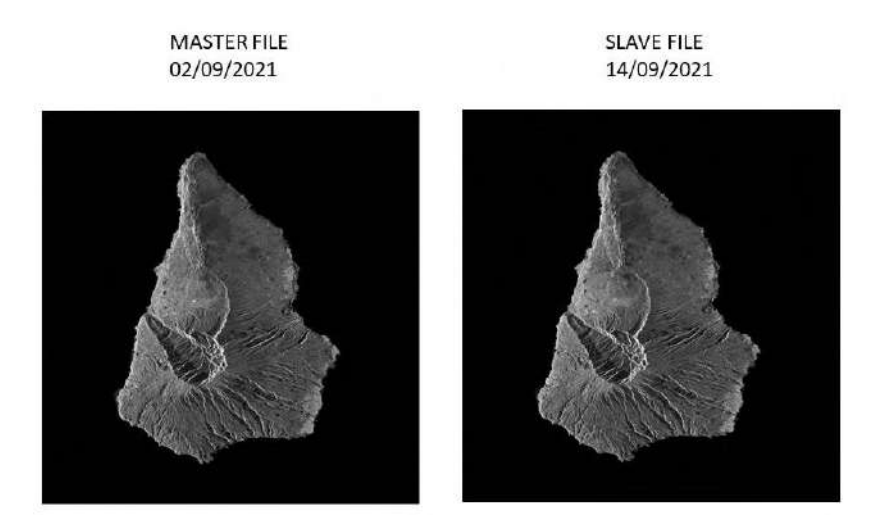


Figure 3.1 Two radar images of the study area. The left one is the master file acquired on the 02nd of September, while the image on the right is the slave radar image acquired on the 14th of September of 2021. Note that the radar images are represented in the geometry of the SAR data acquisition; the georeferentiation is done in the later step.

Once the co-registration is done, the next step is to create an initial interferogram by differentiating the phase values of each pixel of both radar images (ϕ_1 - ϕ_2) [6]. The phase difference between them is calculated (Fig. 3.2), resulting in an interferogram with a high contribution of noise that manifests as fringes in the interferogram. These fringes can be attributed to the ground deformation values and the different orbital geometries of both images, the topography influence, atmospheric conditions and the noise [1, 7]. The first interferogram with those ground deformation, geometrical and topographical fringes and the noise is represented by Figure 3.2.

After the initial interferogram generation, the effect of the orbit and topography is mitigated to create a flattened interferogram. To eliminate the orbital effects, the synthetic interferogram is created (Fig. 3.3) to reproduce the synthetic phase. This is subsequently reduced from the initial interferogram [6]. Also, the fringes associated with the altitude of ambiguity h_a are eliminated. Those represent the height difference required to produce a single topographic fringe. The altitude of ambiguity depends on the altitude of the antenna SAR, the wavelength, incidence angle θ , and the baseline [1, 6]. A good-resolution Digital Elevation Model (DEM) is applied to achieve this goal in the processing software. Once the topographical effect is removed, the interferogram contains the deformation fringes, path delays, phase ramps, noise, etc. [1].

$$h_a = \frac{H\lambda tan\theta}{2b} \tag{3.1}$$

The equation 3.1 refers to the altitude ambiguity h_a , where H is the SAR altitude (693 km for Sentinel-1), λ represents the wavelength (5.6 cm in the case of the Sentinel-1 data), θ is the incidence angle of the sampling dataset (between the range of 18.3° and 46.8°) and b represents the perpendicular component of the baseline (separation of image acquisition points, also known as a temporal

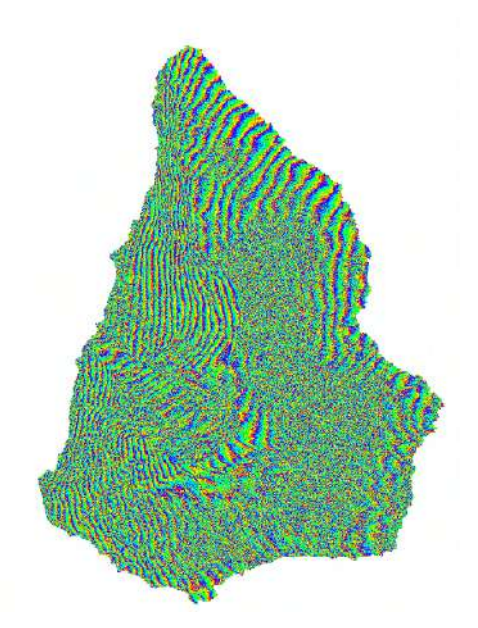


Figure 3.2 Initial interferogram ϕ_1 - ϕ_2 of two SAR images of the same area and similar acquisition geometries. The resulting interferogram contains the fringes created by the ground deformation previous to the eruption of Tajogaite, orbital differences, topography, atmospheric perturbances and noise. The interferogram is not georeferenced.

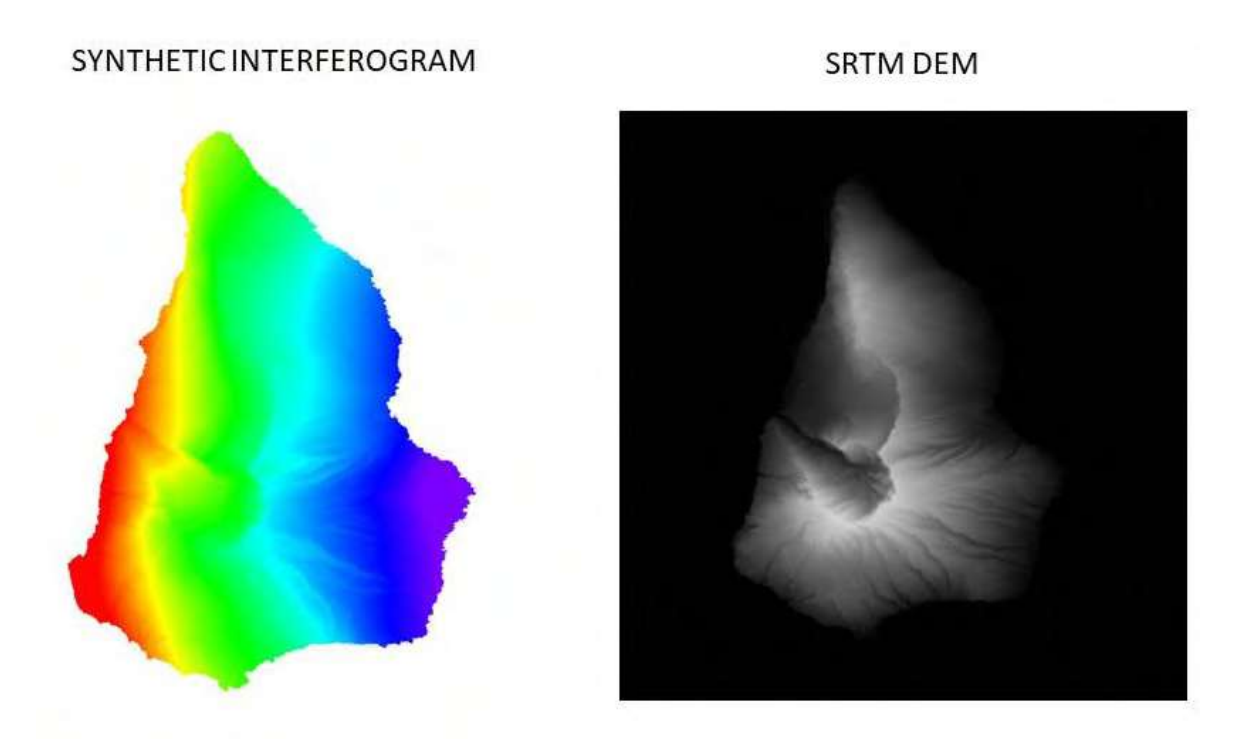


Figure 3.3 Synthetic interferogram (left) and Digital Elevation Model (DEM) (right) used to remove the topographic effects on the interferogram.

baseline or the time interval between SAR trajectories, refers to the distance between successive SAR acquisitions) with respect to the incidence angle [1, 6].

After eliminating topographic and orbital effects, the final product of this first step of phase processing is archived (Fig. 3.4) [6].

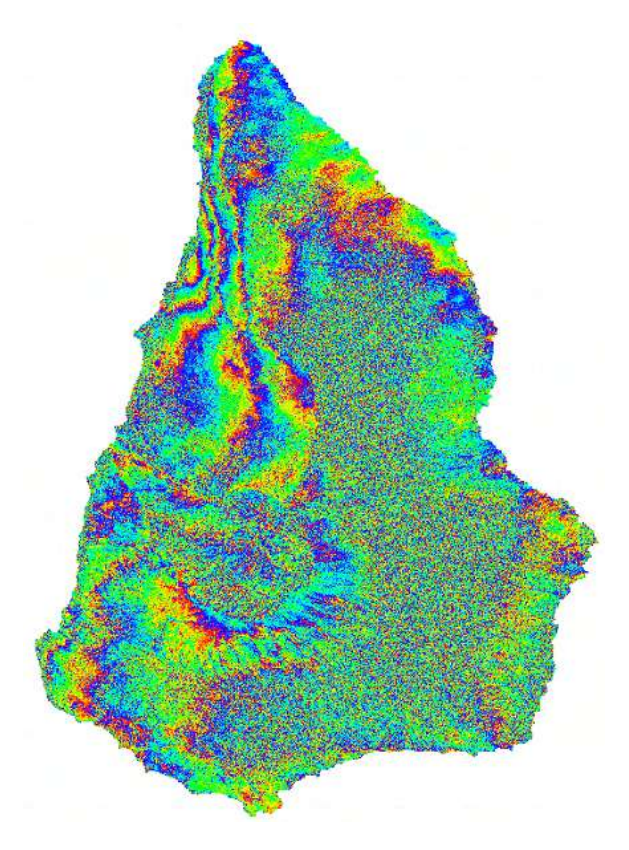


Figure 3.4 Differential interferogram as a product of topographic and orbital effects removed. The fringes are between $-\pi$ and π . The interferogram is not georeferenced.

3.2 Adaptive filter and coherence generation

Once the interferogram is done and the effects of the topography are removed, the phase noise elimination of the interferogram is the following step [7]. To obtain this goal, the generation of a coherence map is necessary. The coherence is an indicator of the quality of the phase of SAR data (the correlation between two images) [6].

Interferometric correlation is performed, where the coherent and incoherent summation ratios are calculated. The coherence values range between 0 and 1, where the values closer to 1 indicate that the pixels are very coherent and taken into account (the coherence between two scenes is very good). Values closer to 0 indicate that the images are not coherent between them and can be interspersed with high values of noise [6]. The coherence value allows us to know the quality of the processed

data. The higher the coherence of the measurement, the lower the acquisition time distance between the master and slave images.

With this parameter, the phase filtering is applied. To achieve our goal, the Goldstein filtering was selected [8, 9, 6].

ESTIMATED COHERENCE

FILTERED INTERFEROGRAM

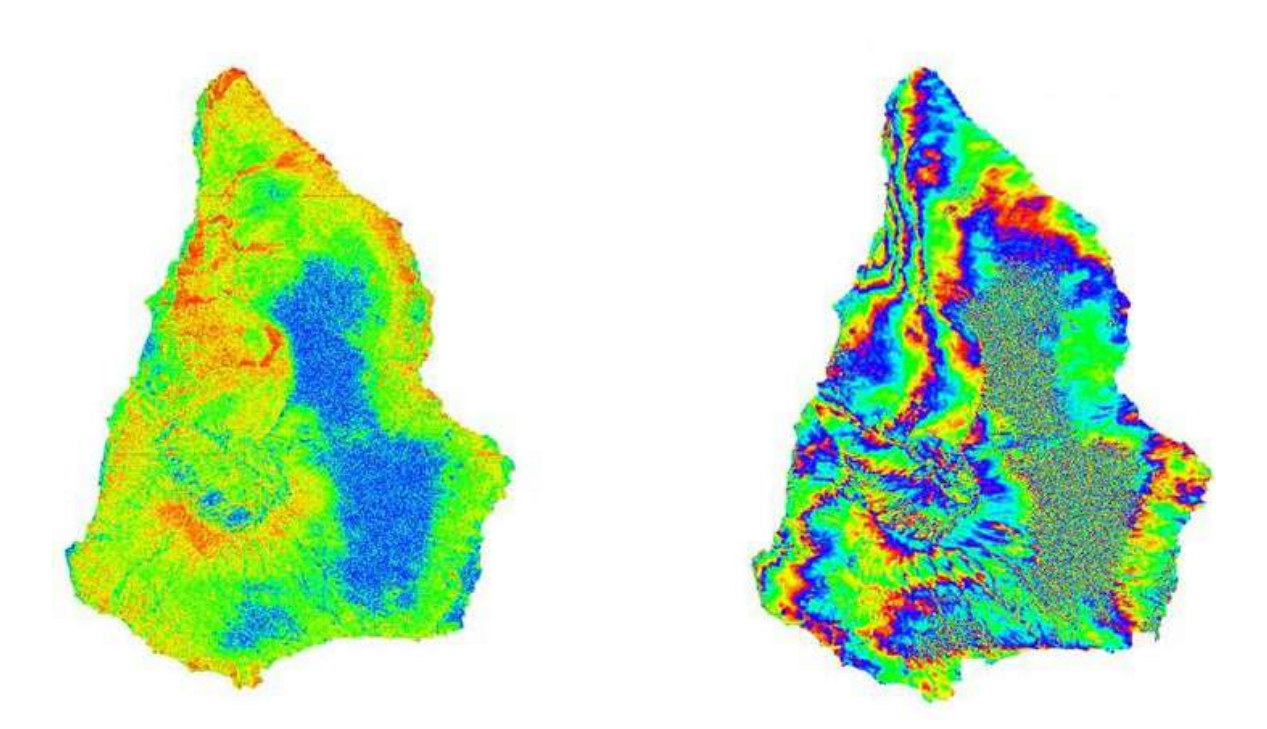


Figure 3.5 The estimated coherence (left) and the filtered interferogram (right). The images are not georeferenced.

Selecting the bandwidth parameter of the filter allows smoothing of the noise and signal frequencies in the image fringes. The α parameter is adjusted according to the needs. This parameter controls the intensity of the filter applied, depending on how coherent the image is. The more incoherent the image, the more intense the filter. This filter improves the fringes' visibility and reduces noise that may appear due to baseline changes. Adjusting the α parameter according to the image coherence produces a cleaner result with reduced noise components [7, 6].

3.3 Phase unwrapping

Wrapped interferograms, observed in previous steps, have a limited phase representation range of 2π . If the observed deformation exceeds this range, the wrapped interferogram does not fully represent the deformation. Therefore, phase unwrapping is necessary. Phase unwrapping resolves the ambiguity of phase change, preventing jumps in the phase observed in the wrapped interferogram. This step

overcomes limitations in phase representation that cannot be addressed by keeping the phase wrapped [6].

The preceding interferogram flattening and coherence file generation step is crucial, as those files are indispensable for phase unwrapping. To achieve the objective of creating the unwrapped interferogram, the Delaunay Minimum Cost Flow (MCF) method was employed [10, 11, 6].

This method is based on the MCF approach, which applies a square grid to the image. Within the entire image, pixels with coherence values lower than the unwrapping threshold are masked. However, the processing example presented here adopted a slight deviation from the standard MCF method. Only pixels with low coherence were considered, rather than the entire image. Subsequently, a grid was created based on these low-coherence pixels, represented by a Delaunay triangular grid. This approach facilitates unwrapping only those pixels with high coherence values [10, 11, 6]. The final product is the unwrapped interferogram showing the ground deformation in radians [rad] (see Fig. 3.6)[6].

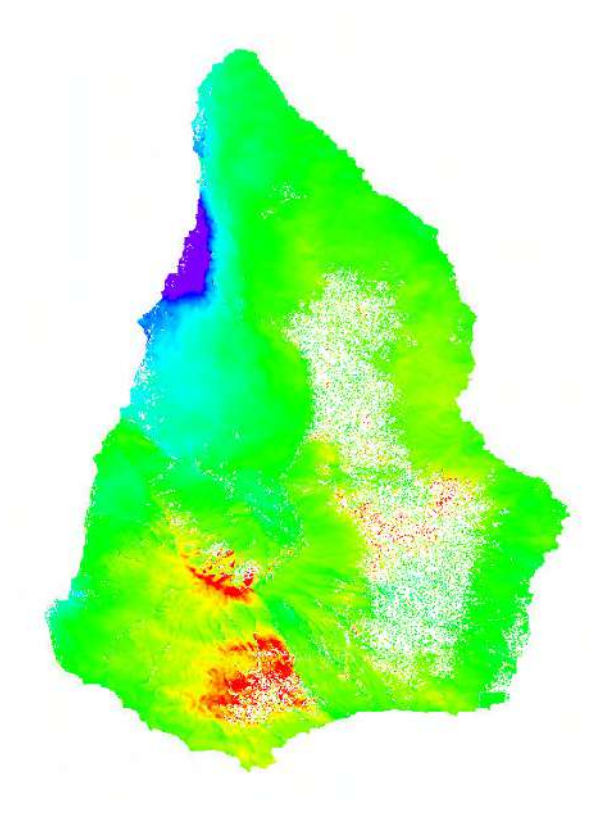


Figure 3.6 Unwrapped phase. The image is not georeferenced.

3.4 Refinement and re-flattening

This next processing step aims to obtain the height (chapter 3.5) and displacement (chapter 3.6) values from the unwrapped phase information. During this stage, refining the data to the orbital

information is possible. Due to the consideration of the orbital information, it is possible to clear the interferograms from the noise affected by the orbital residuals and remove phase error, orbital shift, etc. [6].

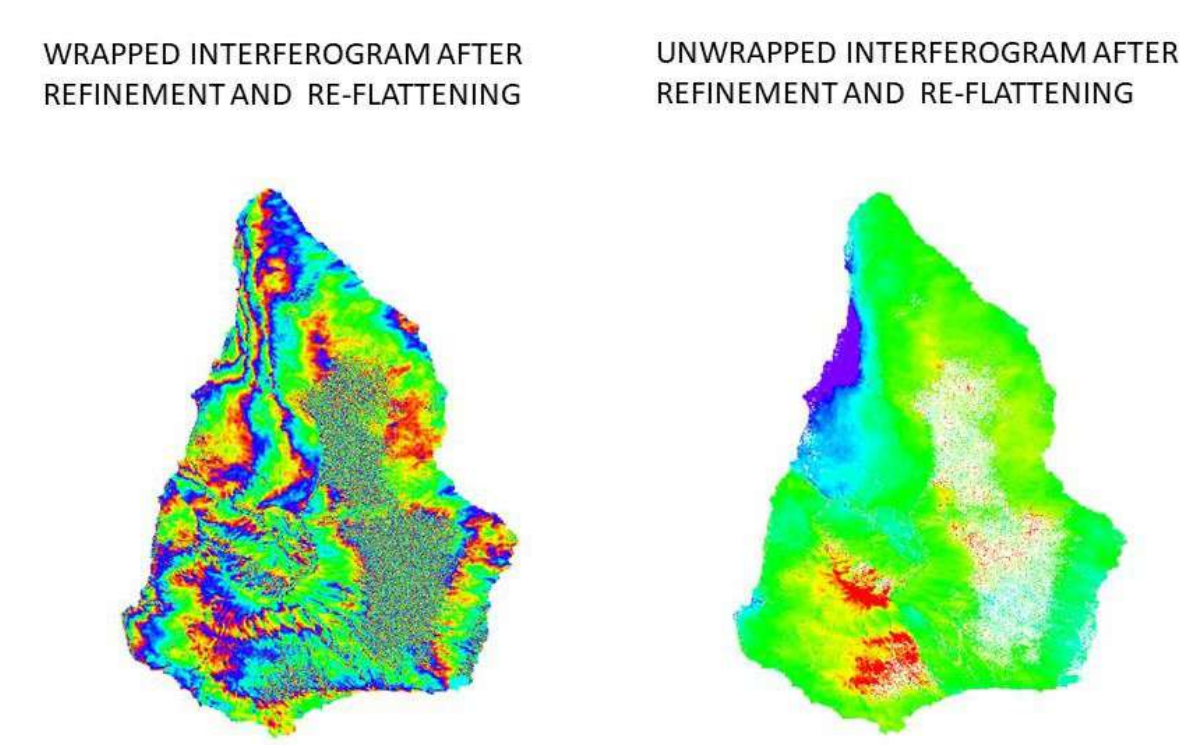


Figure 3.7 Wrapped (left) and unwrapped (right) interferograms after refinement and re-flattening.

The creation of Ground Control Points (GCP) is executed during this stage. The GCP are the points selected manually or automatically (Chapter 4) used to georeference the images and apply the orbital corrections to the SAR dataset. To use the GCP correctly, the DEM file is mandatory, as the GCP points are strictly linked to the correctly georeferenced DEM. Those GCPs help to correct the orbital residuals [6].

The wrapped and unwrapped interferograms after refinement and re-flattening steps are represented in the figure (Fig. 3.7)

3.5 Phase to height conversion and geocoding

Once the unwrapped interferogram is fully calibrated (right panel in Fig. 3.7), we combine it with the synthetic interferogram phases with an aim to convert the input data into height maps and, consequently, convert it into the georeferenced maps. The DEM file is mandatory for geocoding to obtain the X, Y and Z coordinates. To obtain the map with the Cartesian coordinates, the Nearest Neighbour approach is used [12, 13, 6].

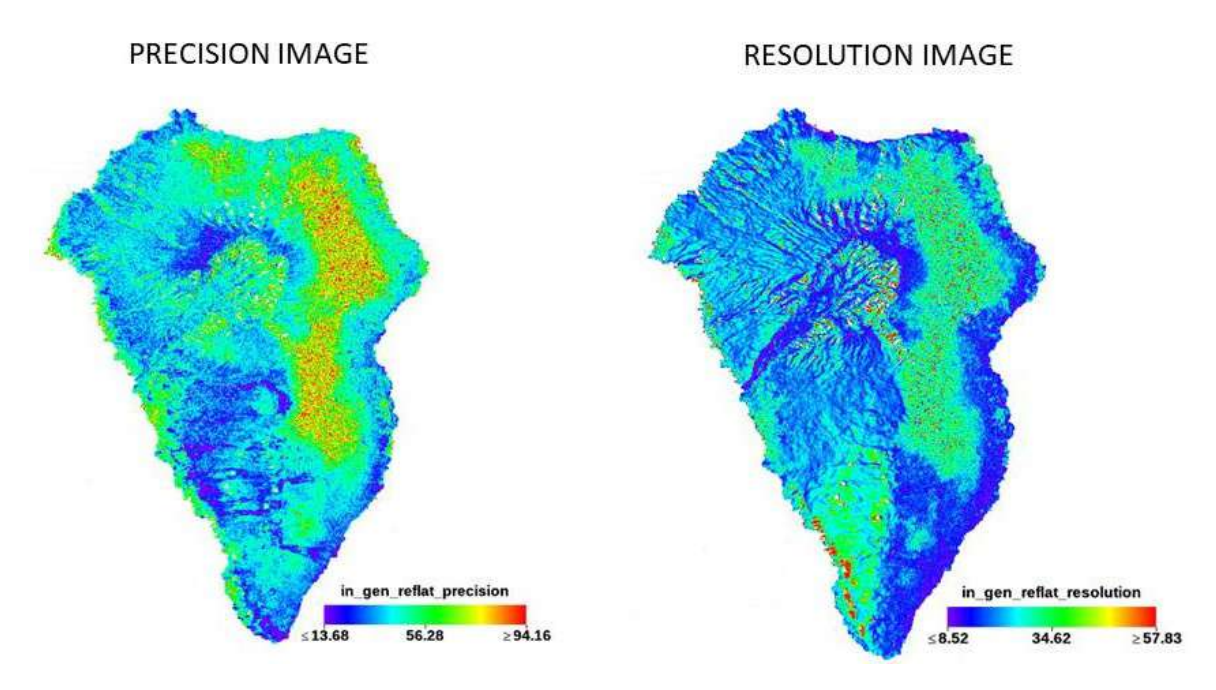


Figure 3.8 Precision (left) and resolution (right) images. The images are georeferenced. Units of measurements are expressed in meters [m].

As a result of this processing stage, we obtain the geocoded files of coherence, DEM, precision and resolution. The precision file is a result of applying the coherence, baseline and wavelength information to obtain the precision of the measurements (see left panel in Fig. 3.8). The higher the precision values, the lower the precision of the measured pixel [12, 13, 6]. On the other hand, the resolution files allow us to obtain information about the pixel resolution in the ground range (distance between the nadir and the object) [12, 13, 6] (see right panel in Fig. 3.8).

3.6 Phase to displacement conversion and geocoding

The unwrapped interferogram is used to create this final step to obtain the geocoded displacement maps [6]. The final products are the displacement maps with the location of each pixel (Northing and Easting) in the cartographic reference system. This step allows the calculation of any vector in Slant Range (SR) displacement (distance between the satellite and the object on the surface). The SR displacements in meters are shown in the Fig. 3.9. The positive values represent the movement of the target on the ground towards the sensor (in the La Palma case study, it reflects the magmatic input in the crust, producing the positive deformation of the flank).

The re-projection of the Slant Range look direction is possible by selecting the direction in the ground and the inclination values by selecting the Displacement Custom Direction values. It is possible to customise the maps depending on the direction of the target's movement [6].

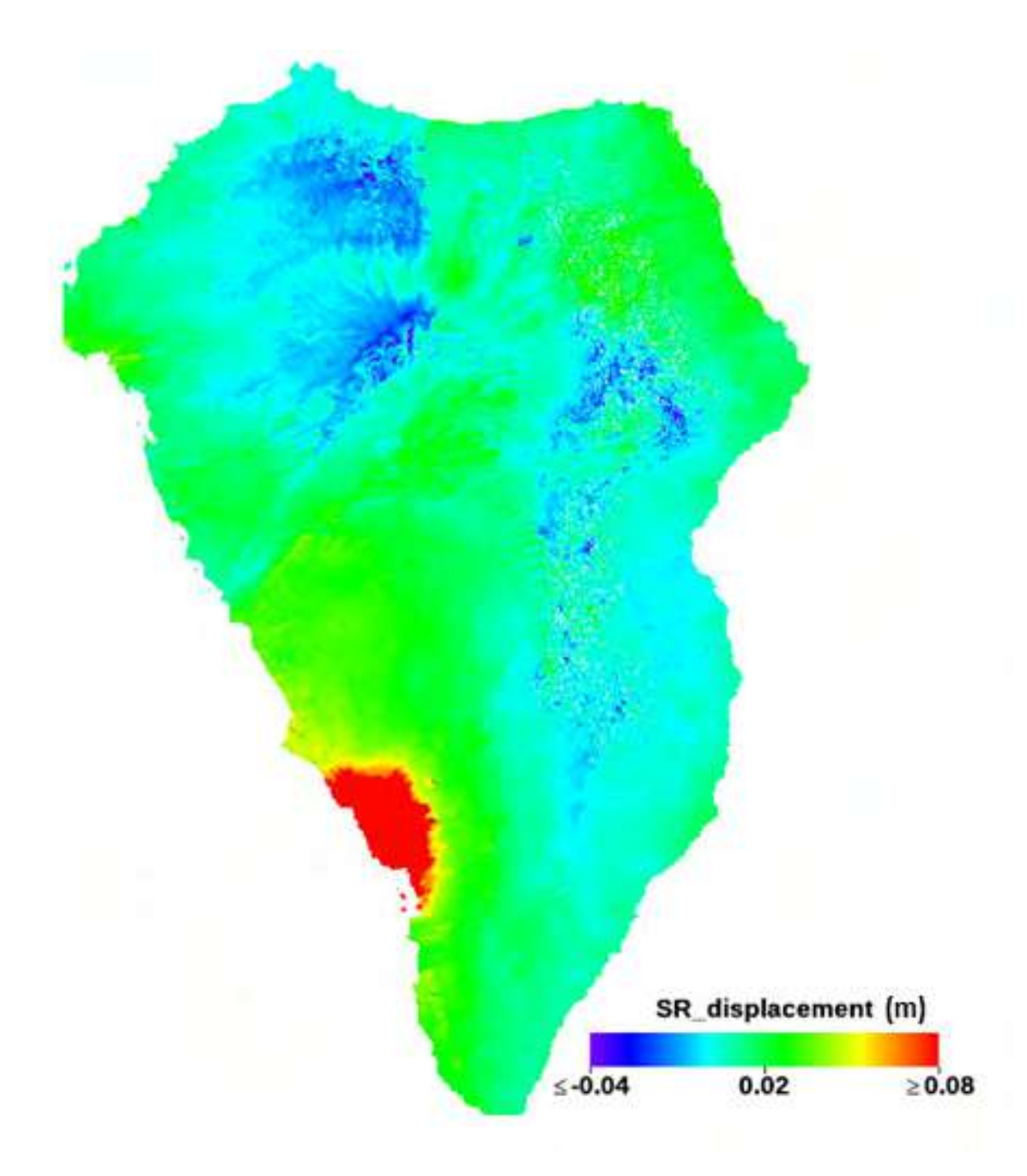


Figure 3.9 Georeferenced Slant range displacement in [m].

Chapter 4

Interferometric Stacking SBAS

In this chapter, the processing of multiple radar images is discussed. Interferogram stacking aims to obtain cumulative and displacement maps of the area over time (spanning months or years). Differential Interferometry (DInSAR) involves similar processing of interferograms with several radar images overlaid (2-4 radar acquisitions). However, the most commonly used interferometric stacking technique with the biggest advantages for large datasets is the Small Baseline Subset (SBAS), explained in the following sections [14]. SBAS processing allows detection of movement in the ground that occurs over a long period and in extensive areas. It also allows the reduction of the images' atmospherical and topographical phase components. The SBAS processing procedure allows obtaining a product of good quality data over a large amount of SAR data within years or months of data acquisition [14, 6]. There exist many products of this processing. However, in this thesis, the main objective is to obtain the cumulative displacement map in Line-Of-Sight (LOS) [14].

As the input of the SBAS processing must be the radar images acquired by the same satellite sensor, the same polarisation and viewing geometry, the Sentinel-1 (S1) dataset was selected. The processing englobes the ascending images between the 16th of July and the 26th of September of 2021 in La Palma island. In total, the seven radar images are taken into account. In order to remove atmospheric phase components, the GACOS atmospheric models of each day of radar acquisition were also taken into account [15, 16, 17, 6].

4.1 Connection graphs

The first step of SBAS data processing is creating connections between the selected radar images that allow generating multiple differential interferograms. These connections are based on the thresholds of temporal and spatial baselines, establishing their maximum and minimum values. This net of interconnected images with small temporal and spatial baselines creates a net of multiple connections of master and slave images [6]. The result of the connection graph step in the La Palma case study resulted in the creation of 20 pairs of master-slave images.

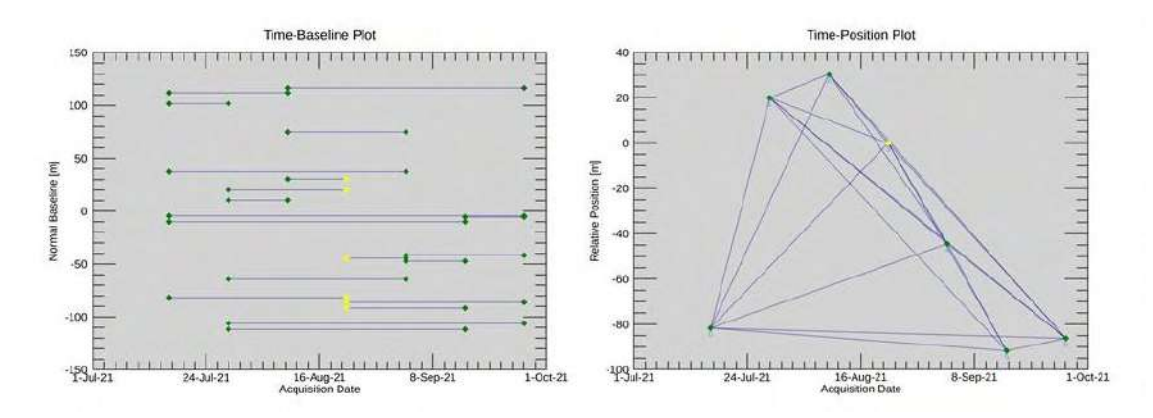


Figure 4.1 Spatial (left) and temporal (right) connection graphs.

In this step, the super master file is also selected and can be chosen automatically or manually. Within this super master image, all the other images are coregistered [6]. In the case of La Palma, the super master file was selected for the 21st of August 2021.

The temporal baseline plot (see the left panel in Fig. 4.1) provides the connections of the files in the temporal baseline between the master and super master file (yellow points) to the input acquisition dates (green points). The spatiotemporal baseline (see the right panel in Fig 4.1) represents the distance (y-axis) from the super master file (yellow point) to the input acquisition dates (green points) and the other spatial connections between the master-slave pairs. Both figures represent 20 pairs of master-slave image connections.

4.2 Interferometric Process

In this second step of SBAS processing, the complete Interferogram Generation and Flattening (Chapter 3.1), Adaptive Filter and Coherence Generation (Chapter 3.2) and Phase Unwrapping (Chapter 3.3) steps are executed automatically. The procedure is similar to the one described in Chapter 3, where the processing parameters remain unchanged. However, this step involves incorporating the full set of seven radar images to generate twenty interferograms, as specified previously (Chapter 4.1).

During the interferogram flattening, it is possible to manually create GCP points to correct the master files. However, the manual selection of GCP points is optional, and the software itself can create those points [6].

Other optional steps in this stage include establishing the area excluded from processing *Avoid Moving Area* or generating a mask zone using *Classification Mask* tool. These and other optional parameters can be incorporated at this stage of processing.

To remove the atmospheric fringes, adding the raster files of the atmospheric models in each sampling date and time is necessary. To do this, the GACOS platform provides those raster files that are selected in the present step [15, 16, 17, 6].

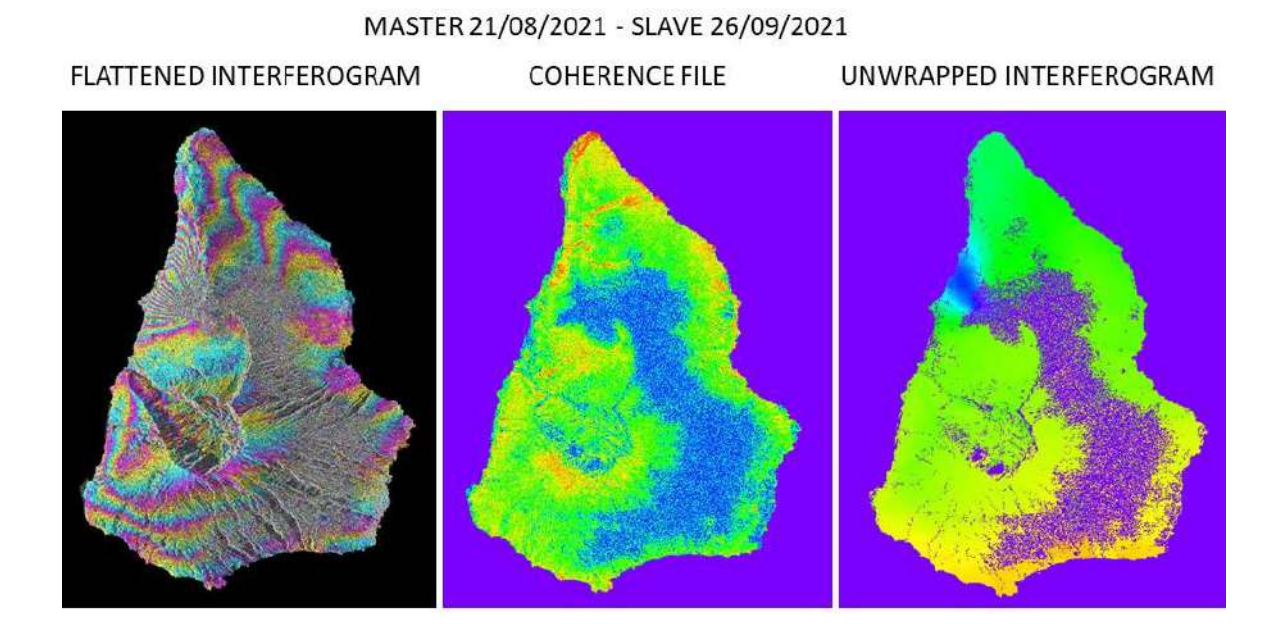


Figure 4.2 Flattened interferogram (left), coherence file (middle) and unwrapped interferogram (right) from the pairs of radar images between 21st of August and 26th of September of 2021. The images are not georeferenced.

Since the output files of this processing step are extensive, including coherence files, flattened interferograms, unwrapped interferograms, among others, for each master-slave pair, Figure 4.2 displays the flattened interferogram, coherence file, and unwrapped interferogram corresponding to the pair of radar images of super master file on 21st of August of 2021 and the slave file on the 26th of September of 2021.

4.3 Inversion: First Step

The First Step of Inversion of the SBAS processing is based on using the unwrapped interferogram (Fig. 4.2) to calculate each pixel's displacement rate and residual height [6]. The selection of the outputs of displacement rates is needed, depending on the processing aims. It is possible to select models that are based on linear, quadratic and cubic models, among others. In the linear model, the outputs are the displacement velocity expressed in [mm/yr]. The quadratic model allows obtaining the displacement acceleration $[mm/yr^2]$ and the displacement acceleration variation $[mm/yr^3]$, the displacement acceleration $[mm/yr^2]$ and the displacement velocity [mm/yr] [6]. In the case of La Palma, the displacement velocity is represented in Fig. 4.3. The positive values represent the SR distance in the ground movement towards the sensor. The negative values indicate the increased distance between the sensor and the target in SR distance [6].

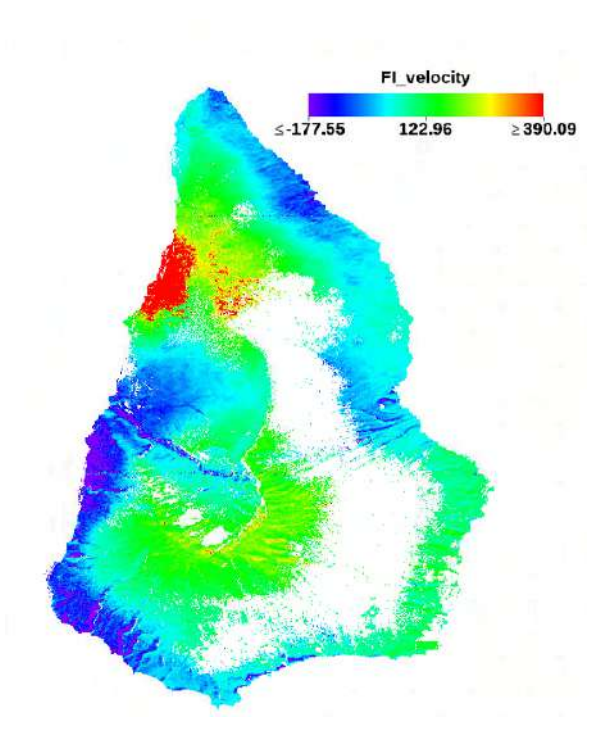


Figure 4.3 Displacement velocity [mm/yr] resulted of the First Inversion of SBAS processing.

This displacement rate is secondly used to redo the flattening of each interferogram in all the interferogram stacks. The flattening of each interferogram allows redoing the unwrapping with better data quality. In this step, the GCP is also selected with an aim to eliminate the orbital fringes. The GCP can be selected manually or automatically using the Super Master flattened or unwrapped interferogram [6]. The results are the re-flattened unwrapped phases and re-flattened filtered interferograms (see Fig. 4.4) [6].

4.4 Inversion: Second Step

In this final inversion step, the re-flattened interferograms, as the results from the previous step on the inversion (Chapter 4.3), are considered with the aim of calculating the displacement rates (the height and displacement velocity) [6]. After estimating the displacements date by date, the atmospheric phase components are estimated to eliminate the atmospheric phases from the interferograms. The atmospheric corrections are performed by two filters. The atmospheric low pass and high pass depend on the spatial or temporal atmospheric distribution, respectively [14].

After the atmospheric corrections, the final output displacement file is represented in the following Fig. 4.5. The units of measurement are in [mm/yr] [6].

MASTER 21/08/2021 - SLAVE 26/09/2021

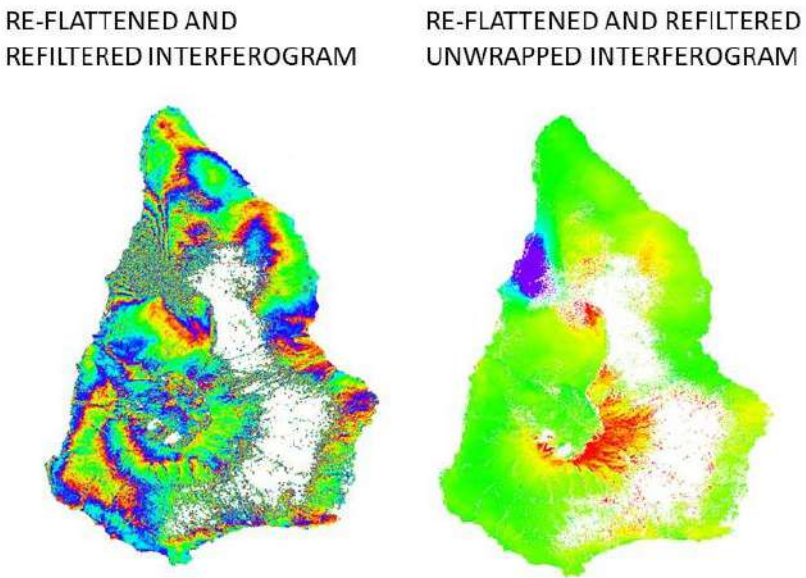


Figure 4.4 Re-flattened and re-filtered wrapped interferogram (left) and unwrapped (right).

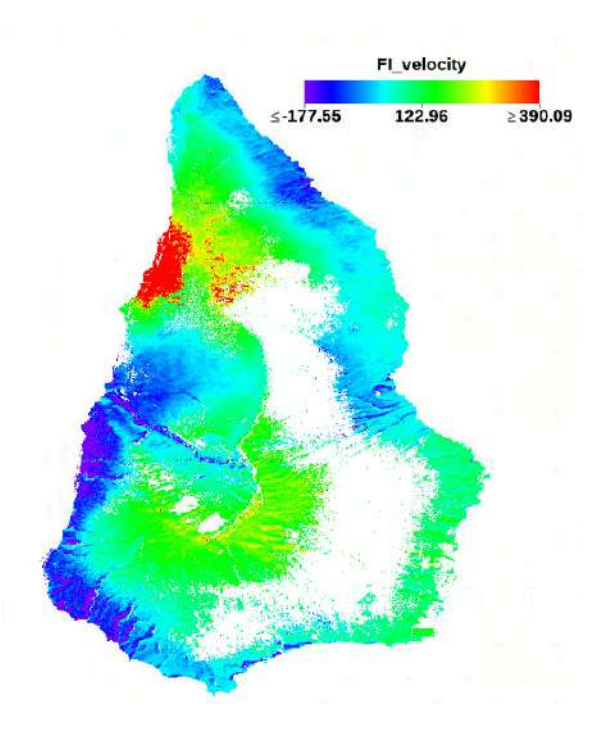


Figure 4.5 Mean displacement velocity in [mm/yr] after atmospheric corrections. The image is not georeferenced.

4.5 Geocoding

Finally, the last step of the processing is to georeference the image in the Cartographic Projection. The first (Chapter 4.3) and second inversion (Chapter 4.4) products are subjected to the geocoding step. During this step, the pixels selected with the high height precision values (resulting from the first inversion step) and the high values of high-velocity precision (from the second inversion) are masked out [14, 6].

In this processing stage, the imperial step is to apply the DEM file to obtain the proper geocoding of all the files. Also, the Height and Velocity Precision Thresholds are important for obtaining good-quality data with low-noise pixels.

The final result is geocoded maps of cumulative deformation for each acquisition date concerning the first acquisition date to which zero values were assigned. These cumulative maps of deformation are expressed in [mm] in the LOS direction. The geocoded process of La Palma is shown in the Fig. 4.6.

4.5 Geocoding

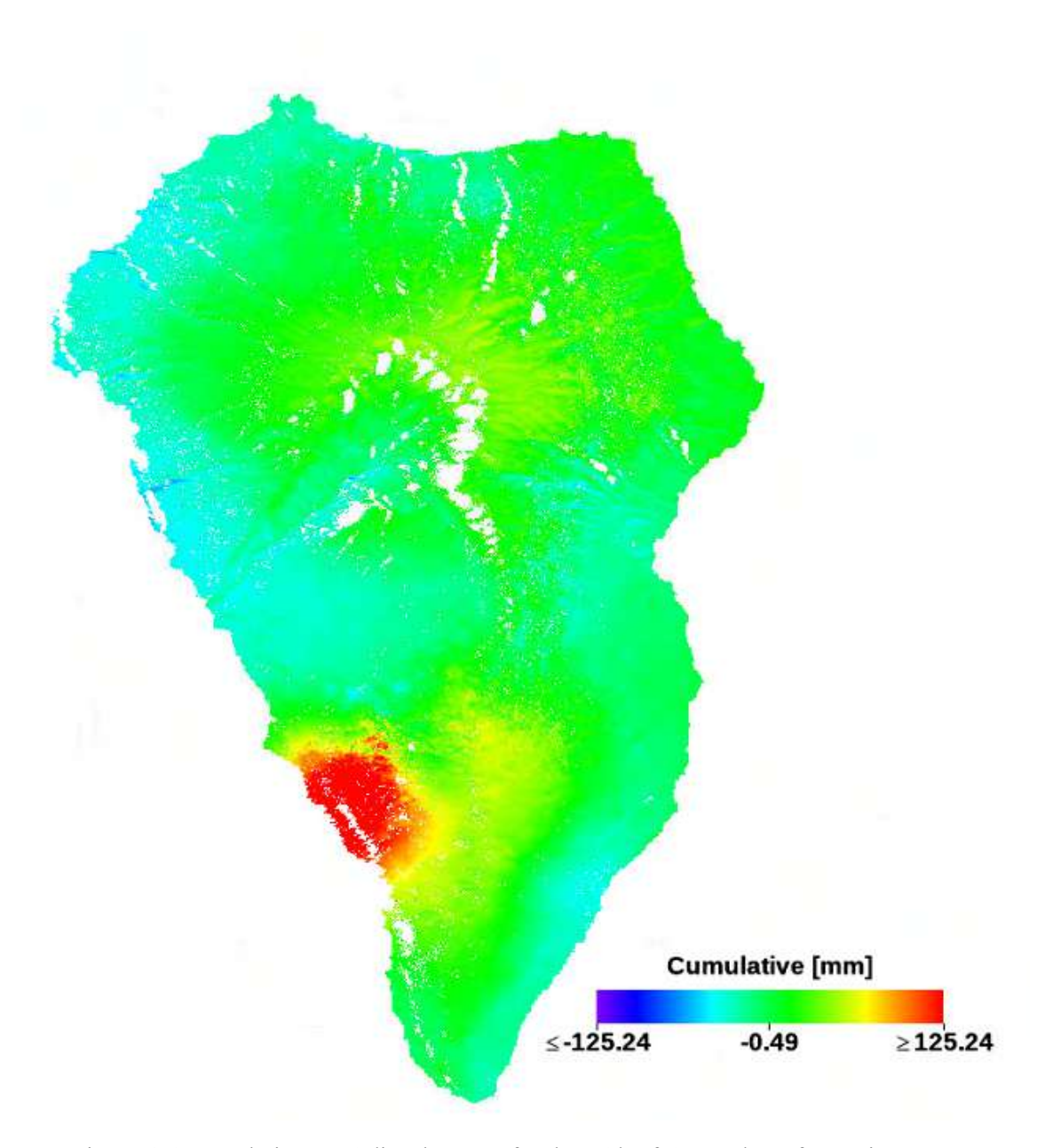


Figure 4.6 Cumulative LOS dispalcement for the 26th of September of 2021 in [mm].

Chapter 5

Independent Component Analysis (ICA)

5.1 Independent Component Analysis

Independent Component Analysis (ICA) is a statistical tool for computational signal processing. It allows separating a mixed signal into a set of independent components, where each constituent signal represents a non-gaussian probability distribution [18]. The main objective of the ICA application is to find random variables that are a linear combination of statistically independent components [19, 18, 20]. The ICA is based on the Principal Component Analysis (PCA) assumption, where the sources constituting the mixed signals are uncorrelated. Still, the product of the PCA application is the signal variance [20]. In the ICA, obtaining the sources is possible by maximising their statistical independence. In other words, the objective of PCA is to maximise the data variance (a measure of data dispersion) along each component. The principal components are linear combinations of the original variables and are orthogonal to each other (Fig. 5.1). In contrast, the principal assumption of ICA is that it focuses on maximising the negentropy (a measure of statistical independence). This means that ICA searches for statistically independent components that are as less correlated as possible and whose distributions can be non-Gaussian. Independent Components are not bound to be orthogonal (Fig. 5.1).

ICA has been applied to various mathematical, physical, and medicinal studies, aiming to separate mixed signals into independent components and uncover the hidden patterns of mixed signals. It has been successfully applied in Geodesy [22, 20, 23]. Ebmeier [20] used the ICA signal decomposition to the two different geographical volcanic areas and different sets of the InSAR data. The author applied the ICA to the Sentinel-1 dataset in the Calbuco (Chile) and Parícutin (México) volcanic areas, retrieving the subsidence behaviour in the middle of the complex signal. With this method, the author [20] described the effectiveness of the ICA in separating the signals where the multiple deformation patterns are active. In this work, the author [20] showed the effectiveness of the signal separation from the atmospheric noise in the data. Assuming the atmosphere is stratified, changes in water vapour are correlated to the topography and deformation patterns can be hidden in the signal [20]. However, if the atmosphere is turbulent, the atmospheric signals can be spatially correlated [20].

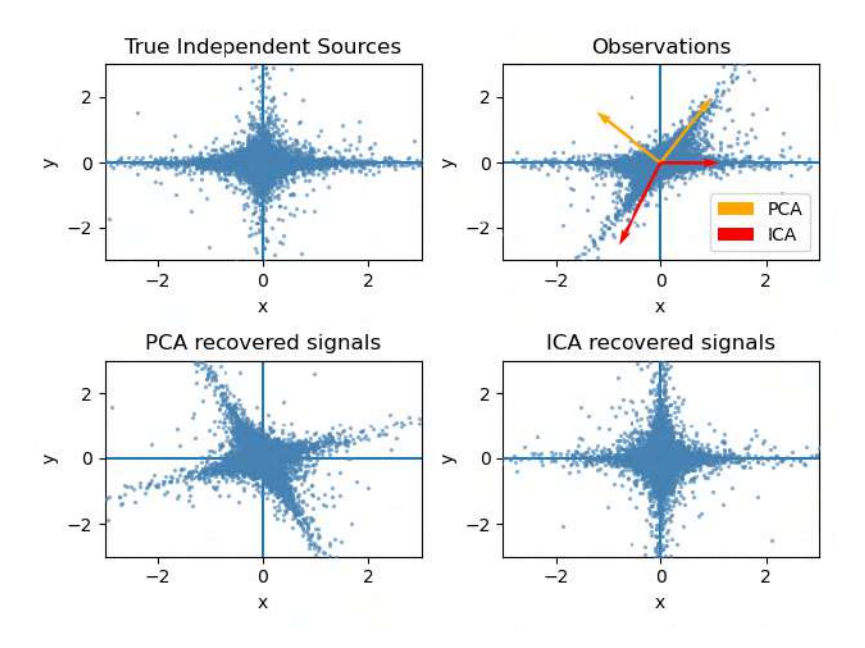


Figure 5.1 Comparison between the PCA and ICA distribution of the features after [21].

In the case of turbulent atmospheric signals, the stacking InSAR tools (Chapter 4) can help reduce the atmospheric noise signals. However, the stacking tools can be less effective if the atmospheric noise has a stratified water vapour signal [20]. The application of the ICA allows this atmospheric signal reduction to be separated from a set of InSAR data. For this reason, the ICA can mitigate the atmospheric signals from the InSAR datasets and uncover the hidden ground deformation patterns.

Figure 5.2 represents the ICA and PCA signal decomposition. The input signals (a) are random one-dimensional functions y_1 , y_2 and y_3 . Those three independent input signals are combined (b) to produce mixed signals [20]. The mixed signals are decomposed into three components by the ICA (c) and PCA (d) statistical algorithms. The ICA algorithm perfectly decomposes the combined signals into three components that maximise the statistically independent components [20]. The ICA successfully recreated the structure of the input signal. On the other hand, the PCA cannot fully separate the signals from the combined one. However, it contains the characteristics of each of the input signals.

5.2 ICA for SBAS DInSAR dataset

In the context of an SBAS DInSAR dataset, the time series is represented as $L(x_i, t_j)$, where L denotes the Line-Of-Sight (LOS) displacement, x_i corresponds to the position of the i-th DInSAR pixel, and t_j represents the time of the j-th DInSAR image. The DInSAR dataset can be decomposed into a finite sum of N components characterised by fixed spatial patterns. If we denote B_k the spatial pattern of the k-th and with A_{jk} the time-varying amplitudes of the k-th component in time t_j , we can write the ICA decomposition result as:

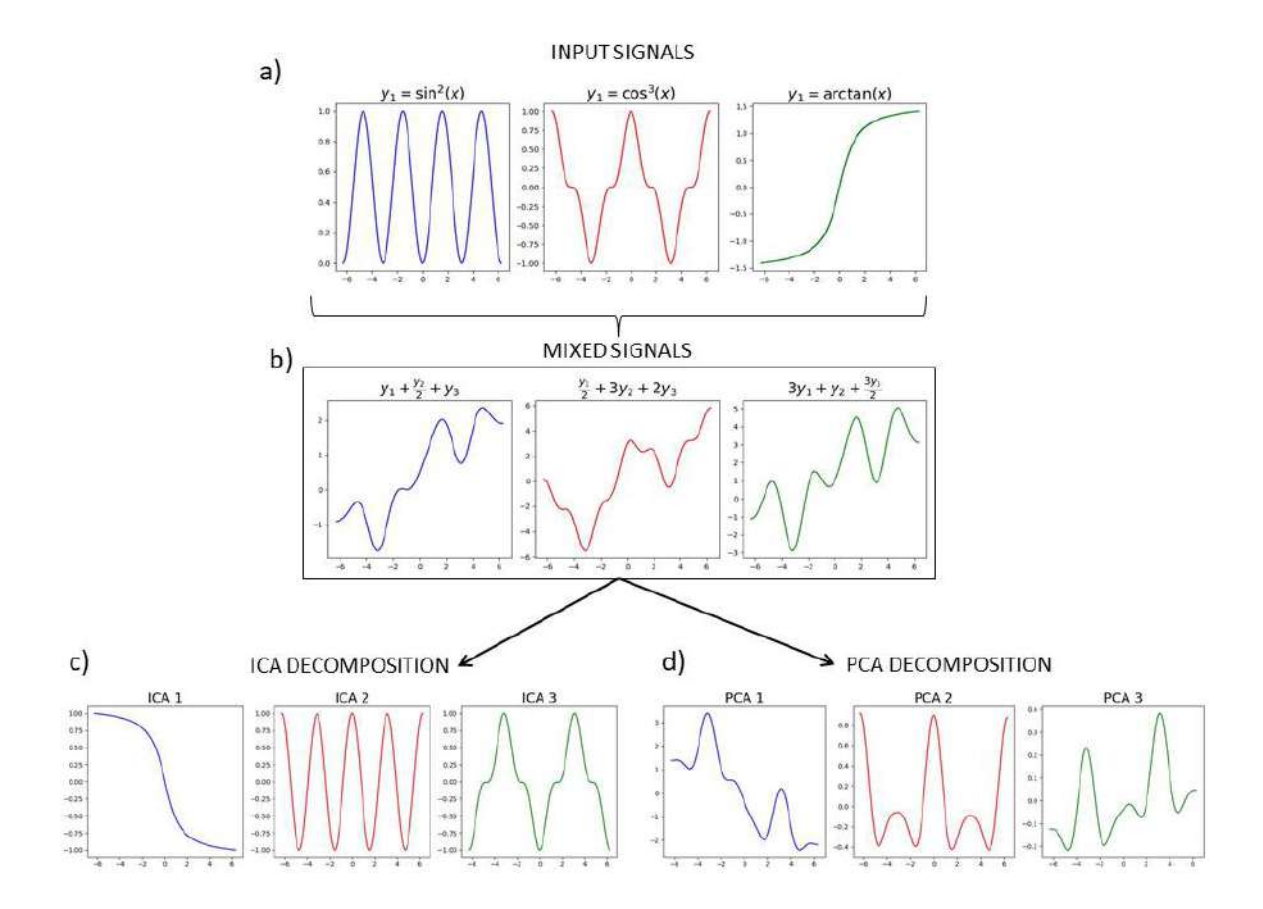


Figure 5.2 Application of ICA and PCA to the mixed signal. The a) represents three independent functions combined into a mixed signals b). The c) represents the decomposed signal into three independent components, and the d) represents the decomposition into three principal components.

$$L(x_i, t_j) = \sum_{k=1}^{N} A_{jk} B_k(x_i)$$
 (5.1)

Once the spatial patterns have been normalised, the sum of squared amplitudes A_{jk} for each independent component k could be used to define its energy. This enables us to sort the components based on their energy and determine the optimal number of components representing the whole signal. This can be realised by setting a threshold below which the contribution to the total energy is negligible. In the studies presented in this thesis, we opted to retain one more component, even if characterised by negligible amplitude values, given that it would host the noise inherent in each DInSAR dataset.

Chapter 6

Volcano Deformation Source Models

6.1 Analytical volcano deformation source models

The term Analytical Volcano Deformation Source Models refers to analytical models used to describe in a simplified manner the sources that generate ground deformations in volcanic environments. These models are mathematical and theoretical simplifications that allow studying the geometry of the deformation source observed on the surface.

A first approximation of the Earth's subsurface is made by studying analytical models of deformation sources, assuming that the space being studied is an elastic half-space. Within this space, forces (stress) act, causing deformation (strain) in the observable environment on the surface. An example of such forces is a magmatic intrusion that creates stress forces in the crust and, consequently, induces ground deformation. The elastic half-space means that the crust is assumed to have an infinitely extending flat surface in all directions. It is a materially homogeneous space and mechanically isotropic (its mechanical properties do not vary according to direction). The elastic half-space is also a good approximation for the forces that act in the short term and are located in the shallow crust [1].

In the elastic half-space, Hooke's law holds true [1]. Hooke's Law describes the elastic behaviour of an isotropic solid material when subjected to deformation forces that do not exceed its elastic limit. This law states that the force required to stretch or compress the solid material is directly proportional to the distance by which the material is deformed [24].

Two elastic constants are considered to describe the relationship between stress and strain in an isotropic and linearly elastic solid. Poisson's ratio (v) describes the proportion of lateral strain in the body with respect to longitudinally applied stress within the material's elastic limit. In other words, it represents the lateral expansion with respect to the longitudinal contraction of the material in the case of uniaxial stress. The other elastic constant is the Rigidity Modulus (μ) expressed in [Pa]. It defines the linear relationship between shear stress and shear strain, describing the stiffness of a material under shear conditions. Both elastic constants can be obtained using seismic wave velocities and other alternative elastic constants [1].

There are four types of point displacement in a half-space. These correspond to tension, dilation, strike-slip, and dip-slip movements. To model the mechanisms that correspond to those types of displacements, we use some of the most important analytical models commonly used in geodetic studies. Those are described in the following.

6.1.1 Mogi point pressure source

The simplest model, representing a point generating pressure in the crust, is known as the Mogi Model [3]. The primary assumption in the mentioned source model revolves around a variation in pressure denoted as ΔP . The author described the relationship of a point pressure source in an elastic half-space, and its surface response manifested as ground deformation at two volcanoes: Sakurajima in Japan and Kilauea in the USA.

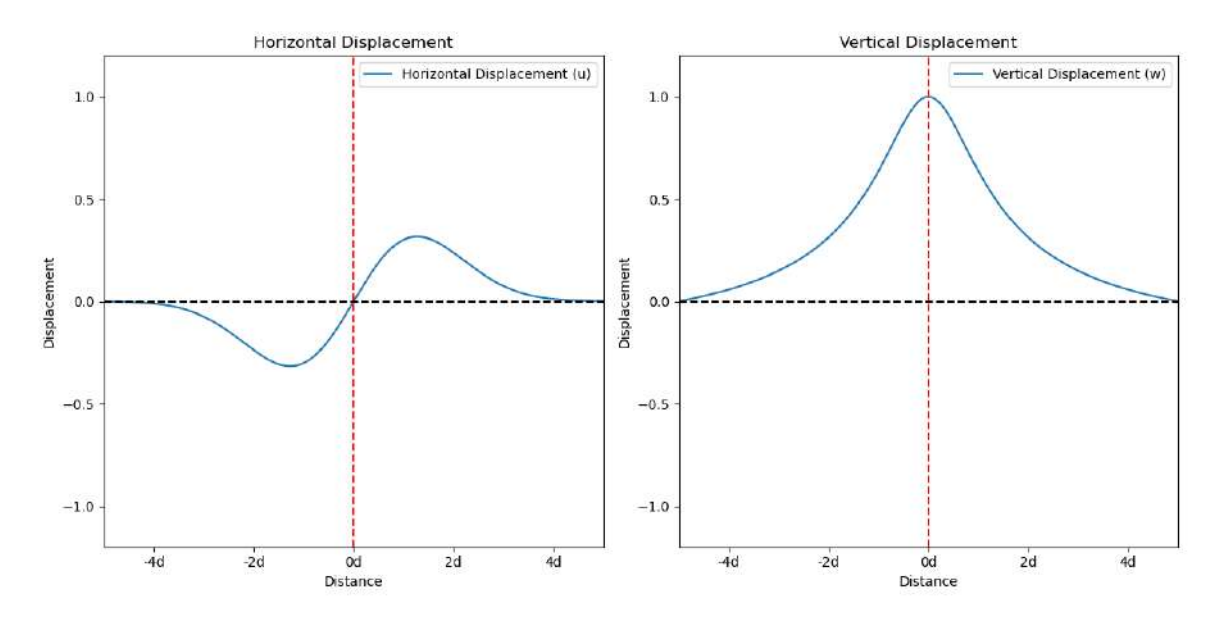


Figure 6.1 Synthetic horizontal and vertical displacement for point pressure source [3].

Ground displacement for Mogi point pressure model is explained by the following equation [1]:

$$\begin{pmatrix} u \\ v \\ w \end{pmatrix} = \alpha^3 \Delta P \frac{(1-v)}{\mu} \begin{pmatrix} \frac{x}{R^3} \\ \frac{y}{R^3} \\ \frac{d}{R^3} \end{pmatrix}$$
(6.1)

Here, (u, v, w) represents the displacement at a point in the surface with coordinates (x, y, 0). The symbol α represents the source ratio, which must be smaller than the depth (d) of the source $\alpha \ll d$ [1]. The Poisson's ratio is represented by v and Rigidity Modulus by mu in the elastic half-space, and ΔP represents the pressure change in the cavity. R denotes the radial distance from the centre of the cavity to the point on the surface. Finally, (x, y, d) represent the Cartesian coordinates of a point and its depth, respectively.

The maximum vertical deformation is observed at a point right above the point source on the surface, while the maximum horizontal deformation is at a distance of 0.7d (where d is the depth of the source) Fig. 6.1 [1].

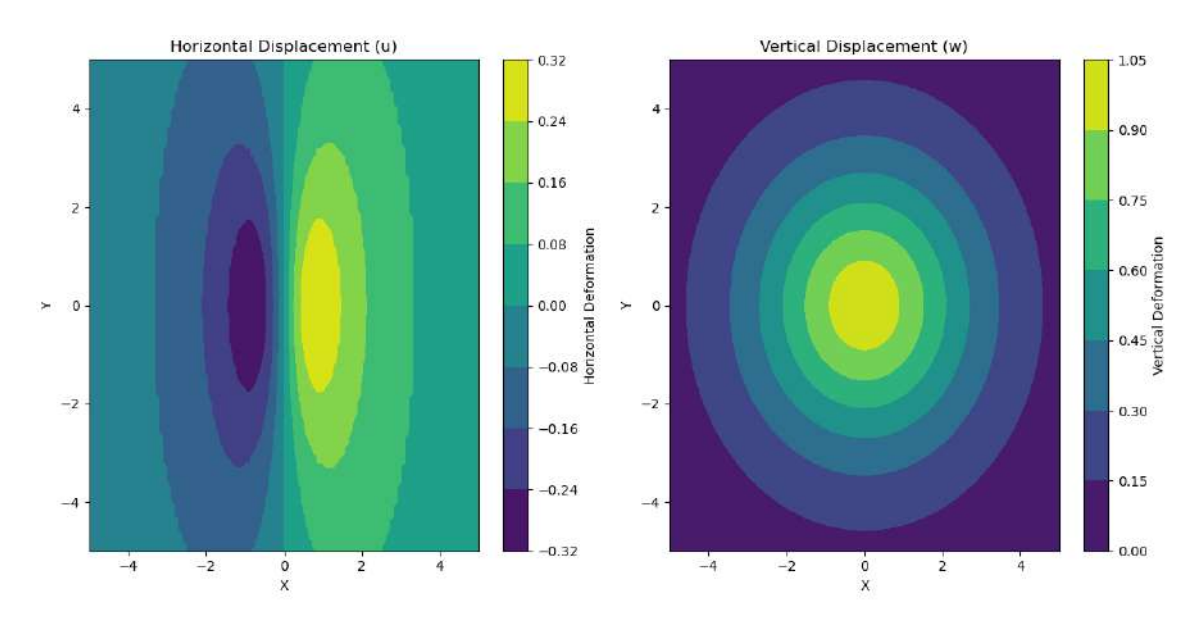


Figure 6.2 Synthetic horizontal and vertical displacement for point pressure source.

A simplified and synthetic representation of ground deformation in horizontal and vertical axes due to the Mogi point pressure source is depicted in Fig. 6.2.

6.1.2 McTigue finite spherical model

In this extended Mogi model, the author McTigue defines the size of the spherical source [25]. By estimating the source ratio, a closer approximation of the source characteristics is achieved, where values for the depth (d), coordinates of the source location (x, y), and the change in volume within it ΔV are obtained.

The displacement values are defined by the following equation [1]:

$$\begin{pmatrix} u \\ v \\ w \end{pmatrix} = (\alpha^3 \Delta P \frac{(1-v)}{\mu} ((1+(\frac{\alpha}{d})^3 (\frac{(1+v)}{2(-7+5v)} + \frac{15d^2(-2+v)}{4R^2(-7+5V)}))) \begin{pmatrix} \frac{x}{R^3} \\ \frac{y}{R^3} \\ \frac{d}{R^3} \end{pmatrix}$$
(6.2)

Where all symbols are the same as in Equation 6.1. Knowing the pressure change values ΔP , details of the volume change within the cavity ΔV are obtained. This volume change represents the alteration that occurs in the elastic half-space when experiencing the pressure change within the finite spherical source. To calculate the volume change ΔV within the cavity, a source radius of 1 km is assumed, and the following equation is applied [1]:

$$\Delta V = \frac{\Delta P}{\mu} \pi \alpha^3 \tag{6.3}$$

The horizontal and vertical deformation patterns are similar to the Mogi source models (Fig. 6.1).

6.1.3 Okada dike-like model

The Okada-like source is one of the most common analytical models for volcanic regions. It refers to the finite rectangular dislocation model, commonly recognized as the intrusion of a magmatic dike. Those models originate in-depth, present small width dimensions, and tend to propagate towards the surface [1, 26]. Its parameters include dip, strike, rake, width, length, depth and height, which determine the variations in horizontal and vertical displacements. However, the horizontal deformation pattern typically exhibits two lobes with maxima on either side of the magmatic intrusion. In the following Fig. 6.3, the 1D horizontal and vertical deformation patterns are depicted for a dike with a dip equal to 90°.

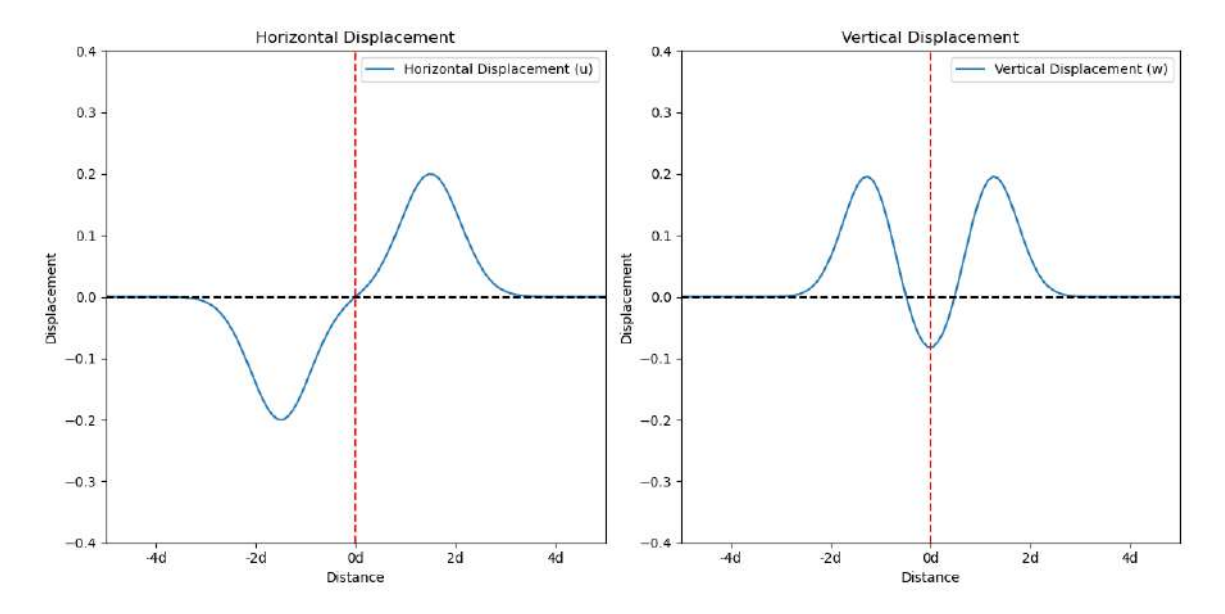


Figure 6.3 Synthetic horizontal and vertical displacement for finite rectangular dislocation model.

The displacement values are defined by the following simplified equation [1]:

$$\begin{pmatrix} u \\ v \\ w \end{pmatrix} = \frac{3M_0}{2\mu\pi} \begin{pmatrix} \frac{xd^2}{R^5} \\ \frac{yd^2}{R^5} \\ \frac{d^3}{R^5} \end{pmatrix}$$
 (6.4)

The symbols represent the same parameters as in the previous Equation 6.1. with the seismic moment parameter M_0 . The maxima of the horizontal deformation on each side of the magmatic intrusion are represented by the 2D synthetic deformation model in Fig. 6.4.

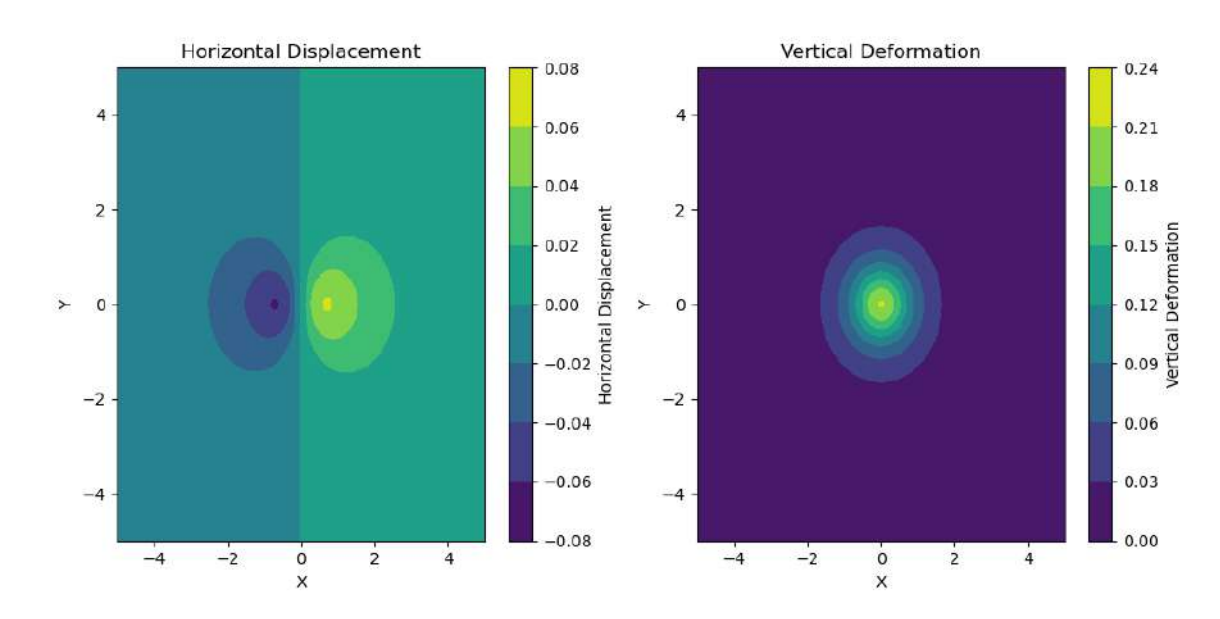


Figure 6.4 Synthetic horizontal and vertical displacement 2D representation for finite rectangular dike-like dislocation model.

6.1.4 Sill-like model

The sill-like magma chamber can be explained by three different models [1] proposed by the following authors: Davis [27], and Yang and Davis [28] proposed finite rectangular tensile dislocations as the mechanism responsible for the observed displacements. Following this, Davis [29] proposed a pressurised oblate sphere, and finally, Fialko et al. [30] proposed a model of finite pressurised horizontal circular cracks. This thesis describes a sill-like model as a horizontal point tensile dislocation model proposed by Davis [29]. The author assume the inflation of an ellipsoidal cavity in an elastic half-space. The cavity is replaced by the material that presents the same properties as the adjacent material of the subsurface [29]. This triaxial ellipsoidal cavity is located at a greater depth than twice the dimension of the ellipsoid (the radius of a sill is much less than its depth [1]). Due to the approximation of this model to the Mogi-like source [3], being extended to the ellipsoid, the displacement components u, v, and w of a point on the surface can also be calculated using Equation 6.5 of Okada [31].

As the shape of the sill is assumed to be ellipsoidal, the deformation response is similar to that observed with the spherical source proposed by McTigue Fig. 6.5 [25]. However, the dimensions and geometry of the deformation can be elongated in the directions where the axis length of the proposed sill source is extended. The maximum horizontal deformation is observed at a distance of d/2, where *d* represents the depth of the centre of the sill-like source [1]. The synthetic horizontal and vertical deformation models are represented in Fig. 6.6 for an ellipsoid whose X-axis is three times larger than the Y-axis.

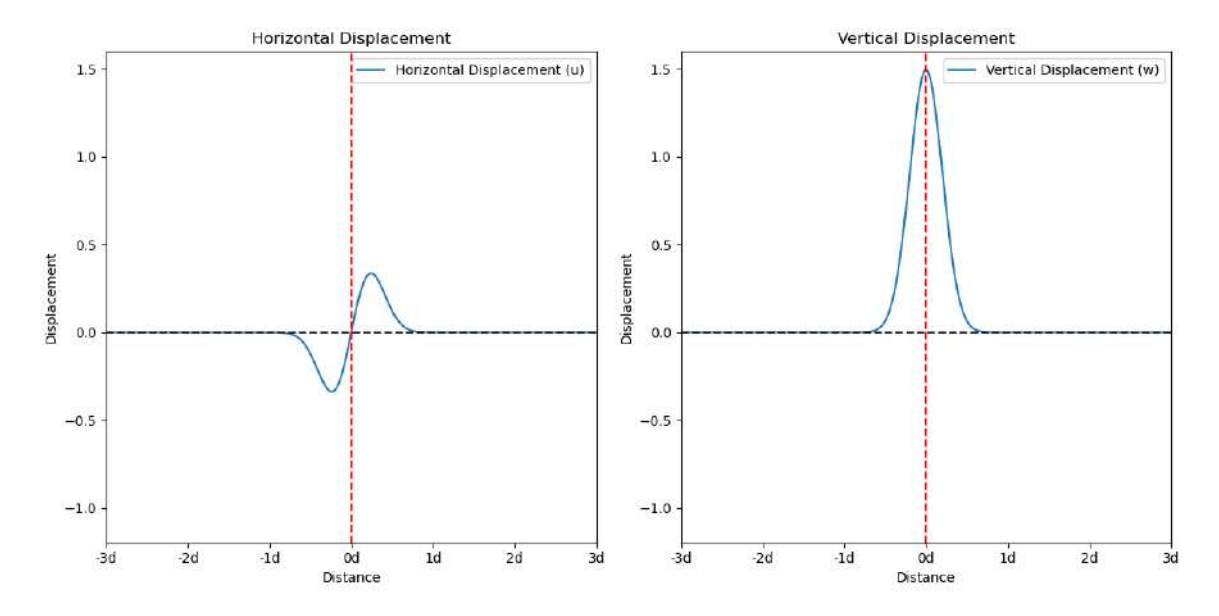


Figure 6.5 Synthetic horizontal and vertical displacement representation for finite rectangular dislocation model.

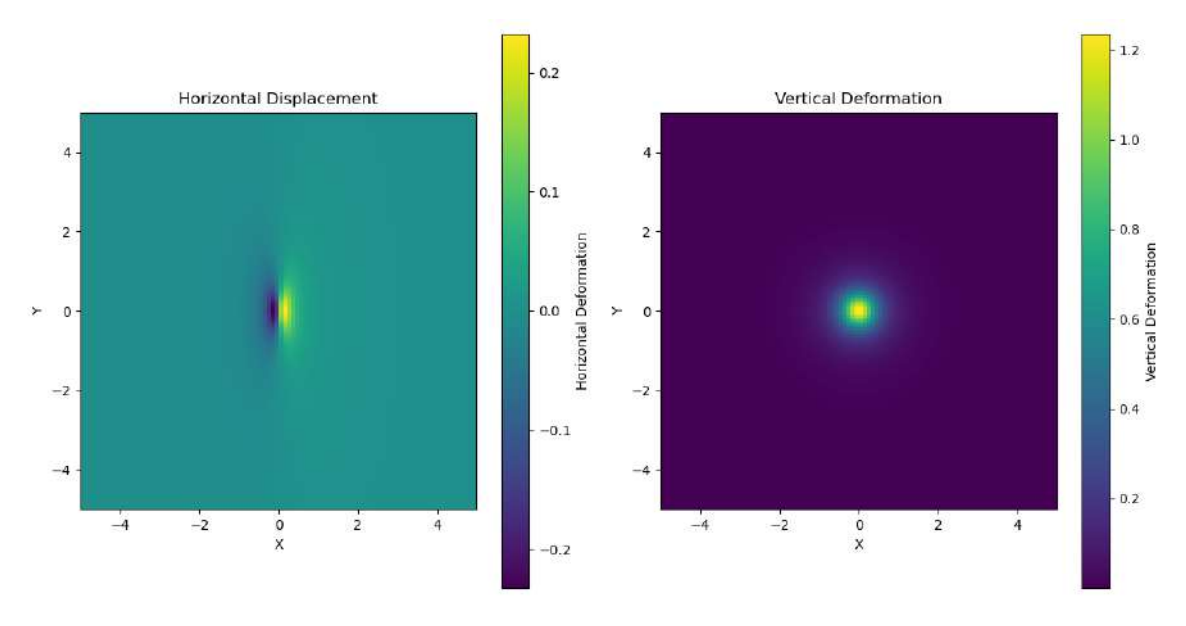


Figure 6.6 Synthetic horizontal and vertical displacement 2D representation for finite rectangular dislocation model.

The sill-like model proposed by Davis [29] is more commonly used in the scientific community due to its simpler and more accurate approximation of the ellipsoidal-shaped source. However, the Fialko [30] model represents a set of horizontally and circularly pressurised cracks widely acknowledged in geophysical studies. This approximation also assumes an elastic half-space medium. Injections or withdrawals of magma cause ground deformation into a finite oblate cavity [30]. The ground deformation corresponds to the volume change in the cavities. Fialko [30] describes that the volume of uplift in the ground can directly approximate the volume increase in the sill-like source.

6.2 Numerical volcano deformation source models

In addition to analytical models, which consider simplified equations and geometries, another method used in volcanic geodesy to tackle more complex problems is the Finite Element Method (FEM) [32, 33]. This approach is a commonly used numerical modelling tool in a wide variety of geophysics problems. Particularly in volcanic geodesy, FEM is employed to model complex geometries that cannot be easily modelled using analytical models. Within the context of FEM, various discretisation techniques are used to approximate the equations, which are obtained through numerical methods [34].

FEM considers medium heterogeneities and allows for a wide range of physical system properties and environmental conditions to be considered. In FEM, a working domain is established where the approximation of solutions for complex equations and geometries is calculated. This domain refers to the delimited study area, simplified into a set of geometries or meshes called finite elements. The use of FEM requires extensive computational capabilities, as it involves the application of equations and algorithms that discretise the problem domain into a mesh [34].

FEM allows for more realistic and precise model simulations, enabling more accurate source geometries to be established that consider a variety of environmental conditions. In structural mechanics, FEM models enable the response of the environment (deformation) to applied force (stress) to be obtained. These models allow for the representation of the geometries of the sources causing the deformations and their properties. To achieve this, a series of environmental characteristics are considered, such as domain heterogeneity, magma properties (pressure, density, viscosity, etc.), study area properties (environment geometry), boundary conditions (topography, etc.), and all external parameters that may influence the model, such as seismic activity, among others [34].

Combining so many environmental characteristics in complex equations allows for a more approximate solution to the problem and, therefore, a clearer view of the model.

To achieve the objectives of this thesis, the Comsol Multiphysics ®software was used to model and optimise source models under complex environmental conditions. The application of FEM allowed for the modelling of a schematic model of three-dimensional finite element modelling (FEM) incorporating Las Cañadas topography and the source's ellipsoidal geometry, represented in Fig. 6.7. The domain was discretised using tetrahedral mesh elements, with a maximum element size of 1,200

m and a minimum element size of 500 m. The ellipsoid model represents the source of ground deformation.

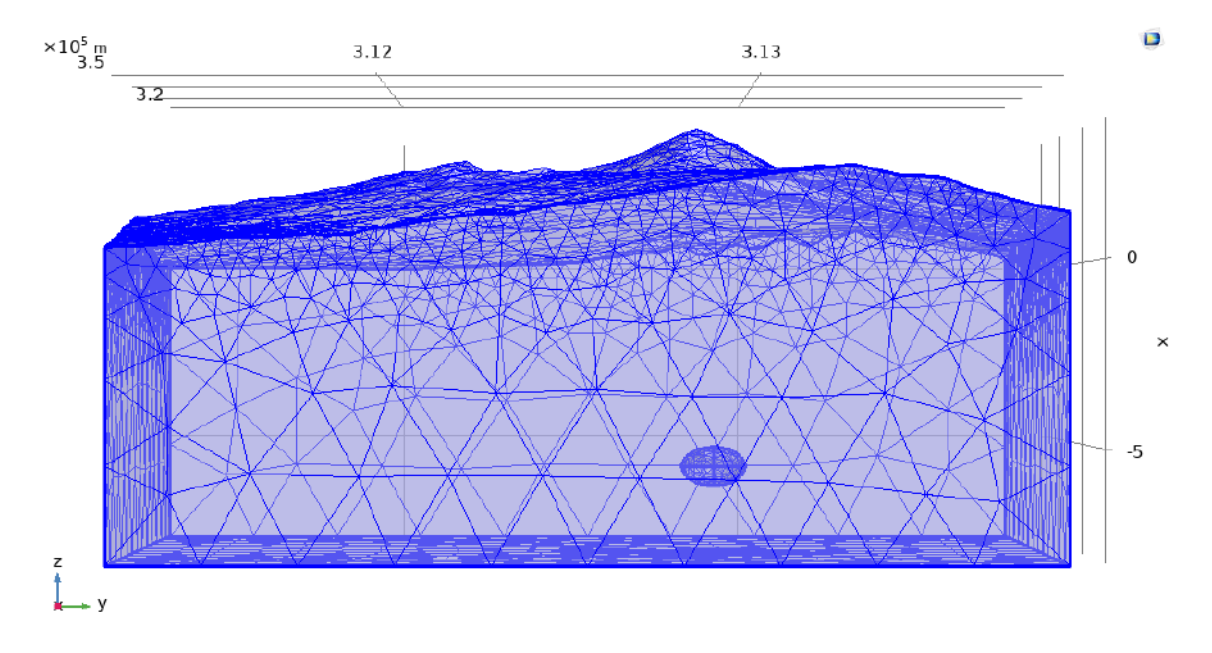


Figure 6.7 Schematic model of FEM in Las Cañadas with the magmatic source beneath the Teide volcano, exhibiting an ellipsoidal shape. Both the domain and the ellipsoid are modelled with the tetrahedral mesh.

The computational domain had dimensions of 33,000 m in width, 25,000 m in height, and 12,000 m in depth. The elastic constants for pressure wave speed were Cp = 4,000 m/s, shear wave velocity was Cs = 2,400 m/s, and the density was $\rho = 2,700$ kg/m³ [35]. The linear elastic material properties with isotropic characteristics were assumed. The bottom boundary of the domain was fixed, and the lateral sides were defined as roller nodes.

The optimised parameters are determined using the Nelder-Mead simplex algorithm and include the following: position in UTM (X, Y, Z); the dimensions of the ellipsoid along the X, Y, and Z axes in meters; and the overpressure in pascals (Pa) [36].

Chapter 7

Inverse Modelling

Inverse models are used to estimate parameters from observed data. They specifically rely on tracing from observable data to the parameters that triggered the observable effects and, more specifically, to find the relationship between model values and observable data [37]. The inverse problem begins by establishing observable data with the aim of reversing the data to obtain the values of the parameters that create the models. One characteristic of inverse modelling is that no perfect model satisfies the data [38]. Many models can fit the observed data very well. However, through the use of inverse modelling, we can approximate the values of the parameters that allow for the creation of models that fit the data well [37].

Starting with describing the data, which are numerical values, we can represent them as elements of a vector. If the data consists of a number N of measurements, we can organise these numbers into the vector d, which has length N. Now, in order to obtain information from the data, we assign numerical values to the parameters. These parameter values are carefully chosen to represent the observed data approximately. These parameters are considered as the elements of a vector m, which has length M [37].

Data:
$$\mathbf{d} = [d_1, d_2, d_3, \dots, d_N]^T$$
 Model Parameters: $\mathbf{m} = [m_1, m_2, m_3, \dots, m_M]^T$ (7.1)

Where T represents transpose. As the main objective of inverse models is to find the connection between the observed data and the model parameters, a quantitative model often describes this relationship [37]. The following equations can express this relationship:

$$f_{1}(\mathbf{d}, \mathbf{m}) = 0$$

$$f_{2}(\mathbf{d}, \mathbf{m}) = 0$$

$$\vdots \text{ or } \mathbf{f}(\mathbf{d}, \mathbf{m}) = 0$$

$$f_{L}(\mathbf{d}, \mathbf{m}) = 0$$

$$(7.2)$$

46 Inverse Modelling

where L represents the number of equations relating the parameters of the model and the observed data [37].

It's worth mentioning that the equations f(d, m) = 0 may not contain sufficient information to establish the model parameters. In some cases, there may also be inconsistencies between these parameters. One of the primary objectives of inverse methods is to address and resolve such issues. In many instances, the equation f(d, m) = 0 can take on various forms, involving highly complex (nonlinear) functions of both the model parameters and the data. However, in many cases, these complex functions can be simplified to more straightforward forms [37].

The selection of variables for model representation is called parameterisation. This step is crucial, as the chosen parameterisation directly influences the modelling results [37].

Inverse modelling of DInSAR data aims to obtain the source parameters of the observed ground deformation. It is based on finding the best fit of analytical or numerical models to the observed dataset. Estimating the best-fit source parameters requires an inverse modelling search for various source parameters to determine the residual values of the selected models.

Linear (Chapter 7.1) and nonlinear (Chapter 7.2) inverse modelling is described in the following section.

7.1 Linear inverse modelling

The inverse modelling is based on linear and nonlinear equations. In this chapter, the use of linear equations is explained. The representation of this linear function is the following:

$$Gm = d (7.3)$$

The matrix G is called data Kernell, drawing analogy with integral equations. In those integral equations, the model and data are the continuous functions d(x) and m(x), where x is an independent variable [38, 37]. The approach to solve the linear inverse problem Gm = d implies measurements of magnitude or length of the estimated model parameters, represented by m_e and the predicted data d_e .

$$d_o = Gm_o \tag{7.4}$$

To measure the magnitude of the estimated model parameters (to adjust the model parameters to the observed data), the Least Squares (LS) method is applied [38, 37]. The basic linear solution for the LQ method is represented in the following function:

$$m = (\mathbf{G}^T \mathbf{G})^{-1} \mathbf{G}^T \mathbf{d} \tag{7.5}$$

The LS method is based on finding the line that minimises the sum of the squared differences between the data and the model line [38, 37]. However, regularisation needs to be applied to avoid overfitting the model to the data. Tikhonov regularisation takes into account the magnitude of the

coefficients of the line. It prevents the coefficients from becoming too large and dominating the method's fit to the data. The Tikhonov regularisation implies smoothness conditions for the model, taking into account the spatial derivatives of the model [38, 37]. Tor the Tikhonov regularisation, the linear inverse models can be expressed by:

$$\delta m = (G^T G + L_{\Theta}^T L_{\Theta})^{-1} G^T \delta_d \tag{7.6}$$

Where δm is the perturbation of the model parameter vector with respect to the reference homogeneous model, G is the kernel matrix, L_{Θ} is the damping matrix, and δ_d is the vector of residuals (computed with respect to the reference homogeneous model) [38, 37].

A second-order Tikhonov regularisation for space and time was applied for the present thesis. Low damping values lead to lower misfit but unreliable noisy models. Conversely, high damping values lead to smoother models but high misfit values. This work used the widely known L-curve approach to establish the optimal damping value [38].

7.2 Nonlinear inverse modelling

Most geophysical problems are nonlinear. In such cases, the problem is addressed by beginning with an initial model and linearizing the forward modelling equation around this model. The initial solution is then refined through iterative processes to improve the solution until reaching an optimal result.

The following equation expresses a forward problem that links the observed deformation data and the model.

$$O = G(m) + \epsilon \tag{7.7}$$

Where O represents the observed deformation, G is the function that relates the source geometry with the m components of the source (depth, length, width, etc.) to the observed deformation in the selected point. ϵ represents the vector of observation error [1]. The relation of the observed deformation and the source parameters is nonlinear, and finding the m parameters allows finding the best fit that minimises the error between the data and the model [1]. In the present thesis, the Nelder-Mead algorithm was employed to optimise the model parameters to tackle the nonlinear problems [36]. This Simplex algorithm is used to find the best model parameters that minimise the difference between the observed data and the estimated values of the model.

This method considers the simplex geometry with N dimensions and N+1 points (vertices). During this method, the initial point is selected to start the algorithm. It searches for the minimum value of the vertex through the imaginary topography of N-dimensions (7.1. The algorithm systematically replaces the vertex with the poorest value with a new point demonstrating optimal characteristics. The minimum value of the final vertex can be in different scales, meaning it can select a global minimum and a local one [36].

48 Inverse Modelling

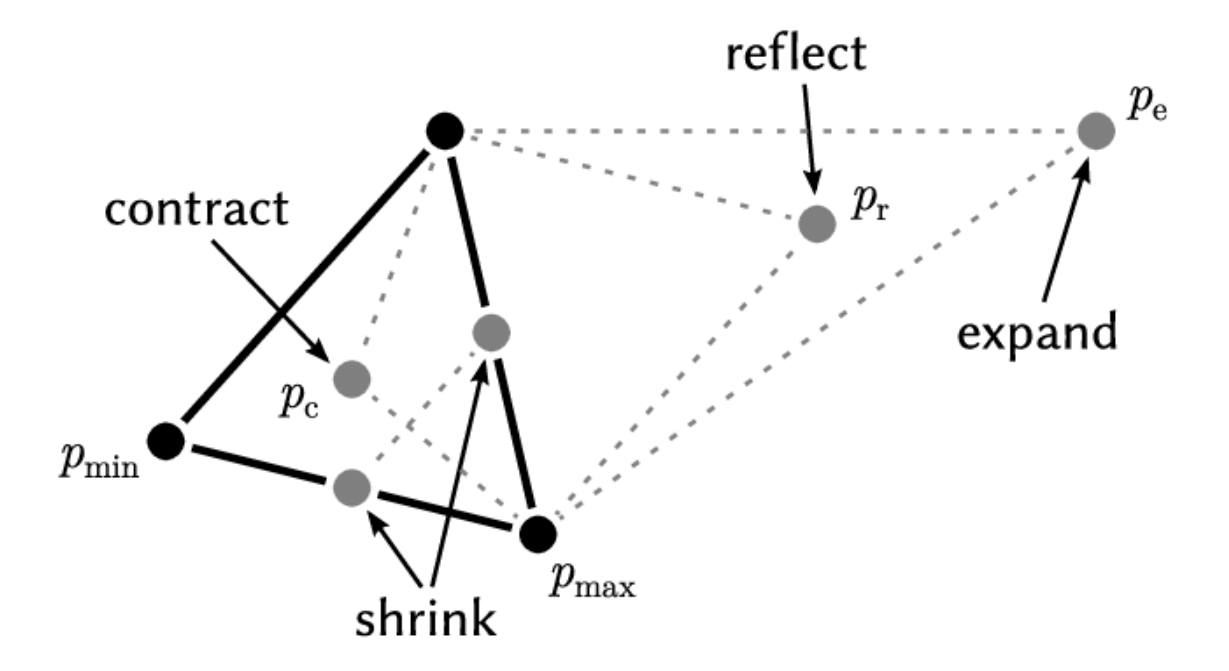


Figure 7.1 An interaction of the Nelder-Mear method over two-dimensional space showing points after [39].

Chapter 8

Elastic interaction between Mauna Loa and Kīlauea evidenced by independent component analysis

Przeor, M., D'Auria, L., Pepe, S., Tizzani, P., and Cabrera-Pérez, I. (2022). Elastic interaction between Mauna Loa and Kīlauea evidenced by independent component analysis. Scientific Reports, 12(1), 19863.

8.1 Introduction

The interaction processes between the two most active Hawaiian volcanoes are still controversial, and despite multiple studies carried out over more than a century, an unambiguous model has yet to be identified. In order to provide new insights to this discussion, we compared the ground deformation patterns in both volcanoes using DInSAR SBAS and Global Positioning System (GPS) datasets. In this work, we processed 10 tracks of ENVISAT ASAR satellite images from 2003-2010, together with available GPS data from 15 stations located around the two summit calderas of Mauna Loa and Kīlauea. We applied the Independent Component Analysis (ICA) to the DInSAR SBAS ground deformation data to reveal relationships between the spatio-temporal patterns of the ground deformation of the two volcanoes. ICA is widely used Data Mining technique, which allows detecting, separating and characterizing hidden patterns into a spatio-temporal dataset [19]. Furthermore, we computed the GPS areal strain time series around Mauna Loa and Kīlauea calderas, comparing them with the results provided by ICA. Subsequently, we present inverse modelling of ground deformation sources, which provides constraints for conceptual models of the shallow feeding system of Mauna Loa and Kīlauea. Conclusively, we realized a 3D numerical modelling of the stress and strain fields produced by the inflation/deflation of the individual ground deformation sources to better understand the mech-

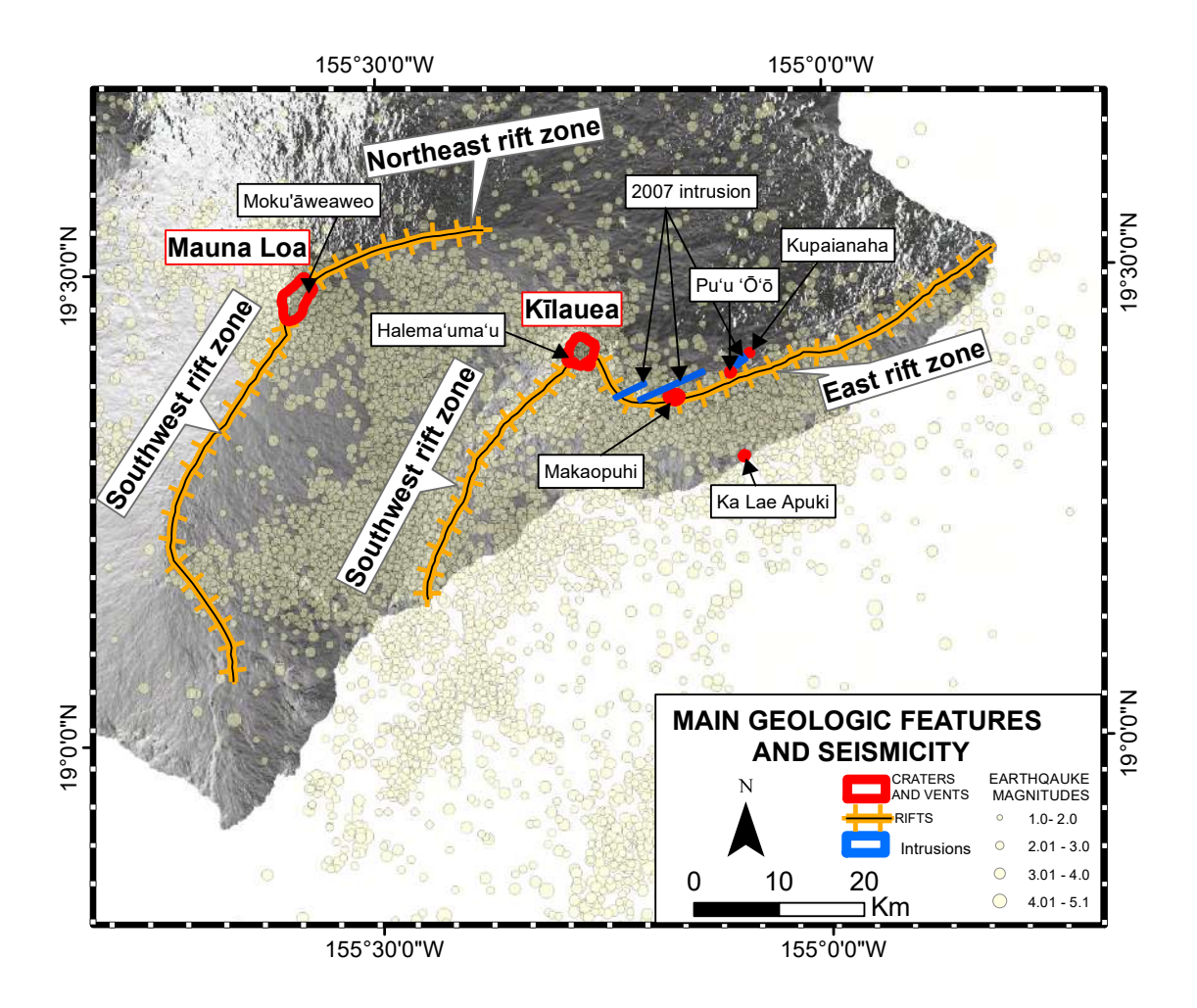


Figure 8.1 Main geologic and seismicity map of Mauna Loa and Kīlauea [41]

anism of their interaction. The details of data processing and modelling are described in the Methods section.

Hawai'i Island is composed of 5 shield volcanoes: Kohala, Mauna Kea, Hualālai, Kīlauea, and Mauna Loa, with the latter being the largest active volcano on Earth. It has erupted 35 times since its first historical eruption in AD 1750 [40]. The summit area of Mauna Loa is composed of a large summit caldera (Moku'āweoweo) and two elongated ridges: the Northeast Rift Zone (NERZ) and the Southwest Rift Zone (SWRZ) (Fig. 1). Kīlauea volcano overlaps the southeastern flank of Mauna Loa. It has been in near- continuous eruption from 1983 to 2018 [40], and its main volcano-tectonic features are the East Rift Zone (ERZ), the Southwest Rift Zone (SWRZ), a large summit caldera, and the Halema'uma'u crater within it [40] (Fig. 8.1).

Recently, several studies have aimed to characterise the nature of the magmatic source responsible for ground deformation at Kīlauea and Mauna Loa volcanoes [41, 42, 43, 44, 45, 46, 47, 48, 49, 50, 51, 52, 53, 54]. The two principal sources at Mauna Loa volcano are associated with shallow

8.1 Introduction 51

dike intrusion into the central conduit of Mauna Loa, and its rift zones [52]. Dike intrusions create compression over the adjacent flanks of the volcano [55, 56] and consequently, they produce ground deformation and earthquakes along the basal decollement zone [57]. In the case of Kīlauea volcano, the general picture is similar to Mauna Loa: the main ground deformation sources are linked to the central feeding system as well as to magmatic intrusions along the rift zones7 that are also responsible for the seismicity near the base of the volcano [58, 59]. The intrusion of dikes and extension of the rift-zone9 also causes the shortening at the base of the edifice and the uplift along the frontal bench [46, 60].

At Mauna Loa, Amelung et al. [52] identified a spheroidal source reservoir beneath the southeast margin of Moku'āweoweo Caldera, connected to an elongated source linked to the rift zones. Pepe et al. [43] showed that the main source of ground deformation at Mauna Loa consists of a vertical pipe connected to dike-shaped reservoirs located along the rift zones.

Poland et al. [41] showed the existence of various magmatic reservoirs beneath Kīlauea: one below the caldera of Halema'uma'u, the Keanakāko'i reservoir, the South Caldera reservoir, and both Rift Zones (East Rift Zone and Southwest Rift Zone). The Halema'uma'u reservoir is the summit storage located between 1 and 2 km depth below the main caldera. The Keanakāko'i is considered a temporal storage, with magma inputs occurring intermittently. The South Caldera reservoir, mentioned by Poland et al. [41] is located at a depth of 3–5 km below the Halema'uma'u caldera and is considered the principal storage of magma at Kīlauea. Both Rift Zones are a set of fractures and vents with directions toward the East and Southwest of the main caldera. A full catalogue of dike intrusions over Kīlauea edifice can be found in Montgomery–Brown et al. [61].

In the last three decades, some relevant deformation episodes took place at Kīlauea and were linked to the Pu'u 'Ō'ō-Kūpa'ianahā eruption (1983–2018) [41, 42, 43, 44, 45, 46, 47, 48, 49, 50, 51, 52, 53, 54, 62]. Volcanic activity at Pu'u 'Ō'ō-Kūpa'ianahā from 1983 to 2001 was characterised by dominant deflation, followed by a new inflation episode starting in 2001 when Kīlauea experienced a new uplift phase. Six months later, similar behaviour at Mauna Loa volcano was observed13. The enhancement of volcanic activity in this period was caused by an increase in the magma supply from the mantle [51].

The sudden inflation that started in 2003 at Kīlauea mainly affected the summit caldera, but was recorded as far away as 50 km from the summit and lasted until 2007 [54]. In 2005, magma accumulation in ERZ led to summit inflation and an increase in the output of SO2 [51]. In the same year, a major collapse of the lava delta occurred [63], and one year later, an uplift episode along the southern part of the Kīlauea summit caldera was registered15. The ground deformation pattern of Kīlauea during 2003–2007 was dominated by inflation along the ERZ and the summit crater [54].

In this work, we consider only the magmatic intrusions that occurred in the summit area of the volcanoes and only during the time interval considered in this study. A major episode of volcanic unrest occurred between 2003-2010, beginning on 17th June 2007 (American Father's Day 2007, FD07). The event entailed changes in volcanic activity and formation of new eruptive vents17. It caused rapid deflation of the Kīlauea summit area due to magma withdrawal to eruptive vents located

along the ERZ, about 8 km away [63, 53, 54]. The first episode of the FD07 eruption lasted for two days. On 21st July of 2007, another eruptive episode began along the ERZ, with vents located about 19 km away from the summit [63, 53]. ERZ vent activity was then continuous, while the summit crater of Halema'uma'u showed increased volcanic gas emission levels until an explosion of Kīlauea's main summit crater on 19th March 2008 [54]. After the FD07 episode until 2008, the ground deformation pattern of Kīlauea was characterised by deflation, and summit seismicity returned to background values [54].

The interaction between the two most active volcanoes of Hawai'i Island has been discussed for over 100 years [49, 50, 64]. Rhodes and Hart [65] confirm that the chemical composition of lavas at Kīlauea and Mauna Loa are different, indicating the magmatic feeding systems are independent (at least at the crustal level). However, geophysical studies seem to indicate the opposite: Klein [49] first noticed the anticorrelation between the two volcanoes, emphasising that an increase in activity at Kīlauea often corresponds to a decrease in Mauna Loa dynamism. Miklius and Cervelli [50] captured the opposite behaviour in the ground deformation patterns of the volcanoes: at the beginning of the high-volume effusive episode in Kīlauea, inflation of Mauna Loa was observed (May 2002). Shirzaei et al. [66] studied the coupling behaviour of both volcanoes between 2003 and 2008. The authors postulate that the causative source of the interaction between the two volcanoes is related to deep-seated mantle surges. Despite being the subject of many studies, the nature and the mechanism of the interaction between the feeding systems of the two volcanoes and their level of interconnection are still contentious and remain unclear.

8.2 Results

The analysis of the observed ground deformation, reported in the first column of Fig. 8.2(A, D, G, J), suggests an anticorrelated behaviour of the ground deformation between Mauna Loa and Kīlauea volcanoes. This is clearly seen in the normalized spatial patterns (indicated as Bk in Eq. 1) of the first component (ICA1) and shown in Fig. 8.2. The anticorrelation between these two volcanoes is demonstrated by the presence of positive values on Mauna Loa and negative values on Kilauea on the ICA1 component for all four selected tracks. The anticorrelation between the two volcanoes is seen only by the ICA1 component on both Mauna Loa and Kīlauea. The temporal variation is shown in Fig. 8.3 with dashed lines, clearly showing the opposite behaviour of Mauna Loa and Kīlauea on all four tracks: when ground deformation of Mauna Loa shows positive values, Kīlauea exhibits negative ones. It should be noted that the sign of the ICA components is arbitrary, being the actual value of the ground deformation modulated by the coefficients Ajk in Eq. (1).

Also, let us remark that, as shown by Fig. 8.2, there are other evidences of the ground deformation far from their summit areas. Column 1 in Fig. 2 shows an example of such deformation in the southeast side of the Kīlauea volcano associated with the faults system mentioned by Shirzaei et al. [66].

The second component of the ground deformation pattern (ICA2 in Fig. 8.2) exhibits significant values only in the area of Kīlauea volcano. The overall shape (Fig. 2) and temporal behaviour (Fig. 3) of the two components are different. The maximum of the ICA2 component at Kīlauea is located on the southern side of the summit caldera, slightly displaced to the south with respect to the maximum of the ICA1 component on the same volcano.

The above-mentioned anticorrelated behaviour in the ground deformation pattern is visible also by considering the LOS deformation time series. In Fig. 8.3, the time series for two selected pixels are shown, which correspond with the summit calderas of Mauna Loa and Kīlauea. The Mauna Loa time series displays an uplift from 2003 until late 2009. Simultaneously, the Kīlauea shows an inflation pattern until 2007 (the FD07 volcanic episode), followed by significant subsidence until late 2009.

At Mauna Loa, the total ground deformation pattern is almost exclusively represented by the first ICA component for all four considered tracks (see panels A, C, E, and G in Fig. 8.3). Minor differences between the ICA1 and the total LOS on this volcano can be attributed to a noisy component that ICA cannot model. In the case of Kīlauea volcano (see panels B, D, F, and H in Fig. ??), the contribution of both components is relevant. The anticorrelation in the temporal pattern of ICA1 is seen by a monotonic increase for Mauna Loa (ICA1, Fig. 8.3), which corresponds to a monotonic decrease in Kīlauea (seen on tracks T343 and T472; Fig. 8.3, dashed line). This difference in the amplitude of the ICA1 on the four considered tracks on Kīlauea can be attributed to the different orbits or, in other words, to the different LOS directions of the considered tracks. Conversely, the second ICA component displays a more complex temporal pattern, with an increase until the FD07 eruption, followed by a decreasing trend until the end of 2009.

The GPS ground deformation patterns show the different behaviour of Mauna Loa and Kīlauea (Figs. S1 and S2). Specifically, since 2009, the patterns of the two volcanoes show an opposite behaviour. This agrees with the results of ICA decomposition, shown in Fig. 8.3. The ICA2 component does not vary much since mid-2009; hence the ground deformation is shown in the anticorrelated ICA1 pattern. This does not hold for the previous interval, where ICA2 is prevalent on the ground deformation at Kīlauea. The ICA analysis of the DInSAR SBAS time series of the satellite tracks highlight the presence of an anticorrelated ground deformation pattern linked to at least two sources located beneath the summit calderas of Mauna Loa and Kīlauea (component ICA1). Furthermore, the presence of another source is evidenced by the ICA2 component beneath Kīlauea alone. In order to better understand the physical mechanisms responsible for the observed ground deformation patterns, we performed inverse modelling of the three detected sources and used Akaike Information Criterion (AIC) [67] to select the appropriate model for each source.

In Table A.14 in supplementary material, we detail the parameters of the three retrieved sources. Based on AIC, the temporal variation of Mauna Loa area displacements (delineated by ICA1) are best explained by a subvertical Okada crack model, with a centroid located at 6.2 km depth (Fig. 8.4; Table A.14). The ICA1 component for Kīlauea is better represented by a simple Mogi [3] source located at 1.2 km depth (Fig. 8.5). The ICA2 component for Kīlauea is best described by a sub-horizontal Okada [31] crack located at 3.5 km depth (Fig. 8.6; Table A.14 in supplementary material).

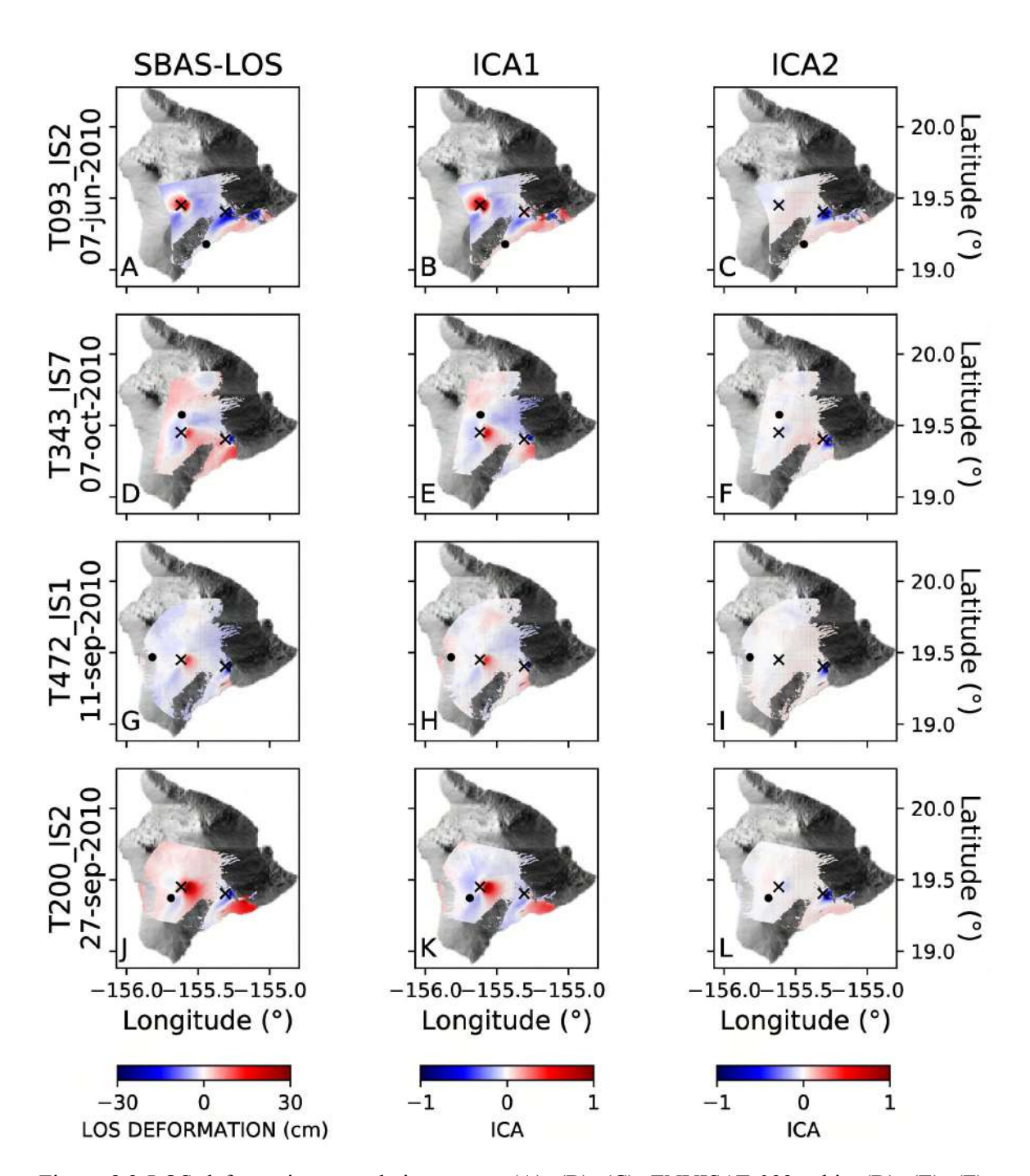


Figure 8.2 LOS deformation cumulative maps. (A), (B), (C): ENVISAT 093 orbit; (D), (E), (F): ENVISAT 343 orbit; (G), (H), (I): ENVISAT 472 orbit; (J), (K), (L): ENVISAT 200 orbit (see Table S2 for track details). Column 1 shows the LOS cumulative displacement DInSAR map; columns 2 and 3 represent the first and second components resulting from applying the ICA decomposition algorithm. The black crosses indicate the points used for extracting the time series shown in Fig. 8.3, while black dots are the reference points used for the DInSAR SBAS processing.

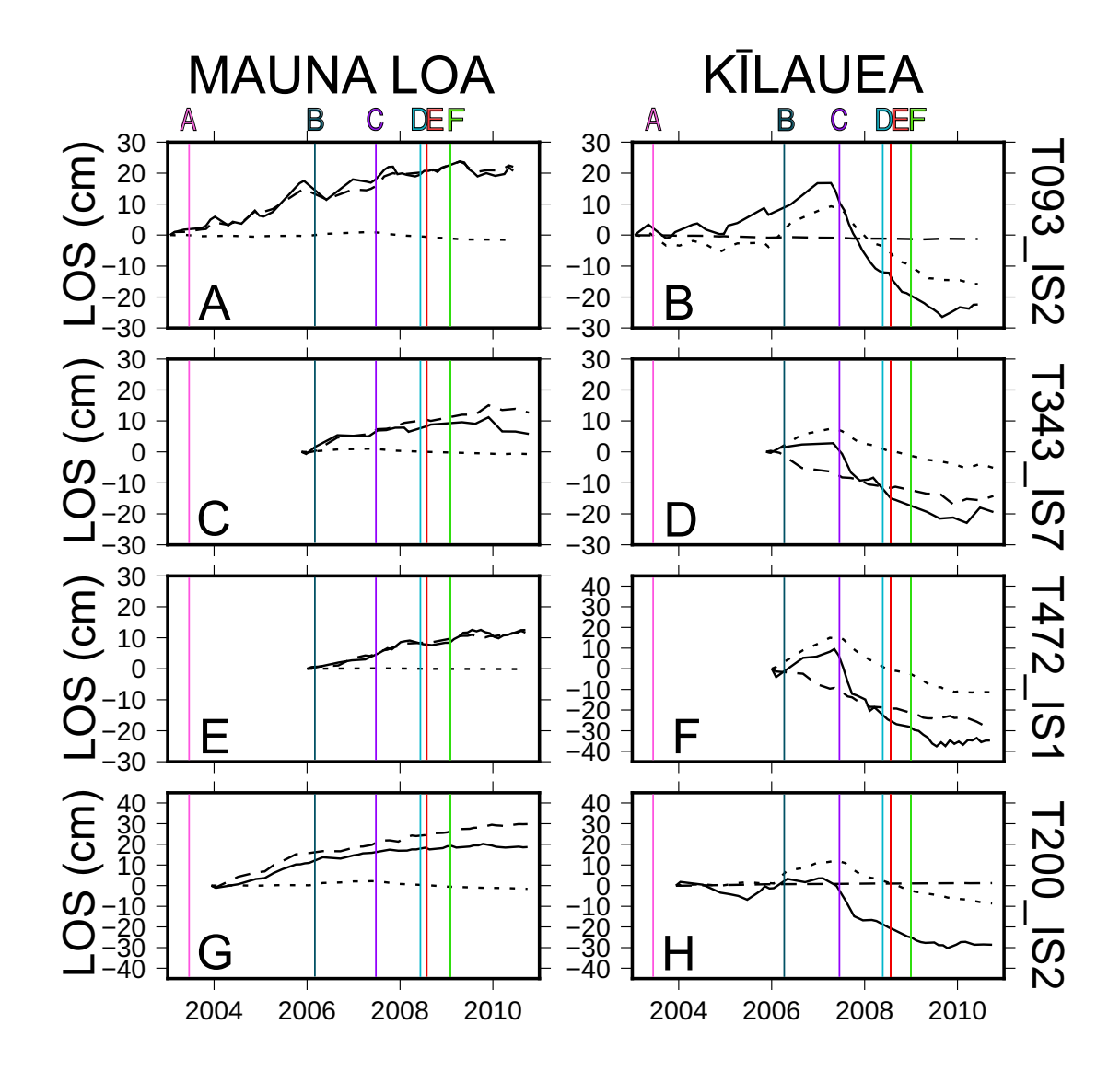


Figure 8.3 LOS displacement time series of Mauna Loa and Kīlauea summits. (A), (C), (E), (G): time series for LOS displacement of Mauna Loa; (B), (D), (F), (H): time series for Kīlauea volcano. Time series of LOS data are shown with continuous black lines; time series of the first component of ICA are indicated with the dashed black lines, while the dotted black lines report the time series of the second component of ICA. Vertical lines mark major volcanic episodes and the date of the beginning of the GPS dataset: (A) Mother's Day flow, which began erupting from Pu'u 'Ō'ō on 12th May 2003; (B) small bench collapse on 30th July 2006; (C) Father's Day eruption on 17th June 2007; (D) explosion on 19th March 2008; (E) the second half of 2008 which represent the time interval where the GPS measurements are available; (F) active vent within Halema'uma'u crater in January 2009.

Figures 4, 5, and 6 show the inverse modelling results for each of the three modelled sources of ground deformation. Each Figure shows the spatial pattern of the ground deformation associated with the relevant ICA, the best-fit analytical model, and the residuals. The panel (B) in the Fig. 8.7, shows a schematic tridimensional perspective of the three sources of ground deformation resulting from inverse modelling. Beneath Mauna Loa volcano, there is an Okada dike-shaped source. In the area of Kīlauea, there are Mogi-like and Okada sill-shaped sources of deformation.

8.3 Discussion

Previous studies of Mauna Loa and Kīlauea hypothesised the presence of a connection between these two volcanoes. In this context, Kīlauea volcano provided considerable geophysical and geochemical data due to its constant activity from 1983 to 2018. However, the lower density of the geophysical monitoring network of Mauna Loa with respect to Kīlauea, poses some difficulties in comparing the geophysical data of the two volcanoes3. This work has provided evidence for two sources associated with ICA1 and showing an anticorrelated temporal relationship between the Mauna Loa and Kīlauea (Fig. 8.3).

The findings of the inverse modelling are consistent with previous studies. Poland et al. [41] postulated the existence of two long-term magma reservoirs beneath the Kīlauea summit. Both reservoirs are connected to the rift zone system. Additionally, there exists a temporary storage area beneath Keanakaoko'i Crater. They highlighted the presence of a shallower magma reservoir located in the eastern margin of Halema'uma'u Crater, at a depth of 1-2 km depth. This source may coincide with the Kīlauea-ICA1 source proposed here, located at 1.2 km depth (Fig. 8.5; Table S3). According to Poland et al. [41], deeper magma storage at Kīlauea is situated at about 3 km depth and displaced to the south of Halema'uma'u Crater. This is consistent with our inversion results, which show a sill-shaped source located at a 3.5 km depth. The inverse model of the second and deeper source of the Kīlauea volcano is given in Fig. 8.6, with parameters detailed in Table A.14 in supplementary material. Our results for the Kīlauea feeding systems are compatible with Poland et al. [41] showing the presence of at least two ground deformation sources active between 2003 and 2010. However, Poland et al. [41] postulate the existence of a spherical or an ellipsoidal source in the southern side of the main caldera of Kīlauea. In contrast, our inversion results indicate the existence of a sill-like reservoir. Let us remark that our source model is related only to the ground deformation pattern related to the second component (ICA2) of decomposition. We again emphasise the effectiveness of ICA in separating the contribution of individual sources, significantly reducing the intrinsic ambiguity in geodetic inverse problems.

At Mauna Loa, previous studies emphasised the relevance of the rift zones as sources of ground deformation [42, 43]. Our findings suggest a dike-like geometrical structure as a primary source during the interval considered (Fig. 8.4). During our analysed period (2003–2010), the ICA decomposition detected only one component of ground deformation in Mauna Loa. This is in agreement

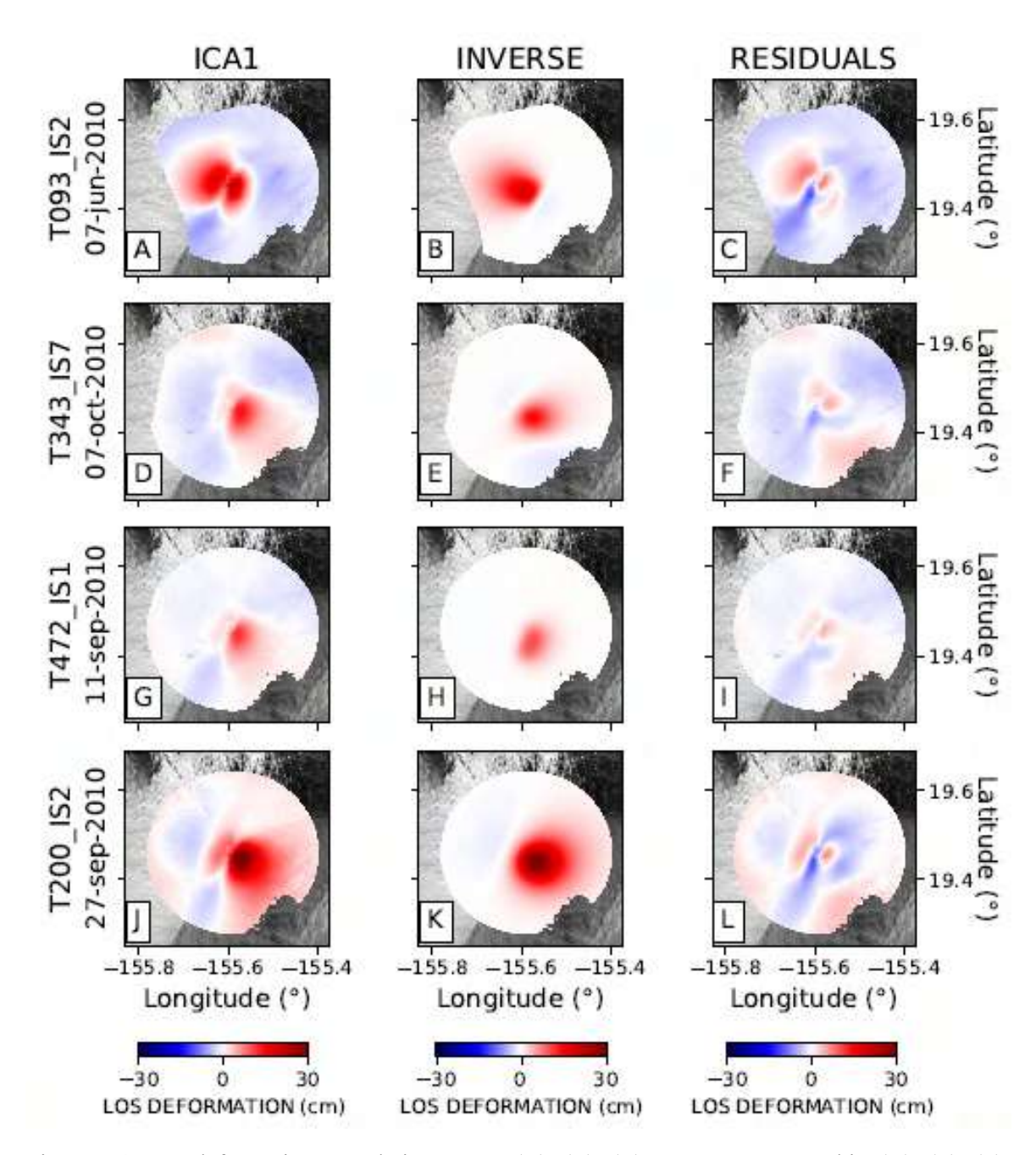


Figure 8.4 LOS deformation cumulative maps. (A), (B), (C): ENVISAT 093 orbit; (D), (E), (F): ENVISAT 343 orbit; (G), (H), (I): ENVISAT 472 orbit; (J), (K), (L): ENVISAT 200 orbit (see Table S2 for track details). Column 1 shows the LOS cumulative displacement DInSAR map; columns 2 and 3 represent the first and second components resulting from applying the ICA decomposition algorithm. The black crosses indicate the points used for extracting the time series shown in Fig. 3, while black dots are the reference points used for the DInSAR SBAS processing.

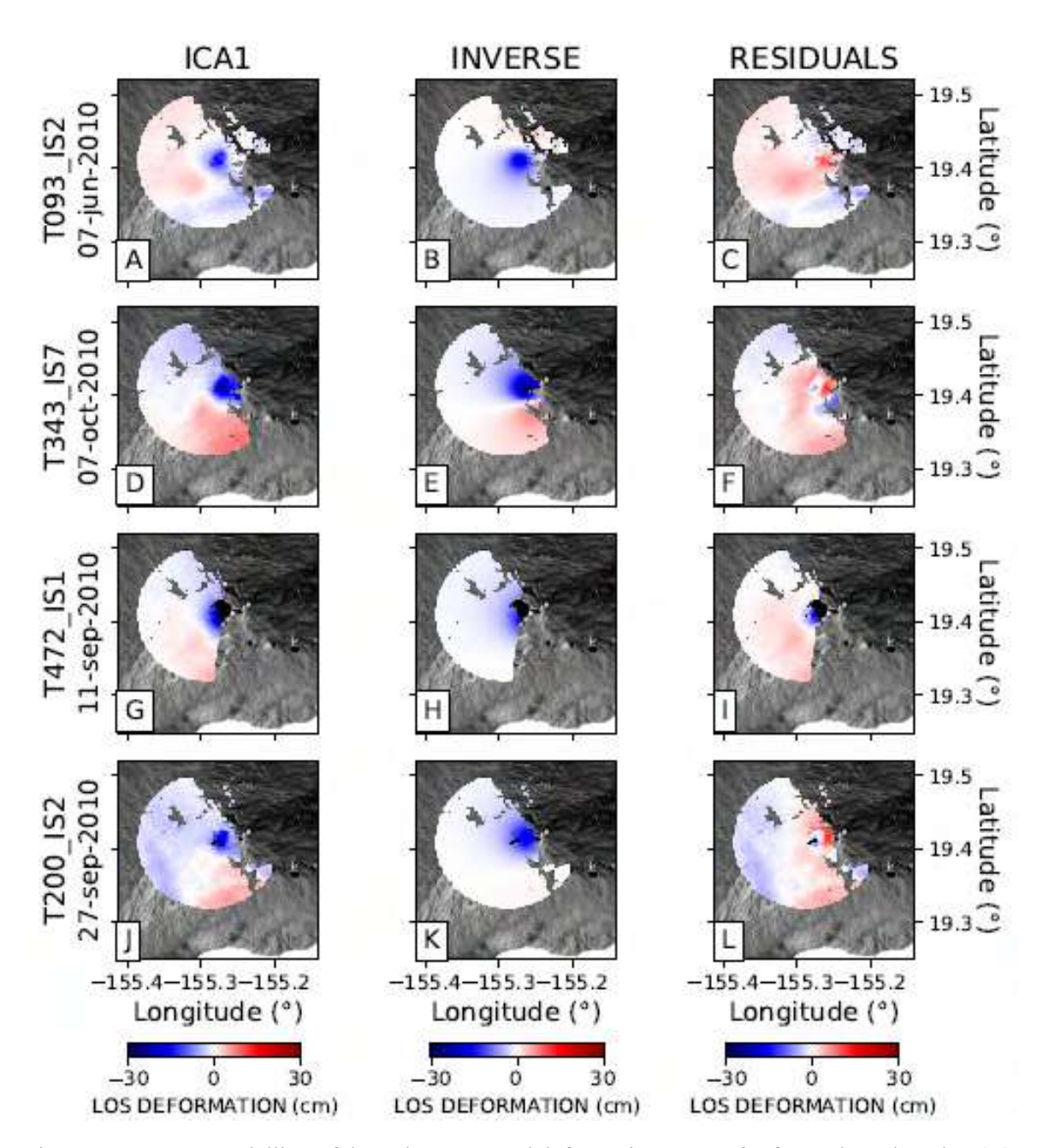


Figure 8.5 Inverse modelling of the Kīlauea ground deformation source for four selected tracks: (A), (B), (C): ENVISAT 093 orbit; D, E, F: ENVISAT 343 orbit; G, H, I: ENVISAT 472 orbit; J, K, L: ENVISAT 200 orbit, respectively. Column 1 represents the first component (ICA1) encompassing a radius of 11 km from Halema'uma'u Crater. Column 2 represents the Mogi analytical model as a result of the inverse modelling. Column 3 shows the residuals of the inverse modelling and the observed data.

with Pepe et al. [43], who, although proposing a more complex geometrical model, showed that the main reservoir and the rift zone acted with synchronous behaviour.

Many authors have already suggested possible connections between Mauna Loa and Kīlauea. Miklius and Cervelli [50] proposed a crustal-level interaction between them: pulses of magma in the plumbing system of Mauna Loa may cause pressure variations in the Kīlauea shallow magma system. Gonnermann et al. [51] explained observed related ground deformation patterns by considering a pore-pressure diffusion within a thin accumulation layer in the asthenosphere. Since the magma composition at Kīlauea is isotopically distinct from Mauna Loa [65], Gonnermann et al. cit-egonnermann2012coupling suggested the interconnection between Mauna Loa and Kīlauea must be explained by the transfer of stress by pore-pressure variations. Shirzaei et al. [66] explain the interconnection between the Mauna Loa magma chamber and the Kīlauea rift zone through pore pressure diffusion in an asthenospheric magma supply system.

We note that volcanic interconnection is even more evident if we consider the temporal evolution of the ground deformation patterns. From 1983 until 2003, both volcanoes were deflating [50, 52, 63, 53, 54]. The time series of DInSAR data (Fig. 8.3) shows the change of the ground deformation that took place in 2003 and was explained by many authors as sudden inflation that started in Kīlauea and lasted until 2007. That inflation resulted in an eruption that started in the northern part of Makaopuhi Crater due to higher magma rates in ERZ3. While Kīlauea showed higher volcanic activity accompanied by ground deflation mostly represented by the continuous and dotted line in Fig. 8.3 in Kīlauea block, Mauna Loa was still experiencing gradual inflation of the ground - continuous and dashed line in Mauna Loa block (Fig. 8.3). Many authors have attempted to explain these opposing ground deformation pattern behaviours, presenting models for the causes. Poland et al. [54] stated that the 2003-2007 episode was an unusual event, caused by the arrival of a new pulse of magma from the mantle. Dzurisin et al. [1] found similar behaviour in the late 70s: when Kīlauea experienced an increase in magma supply, inflation of Mauna Loa was also observed. Poland et al. [41] explained this similar behaviour by magma input to the deep storage zone that affected both volcanoes.

The DInSAR SBAS time series analysis via the ICA decomposition technique provides a powerful tool for assessing and highlighting the relationship between the magmatic systems of the two volcanoes, and can be used to constrain the underlying physical mechanism of their possible connection. Interconnection between the two volcanic systems is best shown by the first independent component of the ground deformation (ICA1). In contrast, ICA2 shows a ground deformation source affecting only Kīlauea volcano. The rapid deflation of Kīlauea from 2007 to 2009 (Fig. 8.3) has a source located beneath Halema'uma'u Crater. Co-incident with deflation of this source, the interconnected source of Kīlauea and Mauna Loa (ICA1) was deflating more gradually (Fig.8.3).

The GPS strain area results support anticorrelated behaviour of these two volcanoes. The 2009 strain area reduction in Mauna Loa and the opposite increment of the strain area in Kīlauea indicates that while Mauna Loa was undergoing a deflation, Kīlauea was experiencing an inflation episode.

Finally, based on the inverse modelling results, we maintain that the pattern associated with the anticorrelated component ICA1 points to a very shallow source beneath Kīlauea. This makes it un-

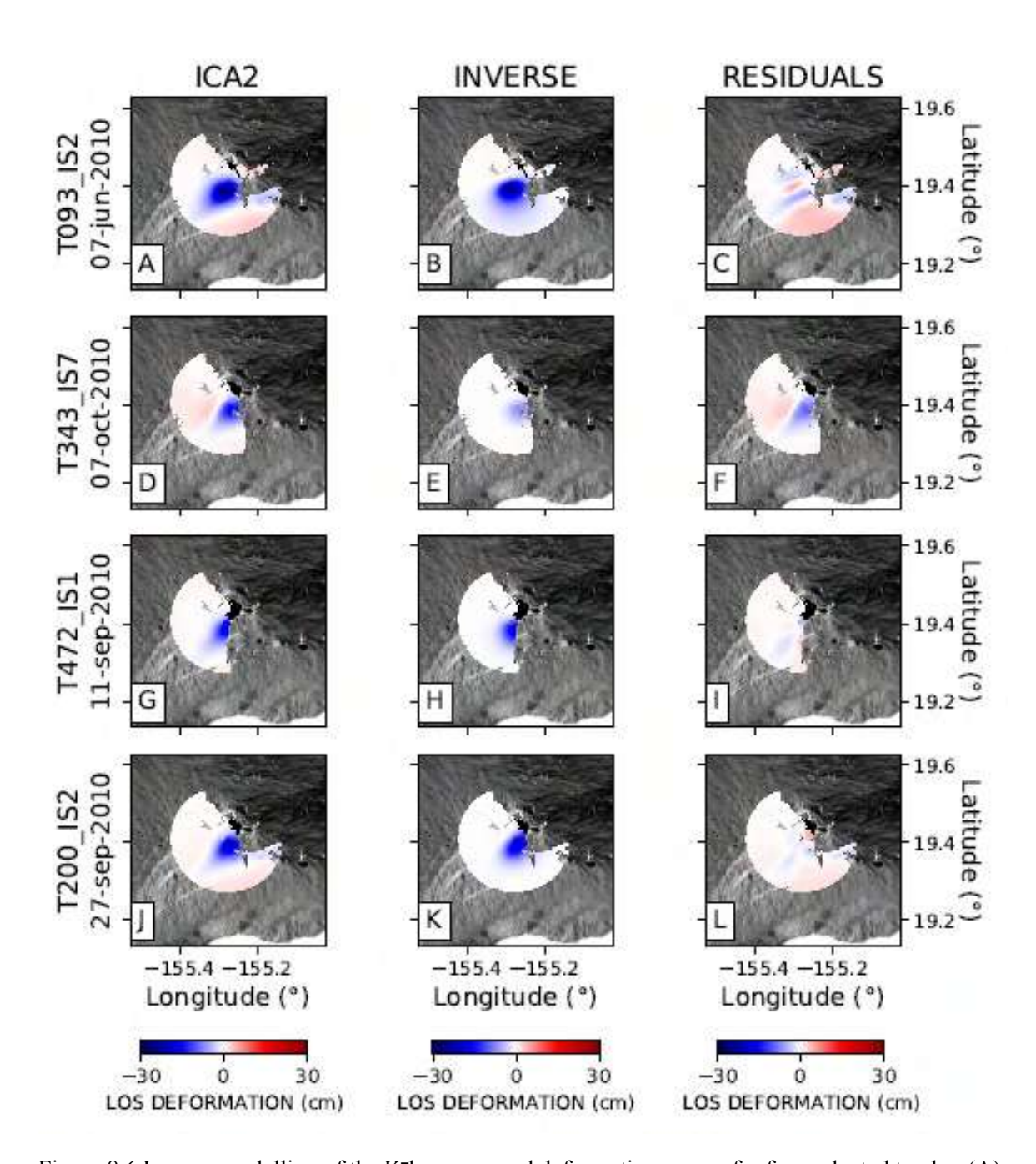


Figure 8.6 Inverse modelling of the Kīlauea ground deformation source for four selected tracks: (A), (B), (C): ENVISAT 093 orbit; (D), (E), (F): ENVISAT 343 orbit; (G), (H), (I): ENVISAT 472 orbit; (J), (K), (L): ENVISAT 200 orbit, respectively. Column 1 represents the first component (ICA2) encompassing a radius of 15 km from Halema'uma'u Crater. Column 2 represents the inverse model. Column 3 shows the residuals.

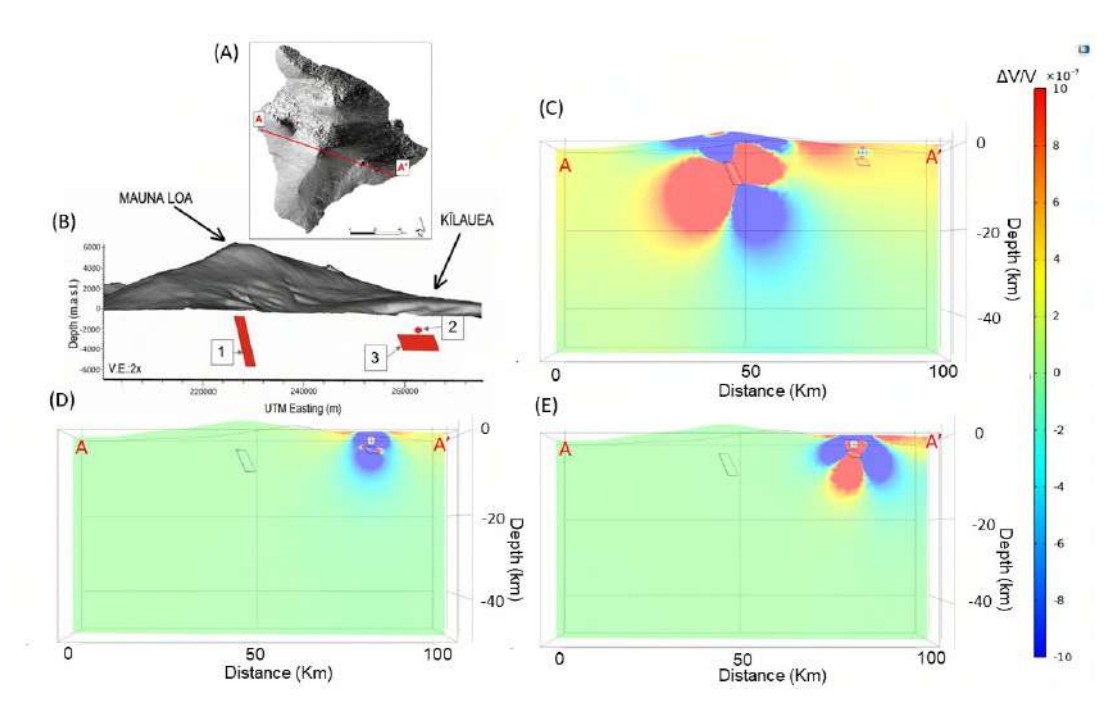


Figure 8.7 3D numerical modelling of strain fields. (A) The Digital Elevation Model of Hawai'i Island, with the red line representing the trace (A-A'), used in panels (C–E). (B) tridimensional representation of the modelled ground deformation sources of Mauna Loa and Kīlauea volcanoes. The sources are numbered according to Table A.14 in the supplementary material. (1) the Mauna Loa dike-shaped source from ICA1; (2) the Kīlauea Mogi-like source from ICA1; (3) the Kīlauea sill-shaped source from ICA2. Storage areas and topography are exaggerated in size for clarity. (C) the volumetric strain field represented along the A-A' trace due to an overpressure applied to the Mauna Loa dike-like source. (D) volumetric strain field along the A-A' trace due to an overpressure applied to the Kīlauea Mogi-like source. (E) volumetric strain field along the A-A' trace due to an overpressure applied to the Kīlauea sill-like source.

likely that there is a direct connection between the magmatic systems of the two volcanoes in the deeper crust. A direct connection at shallow depths would provide a further source of ground deformation, which has never been observed. Furthermore, it would contradict petrological and geochemical evidence [65]. On the other hand, the existence of a second component, related to Kīlauea alone, suggests a more complex configuration of the plumbing system of Kīlauea, characterised by multiple reservoirs.

The spatial configuration suggests a possible explanation for the observed anticorrelation between the ground deformation sources related to ICA1 (numbered 1 and 2 in Fig. 8.7). Their respective geometries make the stress field, caused by the inflation of one source, act on the other with forces directed inward along its external surface. At the same time, because of its sill-like geometry, the source related to ICA2 (number 3 in Fig. 7) would be less sensitive to these changes in the stress field, explaining its independent temporal behaviour. In practice, the dike-shaped source of Mauna Loa would be capable of affecting the shallow volumetric (Mogi-like) source of Kīlauea, but not the deeper sill-shaped source.

To corroborate our hypothesis, we performed a quantitative numerical model of the interaction between the plumbing systems of Mauna Loa and Kīlauea. The Figs. 8.7 and A.13 in supplementary material show the volumetric strain and stress fields as the consequence of internal overpressure applied to each source independently. We selected the overpressure values for each source to reproduce approximately the maximum observed ground deformation above each source. Figure 7 shows the volumetric strain produced by a pressure change inside the Mauna Loa dike-shaped source (see panel (C) in Fig. 8.7). It can be seen that the strain field in the surroundings of the shallow source at Kīlauea is perturbed. The Mauna Loa Okada source does not significantly affect the deeper Kilauea reservoir. Furthermore, panels (D) and (E) in Fig. 8.7 show that pressure changes inside the Kīlauea sources does not significantly affect Mauna Loa. Therefore we conclude that the interaction through stress-transfer is effective only between the Mauna Loa dike with respect to the shallow Mogi-shaped Kīlauea reservoir. In the supplementary Fig. A.13, we also show the corresponding isotropic component of the perturbed stress field.

8.4 Methods

8.4.1 DInSAR SBAS time series

In this work, was utilised the large amount of satellite data acquired over eight years (2003–2010) across Hawai'i Island. Specifically, C-band (wavelength of ≈ 5.6 cm) ASAR ENVISAT images from the European Space Agency (ESA) were acquired along both ascending and descending orbits from 2003-2010 (see Fig. A.15 in the supplementary material). Four tracks were selected: T093 along an ascending orbit, and T343, T472, and T200 (Fig. A.15 in supplementary material) along descending orbits. The tracks have different swathes: I2, I7, I1, and I2, respectively (see Table S2 for tracks details). We analysed a catalog of 394 SAR images covering both Mauna Loa and Kīlauea volca-

8.4 Methods

noes, with look angles ranging from 15.0° (I1) to 45.2°(I7) [43]. All the interferograms of the considered tracks were analysed automatically, and noisy interferograms were discarded. We performed a multitemporal analysis using the Small Baseline (SBAS) technique that provided a Line-Of-Sight (LOS) time series for coherent pixels of the SAR images. SBAS algorithms allow the production of a deformation time series for each coherent pixel [68]. For data processing, we employed the Grid Processing On-Demand (G-POD) platform of ESA that applies the SBAS algorithm and can process large volumes of DInSAR data [5]. Tracks covering only one of the two volcanoes were discarded from the analysis (see Figs. A.4, A.5, A.6, and Table A.17 in the supplementary material).

8.4.2 Independent component analysis (ICA) of DInSAR SBAS time series

Independent Component Analysis is a multivariate statistical tool that allows the separation of a spatio-temporal dataset into discrete components, for which the relative statistical independence is maximised [18]. ICA is a widely recognized technique that allows the detection of "hidden" patterns in complex datasets [18]. An advantage of using ICA in volcano geodesy is that it allows simplification of the inverse problem by separating the contribution of different causative ground deformation sources. ICA was highlighted by Ebmeier [20] as a valuable tool in the detection of different sources responsible for observed ground deformation patterns1. For Hawai'i Island, each track dataset consists of a set of time series L(xi, tj), where L is the LOS displacement for a given track, xi is the spatial position of the i-th DInSAR pixel, tj is the time of the j-th DInSAR image.

Using ICA, the original dataset can be decomposed into a finite sum of N components with a fixed spatial pattern B(xi) and time-varying amplitudes. In practice, the observed LOS displacement time series for a given track can be represented as:

$$L(i, t_j) = \sum_{k=1}^{N} A_{jk} B_k(x_i)$$
 (8.1)

where Bk is the normalised spatial pattern corresponding to the k-th ICA component, and Ajk is the amplitude of the k-th ICA component at time tj.

In the model of Eq. (1), the LOS displacement is expressed through a linear combination of the normalised spatial patterns Bk, through the time-varying coefficients Ajk. Once the Bk are known from ICA, the coefficients Ajk can be determined by solving the linear system of Eq. (1) using a least-squares approach. This model implies that using only a limited number of components, as is usual when performing ICA, the sum on the right side of Eq. (1) cannot fully model the whole signal L. If the number of selected components is sufficient, this missing value is generally related only to the incoherent noisy part of the signal.

The ICA components can be ordered based on their energy, defined as the sum of squared Ajk for each k. This allows a consistent sorting of the retrieved components, irrespective of the specific ICA algorithm used. In our case, using three components was sufficient since additional components had negligible amplitude values.

The first and the second components (ICA1, ICA2) were associated with a clear and meaningful signal, while the third component (ICA3) was mainly composed of noise; hence it was not considered further. In Table A.16 (in supplementary material) we show the percentage of the energy of the ICA signal in every component for each track of the study. It should be noted that for the purposes of ICA decomposition, it is recommended to have a minimum of 3 components so that at least one of them includes the noisy part of the signal [19, 18, 20].

8.4.3 Nonlinear inverse modelling

To model the observed ground deformation, we tested four analytical source models [1]: the Mogi point source [3], the spheroidal source [25], the closed pipe [69] and the rectangular crack [31]. In all cases, we performed the modelling assuming a Poisson's ratio of 0.25 within a half-space. We selected the best model for each ICA and each volcano following the Akaike Information Criterion (AIC) [67]. We performed a non-linear inversion of each track for all previous source models for each ICA and each volcano. The inverse method relies on a non-linear optimisation of a misfit function using the Nelder-Mead simplex algorithm [36]. The misfit function is defined as the sum of the squared residuals between the observed and synthetic data. The synthetic data, computed using the aforementioned analytical models, were projected along the LOS corresponding to each track. The final models resulted from averaging the results obtained for each track. We obtained a source model for Mauna Loa, corresponding to ICA1, and two models for Kīlauea, corresponding to ICA1 and ICA2, respectively.

8.4.4 GPS data

GPS stations up to 10 km from the summit calderas of the two volcanoes were selected (Fig. A.16 in supplementary material). For Mauna Loa and Kīlauea volcanoes, 8 and 7 stations were selected, respectively, with data from 2008 to 2011. The GPS daily solutions were downloaded from the Nevada University repository (http://geodesy.unr.edu) [70]. We used horizontal components to compare results obtained through the ICA decomposition of DInSAR SBAS data with GPS time series since vertical components have a higher signal/noise ratio. The areal strain time series was computed since it does not require the assumption of a reference point on the island (Fig. ??. The areal strain is a geodetic method widely applied in active volcanic areas and has been described by many authors [71, 72, 73, 74]. For this purpose, we computed the area for triplets of GPS stations covering more than half of the summit calderas (see Figs. A.7, A.8 in supplementary material). We did not use triplets with significant temporal data gaps or whose signal was too noisy. Accordingly, we used 11 triplets for the main crater of Mauna Loa and 15 triplets for Kīlauea's summit caldera. We studied the temporal variation in the area of a given triplet of stations, determining the areal strain time series A(t) as:

$$\Delta A(t) = A(t_0) - A\left(\frac{t}{A}\right)(t_0) \tag{8.2}$$

8.4 Methods

with A(t) being the times series of the area of a given triplet and A(t0) the area at the initial time of the series. We did not consider the detailed spatial variations of the areal strain since we are making only a qualitative comparison of the trend of DInSAR SBAS and areal strain data here. Most of the GPS stations at Kīlauea began operation in the first quarter of 2008. Hence, we computed the areal strain time series for this volcano beginning in mid-2008, when the GPS network was fully operative. Therefore, we also begin the comparison with the Mauna Loa time series from June 2008 (although more data is available).

8.4.5 Numerical modelling of the stress and strain fields

To validate the stress-transfer model, we realized a finite-element tridimensional elastic modelling using the software COMSOL Multiphysics®. The model includes the topography of Hawaii Island and the sources of the ground deformation determined by non-linear inversion. The size of the computational domain was $100 \times 100 \times 70 \text{ km}3$. The linear elastic material characteristics were assumed as isotropic, with elastic constants retrieved from the 1D velocity model of Lin et al. [75]. The boundary conditions of the domain were chosen to be fixed on the bottom and lateral sides. The computational domain was built as tetrahedral mesh elements with dimensions ranging between 150 and 3500 m. As explained in the "Discussion" section, we applied an overpressure to each source, calculating the corresponding perturbation of the stress and strain fields Fig. 8.10.

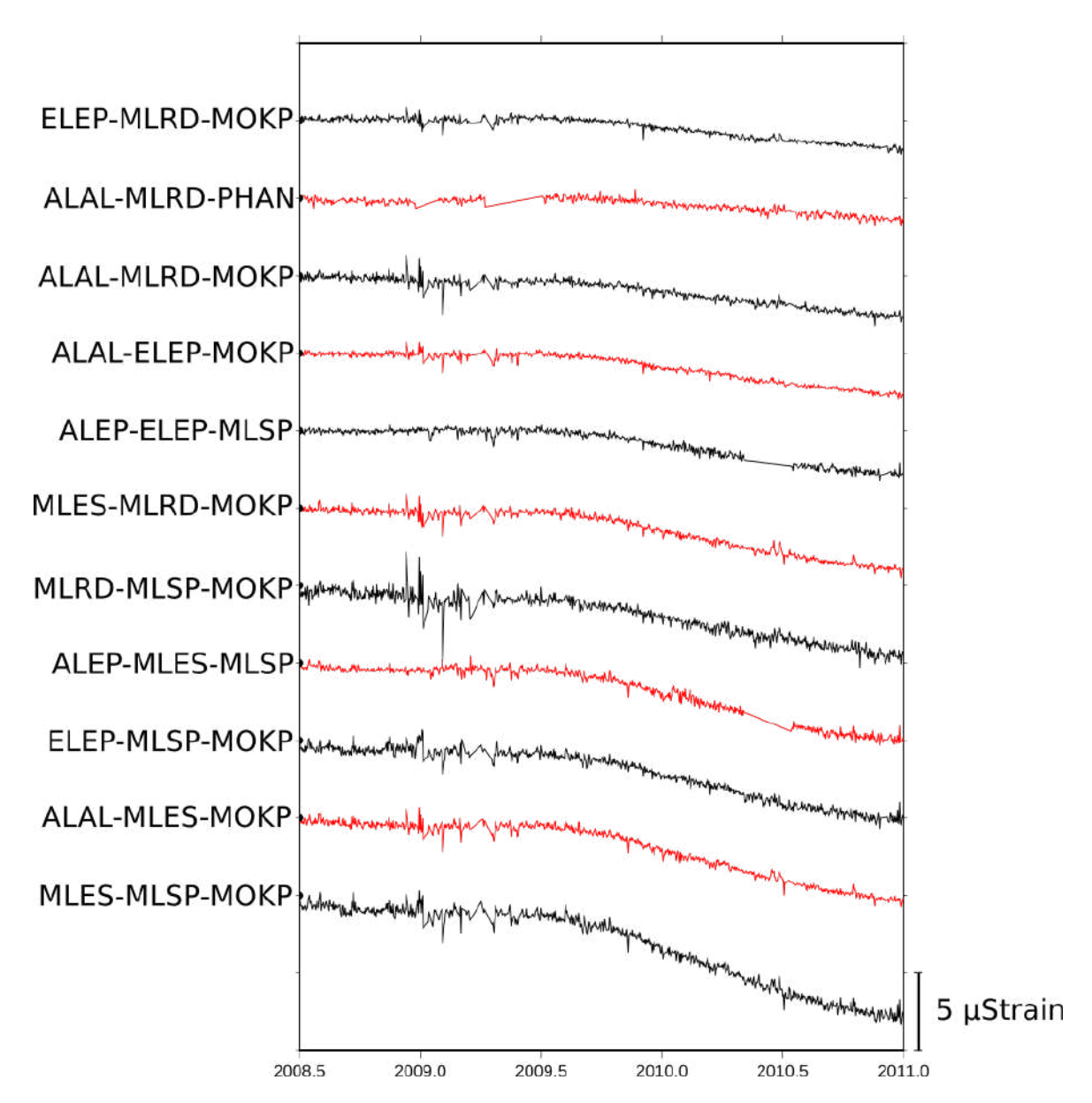


Figure 8.8 Areal strain time series for Mauna Loa GPS stations. The labels are triplets of GPS stations surrounding the summit cone of Moku \Box āweoweo Caldera (see Figure S2 for locations). The y-axis on the right shows the aerial strain scale in μ strain, the dimension of the vertical axis is 5 μ strain, Time series colours are alternated in black and red.

8.4 Methods

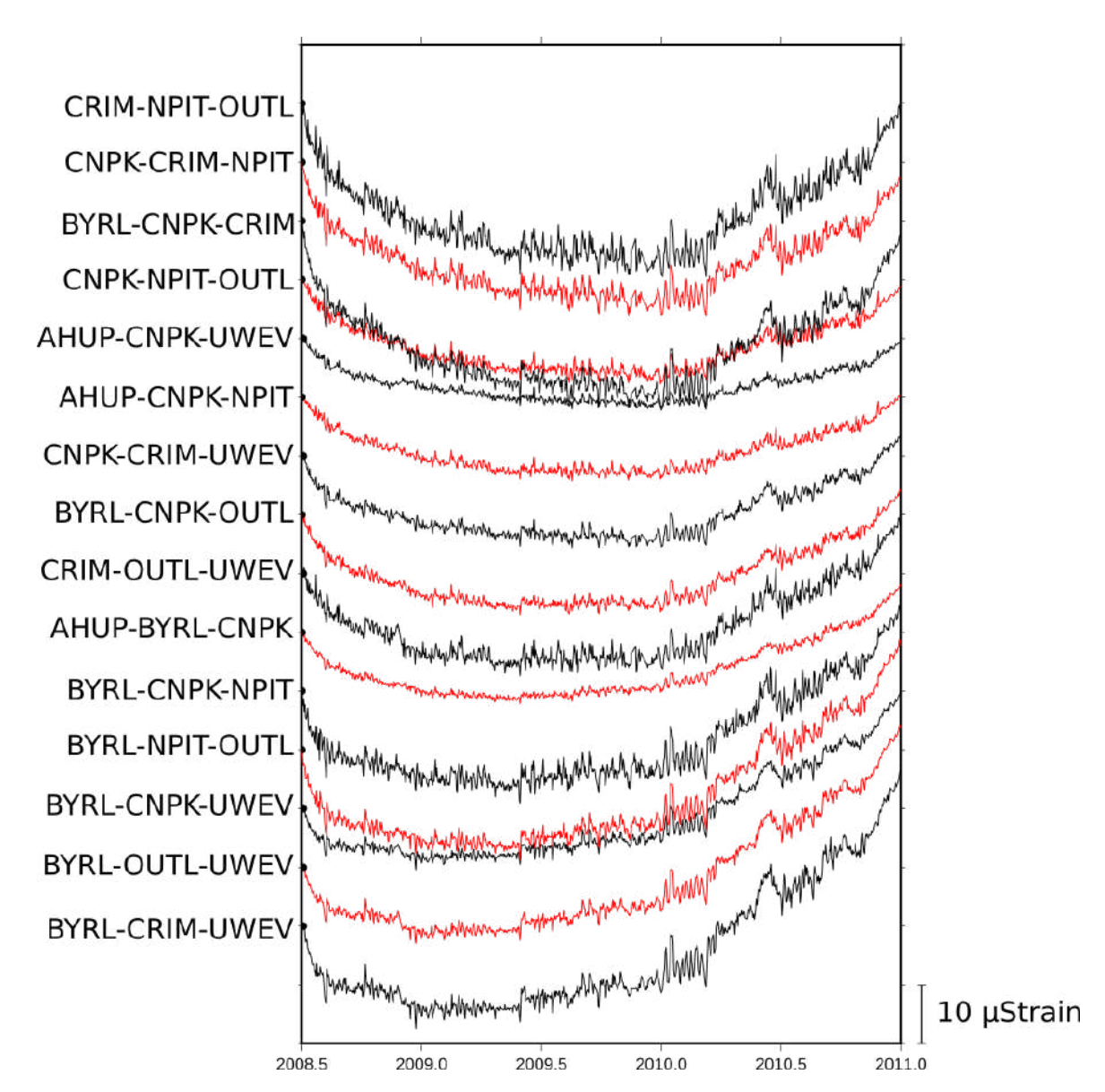


Figure 8.9 Areal strain time series for Kīlauea GPS stations. The labels are triplets of GPS stations surrounding the summit cone of Halema \Box uma \Box u Crater (see Figure S2 for the locations). The y-axis on the right shows the aerial strain scale in μ strain, the dimension of the vertical axis is 10 μ strain, being marked by ticks. Note that the axis scale in this figure is different from that of Figure 8.8. Time series colours are alternated in black and red.

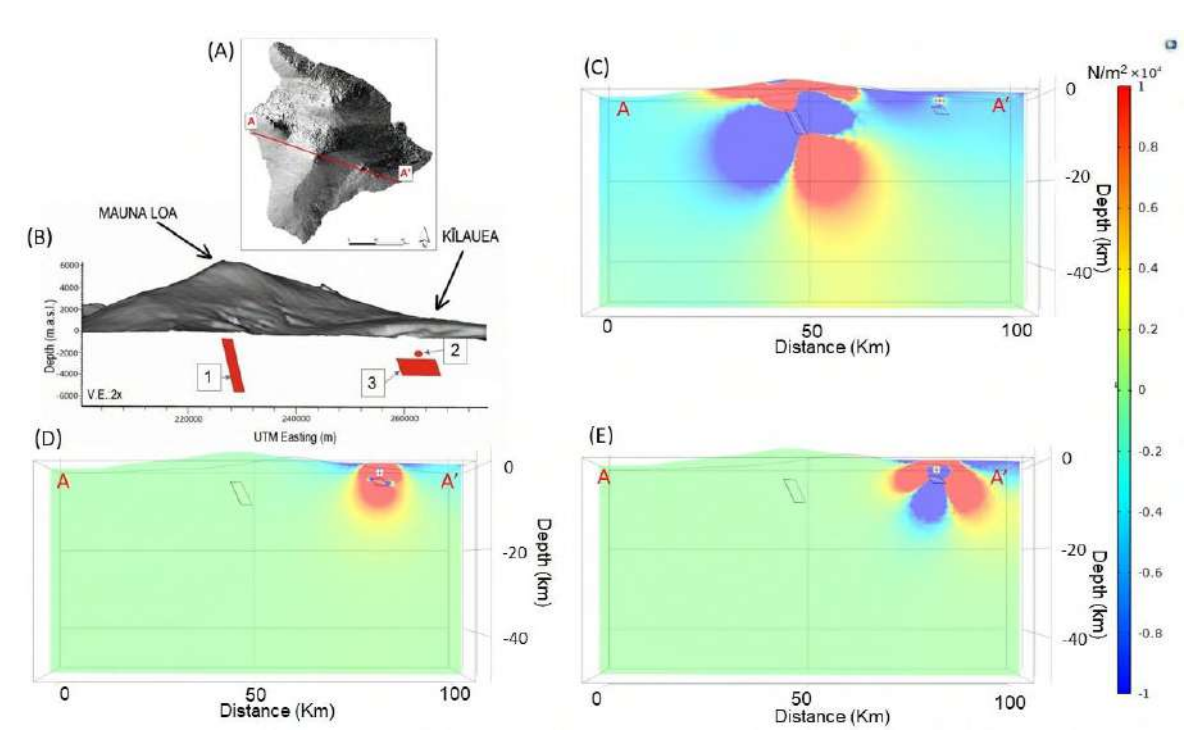


Figure 8.10 3D numerical modelling of stress fields. (A) The Digital Elevation Model of Hawai'i Island, with the red line representing the trace (A-A'), used in panels (C-E). (B) tridimensional representation of the modelled ground deformation sources of Mauna Loa and Kīlauea volcanoes. The sources are numbered according to Table S1 in the supplementary material. 1) the Mauna Loa dikeshaped source from ICA1; 2) the Kīlauea Mogi-like source from ICA1; 3) the Kīlauea sill-shaped source from ICA2. Storage areas and topography are exaggerated in size for clarity. (C) stress field represented along the A-A' trace due to an overpressure applied to the Mauna Loa dike-like source. (D) stress field along the A-A' trace due to an overpressure applied to the Kīlauea Mogi-like source. (E) stress field along the A-A' trace due to an overpressure applied to the Kīlauea sill-like source.

Chapter 9

Geodetic imaging of magma ascent through a bent and twisted dike during the Tajogaite eruption of 2021 (La Palma, Canary Islands)

Przeor, M., Castaldo, R., D'Auria, L., Pepe, A., Pepe, S., Sagiya, T., Solaro, G., Tizzani, P., Barrancos J., and Pérez, N. (2024). Geodetic imaging of magma ascent through a bent and twisted dike during the Tajogaite eruption of 2021 (La Palma, Canary Islands). Scientific Reports, 14(1), 212.

9.1 Introduction

The Canary Islands are located off the northwest coast of Africa, 150 km from the African coastline (Fig. 9.1). The Canaries originated in the intraplate region of the African plate and extend along a 500 km wide alignment from East to West, in the framework of -13°W and -18°W longitudes and 27°N and 30°N latitudes. The formation of the Canaries started in the Oligocene and is still in process [76, 77]. The most ancient islands are Fuerteventura and Lanzarote, the easternmost located of all Archipelago. Its formation continued with the direction to the West, being the most recent islands of El Hierro and La Palma.

La Palma Island formation started in the Pliocene, 4 My ago, as a seamount sequence that lasted about 1 My [77]. Between 3 and 2 My, the island emerged from the ocean, and a rapid elevation of the island caused the giant landslide. The subsequent formation of the Garafía Edifice and Taburiente Domain was also interrupted by a gravitational landslide. The formation of the Cumbre Nueva Domain was centred on the South of the Taburiente Domain.

Consequently, the Cumbre Vieja Domain started its formation 0.123 My ago [77]. This N-S volcanic ridge is still active and hosted all the historical eruptions of the island of La Palma. The latest

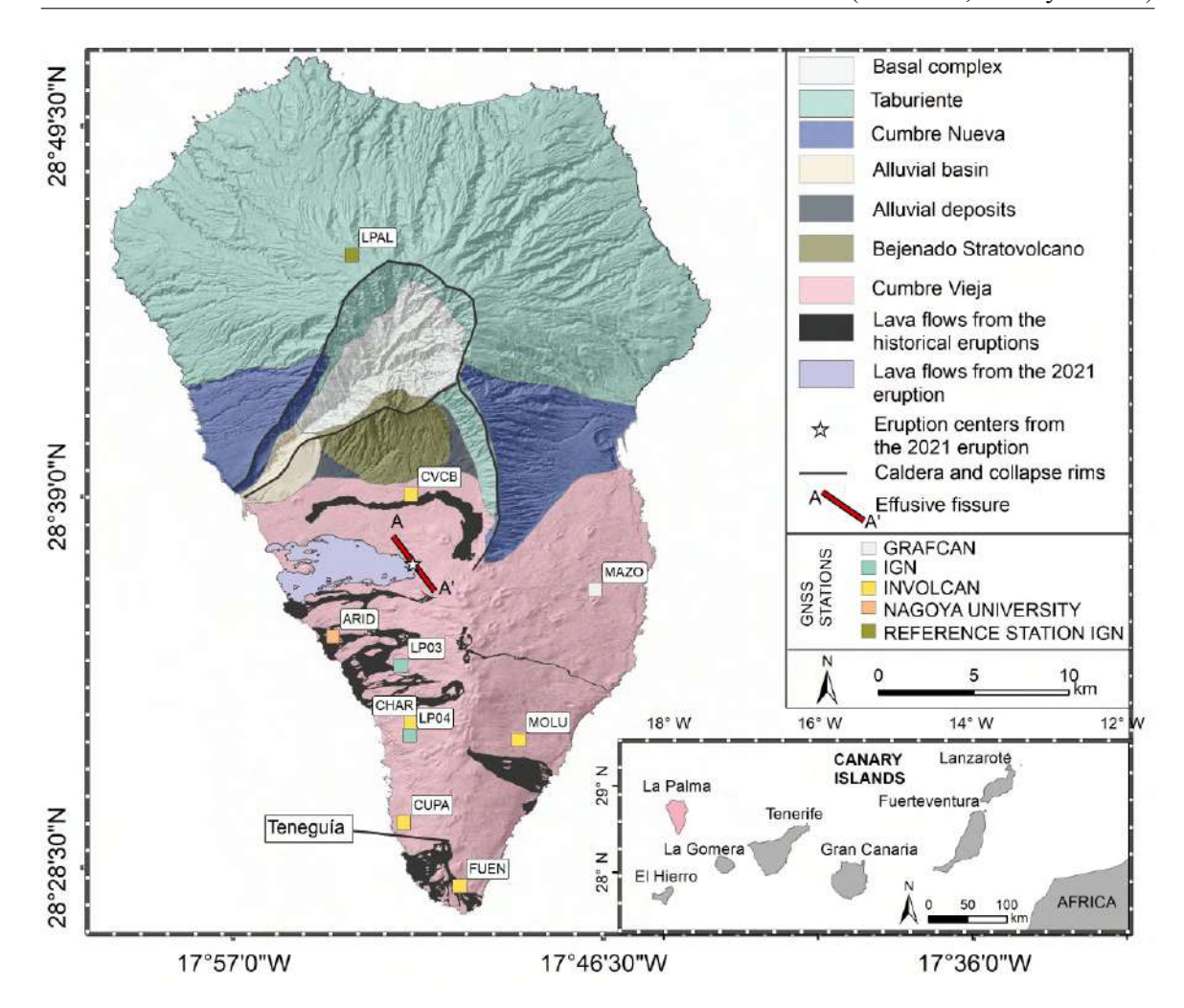


Figure 9.1 The geological map and the GNSS permanent stations location of La Palma. The lower right-hand side panel shows the location of the island of La Palma (in red) within the Canaries. The legend explains the meaning of the colour shades on the map and the GNSS station. The NW–SE alignment of the effusive fissure of the 2021 eruption is represented by the red line (A–A').

eruption in La Palma in the past century (Teneguía eruption of 1971) emerged in the southernmost part of the island (Fig. 9.1).

On Sept. 19th, 2021, in the N.W. of the Cumbre Vieja ridge, a new volcanic eruption on the island started and lasted 85 days [78]. The eruption's consequences (gas emissions, a large volume of lava flows, and tephra dispersion) resulted in one fatality due to indirect causes and enormous economic and social losses [79]. The volcanic precursors, like ground deformation, seismicity, and gas emissions, were noticed eight days before the eruption onset [78]. The permanent volcano monitoring stations of Instituto Volcanológico de Canarias (INVOLCAN) assessed the ground deformation and the pre-eruptive seismicity migration. The Global Navigation Satellite System (GNSS), the Sentinel-1 (S-1) satellite constellation, and seismic stations collected the data of the pre-and early-eruptive phases used in the present study. The first evidence of the magmatic intrusion began on Sept. 11th

[78, 80], with a seismic swarm of volcano-tectonic character, with a depth of 10 km or less. The upward migration of the hypocenters lasted only eight days until magma emerged to the surface. Considerable ground deformation appeared on continuous GNSS (cGNSS) stations of INVOLCAN on Sept. 12th and continued increasing to reach its maximum three days after the eruption onset.

This study analyses magmatic and hydrothermal sources that caused the pre-eruptive ground deformation in La Palma. To this aim, we processed a sequence of Synthetic Aperture Radar (SAR) images collected by the Sentinel-1 (A and B) satellites from January to November 2021. We used the multi-temporal differential interferometric SAR (DInSAR) and Small Baseline Subset (SBAS) method6. Subsequently, we analysed the InSAR-driven ground displacement measurements and the available cGNSS dataset from Sept. 8th until Sept. 28th, 2021. Accordingly, we performed a preliminary non-linear inversion to determine the dip of the shallow part of the dike. The geometry of the deeper part has been constrained by using the relocated hypocenters of D'Auria et al. [78]. Later on, following D'Auria et al. [81] and Pepe et al. [43], we applied the Geodetic Imaging technique to the DInSAR and cGNSS datasets to understand the ascent path of magma and the spatiotemporal dike aperture kinematics.

Previous studies evidenced the importance of advanced modelling of the ground deformation sources to understand the dynamics of a magmatic plumbing system [81, 43, 23, 82, 83]. The results of this study are supported by previous studies about local earthquake seismic tomography (LET) of La Palma [78], Ambient Noise Tomography (ANT) [84], deformation inverse modelling [82, 83], petrological studies [85] and gravity surveys by Montesinos et al.[86].

In this study, we denote the eight days preceding the eruption as the pre-eruptive phase and the dates between Sept. 19th and 28th as the early-eruptive phase. Geodetic imaging proved to be an effective tool for understanding and visualising the complex magmatic ascent process on La Palma island during both phases.

9.2 Results

9.2.1 Preliminary non-linear inversion and dike geometry

Based on the results of previous studies [82], we assume that the shallow part of the conduit consists of a southwestward dipping dike. Therefore, we performed a non-linear inverse modelling to constrain the dip of this shallow part of the conduit (see the Methods section for more details). Figures B.1 and B.2 in the supplementary materials represent the data, the model, and the residuals for each displacement map for both orbits.

We modelled the source using a simple rectangular dike geometry 15, constraining the azimuth (125°), following the surface orientation of the eruptive fissures (Fig. 9.1) [87]. The retrieved best-fit value of the dip was 50° westward. The location and the geometry of the shallow dike have been adjusted to one of two shallow seismicity clusters corresponding to the dike ascent. However, the second shallow seismicity cluster is unrelated to the dike intrusion process. Previous studies [78,

80] demonstrated that it is related to hydrothermal activity triggered by the fluids released by the ascending magma. It is located to the South of the eruptive vents, and it is not relevant for modelling the dike geometry (Fig. 9.2).

However, this shallow dike alone cannot accurately describe the pre-eruptive intrusion process. The 3D pre-eruptive seismicity pattern3 shows a north-westward and upward migration of the hypocenters until Sept. 18th. This suggests that the lower part of the dike generated by the magmatic intrusion, starting at about 10 km depth, has an eastward dip. Therefore, a curved dike is a more appropriate geometry for the ground deformation source. To model the geometry of the lower part of the dike, we performed a geometrical fit with the hypocenters distribution using a simple rectangular geometry. The best-fit azimuth and dip are respectively 89° and 67° southward.

The final geometry results from merging these two dikes at a depth of about 3 km. This depth was selected based on the earthquake distribution, which shows a different trend starting from this depth [78]. The resulting geometry is that of a bent and twisted dike schematically shown in Figure 9.2.

9.2.2 Geodetic imaging

Using the dike geometry described in the previous section and applying the geodetic imaging technique described in section 5.4, we obtained a spatiotemporal imaging of the dike opening function. In the following, we describe in detail this result by showing both the absolute opening function (i.e., relative to the first image) and the differential one (i.e., relative to the previous image) (Figs. ??). For clarity, the dike opening function is shown on a 2D image. In each image, we also show the projection of all the earthquake hypocenters (represented with black dots) recorded between 11th and 28th Sept. 2021, while the earthquakes recorded between each image and the previous one are represented with green dots.

There is no visible deformation in the first two images of both orbits (Sept. 8th and 10th) (Fig. 9.3A-D). Until Sept. 11th, neither seismicity indicated relevant magma movement at depth.

Between Sept. 11th and 14th, the most relevant precursor of the approaching eruption was the north-westward and upward migration of the seismicity starting from a depth of about 10 km [78]. The ground deformation began to be significant on Sept. 14th, reflecting magma accumulation at a depth between 6 and 8 km (see R1 in Fig. 9.4A). The seismicity comprised two clusters located between 6 and 10 km. The first one, denoted S1, connects R1 with the magma chamber, located at more than 10 km depth by the local earthquake tomography3. The second cluster, S2, corresponds to the location of the magma accumulation zone in R1 (see Figure 9.4A). The dike opening marked with the R2 is located along the primary magma pathway toward the surface. Conversely, the R3 is situated to the SW of the primary pathway, between 3 and 6 km depth.

The descending orbit from Sept. 16th shows that the dike opening R1 increased its magnitude and extends in depth between 5 and 8 km, with an approximate width of about 3 km (Figs. 9.4C-D). The R2 accumulation zone also increases its magnitude and area, reaching a diameter of approximately

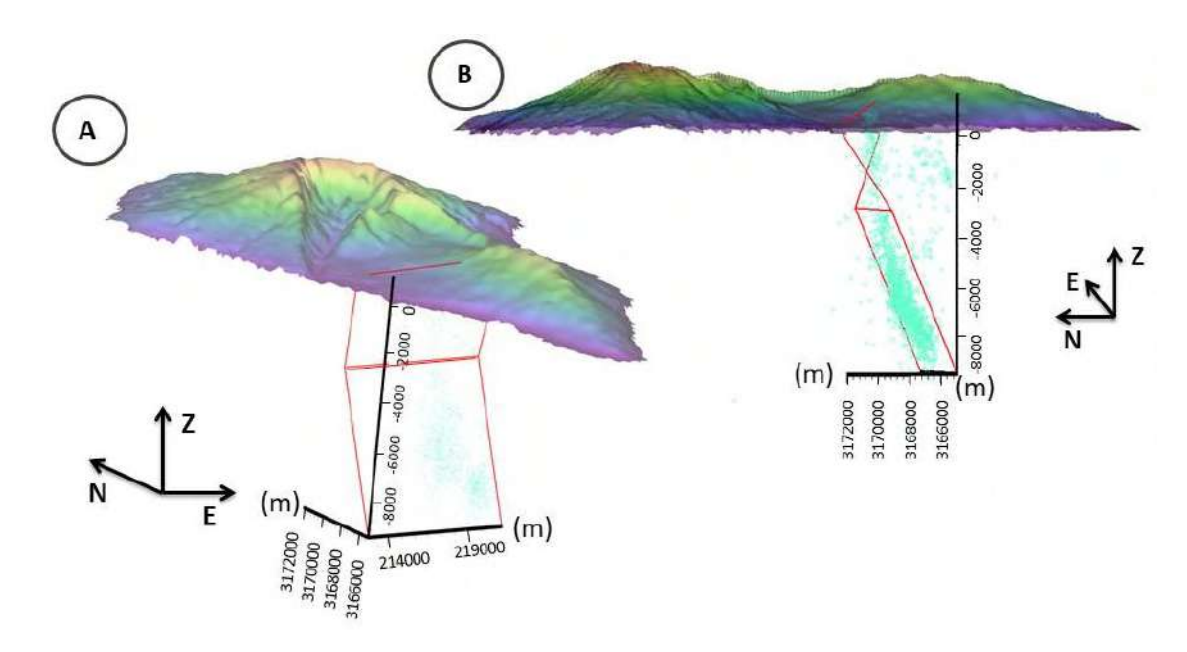


Figure 9.2 Tridimensional representation of the dike geometry and the topography of La Palma island. Panel A is a view from S.W., while B is from W. Earthquake hypocenters are represented as cyan circles. The axes are represented in meters (m).

2 km. The magma ascent was associated with a new cluster of seismicity migrating upward from S2 to S3. In this interval, we also observe a sparse, shallow cluster located between 0 and 3 km depth, represented by S4. The location of this cluster is spatially separated from the main seismicity related to the dike intrusion process [78, 84].

On Sept. 20th, one day after the beginning of the eruption, the previously observed accumulation zones R1 and R2 merged, forming a single accumulation zone extending between 3 and 9 km, with a width of about 3 km, indicated as R4 in Figure 9.5. The seismic cluster S5 is shallower than the previous ones, extended from the surface until 6 km depth. In this image, we can also observe a shallow magma accumulation zone (R5 in Fig. 9.5), which extends between 0 and 2 km depth with a width of about 1 km and coincides with the location of the eruptive vent. We also observe an increase in the dike aperture of the accumulation zone R3 located at a depth between 3 and 4 km.

Since the beginning of the eruption, the strong volcanic tremor prevented the detection of low-magnitude seismicity [78]. However, on Sept. 22nd, the seismicity was mainly located at a shallow depth between 0 and 2 km, which is denoted as S6 in Figure 9.5. At the same time, the accumulation zone R4 shows a marked change, with a decrease in the dike opening in the lower part and an increase in the upper part (see R4A and R4B in Fig. 9.5D). We also observe a decrease in the opening in the R3 zone. We also observe the appearance of a new accumulation zone (R6), between 2 and 4 km, located right above R3 (Fig. 9.5C-D).

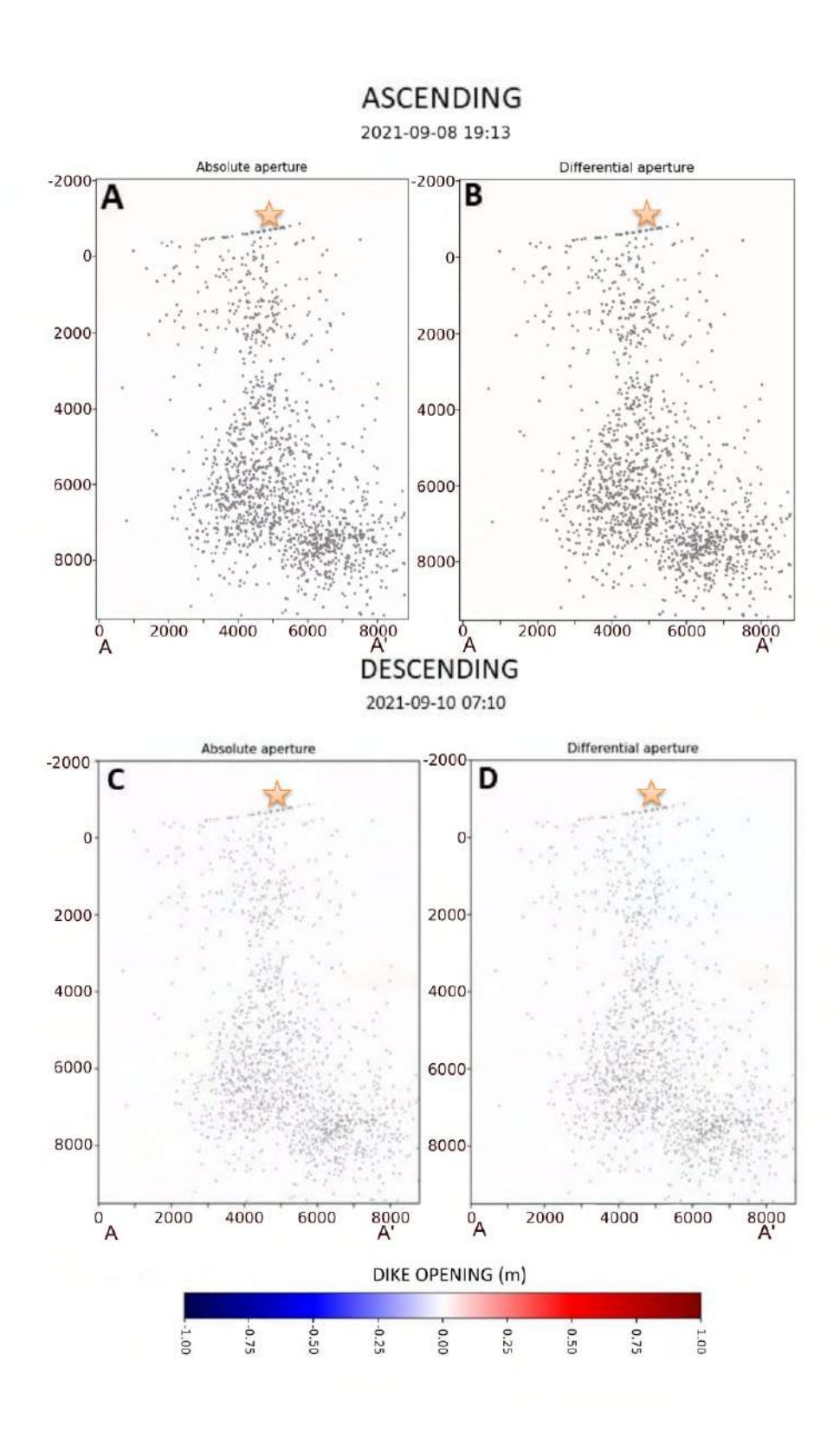


Figure 9.3 Distribution of absolute and differential dike opening for the 8th (ascending orbit) and Sept. 10th 2021 (descending orbit). Grey dots represent the projection on the dike of all the seismic events located between Sept. 11th and 28th. The seismic events colour in the images of Sept. 8th is represented with dark grey in order to highlight the total of earthquakes produced in the analysed period. Orange stars indicate the future location of the main eruptive vent.

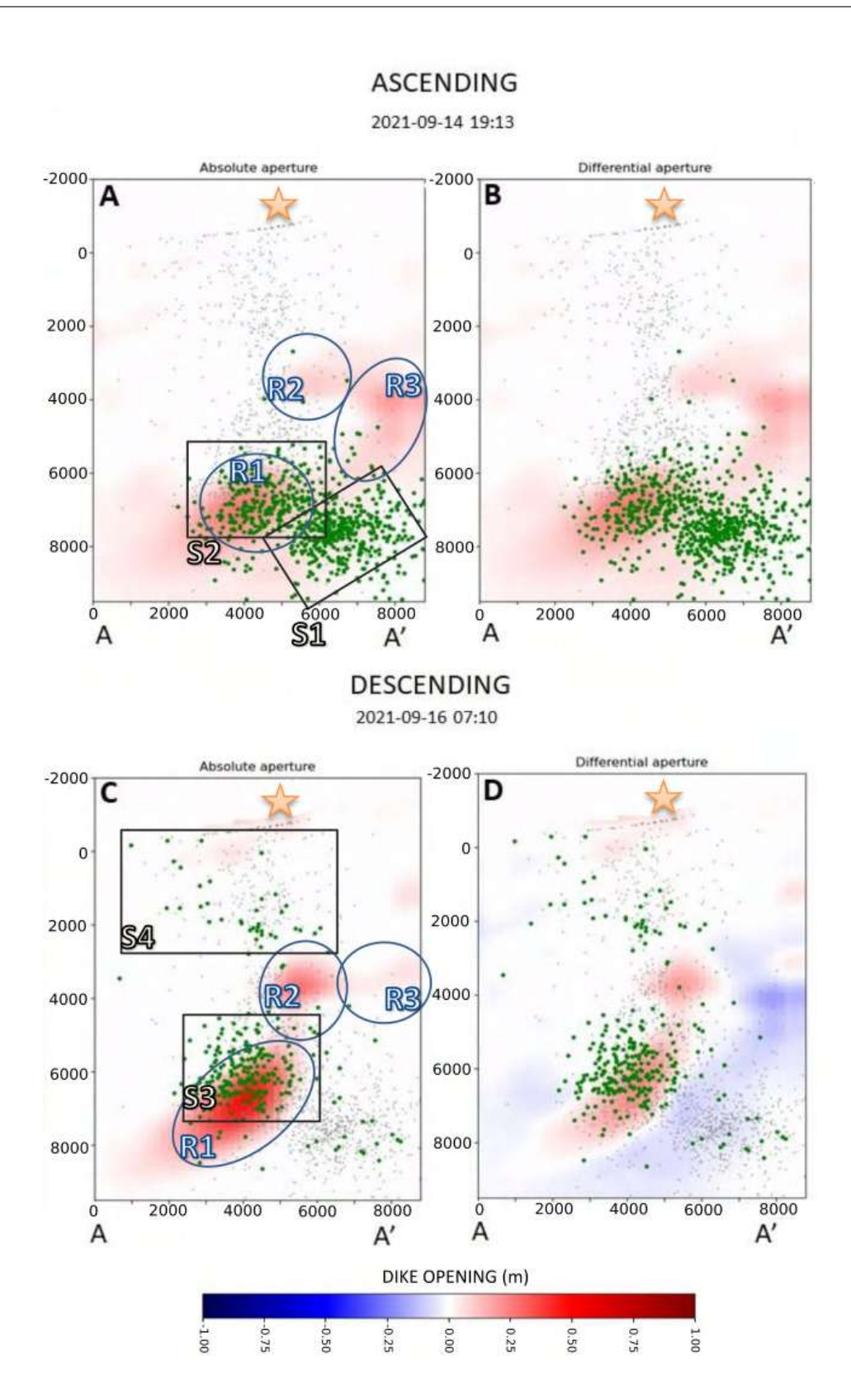


Figure 9.4 Distribution of absolute and differential dike opening for the 14th (ascending orbit) and Sept. 16th 2021 (descending orbit). Grey dots represent the projection on the dike of all the seismic events located between Sept. 11th and 28th, while green dots represent seismic events that occurred between two successive images. Blue ellipsoids and black squares represent, respectively, the features in the dike opening function and the clusters of seismic events discussed in the text. Orange stars indicate the future location of the main eruptive vent.

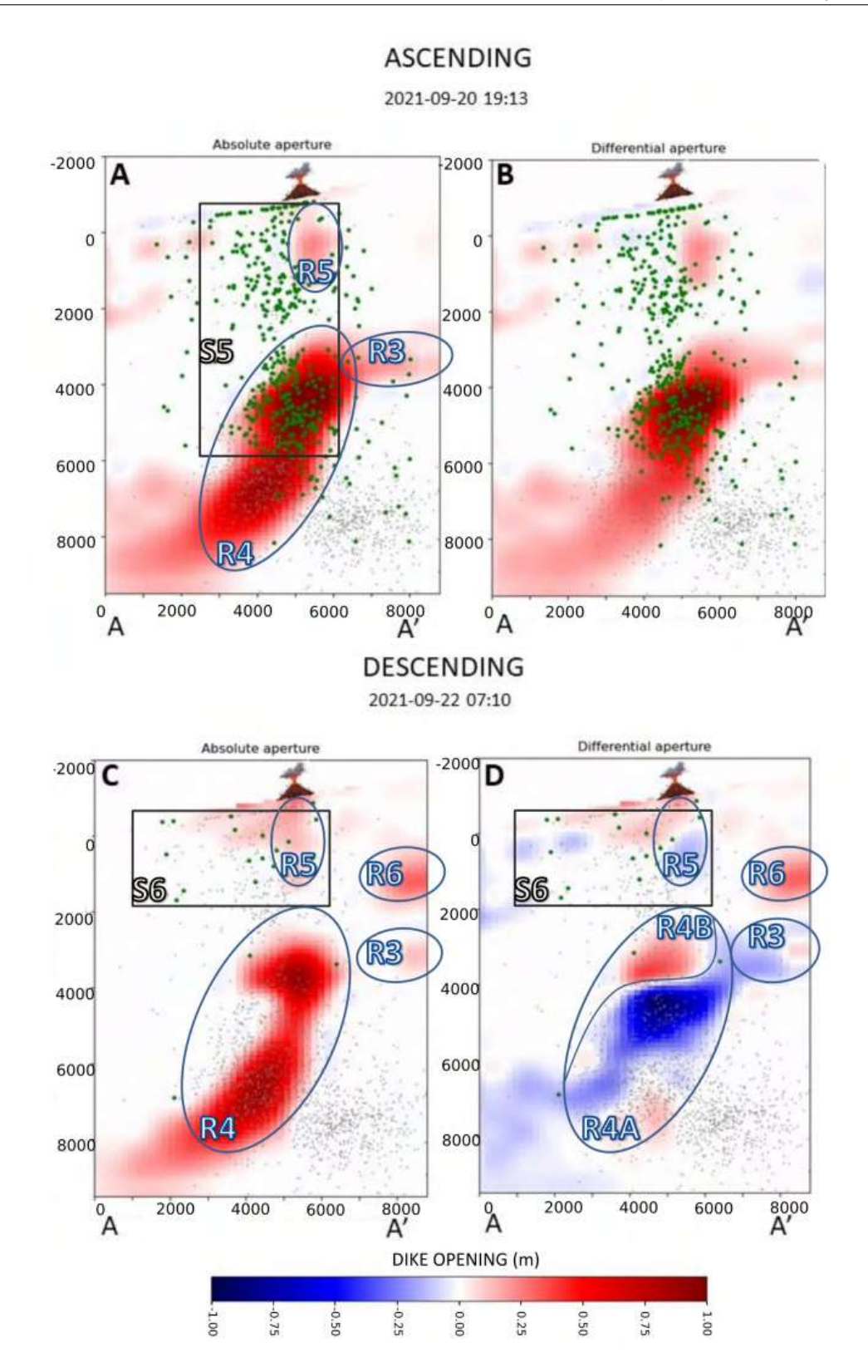


Figure 9.5 Distribution of absolute and differential dike opening for the 20th (ascending orbit) and Sept. 22nd, 2021 (descending orbit). The volcano symbol indicates the position of the main eruptive vent.

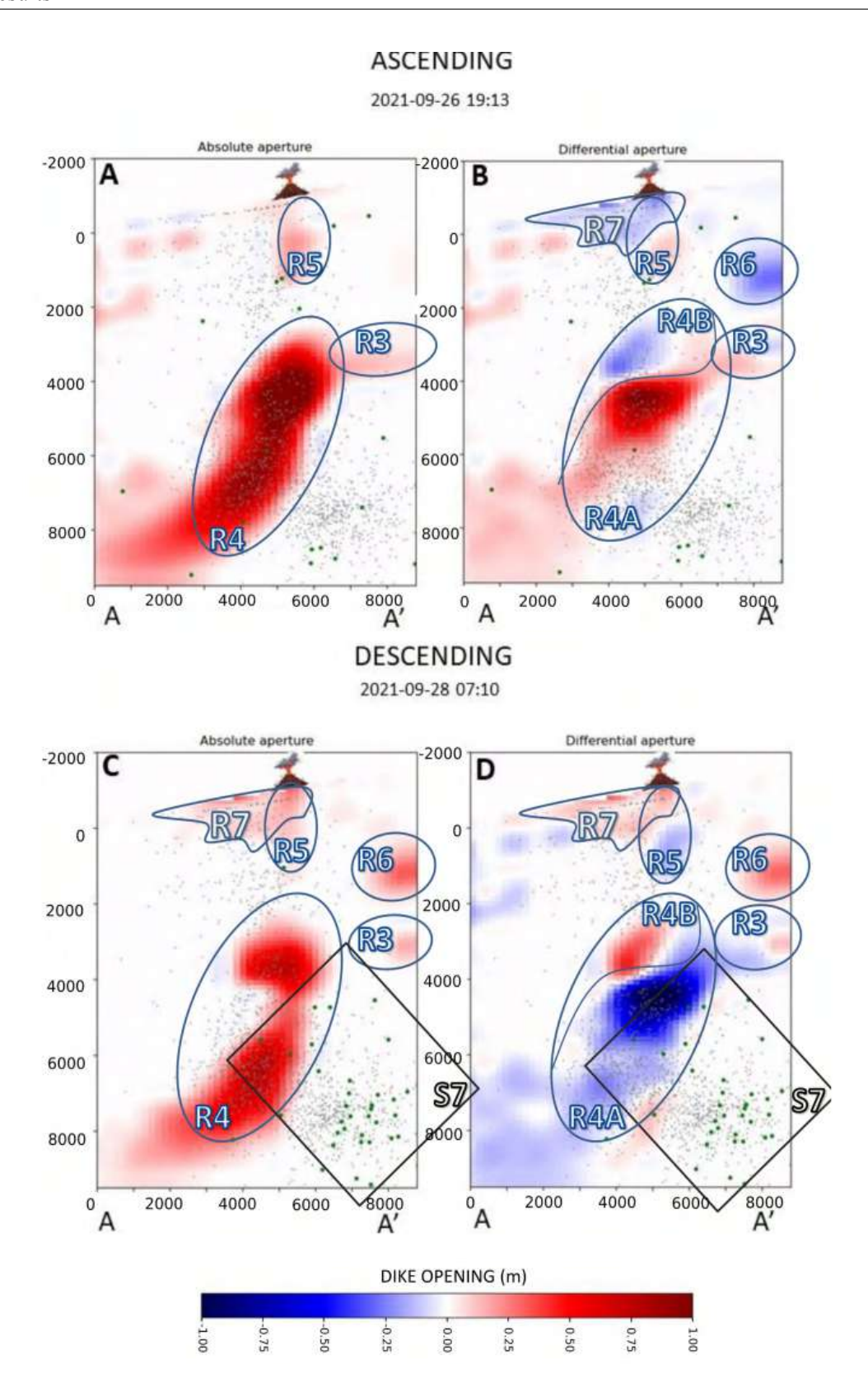


Figure 9.6 Distribution of absolute and differential dike opening for the 26th (ascending orbit) and Sept. 28th, 2021 (descending orbit). The meaning of the symbols is the same as in Fig. 9.5

In the image of Sept. 26th, we observe a marked decrease in the dike opening right beneath the vent (R7 in Fig. 9.6). The zone R4 shows a reversal in its behaviour, with replenishment of its lower part. Analogously, the zones R3 and R6 show a similar reversal.

On Sept. 28th, we observed a renewed increase in the magnitude of R7, R6, and R3. The zone R4 shows a deflation, except for its upper part, and a significant reduction in width. On this date, we also observed the appearance of a deeper seismicity, located mainly below 6 km depth (Fig. 9.6C-D).

9.3 Discussion

The complex dike geometry depicted in this work results from a joint analysis of geodetic and seismic data. A straightforward evidence that the geometry we depicted is realistic comes from the time series of horizontal cumulative displacement of the ARID station (see supplementary Fig. B.14). It can be seen that until Sept. 18th, the displacement is mainly toward the W. After it changes abruptly to SW because the magma reached the upper part of the conduit, having a different orientation.

Different factors can affect the propagation of dikes: the stress field, the mechanical properties of the rocks, and the buoyancy of the magma [88]. First, we notice that the dike bends around a high-velocity body identified by the seismic tomography model of D'Auria et al. [78]. This can explain the north-westward migration of the intrusion during the pre-eruptive phase. The subsequent deviation toward the East and the development of its twisted geometry can be explained, taking into account the internal stress field of the volcano. Following Dahm et al. [89] and Maccaferri et al. [90], gravitational loads make magmatic intrusions move towards higher topography zones. In the case of La Palma, the highest altitudes are located along the N-S dorsal of the Cumbre Vieja domain (Fig. 9.1). Therefore, the eastward bending is compatible with the effect of gravitational loads due to the topography of the volcano. Actually, the majority of the historical and prehistoric vents of Cumbre Vieja are located close to the summit of the ridge1.

The geodetic imaging results (Figs. ??) give a detailed overview of the kinematics of the magma movement within the dike and its relationship with seismicity. In Figure 9.7, we represent, with a schematic cartoon, our interpretation of this process on some key dates. Our study reveals that the magma started accumulating beneath the Cumbre Vieja volcano at a depth of 6-8 km (zone R1 in Fig. 9.4) at least five days before the eruption (Sept. 14th). The simultaneous seismicity, occurring between 7 and 10 km (S1 in Fig. 9.4), possibly reflects the nucleation of the dike from the huge magma chamber, identified by D'Auria et al. [78], beneath 10 km depth. On the other hand, the cluster S2 can be related to the local stress field perturbed by the accumulation of magma within the zone R1 (Fig. 9.7A). At the same time, the zones R2 and R3 seem to evidence a further minor accumulation zone beneath 4 km depth (Figs. 9.4A and 9.7A). Considering previous studies concerning the internal structure of La Palma [91, 92, 78], we know that the first few km of the crust beneath Cumbre Vieja is characterised by low seismic velocities corresponding to low resistivity and low-density values. As discussed by Rivalta et al.17 [88], the presence of crustal layering can significantly affect the dike propagation speed. We postulate that the different rheology of the first few

km caused a temporary decrease in the dike ascent rate, causing the local accumulation in R2 and R3 (Figs. 9.4A and 9.7A).

The seismicity focused on two clusters on Sept. 16th (see Figs. 9.4C and 9.7B). The deeper one (S3) occurred between 4 and 7 km deep and is located atop the accumulation zone R1. This cluster possibly reflected the pressurisation of R1 and the upward propagation of the crack tip. At the same time, we observe an increase in the dike opening in R2 and R3, which we interpret as the transfer of magma toward a blind lateral branch of the main dike (Fig. 9.7B). Conversely, cluster S4 does not seem to be directly associated with a magmatic process. Following Cabrera-Pérez et al. [84], we interpret this cluster as related to the ascent of the hydrothermal fluids exalted from the magma itself that generated the pressurisation of a shallow hydrothermal system. The presence of this hydrothermal system has already been highlighted by previous studies [92, 93, 78]. Furthermore, the study of Pankhurst et al. [85] revealed that the first stages of the eruption presented more hydrated minerals, meaning that the ascending magma was fluid-rich.

The image of Sept. 20th is the first after the beginning of the eruption. The dike opening function clearly shows the opening of the pathway toward the eruptive vent (zone R5 in Figs. 9.5 and 9.7C). The seismicity pattern indicates that the magma approached the surface very quickly during the morning of Sept. 19th [78]. This rapid acceleration in the magma ascent rate when approaching the surface has been studied by Rivalta and Dahm [94], which explained the physical mechanism of this process in terms of depth-dependent fracture toughness. The secondary blind branch R3 in the southeastern direction of the main dike was also increasing its aperture. As mentioned before, we believe this branch stopped its upward movement by a rheological boundary. Secondary branches departing from the main magmatic reservoir were also observed by Fernández et al. [83]. Their model shows two branches of magma that appeared due to zones of structural weakness in the crust. Montesinos et al. [86], using gravity data, showed the possible appearance of a blind magma ascent path in the Jedey zone that could coincide with the R3 branch found in the present study. Also, the observed secondary branch R3 was possibly linked to the sill-like source mentioned by De Luca et al. [82]. Also, Muñoz et al. [87] suggest that the dike developed multiple paths that could not reach the surface due to complex factors.

The main changes observed in the image of Sept. 22nd are the appearance of a further lateral branch (R6 in Figs. 9.5 and 9.7D) and a change in the magma distribution within the main feeding conduit R4 (Fig. 9.5D). We also observe the persistence of the lateral branch R3 (Figs. 9.5D and 9.7D).

Between Sept. 22nd and 26th, there was a visible reduction in the dike opening in the shallow part of the conduit (Figs. 9.6 and 7E). On Sept. 27th, a temporal stop of the eruptive activity was observed, associated with a marked drop in the volcanic tremor amplitude lasting about 10h [78, 95, 96]. The reduction observed in the image of Sept. 26th may be a precursor of the partial conduit collapse, which caused the temporary stoppage of volcanic activity the next day. Also, the shallower part of the main magmatic conduit (R4B) and secondary branch R6 shows a reduction possibly related to the lack of magma in the portion of the conduit located above 4 km depth.

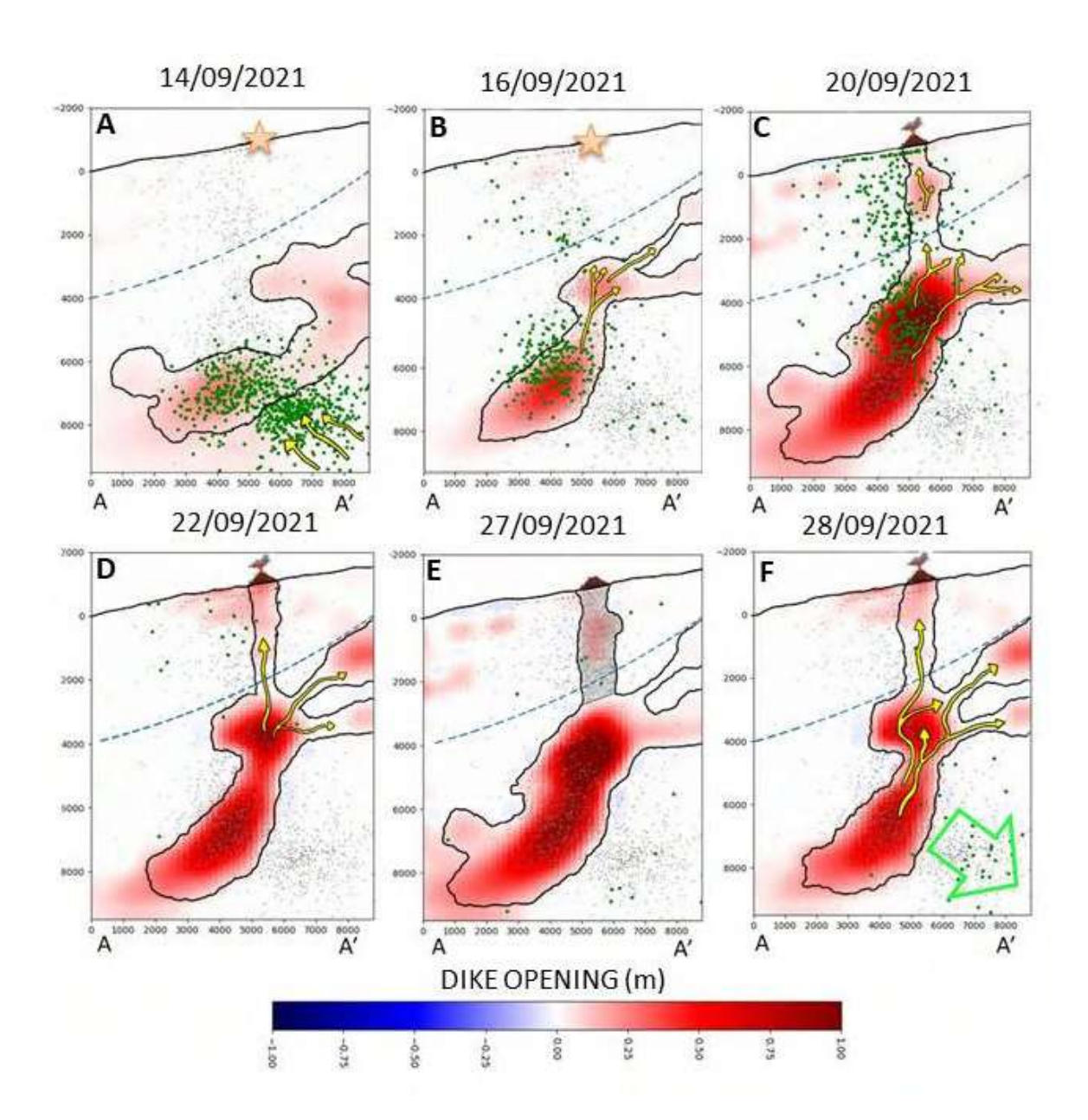


Figure 9.7 Schematic model of the plumbing system dynamics for key dates. Orange stars represent the location of the future site of the volcanic vent in the days preceding the eruption. The symbols of the volcano represent the location of the actual volcanic vent. Yellow arrows represent the magma ascent directions, while the green arrow indicates the incipient collapse of the magma reservoir. The blue dashed lines represent the limit of the rheological boundary discussed in the text.

The eruptive activity resumed in the afternoon of Sept. 27th. The image of Sept. 28th shows a dike aperture similar to Sept. 22nd, indicating that the primary process of the magma accumulation in the shallow crust went back to the initial scenario. However, as shown by Pankhurst et al. [85], the magma erupted after Sept. 27th proceeded from a deeper reservoir, as testified by petrological analysis. Therefore, we believe that the renewed eruptive activity was driven by the arrival of a new magmatic batch with a more primitive composition. This also agrees with the appearance of a new seismic cluster (S7 in Fig. 9.6C-D), which has been interpreted by D'Auria et al. [78] as the effect of the collapse of a magmatic reservoir located below 10 km depth because of its emptying due to the withdrawal of magma.

The modelling of the ground deformation source associated with the 2021 Cumbre Vieja eruption has already been analysed in previous studies, although using different approaches. In the following, we remark on the similarities and differences between their findings compared with the results of our study. De Luca et al. [82] used a combination of elementary sources to perform a static imaging of the plumbing system. We used a complex geometry, using finite-element modelling, to image the spatio-temporal evolution of the plumbing system before and during the earliest phases of the eruption. De Luca et al. [82] showed the existence of the sill-like source during the pre-eruptive phase and the presence of two dike-like sources active during the co-eruptive phases. The sill-like source was located at the 4675 m depth b.s.l. and was active between the 8th and 16th of September, corresponding mainly to the temporary accumulation of magma in its path towards the surface. This sill proposed by De Luca et al. [82] can be well explained by one of the lateral blind branches resulting from our inversion. Secondly, in the co-eruptive phase, they found evidence that the shallow magmatic plumbing system feeding the eruption was composed of two dikes and sills interconnected to the main reservoir, as also evidenced by the present study with the interconnection of the dike to the lateral branches during the pre- and early-eruptive phases. Their models encompass the 10 km depth limit, as well as the model presented in this study. However, De Luca et al. [82] only provided a static model of the ground deformation source, although the overall dike opening they retrieved matches pretty well with our image of Sept. 22nd (Fig. 9.5).

Conversely, Fernández et al. [83] analysed the spatiotemporal evolution of the ground deformation source. However, they used a completely different modelling approach based on an improved version of the 3D multisource modelling algorithm of Camacho et al. [91], which approximates the ground deformation sources as a combination of elementary pressure and fault slip sources. We believe this approach to be not entirely appropriate with volcanological observations of the Tajogaite eruption, which clearly evidenced a dike as the most likely geometry, at least for the shallow plumbing system. Therefore, in our approach, we tried to reproduce a physically realistic geometry and mechanism for the causative source of ground deformation. Also, their model evidences the deep source southward to the eruptive vent, as evidenced by the models presented in this study.

Additionally, we found the beginning of the deformation process related to the magmatic intrusion on Sept. 12th, while Fernández et al. [83] found evidence of magma accumulation that started in May of 2021. However, their overall results are in agreement with our findings, especially concerning the

presence of lateral branches in the plumbing system. Additionally, our approach allowed a direct computation of the dike opening function and established its temporal and spatial relationship with the seismicity.

Montesinos et al. [86] used gravimetric and GNSS data acquired before and after the eruption and took into account the pre-eruptive seismicity to constrain the geometry of the plumbing system. They determined a complex geometry of the feeding system composed of interconnected dikes and sills. Their model also evidences the presence of a lateral blind branch of the plumbing system. Furthermore, they highlighted the temporary ascent of the magma on Sept. 14th due to the presence of horizontal layering within the crust.

To assess the reliability of our findings, we performed several checkerboards and tests over the synthetic dataset. In Figures B.3, B.4, B.5, and B.6 in the supplementary material, we represent the checkerboard test results for different spatial resolutions. We notice that our dataset is able to resolve anomalies of about 1 km size until a depth of 2 km (Fig. B.3 in the supplementary material), anomalies of 2 km until about 4 km depth (Fig. B.4 in the supplementary material), anomalies of 5 km along the whole model, until a depth of 10 km (Fig. B.6 in the supplementary material). This confirms that our model is able to resolve the features described above. Furthermore, we conducted some additional synthetic tests to understand the limitations of our approach better. In Figure B.7 of the supplementary material, we see that, except for the lower left corner, our inverse method is able to detect the presence of magma along the whole domain. However, in Figures B.8 and B.9 of the supplementary material, we observe a clear decrease in the spatial resolution at depth. This may justify the lack of evidence of the connection between the main magma conduit (R4) and the deeper magma chamber. Finally, in Figure B.10 of the supplementary material, we perform a synthetic test over a realistic geometry of the magmatic system, showing that our inverse model is able to retrieve all the relevant features.

We also need to mention, that the difference in the acquisition geometry between ascending and descending orbits can slightly affect the results. Actually, some of the minor variations observed in the differential dike aperture models can be artefacts related to this effect.

9.4 Data and Methods

9.4.1 Data and processing of GNSS time series

In this work, we used the permanent GNSS stations in La Palma island belonging to the Instituto Volcanológico de Canarias (INVOLCAN), the Nagoya University, and GRAFCAN (Fig. 9.1). Solutions are analysed by GAMIT/GLOBK Software [4]. For processing, we used a total of 27 stations. We removed the regional tectonic component from the solutions using the Nubian plate reference described by Saria et al. [97]. We also used solutions from three stations of Instituto Geográfico Nacional (IGN) denoted LP03, LP04, and LPAL. We selected these three stations of the IGN as the

9.4 Data and Methods

data from other stations of the IGN are not public. Figure 9.8 shows the time series of some of the stations used in this study.

In Figure B.11 (in the supplementary materials), we compare data and the synthetic model resulting from the Geodetic Imaging technique for the three components of the GNSS data for all the stations used for this study. The stations closest to the eruptive vent (ARID) experienced the most significant deformation (Fig. 9.8). The deformation of ARID commenced on Sept. 14th (see Fig. 9.1) with 2.2 cm in the vertical component. It continued increasing in the following days, and on the day of the eruption, on Sept. 19th, the vertical deformation was already 11.4 cm, 15.3 cm toward the West, and 3.2 cm to the South. During the first week of eruption, the deformation continued increasing until it reached its maximum value in the ARID station, reaching 15.0 cm in the vertical component on Sept. 22nd (Fig. 9.8). Some GNSS stations at a higher distance from the eruptive vent also showed a deformation signal caused by the magmatic processes. Stations MOLU and FUEN (Fig. 9.1) began showing significant deformation on Sept. 12th. MOLU reached its maximum on Sept. 28th with 3.6 cm towards the East, 2.6 cm to the South, and 0.6 cm in the vertical component (Fig. 9.8). The deformed values did not return to their pre-eruptive stage and fluctuated during the eruption, showing a nearly steady deflation in the following months.

9.4.2 DInSAR Sentinel-1 data and processing

Two sets of synthetic aperture radar (SAR) images were acquired from complementary (ascending/descending) orbits between January and November 2021 through the constellation of twin radar sensors S-1A and S-1B, operating at the C band (wavelength of approximately 5.6 cm) and gathering images through the Interferometric Wide (I.W.) mode. They were independently processed using the multi-temporal interferometric SAR (Mt-InSAR) Small Baseline Subset (SBAS) technique [14]. The area covered by the used SAR images encompasses the whole island of La Palma (Fig. 9.9). The relevant parameters of the SAR datasets are listed in Table B.15 (in supplementary material). For every detected coherent distributed scatterer (D.S.) on the ground, the corresponding time-series of the LOS-projected ground displacement components were generated. According to Berardino et al. [14], Casu et al. [68] and Lanari et al. [98], the implemented SBAS processing chain operates on sequences of multi-look small baseline (S.B.) interferograms (in particular, 20 (range) x 4 (azimuth) looks were considered in our work) and includes specific steps for: i) the space-time phase unwrapping [43], ii) the estimation and compensation of phase artefacts in the generated SAR interferograms (i.e., the removal of residual topographic phases [14]), iii) the space-time noise-filtering of the sequence of small baseline multi-look SAR interferograms [96] and iv) the compensation of the atmospheric phase screen (APS). Specifically, before their inversion, the noise-filtered, unwrapped interferograms were analysed to retrieve and compensate the APS components by implementing an ad-hoc strategy. First, on every single interferogram, the phase components that are spatially highly correlated with the topography were estimated and filtered out. Then, we applied the methodology proposed in Tymofyeyeva and Fialko [99] that allows discriminating and filtering out the APS time

uncorrelated components in a sequence of SAR images by implementing a stacking operation on couples of S.B. SAR interferograms made with a common SAR image and characterized by the same time span (i.e., temporal baseline). The estimated tropospheric and time-uncorrelated APS components were finally subtracted from the unwrapped interferograms inverted through the SBAS method to obtain the relevant ground displacement time series. The residual APS components were then further compensated with a space-time filter (e.g., see Ferretti et al. [100], Berardino et al. [14], Yang and Buckley [101]). Finally, the interferometric ground deformation products were geocoded, i.e., converted from radar to geographical coordinates. Figures B.12 and B.13 of the supplementary material show the generated LOS-projected mean displacement velocity maps from the ascending and descending orbit tracks, respectively. Then, we concentrated on the short interval between Sept. 8th and 28th, 2021, with an aim to analyse pre- and early-eruptive ground deformation. Accordingly, we extracted the layers corresponding to the selected SAR acquisitions from the generated LOS-projected ground displacement time series and performed the analyses detailed hereinafter.

Starting from the ground displacement time series obtained by separately processing through the SBAS approach the available ascending/descending S-1 SAR images, we focused on the retrieved cumulative ground deformations, calculated with respect to the first images of the two datasets acquired in January 2021. More specifically, the analyses addressed in our study refer to the time interval Sept. 8th - Sept. 28th, representing the core of the analyses shown in this study. Note that the obtained ground deformation values only represented the projection of the ground displacement along the relevant radar-to-target line-of-sight (LOS) directions and were calculated by assuming as a time reference the date of the first available SAR images of the ascending and descending time series, respectively, collected on the first days of January 2021. Figure 9.9 shows the pre- and early-eruptive cumulative LOS deformation maps for the processed ascending and descending orbits. The ground deformation and the magma ascent were rapid. In Figure 9.9A, on Sept. 14th, the deformation shows a slight deformation. Two days later, on Sept. 16th, the descending orbit (Fig. 9.9C) captured a significant ground movement on the southern side of the forthcoming eruptive vent. On Sept. 19th at 14:02 GMT, the eruption started, but that day, Sentinel-1 did not acquire the data over the Canaries. One day after the eruption began, on Sept. 20th, the ascending orbit captured significant deformation in the southwestern side of the eruptive vent (Fig. 9.9B). The descending orbit that acquired the data on Sept. 22nd also captured considerable ground deformation (Fig. 9.9D). Its spatial deformation map differs slightly from the ascending orbit due to differences in the illumination geometries between the orbits and the different acquisition times that capture distinctive rapidly-evolving ground displacement signals from one date to another.

9.4.3 Non-linear inversion for the shallow dike geometry

To determine the inclination of the shallow part of the dike, we performed a non-linear inversion using the analytical ground deformation model of Okada [31], fixing the azimuth and letting the

9.4 Data and Methods

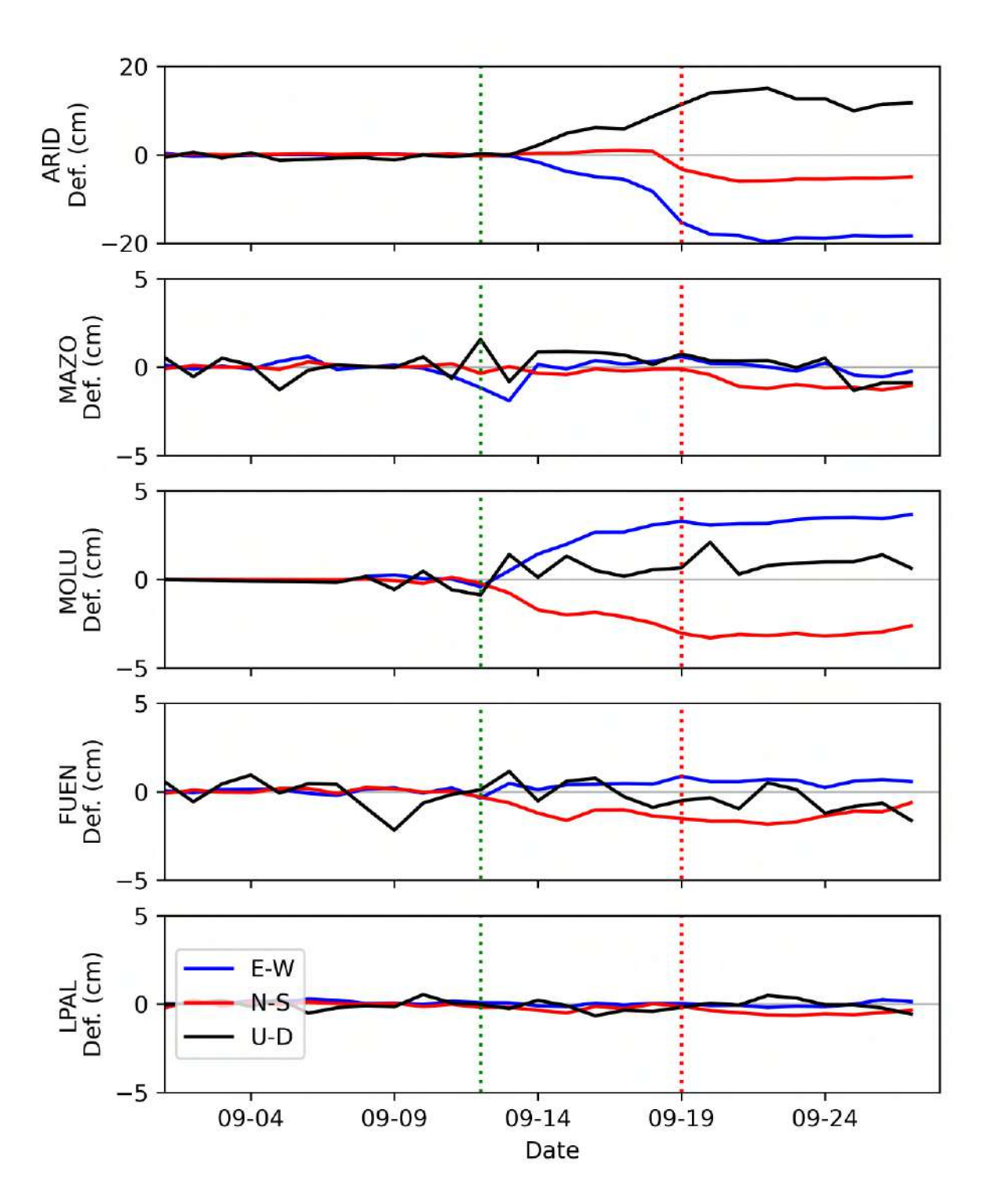


Figure 9.8 Solutions of some GNSS permanent stations solutions. Blue, red, and black horizontal lines show the E–W, N–S, and U–D components of deformation, respectively. The vertical red dotted line marks the day the eruption began, while the green dotted vertical line marks the day when the first significant deformation was recorded at stations MOLU and FUEN.

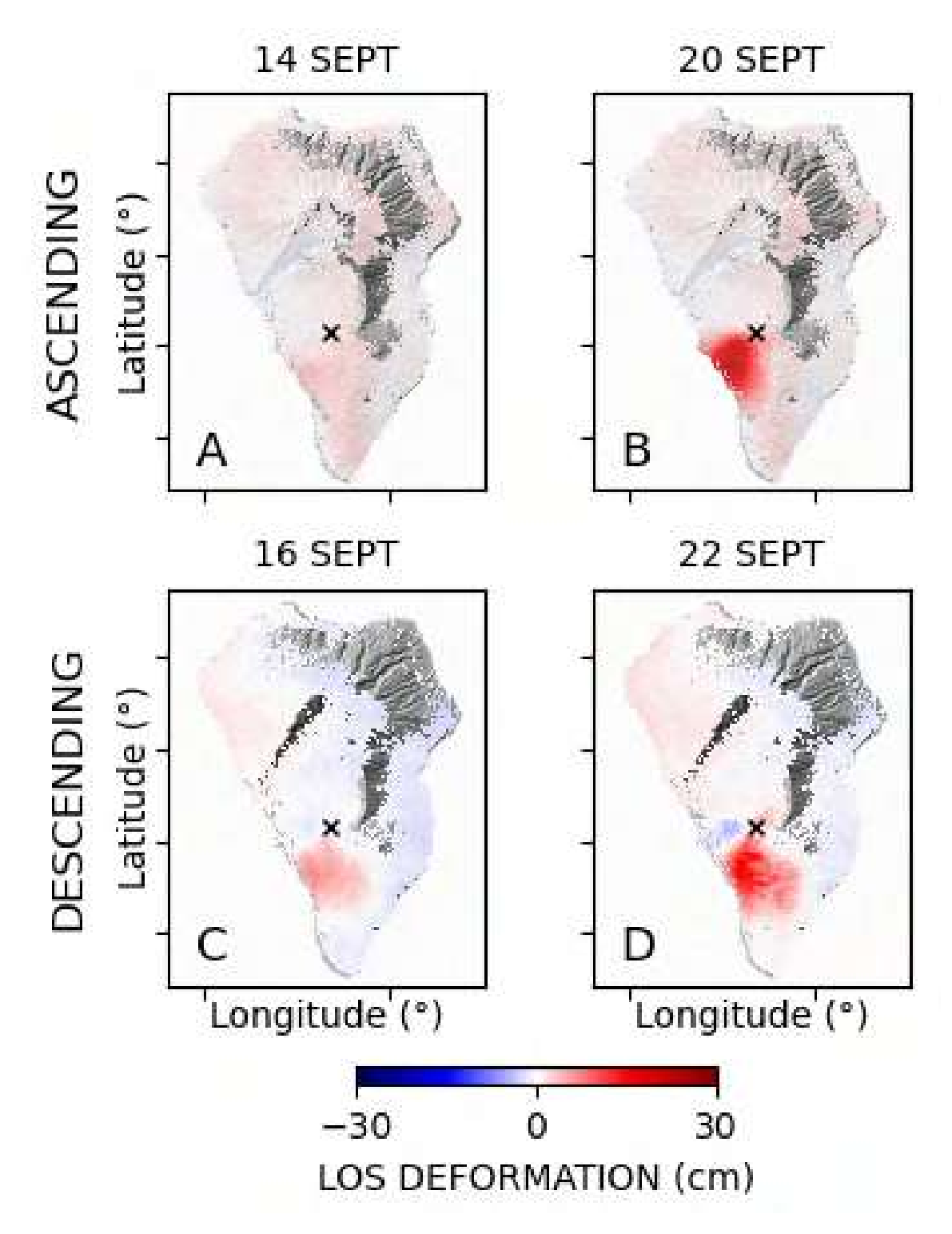


Figure 9.9 DInSAR deformation maps for La Palma in pre-and (A and C panel) and early-eruptive (B and D panel) phases. (A and B) represent the ascending orbit, while (C and D) represent the descending one. Black crosses show the location of the eruptive vents.

9.4 Data and Methods

inclination, the width, the length and the opening to vary. We determined the best-fit model using the Nelder-Mead [36] simplex algorithm.

9.4.4 Geodetic imaging

We applied a non-linear inversion technique of the spatiotemporal pattern of the dike opening following the approach of D'Auria et al. [81].

The dike opening function o(x,y,t) has been discretised into a set of 15x24 rectangular cells (Figs. ??) for each of the 8 DInSAR images used in this work. The computation of the Green's function for each cell has been performed within the finite element modelling environment COMSOL MultiPhysics®, using a 3D model that takes into account the topography and the bathymetry around the island. We used a lateral extent of the computational domain of 9 km. This width is sufficient to encompass all the areas affected by the eruptive phenomena. Furthermore, enlarging this length would negatively affect the resolution and the reliability of the final results. We performed the inversion using different sizes of the computational domain, obtaining similar results.

The opening function of the first image is constrained to 0, the first image being used as a reference for the rest of the dataset. Therefore, this allows the inverse problem formulation as a linear system for a total of 15x24x7 unknown. We used a second-order Tikhonov regularisation for both space and time. As with any inverse method, ours shows a trade-off between model resolution and fit with the data. The damping parameter controls this trade-off. Low damping values lead to lower misfit but unreliable noisy models. Conversely, high damping values lead to smoother models but high misfit values. In this work, we used the widely known L-curve approach [38] to establish the optimal damping value. Since we used a positivity constraint for the opening function, we solved the inverse problem through a non-linear Sequential Least Squares Programming (SLSQP) algorithm.

The final models cannot justify all the observed ground deformation because of the intrinsic limitations related to the inverse method and the lack of details of the 3D model of the mechanical properties of the Cumbre Vieja volcano.

To check the resolution, we performed various checkerboard tests (see Figs. ?? in the supplementary material) and a synthetic test with a realistic dike opening function (see Figs. ?? in the supplementary material). We used the same data acquisition geometry as the actual data (GNSS three components, Ascending DInSAR and Descending DInSAR). The standard deviation of the Gaussian noise added to the synthetic data mimics those assumed for actual data: 10 mm for DInSAR, 5 mm for horizontal GNSS components, and 10 mm for vertical GNSS components.

Chapter 10

Independent Component Analysis and Finite element modelling of the 2004-2005 ground deformation in Tenerife (Canary Islands)

Przeor, M., D'Auria, L., Pepe, S., Tizzani, P., Barone, A., Vitale, A., Pérez, N. and Castaldo, R. (2024). Independent Component Analysis and Finite element modelling of the 2004-2005 ground deformation in Tenerife (Canary Islands). Front. Earth Sci. Sec. Solid Earth Geophysics. Volume 12 - 2024; doi: 10.3389/feart.2024.1412827

10.1 Introduction

Tenerife is the largest island in the Canaries. Due to its high population density and five historical eruptions in the last five centuries, it is considered a region with a moderate volcanic risk [102]. The island's formation began as a Shield Volcanic Complex (SVC) in the Miocene period, possibly consisting of three independent islands: Anaga, Teno, and Roque del Conde massifs [77]. Its structural evolution was completed during the Pliocene, followed by a stage of formation of the central part of the island known as the Las Cañadas edifice. This building phase merged the previous shield volcanoes into a single island. During the Pleistocene, the ongoing formation of Las Cañadas caldera was also marked by numerous strombolian eruptions with vents located along the rifts (NE-SW, N-S and NWSE) connecting Las Cañadas and the older shield volcanoes. The rapid development of Las Cañadas was later followed by destructive episodes characterised by massive lateral collapses, leading to the formation of the current Las Cañadas Caldera [77]. Strombolian activity in the rifts remained prominent, and Las Cañadas Caldera was filled with salic eruptions, creating the Teide-Pico Viejo complex and peripheral eruptions within the Las Cañadas domain. The Holocene activity

was concentrated on eruptions occurring in the island's rifts but also affecting the Las Cañadas domain. From the 16th century to the present, five historical eruptions were concentrated mainly on the NW-SE and NE-SW dorsals, with only one occurring on the Teide-Pico Viejo complex. However, even though historical eruptions displayed basaltic fissure volcanic activity, Teide-Pico Viejo's activity included effusive and explosive eruptions of phonolitic magmas. The most recent explosive eruption in Tenerife was the sub-Plinian eruption of Montaña Blanca, which occurred approximately 2000 years ago 10.1 [77]. The most recent eruption of the Teide stratovolcano complex occurred roughly 800 years ago and is evident in the phonolitic lava flows that descend from the summit cone [77]. Currently, the Teide stratovolcano is dormant; its background volcanic activity consists mainly of a continuous microseismicity of Volcano-Tectonic (VT) and Long-Period (LP) events, fumarole activity in the crater of Teide and diffuse degassing [35].

At the beginning of 2001, anomalous seismic activity on the island began, with higher-than-background seismicity values registered by Instituto Geográfico Nacional (IGN) [103, 104, 105] and geochemical anomalies [106, 107, 108]. The most critical episode that prompted a "volcanic unrest alert" to be issued to the local government was the intense seismic activity that started in April 2004 and persisted until July 2005 [104, 105, 108]. This seismicity was characterised by volcano-tectonic events located within the Las Cañadas domain and some long-period events [104].

During this period of seismic unrest, the chemical composition of gases in Teide fumaroles indicated the presence of magmatic SO2, and there was also an increase in diffuse CO2 emissions in the northwest rift zone [108]. Furthermore, in the local galleries within the southern rift of the island, it was observed an increase in radon emission (220Rn and 222Rn) and an increase in the SO2/Cl ratio in the groundwater [107]. Gottsmann et al. [103] evidenced a gravity increase in the northern flank of the Teide-Pico Viejo volcanic complex and a lack of significant ground deformation. However, Fernández et al. [109] identified evidence of ground deformation of just a few centimeters in the Teide-Pico Viejo volcanic complex in 2004. At the same time, these authors also identified continuous subsidence in Las Cañadas triggered by the compressional state of the volcanic edifice [109]. The intense seismic activity persisted until July 2005 and gradually decreased throughout the early months of the following year [104]. The observed volcanic crisis did not culminate in an eruption, and, as mentioned by Melián et al. [107], the possibility of the reactivation of the Teide-Pico Viejo was low.

Even though a ground deformation in 2004 was observed [109], until now, no modelling of the causative source has been presented. We believe that a better understanding of this episode would allow a better understanding of the dynamics of the volcanic hydrothermal system of Tenerife and, consequently, would provide a useful tool for the interpretation of future volcanic unrest episodes on the island.

We first performed data processing employing the Differential Interferogram Satellite Aperture Radar (DInSAR) by using the Small BAseline Subset (SBAS) algorithm 10.3. Then we applied the Independent Component Analysis (ICA) to the 2004–2005 ground deformation occurring in Tenerife, obtaining the decomposition of the signal in different components. Applying the ICA to this dataset

10.1 Introduction 91

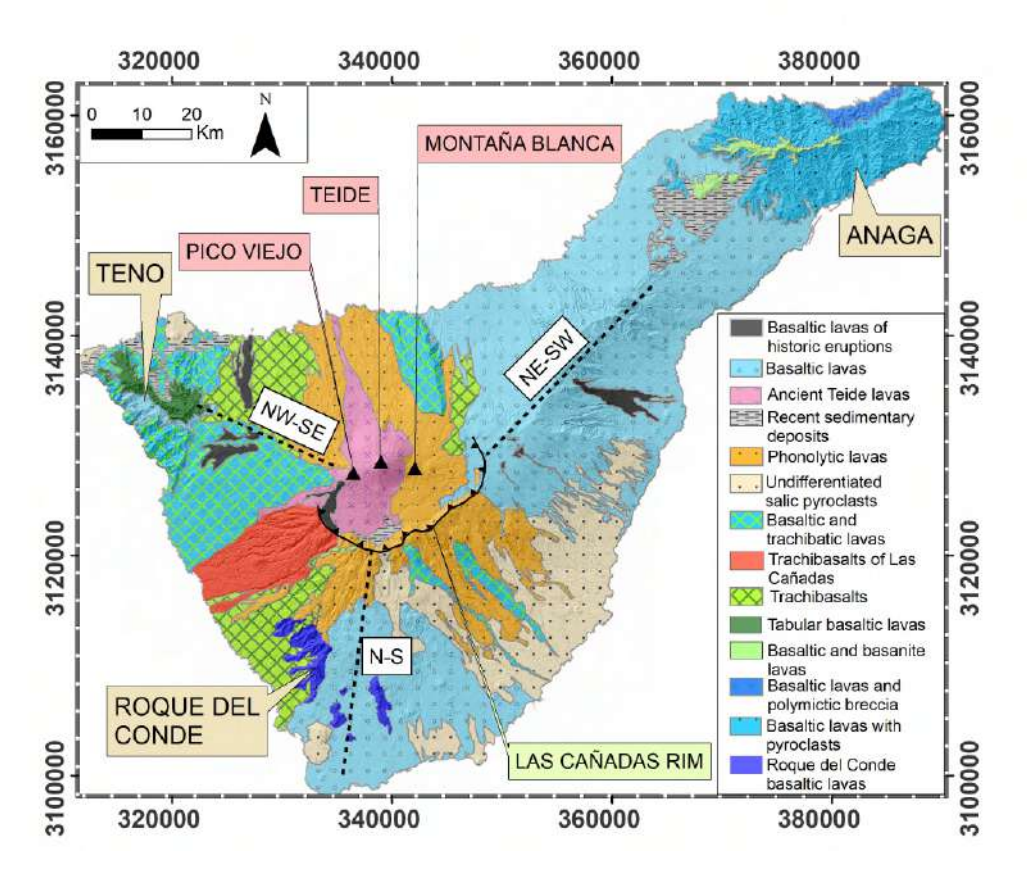


Figure 10.1 Geological map of Tenerife after Barrera et al. [77]. The legend explains the meaning of the color shades on the map. The three SVCs are marked with the tanned yellow square with the SVCs' names included. The rim of the caldera is shown with the black line with the triangles. Black triangles represent the volcanoes Pico Viejo, Teide, and Montaña Blanca. A dashed black line represents the three rifts.

allowed us to identify a consistent ground deformation pattern that we attributed to a causative volcanic source. We modelled this pattern using a non-linear optimisation within a Finite Element (FE) environment to study the geometry of the source in detail.

Interferogram stacking (DInSAR SBAS) is a widely known method for processing the SAR data in order to obtain time series of cumulative deformation in the area of interest. In this method, the multiple interferograms with the Small Baseline between the SAR images are overlaid, allowing to obtain small displacement information along the long time periods. The DInSAR SBAS method was proposed by Bernandino et al. [14] using the SAR images acquisitions with a small orbital separation (SBAS), allowing limiting the observed spatial decorrelation phenomena. This method was widely applied to study volcanic behaviours [110, 111, 5, 43] where prolonged deformation in time within the volcanic areas was observed. The Independent Component Analysis (ICA) represents a valuable statistical tool for analysing complex datasets [19, 18]. It allows the decomposition of a mixture of signals under the assumption that the individual sources are statistically independent and non-Gaussian [20]. ICA enables the separation of a dataset into nonorthogonal components that exhibit minimal statistical dependence between them. This valuable technique was first introduced for computational signal processing. However, it has also been applied in various geophysical applications like volcano seismology [112] and volcano geodesy [22, 20, 23].

The ICA in the volcano geodesy context has been applied to GNSS and DInSAR datasets and has shown its effectiveness in reducing the noise and uncovering hidden ground deformation patterns within complex DInSAR datasets. Ebmeier [20] showcased its effectiveness in separating the causative sources of complex ground deformation. Subsequently, Przeor et al. [23] used ICA to separate independent components of ground deformation in Hawaii, highlighting its ability to identify simultaneous but independent sources acting beneath Mauna Loa and Kīlauea volcanoes.

The observed ground deformation was modeled within the Finite Element environment in order to modelise the geometry and the location of the source responsible for the observed anomalies. This method is commonly applied to the DInSAR dataset, which helps visualizing the magmatic or hydrothermal sources. The application of this method to the DInSAR SABS dataset of Sentinel-1 allowed modelise the magmatic source injection during the pre-eruptive episode in La Palma (Tajogaite eruption of 2021); [82].

10.2 Data and Methods

10.2.1 SBAS DInSAR time series

The data used in this study were collected by the European Space Agency (ESA) through the ASAR sensor onboard the Envisat satellite acquired on C-band wavelength (≈5.6 cm). The satellite images acquired along ascending orbits were analyzed by the Grid Processing On Demand (G-POD) platform of ESA applying the multitemporal analysis using the Small BAseline Subset (SBAS) to obtain the Line-Of-Sight (LOS) time series for the coherent pixels of the SAR dataset [5]. The obtained

10.2 Data and Methods 93

180 interferograms were processed with a maximum temporal baseline of 150 days and a maximum spatial baseline of 400 m. We achieved the time series for each coherent pixel for the ascending orbit encompassing the island of Tenerife between 2003 and 2010. However, since the ground deformation occurred between 2004 and 2005, we focused on the dataset encompassing this interval. We did not evidence of any ground deformation pattern in the subsequent period in the processed dataset. baseline of 150 days and a maximum spatial baseline of 400 m. We achieved the time series for each coherent pixel for the ascending orbit encompassing the island of Tenerife between 2003 and 2010. However, since the ground deformation occurred between 2004 and 2005, we focused on the dataset encompassing this interval. We did not evidence of any ground deformation pattern in the subsequent period in the processed dataset.

10.2.2 Independent Component Analysis (ICA) of SBAS DInSAR time series

In the context of an SBAS DInSAR dataset, the time series is represented as L (xi, tj), where L denotes the Line-Of-Sight (LOS) displacement, xi corresponds to the position of the ith DInSAR pixel, and tj represents the time of the jth DInSAR image. The DInSAR dataset can be decomposed into a finite sum of N components characterised by fixed spatial patterns. If we denote Bk the spatial pattern of the kth and with Ajk the time-varying amplitudes of the kth component in time tj, we can write the ICA decomposition result as:

$$L(x_i, t_j) = \sum_{k=1}^{N} A_{jk} B_k(x_i)$$
 (10.1)

Once the spatial patterns have been normalised, the sum of squared amplitudes Ajk for each independent component k defines its energy. This enables us to sort the components based on their energy and determine the optimal number of components representing the whole signal. This can be realised by setting a threshold below which the contribution to the total energy is negligible. We opted to retain one more component, even if characterised by negligible amplitude values, given that it would host the noise inherent in each DInSAR dataset. In the case of the ascending SBAS DInSAR dataset for Tenerife, we used four components.

10.2.3 Non-linear source modeling through the Finite Element Modeling

To model a causative source of ground deformation, represented by an individual ICA component, we employed the Comsol Multiphysics® software environment. We built a three-dimensional mesh taking into account Tenerife Island's topography. The computational domain had dimensions of 33,000 m along the EW direction, 25,000 m along the NS direction, and 12,000 m in depth, to cover all the Las Cañadas caldera. We assumed isotropic linear elastic material properties. The elastic constants are calculated assuming an average P-wave velocity of 4,000 m/s, S-wave velocity of 2,400 m/s, and a 2,700 kg/m³ density. The seismic wave velocity values have been estimated from the seismic tomography model of Koulakov et al. [35].

X (UTM)	Y (UTM)	Depth (m)	Rx (m)	Ry (m)	Rz (m)
340078	3128959	-1603	1421.6	893.5	536

Figure 10.2 Optimized source parameters.

The domain was discretised using tetrahedral mesh elements, with a maximum element size of 1,200 m and a minimum element size of 500 m. As a starting model, we chose a three-axis body representing the causative sources of the observed ground deformation. The parameters used to define the source model are seven: the centre position in UTM (X, Y, Z); the dimensions of the ellipsoid axes along the X, Y, and Z-axes in meters; and the overpressure in pascals (Pa). The best-fit model has been retrieved through a non-linear optimisation using the Nelder and Mead [36] simplex algorithm. The number of iterations required to reach the minimum was 1,000, and an objective function used was the residual sum of squares.

10.3 Results

10.3.1 SBAS DInSAR time series

The 2003–2005 SBAS DInSAR mean LOS velocity map computed along ascending orbit reveals four local deformation patterns on the island (Fig. 10.3). At first sight, three areas of deformation with negative values are visible, one located in the NESW rift and two in the NW-SE rift, highlighted by black squares in Fig. 10.3. These ground deformation anomalies were previously identified by [109] and associated with water withdrawal from the island's galleries. As this study aims to identify ground deformation caused by volcanic or hydrothermal activity, we chose not to focus on these hydric ground deformation behaviours. The central area of Tenerife, in the Teide volcano, exhibits a positive ascending LOS deformation of a few cm/year. The deformation encompasses all of the Teide volcano area; however, the deformation is interspersed with other patterns visible on the DInSAR dataset. The application of ICA helped us to understand the geometry and more precise location of the area affected by the ground deformation at Teide. To better analyze the ICA patterns, we selected a radius of 9 km from the summit cone of Teide, shown by the black circle in Figure 10.3.

10.3.2 Application of the ICA to the DInSAR dataset

The results of ICA decomposition to the SBAS DInSAR dataset within the area of 9 km of radius from the summit of the Teide volcano revealed the presence of at least four components (Fig. 10.4), sorted in descending order by their energy. Among these, three exhibited significant ground deformation values, while the fourth component had low amplitude energy and primarily consisted of noise.

10.3 Results 95

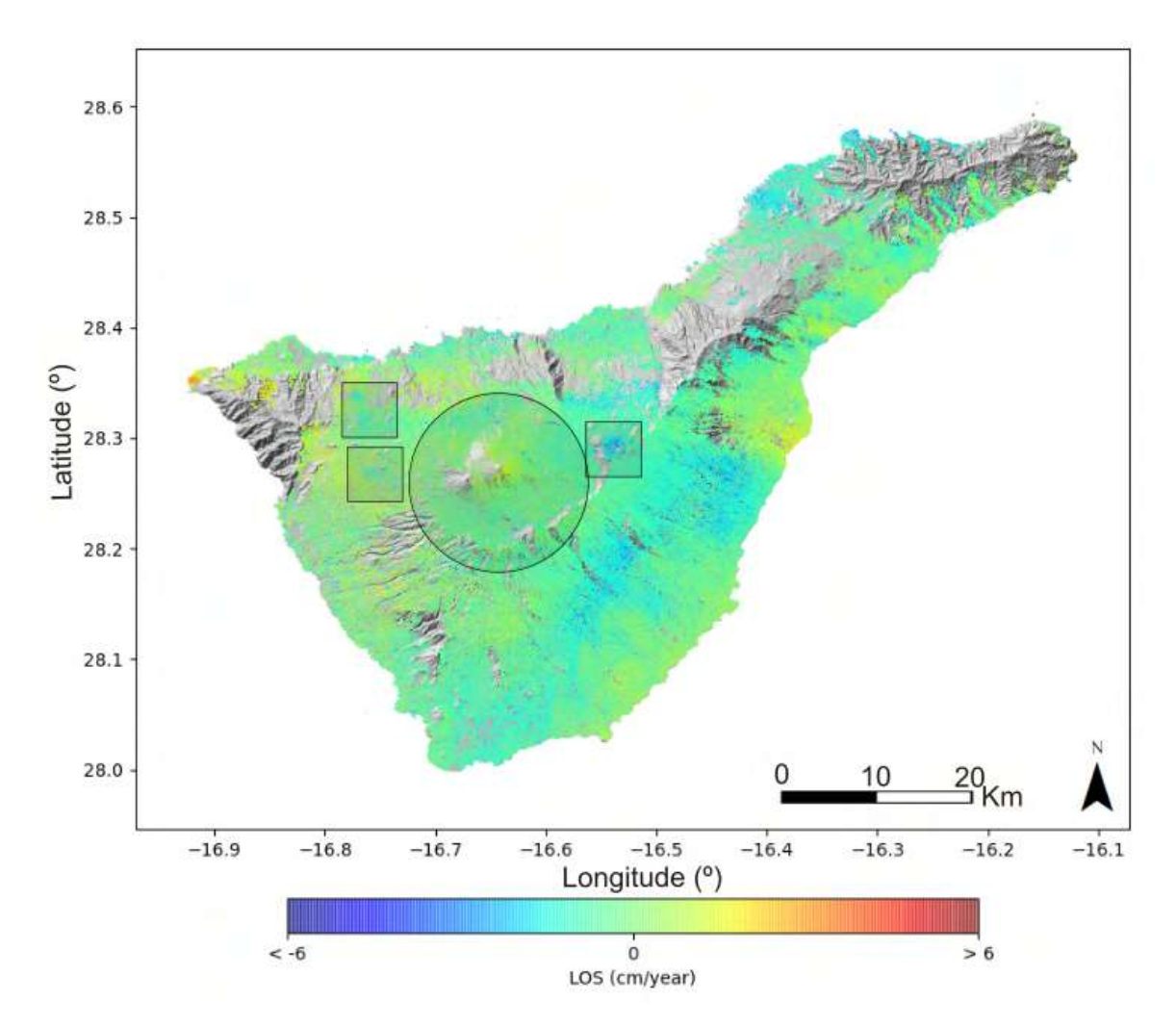


Figure 10.3 The 2003 - 2005 SBAS-DInSAR mean velocity map represented in Line-Of-Sight (cm/year). The gray circle shows the area of interest, where the ICA decomposition is applied, while the three gray squares represent the zones of the local negative deformation, discussed by Fernández et al. [109].

The first component of the ICA decomposition (ICA1) exhibits a highly localized and high-energy pattern, with the maximum within the summit cone of the Teide volcano (see panel A in Fig. 10.4), displaying a circular symmetry with an approximate radius of 3 km. The second and third components of the ICA decomposition (ICA2 and ICA3; panels B and C of Fig. 10.4) likely represent topographical or atmospheric artefacts with high ICA energy values (Table 10.5). The ICA2 represents the negative values on the northern flank of the complex volcano and higher positive values on the southern side of the Teide. The positive values are located exactly in the edge of the Las Cañadas rim while the negative ones are located in the northern side of the flank of Teide. The topography in Tenerife is abrupt and presents very complex features. The SBAS method cannot eliminate the whole signal corresponding to the topography, however, by applying the ICA we can discard the left pattern of topography from the data. The ICA3 is less energetic and does not have locally concentrated anomalies. However, as the SBAS method can still allow atmospheric artefacts in the dataset, we associate this pattern with the atmospheric noise. The final component (ICA4; panel D of Fig.10.4) displays a negligible signal pattern and possesses low energy (Table 10.5), indicating that it primarily represents signal noise.

10.3.3 Non-linear optimization in Finite Element Modeling

The inverse modeling was carried out on the first component of the ICA (ICA1) due to (i) its high ICA energy, (ii) the location in the area of the highest interest, and (iii) the potential volcanic or hydrothermal origin of deformation. In the following, we provide details of the optimization results. The results of the inverse modeling, as indicated by the local maximum in the Teide summit cone, exhibit a substantial adjustment with the observed data (Fig. 10.6). The parameters defining the source responsible for the observed deformation were determined based on an ellipsoidal geometry positioned at 1600 m a.s.l. This source is situated beneath the summit zone of the Teide volcano, with dimensions of 1420 m, 893 m, and 536 m along the X, Y, and Z axes, respectively. The location of the source in UTM was the following: X= 340075 m E; Y= 3128959 m N (UTM zone 28 R). The geometry of this source demonstrated nearly perfect alignment with the ICA1 data, resulting in low residuals (Fig. 10.6, panel C).

10.4 Discussion and Conclusion

The detected ground deformation in Tenerife was analyzed by applying ICA to the DInSAR dataset, which was achieved by data processing of the ascending Envisat satellite images. The main volcanic deformation source in Tenerife was identified in the first ICA component, primarily concentrated between 2004 and 2005. The geometry of the source was derived through inverse modeling, assuming a three-axial ellipsoidal source located beneath the Teide and Montaña Blanca volcanoes at 1,600 m a.s.l. (Fig. 10.7). Our results show a deformation source elongated mainly along the E-W axis. The current study findings strongly suggest that a ground deformation source was activated during the

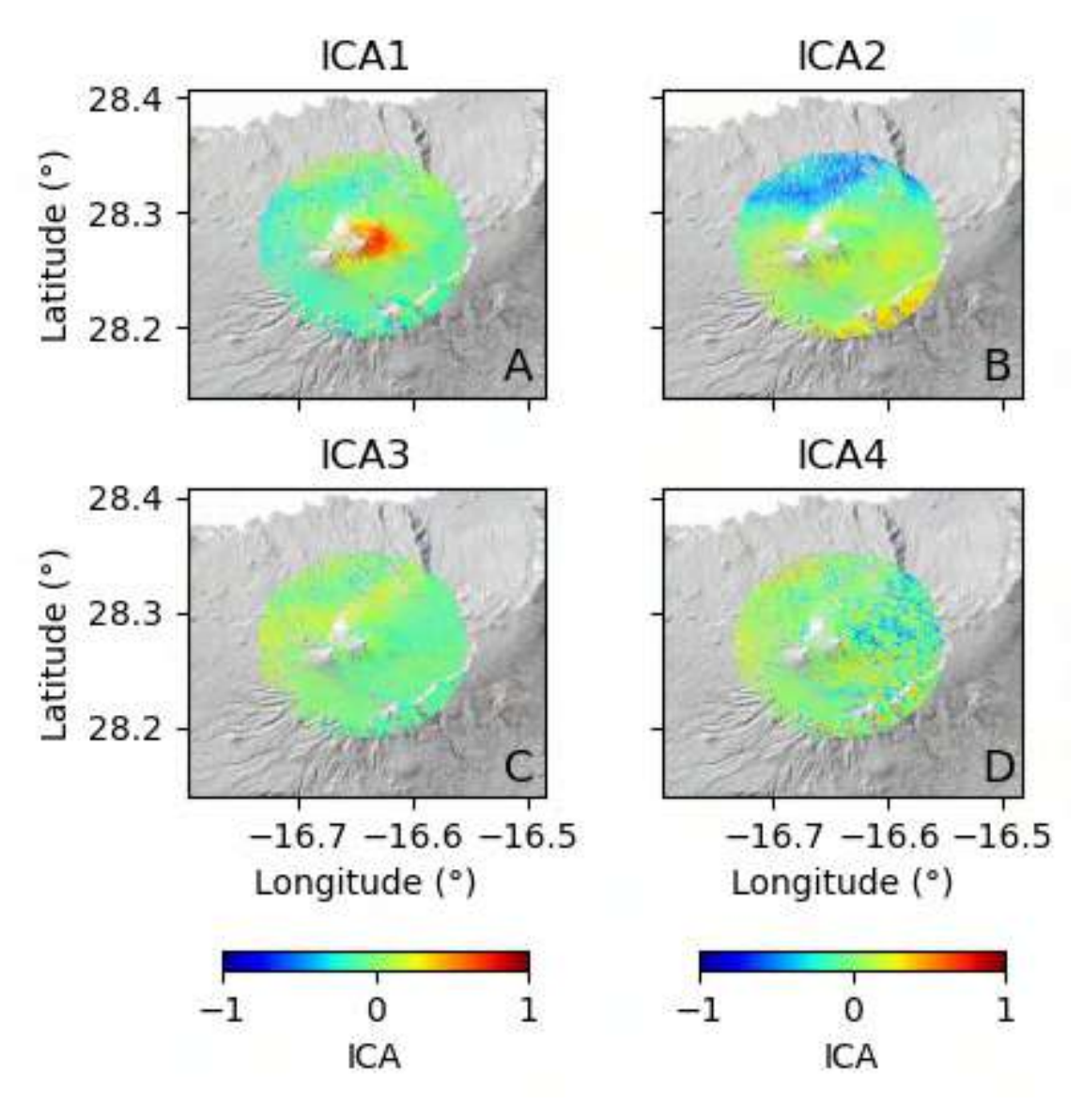


Figure 10.4 Four independent component maps (A-D) extracted by ICA within the selected area of a 9 km radius from the summit of the Teide volcano. The amplitude of the ground deformation pattern components is normalized.

COMPONENT	ENERGY (%)		
ICA1	32.4		
ICA2	31.9		
ICA3	24.7		
ICA4	11.0		

Figure 10.5 ICA components and their respective energy.

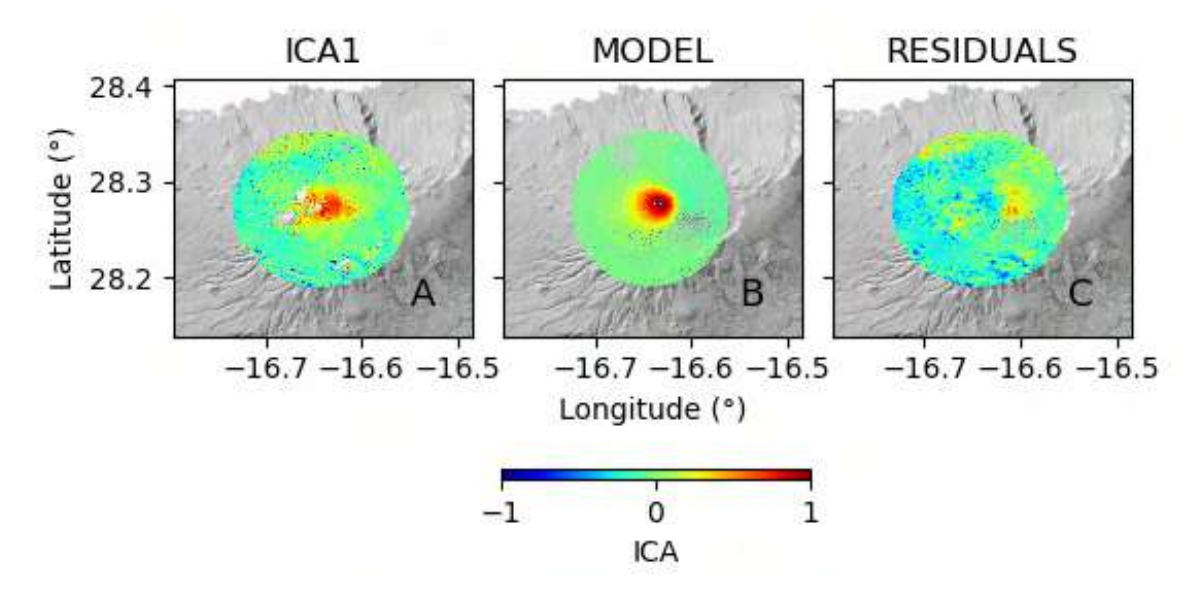


Figure 10.6 Modelling result: (A) data, (B) model, and (C) residuals for the inverse modeling of the first component of the ICA decomposition, respectively. TThe amplitude of the ground deformation pattern components is normalized.

seismic crisis in 2004–2005. These results are compatible with the conclusions of previous studies, where a volcanic or hydrothermal origin in the Teide volcano was distinctly established through various geophysical and geochemical methods [113, 103, 114, 106, 104, 102, 115, 116, 109, 105, 117, 107, 108] In the following, we describe the similarities and differences observed between the previous studies and the present one.

The most significant feature during the crisis of 2004–2005 was primarily focused on seismic activity in the area of the Teide volcano and the NW rift of the island ([114, 104]). Tárraga et al. [114] postulated the existence of volcanic tremor caused by convective processes in the reservoir beneath the Teide-Pico Viejo volcanic complex triggered by new inputs of magma. However, according to Almendros et al. [104], the 2004–2005 crisis was marked by anomalous seismic events triggered by deep magma injection under the NW flank of Teide. This new input of magma triggered the VT earthquakes, the release of magmatic gases, and, consequently, LP events. Ultimately, the injection of magma into the crust disturbed the local aquifers in Las Cañadas and induced volcanic tremor beneath the Teide volcano. Both authors confirm the evidence of the magmatic reactivation of the Teide volcano.

Additionally, Gottsmann et al. [103], through joint microgravity and ground deformation surveys realized in May 2004 and July 2005, observed changes in the gravity field but found no evidence of significant ground deformation caused by volcanic phenomena. They could not detect these slight changes in ground deformation due to the lack of a network covering the area of interest and the temporary nature of the stations. However, applying the Envisat ASAR dataset that covers all the areas of interest and samples the data every 35 days during the 9 years of analysed period, we were able to detect even small changes in the ground deformation behavior. In addition, the ICA method decomposes the raw DInSAR SBAS signal into independent signal behaviours, letting the small changes in the ground deformation be noticed.

Gottsmann et al. [103] proposed three possible scenarios for the observed gravity increase: 1) new magma inputs, 2) migration of hydrothermal fluids, or 3) a hybrid process involving both a new magma input and hydrothermal fluid migration. To support the hypothesis of hydrothermal fluid migration, the authors conducted an inversion of the gravity data and determined that a hydrothermal reservoir was responsible for the observed changes. Their results indicate the existence of the source at a depth of 1,9 +- 0.12 km below the surface, which is approximately consistent with our results showing the source at a depth of 1,600 m a.s.l. Ultimately, Gottsmann et al. [103] concluded that the movement of hydrothermal fluids is the most likely scenario to explain the gravity changes and the absence of ground deformation. However, the present study allowed us to uncover hidden deformation patterns in the Teide volcano, providing further insight into the dynamics of the 2004–2005 unrest.

Additionally, Martí et al. [105] evaluated seismic and microgravimetric observations, finding clear evidence of volcanic activity on the Teide volcano. Their discussion was based on the number and location of VT and LP events, tremor, and perturbations in the gravity field. They also reported increased activity in the fumaroles of Teide and the appearance of new fractures with gas emissions

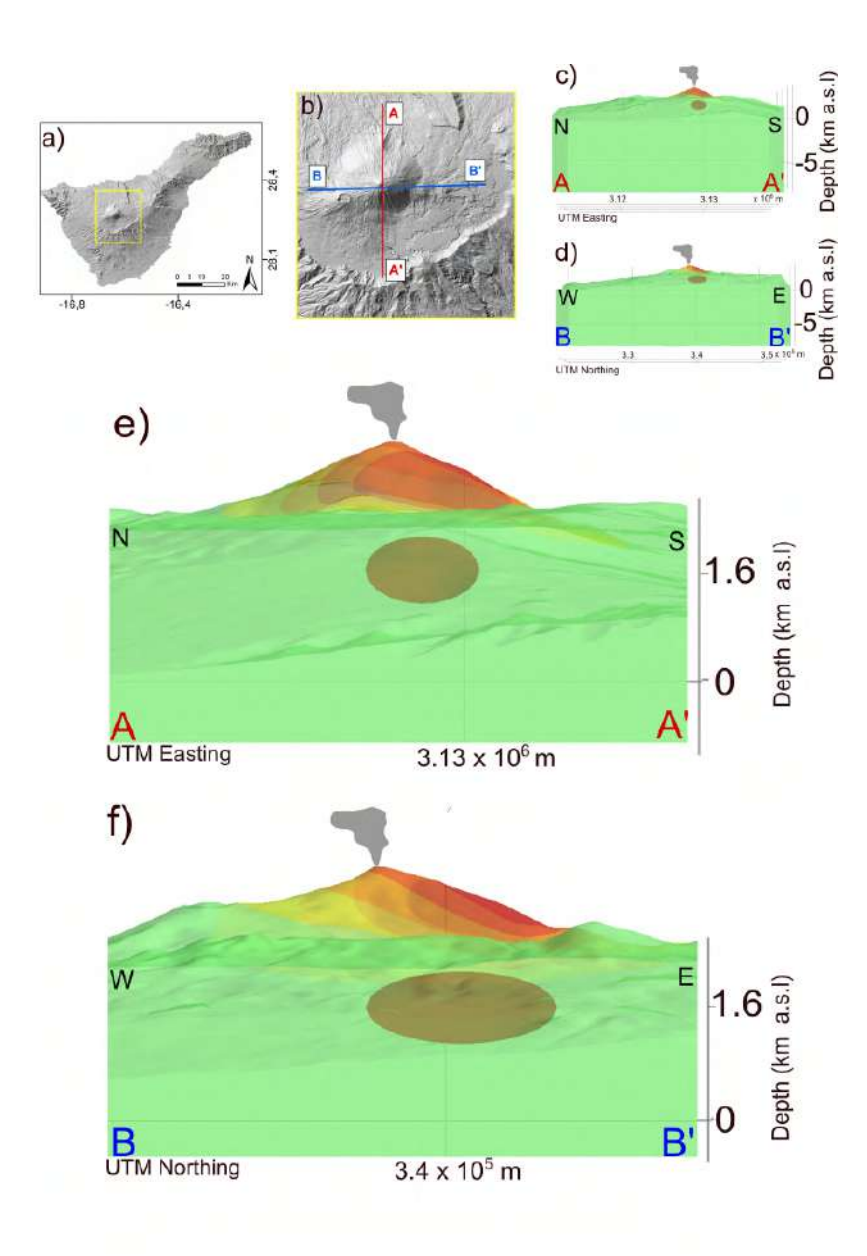


Figure 10.7 Three-dimensional model of the retrieved source, responsible of 2004-2005 the ground deformation. (A) map of Tenerife island, with the yellow box indicating the zoom of Las Cañadas region. (B) Las Cañadas region, featuring the N-S (A-A') and E-W (B-B') profiles employed to represent the vertical sections of topography and the source. (C-D) the N-S and E-W sections of the topography in Las Cañadas and the ground deformation modeled source, while (E-F) show the enlarged views of panels (C-D).

in La Orotava. These anomalies were interpreted as disturbances in the background activity of the Teide-Pico Viejo volcanic complex. The authors postulate that new magma inputs can trigger the reactivation of the phonolitic reservoir beneath the Teide-Pico Viejo volcanic complex in the future.

Furthermore, Fernández et al. [109] identified three distinct areas affected by ground deformation in Tenerife using DInSAR SBAS data from the ERS-1 and ERS-2 sensors between 1995 and 2005. The primary one was characterized as the compressional state of the island, attributed to the gravitational load of the edifice. Additionally, there were very localized subsidence zones in the rifts of the island, which were attributed to water withdrawal in the galleries, evidenced by Fernández et al. [109] and also shown in Fig. 10.3 in the present study. The authors also observed disturbances in ground deformation in the Teide volcano associated with the volcanic crisis; however, they did not perform modeling of the causative source for the observed ground deformation between 2004 and 2005.

Finally, through the geochemical analysis, Melián et al. [107] observed a change in the composition of fumaroles in the Teide crater, resulting in a higher contribution of magmatic gases between 2001 and 2005. Pérez et al. [108] reported temporal changes in the gas composition of Teide's fumaroles, including increased CO2 efflux in the Teide summit cone and crater since 2001. They highlighted that the Teide volcanic and hydrothermal system undergoes temporal degassing episodes caused by magmatic fluid injection into the hydrothermal system, which was evident in 2004 and triggered by magma movements beneath Teide. Additionally, they rejected the previously proposed hypothesis by Martí et al. [105] regarding the reactivation of the phonolitic storage of Teide-Pico Viejo due to the analysis of gas compositions in fumaroles by Melián et al. [107] and SO2 emissions reported by Weber et al. [106].

The reactivation of an ellipsoidal-like source beneath the Teide volcano offers a comprehensive understanding of the seismic, gravimetric, and geochemical anomalies that occurred during the 2004–2005 crisis.

First of all, we observe that the ground deformation source we identified is located at a shallower depth and is displaced about 5 km to the SE with respect to the northern seismic cluster active during 2004 [117]. This seismic cluster has been interpreted by different authors as the effect of a magmatic intrusion in the north-western part of Tenerife [103, 117]. The volume affected bythis cluster has shown limited activity in the following years [35].

Secondly, Gottsmann et al. [103] evidenced that the observed gravity variations are compatible with a density increase caused by the filling of rock porosity with hydrothermal fluids. They assume a volume fraction of 30 percent and infer a source having a radius of around 80 m. Assuming a larger source volume, the volume fraction decreases. Our source model has a volume of approximately 2.8 × 109 m3, which implies a much lower volume fraction. Another possibility is that the source thickness would be much lower than its areal extension or, in other words, it consists of a sill-shaped geometry. Unfortunately, geodetic data alone, are not able to precisely constrain the thickness of the causative source. However, both interpretations are compatible with the observed ground deformation, gravity variations, and geochemical variations.

Concerning the source of the hydrothermal fluids, the most likely mechanism is the degassing of the magma batch which likely intruded at depth in the northwestern sector of the island. A similar mechanism is possibly related to the recent seismological and geochemical anomalies observed in Tenerife [118, 119, 120]. This magmatic injection episode did not show up in the ground deformation pattern, possibly because of the depth of the intrusion (>5 km) and the limited amount of magma involved. We note that eruptions occurring along the NW dorsal of Tenerife have generally a Strombolian character and are fed by basaltic magmas. This contrasts with the central Teide- Las Cañadas complex, where phonolitic eruptions with both effusive and explosive typologies occurred in the past. This was explained by Koulakov et al. [35] by considering the difference in the crustal structure beneath these two areas. In the former, the rigid crust does not allow a long-term residence of primitive basaltic magmas, which quickly reach the surface through a network of dikes. In the latter, the presence of a ductile regime allows the stationing and the differentiation of magmas toward phonolitic composition. In this context, we postulate that the 2004–2005 unrest represents a "failed" eruption along the NW dorsal in Tenerife.

Our work highlights two relevant points from the volcano monitoring point of view. First, the most likely precursor of an eruption in the NE dorsal of Tenerife is deep seismicity related to the magmatic intrusion process. This is similar to what was observed during the 2021 Tajogaite eruption on the island of La Palma [78]. Second, the ground deformation pattern should be interpreted carefully. We have shown how it can be related to a hydrothermal causative source instead of a magmatic intrusion.

Chapter 11

Conclusions

11.1 Conclusions for Elastic interaction between Mauna Loa and Kīlauea evidenced by ICA

The application of ICA decomposition to four DInSAR SBAS datasets revealed an anticorrelated behaviour between Mauna Loa and Kīlauea volcanoes during the studied interval 2003–2010. At the same time, another pattern of ground deformation has been identified and is linked to independent behaviour at Kīlauea alone. The GPS dataset and inverse modelling results support these findings. Moreover, another significant result from our analysis is the evidence of a single ground deformation source at Mauna Loa during the studied time interval. This was previously suggested by Pepe et al.[43], who showed that the central conduit dynamics and the dikes along the rift zones displayed almost synchronous inflation. Kīlauea displays a greater complexity, with at least two sources simultaneously active.

We highlight that the connection between Mauna Loa and Kīlauea occurs at shallow depths in the first few kilometers of the crust, through a stress transfer mechanism. Stress transfer at Mauna Loa and Kīlauea has been considered by various authors to explain the dynamics of intrusions along rift zones [52, 55] and the interaction between earthquakes and eruptions [42, 43] at both volcanoes. This interconnection is created by the Mauna Loa reservoir perturbing the Kīlauea shallowest source. Conversely, the sources below the Kīlauea do not effectively influence the Mauna Loa reservoir. In practice, the inflation of Mauna Loa makes the stress field in the surroundings of Kīlauea less favourable for the ascent of magma into its shallow reservoir. The opposite mechanism, with Kīlauea affecting Mauna Loa, seems less favorable. The respective geometries of the sources (Fig. 8.7) make an effective mechanical interaction possible only between the dike-shaped source of Mauna Loa to the shallow volumetric source of Kīlauea. The sill-shaped geometry of the deeper Kīlauea source means it is less affected by this interaction process, as also confirmed by numerical modelling.

An important result of this work is the application of ICA to ground deformation datasets. This statistical tool has been demonstrated to effectively detect and separate individual independent sources within complex spatiotemporal ground deformation patterns. This approach greatly simplifies the

104 Conclusions

study of complex ground deformation sources, whose components can be modelled independently. Using more advanced inverse modelling tools [43] can shed further light on the spatial complexity of the Kīlauea plumbing system. Further studies should be devoted to analyzing the interaction between ground deformation sources over a larger time span.

11.2 Conclusions for Geodetic Imaging of magma ascent of the Tajogaite eruption of 2021

We propose a novel model of the spatiotemporal evolution of the magmatic system preceding and accompanying the first 10 days of the 2021 Cumbre Vieja eruption. For this purpose, we applied a Geodetic Imaging technique [81, 121] to reconstruct the kinematics of the plumbing system during the pre- and early-eruptive phases. The main finding of our study is that the causative source of the ground deformation was a dike with a bent and twisted geometry connecting a magmatic reservoir located below 10 km depth with the surface. Its azimuth changed from E-W in the deepest parts to NW–SE on the surface, while its dip changed from southward to southwestward.

We found an excellent agreement between the temporal evolution of the dike opening and the upward migration of pre-eruptive hypocenters. The upward propagation of the magma was very rapid (about 8 days) and strongly accelerated during the last day. The overall geometry of the dike intrusion process shows the presence of at least two blind lateral branches whose propagation stopped before reaching the surface. The eruption's onset is clearly evidenced by a dike opening right beneath the eruptive vent accompanied by intense shallow seismicity. On Sept. 27th, the eruption stopped for a few hours. We interpret it as an effect of a temporary collapse of the dike, as confirmed by the dike opening model, which shows an incipient collapse already starting the day before

In conclusion, we state that the Geodetic imaging technique is an excellent tool for better understanding magma ascent processes. Our results provide evidence of the complexity of the dike propagation processes and the temporal changes in the shallow plumbing system before and during an eruption.

11.3 Independent component analysis and finite element modelling of the 2004–2005 ground deformation in Tenerife (Canary islands)

Concerning the source of the hydrothermal fluids, the most likely mechanism is the degassing of the magma batch which likely intruded at depth in the northwestern sector of the island. A similar mechanism is possibly related to the recent seismological and geochemical anomalies observed in Tenerife [118, 119, 120]. This magmatic injection episode did not show up in the ground deformation pattern, possibly because of the depth of the intrusion (>5 km) and the limited amount of magma involved. We note that eruptions occurring along the NW dorsal of Tenerife have generally a Strombolian character and are fed by basaltic magmas. This contrasts with the central Teide- Las Cañadas complex,

11.4 General conclusions 105

where phonolitic eruptions with both effusive and explosive typologies occurred in the past. This was explained by Koulakov et al. [35] by considering the difference in the crustal structure beneath these two areas. In the former, the rigid crust does not allow a long-term residence of primitive basaltic magmas, which quickly reach the surface through a network of dikes. In the latter, the presence of a ductile regime allows the stationing and the differentiation of magmas toward phonolitic composition. In this context, we postulate that the 2004–2005 unrest represents a "failed" eruption along the NW dorsal in Tenerife.

Our work highlights two relevant points from the volcano monitoring point of view. First, the most likely precursor of an eruption in the NE dorsal of Tenerife is deep seismicity related to the magmatic intrusion process. This is similar to what was observed during the 2021 Tajogaite eruption on the island of La Palma [78]. Second, the ground deformation pattern should be interpreted carefully. We have shown how it can be related to a hydrothermal causative source instead of a magmatic intrusion.

Our work highlights two relevant points from the volcano monitoring point of view. First, the most likely precursor of an eruption in the NE dorsal of Tenerife is deep seismicity related to the magmatic intrusion process. This is similar to what was observed during the 2021 Tajogaite eruption on the island of La Palma [78]. Second, the ground deformation pattern should be interpreted carefully. We have shown how it can be related to a hydrothermal causative source instead of a magmatic intrusion.

11.4 General conclusions

Applying the ICA to the DInSAR SBAS dataset in different volcanic areas revealed the presence of hidden ground deformation patterns operating within the studied regions. In the case of Hawaii island, it was possible to understand and model the characteristics of magmatic sources in these volcanoes and comprehend complex volcanic interaction within the crust involving two volcanoes. We gained insight into how the volcanoes of Mauna Loa and Kilauea exhibit contrasting behaviours due to stress transfer mechanisms.

La Palma island and its most recent Tajogaite eruption in 2021 provided an excellent opportunity to employ Geodetic Imaging techniques, allowing us to visualize the kinematic processes occurring before and during the eruption. Modelling the sources responsible for ground deformation and subsequently simulating their ascent facilitated understanding and imaging of the internal crustal structure of La Palma, along with the specific ascent paths utilized by magma as it rose toward the surface.

Finally, applying the ICA to the DInSAR SBAS dataset of Tenerife enabled us to comprehend the mechanism of the degassing of the magma batch responsible for the seismic crisis of 2004-2005. The ground deformation source modelling also revealed hydrothermal activity within the Teide-Pico Viejo volcanic complex in the crust. This study underscored the importance of future research aimed

106 Conclusions

at understanding volcanic processes on the island, which can aid in identifying magmatic or hydrothermal sources beneath the islands and, in the future, modelling potential volcanic scenarios.

This study focuses on comprehending processes occurring in volcanic areas by utilising the DIn-SAR SBAS dataset and subsequently analysing its hidden ground deformation patterns. Subsequent modelling of the observed ground deformation data can enhance our understanding of processes occurring in the studied areas, thereby enabling anticipation of potential future volcanic scenarios on the islands. These findings are of great importance in volcanic regions as they allow society to prepare for future volcanic phenomena.

The results of this work show detailed, high-resolution ground deformation models that provide significant insight into volcano dynamics. Future studies will focus on analyzing more complex datasets and integrating gravity and other geophysical datasets. An interesting addition to this thesis is modelling the kinematic ascent of magma, which could be applied to other volcanic areas, such as Iceland's current volcanic activity (which commenced in 2023). These studies could potentially provide insights into imaging and understanding the paths of magmatic branches and their magnitude, aiding in the prediction of forthcoming volcanic scenarios.

- [1] Daniel Dzurisin, Robert Y Koyanagi and Thomas T M English. "Magma supply and storage at Kilauea volcano, Hawaii, 1956–1983". In: *Journal of Volcanology and Geothermal Research* 21 (1984). https://doi.org/10.1016/0377-0273(84)90022-2, pp. 177–206.
- [2] Antonio Parascandola. *I fenomeni bradisismici del Serapeo di Pozzuoli*. Stabilmento tipografico G. Genovese, 1947.
- [3] Kiyoo Mogi. "Relations between the eruptions of various volcanoes and the deformations of the ground surfaces around them". In: *Earthquake Research Institute* 36 (1958), pp. 99–134.
- [4] TA Herring, RW King, SC McClusky et al. "Introduction to gamit/globk". In: *Massachusetts Institute of Technology, Cambridge, Massachusetts* (2010).
- [5] Claudio De Luca et al. "An on-demand web tool for the unsupervised retrieval of Earth's surface deformation from SAR data: The P-SBAS service within the ESA G-POD environment". In: *Remote Sensing* 7 (2015), pp. 15630–15650.
- [6] SarMap S.A. *SARscape Help Unit of Measure*. Accessed: 2024-06-13. Caslano, Switzerland, 2022.
- [7] A Monti Guarnieri et al. "Multi-mode ENVISAT ASAR interferometry: techniques and preliminary results". In: *IEE Proceedings-Radar, Sonar and Navigation* 150.3 (2003), pp. 193–200.
- [8] Richard M Goldstein and Charles L Werner. "Radar interferogram filtering for geophysical applications". In: *Geophysical research letters* 25.21 (1998), pp. 4035–4038.
- [9] Ireneusz Baran et al. "A modification to the Goldstein radar interferogram filter". In: *IEEE Transactions on Geoscience and Remote Sensing* 41.9 (2003), pp. 2114–2118.
- [10] Mario Costantini. "A novel phase unwrapping method based on network programming". In: *IEEE Transactions on geoscience and remote sensing* 36.3 (1998), pp. 813–821.
- [11] A Reigher and J Moreira. "Phase unwrapping by fusion of local and global methods". In: IGARSS'97. 1997 IEEE International Geoscience and Remote Sensing Symposium Proceedings. Remote Sensing-A Scientific Vision for Sustainable Development. Vol. 2. IEEE. 1997, pp. 869–871.
- [12] Wolfgang Goblirsch and Paolo Pasquali. "Algorithms for calculation of digital surface models from the unwrapped interferometric phase". In: *IGARSS'96. 1996 International Geoscience and Remote Sensing Symposium.* Vol. 1. IEEE. 1996, pp. 656–658.
- [13] Francesco Holecz et al. "Height model generation, automatic geocoding and a mosaicing using airborne AeS-1 InSAR data". In: *IGARSS'97. 1997 IEEE International Geoscience and Remote Sensing Symposium Proceedings. Remote Sensing-A Scientific Vision for Sustainable Development.* Vol. 4. IEEE. 1997, pp. 1929–1931.
- [14] P. Berardino et al. "A new algorithm for surface deformation monitoring based on small baseline differential SAR interferograms". In: *IEEE Transactions on Geoscience and Remote Sensing* ().

[15] Chen Yu, Nigel T Penna and Zhenhong Li. "Generation of real-time mode high-resolution water vapor fields from GPS observations". In: *Journal of Geophysical Research: Atmospheres* 122.3 (2017), pp. 2008–2025.

- [16] Chen Yu et al. "Generic atmospheric correction model for interferometric synthetic aperture radar observations". In: *Journal of Geophysical Research: Solid Earth* 123.10 (2018), pp. 9202–9222.
- [17] Chen Yu, Zhenhong Li and Nigel T Penna. "Interferometric synthetic aperture radar atmospheric correction using a GPS-based iterative tropospheric decomposition model". In: *Remote Sensing of Environment* 204 (2018), pp. 109–121.
- [18] Aapo Hyvärinen and Erkki Oja. "Independent component analysis: algorithms and applications". In: *Neural Networks* 13 (2000), pp. 411–430.
- [19] Pierre Comon. "Independent component analysis, a new concept?" In: *Signal processing* 36.3 (1994), pp. 287–314.
- [20] Susanna Ebmeier. "Application of independent component analysis to multitemporal In-SAR data with volcanic case studies". In: *Journal of Geophysical Research: Solid Earth* 121 (2016), pp. 8970–8986.
- [21] Scikit-learn contributors. *ICA vs PCA*. Accessed: 2024-06-13. 2024. URL: https://scikit-learn.org/stable/auto_examples/decomposition/plot_ica_vs_pca.html#sphx-glr-auto-examples-decomposition-plot-ica-vs-pca-py.
- [22] M Bottiglieri et al. "Independent component analysis as a tool for ground deformation analysis". In: *Geophysical Journal International* 168.3 (2007), pp. 1305–1310.
- [23] M. Przeor et al. "Elastic interaction between Mauna Loa and Kīlauea evidenced by independent component analysis". In: *Scientific Reports* 12 (2022), p. 19863. DOI: 10.1038/s41598-022-24308-0.
- [24] Jan Rychlewski. "On Hooke's law". In: *Journal of Applied Mathematics and Mechanics* 48.3 (1984), pp. 303–314.
- [25] Douglas McTigue. "Elastic stress and deformation near a finite spherical magma body: resolution of the point source paradox". In: *Journal of Geophysical Research: Solid Earth* 92 (1987), pp. 12931–12940.
- [26] David D Pollard and Gary Holzhausen. "On the mechanical interaction between a fluid-filled fracture and the Earth's surface". In: *Tectonophysics* 53.1-2 (1979), pp. 27–57.
- [27] Paul M Davis. "Surface deformation associated with a dipping hydrofracture". In: *Journal of Geophysical Research: Solid Earth* 88.B7 (1983), pp. 5826–5834.
- [28] Xue-Min Yang and Paul M Davis. "Deformation due to a rectangular tension crack in an elastic half-space". In: *Bulletin of the Seismological Society of America* 76.3 (1986), pp. 865–881.
- [29] Paul M Davis. "Surface deformation due to inflation of an arbitrarily oriented triaxial ellipsoidal cavity in an elastic half-space, with reference to Kilauea volcano, Hawaii". In: *Journal of Geophysical Research: Solid Earth* 91.B7 (1986), pp. 7429–7438.
- [30] Yuri Fialko, Yakov Khazan and Mark Simons. "Deformation due to a pressurized horizontal circular crack in an elastic half-space, with applications to volcano geodesy". In: *Geophysical Journal International* 146.1 (2001), pp. 181–190.
- [31] Yoshimitsu Okada. "Surface deformation due to shear and tensile faults in a half-space". In: *Bulletin of the Seismological Society of America* 75 (1985), pp. 1135–1154.
- [32] Olek C Zienkiewicz and Robert L Taylor. *The finite element method: The basis*. Butterworth Heinemann, 2000.

[33] Olek C Zienkiewicz and Robert L Taylor. *The finite element method for solid and structural mechanics*. Elsevier, 2005.

- [34] Tirupathi Chandrupatla and Ashok Belegundu. *Introduction to finite elements in engineering*. Cambridge University Press, 2021.
- [35] Ivan Koulakov et al. "Local earthquake seismic tomography reveals the link between crustal structure and volcanism in Tenerife (Canary Islands)". In: *Journal of Geophysical Research: Solid Earth* 128.3 (2023), e2022JB025798.
- [36] John A Nelder and Roger Mead. "A simplex method for function minimization". In: *The computer journal* 7.4 (1965), pp. 308–313.
- [37] William Menke. Geophysical data analysis: Discrete inverse theory. Academic press, 2018.
- [38] Richard C Aster, Brian Borchers and Clifford H Thurber. *Parameter estimation and inverse problems*. Elsevier, 2018.
- [39] Wikipedia contributors. *Nelder-Mead method*. Accessed: 2024-06-13. 2023. URL: https://en.wikipedia.org/wiki/Nelder%E2%80%93Mead method.
- [40] Edward Venzke. "Global volcanism program. Volcanoes of the World". In: 4.1 (2013), p. 1280.
- [41] Michael P Poland, Asta Miklius and Emily Montgomery-Brown. "Magma supply, storage, and transport at shield-stage Hawaiian volcanoes. Characteristics of Hawaii. Volcanoes". In: 179 (2015), pp. 179–234.
- [42] Thomas R Walter and Falk Amelung. "Volcano-earthquake interaction at Mauna Loa volcano, Hawaii". In: *Journal of Geophysical Research: Solid Earth* 111.B5 (2006).
- [43] Susi Pepe et al. "The use of massive deformation datasets for the analysis of spatial and temporal evolution of Mauna Loa volcano (Hawaii)". In: *Remote Sensing* 10 (2018), p. 968.
- [44] Paul G Okubo, Harley M Benz and Bernard A Chouet. "Imaging the crustal magma sources beneath Mauna Loa and Kilauea volcanoes, Hawaii". In: *Geology* 25 (1997), pp. 867–870.
- [45] Nicolas Le Corvec and Thomas R Walter. "Volcano spreading and fault interaction influenced by rift zone intrusions: insights from analogue experiments analyzed with digital image correlation technique". In: *Journal of Volcanology and Geothermal Research* 183 (2009), pp. 170–182.
- [46] Roger P Denlinger and Paul Okubo. "Structure of the mobile south flank of Kilauea volcano, Hawaii". In: *Journal of Geophysical Research: Solid Earth* 100 (1995), pp. 24499–24507.
- [47] Jason K Morgan et al. "Overthrusting and sediment accretion along Kilauea's mobile south flank, Hawaii: evidence for volcanic spreading from marine seismic reflection data". In: *Geology* 28 (2000), pp. 667–670.
- [48] Andrea Borgia. "Dynamic basis of volcanic spreading". In: *Journal of Geophysical Research: Solid Earth* 99 (1994), pp. 17791–17804.
- [49] Fred W Klein. "Patterns of historical eruptions at Hawaiian volcanoes". In: *Journal of Volcanology and Geothermal Research* 12 (1982), pp. 1–35.
- [50] Asta Miklius and Peter Cervelli. "Interaction between Kilauea and Mauna Loa". In: *Nature* 421 (2003), pp. 229–229.
- [51] Helge M Gonnermann et al. "Coupling at Mauna Loa and Kīlauea by stress transfer in an asthenospheric melt layer". In: *Nature Geoscience* 5.11 (2012).
- [52] Falk Amelung et al. "Stress control of deep rift intrusion at Mauna Loa volcano, Hawaii". In: *Science* 316 (2007), pp. 1026–1030.
- [53] Michael P Poland, A J Sutton and Terrence M Gerlach. "Magma degassing triggered by static decompression at Kīlauea volcano, Hawai'i". In: *Geophysical Research Letters* 36.16 (2009).

[54] Michael P Poland et al. "A mantle-driven surge in magma supply to Kīlauea volcano during 2003–2007". In: *Nature Geoscience* 5 (2012), pp. 295–300.

- [55] Donald A Swanson, Wendell A Duffield and Richard S Fiske. *Displacement of the south flank of Kilauea volcano; the result of forceful intrusion of magma into the rift zones*. Tech. rep. US Government Printing Office, 1976.
- [56] Robert Decker et al. "Seismicity and surface deformation of Mauna Loa volcano, Hawaii". In: EOS Trans. Am. Geophys. Union 64 (1983), pp. 545–547.
- [57] Max Wyss. "Regular intervals between Hawaiian earthquakes: implications for predicting the next event". In: *Science* 234 (1986), pp. 726–728.
- [58] Susan Owen et al. "Rapid deformation of the south flank of Kilauea volcano, Hawaii". In: *Science* 267 (1995), pp. 1328–1332.
- [59] Paul T Delaney et al. "Volcanic spreading at Kilauea, 1976–1996". In: *Journal of Geophysical Research: Solid Earth* 103 (1998), pp. 18003–18023.
- [60] Andrea Borgia, B Treves et al. "Volcanic plates overriding the ocean crust: structure and dynamics of Hawaiian volcanoes". In: *Geological Society, London, Special Publications* 60 (1992), pp. 277–299.
- [61] Emily K Montgomery-Brown and Asta Miklius. "Periodic dike intrusions at Kīlauea volcano, Hawai'i". In: *Geology* 49 (2021), pp. 397–401.
- [62] Julia K Morgan and David A Clague. "Volcanic spreading on Mauna Loa volcano, Hawaii: Evidence from accretion, alteration, and exhumation of volcaniclastic sediments". In: *Geology* 31 (2003), pp. 411–414.
- [63] Michael P Poland. "Asar images a diverse set of deformation patterns at Kīlauea volcano, Hawaii". In: *Envisat Symposium 2007 SP-636*. 2007.
- [64] Thomas A Jaggar. "Report of the Hawaiian Volcano Observatory of the Massachusetts Institute of Technology and the Hawaiian Volcano Research Association". In: *Society of Arts of the Massachusetts Institute of Technology* (1912).
- [65] J Rhodes and S Hart. "Episodic trace element and isotopic variations in historical Mauna Loa lavas: Implications for magma and plume dynamics". In: *Washington, DC Am. Geophys. Union Geophys. Monogr. Ser.* 92 (1995), pp. 263–288.
- [66] Manoochehr Shirzaei, Thomas R Walter and Roland Bürgmann. "Coupling of Hawaiian volcanoes only during overpressure condition". In: *Geophysical Research Letters* 40.10 (2013), pp. 1994–1999.
- [67] Hirotugu Akaike. "A new look at the statistical model identification". In: *IEEE Transactions on Automatic Control* 19 (1974), pp. 716–723.
- [68] Francesco Casu, Mariarosaria Manzo and Riccardo Lanari. "A quantitative assessment of the SBAS algorithm performance for surface deformation retrieval from DInSAR data". In: *Remote Sensing of Environment* 102 (2006), pp. 195–210.
- [69] Alessandro Bonaccorso and Paul M Davis. "Models of ground deformation from vertical volcanic conduits with application to eruptions of Mount St. Helens and Mount Etna". In: *Journal of Geophysical Research: Solid Earth* 104 (1999), pp. 10531–10542.
- [70] Geoffrey Blewitt and William C Hammond. "Harnessing the GPS data explosion for interdisciplinary science". In: *Eos, Transactions American Geophysical Union* 2019 (2018), pp. 1–8
- [71] AJ Haines and WE Holt. "A procedure for obtaining the complete horizontal motions within zones of distributed deformation from the inversion of strain rate data". In: *Journal of Geophysical Research: Solid Earth* 98.B7 (1993), pp. 12057–12082.

[72] Hans-Georg Scherneck et al. "Fennoscandian strain rates from BIFROST GPS: A gravitating, thick-plate approach". In: *Journal of Geodynamics* 50 (2010). https://doi.org/10.1016/j.jog.2009.11.005, pp. 19–26.

- [73] Valentina Bruno et al. "Ground deformations and volcanic processes as imaged by CGPS data at Mt. Etna (Italy) between 2003 and 2008". In: *Journal of Geophysical Research: Solid Earth* 117.B7 (2012).
- [74] Diane Rivet et al. "Long-term dynamics of Piton de la Fournaise volcano from 13 years of seismic velocity change measurements and GPS observations". In: *Journal of Geophysical Research: Solid Earth* 119 (2014), pp. 7654–7666.
- [75] Guoqing Lin et al. "Three-dimensional seismic velocity structure of Mauna Loa and Kilauea volcanoes in Hawaii from local seismic tomography". In: *Journal of Geophysical Research: Solid Earth* 119 (2014), pp. 4377–4392.
- [76] E. Ancochea et al. "Constructive and destructive episodes in the building of a young oceanic island, La Palma, Canary Islands, and genesis of the Caldera de Taburiente". In: *Journal of Volcanology and Geothermal Research* 60.3–4 (1994), pp. 243–262. DOI: 10.1016/0377-0273(94)90022-1.
- [77] J. L. Barrera Morate and R. García Moral. *Mapa Geológico de Canarias*. GRAFCAN. 2011.
- [78] L. D'Auria et al. "Rapid magma ascent beneath La Palma revealed by seismic tomography". In: *Scientific Reports* 12.1 (2022), p. 17654. DOI: 10.1038/s41598-022-37286-3.
- [79] J. C. Carracedo et al. "The 2021 eruption of the Cumbre Vieja volcanic ridge on La Palma, Canary Islands". In: *Geology Today* 38.3 (2022), pp. 94–107. DOI: 10.1111/gto.12397.
- [80] I. Cabrera-Pérez et al. "Spatio-temporal velocity variations observed during the pre-eruptive episode of La Palma 2021 eruption inferred from ambient noise interferometry". In: *Scientific Reports* 13.1 (2023), p. 12039. DOI: 10.1038/s41598-023-11202-y.
- [81] Luca D'Auria et al. "Magma injection beneath the urban area of Naples: a new mechanism for the 2012–2013 volcanic unrest at Campi Flegrei caldera". In: *Scientific reports* 5.1 (2015), p. 13100.
- [82] C. De Luca et al. "Pre-and co-eruptive analysis of the September 2021 eruption at Cumbre Vieja volcano (La Palma, Canary Islands) through DInSAR measurements and analytical modeling". In: *Geophysical Research Letters* 49.7 (2022), e2021097293. DOI: 10.1029/2021GL097293.
- [83] J. Fernández et al. "Shallow magmatic intrusion evolution below La Palma before and during the 2021 eruption". In: *Scientific Reports* 12.1 (2022), p. 20257. DOI: 10.1038/s41598-022-43315-8.
- [84] I. Cabrera-Pérez et al. "Geothermal and structural features of La Palma island (Canary Islands) imaged by ambient noise tomography". In: *Scientific Reports* 13.1 (2023), p. 12892. DOI: 10.1038/s415.
- [85] M. J. Pankhurst et al. "Rapid response petrology for the opening eruptive phase of the 2021 Cumbre Vieja eruption, La Palma, Canary Islands". In: *Volcanica* 5 ().
- [86] Fuensanta G Montesinos et al. "Insights into the Magmatic Feeding System of the 2021 Eruption at Cumbre Vieja (La Palma, Canary Islands) Inferred from Gravity Data Modeling". In: *Remote Sensing* 15.7 (2023), p. 1936.
- [87] Valeria Muñoz et al. "Satellite radar and camera time series reveal transition from aligned to distributed crater arrangement during the 2021 eruption of Cumbre Vieja, La Palma (Spain)". In: *Remote Sensing* 14.23 (2022), p. 6168.

[88] E Rivalta et al. "A review of mechanical models of dike propagation: Schools of thought, results and future directions". In: *Tectonophysics* 638 (2015), pp. 1–42.

- [89] Torsten Dahm. "Numerical simulations of the propagation path and the arrest of fluid-filled fractures in the Earth". In: *Geophysical Journal International* 141.3 (2000), pp. 623–638.
- [90] Francesco Maccaferri, Maurizio Bonafede and Eleonora Rivalta. "A quantitative study of the mechanisms governing dike propagation, dike arrest and sill formation". In: *Journal of Volcanology and Geothermal Research* 208.1-2 (2011), pp. 39–50.
- [91] Antonio G Camacho et al. "Structural results for La Palma island using 3-D gravity inversion". In: *Journal of Geophysical Research: Solid Earth* 114.B5 (2009).
- [92] Federico Di Paolo et al. "La Palma island (Spain) geothermal system revealed by 3D magnetotelluric data inversion". In: *Scientific reports* 10.1 (2020), p. 18181.
- [93] Iván Cabrera-Pérez et al. "A nonlinear multiscale inversion approach for ambient noise tomography". In: *Geophysical Journal International* 225.2 (2021), pp. 1158–1173.
- [94] Eleonora Rivalta and Torsten Dahm. "Acceleration of buoyancy-driven fractures and magmatic dikes beneath the free surface". In: *Geophysical Journal International* 166.3 (2006), pp. 1424–1439.
- [95] Jorge E Romero et al. "The initial phase of the 2021 Cumbre Vieja ridge eruption (Canary Islands): Products and dynamics controlling edifice growth and collapse". In: *Journal of Volcanology and Geothermal Research* 431 (2022), p. 107642.
- [96] Costanza Bonadonna et al. "Physical Characterization of Long-Lasting Hybrid Eruptions: The 2021 Tajogaite Eruption of Cumbre Vieja (La Palma, Canary Islands)". In: *Journal of Geophysical Research: Solid Earth* 127.11 (2022), e2022JB025302.
- [97] E Saria et al. "A new velocity field for Africa from combined GPS and DORIS space geodetic Solutions: Contribution to the definition of the African reference frame (AFREF)". In: *Journal of Geophysical Research: Solid Earth* 118.4 (2013), pp. 1677–1697.
- [98] Riccardo Lanari et al. "An overview of the small baseline subset algorithm: A DInSAR technique for surface deformation analysis". In: *Deformation and Gravity Change: Indicators of Isostasy, Tectonics, Volcanism, and Climate Change* (2007), pp. 637–661.
- [99] Ekaterina Tymofyeyeva and Yuri Fialko. "Mitigation of atmospheric phase delays in InSAR data, with application to the eastern California shear zone". In: *Journal of Geophysical Research: Solid Earth* 120.8 (2015), pp. 5952–5963.
- [100] Alessandro Ferretti, Claudio Prati and Fabio Rocca. "Permanent scatterers in SAR interferometry". In: *IEEE Transactions on geoscience and remote sensing* 39.1 (2001), pp. 8–20.
- [101] Dochul Yang and Sean M Buckley. "Estimating high-resolution atmospheric phase screens from radar interferometry data". In: *IEEE transactions on geoscience and remote sensing* 49.8 (2011), pp. 3117–3128.
- [102] Juan Carlos Carracedo et al. "Eruptive and structural history of Teide Volcano and rift zones of Tenerife, Canary Islands". In: *Geological Society of America Bulletin* 119.9-10 (2007), pp. 1027–1051.
- [103] Joachim Gottsmann et al. "New evidence for the reawakening of Teide volcano". In: *Geophysical Research Letters* 33.20 (2006).
- [104] Javier Almendros et al. "Array analyses of volcanic earthquakes and tremor recorded at Las Cañadas caldera (Tenerife Island, Spain) during the 2004 seismic activation of Teide volcano". In: *Journal of Volcanology and Geothermal Research* 160.3-4 (2007), pp. 285–299.

[105] J Martí and A Geyer. "Central vs flank eruptions at Teide–Pico Viejo twin stratovolcanoes (Tenerife, Canary Islands)". In: *Journal of Volcanology and Geothermal Research* 181.1-2 (2009), pp. 47–60.

- [106] K Weber et al. "Ground-based remote sensing of gas emissions from Teide volcano (Tenerife, Canary Islands, Spain): First results". In: *Remote Sensing of Clouds and the Atmosphere XI*. Vol. 6362. SPIE. 2006, pp. 384–393.
- [107] G Melián et al. "A magmatic source for fumaroles and diffuse degassing from the summit crater of Teide Volcano (Tenerife, Canary Islands): a geochemical evidence for the 2004–2005 seismic–volcanic crisis". In: *Bulletin of Volcanology* 74 (2012), pp. 1465–1483.
- [108] Nemesio M Pérez et al. "An increasing trend of diffuse CO2 emission from Teide volcano (Tenerife, Canary Islands): geochemical evidence of magma degassing episodes". In: *Journal of the Geological Society* 170.4 (2013), pp. 585–592.
- [109] J Fernández et al. "Gravity-driven deformation of Tenerife measured by InSAR time series analysis". In: *Geophysical Research Letters* 36.4 (2009).
- [110] P Tizzani et al. "Surface deformation of Long Valley caldera and Mono Basin, California, investigated with the SBAS-InSAR approach". In: *Remote Sensing of Environment* 108.3 (2007), pp. 277–289.
- [111] Antonio Pepe et al. "Surface deformation of active volcanic areas retrieved with the SBAS-DInSAR technique: an overview". In: *Annals of Geophysics* (2008).
- [112] Fausto Acernese et al. "Properties of seismic noise at the Virgo site". In: *Classical and Quantum Gravity* 21.5 (2004), S433.
- [113] Alicia García et al. "Monitoring the reawakening of Canary Islands' Teide volcano". In: *Eos, Transactions American Geophysical Union* 87.6 (2006), pp. 61–65.
- [114] M Tárraga et al. "On the predictability of volcano-tectonic events by low frequency seismic noise analysis at Teide-Pico Viejo volcanic complex, Canary Islands". In: *Natural Hazards and Earth System Sciences* 6.3 (2006), pp. 365–376.
- [115] Joachim Gottsmann et al. "Shallow structure beneath the Central Volcanic Complex of Tenerife from new gravity data: implications for its evolution and recent reactivation". In: *Physics of the Earth and Planetary Interiors* 168.3-4 (2008), pp. 212–230.
- [116] Alvaro Márquez et al. "Spreading and potential instability of Teide volcano, Tenerife, Canary Islands". In: *Geophysical Research Letters* 35.5 (2008).
- [117] I Domínguez Cerdeña, Carmen del Fresno and Luis Rivera. "New insight on the increasing seismicity during Tenerife's 2004 volcanic reactivation". In: *Journal of Volcanology and Geothermal Research* 206.1-2 (2011), pp. 15–29.
- [118] Luca D'Auria et al. "The 2016 Tenerife (Canary Islands) long-period seismic swarm". In: *Journal of Geophysical Research: Solid Earth* 124.8 (2019), pp. 8739–8752.
- [119] Eleazar Padrón et al. "Changes in diffuse degassing from the summit crater of Teide volcano (Tenerife, Canary Islands) prior to the 2016 Tenerife long-period seismic swarm". In: *Journal of Geophysical Research: Solid Earth* 126.3 (2021), e2020JB020318.
- [120] Cecilia Amonte et al. "Hydrogeochemical temporal variations related to changes of seismic activity at Tenerife, Canary Islands". In: *Bulletin of Volcanology* 83.4 (2021), p. 24.
- [121] DW Vasco et al. "Geodetic imaging: reservoir monitoring using satellite interferometry". In: *Geophysical Journal International* 149.3 (2002), pp. 555–571.

Appendix A

Supplementary material for: Elastic interaction between Mauna Loa and Kīlauea evidenced by ICA

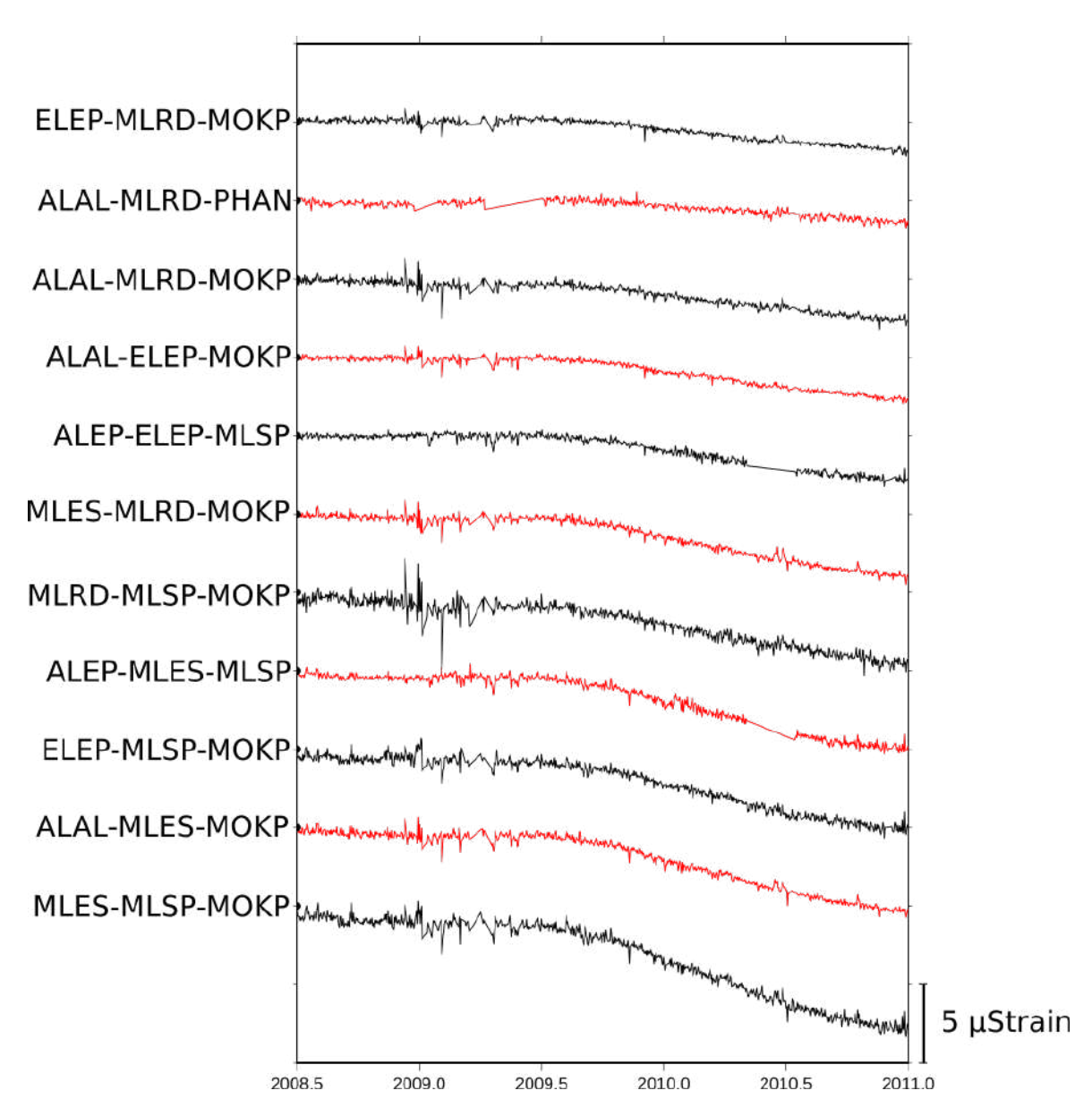


Figure A.1 Areal strain time series for Mauna Loa GPS stations. The labels are triplets of GPS stations surrounding the summit cone of Moku \Box āweoweo Caldera (see Figure S2 for locations). The y-axis on the right shows the aerial strain scale in μ strain, the dimension of the vertical axis is 5 μ strain, Time series colours are alternated in black and red.

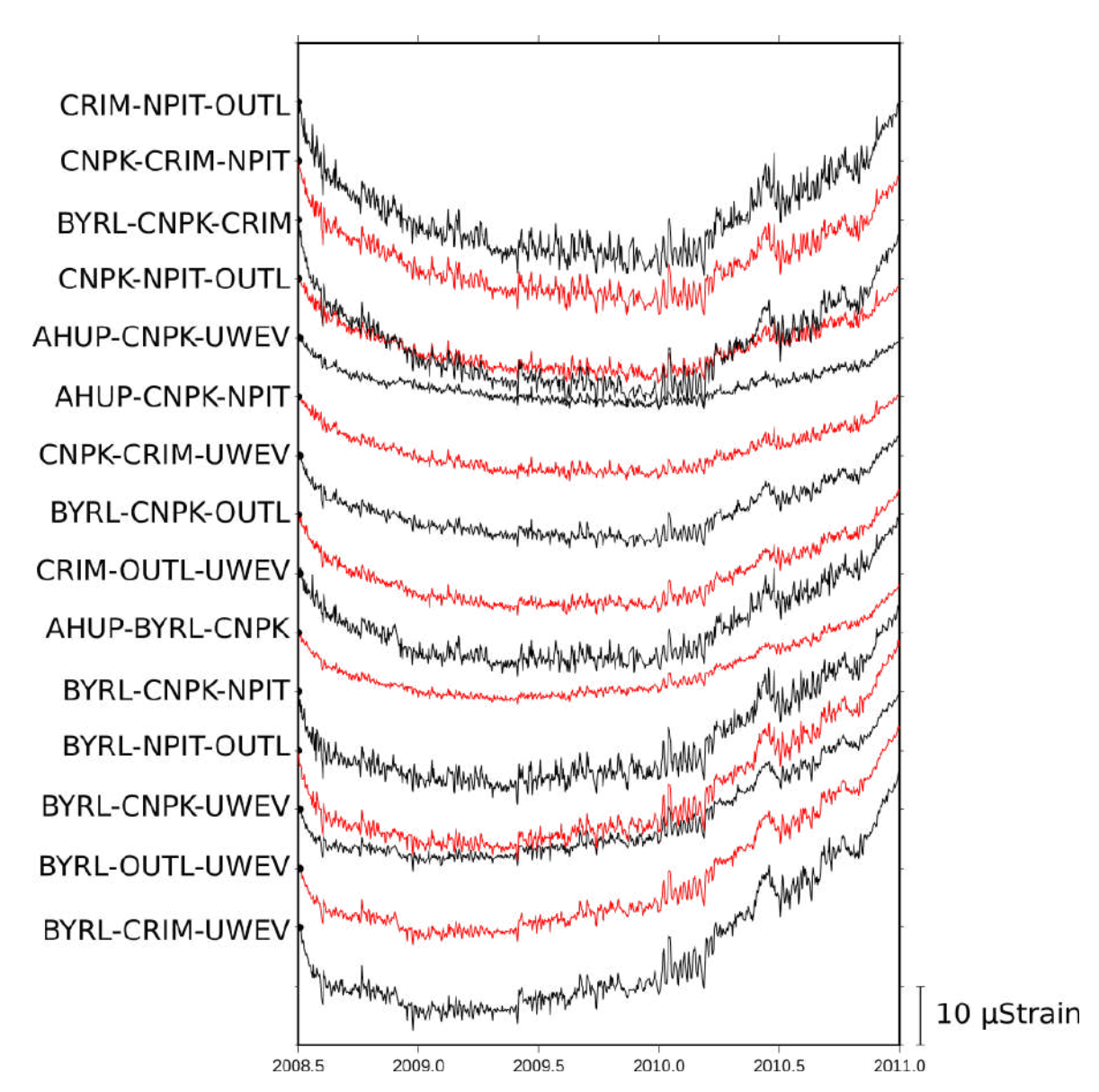


Figure A.2 Areal strain time series for Kīlauea GPS stations. The labels are triplets of GPS stations surrounding the summit cone of Halema \Box uma \Box u Crater (see Figure S2 for the locations). The y-axis on the right shows the aerial strain scale in μ strain, the dimension of the vertical axis is 10 μ strain, being marked by ticks. Note that the axis scale in this figure is different from that of Figure S1. Time series colours are alternated in black and red.

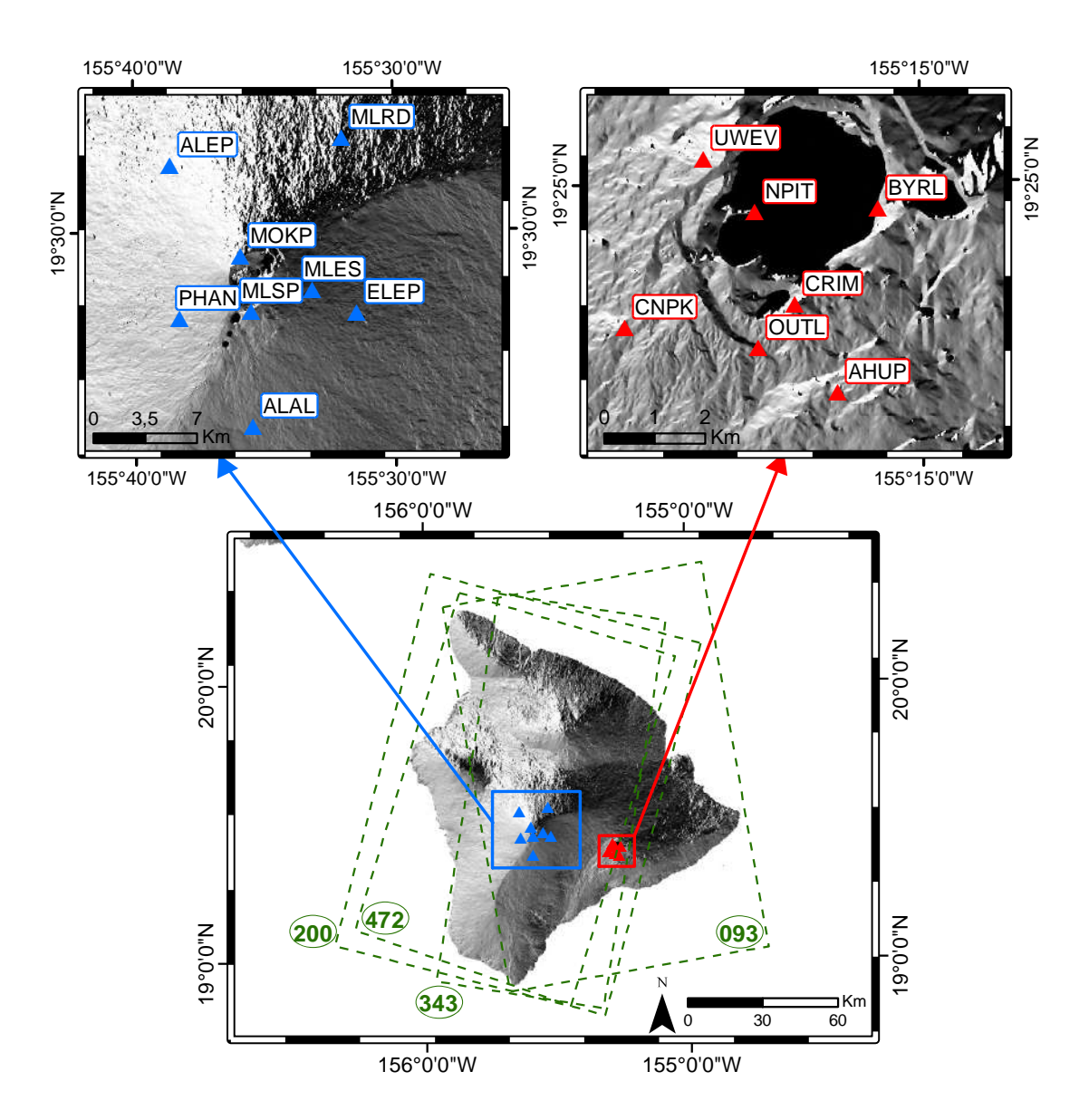


Figure A.3 Location of satellite tracks and GPS stations. The lower map shows Hawai'i Island. The blue rectangle shows the GPS study area of Mauna Loa, while the red rectangle represents the area of Kīlauea GPS stations. Green rectangles mark ENVISAT satellite data tracks along ascending (093) and descending orbits (343, 472, and 200). The upper maps show Mauna Loa and Kīlauea summits, respectively, with blue triangles representing the GPS stations of Mauna Loa and red triangles, GPS stations of Kīlauea.

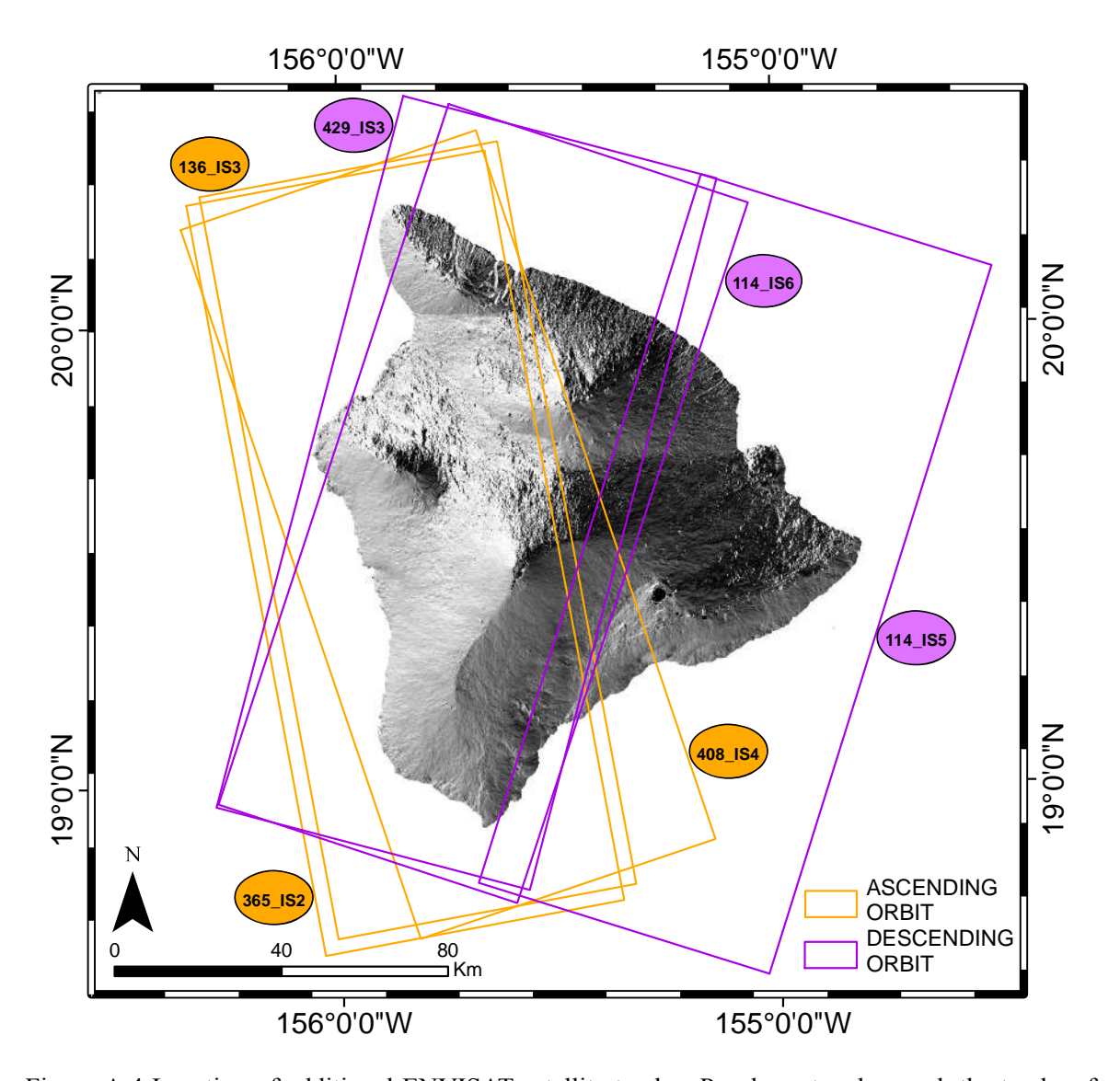


Figure A.4 Location of additional ENVISAT satellite tracks. Purple rectangles mark the tracks of ENVISAT satellite along descending orbits with swaths varying from I3 to I6 (26.0° to 42.8°); orange rectangles mark the tracks of ENVISAT satellite along ascending orbits with swaths varying from I2 to I4 (19.2° to 36.3°).

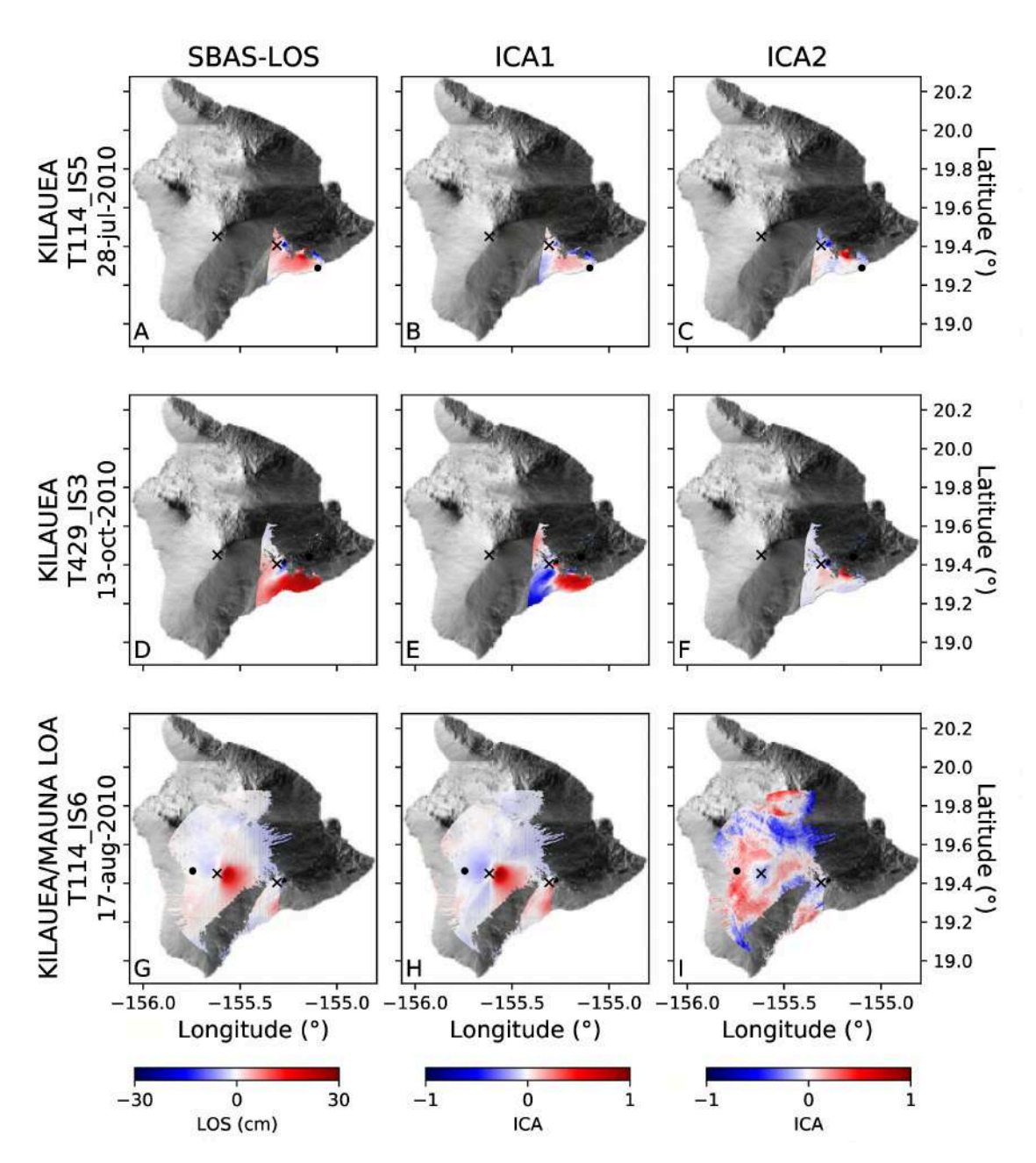


Figure A.5 LOS deformation maps of Mauna Loa. A,B,C: ENVISAT 136 (IS3) orbit; D,E,F: ENVISAT 365 (IS2) orbit; G,H,I: ENVISAT 408 (IS4) orbit (see table S4 for track details). Column 1 shows raw data; columns 2 and 3 represent respectively the first and the second component resulting from applying the ICA decomposition algorithm. Black crosses: see figure 2 for description, while black dots are the reference points used to the SBAS-LOS performance.

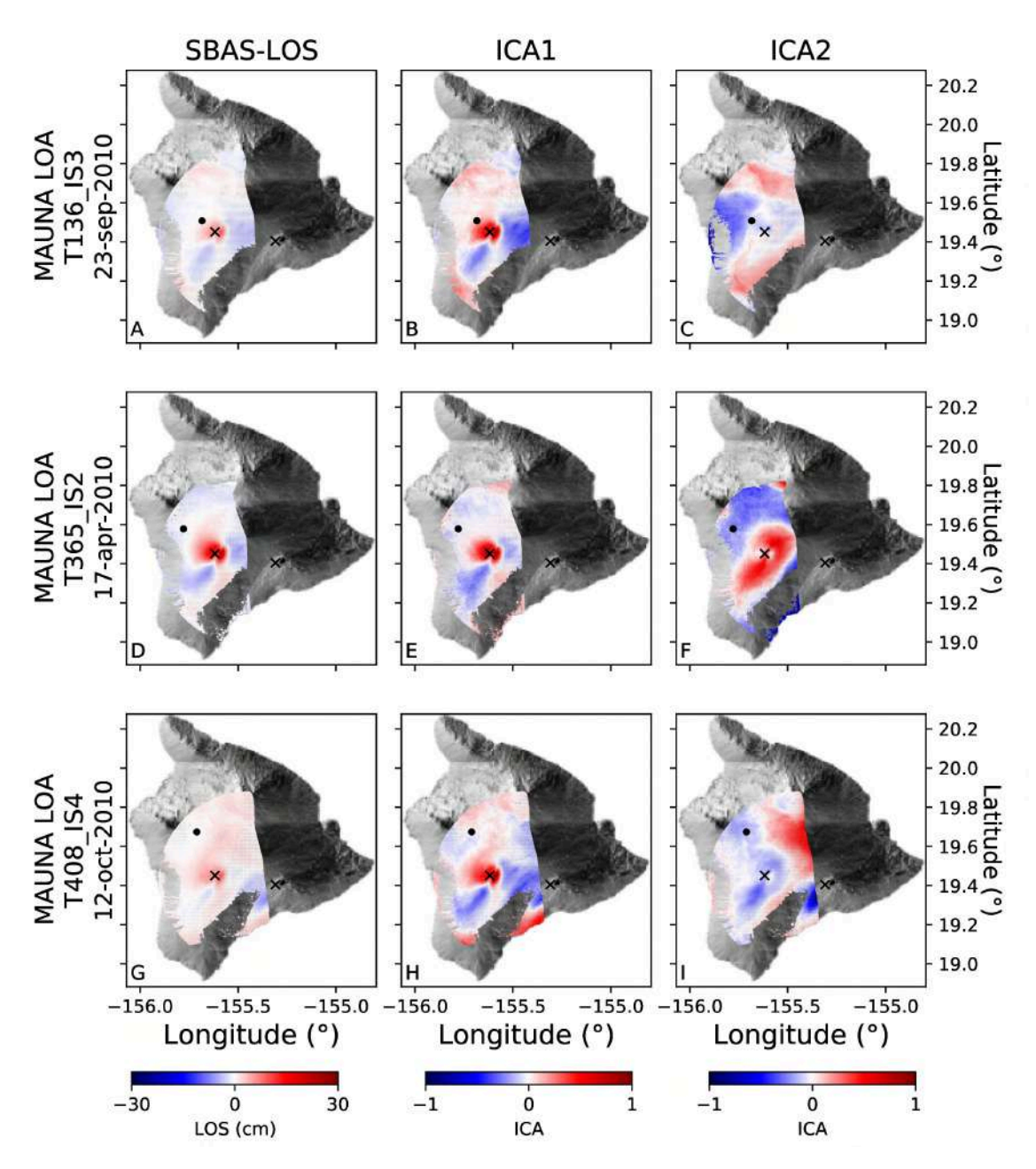


Figure A.6 LOS deformation maps of Kīlauea. A,B,C: ENVISAT 114 (IS5) orbit; D,E,F: ENVISAT 429 (IS3) orbit; G,H,I: ENVISAT 114 (IS6) orbit (see table S1 for track details). Column 1 shows raw data; columns 2 and 3 represent respectively the first and the second component resulting from applying the ICA decomposition algorithm. Black crosses: see figure 2 for description, while black dots are the reference points used to the SBAS-LOS performance.

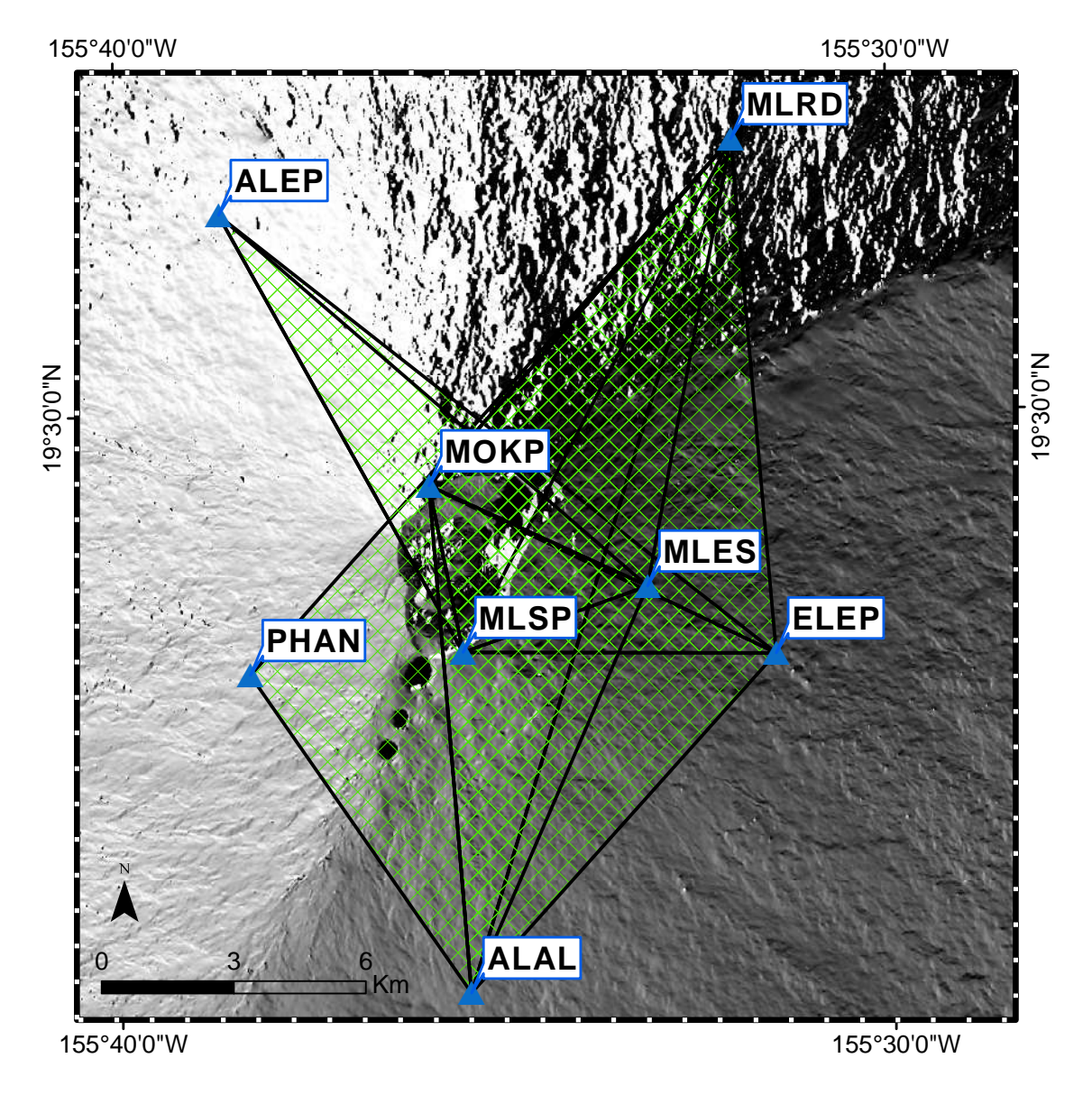


Figure A.7 Mauna Loa GPS station triples used for computing the areal strain time series. Blue triangles represent the GPS stations on Mauna Loa summit Caldera. Every triplet of stations is bordered by black lines and filled by a green grid.

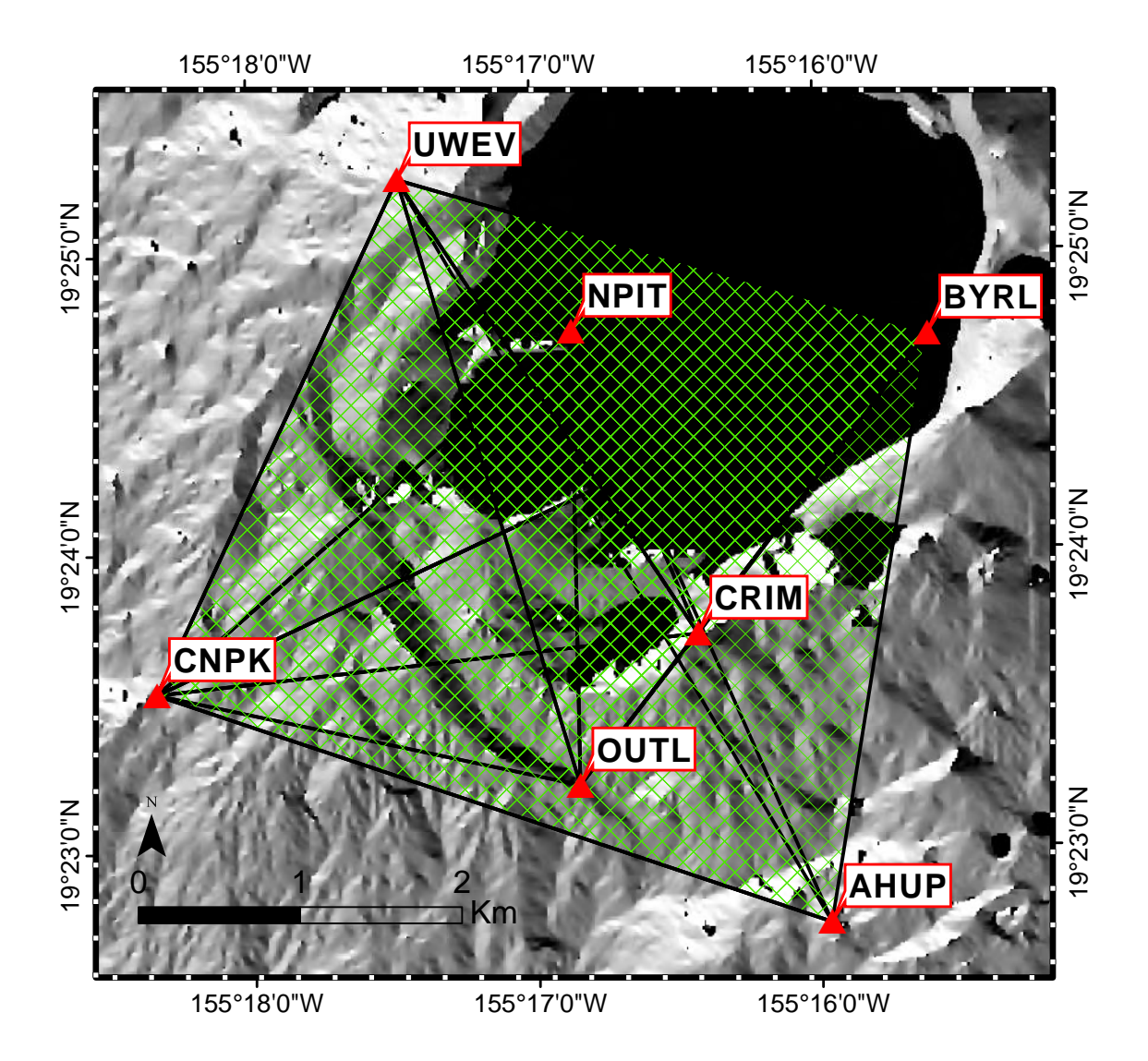


Figure A.8 Kīlauea GPS station triples used for computing the areal strain time series. Red triangles represent the GPS stations in Kīlauea summit Caldera. Every triplet of stations is bordered by black lines and filled by a green grid.

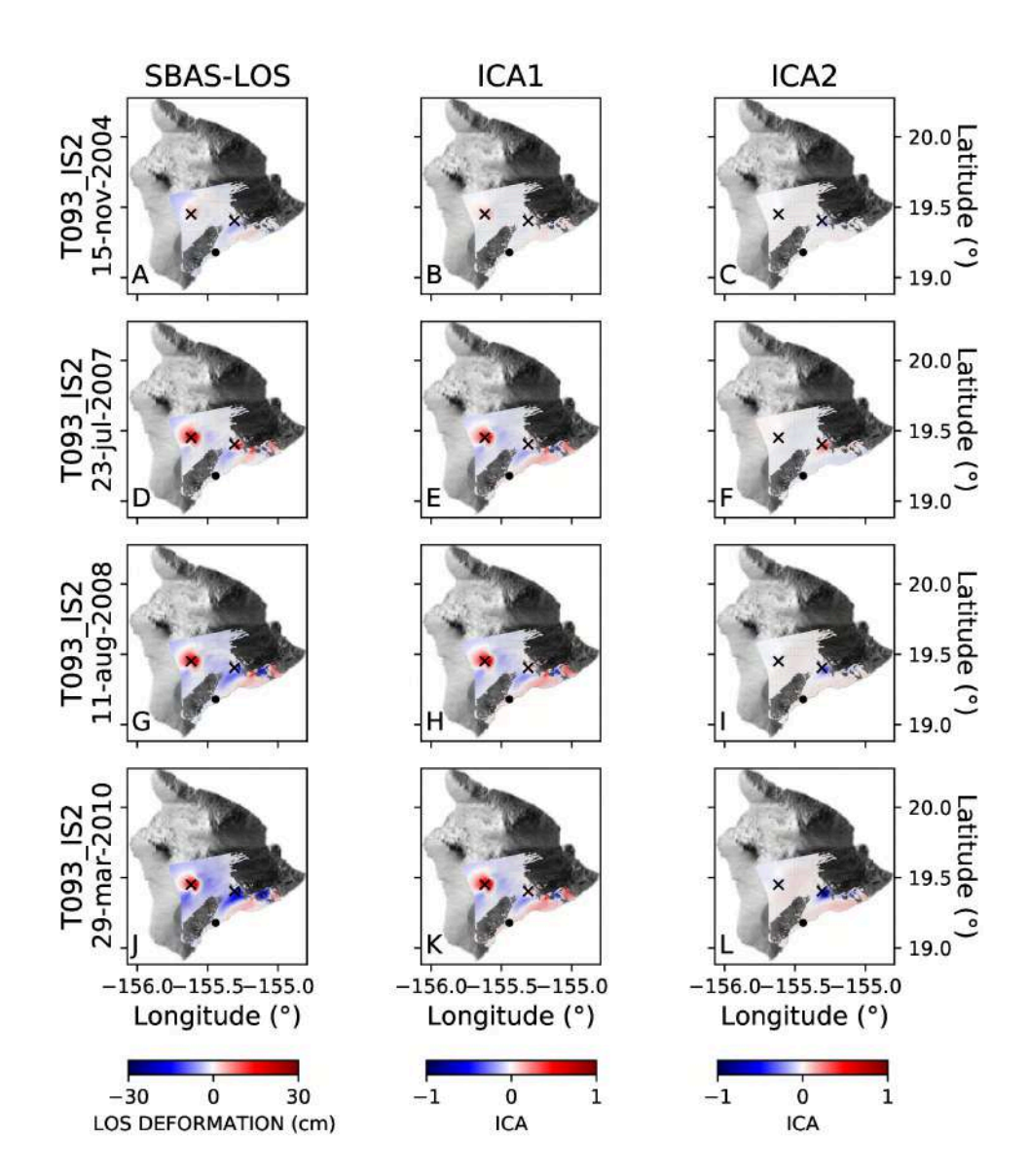


Figure A.9 LOS deformation cumulative maps, first and second component of ICA decomposition of ENVISAT 093 orbit for four different intervals. A, D, G, J: LOS cumulative displacement DInSAR map; B, E, H, J (column 2) and C, F, I, L: (column 3) represent respectively the first and the second component resulting from applying the ICA decomposition algorithm. The black crosses indicate the points used for extracting the time series shown in figure 4, while black dots are the reference points used for the DInSAR SBAS processing.

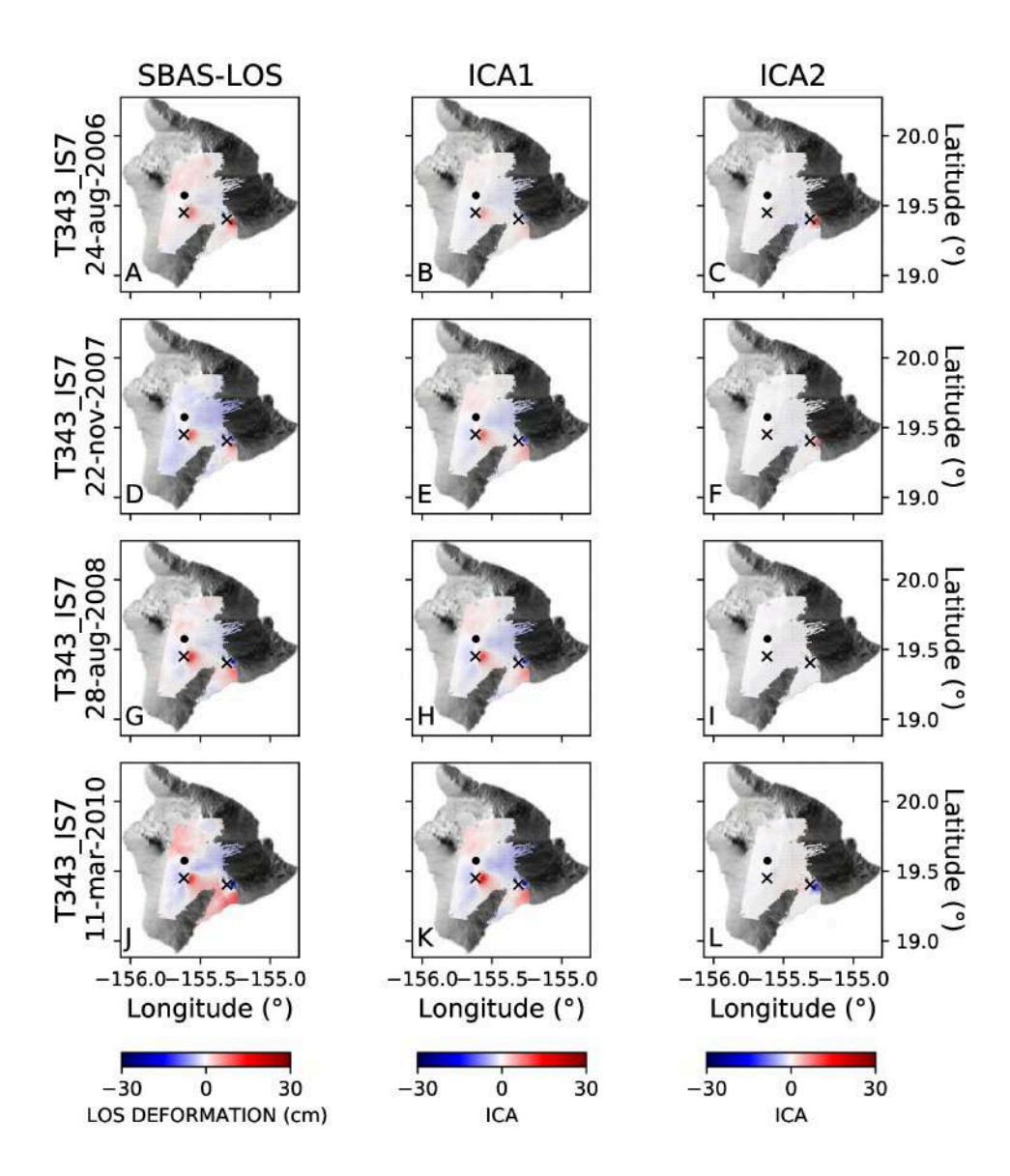


Figure A.10 LOS deformation cumulative maps, first and second component of ICA decomposition of ENVISAT 343 orbit for four different intervals. A, D, G, J: LOS cumulative displacement DInSAR map; B, E, H, J (column 2) and C, F, I, L: (column 3) represent respectively the first and the second component resulting from applying the ICA decomposition algorithm. The black crosses indicate the points used for extracting the time series shown in figure 4, while black dots are the reference points used for the DInSAR SBAS processing.

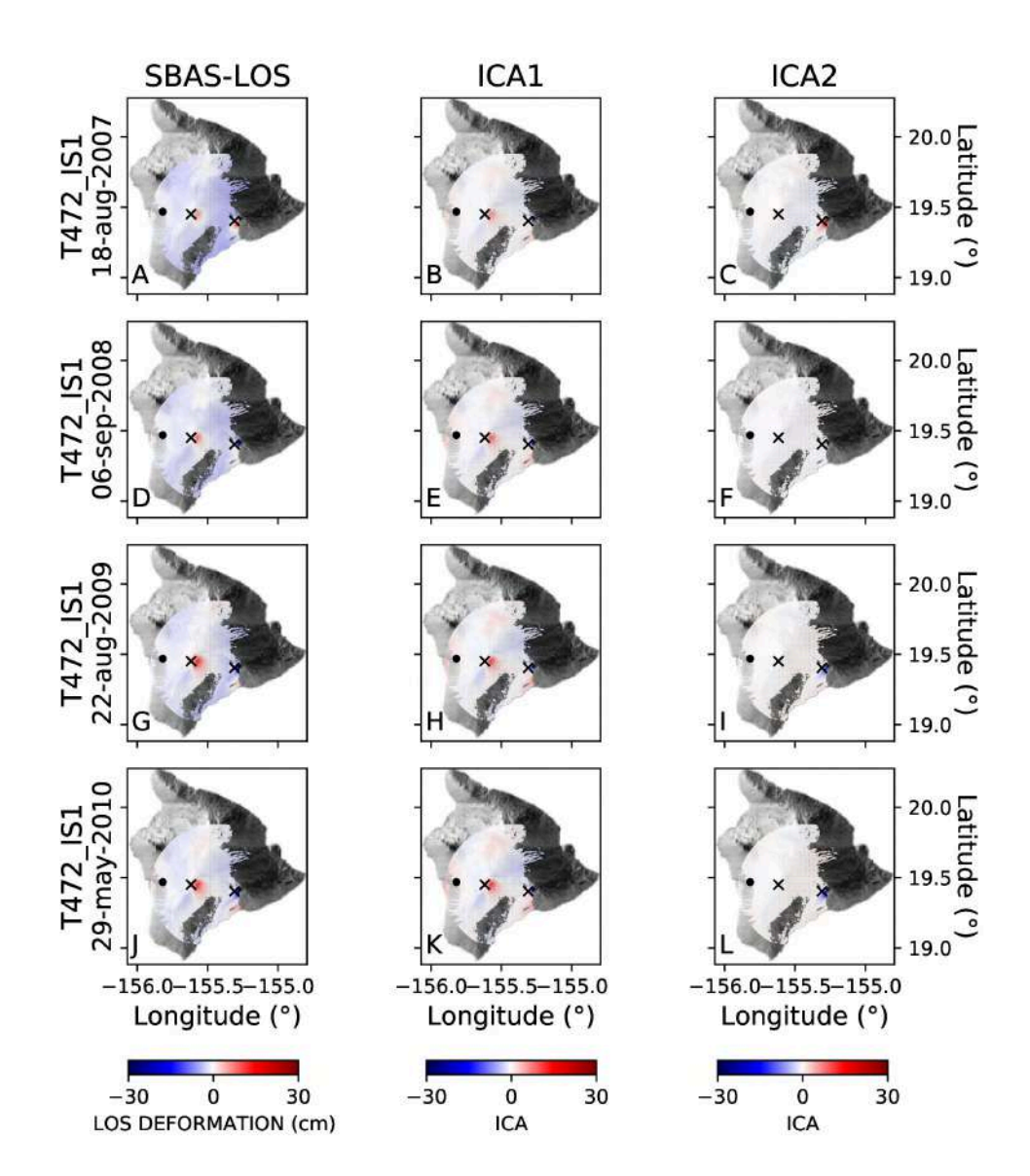


Figure A.11 LOS deformation cumulative maps, first and second component of ICA decomposition of ENVISAT 472 orbit for four different intervals. A, D, G, J: LOS cumulative displacement DInSAR map; B, E, H, J (column 2) and C, F, I, L: (column 3) represent respectively the first and the second component resulting from applying the ICA decomposition algorithm. The black crosses indicate the points used for extracting the time series shown in figure 4, while black dots are the reference points used for the DInSAR SBAS processing.

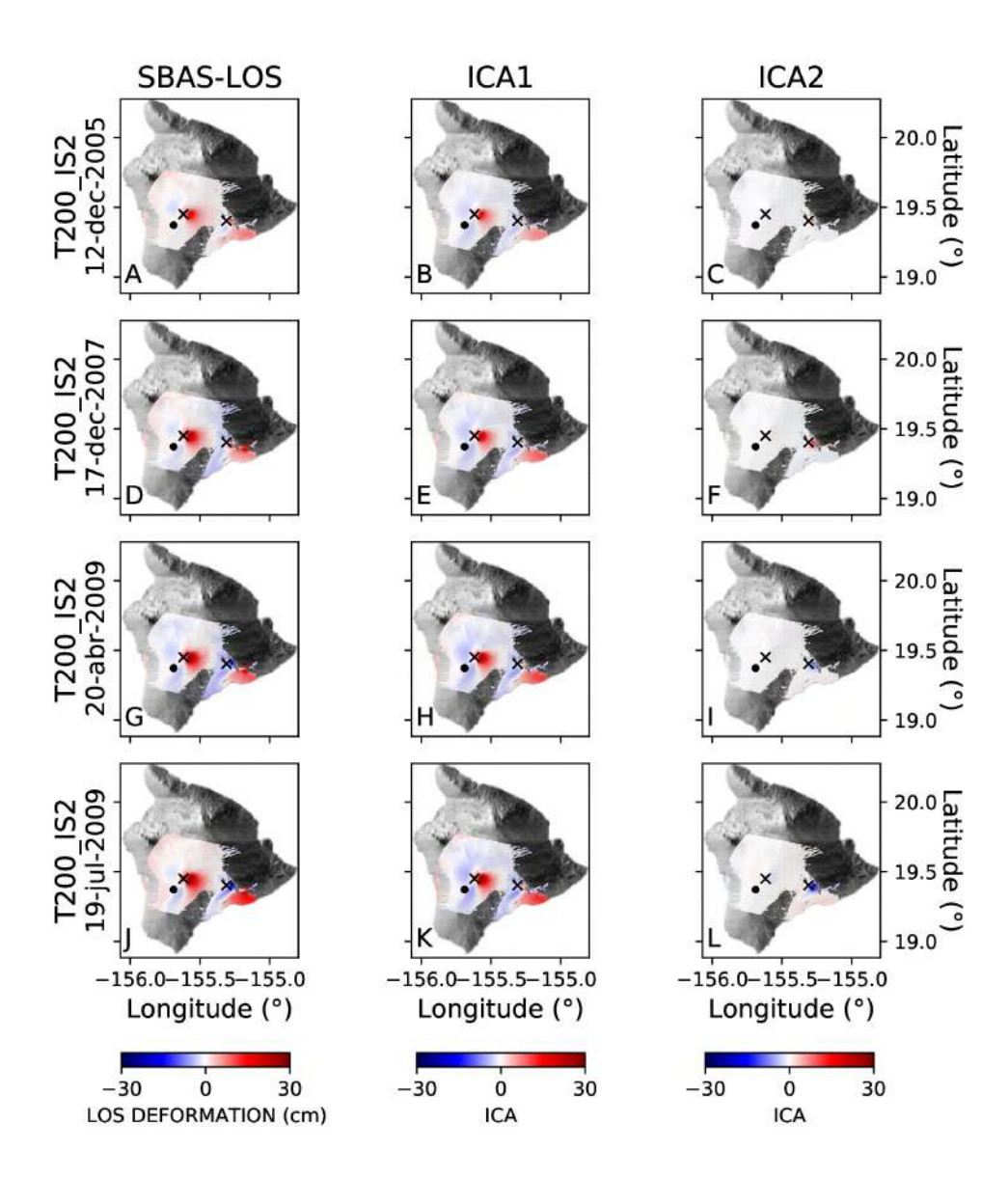


Figure A.12 LOS deformation cumulative maps, first and second component of ICA decomposition of ENVISAT 200 orbit for four different intervals. A, D, G, J: LOS cumulative displacement DInSAR map; B, E, H, J (column 2) and C, F, I, L: (column 3) represent respectively the first and the second component resulting from applying the ICA decomposition algorithm. The black crosses indicate the points used for extracting the time series shown in figure 8.4, while black dots are the reference points used for the DInSAR SBAS processing.

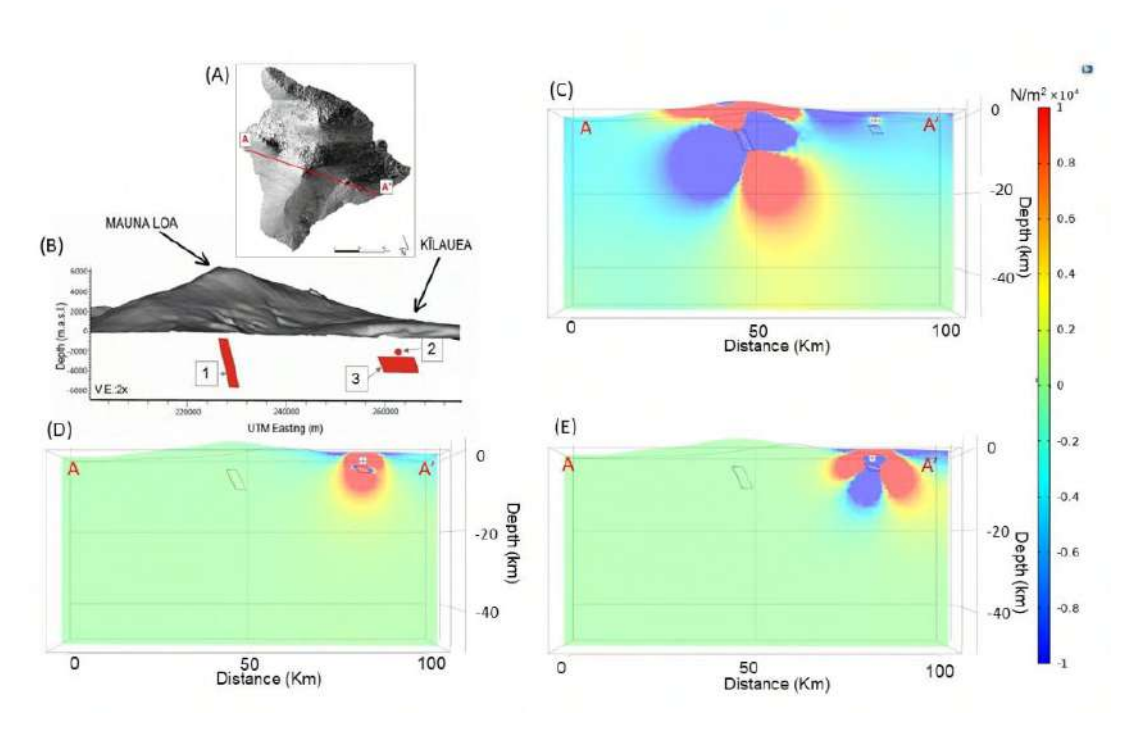


Figure A.13 3D numerical modelling of stress fields. (A) The Digital Elevation Model of Hawai'i Island, with the red line representing the trace (A-A'), used in panels (C-E). (B) tridimensional representation of the modelled ground deformation sources of Mauna Loa and Kīlauea volcanoes. The sources are numbered according to Table S1 in the supplementary material. 1) the Mauna Loa dikeshaped source from ICA1; 2) the Kīlauea Mogi-like source from ICA1; 3) the Kīlauea sill-shaped source from ICA2. Storage areas and topography are exaggerated in size for clarity. (C) stress field represented along the A-A' trace due to an overpressure applied to the Mauna Loa dike-like source. (D) stress field along the A-A' trace due to an overpressure applied to the Kīlauea sill-like source. (E) stress field along the A-A' trace due to an overpressure applied to the Kīlauea sill-like source.

Source		Lat. (ºN)	Long. (ºW)	Depth (m)	Azimut h (º)	Dip	Length (m)	Width (m)
Mauna	Mean	19.43	-155.58	6204.6	28.2	62.1	3982.1	5572.4
Loa								
(ICA1)	Std	0.009	0.015	1870.1	8.9	54.3	3646.1	4396.2
OKADA	******							
Kīlauea	Mean	19.40	-155.26	1202.5	X	X	х	X
(ICA1)								
MOGI	Std	0.011	0.008	471.9	X	X	X	X
Kīlauea	Mean	19.40	-155.26	3566.6	67.0	29.8	7708.1	3136.1
(ICA2) OKADA	Std	0.012	0.03	560.3	17.6	14.1	3577.8	2941.8

Figure A.14 Parameters of modelled sources of ground deformation. The results are the mean value and standard deviation of the modelled parameters of separated inversions of each track.

TRACK	SWATH	LOOK	ORBIT	START	STOP
		ANGLE		TIME	TIME
093	IS2	19.2º-26.7º	ASCENDING	20/01/2003	07/06/2010
343	IS7	42.5°-45.2°	DESCENDING	17/11/2005	07/10/2010
472	IS1	15.0°-22.9°	DESCENDING	31/12/2005	11/09/2010
200	IS2	19.2º-26.7º	DESCENDING	08/12/2003	27/09/2010

Figure A.15 Inventory of the four analysed ENVISAT satellite data tracks in the 2003-2010 period, covering both volcanoes.

	TRACK 093	TRACK 343	TRACK 472	TRACK 200
Component 1	75.30%	82.30%	63.10%	84.20%
Component 2	19.40%	14.70%	32.60%	8.20%
Component 3	5.30%	2.90%	4.30%	7.60%

Figure A.16 Percentage of energy of every component of decomposition for each track.

TRACK	SWATH	LOOK	ORBIT	START	STOP
		ANGLE	OKDII	TIME	TIME
114	IS5	35.8°-39.4°	DESCENDING	16/11/2004	28/07/2009
429	IS3	26.0°-31.4°	DESCENDING	12/02/2003	13/10/2010
136	IS3	26.0°-31.4°	ASCENDING	27/01/2005	23/09/2010
365	IS2	19.2°-26.7°	ASCENDING	08/02/2003	17/04/2010
408	IS4	31.0°-36.3°	ASCENDING	27/12/2005	12/10/2010
114	IS6	39.1°-42.8°	DESCENDING	07/08/2005	17/08/2010

 $Figure\ A.17\ Inventory\ of\ the\ 6\ analyzed\ and\ discarded\ tracks\ of\ ENVISAT\ satellite\ data\ in\ 2003-2010\ period.$

Appendix B

Supplementary material for: Geodetic imaging of magma ascent through a bent and twisted dike during the Tajogaite eruption of 2021 (La Palma, Canary Islands

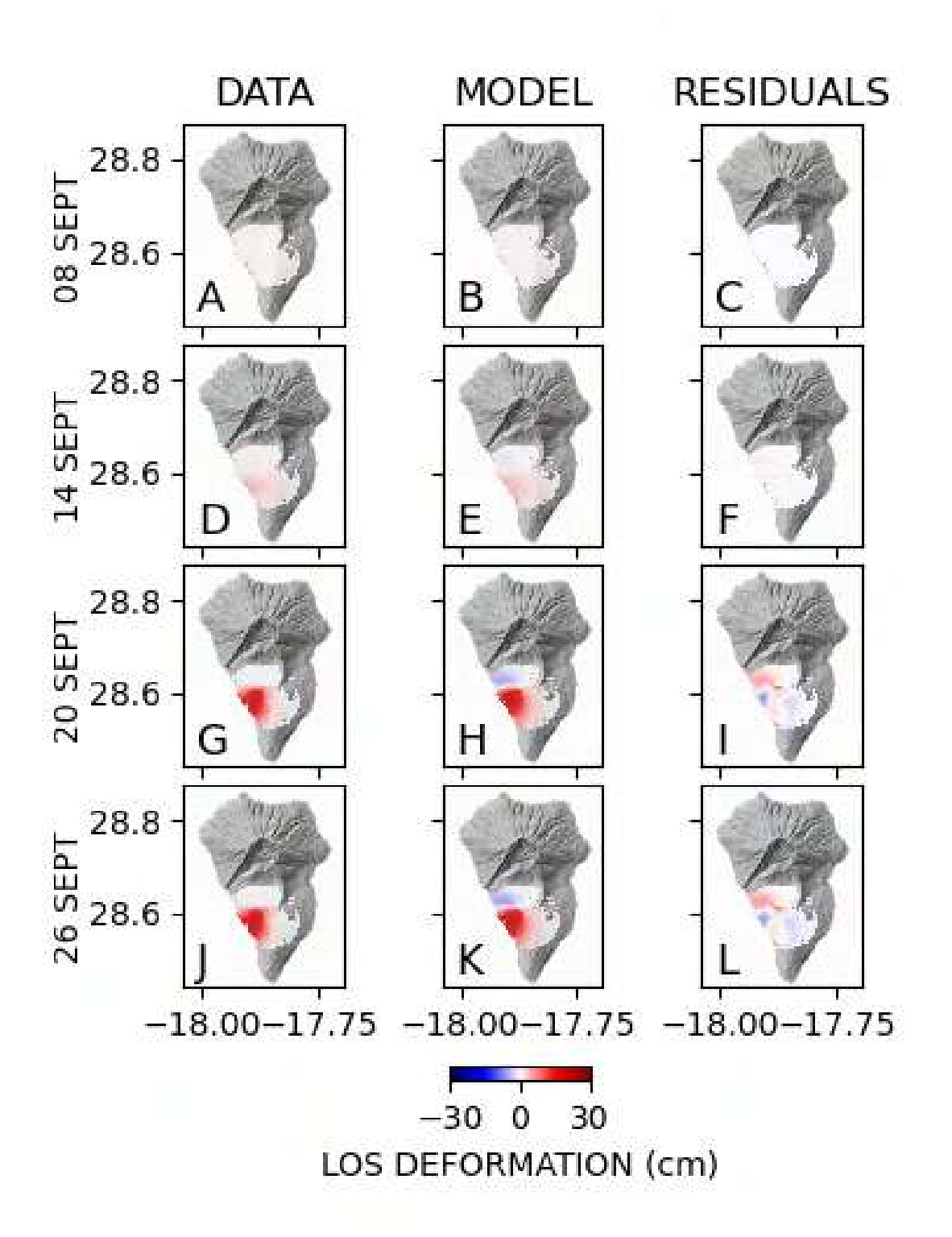


Figure B.1 Data, model, and residuals for the source of the ground deformation on La Palma (columns 1, 2, and 3, respectively) for each data acquisition date of the ascending orbit.

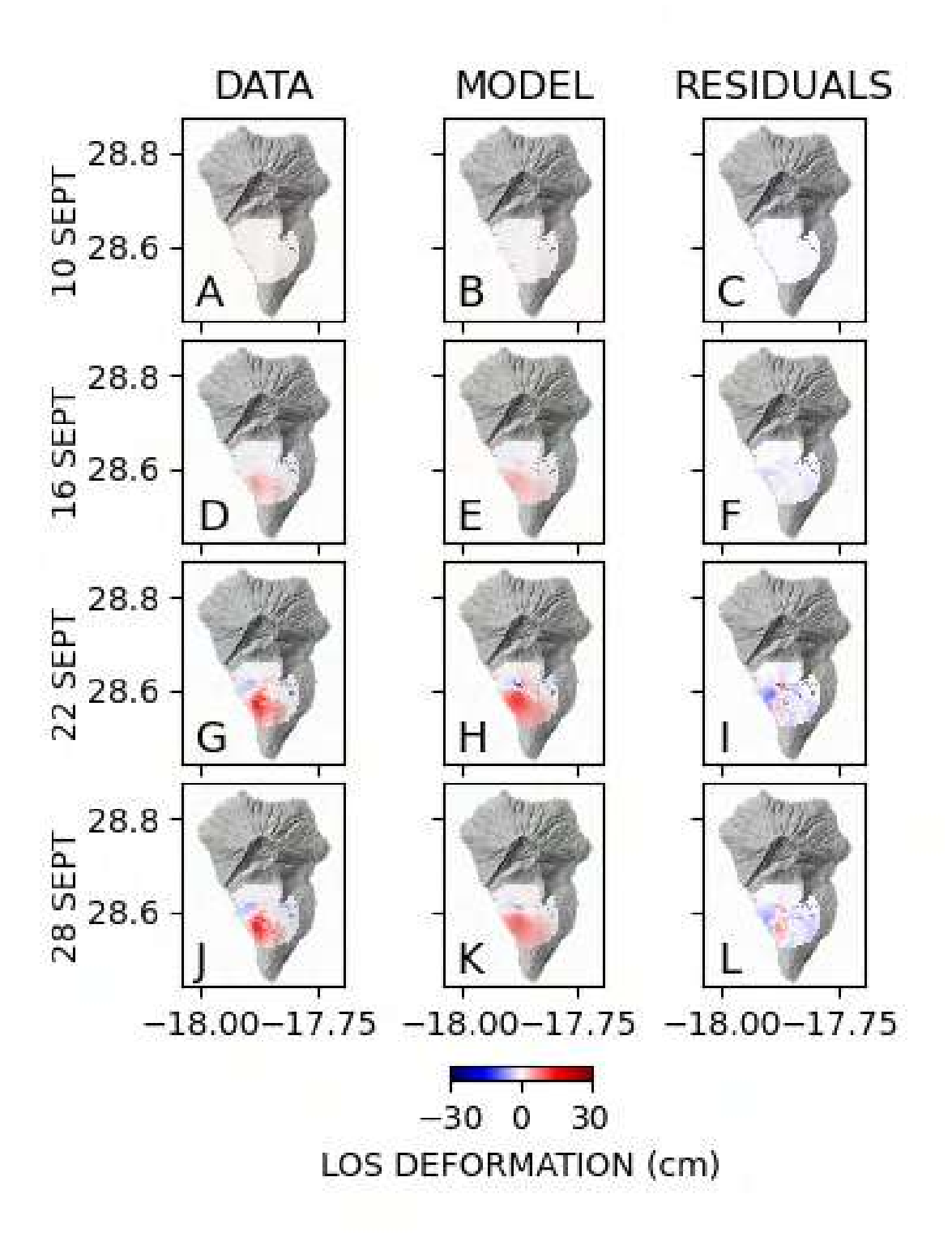


Figure B.2 Data, model, and residuals for the source of the ground deformation on La Palma (columns 1, 2, and 3, respectively) for each of the data acquisition dates of the descending orbit.

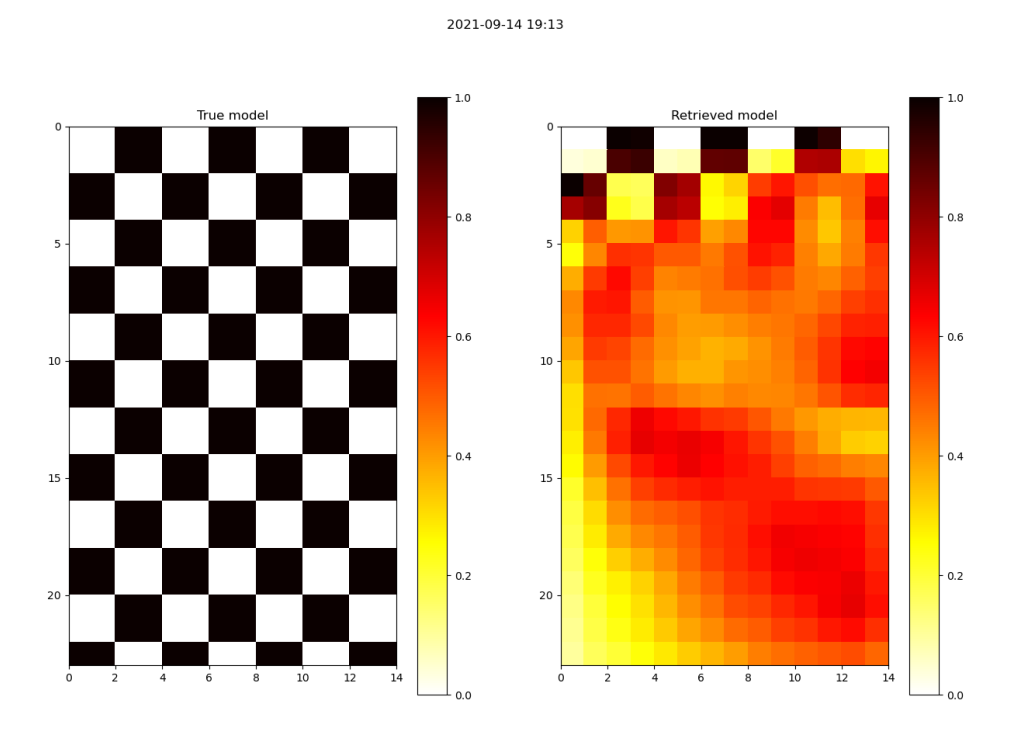


Figure B.3 Checkerboard test for anomalies of 1 km. The left-hand side panel represents the true model while the right-hand side panel shows the retrieved model.

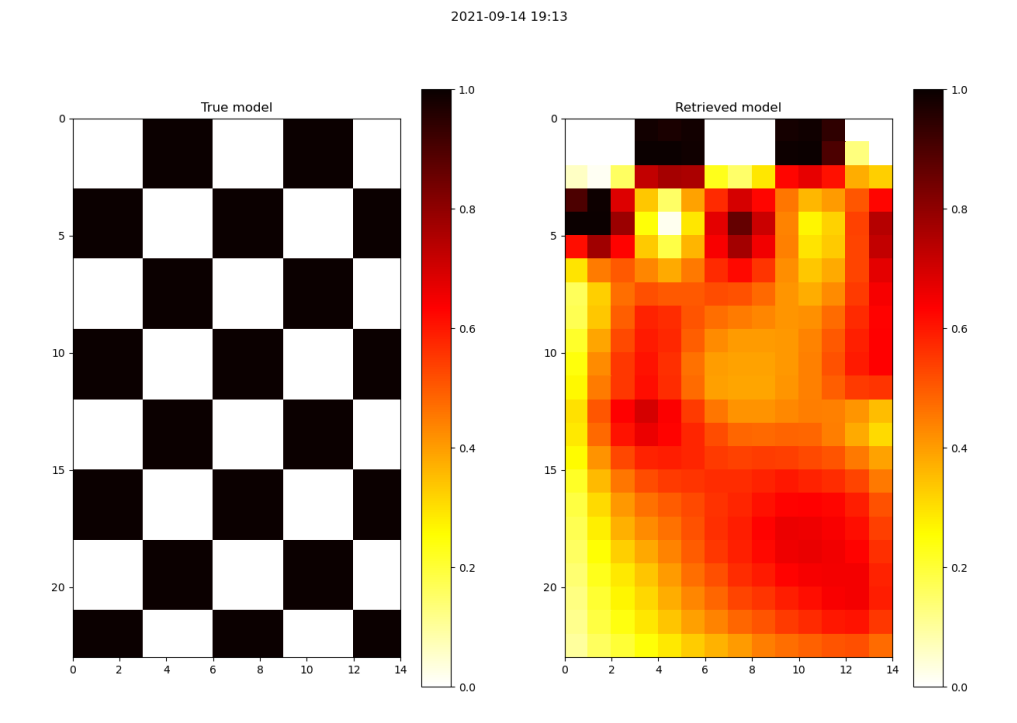


Figure B.4 Checkerboard test for anomalies of 2 km. The left-hand side panel represents the true model while the right-hand side panel shows the retrieved model.

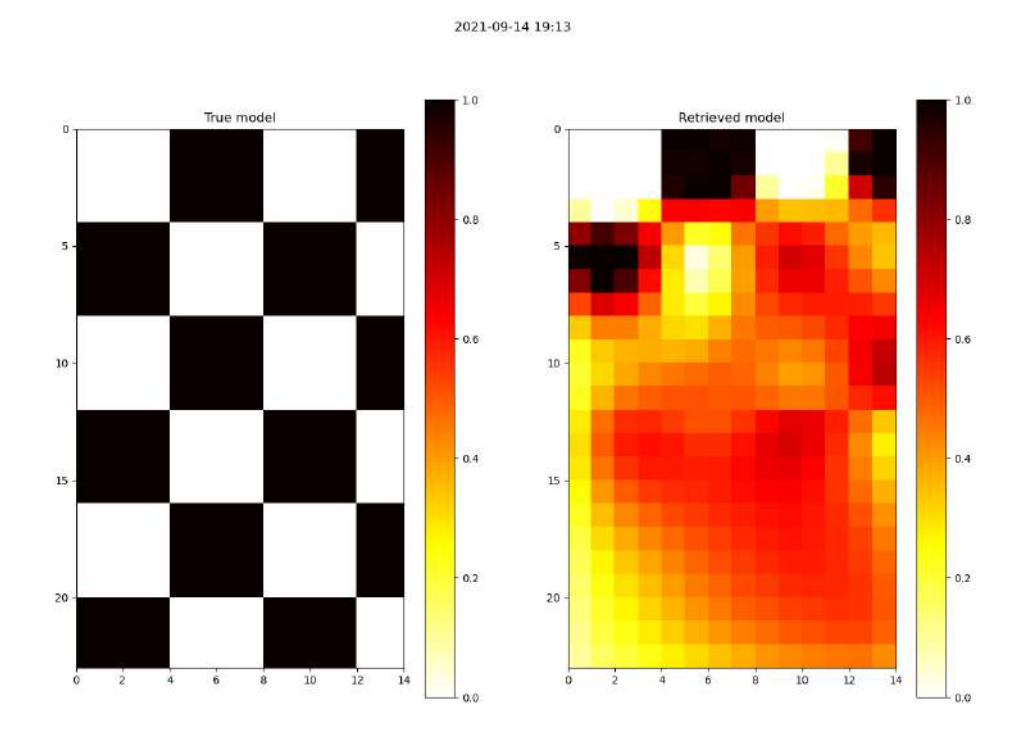


Figure B.5 Checkerboard test for anomalies of 2.5 km. The left-hand side panel represents the true model while the right-hand side panel shows the retrieved model.

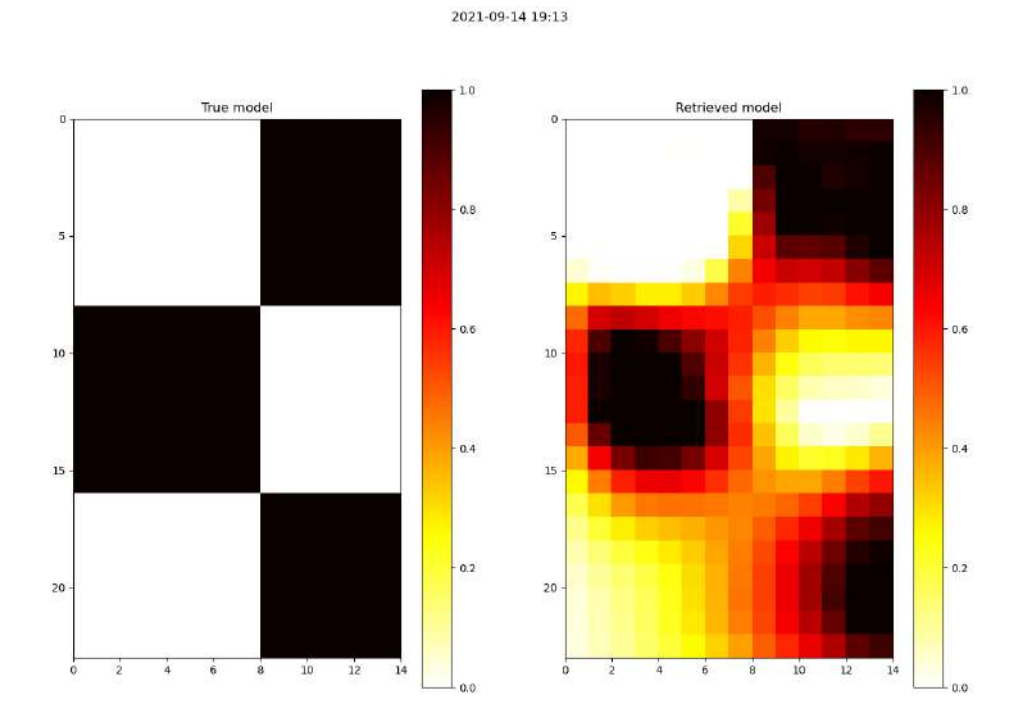


Figure B.6 Checkerboard test for anomalies of 5 km. The left-hand side panel represents the true model while the right-hand side panel shows the retrieved model.

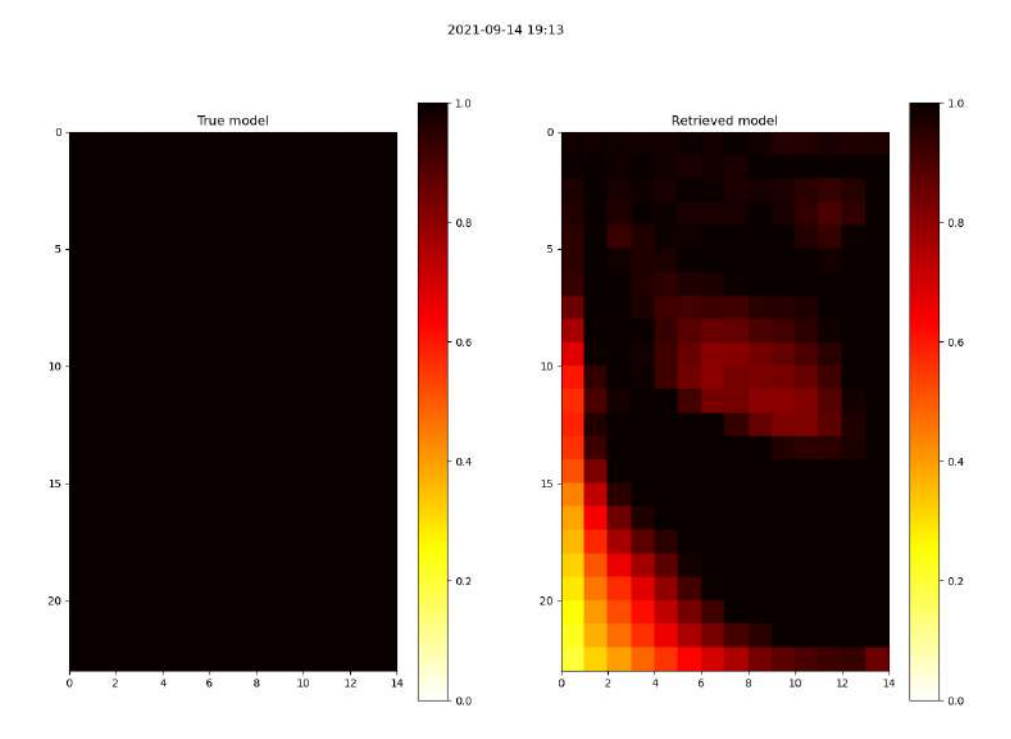


Figure B.7 Synthetic tests for the true model (left-hand side panel) and the retrieved model (right-hand side panel).

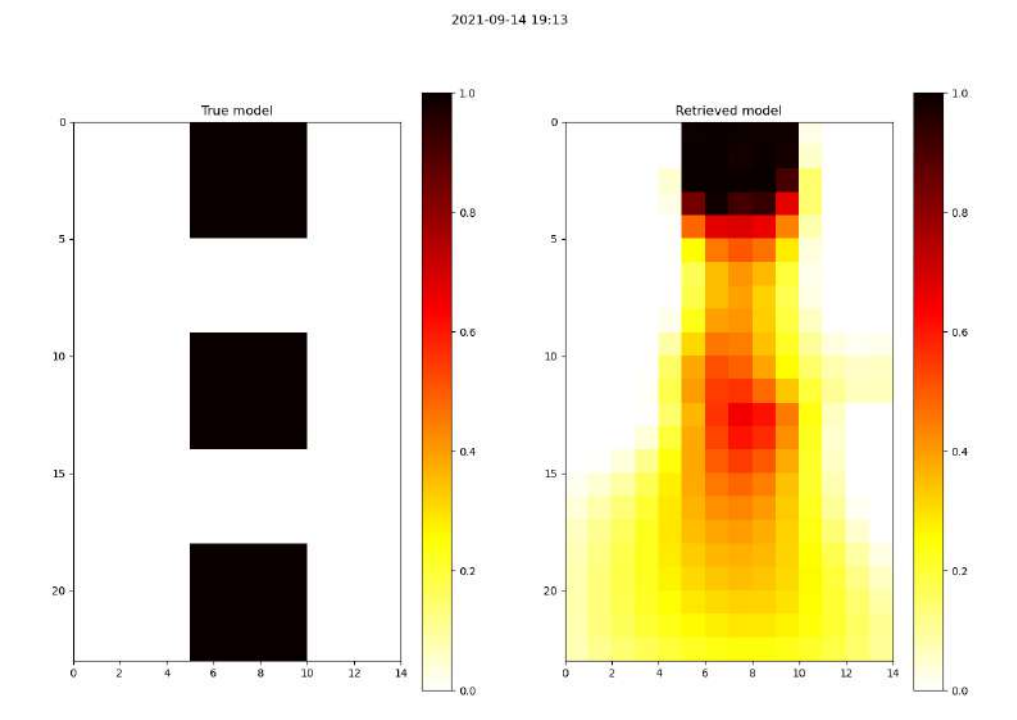


Figure B.8 Synthetic tests for the true model (left-hand side panel) and the retrieved model (right-hand side panel).

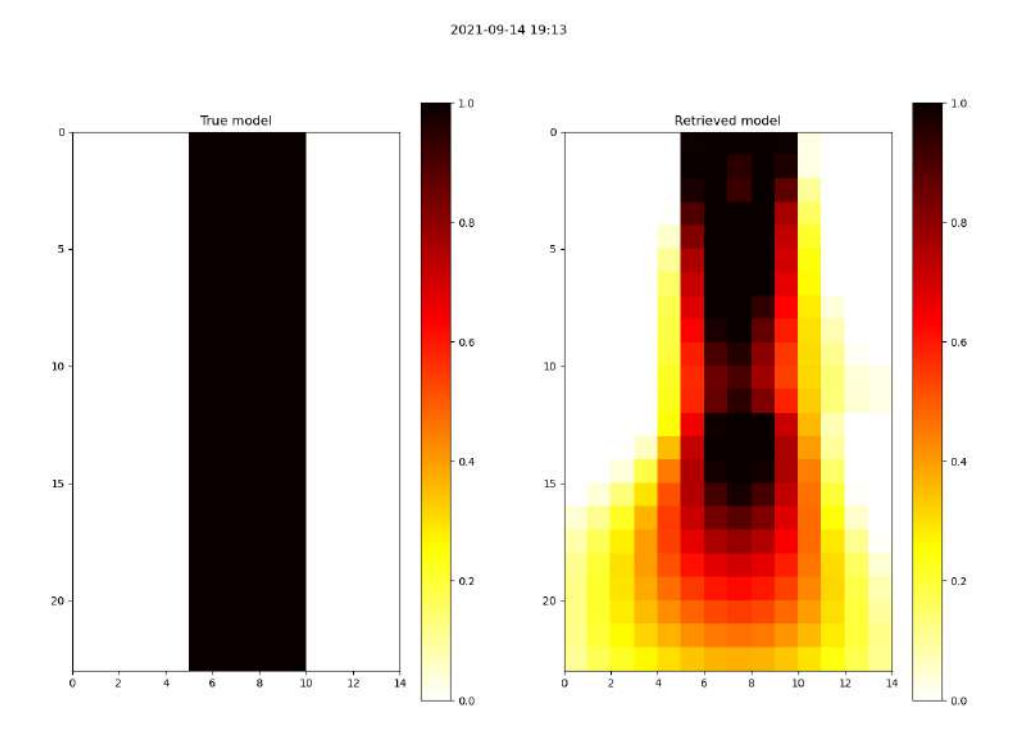


Figure B.9 Synthetic tests for the true model (left-hand side panel) and the retrieved model (right-hand side panel).

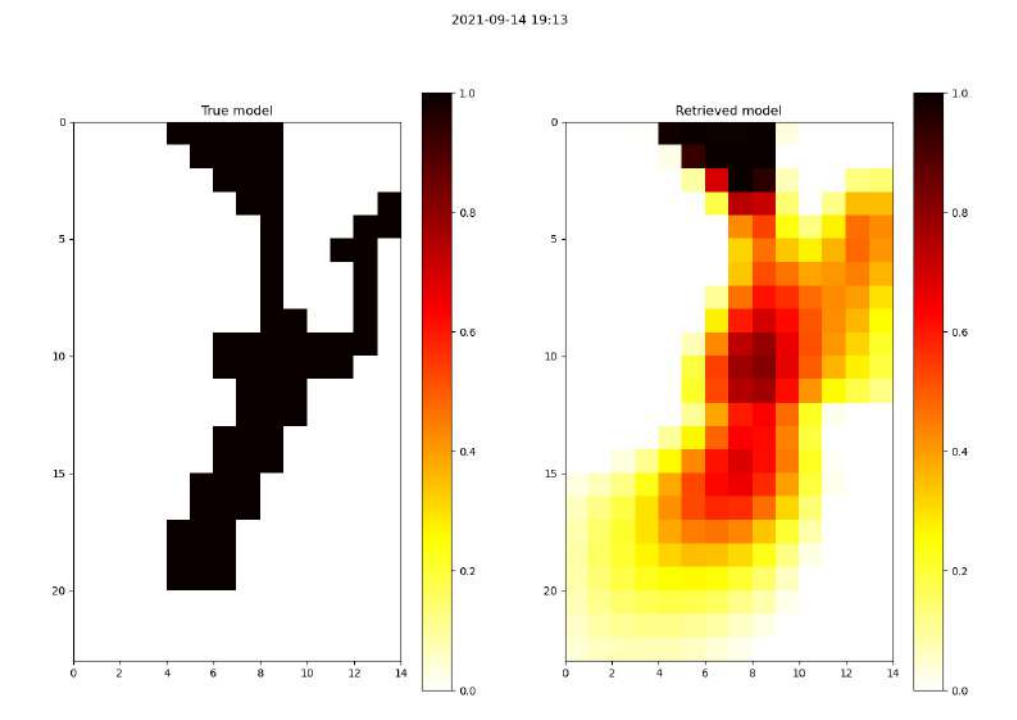


Figure B.10 Synthetic tests for the true model (left-hand side panel) and the retrieved model (right-hand side panel).

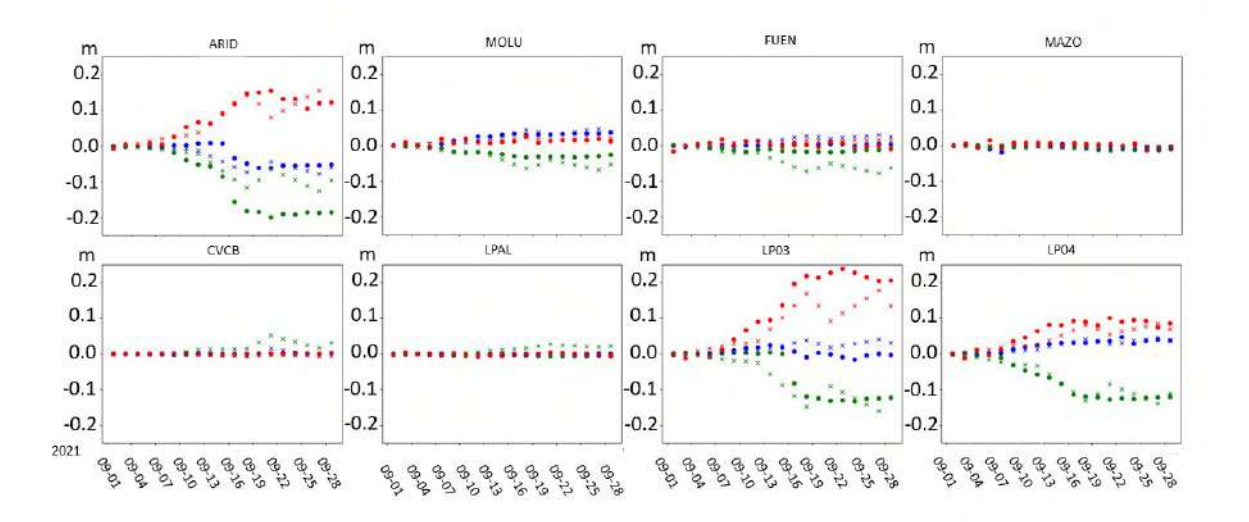
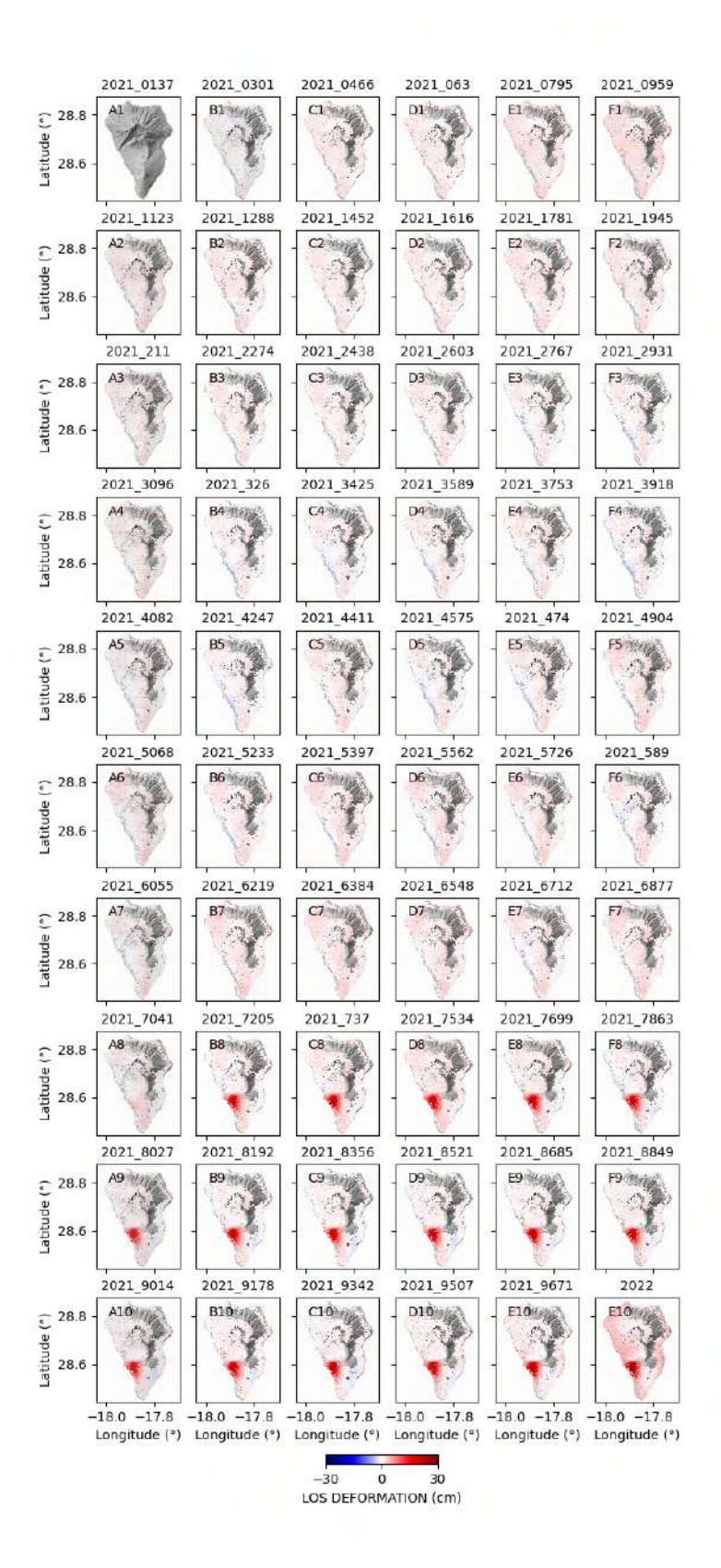
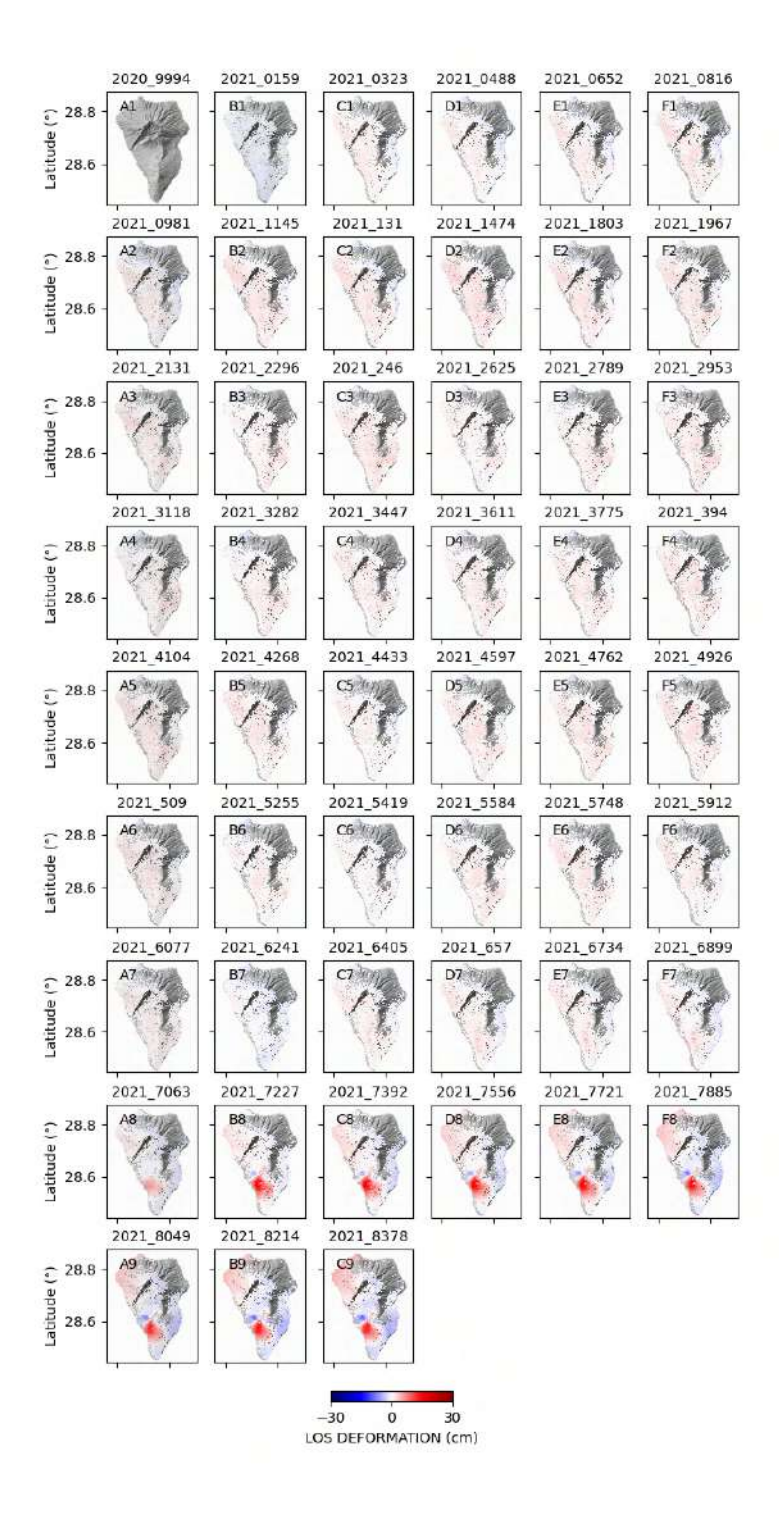


Figure B.11 Data and synthetic model resulting from the Geodetic Imaging technique, for the three components of the GNSS data for all the stations used for this study. Each point represents the daily data solution while each x-symbol represents the synthetic model solution. Red, blue, and green colors represent the vertical, N-S, and E-W components, respectively.





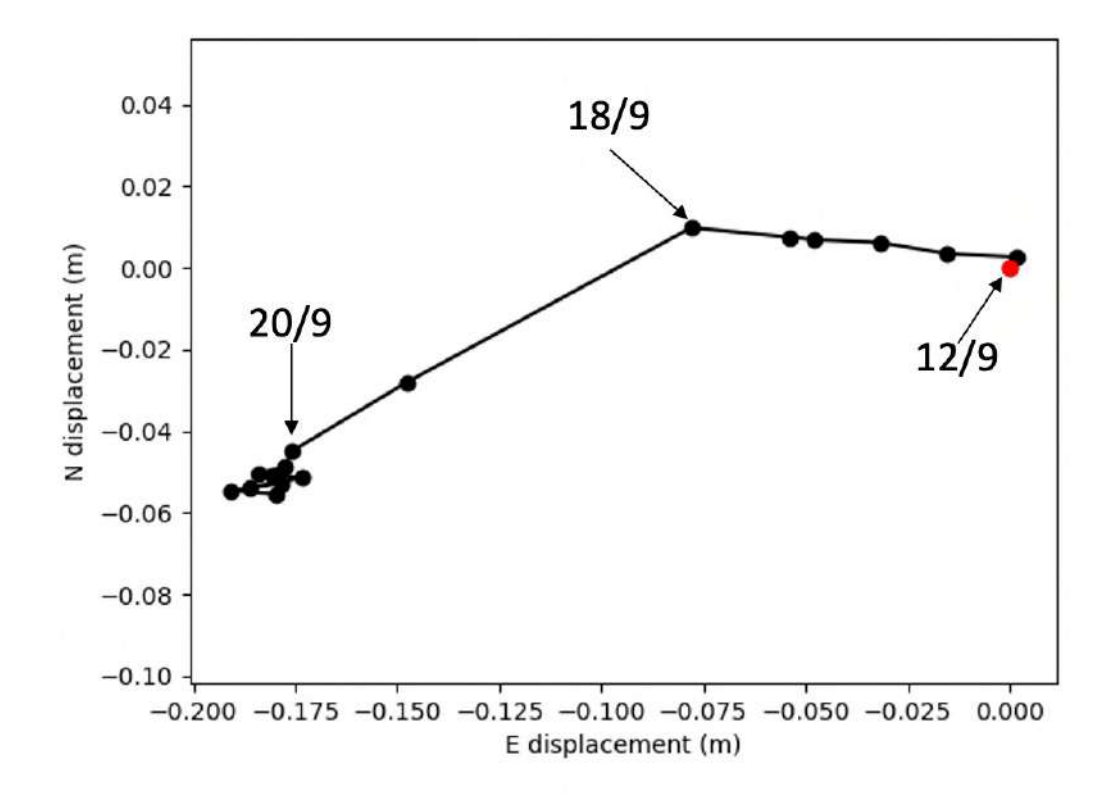


Figure B.14 Horizontal cumulative displacement of GNSS station ARID. We represent the cumulative horizontal displacement from the 12th to the 28th of September 2021. Each point represents a daily solution. The red point marks the beginning of the time series. We annotated relevant dates as discussed in the text.

Main Sentinel-1 SAR data parameters					
Satellite	ite Sentinel-1A Sentinel-1B				
Orbit	Ascending	Descending			
Beam mode	IW				
Path	60	169			
Frame	87	498			
Number of SLC images	51	51			
Time interval	January 2021-November 2021	January 2021-November 2021			

Figure B.15 SAR datasets' key parameters for data acquired in this study.

Appendix C

Thesis Publications

scientific reports



OPEN

Elastic interaction between Mauna Loa and Kīlauea evidenced by independent component analysis

Monika Przeor^{1,2⊠}, Luca D'Auria^{1,2}, Susi Pepe³, Pietro Tizzani³ & Iván Cabrera-Pérez¹

The contrasting dynamics between Mauna Loa and Kīlauea have been studied over the last 100 years from multiple viewpoints. The fact that dynamic changes of one volcano trigger a dynamic response of the other volcano indicates a connection may exist. Petrological works show a direct relationship between the magmatic systems of these two volcanoes is not possible. We analysed DInSAR data and GPS measurements of ground deformation patterns associated with the activity of Mauna Loa and Kīlauea volcanoes. The DInSAR SBAS dataset spans the interval between 2003 and 2010, and was acquired along ascending and descending orbits of the ENVISAT (ESA) satellite under different look angles. Of the 10 tracks that cover the Big Island (Hawai'i), 4 cover both volcanic edifices. Using GPS measurements, we computed the areal strain on 15 triplets of stations for Kīlauea volcano and 11 for Mauna Loa volcano. DInSAR data was analysed by applying Independent Component Analysis (ICA) to decompose the time-varying ground deformation pattern of both volcanoes. The results revealed anticorrelated ground deformation behaviour of the main calderas of Mauna Loa and Kīlauea, meaning that the opposite response is seen in the ground deformation of one volcano with respect to the other. At the same time, Kīlauea exhibits a more complex pattern, with an additional component, which appears not to be correlated with the dynamics of Mauna Loa. The GPS areal strain time series support these findings. To corroborate and help interpret the results, we performed inverse modelling of the observed ground deformation pattern using analytical source models. The results indicate that the ground deformation of Mauna Loa is associated with a dike-shaped source located at 6.2 km depth. In comparison, the anticorrelated ground deformation of Kīlauea is associated with a volumetric source at 1.2 km depth. This excludes a hydraulic connection as a possible mechanism to explain the anticorrelated behaviour; instead, we postulate a stress-transfer mechanism. To support this hypothesis, we performed a 3D numerical modelling of stress and strain fields in the study area, determining the elastic interaction of each source over the others. The most relevant finding is that the Mauna Loa shallow plumbing system can affect the shallowest magmatic reservoir of Kīlauea, while the opposite scenario is unlikely. Conversely, the second independent component observed at Kīlauea is associated to a sill-shaped source located at a depth of 3.5 km, which is less affected by this interaction process.

The interaction processes between the two most active Hawaiian volcanoes are still controversial, and despite multiple studies carried out over more than a century, an unambiguous model has yet to be identified. In order to provide new insights to this discussion, we compared the ground deformation patterns in both volcanoes using DInSAR SBAS and Global Positioning System (GPS) datasets. In this work, we processed 10 tracks of ENVISAT ASAR satellite images from 2003-2010, together with available GPS data from 15 stations located around the two summit calderas of Mauna Loa and Kīlauea. We applied the Independent Component Analysis (ICA) to the DInSAR SBAS ground deformation data to reveal relationships between the spatio-temporal patterns of the ground deformation of the two volcanoes. ICA is widely used Data Mining technique, which allows detecting, separating and characterizing hidden patterns into a spatio-temporal dataset¹. Furthermore, we computed the GPS areal strain time series around Mauna Loa and Kīlauea calderas, comparing them with the results provided

¹Instituto Volcanológico de Canarias (INVOLCAN), San Cristóbal de La Laguna, Spain. ²Instituto Tecnológico y de Energías Renovables (ITER), Granadilla de Abona, Spain. ³Istituto per il Rilevamento Elettromagnetico dell'Ambiente (IREA-CNR), Napoli, Italy. [™]email: mprzeor@iter.es

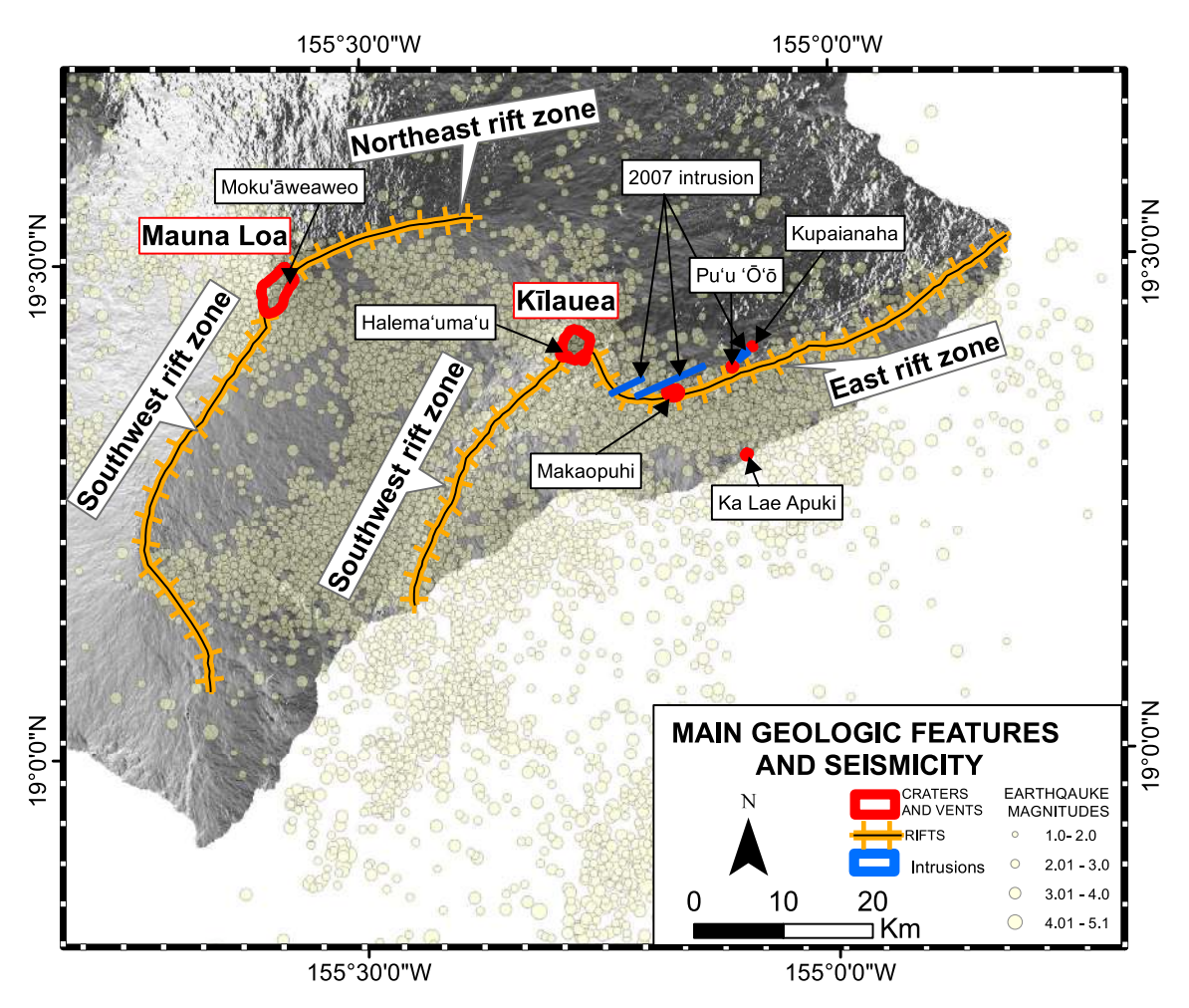


Figure 1. Main geologic and seismicity map of Mauna Loa and Kīlauea³.

by ICA. Subsequently, we present inverse modelling of ground deformation sources, which provides constraints for conceptual models of the shallow feeding system of Mauna Loa and Kīlauea. Conclusively, we realized a 3D numerical modelling of the stress and strain fields produced by the inflation/deflation of the individual ground deformation sources to better understand the mechanism of their interaction. The details of data processing and modelling are described in the Methods section.

Hawai'i Island is composed of 5 shield volcanoes: Kohala, Mauna Kea, Hualālai, Kīlauea, and Mauna Loa, with the latter being the largest active volcano on Earth. It has erupted 35 times since its first historical eruption in AD 1750². The summit area of Mauna Loa is composed of a large summit caldera (Moku'āweoweo) and two elongated ridges: the Northeast Rift Zone (NERZ) and the Southwest Rift Zone (SWRZ); (Fig. 1). Kīlauea volcano overlaps the southeastern flank of Mauna Loa. It has been in near- continuous eruption from 1983 to 2018², and its main volcano-tectonic features are the East Rift Zone (ERZ), the Southwest Rift Zone (SWRZ), a large summit caldera, and the Halema'uma'u crater within it² (Fig. 1).

Recently, several studies have aimed to characterise the nature of the magmatic source responsible for ground deformation at Kīlauea and Mauna Loa volcanoes^{3–17}. The two principal sources at Mauna Loa volcano are associated with shallow dike intrusion into the central conduit of Mauna Loa, and its rift zones¹⁴. Dike intrusions create compression over the adjacent flanks of the volcano^{18,19} and consequently, they produce ground deformation and earthquakes along the basal decollement zone²⁰. In the case of Kīlauea volcano, the general picture is similar to Mauna Loa: the main ground deformation sources are linked to the central feeding system as well as to magmatic intrusions along the rift zones⁷ that are also responsible for the seismicity near the base of the volcano^{21,22}. The intrusion of dikes and extension of the rift-zone⁹ also causes the shortening at the base of the edifice and the uplift along the frontal bench^{8,23}.

At Mauna Loa, Amelung et al. ¹⁴ identified a spheroidal source reservoir beneath the southeast margin of Moku'āweoweo Caldera, connected to an elongated source linked to the rift zones. Pepe et al. ⁵, showed that the main source of ground deformation at Mauna Loa consists of a vertical pipe connected to dike-shaped reservoirs located along the rift zones.

Poland et al.³ showed the existence of various magmatic reservoirs beneath Kīlauea: one below the caldera of Halema'uma'u, the Keanakāko'i reservoir, the South Caldera reservoir, and both Rift Zones (East Rift Zone and Southwest Rift Zone). The Halema'uma'u reservoir is the summit storage located between 1 and 2 km depth below the main caldera. The Keanakāko'i is considered a temporal storage, with magma inputs occurring intermittently.

The South Caldera reservoir, mentioned by Poland et al.³ is located at a depth of 3–5 km below the Halema'uma'u caldera and is considered the principal storage of magma at Kīlauea. Both Rift Zones are a set of fractures and vents with directions toward the East and Southwest of the main caldera. A full catalogue of dike intrusions over Kīlauea edifice can be found in Montgomery–Brown et al.²⁴.

In the last three decades, some relevant deformation episodes took place at Kīlauea and were linked to the Pu'u 'Õō-Kūpa'ianahā eruption (1983–2018)^{3–17,25}. Volcanic activity at Pu'u 'Õō-Kūpa'ianahā from 1983 to 2001 was characterised by dominant deflation, followed by a new inflation episode starting in 2001 when Kīlauea experienced a new uplift phase. Six months later, similar behaviour at Mauna Loa volcano was observed¹³. The enhancement of volcanic activity in this period was caused by an increase in the magma supply from the mantle¹³.

The sudden inflation that started in 2003 at Kīlauea mainly affected the summit caldera, but was recorded as far away as 50 km from the summit and lasted until 2007^{17} . In 2005, magma accumulation in ERZ led to summit inflation and an increase in the output of SO_2^{13} . In the same year, a major collapse of the lava delta occurred¹⁵, and one year later, an uplift episode along the southern part of the Kīlauea summit caldera was registered¹⁵. The ground deformation pattern of Kīlauea during 2003–2007 was dominated by inflation along the ERZ and the summit crater¹⁷.

In this work, we consider only the magmatic intrusions that occurred in the summit area of the volcanoes and only during the time interval considered in this study. A major episode of volcanic unrest occurred between 2003-2010, beginning on 17th June 2007 (American Father's Day 2007, FD07). The event entailed changes in volcanic activity and formation of new eruptive vents¹⁷. It caused rapid deflation of the Kīlauea summit area due to magma withdrawal to eruptive vents located along the ERZ, about 8 km away¹⁵⁻¹⁷. The first episode of the FD07 eruption lasted for two days. On 21st July of 2007, another eruptive episode began along the ERZ, with vents located about 19 km away from the summit^{15,16}. ERZ vent activity was then continuous, while the summit crater of Halema'uma'u showed increased volcanic gas emission levels until an explosion of Kīlauea's main summit crater on 19th March 2008¹⁷. After the FD07 episode until 2008, the ground deformation pattern of Kīlauea was characterised by deflation, and summit seismicity returned to background values¹⁷.

The interaction between the two most active volcanoes of Hawai'i Island has been discussed for over 100 years ^{11,12,26}. Rhodes and Hart²⁷ confirm that the chemical composition of lavas at Kīlauea and Mauna Loa are different, indicating the magmatic feeding systems are independent (at least at the crustal level). However, geophysical studies seem to indicate the opposite: Klein¹¹ first noticed the anticorrelation between the two volcanoes, emphasising that an increase in activity at Kīlauea often corresponds to a decrease in Mauna Loa dynamism. Miklius and Cervelli¹² captured the opposite behaviour in the ground deformation patterns of the volcanoes: at the beginning of the high-volume effusive episode in Kīlauea, inflation of Mauna Loa was observed (May 2002). Shirzaei et al. ²⁸ studied the coupling behaviour of both volcanoes between 2003 and 2008. The authors postulate that the causative source of the interaction between the two volcanoes is related to deep-seated mantle surges. Despite being the subject of many studies, the nature and the mechanism of the interaction between the feeding systems of the two volcanoes and their level of interconnection are still contentious and remain unclear.

Results

The analysis of the observed ground deformation, reported in the first column of Fig. 2(A, D, G, J), suggests an anticorrelated behaviour of the ground deformation between Mauna Loa and Kīlauea volcanoes. This is clearly seen in the normalized spatial patterns (indicated as B_k in Eq. 1) of the first component (ICA1), and shown in Fig. 2. The anticorrelation between these two volcanoes is demonstrated by the presence of positive values on Mauna Loa and negative values on Kilauea on the ICA1 component for all four selected tracks. The anticorrelation between the two volcanoes is seen only by the ICA1 component on both Mauna Loa and Kīlauea. The temporal variation is shown in Fig. 3 with dashed lines, clearly showing the opposite behaviour of Mauna Loa and Kīlauea on all four tracks: when ground deformation of Mauna Loa shows positive values, Kīlauea exhibits negative ones. It should be noted that the sign of the ICA components is arbitrary, being the actual value of the ground deformation modulated by the coefficients $A_i k$ in Eq. (1)1.

Also, let us remark that, as shown by Fig. 2, there are other evidences of the ground deformation far from their summit areas. Column 1 in Fig. 2 shows an example of such deformation in the southeast side of the Kīlauea volcano associated with the faults system mentioned by Shirzaei et al.²⁹.

The second component of the ground deformation pattern (ICA2 in Fig. 2) exhibits significant values only in the area of Kīlauea volcano. The overall shape (Fig. 2) and temporal behaviour (Fig. 3) of the two components are different. The maximum of the ICA2 component at Kīlauea is located on the southern side of the summit caldera, slightly displaced to the south with respect to the maximum of the ICA1 component on the same volcano.

The above-mentioned anticorrelated behaviour in the ground deformation pattern is visible also by considering the LOS deformation time series. In Fig. 3, the time series for two selected pixels are shown, which correspond with the summit calderas of Mauna Loa and Kīlauea. The Mauna Loa time series displays an uplift from 2003 until late 2009. Simultaneously, the Kīlauea shows an inflation pattern until 2007 (the FD07 volcanic episode), followed by significant subsidence until late 2009.

At Mauna Loa, the total ground deformation pattern is almost exclusively represented by the first ICA component for all four considered tracks (see panels A, C, E, and G in Fig. 3). Minor differences between the ICA1 and the total LOS on this volcano can be attributed to a noisy component that ICA cannot model. In the case of Kīlauea volcano (see panels B, D, F, and H in Fig. 3), the contribution of both components is relevant. The anticorrelation in the temporal pattern of ICA1 is seen by a monotonic increase for Mauna Loa (ICA1, Fig. 3), which corresponds to a monotonic decrease in Kīlauea (seen on tracks T343 and T472; Fig. 3, dashed line). This difference in the amplitude of the ICA1 on the four considered tracks on Kīlauea can be attributed to the different orbits or, in other words, to the different LOS directions of the considered tracks. Conversely, the second

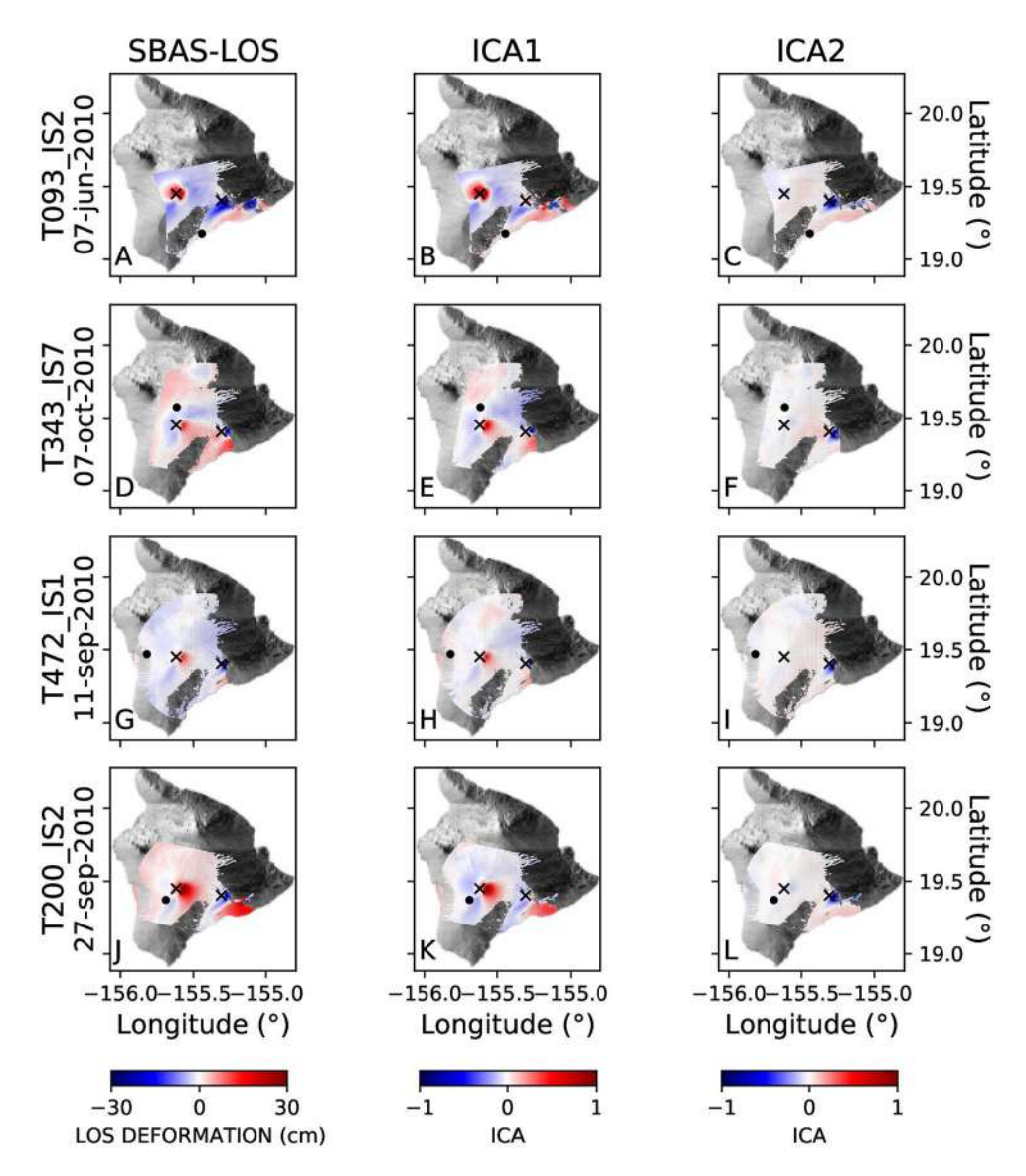


Figure 2. LOS deformation cumulative maps. (**A**), (**B**), (**C**): ENVISAT 093 orbit; (**D**), (**E**), (**F**): ENVISAT 343 orbit; (**G**), (**H**), (**I**): ENVISAT 472 orbit; (**J**), (**K**), (**L**): ENVISAT 200 orbit (see Table S2 for track details). Column 1 shows the LOS cumulative displacement DInSAR map; columns 2 and 3 represent the first and second components resulting from applying the ICA decomposition algorithm. The black crosses indicate the points used for extracting the time series shown in Fig. 3, while black dots are the reference points used for the DInSAR SBAS processing.

ICA component displays a more complex temporal pattern, with an increase until the FD07 eruption, followed by a decreasing trend until the end of 2009.

The GPS data analysis reveals similar patterns to the SBAS time series for both volcanoes (Figs. S1 and S2 in supplementary material). The vertical axis is in order of 5 and 10 μ strain, respectively. Mauna Loa volcano displays slow strain rates until the second part of 2009, when the rate increases significantly in triplets of stations located in the southeast part of the summit caldera. Although the last four triplets (those located in the SE part of the main crater) dominantly see the decrease in strain area that began in mid-2009, the other triplets of stations show a smaller but evident decrease too. From mid-2008 to mid-2009, the strain area of Kīlauea diminished (Fig. S2). After the second half of 2009, GPS stations in Kīlauea crater and its surroundings record a significant increase in the strain area.

The GPS ground deformation patterns show the different behaviour of Mauna Loa and Kīlauea (Figs. S1 and S2). Specifically, since 2009, the patterns of the two volcanoes show an opposite behaviour. This agrees with the results of ICA decomposition, shown in Fig. 3. The ICA2 component does not vary much since mid-2009; hence the ground deformation is shown in the anticorrelated ICA1 pattern. This does not hold for the previous interval, where ICA2 is prevalent on the ground deformation at Kīlauea.

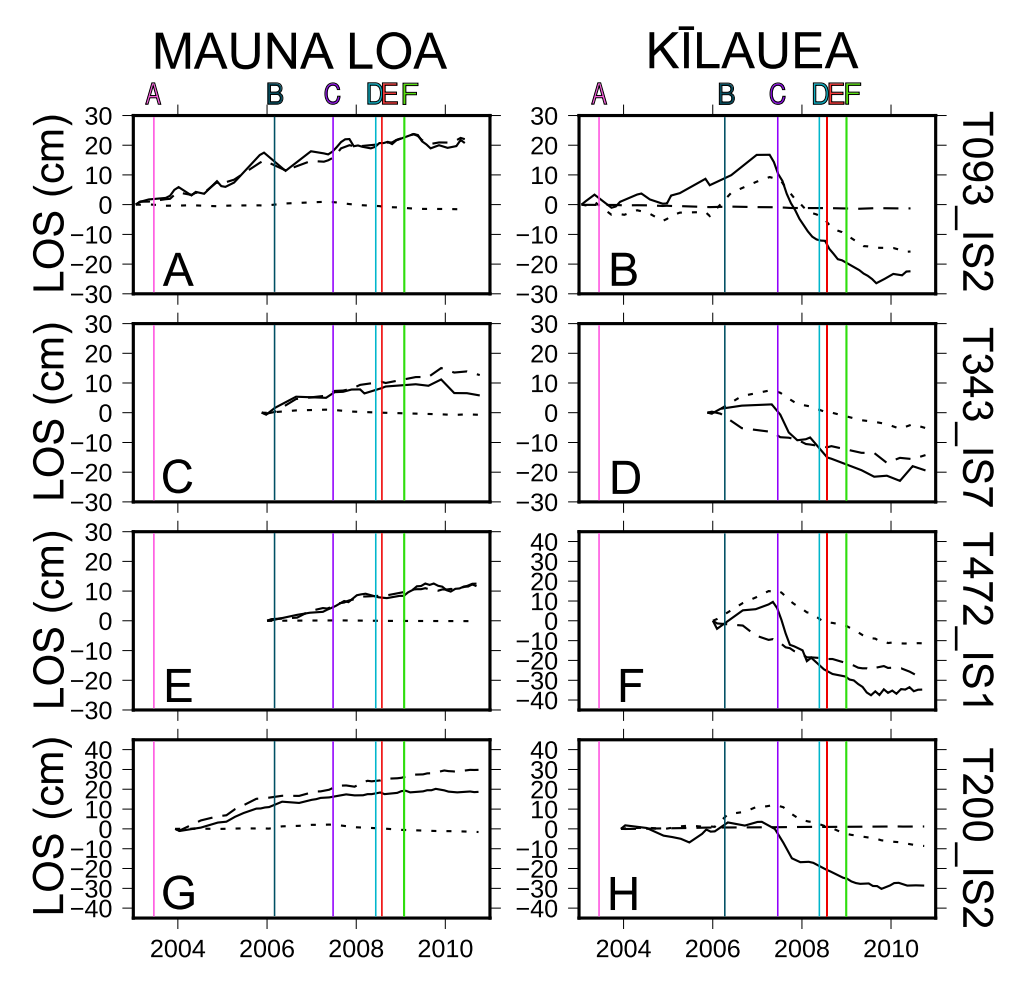


Figure 3. LOS displacement time series of Mauna Loa and Kīlauea summits. (**A**), (**C**), (**E**), (**G**): time series for LOS displacement of Mauna Loa; (**B**), (**D**), (**F**), (**H**): time series for Kīlauea volcano. Time series of LOS data are shown with continuous black lines; time series of the first component of ICA are indicated with the dashed black lines, while the dotted black lines report the time series of the second component of ICA. Vertical lines mark major volcanic episodes and the date of the beginning of the GPS dataset: (**A**) Mother's Day flow, which began erupting from Pu'u 'Õ'ō on 12th May 2003; (**B**) small bench collapse on 30th July 2006; (**C**) Father's Day eruption on 17th June 2007; (**D**) explosion on 19th March 2008; (**E**) the second half of 2008 which represent the time interval where the GPS measurements are available; (**F**) active vent within Halema'uma'u crater in January 2009.

The ICA analysis of the DInSAR SBAS time series of the satellite tracks highlight the presence of an anticorrelated ground deformation pattern linked to at least two sources located beneath the summit calderas of Mauna Loa and Kīlauea (component ICA1). Furthermore, the presence of another source is evidenced by the ICA2 component beneath Kīlauea alone. In order to better understand the physical mechanisms responsible for the observed ground deformation patterns, we performed inverse modelling of the three detected sources and used Akaike Information Criterion (AIC)³⁰ to select the appropriate model for each source.

In Table S1 in supplementary material, we detail the parameters of the three retrieved sources. Based on AIC, the temporal variation of Mauna Loa area displacements (delineated by ICA1) are best explained by a subvertical Okada crack model, with a centroid located at 6.2 km depth (Fig. 4; Table S1). The ICA1 component for Kīlauea is better represented by a simple Mogi³¹ source located at 1.2 km depth (Fig. 5). The ICA2 component for Kīlauea is best described by a sub-horizontal Okada³² crack located at 3.5 km depth (Fig. 6; Table S1 in supplementary material).

Figures 4, 5, and 6 show the inverse modelling results for each of the three modelled sources of ground deformation. Each Figure shows the spatial pattern of the ground deformation associated with the relevant ICA, the best-fit analytical model, and the residuals.

The panel (B) in the Fig. 7, shows a schematic tridimensional perspective of the three sources of ground deformation resulting from inverse modelling. Beneath Mauna Loa volcano, there is an Okada dike-shaped source. In the area of Kīlauea, there are Mogi-like and Okada sill-shaped sources of deformation.

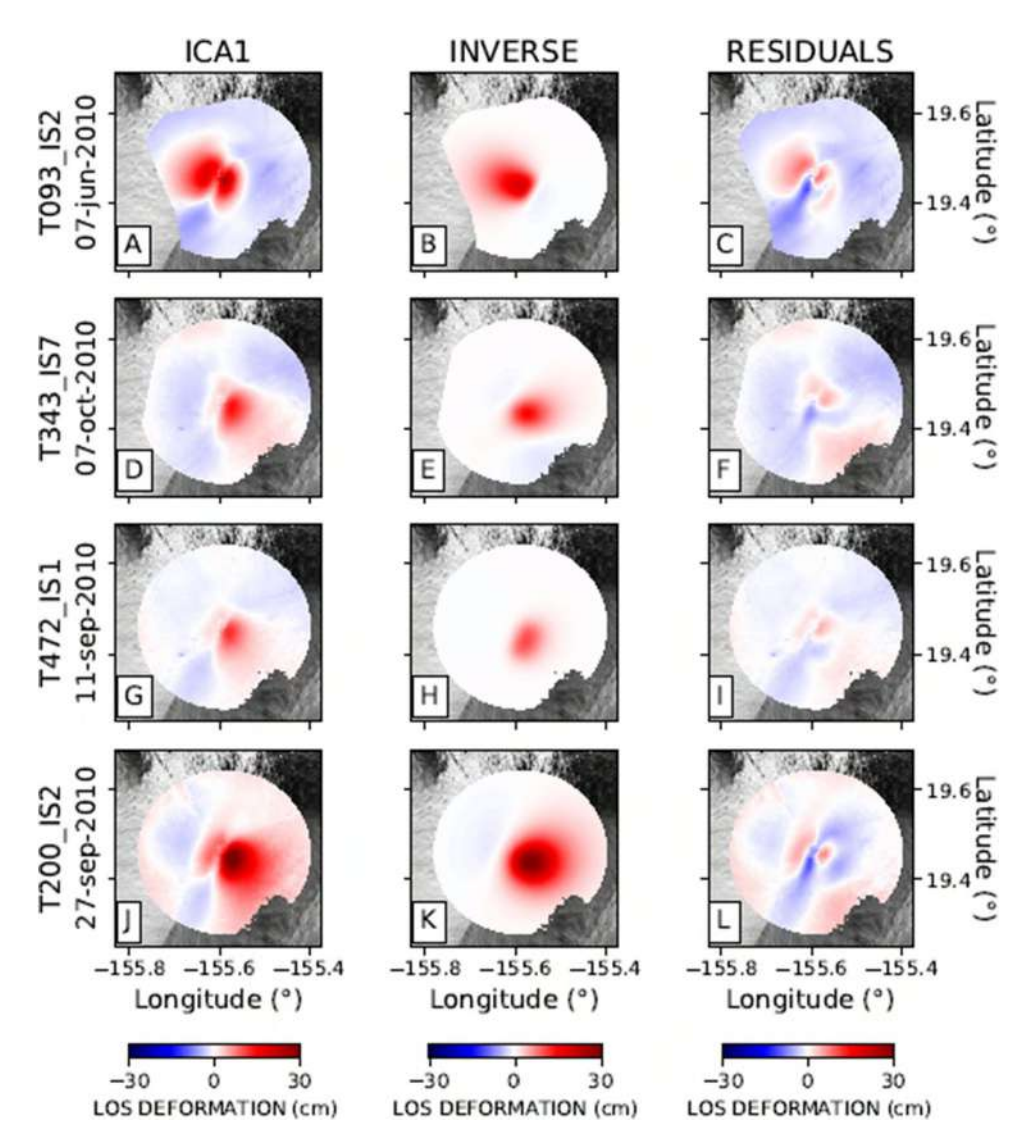


Figure 4. Inverse modelling of the Mauna Loa ground deformation source for four selected tracks: (**A**), (**B**), (**C**): ENVISAT 093 orbit; (**D**), (**E**), (**F**): ENVISAT 343 orbit; (**G**), (**H**), (**I**): ENVISAT 472 orbit; (**J**), (**K**), (**L**): ENVISAT 200 orbit, respectively. Column 1 represents the first component (ICA1) encompassing a radius of 20 km from Moku'āweoweo Crater. Column 2 represents the inverse model. Column 3 shows the residuals.

Discussion

Previous studies of Mauna Loa and Kīlauea hypothesised the presence of a connection between these two volcanoes. In this context, Kīlauea volcano provided considerable geophysical and geochemical data due to its constant activity from 1983 to 2018. However, the lower density of the geophysical monitoring network of Mauna Loa with respect to Kīlauea, poses some difficulties in comparing the geophysical data of the two volcanoes³. This work has provided evidence for two sources associated with ICA1 and showing an anticorrelated temporal relationship between the Mauna Loa and Kīlauea (Fig. 3).

The findings of the inverse modelling are consistent with previous studies. Poland et al.³ postulated the existence of two long-term magma reservoirs beneath the Kīlauea summit. Both reservoirs are connected to the rift zone system. Additionally, there exists a temporary storage area beneath Keanakaoko'i Crater. They highlighted the presence of a shallower magma reservoir located in the eastern margin of Halema'uma'u Crater, at a depth of 1–2 km depth. This source may coincide with the Kīlauea-ICA1 source proposed here, located at 1.2 km depth (Fig. 5; Table S3). According to Poland et al.³, deeper magma storage at Kīlauea is situated at about 3 km depth and displaced to the south of Halema'uma'u Crater. This is consistent with our inversion results, which show a sill-shaped source located at a 3.5 km depth. The inverse model of the second and deeper source of the Kīlauea volcano is given in Fig. 6, with parameters detailed in Table S1 in supplementary material. Our results for the Kīlauea feeding systems are compatible with Poland et al.³ showing the presence of at least two ground deformation sources active between 2003 and 2010. However, Poland et al.³ postulate the existence of a spherical or an ellipsoidal source in the southern side of the main caldera of Kīlauea. In contrast, our inversion results indicate the existence of a sill-like reservoir. Let us remark that our source model is related only to the

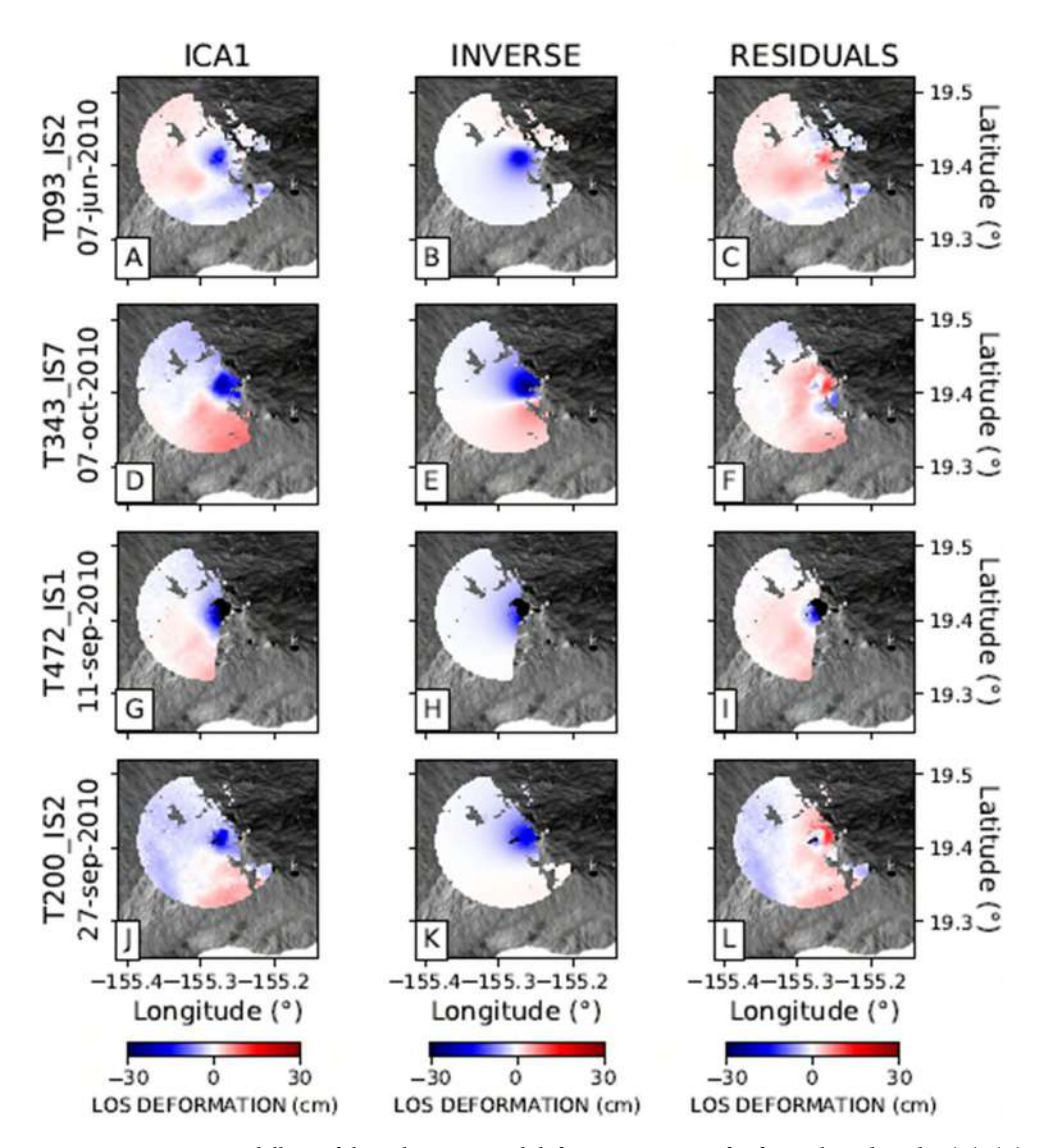


Figure 5. Inverse modelling of the Kilauea ground deformation source for four selected tracks: (A), (B), (C): ENVISAT 093 orbit; D, E, F: ENVISAT 343 orbit; G, H, I: ENVISAT 472 orbit; J, K, L: ENVISAT 200 orbit, respectively. Column 1 represents the first component (ICA1) encompassing a radius of 11 km from Halema'uma'u Crater. Column 2 represents the Mogi analytical model as a result of the inverse modelling. Column 3 shows the residuals of the inverse modelling and the observed data.

ground deformation pattern related to the second component (ICA2) of decomposition. We again emphasise the effectiveness of ICA in separating the contribution of individual sources, significantly reducing the intrinsic ambiguity in geodetic inverse problems.

At Mauna Loa, previous studies emphasised the relevance of the rift zones as sources of ground deformation^{4,5}. Our findings suggest a dike-like geometrical structure as a primary source during the interval considered (Fig. 4). During our analysed period (2003–2010), the ICA decomposition detected only one component of ground deformation in Mauna Loa. This is in agreement with Pepe et al.⁵, who, although proposing a more complex geometrical model, showed that the main reservoir and the rift zone acted with synchronous behaviour.

Many authors have already suggested possible connections between Mauna Loa and Kīlauea. Miklius and Cervelli¹² proposed a crustal-level interaction between them: pulses of magma in the plumbing system of Mauna Loa may cause pressure variations in the Kīlauea shallow magma system. Gonnermann et al.¹³ explained observed related ground deformation patterns by considering a pore-pressure diffusion within a thin accumulation layer in the asthenosphere. Since the magma composition at Kīlauea is isotopically distinct from Mauna Loa²⁷, Gonnermann et al.¹³ suggested the interconnection between Mauna Loa and Kīlauea must be explained by the transfer of stress by pore-pressure variations. Shirzaei et al.²⁸ explain the interconnection between the Mauna Loa magma chamber and the Kīlauea rift zone through pore pressure diffusion in an asthenospheric magma supply system.

We note that volcanic interconnection is even more evident if we consider the temporal evolution of the ground deformation patterns. From 1983 until 2003, both volcanoes were deflating ^{12,14–17}. The time series of DInSAR data (Fig. 3) shows the change of the ground deformation that took place in 2003 and was explained by many authors as sudden inflation that started in Kīlauea and lasted until 2007. That inflation resulted in an

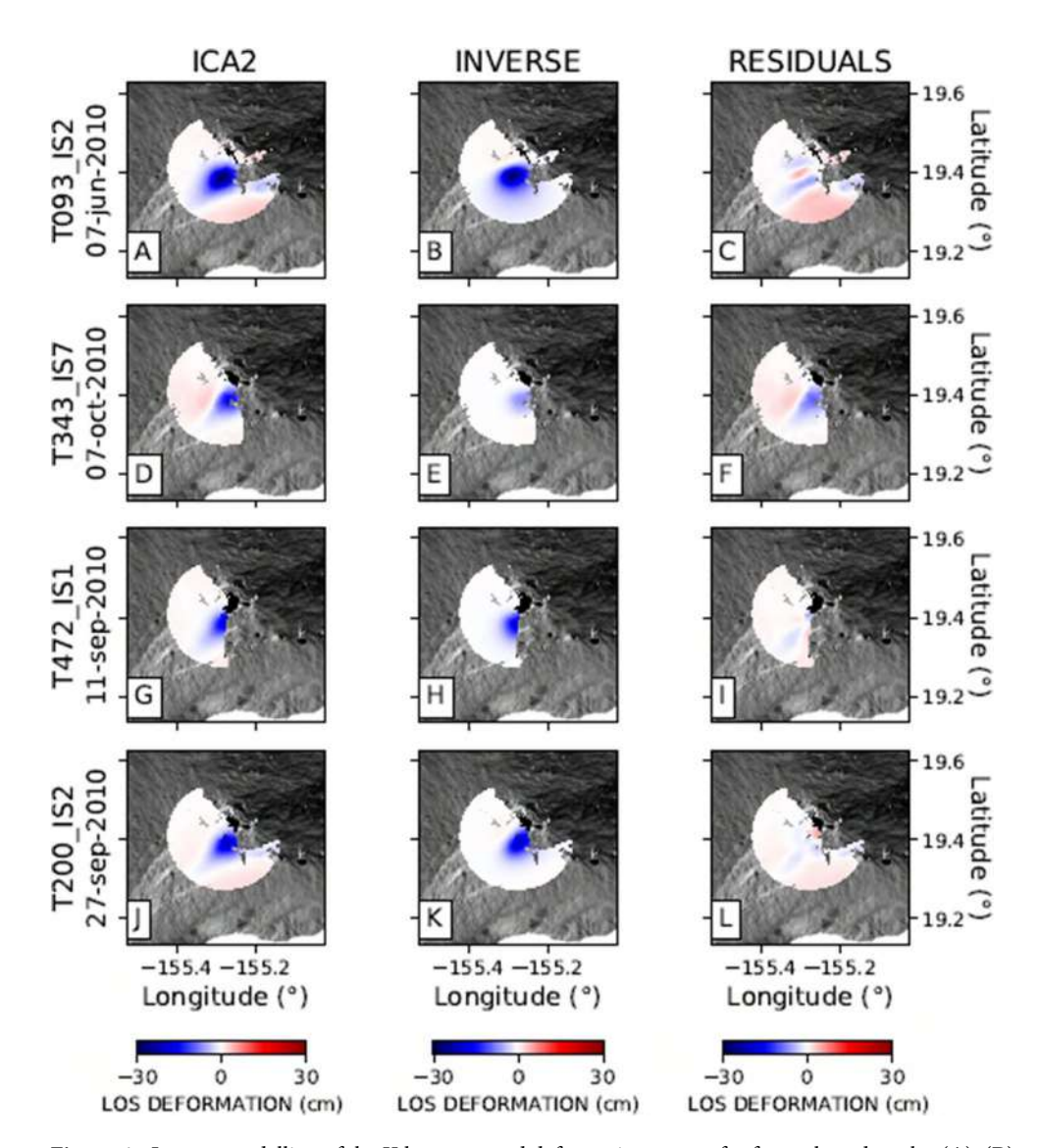


Figure 6. Inverse modelling of the Kilauea ground deformation source for four selected tracks: (A), (B), (C): ENVISAT 093 orbit; (D), (E), (F): ENVISAT 343 orbit; (G), (H), (I): ENVISAT 472 orbit; (J), (K), (L): ENVISAT 200 orbit, respectively. Column 1 represents the first component (ICA2) encompassing a radius of 15 km from Halema'uma'u Crater. Column 2 represents the inverse model. Column 3 shows the residuals.

eruption that started in the northern part of Makaopuhi Crater due to higher magma rates in ERZ³. While Kīlauea showed higher volcanic activity accompanied by ground deflation mostly represented by the continuous and dotted line in Fig. 3 in Kīlauea block, Mauna Loa was still experiencing gradual inflation of the ground - continuous and dashed line in Mauna Loa block (Fig. 3). Many authors have attempted to explain these opposing ground deformation pattern behaviours, presenting models for the causes. Poland et al.¹¹ stated that the 2003-2007 episode was an unusual event, caused by the arrival of a new pulse of magma from the mantle. Dzurisin et al.³³ found similar behaviour in the late 70s: when Kīlauea experienced an increase in magma supply, inflation of Mauna Loa was also observed. Poland et al.³ explained this similar behaviour by magma input to the deep storage zone that affected both volcanoes.

The DInSAR SBAS time series analysis via the ICA decomposition technique provides a powerful tool for assessing and highlighting the relationship between the magmatic systems of the two volcanoes, and can be used to constrain the underlying physical mechanism of their possible connection. Interconnection between the two volcanic systems is best shown by the first independent component of the ground deformation (ICA1). In contrast, ICA2 shows a ground deformation source affecting only Kīlauea volcano. The rapid deflation of Kīlauea from 2007 to 2009 (Fig. 3) has a source located beneath Halema'uma'u Crater. Co-incident with deflation of this source, the interconnected source of Kīlauea and Mauna Loa (ICA1) was deflating more gradually (Fig.3).

The GPS strain area results support anticorrelated behaviour of these two volcanoes. The 2009 strain area reduction in Mauna Loa and the opposite increment of the strain area in Kīlauea indicates that while Mauna Loa was undergoing a deflation, Kīlauea was experiencing an inflation episode.

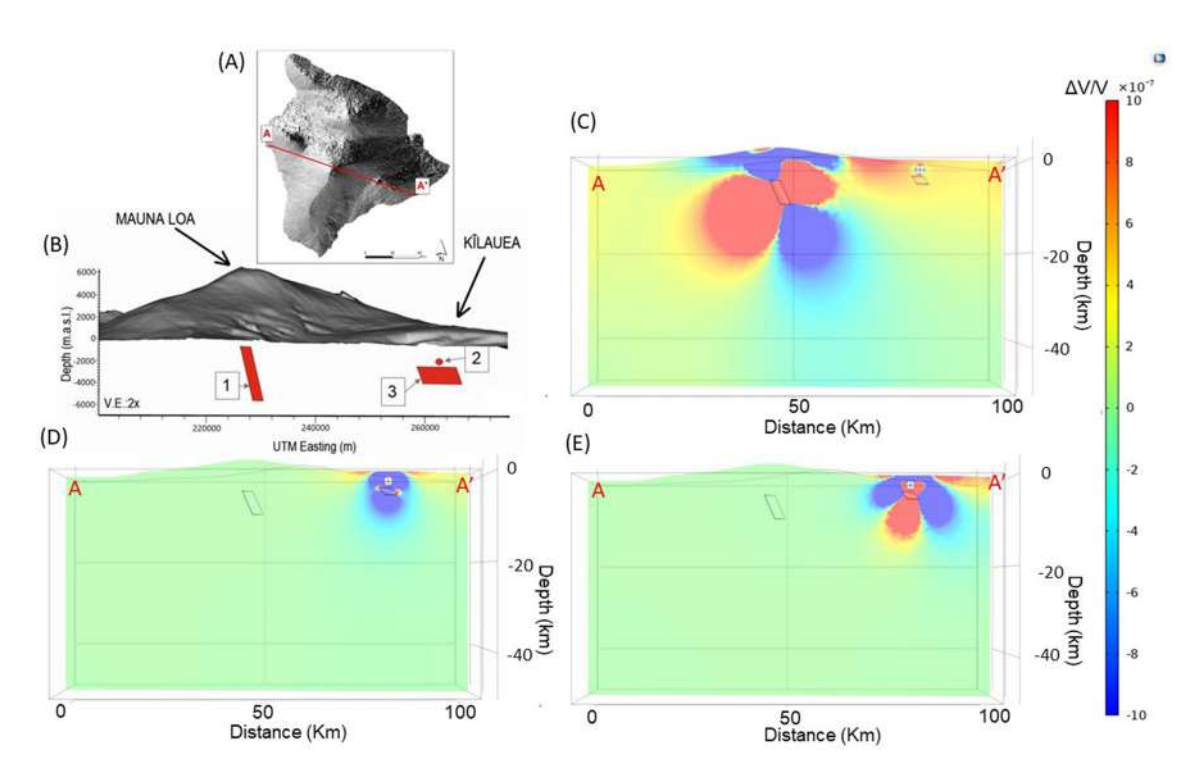


Figure 7. 3D numerical modelling of strain fields. (**A**) The Digital Elevation Model of Hawai'i Island, with the red line representing the trace (A-A'), used in panels (**C**-**E**). (**B**) tridimensional representation of the modelled ground deformation sources of Mauna Loa and Kīlauea volcanoes. The sources are numbered according to Table S1 in the supplementary material. (1) the Mauna Loa dike-shaped source from ICA1; (2) the Kīlauea Mogi-like source from ICA1; (3) the Kīlauea sill-shaped source from ICA2. Storage areas and topography are exaggerated in size for clarity. (**C**) the volumetric strain field represented along the A-A' trace due to an overpressure applied to the Mauna Loa dike-like source. (**D**) volumetric strain field along the A-A' trace due to an overpressure applied to the Kīlauea Mogi-like source. (**E**) volumetric strain field along the A-A' trace due to an overpressure applied to the Kīlauea sill-like source.

Finally, based on the inverse modelling results, we maintain that the pattern associated with the anticorrelated component ICA1 points to a very shallow source beneath Kīlauea. This makes it unlikely that there is a direct connection between the magmatic systems of the two volcanoes in the deeper crust. A direct connection at shallow depths would provide a further source of ground deformation, which has never been observed. Furthermore, it would contradict petrological and geochemical evidence²⁷. On the other hand, the existence of a second component, related to Kīlauea alone, suggests a more complex configuration of the plumbing system of Kīlauea, characterised by multiple reservoirs.

The spatial configuration suggests a possible explanation for the observed anticorrelation between the ground deformation sources related to ICA1 (numbered 1 and 2 in Fig. 7). Their respective geometries make the stress field, caused by the inflation of one source, act on the other with forces directed inward along its external surface. At the same time, because of its sill-like geometry, the source related to ICA2 (number 3 in Fig. 7) would be less sensitive to these changes in the stress field, explaining its independent temporal behaviour. In practice, the dike-shaped source of Mauna Loa would be capable of affecting the shallow volumetric (Mogi-like) source of Kīlauea, but not the deeper sill-shaped source.

To corroborate our hypothesis, we performed a quantitative numerical model of the interaction between the plumbing systems of Mauna Loa and Kīlauea. The Figs. 7 and S13 in supplementary material show the volumetric strain and stress fields as the consequence of internal overpressure applied to each source independently. We selected the overpressure values for each source to reproduce approximately the maximum observed ground deformation above each source. Figure 7 shows the volumetric strain produced by a pressure change inside the Mauna Loa dike-shaped source (see panel (C) in Fig. 7). It can be seen that the strain field in the surroundings of the shallow source at Kīlauea is perturbed. The Mauna Loa Okada source does not significantly affect the deeper Kilauea reservoir. Furthermore, panels (D) and (E) in Fig. 7 show that pressure changes inside the Kīlauea sources does not significantly affect Mauna Loa. Therefore we conclude that the interaction through stress-transfer is effective only between the Mauna Loa dike with respect to the shallow Mogi-shaped Kīlauea reservoir. In the supplementary Fig. S13, we also show the corresponding isotropic component of the perturbed stress field.

Conclusions

The application of ICA decomposition to four DInSAR SBAS datasets revealed an anticorrelated behaviour between Mauna Loa and Kīlauea volcanoes during the studied interval 2003–2010. At the same time, another pattern of ground deformation has been identified and is linked to independent behaviour at Kīlauea alone. The

GPS dataset and inverse modelling results support these findings. Moreover, another significant result from our analysis is the evidence of a single ground deformation source at Mauna Loa during the studied time interval. This has been previously suggested by Pepe et al.⁵, who showed the central conduit dynamics and the dikes along the rift zones displayed an almost synchronous inflation. Kīlauea displays a greater complexity, with at least two sources simultaneously active.

We highlight that the connection between Mauna Loa and Kīlauea occurs at shallow depths in the first few kilometers of the crust, through a stress transfer mechanism. Stress transfer at Mauna Loa and Kīlauea has been considered by various authors to explain the dynamics of intrusions along rift zones ^{14,18} and the interaction between earthquakes and eruptions ^{4,5} at both volcanoes. This interconnection is created by the Mauna Loa reservoir perturbing the Kīlauea shallowest source. Conversely, the sources below the Kīlauea do not effectively influence the Mauna Loa reservoir. In practice, the inflation of Mauna Loa makes the stress field in the surroundings of Kīlauea less favourable for the ascent of magma into its shallow reservoir. The opposite mechanism, with Kīlauea affecting Mauna Loa, seems less favorable. The respective geometries of the sources (Fig. 7) make an effective mechanical interaction possible only between the dike-shaped source of Mauna Loa to the shallow volumetric source of Kīlauea. The sill-shaped geometry of the deeper Kīlauea source means it is less affected by this interaction process, as also confirmed by numerical modelling.

An important result of this work is the application of ICA to ground deformation datasets. This statistical tool has been demonstrated to effectively detect and separate individual independent sources within complex spatiotemporal ground deformation patterns. This approach greatly simplifies the study of complex ground deformation sources, whose components can be modelled independently. Using more advanced inverse modelling tools⁵ can shed further light on the spatial complexity of the Kīlauea plumbing system. Further studies should be devoted to analyzing the interaction between ground deformation sources over a larger time span.

Methods

DInSAR SBAS time series. In this work, was utilised the large amount of satellite data acquired over eight years (2003–2010) across Hawai'i Island. Specifically, C-band (wavelength of \approx 5.6 cm) ASAR ENVISAT images from the European Space Agency (ESA) were acquired along both ascending and descending orbits from 2003-2010 (see Fig. S3 in the supplementary material). Four tracks were selected: T093 along an ascending orbit, and T343, T472, and T200 (Fig. S3 in supplementary material) along descending orbits. The tracks have different swathes: I2, I7, I1, and I2, respectively (see Table S2 for tracks details). We analysed a catalog of 394 SAR images covering both Mauna Loa and Kīlauea volcanoes, with look angles ranging from 15.0° (I1) to 45.2° (I7)⁵. All the interferograms of the considered tracks were analysed automatically, and noisy interferograms were discarded. We performed a multitemporal analysis using the Small Baseline (SBAS) technique that provided a Line-Of-Sight (LOS) time series for coherent pixels of the SAR images. SBAS algorithms allow the production of a deformation time series for each coherent pixels of the SAR images. SBAS algorithms allow the Processing On-Demand (G-POD) platform of ESA that applies the SBAS algorithm and can process large volumes of DInSAR data³⁵. Tracks covering only one of the two volcanoes were discarded from the analysis (see Figs. S4, S5, S6, and Table S4 in the supplementary material).

Independent component analysis (ICA) of DInSAR SBAS time series. Independent Component Analysis is a multivariate statistical tool that allows the separation of a spatio-temporal dataset into discrete components, for which the relative statistical independence is maximised³⁶. ICA is a widely recognized technique that allows the detection of "hidden" patterns in complex datasets³⁶. An advantage of using ICA in volcano geodesy is that it allows simplification of the inverse problem by separating the contribution of different causative ground deformation sources. ICA was highlighted by Ebmeier³⁷ as a valuable tool in the detection of different sources responsible for observed ground deformation patterns¹. For Hawai'i Island, each track dataset consists of a set of time series L(xi, tj), where L is the LOS displacement for a given track, xi is the spatial position of the i-th DInSAR pixel, tj is the time of the j-th DInSAR image.

Using ICA, the original dataset can be decomposed into a finite sum of N components with a fixed spatial pattern $B_i(xi)$ and time-varying amplitudes. In practice, the observed LOS displacement time series for a given track can be represented as:

$$L(i, t_j) = \sum_{k=1}^{N} A_{jk} B_k(x_i),$$
 (1)

where B_k is the normalised spatial pattern corresponding to the k-th ICA component, and A_{jk} is the amplitude of the k-th ICA component at time t_j .

In the model of Eq. (1), the LOS displacement is expressed through a linear combination of the normalised spatial patterns B_k , through the time-varying coefficients A_{jk} . Once the B_k are known from ICA, the coefficients A_{jk} can be determined by solving the linear system of Eq. (1) using a least-squares approach. This model implies that using only a limited number of components, as is usual when performing ICA, the sum on the right side of Eq. (1) cannot fully model the whole signal L. If the number of selected components is sufficient, this missing value is generally related only to the incoherent noisy part of the signal.

The ICA components can be ordered based on their energy, defined as the sum of squared A_{jk} for each k. This allows a consistent sorting of the retrieved components, irrespective of the specific ICA algorithm used. In our case, using three components was sufficient since additional components had negligible amplitude values.

The first and the second components (ICA1, ICA2) were associated with a clear and meaningful signal, while the third component (ICA3) was mainly composed of noise; hence it was not considered further. In Table S3 (in

supplementary material) we show the percentage of the energy of the ICA signal in every component for each track of the study. It should be noted that for the purposes of ICA decomposition, it is recommended to have a minimum of 3 components so that at least one of them includes the noisy part of the signal^{1,36,37}.

Non-linear inverse modelling. To model the observed ground deformation, we tested four analytical source models³³: the Mogi point source³¹, the spheroidal source³⁸, the closed pipe³⁹ and the rectangular crack³². In all cases, we performed the modelling assuming a Poisson's ratio of 0.25 within a half-space. We selected the best model for each ICA and each volcano following the Akaike Information Criterion (AIC)³⁰. We performed a non-linear inversion of each track for all previous source models for each ICA and each volcano. The inverse method relies on a non-linear optimisation of a misfit function using the Nelder-Mead simplex algorithm⁴⁰. The misfit function is defined as the sum of the squared residuals between the observed and synthetic data. The synthetic data, computed using the aforementioned analytical models, were projected along the LOS corresponding to each track. The final models resulted from averaging the results obtained for each track. We obtained a source model for Mauna Loa, corresponding to ICA1, and two models for Kīlauea, corresponding to ICA1 and ICA2, respectively.

GPS data. GPS stations up to 10 km from the summit calderas of the two volcanoes were selected (Fig. S3 in supplementary material). For Mauna Loa and Kīlauea volcanoes, 8 and 7 stations were selected, respectively, with data from 2008 to 2011. The GPS daily solutions were downloaded from the Nevada University repository (http://geodesy.unr.edu)⁴¹.

We used horizontal components to compare results obtained through the ICA decomposition of DInSAR SBAS data with GPS time series, since vertical components have a higher signal/noise ratio. The areal strain time series was computed since it does not require the assumption of a reference point on the island. The areal strain is a geodetic method widely applied in active volcanic areas and has been described by many authors^{42–45}. For this purpose, we computed the area for triplets of GPS stations covering more than half of the summit calderas (see Figs. S7, S8 in supplementary material). We did not use triplets with significant temporal data gaps or whose signal was too noisy. Accordingly, we used 11 triplets for the main crater of Mauna Loa and 15 triplets for Kilauea's summit caldera. We studied the temporal variation in the area of a given triplet of stations, determining the areal strain time series $\delta A(t)$ as:

$$\delta A(t) = (A(t_0) - A\frac{(t)}{A}(t_0)), \tag{2}$$

with $\delta A(t)$ being the times series of the area of a given triplet and $A(t_0)$ the area at the initial time of the series. We did not consider the detailed spatial variations of the areal strain since we are making only a qualitative comparison of the trend of DInSAR SBAS and areal strain data here. Most of the GPS stations at Kīlauea began operation in the first quarter of 2008. Hence, we computed the areal strain time series for this volcano beginning in mid-2008, when the GPS network was fully operative. Therefore, we also begin the comparison with the Mauna Loa time series from June 2008 (although more data is available).

Numerical modelling of the stress and strain fields. To validate the stress-transfer model, we realized a finite-element tridimensional elastic modelling using the software COMSOL Multiphysics *. The model includes the topography of Hawaii Island and the sources of the ground deformation determined by non-linear inversion. The size of the computational domain was $100 \times 100 \times 70 \text{ km}^3$. The linear elastic material characteristics were assumed as isotropic, with elastic constants retrieved from the 1D velocity model of Lin et al. 46. The boundary conditions of the domain were chosen to be fixed on the bottom and lateral sides. The computational domain was built as tetrahedral mesh elements with dimensions ranging between 150 and 3500 m. As explained in the "Discussion" section, we applied an overpressure to each source, calculating the corresponding perturbation of the stress and strain fields.

Data availability

The DInSAR SBAS datasets used and/or analysed during the current study available from the corresponding author on reasonable request. The GPS daily solutions were downloaded from the Nevada University repository (http://geodesy.unr.edu).

Received: 4 May 2022; Accepted: 14 November 2022

Published online: 18 November 2022

References

- 1. Comon, P. Independent component analysis, a new concept?. Signal Process. 36, 287–314 (1994).
- 2. Venzke, E. Global volcanism program. Volcanoes of the World, 4(1), 1280 (2013).
- 3. Poland, M. P., Miklius, A. & Montgomery-Brown, E. Magma supply, storage, and transport at shield-stage Hawaiian volcanoes. *Charact. Hawaii. Volcanoes* 179, 179–234 (2015).
- 4. Walter, T. R. & Amelung, F. Volcano-earthquake interaction at Mauna Loa volcano, Hawaii. *J. Geophys. Res. Solid Earth* 111(B5) (2006).
- 5. Pepe, S. et al. The use of massive deformation datasets for the analysis of spatial and temporal evolution of Mauna Loa volcano (hawai'i). Remote Sens. 10, 968 (2018).
- 6. Okubo, P. G., Benz, H. M. & Chouet, B. A. Imaging the crustal magma sources beneath Mauna Loa and kilauea volcanoes, Hawaii. *Geology* 25, 867–870 (1997).

- 7. Le Corvec, N. & Walter, T. R. Volcano spreading and fault interaction influenced by rift zone intrusions: insights from analogue experiments analyzed with digital image correlation technique. *J. Volcanol. Geoth. Res.* 183, 170–182 (2009).
- Denlinger, R. P. & Okubo, P. Structure of the mobile south flank of kilauea volcano, Hawaii. J. Geophys. Res. Solid Earth 100, 24499–24507 (1995).
- 9. Morgan, J. K., Moore, G. F., Hills, D. J. & Leslie, S. Overthrusting and sediment accretion along kilauea's mobile south flank, Hawaii: evidence for volcanic spreading from marine seismic reflection data. *Geology* 28, 667–670 (2000).
- 10. Borgia, A. Dynamic basis of volcanic spreading. J. Geophys. Res. Solid Earth 99, 17791-17804 (1994).
- 11. Klein, F. W. Patterns of historical eruptions at Hawaiian volcanoes. J. Volcanol. Geoth. Res. 12, 1-35 (1982).
- 12. Miklius, A. & Cervelli, P. Interaction between kilauea and Mauna Loa. Nature 421, 229-229 (2003).
- 13. Gonnermann, H. M. et al. Coupling at Mauna Loa and Kīlauea by stress transfer in an asthenospheric melt layer. Nat. Geosci. 5, 826–829 (2012).
- 14. Amelung, F., Yun, S.-H., Walter, T. R., Segall, P. & Kim, S.-W. Stress control of deep rift intrusion at Mauna Loa volcano, Hawaii. *Science* 316, 1026–1030 (2007).
- Poland, M. P. Asar images a diverse set of deformation patterns at Kīlauea volcano, Hawaii. In Envisat Symposium 2007 SP-636 (2007).
- Poland, M. P., Sutton, A. J. & Gerlach, T. M. Magma degassing triggered by static decompression at Kīlauea volcano, Hawai 'i. Geophys. Res. Lett. 36(16) (2009).
- 17. Poland, M. P., Miklius, A., Jeff Sutton, A. & Thornber, C. R. A mantle-driven surge in magma supply to Kīlauea volcano during 2003–2007. Nat. Geosci. 5, 295–300 (2012).
- 18. Swanson, D. A., Duffield, W. A. & Fiske, R. S. Displacement of the south flank of kilauea volcano; the result of forceful intrusion of magma into the rift zones. Tech. Rep., US Govt. Print. Off., (1976).
- Decker, R. et al. Seismicity and surface deformation of Mauna Loa volcano, Hawaii. EOS Trans. Am. Geophys. Union 64, 545–547 (1983).
- 20. Wyss, M. Regular intervals between hawaiian earthquakes: implications for predicting the next event. Science 234, 726–728 (1986).
- 21. Owen, S. et al. Rapid deformation of the south flank of kilauea volcano, Hawaii. Science 267, 1328-1332 (1995).
- 22. Delaney, P. T. et al. Volcanic spreading at kilauea, 1976-1996. J. Geophys. Res. Solid Earth 103, 18003-18023 (1998).
- Borgia, A. & Treves, B. Volcanic plates overriding the ocean crust: structure and dynamics of hawaiian volcanoes. Geological Society, London, Special Publications 60, 277–299 (1992).
- 24. Montgomery-Brown, E. K. & Miklius, A. Periodic dike intrusions at kı-lauea volcano, Hawai'i. Geology 49, 397–401 (2021).
- 25. Morgan, J. K. & Clague, D. A. Volcanic spreading on Mauna Loa volcano, Hawaii: Evidence from accretion, alteration, and exhumation of volcaniclastic sediments. *Geology* 31, 411–414 (2003).
- 26. Jaggar, T. A. Report of the Hawaiian Volcano Observatory of the Massachusetts Institute of Technology and the Hawaiian Volcano Research Association. Society of Arts of the Massachusetts Institute of Technology (1912).
- 27. Rhodes, J. & Hart, S. Episodic trace element and isotopic variations in historical Mauna Loa lavas: Implications for magma and plume dynamics. *Wash. DC Am. Geophys. Union Geophys. Monogr. Ser.* **92**, 263–288 (1995).
- 28. Shirzaei, M., Walter, T. R. & Bürgmann, R. Coupling of Hawaiian volcanoes only during overpressure condition. *Geophys. Res. Lett.* 40, 1994–1999 (2013).
- 29. Shirzaei, M., Bürgmann, R., Foster, J., Walter, T. & Brooks, B. Aseismic deformation across the hilina fault system, hawaii, revealed by wavelet analysis of insar and gps time series. *Earth Planet. Sci. Lett.* **376**, 12–19 (2013).
- 30. Akaike, H. A new look at the statistical model identification. *IEEE Trans. Autom. Control* **19**, 716–723 (1974).
- 31. Mogi, K. Relations between the eruptions of various volcanoes and the deformations of the ground surfaces around them. *Earthq. Res. Inst.* **36**, 99–134 (1958).
- 32. Okada, Y. Surface deformation due to shear and tensile faults in a half-space. Bull. Seismol. Soc. Am. 75, 1135-1154 (1985).
- 33. Dzurisin, D., Koyanagi, R. Y. & English, T. T. Magma supply and storage at kilauea volcano, Hawaii, 1956–1983. *J. Volcanol. Geoth. Res.* 21, 177–206. https://doi.org/10.1016/0377-0273(84)90022-2 (1984).
- 34. Casu, F., Manzo, M. & Lanari, R. A quantitative assessment of the sbas algorithm performance for surface deformation retrieval from dinsar data. *Remote Sens. Environ.* **102**, 195–210 (2006).
- 35. De Luca, C. et al. An on-demand web tool for the unsupervised retrieval of Earth's surface deformation from sar data: The p-sbas service within the esa g-pod environment. Remote Sens. 7, 15630–15650 (2015).
- 36. Hyvärinen, A. & Oja, E. Independent component analysis: algorithms and applications. Neural Netw. 13, 411-430 (2000).
- 37. Ebmeier, S. Application of independent component analysis to multitemporal insar data with volcanic case studies. *J. Geophys. Res. Solid Earth* 121, 8970–8986 (2016).
- 38. McTigue, D. Elastic stress and deformation near a finite spherical magma body: resolution of the point source paradox. *J. Geophys. Res. Solid Earth* **92**, 12931–12940 (1987).
- 39. Bonaccorso, A. & Davis, P. M. Models of ground deformation from vertical volcanic conduits with application to eruptions of Mount St. Helens and Mount Etna. *J. Geophys. Res. Solid Earth* 104, 10531–10542 (1999).
- Nelder, J. A. & Mead, R. A simplex method for function minimization. Computer J. 7, 308–313, https://doi.org/10.1093/comjnl/7.4.308 (1965). https://academic.oup.com/comjnl/article-pdf/7/4/308/1013182/7-4-308.pdf.
- 41. Blewitt, B. G. & Hammond, W. C. Harnessing the gps data explosion for interdisciplinary science. Eos, Trans. Am. Geophys. Union, 2019 1–8 (2018).
- Haines, A. J. & Holt, W. E. A procedure for obtaining the complete horizontal motions within zones of distributed deformation from the inversion of strain rate data. J. Geophys. Res. Solid Earth 98, 12057–12082, https://doi.org/10.1029/93JB00892 (1993). https://agupubs.onlinelibrary.wiley.com/doi/pdf/10.1029/93JB00892.
- 43. Scherneck, H.-G., Lidberg, M., Haas, R., Johansson, J. M. & Milne, G. Fennoscandian strain rates from bifrost gps: A gravitating, thick-plate approach. *J. Geodyn.* 50, 19–26, https://doi.org/10.1016/j.jog.2009.11.005 (2010).
- 44. Bruno, V. et al. Ground deformations and volcanic processes as imaged by cgps data at mt. Etna (italy) between 2003 and 2008. J. Geophys. Res. Solid Earth https://doi.org/10.1029/2011JB009114 (2012). https://agupubs.onlinelibrary.wiley.com/doi/pdf/10.1029/2011JB009114.
- Rivet, D., Brenguier, F., Clarke, D., Shapiro, N. M. & Peltier, A. Long-term dynamics of piton de la fournaise volcano from 13 years of seismic velocity change measurements and gps observations. J. Geophys. Res. Solid Earth 119, 7654–7666 (2014).
- 46. Lin, G., Shearer, P. M., Matoza, R. S., Okubo, P. G. & Amelung, F. Three-dimensional seismic velocity structure of Mauna Loa and kilauea volcanoes in Hawaii from local seismic tomography. *J. Geophys. Res. Solid Earth* 119, 4377–4392 (2014).

Acknowledgements

We warmly thank Dr. Beverley Coldwell for her accurate and valuable proofreading. Also, we are grateful to both reviewers, who provided a very detailed review with a lot of useful comments and constructive suggestions.

Author contributions

All the authors contributed to the conceptualisation of the article. M.P. and S.P. contributed to the data curation, L.D. and I.C.P. developed some of the software used in the analysis, all the authors contributed in writing and revising the paper.

Funding

This research was funded by Tenerife Volcano Disaster Assistance Team (TFassistance), financed by the TFinnova Program of the Cabildo Insular de Tenerife (Spain) and by the project VOLRISKMAC II (MAC2/3.5b/328; www. volriskmac.com) co-financed by the Program MAC 2014-2020 of the European Commission MAC 2014-2020 Cooperation Transnational Programs.

Competing interests

The authors declare no competing interests.

Additional information

 $\label{lem:supplementary material available at https://doi.org/10.1038/s41598-022-24308-0.}$

Correspondence and requests for materials should be addressed to M.P.

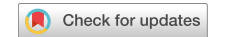
Reprints and permissions information is available at www.nature.com/reprints.

Publisher's note Springer Nature remains neutral with regard to jurisdictional claims in published maps and institutional affiliations.

Open Access This article is licensed under a Creative Commons Attribution 4.0 International License, which permits use, sharing, adaptation, distribution and reproduction in any medium or format, as long as you give appropriate credit to the original author(s) and the source, provide a link to the Creative Commons licence, and indicate if changes were made. The images or other third party material in this article are included in the article's Creative Commons licence, unless indicated otherwise in a credit line to the material. If material is not included in the article's Creative Commons licence and your intended use is not permitted by statutory regulation or exceeds the permitted use, you will need to obtain permission directly from the copyright holder. To view a copy of this licence, visit http://creativecommons.org/licenses/by/4.0/.

© The Author(s) 2022

scientific reports



OPEN Geodetic imaging of magma ascent through a bent and twisted dike during the Tajogaite eruption of 2021 (La Palma, Canary Islands)

Monika Przeor^{1,2⊠}, Raffaele Castaldo³, Luca D'Auria^{1,2}, Antonio Pepe³, Susi Pepe³, Takeshi Saqiya⁴, Giuseppe Solaro³, Pietro Tizzani³, José Barrancos Martínez^{1,2} & Nemesio Pérez^{1,2}

On Sept. 19th, 2021, the largest historical eruption on the island of La Palma began, which had a significant scientific, social, and economic impact. The 2021 Tajogaite eruption was characterised by short precursors, lasting only 8 days. The seismicity started on Sept. 11th with a westward and upward migration of hypocenters. Permanent GNSS stations started recording deformation on Sept. 12th on the island's western side, which reached more than 15 cm just before the eruption. After the eruption onset, the ground deformation increased, reaching a maximum on Sept. 22nd and showing a nearly steady deflation trend in the following months. To better understand the dynamics of the eruption, we exploited a joint dataset of GNSS and Sentinel-1 SBAS time series along both ascending and descending orbits. To obtain the geometry of the causative source of the ground deformation, we combined the result of a preliminary non-linear inversion and the precise location of the seismicity. The resulting geometry of the source is that of a twisted dike bending eastward. We performed inverse modelling to obtain the spatiotemporal kinematics of the opening function of the dike. The forward modelling has been realised using a 3D finite-element approach considering the island's topography. Our findings reveal a close correspondence between the magmatic intrusion and pre-eruptive seismicity. The ascent of the magma occurred along two branches, and the rheology of a previously identified ductile layer strongly affected the magma propagation process. Finally, we found evidence of an early shallow deformation, which we interpret as the effect of ascending hydrothermal fluids. Our findings highlight the need for advanced modelling to understand pre-eruptive processes in basaltic volcanoes.

The Canary Islands are located off the northwest coast of Africa, 150 km from the African coastline (Fig. 1). The Canaries originated in the intraplate region of the African plate and extend along a 500 km wide alignment from East to West, in the framework of – 13° W and – 18° W longitudes and 27° N and 30° N latitudes. The formation of the Canaries started in the Oligocene and is still in process^{1,2}. The most ancient islands are Fuerteventura and Lanzarote, the easternmost located of all Archipelago. Its formation continued with the direction to the West, being the most recent islands of El Hierro and La Palma.

La Palma Island formation started in the Pliocene, 4 My ago, as a seamount sequence that lasted about 1 My². Between 3 and 2 My, the island emerged from the ocean, and a rapid elevation of the island caused the giant landslide. The subsequent formation of the Garafía Edifice and Taburiente Domain was also interrupted by a gravitational landslide. The formation of the Cumbre Nueva Domain was centred on the South of the Taburiente Domain.

Consequently, the Cumbre Vieja Domain started its formation 0.123 My ago². This N-S volcanic ridge is still active and hosted all the historical eruptions of the island of La Palma. The latest eruption in La Palma in the past century (Teneguía eruption of 1971) emerged in the southernmost part of the island (Fig. 1).

¹Instituto Volcanológico de Canarias (INVOLCAN), Granadilla de Abona, Tenerife, Canary Islands, Spain. ²Instituto Tecnológico y de Energías Renovables (ITER), Granadilla de Abona, Tenerife, Canary Islands, Spain. ³Istituto Per il Rilevamento Elettromagnetico dell'Ambiente (CNR-IREA), Naples, Italy. Anagoya University, Nagoya, ${\sf Japan.}^{\boxtimes}{\sf email:mprzeor@iter.es}$

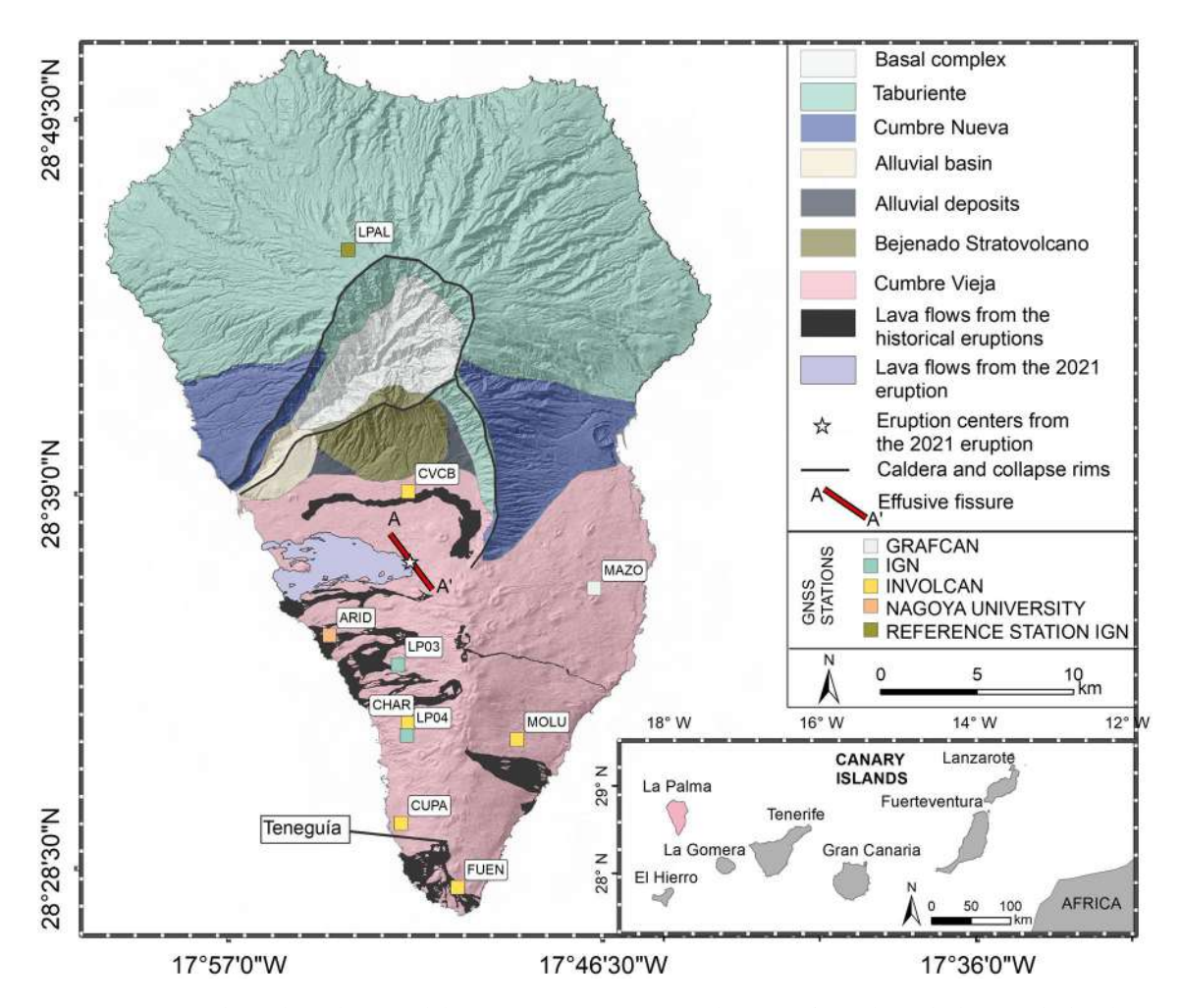


Figure 1. The geological map and the GNSS permanent stations location of La Palma. The lower right-hand side panel shows the location of the island of La Palma (in red) within the Canaries. The legend explains the meaning of the colour shades on the map and the GNSS station. The NW–SE alignment of the effusive fissure of the 2021 eruption is represented by the red line (A–A').

On Sept. 19th, 2021, in the N.W. of the Cumbre Vieja ridge, a new volcanic eruption on the island started and lasted 85 days³. The eruption's consequences (gas emissions, a large volume of lava flows, and tephra dispersion) resulted in one fatality due to indirect causes and enormous economic and social losses⁴. The volcanic precursors, like ground deformation, seismicity, and gas emissions, were noticed 8 days before the eruption onset³. The permanent volcano monitoring stations of Instituto Volcanológico de Canarias (INVOLCAN) assessed the ground deformation and the pre-eruptive seismicity migration. The Global Navigation Satellite System (GNSS), the Sentinel-1 (S-1) satellite constellation, and seismic stations collected the data of the pre-and early-eruptive phases used in the present study. The first evidence of the magmatic intrusion began on Sept. 11th³.⁵, with a seismic swarm of volcano-tectonic character, with a depth of 10 km or less. The upward migration of the hypocenters lasted only 8 days until magma emerged to the surface. Considerable ground deformation appeared on continuous GNSS (cGNSS) stations of INVOLCAN on Sept. 12th and continued increasing to reach its maximum 3 days after the eruption onset.

This study analyses magmatic and hydrothermal sources that caused the pre-eruptive ground deformation in La Palma. To this aim, we processed a sequence of Synthetic Aperture Radar (SAR) images collected by the Sentinel-1 (A and B) satellites from January to November 2021. We used the multi-temporal differential interferometric SAR (DInSAR) and Small Baseline Subset (SBAS) method⁶. Subsequently, we analysed the InSAR-driven ground displacement measurements and the available cGNSS dataset from Sept. 8th to Sept. 28th, 2021. Accordingly, we performed a preliminary non-linear inversion to determine the dip of the shallow part of the dike. The geometry of the deeper part has been constrained by using the relocated hypocenters of D'Auria et al.³. Later on, following D'Auria et al.⁷ and Pepe et al.⁸, we applied the Geodetic Imaging technique to the DInSAR and cGNSS datasets to understand the ascent path of magma and the spatiotemporal dike aperture kinematics.

Previous studies evidenced the importance of advanced modelling of the ground deformation sources to understand the dynamics of a magmatic plumbing system⁷⁻¹¹. The results of this study are supported by previous studies about local earthquake seismic tomography (LET) of La Palma³, Ambient Noise Tomography (ANT)¹², deformation inverse modelling^{10,11}, petrological studies¹³ and gravity surveys by Montesinos et al.¹⁴.

In this study, we denote the 8 days preceding the eruption as the pre-eruptive phase and the dates between Sept. 19th and 28th as the early-eruptive phase. Geodetic imaging proved to be an effective tool for understanding and visualising the complex magmatic ascent process on La Palma island during both phases.

Results

Preliminary non-linear inversion and dike geometry

Based on the results of previous studies¹⁰, we assume that the shallow part of the conduit consists of a southwestward dipping dike. Therefore, we performed a non-linear inverse modelling to constrain the dip of this shallow part of the conduit (see the Methods section for more details). Figures S1 and S2 in the supplementary materials represent the data, the model, and the residuals for each displacement map for both orbits.

We modelled the source using a simple rectangular dike geometry¹⁵, constraining the azimuth (125°), following the surface orientation of the eruptive fissures (Fig. 1)¹⁶. The retrieved best-fit value of the dip was 50° westward. The location and the geometry of the shallow dike have been adjusted to one of two shallow seismicity clusters corresponding to the dike ascent. However, the second shallow seismicity cluster is unrelated to the dike intrusion process. Previous studies^{3,5} demonstrated that it is related to hydrothermal activity triggered by the fluids released by the ascending magma. It is located to the South of the eruptive vents, and it is not relevant for modelling the dike geometry (Fig. 2).

However, this shallow dike alone cannot accurately describe the pre-eruptive intrusion process. The 3D pre-eruptive seismicity pattern³ shows a north-westward and upward migration of the hypocenters until Sept. 18th. This suggests that the lower part of the dike generated by the magmatic intrusion, starting at about 10 km depth, has an eastward dip. Therefore, a curved dike is a more appropriate geometry for the ground deformation source. To model the geometry of the lower part of the dike, we performed a geometrical fit with the hypocenters distribution using a simple rectangular geometry. The best-fit azimuth and dip are respectively 89° and 67° southward.

The final geometry results from merging these two dikes at a depth of about 3 km. This depth was selected based on the earthquake distribution, which shows a different trend starting from this depth³. The resulting geometry is that of a bent and twisted dike schematically shown in Fig. 2.

Geodetic imaging

Using the dike geometry described in the previous section and applying the geodetic imaging technique described in "Geodetic imaging" section, we obtained a spatiotemporal imaging of the dike opening function. In the following, we describe in detail this result by showing both the absolute opening function (i.e., relative to the first image) and the differential one (i.e., relative to the previous image) (Figs. 3, 4, 5, and 6). For clarity, the dike opening function is shown on a 2D image. In each image, we also show the projection of all the earthquake hypocenters (represented with black dots) recorded between 11 and 28th Sept. 2021, while the earthquakes recorded between each image and the previous one are represented with green dots.

There is no visible deformation in the first two images of both orbits (Sept. 8th and 10th) (Fig. 3A–D). Until Sept. 11th, neither seismicity indicated relevant magma movement at depth.

Between Sept. 11th and 14th, the most relevant precursor of the approaching eruption was the north-west-ward and upward migration of the seismicity starting from a depth of about 10 km³. The ground deformation began to be significant on Sept. 14th, reflecting magma accumulation at a depth between 6 and 8 km (see R1 in Fig. 4A). The seismicity comprised two clusters located between 6 and 10 km. The first one, denoted S1, connects R1 with the magma chamber, located at more than 10 km depth by the local earthquake tomography³. The

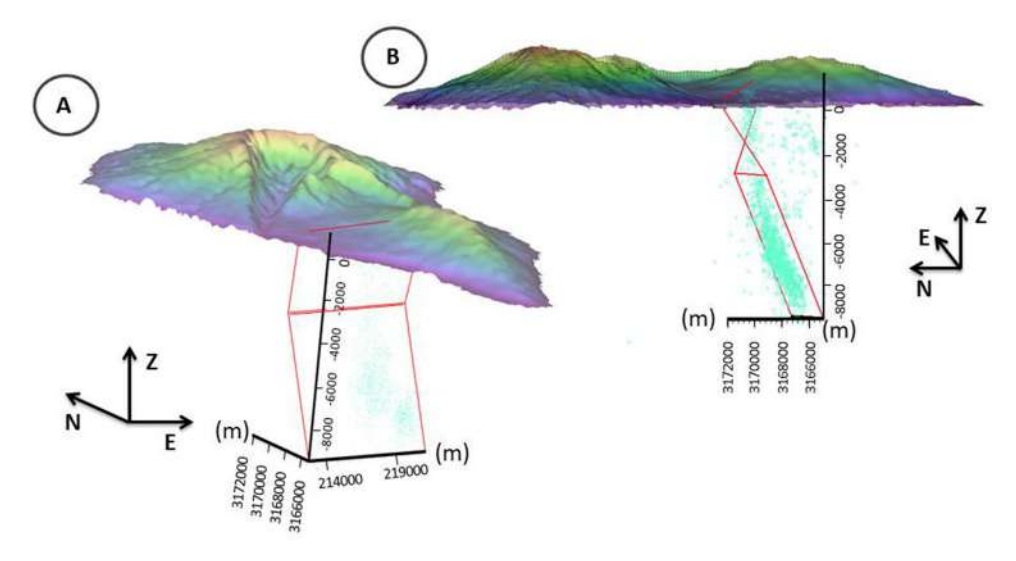


Figure 2. Tridimensional representation of the dike geometry and the topography of La Palma island. Panel A is a view from S.W., while B is from W. Earthquake hypocenters are represented as cyan circles. The axes are represented in meters (m).

2021-09-08 19:13

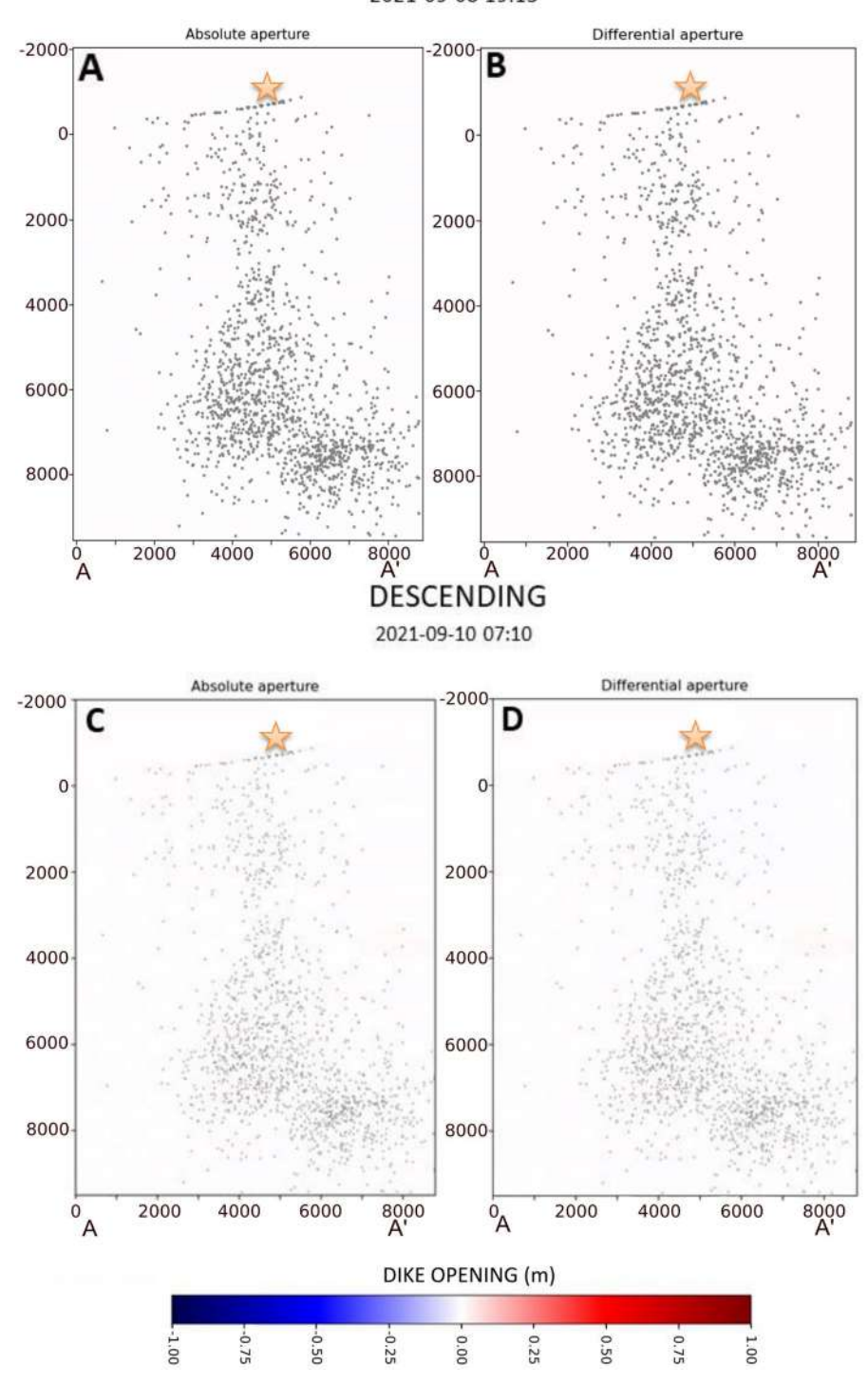


Figure 3. Distribution of absolute and differential dike opening for the 8th (ascending orbit) and Sept. 10th 2021 (descending orbit). Grey dots represent the projection on the dike of all the seismic events located between Sept. 11th and 28th. The seismic events colour in the images of Sept. 8th is represented with dark grey in order to highlight the total of earthquakes produced in the analysed period. Orange stars indicate the future location of the main eruptive vent.

2021-09-14 19:13

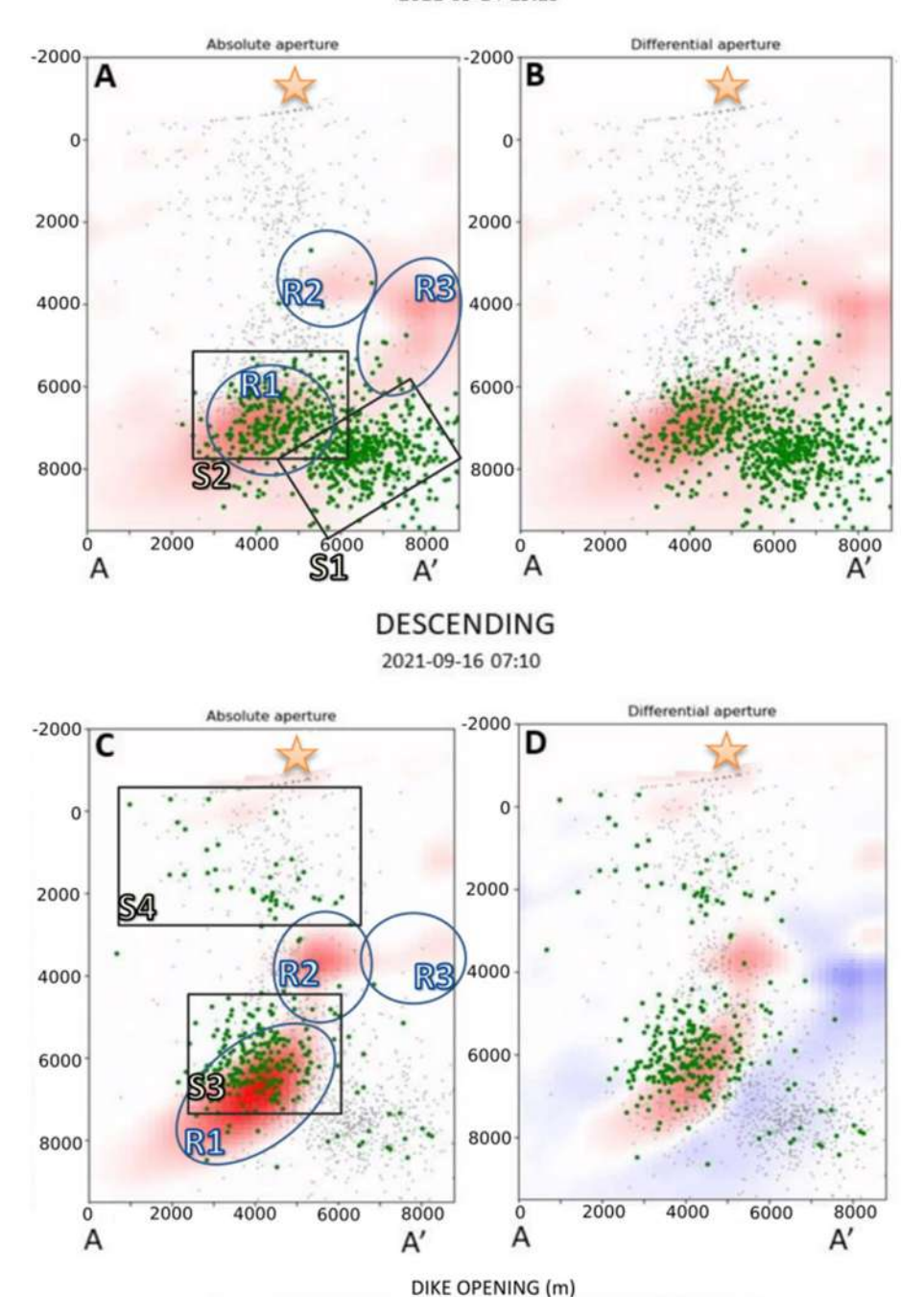
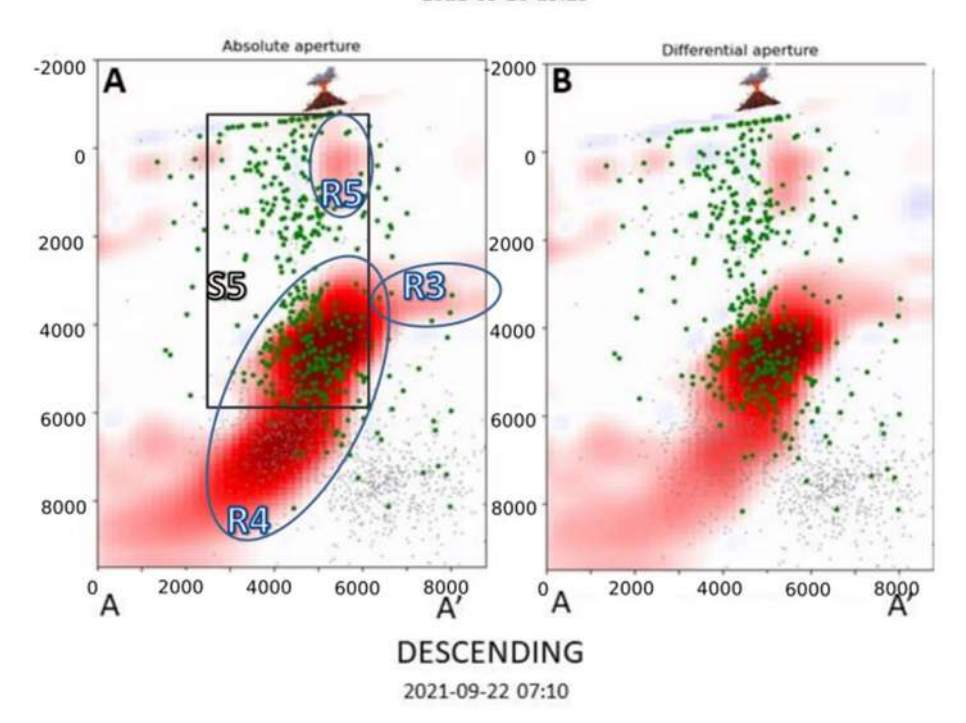


Figure 4. Distribution of absolute and differential dike opening for the 14th (ascending orbit) and Sept. 16th 2021 (descending orbit). Grey dots represent the projection on the dike of all the seismic events located between Sept. 11th and 28th, while green dots represent seismic events that occurred between two successive images. Blue ellipsoids and black squares represent, respectively, the features in the dike opening function and the clusters of seismic events discussed in the text. Orange stars indicate the future location of the main eruptive vent.

2021-09-20 19:13



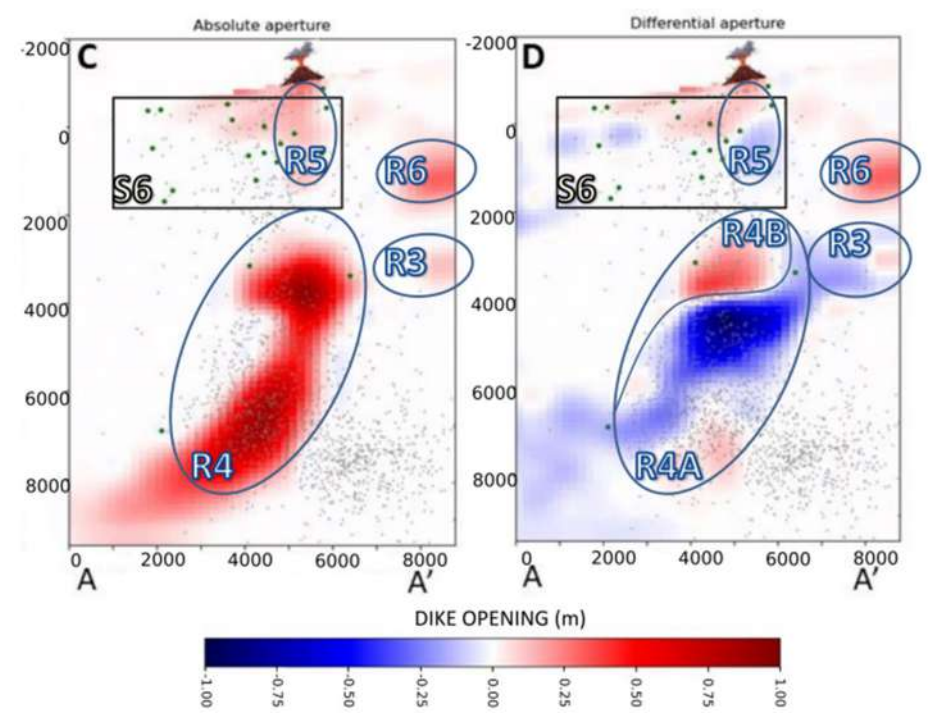
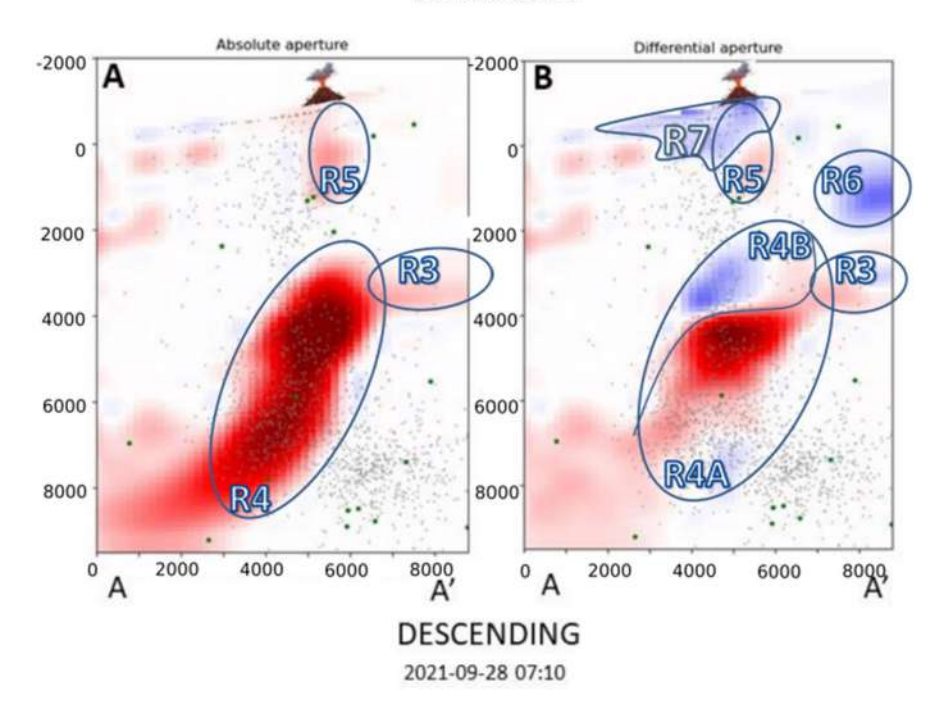


Figure 5. Distribution of absolute and differential dike opening for the 20th (ascending orbit) and Sept. 22nd, 2021 (descending orbit). The volcano symbol indicates the position of the main eruptive vent.

second cluster, S2, corresponds to the location of the magma accumulation zone in R1 (see Fig. 4A). The dike opening marked with the R2 is located along the primary magma pathway toward the surface. Conversely, the R3 is situated to the SW of the primary pathway, between 3 and 6 km depth.

The descending orbit from Sept. 16th shows that the dike opening R1 increased its magnitude and extends in depth between 5 and 8 km, with an approximate width of about 3 km (Fig. 4C,D). The R2 accumulation zone also increases its magnitude and area, reaching a diameter of approximately 2 km. The magma ascent was associated

2021-09-26 19:13



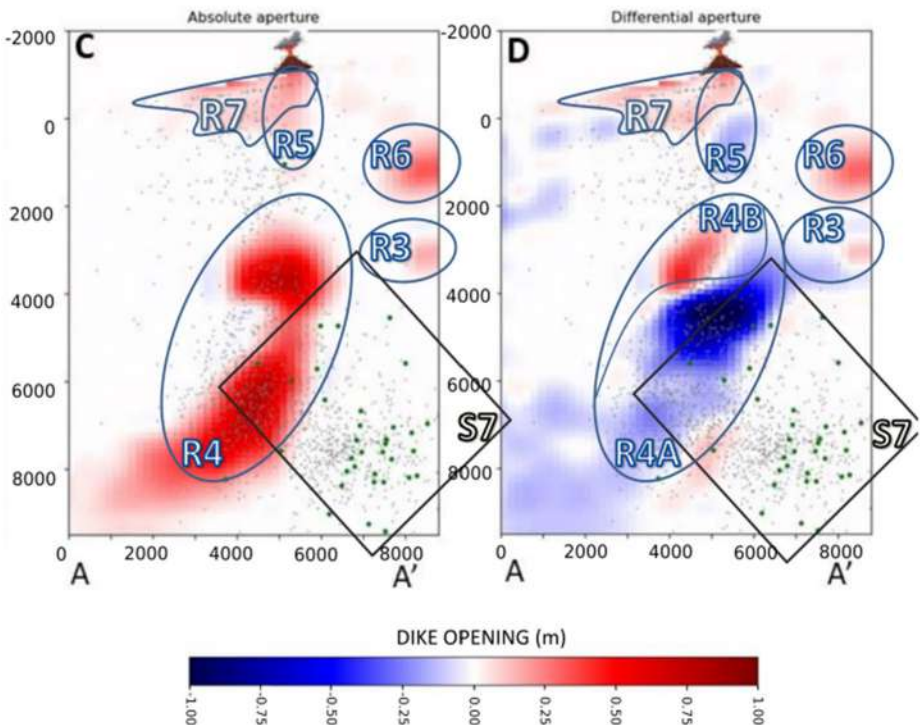


Figure 6. Distribution of absolute and differential dike opening for the 26th (ascending orbit) and Sept. 28th, 2021 (descending orbit). The meaning of the symbols is the same as in Fig. 5.

with a new cluster of seismicity migrating upward from S2 to S3. In this interval, we also observe a sparse, shallow cluster located between 0 and 3 km depth, represented by S4. The location of this cluster is spatially separated from the main seismicity related to the dike intrusion process 3,12 .

On Sept. 20th, 1 day after the beginning of the eruption, the previously observed accumulation zones R1 and R2 merged, forming a single accumulation zone extending between 3 and 9 km, with a width of about 3 km, indicated as R4 in Fig. 5. The seismic cluster S5 is shallower than the previous ones, extended from the surface

until 6 km depth. In this image, we can also observe a shallow magma accumulation zone (R5 in Fig. 5), which extends between 0 and 2 km depth with a width of about 1 km and coincides with the location of the eruptive vent. We also observe an increase in the dike aperture of the accumulation zone R3 located at a depth between 3 and 4 km

Since the beginning of the eruption, the strong volcanic tremor prevented the detection of low-magnitude seismicity³. However, on Sept. 22nd, the seismicity was mainly located at a shallow depth between 0 and 2 km, which is denoted as S6 in Fig. 5. At the same time, the accumulation zone R4 shows a marked change, with a decrease in the dike opening in the lower part and an increase in the upper part (see R4A and R4B in Fig. 5D). We also observe a decrease in the opening in the R3 zone. We also observe the appearance of a new accumulation zone (R6), between 2 and 4 km, located right above R3 Fig. 5C,D.

In the image of Sept. 26th, we observe a marked decrease in the dike opening right beneath the vent (R7 in Fig. 6). The zone R4 shows a reversal in its behaviour, with replenishment of its lower part. Analogously, the zones R3 and R6 show a similar reversal.

On Sept. 28th, we observed a renewed increase in the magnitude of R7, R6, and R3. The zone R4 shows a deflation, except for its upper part, and a significant reduction in width. On this date, we also observed the appearance of a deeper seismicity, located mainly below 6 km depth (Fig. 6C,D).

Discussion

The complex dike geometry depicted in this work results from a joint analysis of geodetic and seismic data. A straightforward evidence that the geometry we depicted is realistic comes from the time series of horizontal cumulative displacement of the ARID station (see supplementary Fig. S14). It can be seen that until Sept. 18th, the displacement is mainly toward the W. After it changes abruptly to SW because the magma reached the upper part of the conduit, having a different orientation.

Different factors can affect the propagation of dikes: the stress field, the mechanical properties of the rocks, and the buoyancy of the magma¹⁷. First, we notice that the dike bends around a high-velocity body identified by the seismic tomography model of D'Auria et al.³. This can explain the north-westward migration of the intrusion during the pre-eruptive phase. The subsequent deviation toward the East and the development of its twisted geometry can be explained, taking into account the internal stress field of the volcano. Following Dahm et al.¹⁸ and Maccaferri et al.¹⁹, gravitational loads make magmatic intrusions move towards higher topography zones. In the case of La Palma, the highest altitudes are located along the N–S dorsal of the Cumbre Vieja domain (Fig. 1). Therefore, the eastward bending is compatible with the effect of gravitational loads due to the topography of the volcano. Actually, the majority of the historical and prehistoric vents of Cumbre Vieja are located close to the summit of the ridge¹.

The geodetic imaging results (Figs. 3, 4, 5, and 6) give a detailed overview of the kinematics of the magma movement within the dike and its relationship with seismicity. In Fig. 7, we represent, with a schematic cartoon, our interpretation of this process on some key dates. Our study reveals that the magma started accumulating beneath the Cumbre Vieja volcano at a depth of 6–8 km (zone R1 in Fig. 4) at least 5 days before the eruption (Sept. 14th). The simultaneous seismicity, occurring between 7 and 10 km (S1 in Fig. 4), possibly reflects the nucleation of the dike from the huge magma chamber, identified by D'Auria et al.³, beneath 10 km depth. On the other hand, the cluster S2 can be related to the local stress field perturbed by the accumulation of magma within the zone R1 (Fig. 7A). At the same time, the zones R2 and R3 seem to evidence a further minor accumulation zone beneath 4 km depth (Figs. 4A and 7A). Considering previous studies concerning the internal structure of La Palma^{3,20,21}, we know that the first few km of the crust beneath Cumbre Vieja is characterised by low seismic velocities corresponding to low resistivity and low-density values. As discussed by Rivalta et al.¹⁷, the presence of crustal layering can significantly affect the dike propagation speed. We postulate that the different rheology of the first few km caused a temporary decrease in the dike ascent rate, causing the local accumulation in R2 and R3 (Figs. 4A and 7A).

The seismicity focused on two clusters on Sept. 16th (see Figs. 4C and 7B). The deeper one (S3) occurred between 4 and 7 km deep and is located atop the accumulation zone R1. This cluster possibly reflected the pressurisation of R1 and the upward propagation of the crack tip. At the same time, we observe an increase in the dike opening in R2 and R3, which we interpret as the transfer of magma toward a blind lateral branch of the main dike (Fig. 7B). Conversely, cluster S4 does not seem to be directly associated with a magmatic process. Following Cabrera-Pérez et al. ¹², we interpret this cluster as related to the ascent of the hydrothermal fluids exalted from the magma itself that generated the pressurisation of a shallow hydrothermal system. The presence of this hydrothermal system has already been highlighted by previous studies 3.21,22. Furthermore, the study of Pankhurst et al. (2021) revealed that the first stages of the eruption presented more hydrated minerals, meaning that the ascending magma was fluid-rich.

The image of Sept. 20th is the first after the beginning of the eruption. The dike opening function clearly shows the opening of the pathway toward the eruptive vent (zone R5 in Figs. 5 and 7C). The seismicity pattern indicates that the magma approached the surface very quickly during the morning of Sept. 19th³. This rapid acceleration in the magma ascent rate when approaching the surface has been studied by Rivalta and Dahm²³, which explained the physical mechanism of this process in terms of depth-dependent fracture toughness. The secondary blind branch R3 in the southeastern direction of the main dike was also increasing its aperture. As mentioned before, we believe this branch stopped its upward movement by a rheological boundary. Secondary branches departing from the main magmatic reservoir were also observed by Fernández et al.¹¹. Their model shows two branches of magma that appeared due to zones of structural weakness in the crust. Montesinos et al.¹⁴, using gravity data, showed the possible appearance of a blind magma ascent path in the Jedey zone that could coincide with the R3 branch found in the present study. Also, the observed secondary branch R3 was possibly linked to the sill-like

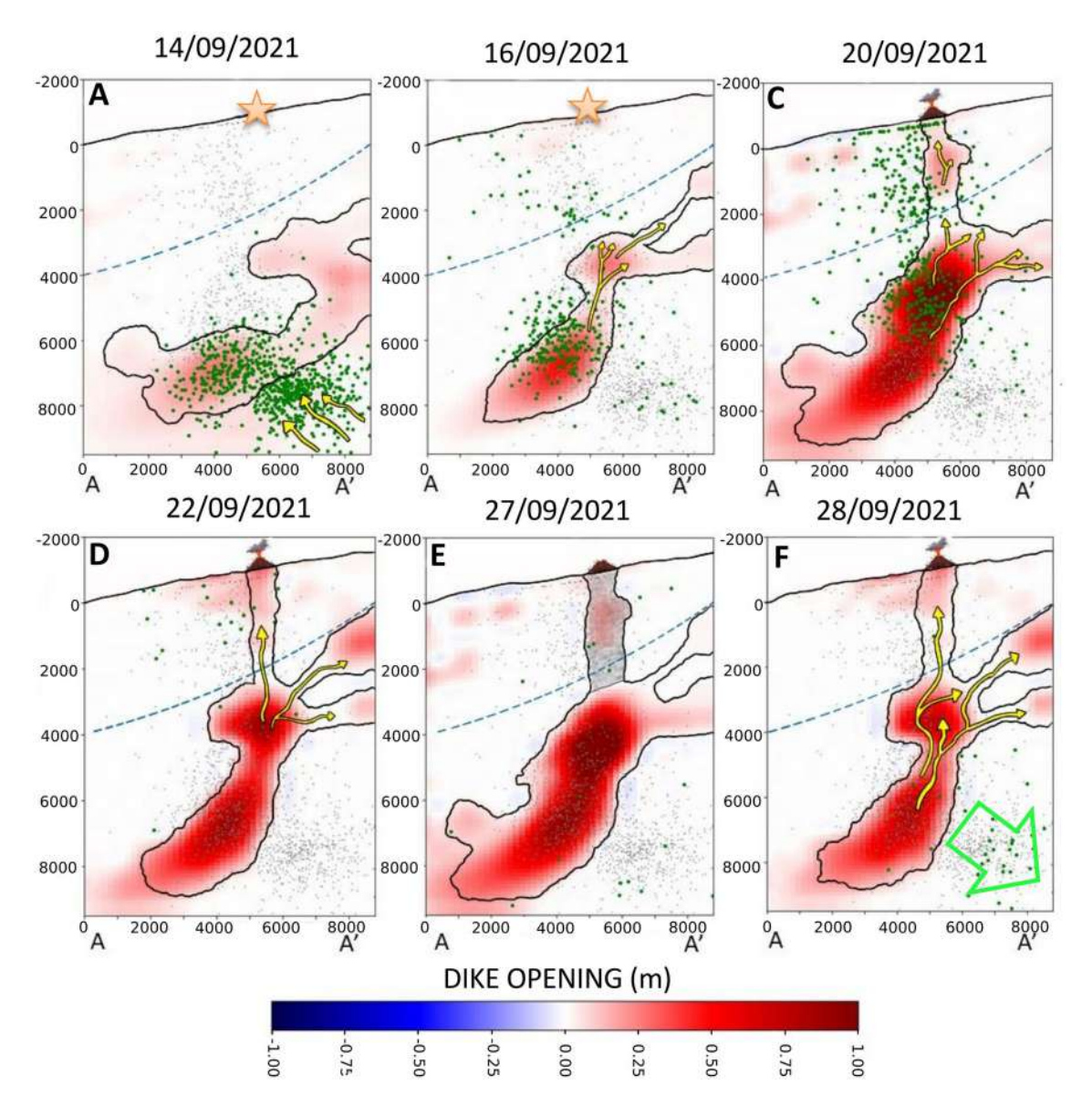


Figure 7. Schematic model of the plumbing system dynamics for key dates. Orange stars represent the location of the future site of the volcanic vent in the days preceding the eruption. The symbols of the volcano represent the location of the actual volcanic vent. Yellow arrows represent the magma ascent directions, while the green arrow indicates the incipient collapse of the magma reservoir. The blue dashed lines represent the limit of the rheological boundary discussed in the text.

source mentioned by De Luca et al. ¹⁰. Also, Muñoz et al. ¹⁶ suggest that the dike developed multiple paths that could not reach the surface due to complex factors.

The main changes observed in the image of Sept. 22nd are the appearance of a further lateral branch (R6 in Figs. 5 and 7D) and a change in the magma distribution within the main feeding conduit R4 (Fig. 5D). We also observe the persistence of the lateral branch R3 (Figs. 5D and 7D).

Between Sept. 22nd and 26th, there was a visible reduction in the dike opening in the shallow part of the conduit (Figs. 6 and 7E). On Sept. 27th, a temporal stop of the eruptive activity was observed, associated with a marked drop in the volcanic tremor amplitude lasting about 10h^{3,24,25}. The reduction observed in the image of Sept. 26th may be a precursor of the partial conduit collapse, which caused the temporary stoppage of volcanic activity the next day. Also, the shallower part of the main magmatic conduit (R4B) and secondary branch R6 shows a reduction possibly related to the lack of magma in the portion of the conduit located above 4 km depth.

The eruptive activity resumed in the afternoon of Sept. 27th. The image of Sept. 28th shows a dike aperture similar to Sept. 22nd, indicating that the primary process of the magma accumulation in the shallow crust went back to the initial scenario. However, as shown by Pankhurst et al.¹³, the magma erupted after Sept. 27th proceeded from a deeper reservoir, as testified by petrological analysis. Therefore, we believe that the renewed eruptive activity was driven by the arrival of a new magmatic batch with a more primitive composition. This also agrees with the appearance of a new seismic cluster (S7 in Fig. 6C,D), which has been interpreted by D'Auria

et al.³ as the effect of the collapse of a magmatic reservoir located below 10 km depth because of its emptying due to the withdrawal of magma.

The modelling of the ground deformation source associated with the 2021 Cumbre Vieja eruption has already been analysed in previous studies, although using different approaches. In the following, we remark on the similarities and differences between their findings compared with the results of our study. De Luca et al. 10 used a combination of elementary sources to perform a static imaging of the plumbing system. We used a complex geometry, using finite-element modelling, to image the spatio-temporal evolution of the plumbing system before and during the earliest phases of the eruption. De Luca et al. 10 showed the existence of the sill-like source during the pre-eruptive phase and the presence of two dike-like sources active during the co-eruptive phases. The sill-like source was located at the 4675 m depth b.s.l. and was active between the 8th and 16th of September, corresponding mainly to the temporary accumulation of magma in its path towards the surface. This sill proposed by De Luca et al. 10 can be well explained by one of the lateral blind branches resulting from our inversion. Secondly, in the co-eruptive phase, they found evidence that the shallow magmatic plumbing system feeding the eruption was composed of two dikes and sills interconnected to the main reservoir, as also evidenced by the present study with the interconnection of the dike to the lateral branches during the pre- and early-eruptive phases. Their models encompass the 10 km depth limit, as well as the model presented in this study. However, De Luca et al. 10 only provided a static model of the ground deformation source, although the overall dike opening they retrieved matches pretty well with our image of Sept. 22nd (Fig. 5).

Conversely, Fernández et al.¹¹ analysed the spatiotemporal evolution of the ground deformation source. However, they used a completely different modelling approach based on an improved version of the 3D multisource modelling algorithm of Camacho et al.²⁰, which approximates the ground deformation sources as a combination of elementary pressure and fault slip sources. We believe this approach to be not entirely appropriate with volcanological observations of the Tajogaite eruption, which clearly evidenced a dike as the most likely geometry, at least for the shallow plumbing system. Therefore, in our approach, we tried to reproduce a physically realistic geometry and mechanism for the causative source of ground deformation. Also, their model evidences the deep source southward to the eruptive vent, as evidenced by the models presented in this study.

Additionally, we found the beginning of the deformation process related to the magmatic intrusion on Sept. 12th, while Fernández et al. 11 found evidence of magma accumulation that started in May of 2021. However, their overall results are in agreement with our findings, especially concerning the presence of lateral branches in the plumbing system. Additionally, our approach allowed a direct computation of the dike opening function and established its temporal and spatial relationship with the seismicity.

Montesinos et al. ¹⁴ used gravimetric and GNSS data acquired before and after the eruption and took into account the pre-eruptive seismicity to constrain the geometry of the plumbing system. They determined a complex geometry of the feeding system composed of interconnected dikes and sills. Their model also evidences the presence of a lateral blind branch of the plumbing system. Furthermore, they highlighted the temporary ascent of the magma on Sept. 14th due to the presence of horizontal layering within the crust.

To assess the reliability of our findings, we performed several checkerboards and tests over the synthetic dataset. In Figures S3, S4, S5, and S6 in the supplementary material, we represent the checkerboard test results for different spatial resolutions. We notice that our dataset is able to resolve anomalies of about 1 km size until a depth of 2 km (Fig. S3 in the supplementary material), anomalies of 2 km until about 4 km depth (Fig. S4 in the supplementary material), anomalies of 5 km along the whole model, until a depth of 10 km (Fig. S5 in the supplementary material) and anomalies of 5 km along the whole model, until a depth of 10 km (Fig. S6 in the supplementary material). This confirms that our model is able to resolve the features described above. Furthermore, we conducted some additional synthetic tests to understand the limitations of our approach better. In Figure S7 of the supplementary material, we see that, except for the lower left corner, our inverse method is able to detect the presence of magma along the whole domain. However, in Figures S8 and S9 of the supplementary material, we observe a clear decrease in the spatial resolution at depth. This may justify the lack of evidence of the connection between the main magma conduit (R4) and the deeper magma chamber. Finally, in Figure S10 of the supplementary material, we perform a synthetic test over a realistic geometry of the magmatic system, showing that our inverse model is able to retrieve all the relevant features.

We also need to mention, that the difference in the acquisition geometry between ascending and descending orbits can slightly affect the results. Actually, some of the minor variations observed in the differential dike aperture models can be artefacts related to this effect.

Conclusions

We propose a novel model of the spatiotemporal evolution of the magmatic system preceding and accompanying the first 10 days of the 2021 Cumbre Vieja eruption. For this purpose, we applied a Geodetic Imaging technique^{7,26} to reconstruct the kinematics of the plumbing system during the pre- and early-eruptive phases. The main finding of our study is that the causative source of the ground deformation was a dike with a bent and twisted geometry connecting a magmatic reservoir located below 10 km depth with the surface. Its azimuth changed from E-W in the deepest parts to NW–SE on the surface, while its dip changed from southward to southwestward.

We found an excellent agreement between the temporal evolution of the dike opening and the upward migration of pre-eruptive hypocenters. The upward propagation of the magma was very rapid (about 8 days) and strongly accelerated during the last day. The overall geometry of the dike intrusion process shows the presence of at least two blind lateral branches whose propagation stopped before reaching the surface. The eruption's onset is clearly evidenced by a dike opening right beneath the eruptive vent accompanied by intense shallow seismicity. On Sept. 27th, the eruption stopped for a few hours. We interpret it as an effect of a temporary collapse of the dike, as confirmed by the dike opening model, which shows an incipient collapse already starting the day before.

In conclusion, we state that the Geodetic imaging technique is an excellent tool for better understanding magma ascent processes. Our results provide evidence of the complexity of the dike propagation processes and the temporal changes in the shallow plumbing system before and during an eruption.

Data and methods

Data and processing of GNSS time series

In this work, we used the permanent GNSS stations in La Palma island belonging to the Instituto Volcanológico de Canarias (INVOLCAN), the Nagoya University, and GRAFCAN (Fig. 1). Solutions are analysed by *GAMIT/GLOBK Software*²⁷. For processing, we used a total of 27 stations. We removed the regional tectonic component from the solutions using the Nubian plate reference described by Saria et al.²⁸. We also used solutions from three stations of Instituto Geográfico Nacional (IGN) denoted LP03, LP04, and LPAL. We selected these three stations of the IGN as the data from other stations of the IGN are not public. Figure 8 shows the time series of some of the stations used in this study.

In Figure S11 (in the supplementary materials), we compare data and the synthetic model resulting from the Geodetic Imaging technique for the three components of the GNSS data for all the stations used for this study. The stations closest to the eruptive vent (ARID) experienced the most significant deformation (Fig. 8). The deformation of ARID commenced on Sept. 14th (see Fig. 1) with 2.2 cm in the vertical component. It continued increasing in the following days, and on the day of the eruption, on Sept. 19th, the vertical deformation was already 11.4 cm, 15.3 cm toward the West, and 3.2 cm to the South. During the first week of eruption, the deformation continued increasing until it reached its maximum value in the ARID station, reaching 15.0 cm in the vertical component on Sept. 22nd (Fig. 8). Some GNSS stations at a higher distance from the eruptive vent also showed a deformation signal caused by the magmatic processes. Stations MOLU and FUEN (Fig. 1) began showing significant deformation on Sept. 12th. MOLU reached its maximum on Sept. 28th with 3.6 cm towards the East, 2.6 cm to the South, and 0.6 cm in the vertical component (Fig. 8). The deformed values did not return to their pre-eruptive stage and fluctuated during the eruption, showing a nearly steady deflation in the following months.

DInSAR Sentinel-1 data and processing

Two sets of synthetic aperture radar (SAR) images were acquired from complementary (ascending/descending) orbits between January and November 2021 through the constellation of twin radar sensors S-1A and S-1B, operating at the C band (wavelength of approximately 5.6 cm) and gathering images through the Interferometric Wide (I.W.) mode. They were independently processed using the multi-temporal interferometric SAR (Mt-InSAR) Small Baseline Subset (SBAS) technique⁶. The area covered by the used SAR images encompasses the whole island of La Palma (Fig. 9). The relevant parameters of the SAR datasets are listed in Table S1 (in supplementary material). For every detected coherent distributed scatterer (D.S.) on the ground, the corresponding time-series of the LOS-projected ground displacement components were generated. According to Berardino et al.6, Casu et al.29 and Lanari et al.30, the implemented SBAS processing chain operates on sequences of multilook small baseline (S.B.) interferograms (in particular, 20 (range) × 4 (azimuth) looks were considered in our work) and includes specific steps for: (1) the space-time phase unwrapping³¹, (2) the estimation and compensation of phase artefacts in the generated SAR interferograms (i.e., the removal of residual topographic phases⁶), (3) the space-time noise-filtering of the sequence of small baseline multi-look SAR interferograms²⁵ and (4) the compensation of the atmospheric phase screen (APS). Specifically, before their inversion, the noise-filtered, unwrapped interferograms were analysed to retrieve and compensate the APS components by implementing an ad-hoc strategy. First, on every single interferogram, the phase components that are spatially highly correlated with the topography were estimated and filtered out. Then, we applied the methodology proposed in Tymofyeyeva and Fialko³² that allows discriminating and filtering out the APS time uncorrelated components in a sequence of SAR images by implementing a stacking operation on couples of S.B. SAR interferograms made with a common SAR image and characterized by the same time span (i.e., temporal baseline). The estimated tropospheric and time-uncorrelated APS components were finally subtracted from the unwrapped interferograms inverted through the SBAS method to obtain the relevant ground displacement time series. The residual APS components were then further compensated with a space-time filter (e.g., see Ferretti et al.³³, Berardino et al.⁶, Yang and Buckley³⁴). Finally, the interferometric ground deformation products were geocoded, i.e., converted from radar to geographical coordinates. Figures S12 and S13 of the supplementary material show the generated LOS-projected mean displacement velocity maps from the ascending and descending orbit tracks, respectively. Then, we concentrated on the short interval between Sept. 8th and 28th, 2021, with an aim to analyse pre- and early-eruptive ground deformation. Accordingly, we extracted the layers corresponding to the selected SAR acquisitions from the generated LOS-projected ground displacement time series and performed the analyses detailed hereinafter.

Starting from the ground displacement time series obtained by separately processing through the SBAS approach the available ascending/descending S-1 SAR images, we focused on the retrieved cumulative ground deformations, calculated with respect to the first images of the two datasets acquired in January 2021. More specifically, the analyses addressed in our study refer to the time interval Sept. 8th–Sept. 28th, representing the core of the analyses shown in this study. Note that the obtained ground deformation values only represented the projection of the ground displacement along the relevant radar-to-target line-of-sight (LOS) directions and were calculated by assuming as a time reference the date of the first available SAR images of the ascending and descending time series, respectively, collected on the first days of January 2021. Figure 9 shows the pre- and early-eruptive cumulative LOS deformation maps for the processed ascending and descending orbits. The ground deformation and the magma ascent were rapid. In Fig. 9A, on Sept. 14th, the deformation shows a slight deformation. Two days later, on Sept. 16th, the descending orbit (Fig. 9C) captured a significant ground movement

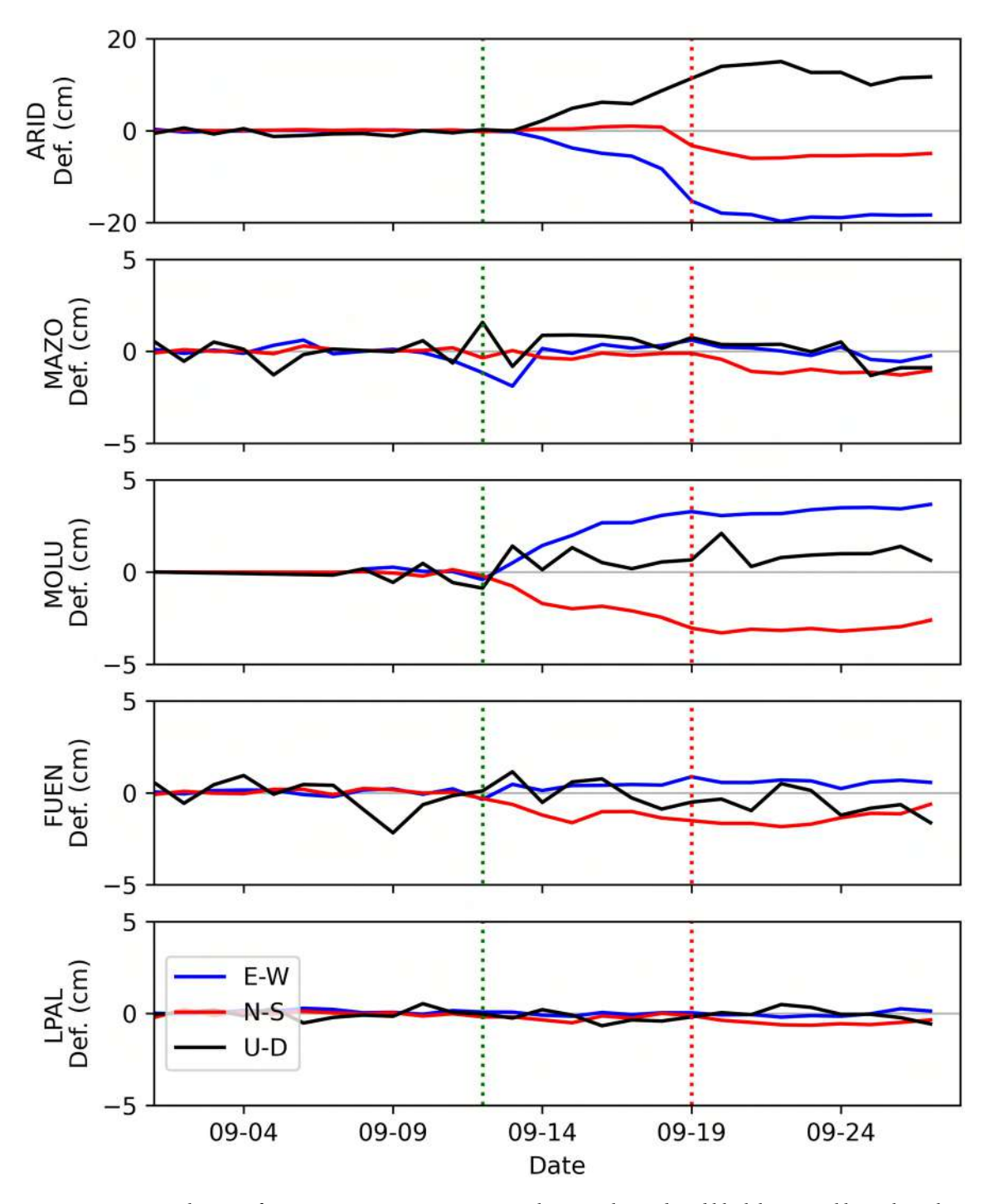


Figure 8. Solutions of some GNSS permanent stations solutions. Blue, red, and black horizontal lines show the E–W, N–S, and U–D components of deformation, respectively. The vertical red dotted line marks the day the eruption began, while the green dotted vertical line marks the day when the first significant deformation was recorded at stations MOLU and FUEN.

on the southern side of the forthcoming eruptive vent. On Sept. 19th at 14:02 GMT, the eruption started, but that day, Sentinel-1 did not acquire the data over the Canaries. One day after the eruption began, on Sept. 20th, the ascending orbit captured significant deformation in the southwestern side of the eruptive vent (Fig. 9B). The descending orbit that acquired the data on Sept. 22nd also captured considerable ground deformation (Fig. 9D). Its spatial deformation map differs slightly from the ascending orbit due to differences in the illumination geometries between the orbits and the different acquisition times that capture distinctive rapidly-evolving ground displacement signals from one date to another.

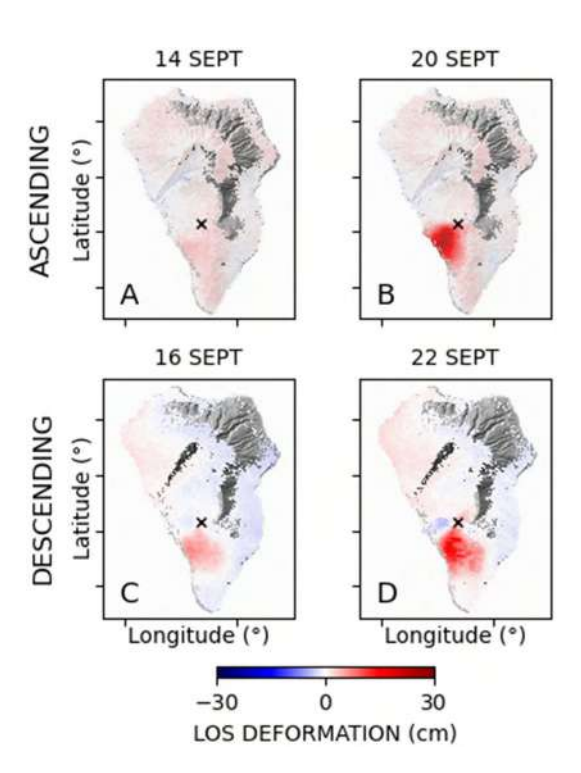


Figure 9. DInSAR deformation maps for La Palma in pre-and (**A** and **C** panel) and early-eruptive (**B** and **D** panel) phases. (**A** and **B**) represent the ascending orbit, while (**C** and **D**) represent the descending one. Black crosses show the location of the eruptive vents.

Non-linear inversion for the shallow dike geometry

To determine the inclination of the shallow part of the dike, we performed a non-linear inversion using the analytical ground deformation model of Okada¹⁵, fixing the azimuth and letting the inclination, the width, the length and the opening to vary. We determined the best-fit model using the Nelder-Mead³⁵ simplex algorithm.

Geodetic imaging

We applied a non-linear inversion technique of the spatiotemporal pattern of the dike opening following the approach of D'Auria et al.⁷.

The dike opening function o(x,y,t) has been discretised into a set of 15×24 rectangular cells (Figs. 3, 4, 5 and 6) for each of the 8 DInSAR images used in this work. The computation of the Green's function for each cell has been performed within the finite element modelling environment COMSOL MultiPhysics*, using a 3D model that takes into account the topography and the bathymetry around the island. We used a lateral extent of the computational domain of 9 km. This width is sufficient to encompass all the areas affected by the eruptive phenomena. Furthermore, enlarging this length would negatively affect the resolution and the reliability of the final results. We performed the inversion using different sizes of the computational domain, obtaining similar results.

The opening function of the first image is constrained to 0, the first image being used as a reference for the rest of the dataset. Therefore, this allows the inverse problem formulation as a linear system for a total of $15 \times 24 \times 7$ unknown. We used a second-order Tikhonov regularisation for both space and time. As with any inverse method, ours shows a trade-off between model resolution and fit with the data. The damping parameter controls this trade-off. Low damping values lead to lower misfit but unreliable noisy models. Conversely, high damping values lead to smoother models but high misfit values. In this work, we used the widely known L-curve approach 36 to establish the optimal damping value. Since we used a positivity constraint for the opening function, we solved the inverse problem through a non-linear Sequential Least Squares Programming (SLSQP) algorithm.

The final models cannot justify all the observed ground deformation because of the intrinsic limitations related to the inverse method and the lack of details of the 3D model of the mechanical properties of the Cumbre Vieja volcano.

To check the resolution, we performed various checkerboard tests (see Figs. S3–S6 in the supplementary material) and a synthetic test with a realistic dike opening function (see Figs. S7–S10 in the supplementary material). We used the same data acquisition geometry as the actual data (GNSS three components, Ascending DInSAR and Descending DInSAR). The standard deviation of the Gaussian noise added to the synthetic data mimics those assumed for actual data: 10 mm for DInSAR, 5 mm for horizontal GNSS components, and 10 mm for vertical GNSS components.

Received: 19 July 2023; Accepted: 28 December 2023

Published online: 02 January 2024

References

- 1. Ancochea, E. et al. Constructive and destructive episodes in the building of a young oceanic island, La Palma, Canary Islands, and genesis of the Caldera de Taburiente. J. Volcanol. Geoth. Res. 60(3–4), 243–262 (1994).
- 2. Barrera Morate, J. L. & García Moral, R. Mapa Geológico de Canarias (GRAFCAN, 2011).
- 3. D'Auria, L. et al. Rapid magma ascent beneath La Palma revealed by seismic tomography. Sci. Rep. 12(1), 17654 (2022).
- 4. Carracedo, J. C. et al. The 2021 eruption of the Cumbre Vieja volcanic ridge on La Palma, Canary Islands. Geol. Today 38(3), 94–107 (2022).
- 5. Cabrera-Pérez, I. et al. Spatio-temporal velocity variations observed during the pre-eruptive episode of La Palma 2021 eruption inferred from ambient noise interferometry. Sci. Rep. 13(1), 12039 (2023).
- 6. Berardino, P., Fornaro, G., Lanari, R. & Sansosti, E. A new algorithm for surface deformation monitoring based on small baseline differential SAR interferograms. *IEEE Trans. Geosci. Remote Sens.* 40(11), 2375–2383 (2002).
- 7. D'Auria, L. et al. Magma injection beneath the urban area of Naples: A new mechanism for the 2012–2013 volcanic unrest at Campi Flegrei caldera Sci. Rep. 5(1) 13100 (2015)
- Flegrei caldera. *Sci. Rep.* **5**(1), 13100 (2015).

 8. Pepe, S. *et al.* The use of massive deformation datasets for the analysis of spatial and temporal evolution of Mauna Loa volcano
- (hawai'i). Remote Sens. 10(6), 968 (2018).

 9. Przeor, M. et al. Elastic interaction between Mauna Loa and Kīlauea evidenced by independent component analysis. Sci. Rep. 12, 19863. https://doi.org/10.1038/s41598-022-24308-0 (2022).
- De Luca, C. et al. Pre-and co-eruptive analysis of the September 2021 eruption at Cumbre Vieja volcano (La Palma, Canary Islands) through DInSAR measurements and analytical modeling. Geophys. Res. Lett. 49(7), e2021097293 (2022).
- 11. Fernández, J. et al. Shallow magmatic intrusion evolution below La Palma before and during the 2021 eruption. Sci. Rep. 12(1), 20257 (2022).
- 12. Cabrera-Pérez, I. *et al.* Geothermal and structural features of La Palma island (Canary Islands) imaged by ambient noise tomog-
- raphy. Sci. Rep. 13(1), 12892 (2023).
- 13. Pankhurst, M. J. et al. Rapid response petrology for the opening eruptive phase of the 2021 Cumbre Vieja eruption, La Palma, Canary Islands. Volcanica 5(1), 1–10 (2022).
- 14. Montesinos, F. G. et al. Insights into the magmatic feeding system of the 2021 Eruption at Cumbre Vieja (La Palma, Canary Islands) inferred from gravity data modeling. Remote Sens. 15(7), 1936 (2023).
- 15. Okada, Y. Surface deformation due to shear and tensile faults in a half-space. Bull. Seismol. Soc. Am. 75(4), 1135-1154 (1985).
- Muñoz, V. et al. Satellite radar and camera time series reveal transition from aligned to distributed crater arrangement during the 2021 Eruption of Cumbre Vieja, La Palma (Spain). Remote Sens. 14(23), 6168 (2022).
- 17. Rivalta, É., Taisne, B., Bunger, A. P. & Katz, R. F. A review of mechanical models of dike propagation: Schools of thought, results and future directions. *Tectonophysics* **638**, 1–42 (2015).
- 18. Dahm, T. Numerical simulations of the propagation path and the arrest of fluid-filled fractures in the Earth. *Geophys. J. Int.* **141**(3), 623–638 (2000).
- 19. Maccaferri, F., Bonafede, M. & Rivalta, E. A quantitative study of the mechanisms governing dike propagation, dike arrest and sill formation. *J. Volcanol. Geotherm. Res.* **208**(1–2), 39–50 (2011).
- Camacho, A. G. et al. Structural results for La Palma island using 3-D gravity inversion. J. Geophys. Res. Solid Earth 114(B5), B05411 (2009).
- 21. Di Paolo, F. *et al.* La Palma island (Spain) geothermal system revealed by 3D magnetotelluric data inversion. *Sci. Rep.* **10**(1), 18181 (2020).
- 22. Cabrera-Pérez, I. et al. A non-linear multiscale inversion approach for ambient noise tomography. Geophy. J. Int. 225(2), 1158–1173 (2021).
- 23. Rivalta, E. & Dahm, T. Acceleration of buoyancy-driven fractures and magmatic dikes beneath the free surface. *Geophy. J. Int.* **166**(3), 1424–1439 (2006).
- 24. Romero, J. E. et al. The initial phase of the 2021 Cumbre Vieja ridge eruption (Canary Islands): Products and dynamics controlling edifice growth and collapse. J. Volcanol. Geotherm. Res. 431, 107642 (2022).
- 25. Bonadonna, C. et al. Physical characterization of long-lasting hybrid eruptions: The 2021 Tajogaite eruption of Cumbre Vieja (La Palma, Canary Islands). J. Geophys. Res. Solid Earth 127(11), e2022JB025302 (2022).
- 26. Vasco, D. W., Wicks, C. Jr., Karasaki, K. & Marques, O. Geodetic imaging: reservoir monitoring using satellite interferometry. *Geophys. J. Int.* 149(3), 555–571 (2002).
- 27. Herring, T. A., King, R. W., & McClusky, S. C. (2010). Introduction to GAMIT/GLOBK Introduction to GAMIT/GLOBK.
- Saria, E., Calais, E., Altamimi, Z., Willis, P. & Farah, H. A new velocity field for Africa from combined GPS and DORIS space geodetic Solutions: Contribution to the definition of the African reference frame (AFREF). J. Geophys. Res. Solid Earth 118(4), 1677–1697 (2013).
- 29. Casu, F., Manzo, M. & Lanari, R. A quantitative assessment of the SBAS algorithm performance for surface deformation retrieval from DInSAR data. *Remote Sens. Environ.* **102**(3–4), 195–210 (2006).
- 30. Lanari, R. et al. An overview of the small baseline subset algorithm: A DInSAR technique for surface deformation analysis. In *Deformation and Gravity Change: Indicators of Isostasy, Tectonics, Volcanism, and Climate Change* (eds Wolf, Detlef & Fernández, José) 637–661 (Springer, 2007).
- 31. Pepe, A. & Lanari, R. On the extension of the minimum cost flow algorithm for phase unwrapping of multitemporal differential SAR interferograms. *IEEE Trans. Geosci. Remote Sens.* **44**(9), 2374–2383 (2006).
- 32. Tymofyeyeva, E. & Fialko, Y. Mitigation of atmospheric phase delays in InSAR data, with application to the eastern California shear zone. J. Geophys. Res. Solid Earth 120, 5952–5963. https://doi.org/10.1002/2015JB011886 (2015).
- 33. Ferretti, A., Prati, C. & Rocca, F. Permanent scatterers in SAR interferometry. IEEE Trans. Geosci. Remote Sens. 39(1), 8-20 (2001).
- Yang, D. & Buckley, S. M. Estimating high-resolution atmospheric phase screens from radar interferometry data. IEEE Trans. Geosci. Remote Sens. 49(8), 3117–3128 (2011).
- 35. Nelder, J. A. & Mead, R. A simplex method for function minimization. Comput. J. 7, 308 (1965).
- 36. Aster, R. C., Borchers, B. & Thurber, C. H. *Parameter estimation and inverse problems* (Elsevier, 2019).

Acknowledgements

We acknowledge the Instituto Geográfico Nacional (IGN) for publishing the graphs of the GNSS time series of the stations LP03 and LP04.

Author contributions

All the authors contributed to the conceptualisation of the article. A.P., T.S., M.P., and S.P. contributed to the data curation. L.D. and R.C. developed some of the software used in the study. All the authors contributed to writing and revising the paper.

Funding

Funging was provided by Cabildo Insular de Tenerife (TFassistance), Interregional MAC Program 2014-2020 and Instituto Tecnológico y de Energías Renovables (ITER) (Grant No. VOLTURMAC (MAC2 / 4.6c / 298)), Gobierno de Canarias (Grant No. CANVolcano), Ministerio de Ciencia e Innovación, Cumbre Vieja Emergencia, Interregional MAC Program 2014-2020 and Instituto Tecnológico y de Energías Renovables (ITER) (Grant No. VolRiskMac II (MAC2/3.5b/328)), Cabildo Insular de La Palma, Spain (Grant No. LPVolcano) and Plan Nacional de I+D (Grant No. DIGIVolcan (PLEC2022-009271)).

Competing interests

The authors declare no competing interests.

Additional information

 $\textbf{Supplementary Information} \ \ \text{The online version contains supplementary material available at $https://doi.org/10.1038/s41598-023-50982-9. }$

Correspondence and requests for materials should be addressed to M.P.

Reprints and permissions information is available at www.nature.com/reprints.

Publisher's note Springer Nature remains neutral with regard to jurisdictional claims in published maps and institutional affiliations.

Open Access This article is licensed under a Creative Commons Attribution 4.0 International License, which permits use, sharing, adaptation, distribution and reproduction in any medium or format, as long as you give appropriate credit to the original author(s) and the source, provide a link to the Creative Commons licence, and indicate if changes were made. The images or other third party material in this article are included in the article's Creative Commons licence, unless indicated otherwise in a credit line to the material. If material is not included in the article's Creative Commons licence and your intended use is not permitted by statutory regulation or exceeds the permitted use, you will need to obtain permission directly from the copyright holder. To view a copy of this licence, visit http://creativecommons.org/licenses/by/4.0/.

© The Author(s) 2024

TYPE Original Research PUBLISHED XX XX 2024 DOI 10.3389/feart.2024.1412827

11

14

15

18 20 21

22

29

30

45

47

37

38

57



89 90

93

61

66

67

70

73

81

82

83

84

85

86

87

 $\mathbf{Q1}$

 $\mathbf{Q2}$

 Q_6

100 101 102

105 106

104

108 110 111

 $\mathbf{Q8}$

112 113

115

116

Check for updates

OPEN ACCESS

EDITED BY Paolo Capuano, University of Salerno, Italy

REVIEWED BY

Umberto Tammaro.

Vesuvius Observatory, National Institute of Geophysics and Volcanology (INGV), Italy Simona Petrosino.

Istituto Nazionale di Geofisica e Vulcanologia, Italy

*CORRESPONDENCE

Monika Przeor.

RECEIVED 05 April 2024 ACCEPTED 28 May 2024 PUBLISHED XX XX 2024

Przeor M, D'Auria L, Pepe S, Tizzani P, Barone A, Vitale A, Castaldo R and Pérez NM (2024), Independent component analysis and finite element modelling of the 2004-2005 ground deformation unrest in Tenerife (Canary islands). Front. Earth Sci. 12:1412827.

doi: 10.3389/feart.2024.1412827

© 2024 Przeor, D'Auria, Pepe, Tizzani, Barone, Vitale, Castaldo and Pérez. This is an open-access article distributed under the terms of the Creative Commons Attribution License (CC BY). The use, distribution of reproduction in other forums is permitted, provided the original author(s) and the copyright owner(s) are credited and that the original publication in this journal is cited, in accordance with accepted academic practice. No use, distribution or reproduction is permitted which does not comply with these

Independent component analysis and finite element modelling of the 2004-2005 ground deformation unrest in Tenerife (Canary islands)

Monika Przeor^{1,2}*, Luca D'Auria^{1,2}, Susi Pepe³, Pietro Tizzani³, Andrea Barone³, Andrea Vitale³, Raffaele Castaldo³ and Nemesio M. Pérez^{1,2}

¹Instituto Tecnológico y de Energías Renovables, Santa Cruz de Tenerife, Spain, ²Instituto Volcanológico de Canarias (Involcan), Santa Cruz de Tenerife, Spain, ³Istituto per il Rilevamento Elettromagnetico dell'Ambiente (IREA-CNR), Napoli, Italy

Historic volcanic activity in Tenerife was concentrated within two of the island's three dorsals and on the Teide-Pico Viejo complex located inside Las Cañadas caldera. Eruptions on the island are primarily characterised by basaltic and trachybasaltic fissural eruptions. However, the Teide-Pico Viejo complex also hosted explosive and effusive phonolitic eruptions. Our study focused on the analysis of the 2004-2005 unrest in Tenerife, which was characterised by an onset of a ground deformation pattern, heightened on-land seismic activity, changes in the chemical composition of fumaroles of the Teide composite volcano, an increase in diffusive emissions of carbon dioxide along the NW rift, and, significant gravity changes. We used the Envisat-ASAR satellite images from 2003 to 2010 to generate the Line-Of-Sight SBAS-DInSAR deformation time series to investigate the source responsible for ground deformation. We applied the Independent Component Analysis (ICA) to separate distinct ground deformation patterns. Specifically, we selected four components for the Independent Component Analysis decomposition: the first one mainly affects the stratovolcano's summit region of Teide and shows a circular symmetry; the second and third components are possibly related to the topography and atmospheric artifacts, while the fourth contains only a noisy signal. We employed a non-linear optimisation approach in a Finite Element modelling environment to determine the source geometry responsible for the first identified ICA pattern of ground deformation within Las Cañadas. We used a three-axis ellipsoidal geometry for the causative source. Our results revealed that the reactivation of a horizontal magmatic body beneath the Teide volcano is the most likely source for the observed deformation between 2004 and 2005.

DInSAR, volcano geodesy, tenerife, finite element modeling, independent component analysis, DInSAR SBAS

Przeor et al. 10.3389/feart.2024.1412827

1 Introduction

Q10

Tenerife is the largest island in the Canaries. Due to its high population density and five historical eruptions in the last five centuries, it is considered a region with a moderate volcanic risk (Carracedo et al., 2007). The island's formation began as a Shield Volcanic Complex (SVC) in the Miocene period, possibly consisting of three independent islands: Anaga, Teno, and Roque del Conde massifs (Barrera Morate and García Moral, 2011). Its structural evolution was completed during the Pliocene, followed by a stage of formation of the central part of the island known as the Las Cañadas edifice. This building phase merged the previous shield volcanoes into a single island. During the Pleistocene, the ongoing formation of Las Cañadas caldera was also marked by numerous strombolian eruptions with vents located along the rifts (NE-SW, N-S and NW-SE) connecting Las Cañadas and the older shield volcanoes. The rapid development of Las Cañadas was later followed by destructive episodes characterised by massive lateral collapses, leading to the formation of the current Las Cañadas Caldera (Barrera Morate and García Moral, 2011). Strombolian activity in the rifts remained prominent, and Las Cañadas Caldera was filled with salic eruptions, creating the Teide-Pico Viejo complex and peripheral eruptions within the Las Cañadas domain. The Holocene activity was concentrated on eruptions occurring in the island's rifts but also affecting the Las Cañadas domain. From the 16th century to the present, five historical eruptions were concentrated mainly on the NW-SE and NE-SW dorsals, with only one occurring on the Teide-Pico Viejo complex. However, even though historical eruptions displayed basaltic fissure volcanic activity, Teide-Pico Viejo's activity included effusive and explosive eruptions of phonolitic magmas. The most recent explosive eruption in Tenerife was the sub-Plinian eruption of Montaña Blanca, which occurred approximately 2000 years ago (Figure 1) (Barrera Morate and García Moral, 2011). The most recent eruption of the Teide stratovolcano complex occurred roughly 800 years ago and is evident in the phonolitic lava flows that descend from the summit cone (Barrera Morate and García Moral, 2011). Currently, the Teide stratovolcano is dormant; its background volcanic activity consists mainly of a continuous microseismicity of Volcano-Tectonic (VT) and Long-Period (LP) events, fumarole activity in the crater of Teide and diffuse degassing (Koulakov et al., 2023).

At the beginning of 2001, anomalous seismic activity on the island began, with higher-than-background seismicity values registered by Instituto Geográfico Nacional (IGN) (Gottsmann et al., 2006; Almendros et al., 2007; Martí et al., 2009) and geochemical anomalies (Weber et al., 2006; Melián et al., 2012; Pérez et al., 2013). The most critical episode that prompted a "volcanic unrest alert" to be issued to the local government was the intense seismic activity that started in April 2004 and persisted until July 2005 (Almendros et al., 2007; Martí et al., 2009; Pérez et al., 2013). This seismicity was characterised by volcano-tectonic events located within the Las Cañadas domain and some long-period events (Almendros et al., 2007).

During this period of seismic unrest, the chemical composition of gases in Teide fumaroles indicated the presence of magmatic SO_2 , and there was also an increase in diffuse CO_2 emissions in the northwest rift zone (Pérez et al., 2013). Furthermore, in the local galleries within the southern rift of the island, it was

observed an increase in radon emission (220Rn and 222Rn) and an increase in the SO₂/Cl ratio in the groundwater (Melián et al., 2012). Gottsmann et al. (2006) evidenced a gravity increase in the northern flank of the Teide-Pico Viejo volcanic complex and a lack of significant ground deformation. However, Fernández et al. (2009) identified evidence of ground deformation of just a few centimeters in the Teide-Pico Viejo volcanic complex in 2004. At the same time, these authors also identified continuous subsidence in Las Cañadas triggered by the compressional state of the volcanic edifice (Fernández et al., 2009). The intense seismic activity persisted until July 2005 and gradually decreased throughout the early months of the following year (Almendros et al., 2007). The observed volcanic crisis did not culminate in an eruption, and, as mentioned by Melián et al. (2012), the possibility of the reactivation of the Teide-Pico Viejo was low.

Even though a ground deformation in 2004 was observed (Fernández et al., 2009), until now, no modelling of the causative source has been presented. We believe that a better understanding of this episode would allow a better understanding of the dynamics of the volcanic hydrothermal system of Tenerife and, consequently, would provide a useful tool for the interpretation of future volcanic unrest episodes on the island.

We first performed data processing employing the Differential Interferogram Satellite Aperture Radar (DInSAR) by using the Small BAseline Subset (SBAS) algorithm (Figure 2). Then we applied the Independent Component Analysis (ICA) to the 2004–2005 ground deformation occurring in Tenerife, obtaining the decomposition of the signal in different components. Applying the ICA to this dataset allowed us to identify a consistent ground deformation pattern that we attributed to a causative volcanic source. We modelled this pattern using a non-linear optimisation within a Finite Element (FE) environment to study the geometry of the source in detail

Interferogram stacking (DInSAR SBAS) is a widely known method for processing the SAR data in order to obtain time series of cumulative deformation in the area of interest. In this method, the multiple interferograms with the Small Baseline between the SAR images are overlaid, allowing to obtain small displacement information along the long time periods. The DInSAR SBAS method was proposed by Bernandino et al. (2002) using the SAR images acquisitions with a small orbital separation (SBAS), allowing limiting the observed spatial decorrelation phenomena. This method was widely applied to study volcanic behaviours (Tizzani et al., 2007; Pepe et al., 2008; De Luca et al., 2015; Pepe et al., 2018) where prolonged deformation in time within the volcanic areas was observed.

The Independent Component Analysis (ICA) represents a valuable statistical tool for analysing complex datasets (Comon, 1994; Hyvärinen and Oja, 2000). It allows the decomposition of a mixture of signals under the assumption that the individual sources are statistically independent and non-Gaussian (Ebmeier, 2016). ICA enables the separation of a dataset into non-orthogonal components that exhibit minimal statistical dependence between them. This valuable technique was first introduced for computational signal processing. However, it has also been applied in various geophysical applications like volcano seismology (Acernese et al., 2004) and volcano geodesy (Bottiglieri et al., 2007; Ebmeier, 2016; Przeor et al., 2022).

Przeor et al. 10.3389/feart,2024.1412827

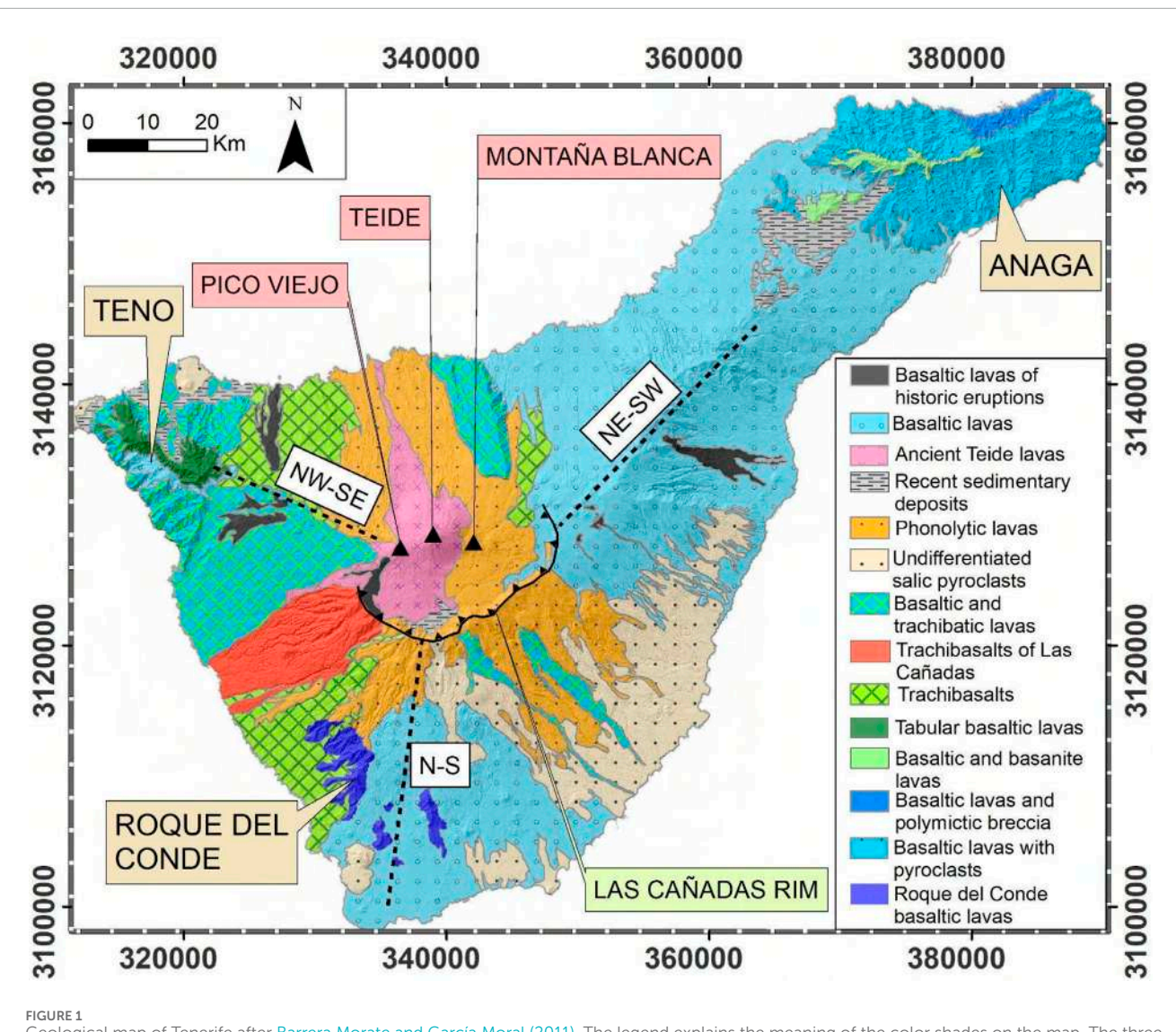


FIGURE 1
Geological map of Tenerife after Barrera Morate and García Moral (2011). The legend explains the meaning of the color shades on the map. The three SVCs are marked with the tanned yellow square with the SVCs' names included. The rim of the caldera is shown with black lines and triangles. Black triangles represent the volcanoes Pico Viejo, Teide, and Montaña Blanca. A dashed black line represents the three rifts.

The ICA in the volcano geodesy context has been applied to GNSS and DInSAR datasets and has shown its effectiveness in reducing the noise and uncovering hidden ground deformation patterns within complex DInSAR datasets. Ebmeier (2016) showcased its effectiveness in separating the causative sources of complex ground deformation. Subsequently, Przeor et al. (2022) used ICA to separate independent components of ground deformation in Hawaii, highlighting its ability to identify simultaneous but independent sources acting beneath Mauna Loa and Kīlauea volcanoes.

Q18

The observed ground deformation was modeled within the Finite Element environment in order to modelise the geometry and the location of the source responsible for the observed anomalies. This method is commonly applied to the DInSAR dataset, which helps visualizing the magmatic or hydrothermal sources. The application of this method to the DInSAR SABS dataset of Sentinel-1 allowed modelise the magmatic source injection during the

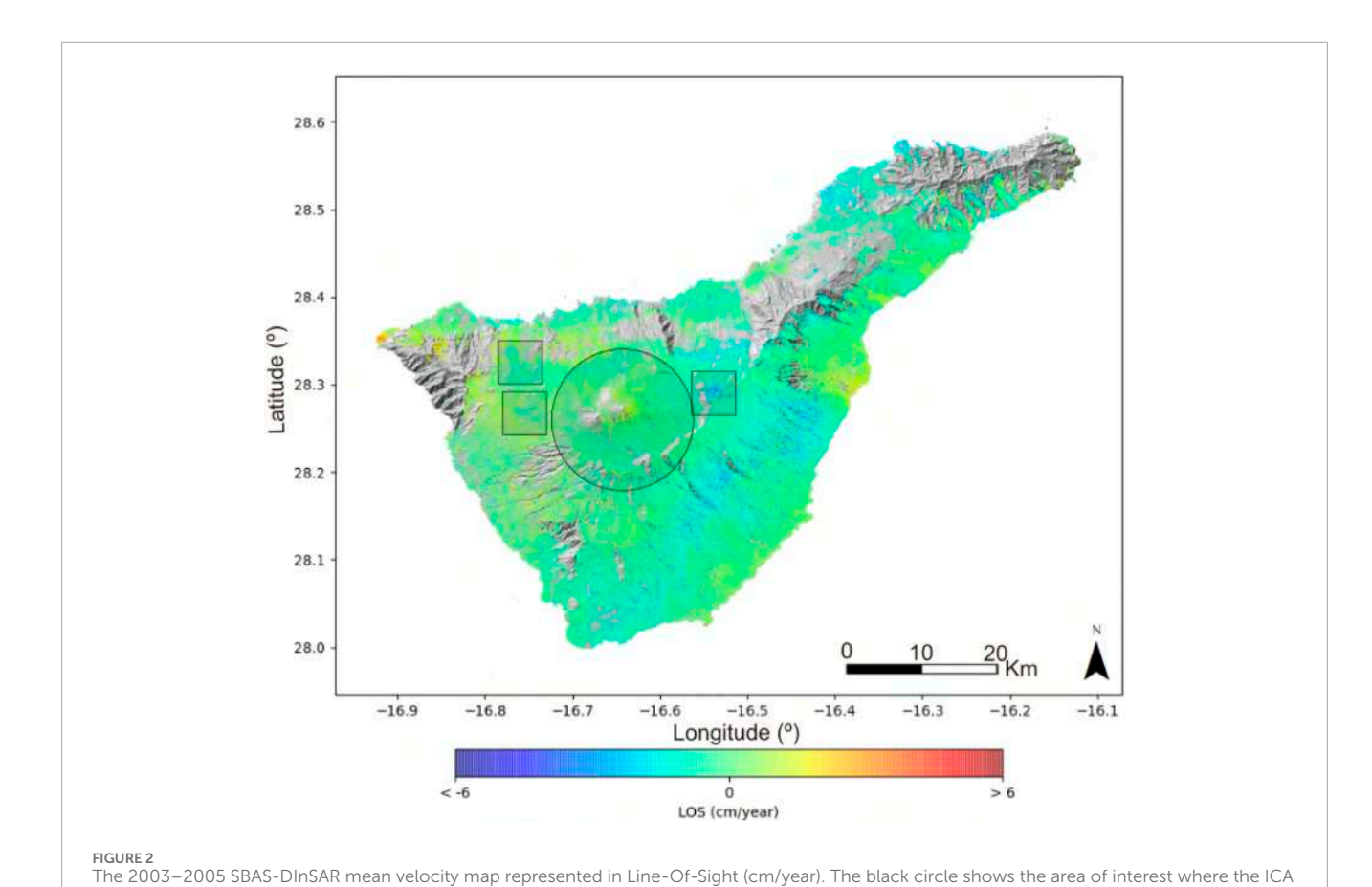
pre-eruptive episode in La Palma (Tajogaite eruption of 2021); (De Luca et al., 2022).

2 Methodology

2.1 SBAS DInSAR time series

The data used in this study were collected by the European Space Agency (ESA) through the ASAR sensor onboard the Envisat satellite acquired on C-band wavelength (\approx 5.6 cm). The satellite images acquired along ascending orbits were analyzed by the Grid Processing On Demand (G-POD) platform of ESA applying the multitemporal analysis using the Small BAseline Subset (SBAS) to obtain the Line-Of-Sight (LOS) time series for the coherent pixels of the SAR dataset (De Luca et al., 2015). The obtained 180 interferograms were processed with a maximum temporal

Przeor et al. 10.3389/feart.2024.1412827



decomposition is applied. In contrast, the three black squares represent the zones of the local negative deformation, discussed by Fernández et al.

baseline of 150 days and a maximum spatial baseline of 400 m. We achieved the time series for each coherent pixel for the ascending orbit encompassing the island of Tenerife between 2003 and 2010. However, since the ground deformation occurred between 2004 and 2005, we focused on the dataset encompassing this interval. We did not evidence of any ground deformation pattern in the subsequent period in the processed dataset.

2.2 Independent component analysis (ICA) of SBAS DInSAR time series

In the context of an SBAS DInSAR dataset, the time series is represented as L (x_i, t_j) , where L denotes the Line-Of-Sight (LOS) displacement, x_i corresponds to the position of the ith DInSAR pixel, and t_j represents the time of the jth DInSAR image. The DInSAR dataset can be decomposed into a finite sum of N components characterised by fixed spatial patterns. If we denote B_k the spatial pattern of the kth and with A_{jk} the time-varying amplitudes of the kth component in time t_j , we can write the ICA decomposition result as:

$$L(x_i, t_j) = \sum_{k=1}^{N} A_{jk} B_k(x_i)$$
 (1)

Once the spatial patterns have been normalised, the sum of squared amplitudes A_{ik} for each independent component k defines

its energy. This enables us to sort the components based on their energy and determine the optimal number of components representing the whole signal. This can be realised by setting a threshold below which the contribution to the total energy is negligible. We opted to retain one more component, even if characterised by negligible amplitude values, given that it would host the noise inherent in each DInSAR dataset. In the case of the ascending SBAS DInSAR dataset for Tenerife, we used four components.

2.3 Non-linear source modeling through the finite element modeling

To model a causative source of ground deformation, represented by an individual ICA component, we employed the Comsol Multiphysics® software environment. We built a three-dimensional mesh taking into account Tenerife Island's topography. The computational domain had dimensions of 33,000 m along the EW direction, 25,000 m along the NS direction, and 12,000 m in depth, to cover all the Las Cañadas caldera. We assumed isotropic linear elastic material properties. The elastic constants are calculated assuming an average P-wave velocity of 4,000 m/s, S-wave velocity of 2,400 m/s, and a 2,700 kg/m³ density. The seismic wave velocity values have been estimated from the seismic tomography model of Koulakov et al. (2023).

Przeor et al. 10.3389/feart.2024.1412827

The domain was discretised using tetrahedral mesh elements, with a maximum element size of $1,200\,\mathrm{m}$ and a minimum element size of $500\,\mathrm{m}$. As a starting model, we chose a three-axis body representing the causative sources of the observed ground deformation. The parameters used to define the source model are seven: the center position in UTM (X, Y, Z); the dimensions of the ellipsoid axes along the X, Y, and Z-axes in meters; and the overpressure in pascals (Pa). The best-fit model has been retrieved through a non-linear optimisation using the Nelder and Mead (1965) simplex algorithm. The number of iterations required to reach the minimum was 1,000, and an objective function used was the residual sum of squares.

3 Results

3.1 SBAS DInSAR time series

The 2003-2005 SBAS DInSAR mean LOS velocity map computed along ascending orbit reveals four local deformation patterns on the island (Figure 2). At first sight, three areas of deformation with negative values are visible, one located in the NE-SW rift and two in the NW-SE rift, highlighted by black squares in Figure 2. These ground deformation anomalies were previously identified by Fernández et al. (2009) and associated with water withdrawal from the island's galleries. As this study aims to identify ground deformation caused by volcanic or hydrothermal activity, we chose not to focus on these hydric ground deformation behaviours. The central area of Tenerife, in the Teide volcano, exhibits a positive ascending LOS deformation of a few cm/year. The deformation encompasses all of the Teide volcano area; however, the deformation is interspersed with other patterns visible on the DInSAR dataset. The application of ICA helped us to understand the geometry and more precise location of the area affected by the ground deformation at Teide. To better analyze the ICA patterns, we selected a radius of 9 km from the summit cone of Teide, shown by the black circle in Figure 2.

3.2 Application of the ICA to the DInSAR dataset

The results of ICA decomposition to the SBAS DInSAR dataset within the area of 9 km of radius from the summit of the Teide volcano revealed the presence of at least four components (Figure 3), sorted in descending order by their energy. Among these, three exhibited significant ground deformation values, while the fourth component had low amplitude energy and primarily consisted of noise. The first component of the ICA decomposition (ICA1) exhibits a highly localized and high-energy pattern, with the maximum within the summit cone of the Teide volcano (see panel A in Figure 3), displaying a circular symmetry with an approximate radius of 3 km.

The second and third components of the ICA decomposition (ICA2 and ICA3; panels B and C of Figure 3) likely represent topographical or atmospheric artifacts with high ICA energy values (Table 2). The ICA2 represents the negative values on the northern flank of the complex volcano and higher positive values on the

southern side of the Teide. The positive values are located exactly in the edge of the Las Cañadas rim while the negative ones are located in the northern side of the flank of Teide. The topography in Tenerife is abrupt and presents very complex features. The SBAS method cannot eliminate the whole signal corresponding to the topography, however, by applying the ICA we can discard the left pattern of topography from the data. The ICA3 is less energetic and does not have locally concentrated anomalies. However, as the SBAS method can still allow having the atmospheric artifacts in the dataset, we associate this pattern with the atmospheric noise. The final component (ICA4; panel D of Figure 3) displays a negligible signal pattern and possesses low energy (Table 2), indicating that it primarily represents signal noise.

3.3 Non-linear optimization in finite element modeling

The inverse modeling was carried out on the first component of the ICA (ICA1) due to 1) its high ICA energy, 2) the location in the area of the highest interest, and 3) the potential volcanic or hydrothermal origin of deformation. In the following, we provide details of the optimization results. The results of the inverse modeling, as indicated by the local maximum in the Teide summit cone, exhibit a substantial adjustment with the observed data (Figure 4). The parameters defining the source responsible for the observed deformation were determined based on an ellipsoidal geometry positioned at 1,600 m a.s.l. This source is situated beneath the summit zone of the Teide volcano, with dimensions of 1,420 m, 893 m, and 536 m along the X, Y, and Z-axes, respectively. The location of the source in UTM was the following: X= 340075 mE; Y= 3128959 mN (UTM zone 28R). The geometry of this source demonstrated nearly perfect alignment with the ICA1 data, resulting in low residuals (Figure 4C).

4 Discussion and conclusion

The detected ground deformation in Tenerife was analyzed by applying ICA to the DInSAR dataset, which was achieved by data processing of the ascending Envisat satellite images. The main volcanic deformation source in Tenerife was identified in the first ICA component, primarily concentrated between 2004 and 2005. The geometry of the source was derived through inverse modeling, assuming a three-axial ellipsoidal source located beneath the Teide and Montaña Blanca volcanoes at 1,600 m a.s.l. (Figure 5). Our results show a deformation source elongated mainly along the E-W axis. The current study findings strongly suggest that a ground deformation source was activated during the seismic crisis in 2004-2005. These results are compatible with the conclusions of previous studies, where a volcanic or hydrothermal origin in the Teide volcano was distinctly established through various geophysical and geochemical methods (García et al., 2006; Gottsmann et al., 2006; Tárraga et al., 2006; Weber et al., 2006; Almendros et al., 2007; Carracedo et al., 2007; Gottsmann et al., 2008; Márquez et al., 2008; Fernández et al., 2009; Martí et al., 2009; Domínguez-Cerdeña et al., 2011; De Barros et al., 2012; Melián et al., 2012; Pérez et al., 2013). In the following, we

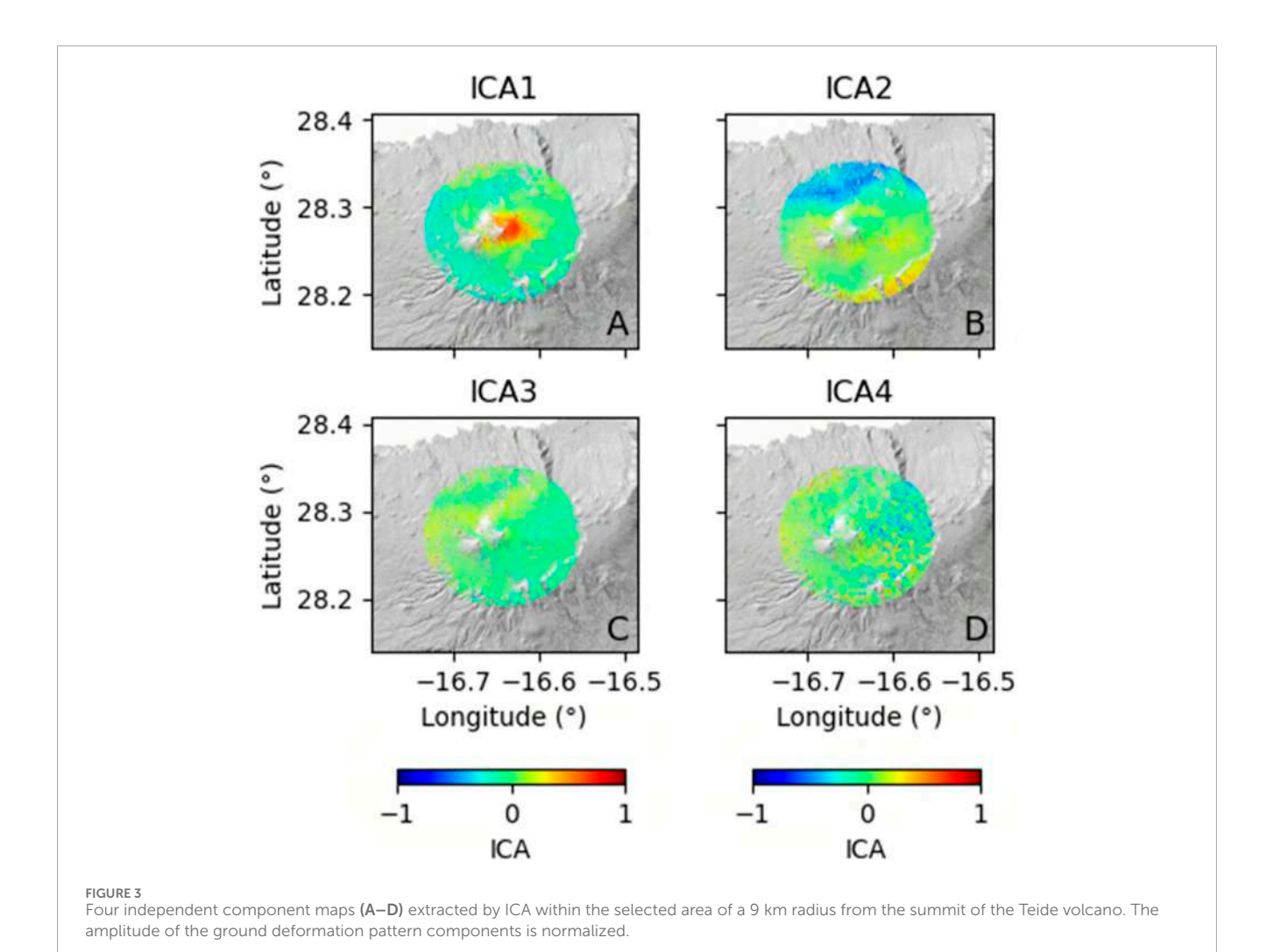


TABLE 1 Optimized source parameters.

X (UTM)	Y (UTM)	Depth m)	Rx m)	Ry m)	Rz m)
340078	3128959	-1,603	1,421.6	893.5	536

TABLE 2 ICA components and their respective energy.

Component	Energy (%)		
ICA1	32.4		
ICA2	31.9		
ICA3	24.7		
ICA4	11.0		

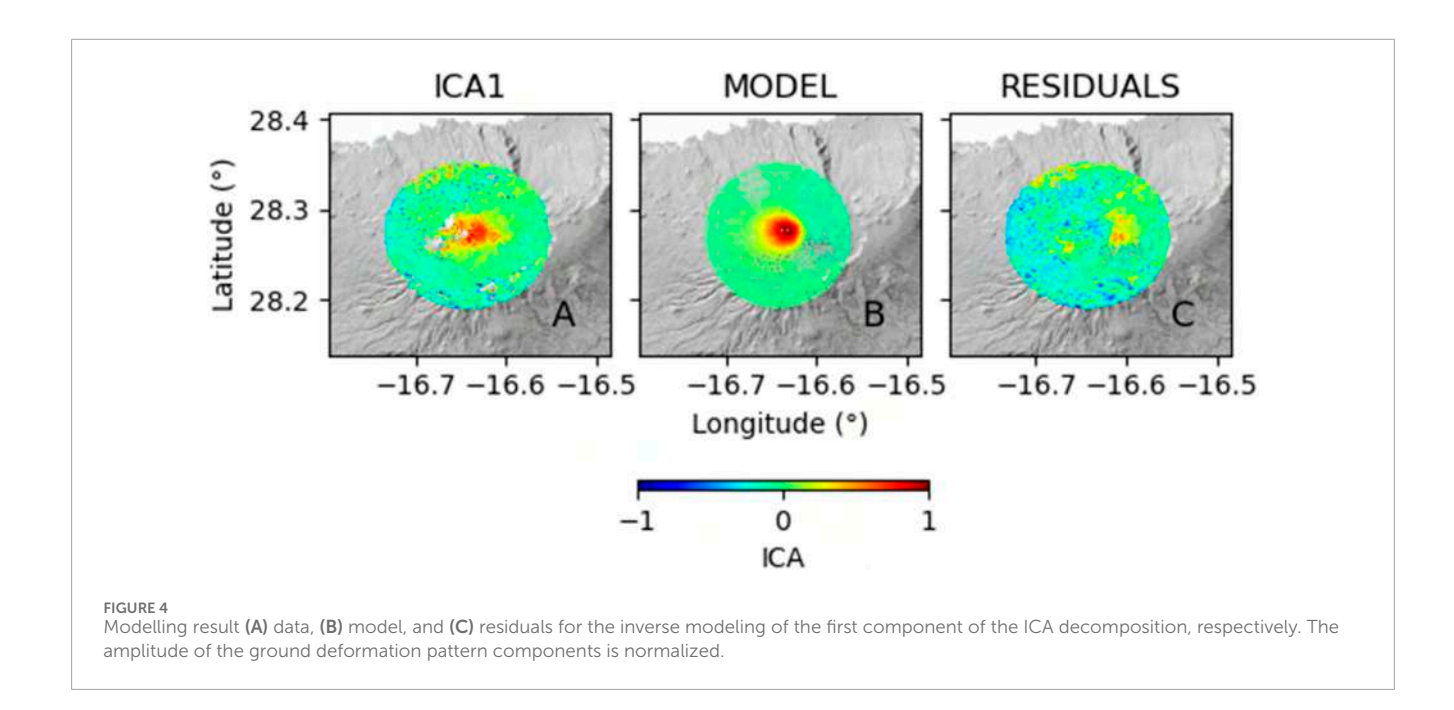
describe the similarities and differences observed between the previous studies and the present one.

The most significant feature during the crisis of 2004–2005 was primarily focused on seismic activity in the area of the Teide volcano

and the NW rift of the island (Tárraga et al., 2006; Almendros et al., 2007). Tárraga et al. (2006) postulated the existence of volcanic tremor caused by convective processes in the reservoir beneath the Teide-Pico Viejo volcanic complex triggered by new inputs of magma. However, according to Almendros et al. (2007), the 2004–2005 crisis was marked by anomalous seismic events triggered by deep magma injection under the NW flank of Teide. This new input of magma triggered the VT earthquakes, the release of magmatic gases, and, consequently, LP events. Ultimately, the injection of magma into the crust disturbed the local aquifers in Las Cañadas and induced volcanic tremor beneath the Teide volcano. Both authors confirm the evidence of the magmatic reactivation of the Teide volcano.

Additionally, Gottsmann et al. (2006), through joint microgravity and ground deformation surveys realized in May 2004 and July 2005, observed changes in the gravity field but found no evidence of significant ground deformation caused by volcanic phenomena. They could not detect these slight changes in ground deformation due to the lack of a network covering the area of interest and the temporary nature of the stations. However, applying the Envisat ASAR dataset that covers all the areas of interest and samples the data every 35 days during the 9 years of analysed

Przeor et al. 10.3389/feart.2024.1412827



period, we were able to detect even small changes in the ground deformation behavior. In addition, the ICA method decomposes the raw DInSAR SBAS signal into independent signal behaviours, letting the small changes in the ground deformation be noticed.

Gottsmann et al. (2006) proposed three possible scenarios for the observed gravity increase: 1) new magma inputs, 2) migration of hydrothermal fluids, or 3) a hybrid process involving both a new magma input and hydrothermal fluid migration. To support the hypothesis of hydrothermal fluid migration, the authors conducted an inversion of the gravity data and determined that a hydrothermal reservoir was responsible for the observed changes. Their results indicate the existence of the source at a depth of 1,9 +- 0.12 km below the surface, which is approximately consistent with our results showing the source at a depth of 1,600 m a.s.l. Ultimately, Gottsmann et al. (2006) concluded that the movement of hydrothermal fluids is the most likely scenario to explain the gravity changes and the absence of ground deformation. However, the present study allowed us to uncover hidden deformation patterns in the Teide volcano, providing further insight into the dynamics of the 2004-2005 unrest.

Additionally, Martí et al. (2009) evaluated seismic and microgravimetric observations, finding clear evidence of volcanic activity on the Teide volcano. Their discussion was based on the number and location of VT and LP events, tremor, and perturbations in the gravity field. They also reported increased activity in the fumaroles of Teide and the appearance of new fractures with gas emissions in La Orotava. These anomalies were interpreted as disturbances in the background activity of the Teide-Pico Viejo volcanic complex. The authors postulate that new magma inputs can trigger the reactivation of the phonolitic reservoir beneath the Teide-Pico Viejo volcanic complex in the future.

Furthermore, Fernández et al. (2009) identified three distinct areas affected by ground deformation in Tenerife using DInSAR SBAS data from the ERS-1 and ERS-2 sensors between 1995 and 2005. The primary one was characterized as the compressional state

of the island, attributed to the gravitational load of the edifice. Additionally, there were very localized subsidence zones in the rifts of the island, which were attributed to water withdrawal in the galleries, evidenced by Fernández et al. (2009) and also shown in Figure 2 in the present study. The authors also observed disturbances in ground deformation in the Teide volcano associated with the volcanic crisis; however, they did not perform modeling of the causative source for the observed ground deformation between 2004 and 2005.

Finally, through the geochemical analysis, Melián et al. (2012) observed a change in the composition of fumaroles in the Teide crater, resulting in a higher contribution of magmatic gases between 2001 and 2005. Pérez et al. (2013) reported temporal changes in the gas composition of Teide's fumaroles, including increased $\rm CO_2$ efflux in the Teide summit cone and crater since 2001. They highlighted that the Teide volcanic and hydrothermal system undergoes temporal degassing episodes caused by magmatic fluid injection into the hydrothermal system, which was evident in 2004 and triggered by magma movements beneath Teide. Additionally, they rejected the previously proposed hypothesis by Martí et al. (2009) regarding the reactivation of the phonolitic storage of Teide-Pico Viejo due to the analysis of gas compositions in fumaroles by Melián et al. (2012) and $\rm SO_2$ emissions reported by Weber et al. (2006).

The reactivation of an ellipsoidal-like source beneath the Teide volcano offers a comprehensive understanding of the seismic, gravimetric, and geochemical anomalies that occurred during the 2004–2005 crisis.

First of all, we observe that the ground deformation source we identified is located at a shallower depth and is displaced about 5 km to the SE with respect to the northern seismic cluster active during 2004 (Domínguez-Cerdeña et al., 2011). This seismic cluster has been interpreted by different authors as the effect of a magmatic intrusion in the north-western part of Tenerife (Gottsmann et al., 2006; Domínguez-Cerdeña et al., 2011). The volume affected by

Przeor et al. 10.3389/feart.2024.1412827

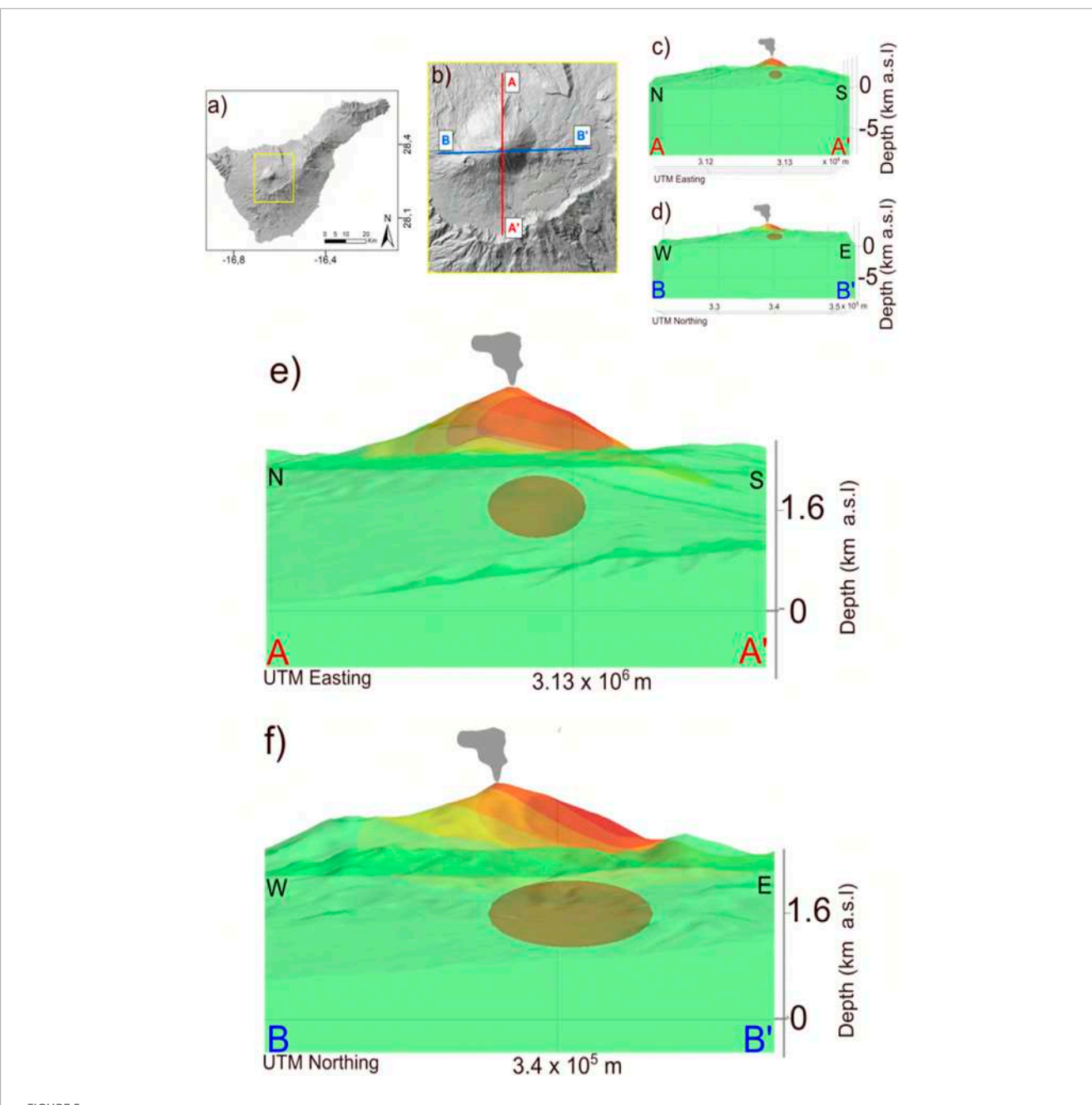


FIGURE 5
Three-dimensional model of the retrieved source responsible for the 2004–2005 ground deformation. (A) Map of Tenerife island, with the yellow box indicating the zoom of the Las Cañadas region. (B) Las Cañadas region, featuring the N-S (A,A') and E-W (B,B') profiles, is employed to represent the vertical sections of topography and the source (C,D) The N-S and E-W sections of the topography in Las Cañadas and the ground deformation modeled source, while (E,F) shows the enlarged views of panels (C,D).

this cluster has shown limited activity in the following years (Koulakov et al., 2023).

Secondly, Gottsmann et al. (2006) evidenced that the observed gravity variations are compatible with a density increase caused by the filling of rock porosity with hydrothermal fluids. They assume a volume fraction of 30% and infer a source having a radius of around 80 m. Assuming a larger source volume, the volume fraction decreases. Our source model has a volume of approximately 2.8×10^9 m³, which implies a much lower volume fraction. Another possibility is that the source thickness would be

much lower than its areal extension or, in other words, it consists of a sill-shaped geometry. Unfortunately, geodetic data alone, are not able to precisely constrain the thickness of the causative source. However, both interpretations are compatible with the observed ground deformation, gravity variations, and geochemical variations.

Concerning the source of the hydrothermal fluids, the most likely mechanism is the degassing of the magma batch which likely intruded at depth in the northwestern sector of the island. A similar mechanism is possibly related to the recent seismological and geochemical anomalies observed in Tenerife (D'Auria et al., 2019;

Padrón et al., 2021; Amonte et al., 2021). This magmatic injection episode did not show up in the ground deformation pattern, possibly because of the depth of the intrusion (>5 km) and the limited amount of magma involved. We note that eruptions occurring along the NW dorsal of Tenerife have generally a Strombolian character and are fed by basaltic magmas. This contrasts with the central Teide-Las Cañadas complex, where phonolitic eruptions with both effusive and explosive typologies occurred in the past. This was explained by Koulakov et al. (2023) by considering the difference in the crustal structure beneath these two areas. In the former, the rigid crust does not allow a long-term residence of primitive basaltic magmas, which quickly reach the surface through a network of dikes. In the latter, the presence of a ductile regime allows the stationing and the differentiation of magmas toward phonolitic composition. In this context, we postulate that the 2004-2005 unrest represents a "failed" eruption along the NW dorsal in Tenerife.

Our work highlights two relevant points from the volcano monitoring point of view. First, the most likely precursor of an eruption in the NE dorsal of Tenerife is deep seismicity related to the magmatic intrusion process. This is similar to what was observed during the 2021 Tajogaite eruption on the island of La Palma (D'Auria et al., 2022). Second, the ground deformation pattern should be interpreted carefully. We have shown how it can be related to a hydrothermal causative source instead of a magmatic intrusion.

Data availability statement

Publicly available datasets were analyzed study. This data can be found here: https://earth.esa. int/eogateway/missions/envisat/data.

Author contributions

MP: Conceptualization, Data curation, Formal Analysis, Investigation, Methodology, Visualization, Writing-original draft,

References

929

931

932

933

935

936

937

939

940

941

943

944

945

946

947

948

949

951

952

953

954

955

956

957

958

959

960

962

963

964

965 966

967

968

969

970

971

973

974

975

976

979

980

981

982

983

985

986

Q16

Q13

Acernese, F., Amico, P., Arnaud, N., Babusci, D., Barillé, R., Barone, F., et al. (2004). Properties of seismic noise at the Virgo site. Class. Quantum Gravity 21 (5), \$433-\$440. doi:10.1088/0264-9381/21/5/008

Almendros, J., Ibáñez, J. M., Carmona, E., and Zandomeneghi, D. (2007). Array analyses of volcanic earthquakes and tremor recorded at Las Cañadas caldera (Tenerife Island, Spain) during the 2004 seismic activation of Teide volcano. J. Volcanol. Geotherm. Res. 160 (3-4), 285-299. doi:10.1016/j.jvolgeores.2006.10.002

Amonte, C., Asensio-Ramos, M., Melián, G. V., Pérez, N. M., Padrón, E., Hernández, P. A., et al. (2021). Hydrogeochemical temporal variations related to changes of seismic activity at Tenerife, Canary Islands. Bull. Volcanol. 83 (4), 24. doi:10.1007/s00445-021-

Barrera Morate, J. L., and García Moral, R. (2011). Mapa Geológico de Canarias. GRAFCAN.

Bottiglieri, M., Falanga, M., Tammaro, U., Obrizzo, F., De Martino, P., Godano, C., et al. (2007). Independent component analysis as a tool for ground deformation analysis. Geophys. J. Int. 168 (3), 1305-1310. doi:10.1111/j.1365-246x.2006.03264.x

Carracedo, J. C., Badiola, E. R., Guillou, H., Paterne, M., Scaillet, S., Torrado, F. P., et al. (2007). Eruptive and structural history of Teide volcano and rift zones of Tenerife, canary islands. Geol. Soc. Am. Bull. 119 (9-10), 1027-1051. doi:10.1130/b26087.1

Comon, P. (1994). Independent component analysis, a new concept? Signal Process 36, 287-314. doi:10.1016/0165-1684(94)90029-9

Writing-review and editing. LD'A: Conceptualization, Data curation, Investigation, Methodology, Software, Writing-review and editing. SP: Data curation, Investigation, Writing-review and editing. PT: Conceptualization, Data curation, Investigation, Supervision, Writing-review and editing. AB: Investigation, Supervision, Writing-review and editing. AV: Investigation, Writing-review and editing. RC: Conceptualization, Data curation, Investigation, Methodology, Software, Supervision, Writing-review

Funding

The author(s) declare that financial support was received for the Q14 research, authorship, and/or publication of this article. TFVolcano, TFAssistance 2023, VolRiskMAc II.

Conflict of interest

The authors declare that the research was conducted in the Q15 absence of any commercial or financial relationships that could be construed as a potential conflict of interest.

The handling editor PC declared a past co-authorship with the author LD.

Publisher's note

All claims expressed in this article are solely those of the authors and do not necessarily represent those of their affiliated organizations, or those of the publisher, the editors and the reviewers. Any product that may be evaluated in this article, or claim that may be made by its manufacturer, is not guaranteed or endorsed by the publisher.

D'Auria, L., Barrancos, J., Padilla, G. D., Pérez, N. M., Hernández, P. A., Melián, G., et al. (2019). The 2016 Tenerife (Canary Islands) long-period seismic swarm. J. Geophys. Res. Solid Earth 124 (8), 8739–8752. doi:10.1029/2019jb017871

D'Auria, L., Koulakov, I., Prudencio, J., Cabrera-Pérez, I., Ibáñez, J. M., Barrancos, J., et al. (2022). Rapid magma ascent beneath La Palma revealed by seismic tomography. Sci. Rep. 12 (1), 17654. doi:10.1038/s41598-022-21818-9

De Barros, L., Martini, F., Bean, C. J., Garcia-Yeguas, A., and Ibáñez, J. (2012). Imaging magma storage below Teide volcano (Tenerife) using scattered seismic wavefields. Geophys. J. Int. 191 (2), 695-706. doi:10.1111/j.1365-246x.2012.

De Luca, C., Cuccu, R., Elefante, S., Zinno, I., Manunta, M., Casola, V., et al. (2015). An on-demand web tool for the unsupervised retrieval of Earth's surface deformation from sar data: the p-sbas service within the esa g-pod environment. Remote Sens. 7, 15630-15650. doi:10.3390/rs71115630

De Luca, C., Valerio, E., Giudicepietro, F., Macedonio, G., Casu, F., and Lanari, R. (2022). Pre-and co-eruptive analysis of the September 2021 eruption at Cumbre Vieja volcano (La Palma, Canary Islands) through DInSAR measurements and analytical modeling. Geophys. Res. Lett. 49 (7), e2021GL097293. doi:10.1029/

Domínguez-Cerdeña, I., del Fresno, C., and Rivera, L. (2011). New insight on the increasing seismicity during Tenerife's 2004 volcanic reactivation. J. Volcanol. Geotherm. Res. 206 (1-2), 15-29. doi:10.1016/j.jvolgeores.2011.06.005

989

990

991

993

994

995

997

998

999

1000

1001

1002

1003

1005

1006

1009

1008

1010 1012

> 1013 1014

1016 1017 1018

1020

1021 1022

1024 1025

1026 1027 1028

1029 1031 1032

1033

1035 1036

1041 1043

1044

Przeor et al. 10.3389/feart.2024.1412827

Application of Ebmeier, (2016).independent S. component InSAR analysis to multitemporal data with volcanic Geophys. Res.Solid 8970-8986. doi:10.1002/ studies. Earth 121, 2016ib013765

1081

1101

Fernández, J., Tizzani, P., Manzo, M., Borgia, A., González, P. J., Martí, J., et al. (2009). Gravity-driven deformation of Tenerife measured by InSAR time series analysis. *Geophys. Res. Lett.* 36 (4). doi:10.1029/2008gl036920

García, A., Ortiz, R., Marrero, J. M., S' nchez, N., Vila, J., Correig, A. M., et al. (2006). Monitoring the reawakening of canary islands' Teide volcano. *Eos, Trans. Am. Geophys. Union* 87 (6), 61–65. doi:10.1029/2006e0060001

Gottsmann, J., Camacho, A. G., Martí, J., Wooller, L., Fernández, J., Garcia, A., et al. (2008). Shallow structure beneath the Central Volcanic Complex of Tenerife from new gravity data: implications for its evolution and recent reactivation. *Phys. Earth Planet. Interiors* 168 (3-4), 212–230. doi:10.1016/j.pepi.2008.06.020

Gottsmann, J., Wooller, L., Martí, J., Fernández, J., Camacho, A. G., González, P. J., et al. (2006). New evidence for the reawakening of Teide volcano. *Geophys. Res. Lett.* 33 (20). doi:10.1029/2006gl027523

Hyvärinen, A., and Oja, E. (2000). Independent component analysis: algorithms and applications. Neural Netw. 13, 411–430. doi:10.1016/s0893-6080(00)00026-5

Koulakov, I., D'Auria, L., Prudencio, J., Cabrera-Pérez, I., Barrancos, J., Padilla, G. D., et al. (2023). Local earthquake seismic tomography reveals the link between crustal structure and volcanism in Tenerife (Canary Islands). *J. Geophys. Res. Solid Earth* 128 (3), e2022JB025798. doi:10.1029/2022jb025798

Márquez, A., López, I., Herrera, R., Martín-González, F., Izquierdo, T., and Carreno, F. (2008). Spreading and potential instability of Teide volcano, Tenerife, canary islands. *Geophys. Res. Lett.* 35 (5). doi:10.1029/2007gl032625

Martí, J., Ortiz, R., Gottsmann, J., Garcia, A., and De La Cruz-Reyna, S. (2009). Characterising unrest during the reawakening of the central volcanic complex on Tenerife, Canary Islands, 2004–2005, and implications for assessing hazards and risk mitigation. *J. Volcanol. Geotherm. Res.* 182 (1-2), 23–33. doi:10.1016/j.jvolgeores.2009.01.028

Melián, G., Tassi, F., Pérez, N., Hernández, P., Sortino, F., Vaselli, O., et al. (2012). A magmatic source for fumaroles and diffuse degassing from the summit crater of Teide Volcano (Tenerife, Canary Islands): a geochemical

evidence for the 2004–2005 seismic–volcanic crisis. $Bull.\ Volcanol.\ 74,\ 1465–1483.$ doi:10.1007/s00445-012-0613-1

Nelder, J. A., and Mead, R. (1965). A simplex method for function minimization. *Comput. J.* 7, 308–313. doi:10.1093/comjnl/7.4.308

Padrón, E., Pérez, N. M., Hernández, P. A., Melián, G., Asensio-Ramos, M., D'Auria, L., et al. (2021). Changes in diffuse degassing from the summit crater of Teide volcano (Tenerife, Canary Islands) prior to the 2016 Tenerife long-period seismic swarm. *J. Geophys. Res. Solid Earth* 126 (3), e2020JB020318. doi:10.1029/2020jb020318

Pepe, A., Manzo, M., Casu, F., Solaro, G., Tizzani, P., Zeni, G., et al. (2008). Surface deformation of active volcanic areas retrieved with the SBAS-DInSAR technique: an overview. *Ann. Geophys.* 51, 247–263.

Pepe, S., D'Auria, L., Castaldo, R., Casu, F., De Luca, C., De Novellis, V., et al. (2018). The use of massive deformation datasets for the analysis of spatial and temporal evolution of Mauna Loa volcano (hawai'i). *Remote Sens.* 10 (6), 968. doi:10.3390/rs10060968

Pérez, N. M., Hernández, P. A., Padrón, E., Melián, G., Nolasco, D., Barrancos, J., et al. (2013). An increasing trend of diffuse CO2 emission from Teide volcano (Tenerife, Canary Islands): geochemical evidence of magma degassing episodes. *J. Geol. Soc.* 170 (4), 585–592. doi:10.1144/jgs2012-125

Przeor, M., D'Auria, L., Pepe, S., Tizzani, P., and Cabrera-Pérez, I. (2022). Elastic interaction between Mauna Loa and Kīlauea evidenced by independent component analysis. *Sci. Rep.* 12 (1), 19863. doi:10.1038/s41598-022-24308-0

Tárraga, M., Carniel, R., Ortiz, R., Marrero, J. M., and García, A. (2006). On the predictability of volcano-tectonic events by low frequency seismic noise analysis at Teide-Pico Viejo volcanic complex, Canary Islands. *Nat. Hazards Earth Syst. Sci.* 6 (3), 365–376. doi:10.5194/nhess-6-365-2006

Tizzani, P., Berardino, P., Casu, F., Euillades, P., Manzo, M., Ricciardi, G. P., et al. (2007). Surface deformation of long valley caldera and mono basin, California, investigated with the SBAS-InSAR approach. *Remote Sens. Environ.* 108 (3), 277–289. doi:10.1016/j.rse.2006.11.015

Weber, K., Fischer, C., Van Haren, G., Bothe, K., Pisirtsidis, S., Laue, M., et al. (2006). "Ground-based remote sensing of gas emissions from Teide volcano (Tenerife, Canary Islands, Spain): first results," in *Remote sensing of clouds and the atmosphere XI* (SPIE), 6362, 384–393. doi:10.1117/12.714411

Q17 1111

Frontiers in Earth Science 10 frontiersin.org

Appendix D

Other Publications

scientific reports



OPEN

Rapid magma ascent beneath La Palma revealed by seismic tomography

Luca D'Auria^{1,2}, Ivan Koulakov^{3,4}, Janire Prudencio^{5,6}, Iván Cabrera-Pérez¹, Jesús M. Ibáñez^{5,6⊠}, Jose Barrancos^{1,2}, Rubén García-Hernández¹, David Martínez van Dorth^{1,2}, Germán D. Padilla^{1,2}, Monika Przeor^{1,2}, Victor Ortega¹, Pedro Hernández^{1,2} & Nemesio M. Peréz^{1,2}

For the first time, we obtained high-resolution images of Earth's interior of the La Palma volcanic eruption that occurred in 2021 derived during the eruptive process. We present evidence of a rapid magmatic rise from the base of the oceanic crust under the island to produce an eruption that was active for 85 days. This eruption is interpreted as a very accelerated and energetic process. We used data from 11,349 earthquakes to perform travel-time seismic tomography. We present high-precision earthquake relocations and 3D distributions of P and S-wave velocities highlighting the geometry of magma sources. We identified three distinct structures: (1) a shallow localised region (<3 km) of hydrothermal alteration; (2) spatially extensive, consolidated, oceanic crust extending to 10 km depth and; (3) a large sub-crustal magma-filled rock volume intrusion extending from 7 to 25 km depth. Our results suggest that this large magma reservoir feeds the La Palma eruption continuously. Prior to eruption onset, magma ascended from 10 km depth to the surface in less than 7 days. In the upper 3 km, melt migration is along the western contact between consolidated oceanic crust and altered hydrothermal material.

On 19 September 2021, an eruption of high social and scientific impact began on the island of La Palma, Canary Islands, Spain (Fig. 1) and lasted 85 days until 13 December 2021. This eruption did not cause any casualties, but it destroyed hundreds of homes, disrupted transport and communication networks, and affected extensive areas of farmland that are key to the local economy. In less than three months, this fissure eruption formed a lava field of $> 12 \text{ km}^2$ with thicknesses of up to tens of meters at some points\(^1\). Among seven previous eruptions on La Palma in the last 500 years\(^2\), the most productive one formed a lava field of just 4.4 km\(^2\) (Fig. 1). The eruptive style has been mainly effusive, but with numerous Strombolian explosions, extensive ash fall, and repeated partial collapses of the cone\(^3\). Intense seismicity activity before and during the eruption has included earthquakes with high magnitudes for this volcano type (up to Ml = 4.3).

Volcano seismology remains one of the most important tools for volcano monitoring. As one of its most significant developments, seismic tomography provides a window into sub-surface structures and their links to magmatic processes^{4,5}. However, obtaining tomographic images during eruptions is complex owing to the requirement of high numbers of seismic stations and earthquakes with adequate spatio-temporal distributions to provide sufficient resolution. In most cases, due to logistical problems, the deployment of arrays with a sufficient number of stations for high-quality tomography study during the most active stage of an eruption is difficult and especially rare when such a dense network operated prior to an eruption culmination. Fortunately, all stages of the La Palma eruption were recorded by two high-quality networks that gave us a unique chance to observe details of the spatial-temporary evolution of seismicity before, during and after the most active stage of the eruption (Figs. 2, and S1–S3 in Supplementary). Furthermore, it provided sufficient material to implement high-quality tomography inversion and to infer the 3D structure of the magma plumbing system *during* the active stage of

¹Instituto Volcanológico de Canarias (INVOLCAN), Calle Álvaro Martín Díaz, 2, San Cristóbal de La Laguna, Tenerife, Spain. ²Instituto Tecnológico Y de Energías Renovables (ITER), Polígono Industrial de Granadilla s/n, 38600 Granadilla de Abona, Tenerife, Spain. ³Trofimuk Institute of Petroleum Geology and Geophysics SB RAS, Prospekt Koptyuga, 3, 630090 Novosibirsk, Russia. ⁴Institute of the Earth's Crust SB RAS, Lermontova 128, Irkutsk, Russia. ⁵Department of Theoretical Physics and Cosmos, Science Faculty, University of Granada, Avd. Fuenteneueva s/n, 18071 Granada, Spain. ⁶Andalusian Institute of Geophysics, Campus de Cartuja, University of Granada, C/Profesor Clavera 12, 18071 Granada, Spain. [∞]email: jibanez@ugr.es

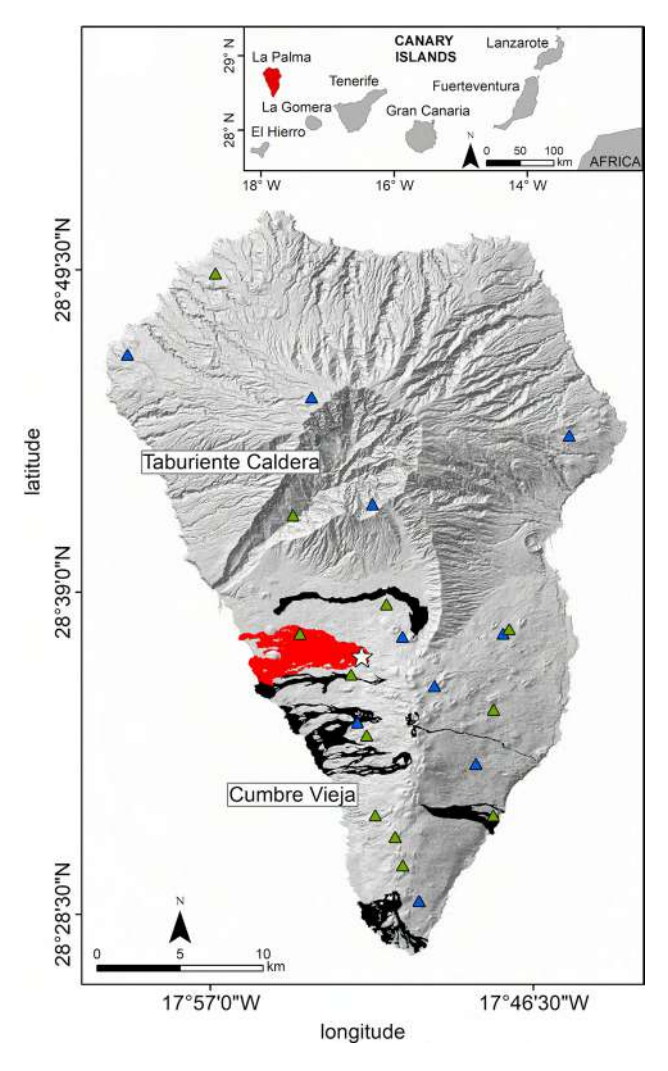


Figure 1. Digital elevation map of La Palma Island with the locations of seismic networks INVOLCAN (green triangles) and IGN (blue triangles). Black shading denotes lava flows from historical eruptions and red shading denotes lava flows from the 2021 activity. The white star is the vent of the 2021 eruption. The digital elevation model and historical lava flows were downloaded from the public graphic repository of GrafCan (www.grafc an.es). The 2021 lava flow was downloaded from the European agency Copernicus Emergency Management Service (httts://emergency.copernicus.eu/mapping/list-of-components/EMSR546). The software used to generate this figure was QGIS 3.22 (https://www.qgis.org).

the eruption. Our results have great scientific and social impact and offer improved understanding of pre- and syn-eruptive activity, along with the possible future volcanic scenarios in La Palma Island.

Previous studies of La Palma and surrounding islands. There is a lack of consensus on the origin and evolution of the Canary Islands archipelago, in part because knowledge of deep structures is scarce and inconclusive. One of the models supports the existence of a mantle plume beneath the western Canary Islands (El Hierro and La Palma)^{6,7}. In this model, material flows from the plume to the east, crossing the north-western African continent, travelling along the base of the oceanic lithosphere below the Canary Islands, and finally flowing into a sub-continental lithospheric corridor beneath the Atlas Mountain system.

Using compressional to shear (P to S) converted seismic phases from teleseismic receiver functions, Lodge et al. 8 studied the crustal and upper mantle structure below La Palma. They identified discontinuities at \sim 8 and 14 km depth, and interpreted the deeper one as Moho. However, it cannot be excluded that the discontinuity at \sim 8 km depth may correspond to the Moho, while that at 14 km might be the trace of magmatic underplating.

Based on P-receiver functions, Martínez-Arévalo et al. suggested that the Moho discontinuity beneath the Canary Islands deepens towards the east, varying in depth from 11.5 to 12.5 km beneath the western islands (El Hierro and La Palma) and up to 20–30 km beneath the eastern islands (Lanzarote and Fuerteventura). They identified a low velocity layer beneath the lithospheric mantle (at 45–65 km depth), which they interpret as a large plume feeding the Canary Islands volcanic system.

From seismic velocity tomography of El Hierro Island, García-Yeguas et al.¹⁰ determined the base of the oceanic crust to be at 10–12 km depth. They did not observe a magma reservoir. Based on their results, they

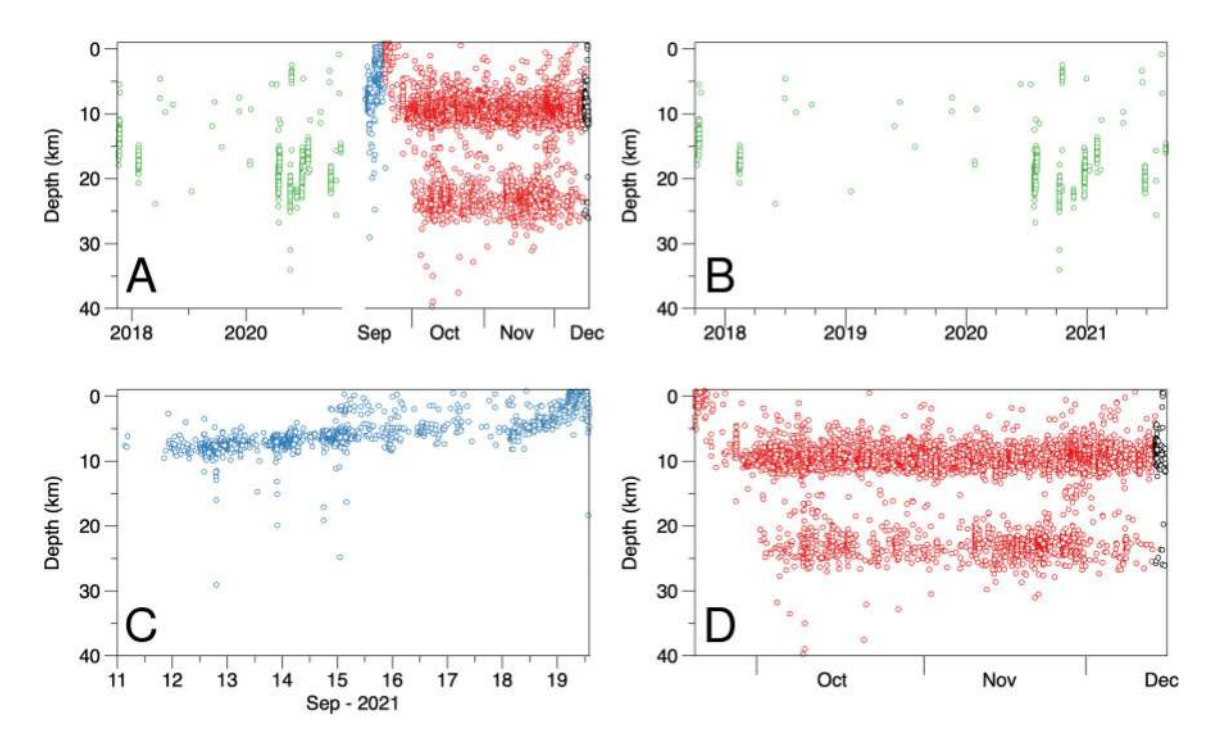


Figure 2. (**A**) Temporal and depth distribution of the used seismicity beneath La Palma (**A**) Seismicity in the entire observation time divided in four periods depicted with different colours. (**B**) Precursory period, from October 2017 to August 2021, plotted in green and zoomed in (**B**). (**C**) Pre-eruptive period in, the week before the start of the eruption. , plotted in blue and zoomed in (**C**). (**D**) Syn-Eruptive and post-eruptive, the seismicity occurred after the start of the eruption up to December 13th 2021, plotted in red, and the post-eruptive, the seismicity after volcanic activity ceased, December 13–16, 2021, plotted in black, all of them represented in (**D**).

suggest that the magma intrusion responsible of the 2011 eruptive process warped the Moho below the island, causing localised thinning of the oceanic crust to < 8 km.

Numerous seismic tomography studies of volcanic regions have identified shallow low-velocity structures that are interpreted as highly fractured, unconsolidated, and/or hydrothermally altered volcanic materials, including those for Deception Island volcano^{11–13}, Avacha group volcanoes¹⁴ and Mt. Etna^{15,16}. Similar anomalies have been observed beneath the island of Tenerife^{17,18}.

Most information on the internal structure of La Palma was derived based on the magnetotelluric sounding¹⁹. The obtained 3D geoelectric model demonstrated high-resistivity zone beneath the Taburiente Caldera, which was interpreted as a trace of old highly consolidated intrusive body. At the same time, this model revealed contrasted low-resistivity anomalies around the Cumbre Vieja that may be associated with the presence of high-fractured and/or hydrothermally altered rocks.

On La Palma, no seismic tomography models nor detailed structural geophysical models were previously constructed. In this study, we present the first seismic velocity model for this area.

Data and algorithms. In this study, we merged datasets derived by the two governmental agencies operating on La Palma prior to and during the eruption: the Instituto Geográfico Nacional (IGN; 11 stations) and the Instituto Volcanológico de Canarias (INVOLCAN; 12 stations) (Fig. 1). Both networks consist of three-component broadband seismic stations sampled with a rate of 100 Hz. The dataset covers the time span from 8 October 2017 to 15 December 2021. The seismic activity (Fig. 2) begins with a seismic swarm at the end of the year 2017. This seismicity, related to the magmatic reactivation process, shows two different space–time characteristics. In the period from 8 October 2017 to August 2021 (Figure S1), seismic activity is recorded mainly at depths between 15 and 20 km, and which in this work we will call precursory activity. On the other hand, we used the term pre-eruptive for the seismic activity associated with the week prior to the eruption (Fig. S2), where a clear migration of seismicity towards the surface is observed, marking the final path followed by the magma until the eruption. Finally, the seismic activity that accompanies the eruptive process was called syn-eruptive seismicity (Fig. S3).

When processing the data, these two agencies used different source location algorithms and different velocity models. Therefore, they provided slightly different solutions for the coordinates and origin times of the same events. When merging, we assumed that both agencies had recorded the same event if the difference between the origin times in the provided solutions was < 1 s. We analysed different values of this threshold and found that when using a smaller value (0.5 s), the number of the common events were much smaller. On the other hand, when using a larger threshold of 2 s, the number of the common events did not increase significantly. From this analysis, we concluded that 1 s is an appropriate value suitable for this case. The merged dataset contains 13,681 events recorded by 23 stations, with 140,078 *P* wave and 155,231 *S* wave picks. Event magnitudes were based on solutions provided by INVOLCAN.

Tomographic inversion was based on the local earthquake tomography code LOTOS²⁰, which has been used to investigate dozens of different volcanoes^{10,21–23}. First, event locations in the reference 1D velocity model were determined using a grid-search method and linear approximation of ray paths¹⁰. We used the topography surface to limit the depths of events; therefore, events can be located above the sea surface. During this step, we selected events with eight or more picks and removed all data with absolute residual values of > 0.5 s for P waves and 0.7 for S waves. After removing outliers, the dataset used for the tomographic procedure included 11,349 events with 121,572 P wave and 127,766 S wave arrival times (mean of 22 picks per event).

Next, we relocated event sources using the gradient method and 3D bending algorithm for ray tracing¹⁰. In the first iteration, the relocation was conducted in the starting 1D model; in subsequent iterations, calculations were performed in the updated 3D model.

The 3D distributions of P and S wave velocity anomalies were parameterised using grid nodes irregularly distributed in the study area according to the ray density. Between the nodes, velocities were approximated continuously using bi-linear interpolation. The minimum grid spacing in both the horizontal and vertical directions was 0.7 km, which is considerably smaller than the size of resolved anomalies in our model. To reduce the influence of parameterisation on the results, we performed inversions in four grids with different basic orientations to the azimuthal direction (0, 22, 45 and 67 degrees) and then averaged them into one regular grid.

The inversion was performed simultaneously for the P and S velocity anomalies, source parameters (corrections of coordinates dx, dy, dz, and origin time dt), and station corrections. To stabilise the solutions, we used two types of regularisation—amplitude damping and flattening—which were performed by adding the corresponding equations to the general system. The values of the damping coefficients were determined from a series of synthetic tests with realistic anomaly sizes and noise levels. The derived sparse matrix was inverted using the Least Squares with QR-factorization (LSQR) method 24,25 .

The optimal 1D reference velocity model was derived after several runs of the complete tomographic procedure. After each trial, we calculated the average *P* and *S* velocities at certain depths and used them for the next iteration. As a result, we obtained a fair balance between high- and low-velocity anomalies at all depth layers.

After inversion in the four grids, the resulting P and S wave velocity anomalies were recalculated in a regular grid and then used for the next iteration, which included source relocation, matrix calculation, and inversion. In total, for the experimental and synthetic data, we performed five iterations, which was a compromise between solution stability and calculation velocity. The calculations enabled considerable variance reduction. In the L1 norm, the average P wave residuals reduced from 0.2397 to 0.0860 s (64.12%) and those for S waves reduced from 0.3058 to 0.1401 s (54.17%).

Seismic tomography results. Figures 3, 4 and 5 show the inversion results of experimental data, including P wave velocity, and S wave velocity anomalies and Vp/Vs ratio in horizontal (Fig. 3) and vertical sections (Fig. 4), as well as in the 3D representation (Fig. 5). In the context of magma-related structures, it is important to present the Vp/Vs ratio, which was calculated by division of the derived P and S absolute velocities. The adequacy of this method was determined by the similar volumes of P and S wave data, and was confirmed using synthetic tests.

In the resulting tomography models, we observe highly heterogeneous structures with the deviations of velocities exceeding 20%. At shallow depths at 0.5 b.s.l. (or 1.5-2 km below surface in the central part of the island), we observe very strong low velocities of P and S waves beneath the southwestern slope of the island (upper row in Fig. 3). This anomaly almost perfectly matches with the locations of most vents of historical eruptions. It may also represent the presence of unconsolidated volcanoclastic deposits^{26–29}. In the vertical sections (Fig. 4), we see that these low-velocity anomalies propagate down to ~ 5 km depth. The Vp/Vs ratio in shallow layers looks patchier but also exhibits a clear connection with the distributions of the vents. On the other hand, the area of the Taburiente Caldera (Fig. 1) in the northern part of the study area coincides with the areas of high velocities Vp and Vs and low Vp/Vs ratio. These findings are consistent with the results of magnetotelluric sounding¹⁹. An anomaly of positive dVp and dVs at the depth of 7 km depth in our results (Fig. 3, middle row) looks very consistent with the high-resistivity anomaly in the deepest Sect. (4–5 km) in Fig. 2 found by Di Paolo et al. ¹⁹. At the shallower Sects. (0.5 km), the seismic anomalies are low in the south and high in the north (upper row in Fig. 3); nearly the same geometry is observed in the MT results at 1.996–2.379 km in which the areas of high resistivity were observed below Taburiente Caldera and low-resistivity anomalies were detected in the area of Cumbre Vieja vents.

At 7 km depth, we observe a prominent high-velocity and low Vp/Vs anomaly beneath the central part of the island. In vertical section A2-B2 in Fig. 4 and the 3D representation in Fig. 5, we see how this high-velocity layer is dissected by a vertically oriented low-velocity anomaly coinciding with a narrow seismicity cluster (see a zoomed fragment in the right column in Fig. 4). This seismicity probably represents the process of upward magma propagation through a new conduit formed due to fracturing of rocks in a brittle "blue" layer. In the lower part of this zone, we observe a "drop-shaped" anomaly of high Vp/Vs ratio that possibly indicates the ascent of partially molten magmas.

In the lower part of the model, below Cumbre Vieja, we observe a prominent anomaly of very high Vp/Vs ratio, which coincides with the distribution of deep seismicity (Fig. 5). Based on a similarity of this anomaly with structures observed beneath many other active volcanoes, we can conclude that it represents a deep conduit that delivers magma from deeper sources.

To assess the spatial resolution of the resulting models and to derive optimal values of controlling parameters for the tomographic procedure, we performed a series of synthetic tests. In all cases, the synthetic model was defined by a set of positive and negative anomalies with respect to the a priori 1D reference model. Synthetic travel times were calculated for the same source-receiver pairs as derived in the main experimental model after

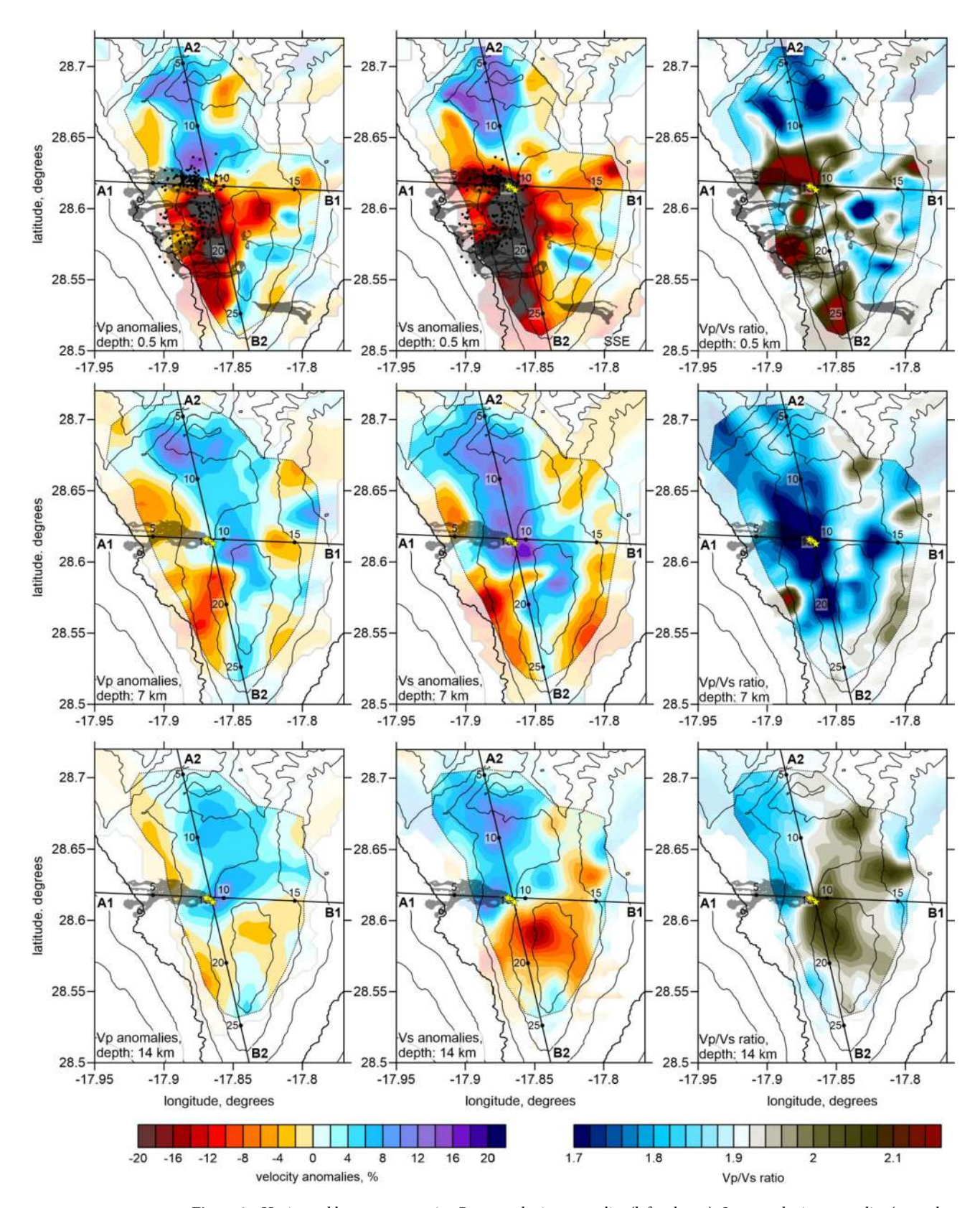


Figure 3. Horizontal layers representing P wave velocity anomalies (left column), S wave velocity anomalies (central column), and Vp/Vs ratio (right column) for three selected depths (0.5, 7 and 14 km depth b.s.l.). Black contour lines represent the topography with the interval of 500 m. In section at 0.5 km depth, all historical lava flows are shown; in other sections, only the flow of the 2021 eruption is presented. The yellow stars depict the vents of the 2021 eruption. The dotted line highlights the resolved areas based on the results of the checkerboard tests. The digital elevation model and historical lava flows were downloaded from the public graphic repository of GrafCan (www.grafcan.es). The 2021 lava flow was downloaded from the European agency Copernicus Emergency Management Service (httts://emergency.copernicus.eu/mapping/list-of-components/EMSR546). The software used to generate this figure was the LOTOS code.

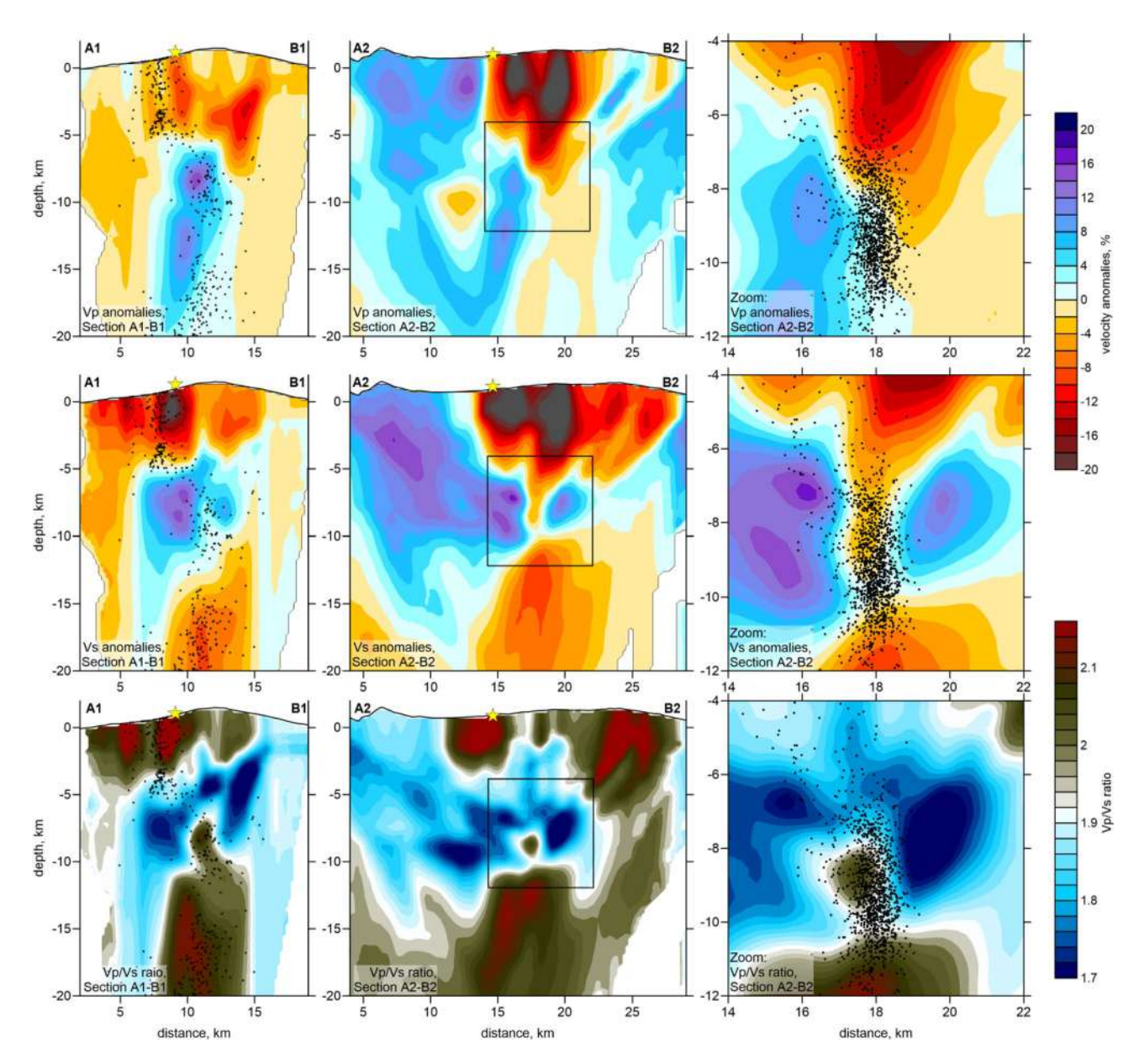


Figure 4. Vertical projections representing P wave velocity anomalies, S wave velocity anomalies, and Vp/Vs ratio. The locations of the profiles are shown in Fig. 3. The central squares of the A2-B2 profiles mark the area that is being zoomed in and is plotted in the right column. The black dots depict the event hypocenters located at distances of less than 0.6 km from the profile. The yellow star indicates the location of the 2021 eruption vent.

five iterations. The derived data were perturbed by random noise with an average deviation of 0.03 s for both P and S data, which enabled the same variance reduction as in the experimental data inversion. Before starting the synthetic model recovery, we "forgot" any information about the sources. Then, calculations were performed based on the same workflow as in the experimental data processing, including source location in the starting 1D model using the grid-search method. During synthetic modelling, we tuned the values of the controlling parameters to derive an optimal quality of the initial model recovery; then, the same controlling parameters were used for the experimental data inversion.

We separately investigated the resolution in the horizontal and vertical directions. In the first series of tests, we defined several checkerboard models with different anomaly sizes in map view. In Figure S4 of Supplementary, we present three tests with anomalies of 2, 3, and 4 km separated by 1 km spacing with zero anomaly values. In all cases, the amplitudes of anomalies were \pm 8%. We defined the opposite signs of the dVp and dVs anomalies to enable contrasted variations of the Vp/Vs ratio. The recovery results are presented in two depth sections. Anomalies of 2 km in size were only resolved in the central part of the study area, where most earthquakes were located. For the models with larger anomalies, fair resolution was observed in most parts of the study area. Based on the results of these tests, we defined a contour of the resolved area, in which the results of experimental data

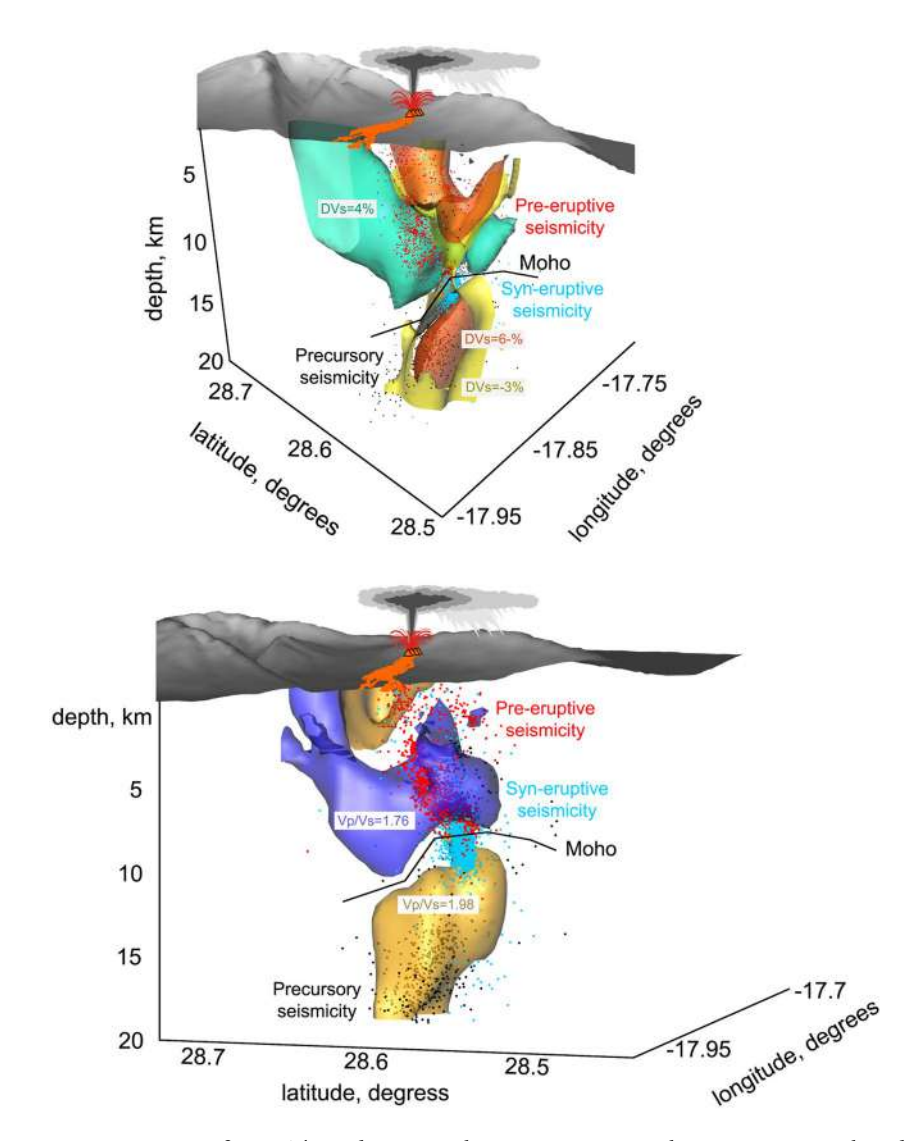


Figure 5. Upper figure. Three-dimensional image representing the main structures based on S waves velocity anomalies. Yellow and orange denotes bodies with lower velocity and green denotes bodies with higher velocity. The black line denotes the potential flexure of the Moho as a consequence of magma intrusion. Coloured dots denote the relocated seismicity according the occurrence phases. **Lower figure.** Same as Upper figure but based in the Vp/Vs ratio. Yellow bodies represent high Vp/Vs ratio and purple body represents low Vp/Vs ratio.

were plotted (dotted line in Fig. 3). From these tests, we confirmed that the distribution of Vp/Vs was correctly recovered, demonstrating the adequacy of the method for this parameter calculation.

In another series of tests shown in Figure S5 of Supplementary, we explored the vertical resolution. Regarding the trade-off between velocity and source coordinates in passive source tomography, as well as dominantly vertical orientations of ray paths, we could expect poorer vertical resolution compared with horizontal resolution. In particular, there was a concern about the capacity of the existing data to provide abrupt changes in velocity at ~ 10 km depth, as observed in the experimental data inversion. To address this problem, we defined models with alternated anomalies defined in each of the vertical sections, in which the main results are presented. Along these sections, the anomalies had a size of 4 km and a spacing of 2 km. In the vertical direction, they formed two rows with an interval of zero values at depths between 6 and 10 km. This test confirmed that major anomalies in the central part of the study area were correctly recovered; however, some diagonal smearing is observed in marginal regions. This effect was taken into account during interpretation.

The synthetic test with realistic anomalies shown in Fig. 6 demonstrates the capacity of the tomography inversion to recover the structures observed in the main model derived from the inversion of experimental data. The synthetic model in this case was defined by a set of polygons distributed along the vertical Section A2-B2. The anomalies of the P and S wave velocities were defined to enable the distributions of the recovered dVp, dVs and Vp/Vs ratio similar to those in the main model in Fig. 4. We see that all structures, which will be used for interpretation of the results in the Discussion section, could be robustly recovered in the case of this synthetic test.

As true event coordinates were presumed to be unknown in the recovery procedure, the synthetic tests allowed us to assess the accuracy of source locations. Figure S6 of Supplementary shows the mislocations of

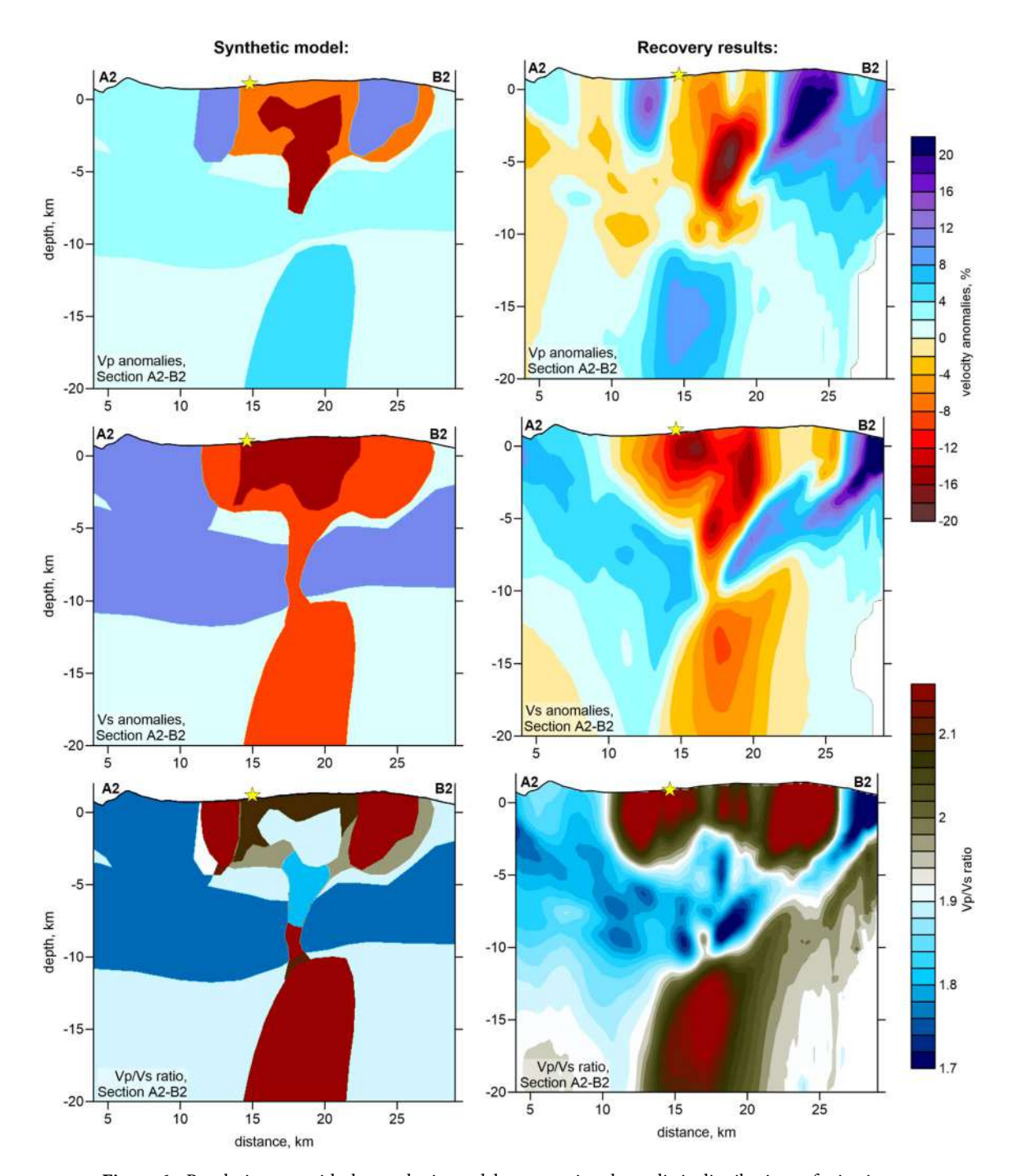


Figure 6. Resolution test with the synthetic model representing the realistic distributions of seismic structures along the section A2–B2. The configuration of the initial synthetic patterns of Vp, Vs anomalies and Vp/Vs ratio are presented in the left column, and the recovery results are shown in the right column. The yellow star indicates the location of the 2021 eruption vent.

events in the model with a vertical checkerboard in Sect. 2 with respect to the true locations. When using the starting 1D velocity model, the average error of source coordinate determination in the L1 norm was 0.68 km. In the final model, the average error reduced to 0.42 km. As expected, the maximum errors were observed for events on the periphery of the network and at the greatest depths. These errors do not significantly affect the interpretation of the results presented in this manuscript.

Discussion

Based on accurate relocations of the seismicity and magnitude determinations at different stages of the eruption development, we have estimated the earthquake Benioff's strain release²⁹ in selected earthquake clusters (Fig. 7). We found that the released seismic strain of intermediate seismicity (5-15 km) is almost four times larger than that of deep and shallow seismicity, suggesting that stress generation in this region is dominating the eruptive

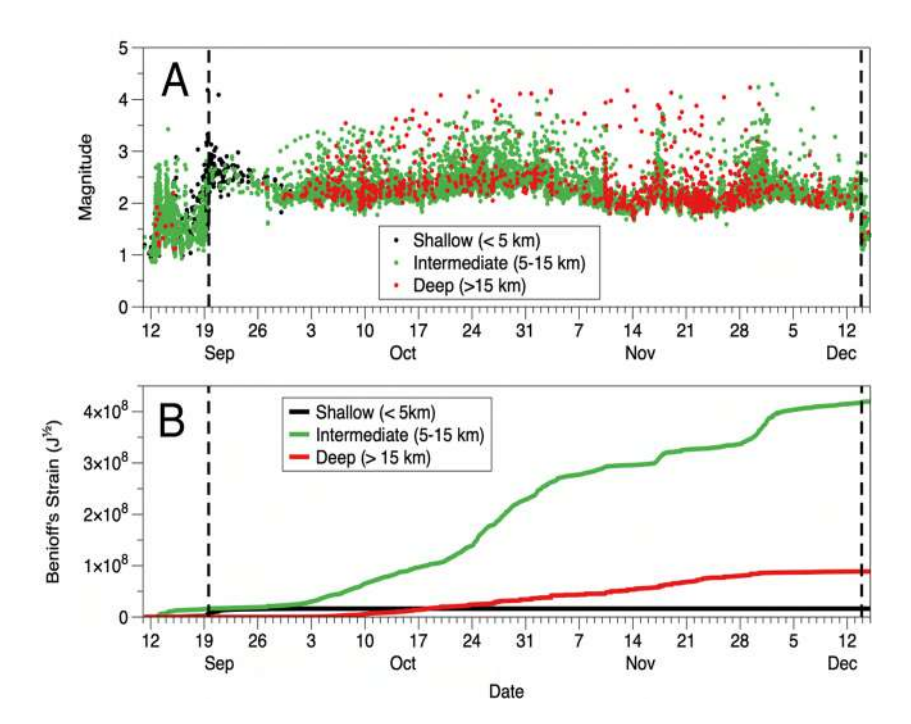


Figure 7. Earthquake magnitudes and Benioff's strain release. (**A**) Magnitudes (Ml) of located earthquakes separated by depth; (**B**) accumulated Benioff's strain release for each depth class. The dashed lines limit the active phase of the eruption.

process. One of the most important characteristics of this seismicity is the difference between pre-eruptive and syn-eruptive seismicity. The pre-eruptive seismicity is of low magnitude and shows evident migrations from the deep towards the surface (Fig. 2, S1 and S2). The syn-eruptive seismicity is of much larger magnitude and presents two focal depth clusters, 10-12 km depth and 20-25 km depth with no apparent migration (Fig. 2 and S3). Note that the upper cluster roughly corresponds to the depth where the pre-eruptive seismicity began on 11 September 2021.

Our seismic tomography results offer improved understanding of pre- and syn-eruptive activity, along with the possible future volcanic scenarios in La Palma Island. Based on the calculated seismic velocity model and the seismicity distribution, we can single out the following observations:

- (1) The western Canary Islands, including La Palma, are underlain by high-velocity oceanic crust. Beneath most islands, the Moho (i.e., the base of the oceanic crust) is at ~ 10–12 km below sea level (bsl); this depth is greater than that between and surrounding the islands and is the expected consequence of isostatic equilibrium^{6,17,19,30}. However, unlike the neighbouring island of El Hierro, where a volcanic unrest was observed in 2012, there is no crustal thickening beneath La Palma. On the contrary, our tomographic images suggest crustal thinning, with a high-velocity body extending from ~ 8 to 10 km bsl.
- (2) Underlying the volcanically active sector of La Palma is a spatially limited by an anomaly with high Vp/Vs>2 and low velocities with negative dVp and dVs of more than 10% extending from the surface to ~ 3 km bsl. This structure has previously been identified as a low-resistivity hydrothermal zone¹⁹.
- (3) The third structure, characterised by high *Vp*, very low *Vs* with the magnitude of more than 10%, and high *Vp/Vs* > 2.05, extends between 7 and 25 km b.s.l. beneath the volcanically active sector of La Palma and represents partially molten material pooled at the base of oceanic crust. Based on our tomographic images, we estimate the volume of this magma-filled rock volume to be around 400 km³, dwarfing the other structures resolved by tomography. The calculation is a conservative estimate based on a simple geometric approximation of the high *Vp/Vs* ratio beneath the Moho. We have not considered the entire low velocity region for this estimate, but only the area covered by iso-lines larger than 1.98, as represented in Fig. 5b. In addition, the upward bending of the Moho seems to indicate that the formation of magma chambers in this same position occurred repeatedly during geological times, leading to a permanent modification of the Moho shape.

Based on these findings, we developed a scenario of the ongoing volcanic activity on La Palma, which is schematically demonstrated in Fig. 8.

(1) For ~2 million years, repeated accumulations of magma³¹ have deformed the base of the oceanic crust beneath La Palma, as evidenced by upward displacement of the Moho and the shape of tomographic struc-

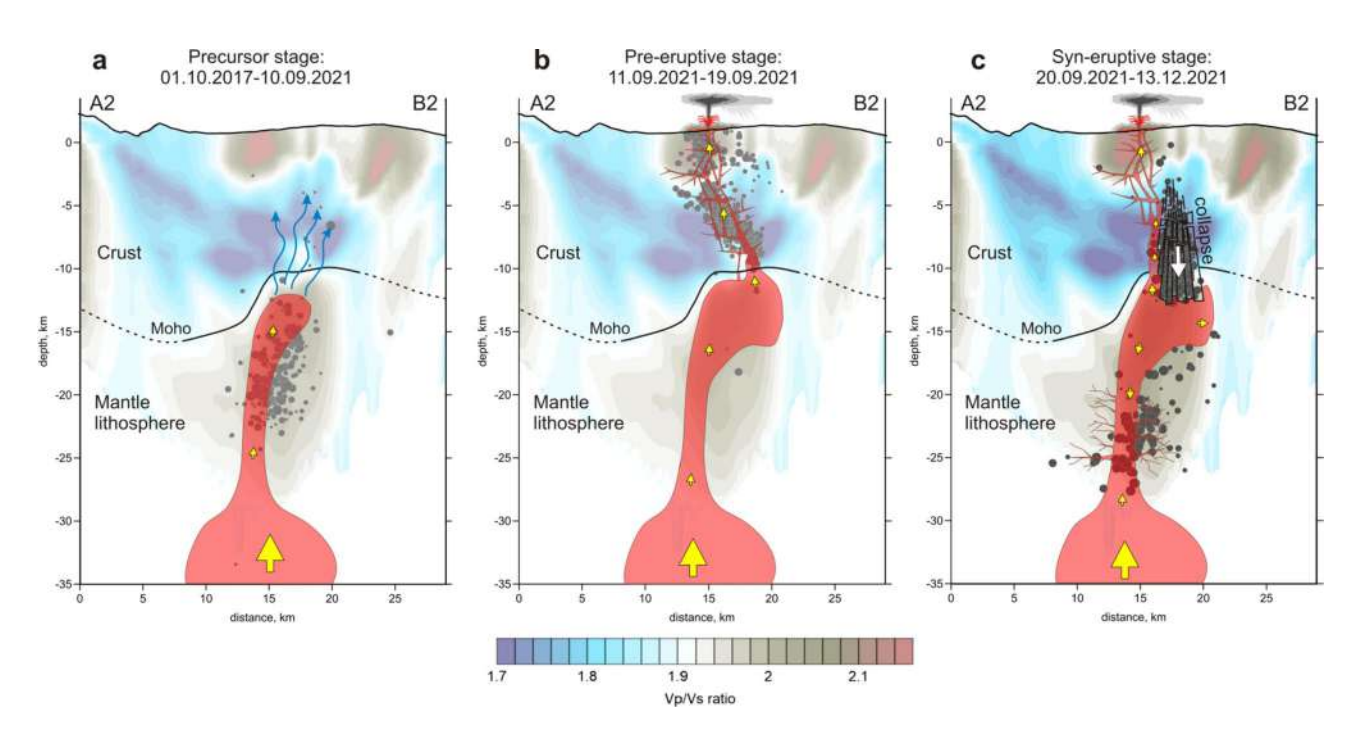


Figure 8. A sketch of the eruptive process preceding and accompanying the 2021 La Palma eruption. Background is the distribution of the Vp/Vs ratio in vertical section A2–B2 in the SSE-NNW direction, same as shown in Fig. 3. Dots are the projections of the event hypocenters in the corresponding time intervals at distances of less than 0.6 km; their size represent the magnitude. (a) Precursor stage. (b) Pre-eruptive stage. (c) Syn-eruptive stage. More description is presented in the main paper.

tures. Between October 2017 and August 2021, at least 9 earthquake swarms (producing \sim 700 well-located earthquakes) recorded magma injections from the mantle to the base of the oceanic crust beneath Cumbre Vieja volcano (the locus of all historical eruptions, including the present activity), causing the accumulation of a large magma-filled rock volume (Fig. 8a). This process, although likely continuous, did not cause significant stress changes, as evidenced by the sporadic and low-magnitude seismicity (Ml < 2.0). Initial earthquakes delineate the upper limit of the reservoir (i.e., the Moho or lower limit of consolidated oceanic crust). The foci of later precursory events trace fluid migration towards the surface and the exchange of stress with consolidated oceanic crust in the months before the eruption (Figs. 8a and S1 of Supplementary).

- During the precursory phase (October 2017—August 2021), the seismicity was mostly grouped into shortlived seismic swarms (Fig. 2). Earthquake hypocentres were mostly located in the depth range 10-25 km and magnitudes were generally lower than 2. After a month of seismic quiescence, in the 7 days before eruption onset (approximately at 14:00 UTC on 19 September), we observe rapid upward migration of the pre-eruptive seismicity indicating magma ascent from 10 km bsl (i.e., the base of the Moho) to the surface along a zone of structural weakness delineated by a low velocity tomographic anomaly associated with seismicity that occurred a few months earlier (Figs. 8b and S2 of Supplementary). For the first 3 km, this low-velocity anomaly is vertical, but close to the surface it follows a NNW-SSE trend and dips ~ 30 degrees towards the current eruptive centre. The migration of seismicity in the shallow crust follows the boundary between consolidated oceanic crust and the hydrothermally altered zone. Despite the highly fractured and brittle nature of the hydrothermal zone, which theoretically offers low resistance to magma ascent, we hypothesise that the contact zone must present even lower mechanical resistance, which is consistent with the small magnitudes of earthquakes in a few days before the eruption that started to increase only a few hours prior to the opening of the vent (Fig. 7a). Similar associations of active volcanic vents with the contact zones between high and low seismic velocities are observed in many cases, such as Mount Saint Helens³², Tolbachik³³ and Colima³⁴, among other examples.
- (3) Seismicity during the first few days of eruption was characterised by energetic volcanic tremor (Figure S7). However, on 29 September, 10 days after eruption onset, an intense seismic swarm (in which most events had magnitudes of Ml > 3.0) occurred along the contact between the magmatic body and lower limit of the oceanic crust (~10 km). This seismicity, which is ongoing just until reaching the current period of eruptive calm on December 13, 2021, can be explained by the collapse of brittle crustal material above the reservoir owing to the continuous extraction of magma to the surface as schematically shown in Fig. 8c. In addition, since early October, a new earthquake cluster (Ml > 3.0) has been observed at ~17–30 km depth (Fig. 2d). This deeper seismicity, which shows no preferential lineation or temporal migration, includes the highest earthquake magnitudes recorded during the eruption (up to Ml = 4.3) and is located above a deep uppermantle magma reservoir (close to the lithosphere base), as reported by previous studies^{35,36}. We attribute this cluster to two possible explanations.

- (4) Magma compression caused by the collapse of crustal material had a piston effect; increased pressure at 12-15 km pushed magma both upwards and downwards (Fig. 8c). The opposing force of magma ascending from the mantle created excessive pressure in the conduit between the upper and lower reservoirs, which triggered fracturing of rocks around the conduit. We do not know any case where exactly the same mechanism occurred. In some way, it looks similar to the case of Katmai-Novarupta, where the collapse of the crater in Katmai pushed the magma in the reservoir and triggered a strong explosive eruption of Novarupta in June 1912³⁷. The existing estimates of focal mechanisms of events during this period show very complex and variable patterns that might take place in the case of an internal collapse presuming the existence of all types of displacements.
- Alternatively, by invoking stress propagation model similar to that of the 2011-2014 eruption of neighbouring El Hierro³⁸, this activity could record the collapse of magmatic reservoir owing to magma withdrawal and corresponding depressurization. It is interesting to note that earthquakes hypocentres during the precursory phase were mostly located within the depth range delimited by the two syn-eruptive clusters. This suggests that precursory seismicity was related to magma-transfer episodes which led to a progressive filling of the intermediate magma chamber, until the onset of the eruption. During the eruption the only significant occurrence of earthquakes within this depth range was observed at the end of November (Fig. 2).

Conclusions

Our tomographic images mark a milestone in the field of volcano seismology, and provide valuable insight into the short-term evolution of a magma plumbing system from the upper mantle to the surface. In particular, given the large size of the magma reservoir that feeds the volcanic eruption it is not possible to discard this magmatic system could cause future new volcanic eruptions on the Island of La Palma.

Among the lessons learned, of relevance for volcano monitoring are:

- 1. The pre-eruptive stage can be faster than expected. In the case of Cumbre Vieja 2021 eruption, it was about 7 days. Furthermore, we observe the rapid ascent of the hypocenters in the very few hours preceding the eruption (Fig. 2). Therefore, we conclude that the decision-making process during a volcanic emergency should not rely on more or less constant trends: sudden changes can occur any time.
- 2. The 3D relocation of hypocenters, is fundamental for understanding precisely the evolution of the seismicity and therefore the dynamics of the magmatic system in near-real-time. A tomographic model, if not already existing, can be obtained quickly, just few days after the onset of a volcanic unrest, if a sufficient number (>500) of earthquakes is available.
- Seismic tomography can identify crustal structure relevant for the propagation of magmatic intrusions. Hence, it provides a valuable tool for volcanic hazard studies.

Data availability

The seismic catalogue of IGN is publicly available at: https://www.ign.es/web/ign/portal/sis-catalogo-terremotos. The seismic catalogue of INVOLCAN is available under request to Dr. Luca D'Auria (ldauria@iter.es). The LOTOS code is publicly available at: www.ivan-art.com/science/LOTOS. An online version of the code with the La Palma dataset is available in: Koulakov Ivan. (2022). Data and program codes to reproduce the results of seismic tomography for La Palma Island [Data set]. Zenodo. https://doi.org/10.5281/zenodo.6589367. The digital elevation model used in all figures and historical lava flows of Figs. 1 and 3 were downloaded from the public graphic repository of GrafCan (www.grafcan.es). The 2021 lava flow was downloaded from the European agency Copernicus Emergency Management Service (httts://emergency.copernicus.eu/mapping/list-of-components/ EMSR546). The software used to generate Fig. 1, Figs. S1, S2 and S3 was QGIS 3.22 (https://www.qgis.org). The software used to generate Figs. 3, 4 and 6, Figs. S4, S5 and S6 is the LOTOS code.

Received: 7 January 2022; Accepted: 4 October 2022 Published online: 21 October 2022

References

- 1. Civico, R. et al. High-resolution digital surface model of the 2021 eruption deposit of Cumbre Vieja volcano, La Palma, Spain. Sci. Data 9(1), 1-7 (2022).
- 2. Ancochea, E. et al. Constructive and destructive episodes in the building of a young oceanic island, La Palma, Canary Islands, and genesis of the Caldera de Taburiente. J. Volc. Geotherm. Res. 60(3-4), 243-262 (1994).
- Romero, J. E. et al. The initial phase of the 2021 Cumbre Vieja ridge eruption (Canary Islands): products and dynamics controlling edifice growth and collapse. J. Volcanol. Geotherm. Res. 431, 107642 (2022).
- Lees, J. M. Seismic tomography of magmatic systems. J. Volcanol. Geotherm. Res. 167(1-4), 37–56 (2007).
 Koulakov, I. & Shapiro, N. in Encyclopedia of Earthquake Engineering 3117–3134 (Springer, Dordrecht, 2015).
- 6. Duggen, S. et al. Flow of Canary mantle plume material through a subcontinental lithospheric corridor beneath Africa to the Mediterranean. Geology 37, 283–286 (2009).
- Van den Bogaard, P. The origin of the canary island seamount province-new ages of old seamounts. Sci. Rep. 3(1), 1–7 (2013).
- 8. Lodge, A., Nippress, S. E. J., Rietbrock, A., García-Yeguas, A. & İbáñez, J. M. Evidence for magmatic underplating and partial melt beneath the Canary Islands derived using teleseismic receiver functions. Phys. Earth Planet. Int. 212, 44-54 (2012)
- 9. Martinez-Arevalo, C., de Lis Mancilla, F., Helffrich, G. & Garcia, A. Seismic evidence of a regional sublithospheric low velocity layer beneath the Canary Islands. Tectonophysics 608, 586-599 (2013).
- 10. García-Yeguas, A. et al. Seismic tomography model reveals mantle magma sources of recent volcanic activity at El Hierro Island (Canary Islands, Spain). Geophys. J. Int. 199(3), 1739-1750 (2014).

- 11. Zandomeneghi, D. et al. Crustal structure of Deception Island volcano from P wave seismic tomography: Tectonic and volcanic implications. *J. Geophys. Rees. Solid Earth* **114**(B6), (2009).
- 12. Luzón, F., Almendros, J. & García-Jerez, A. Shallow structure of deception island, Antarctica, from correlations of ambient seismic noise on a set of dense seismic arrays. *Geophys. J. Int.* 185(2), 737–748. https://doi.org/10.1111/j.1365-246x.2011.04962.x (2011).
- 13. Prudencio, J. et al. The 3D attenuation structure of Deception Island (Antarctica). Surv. Geophys. 36(3), 371-390 (2015).
- Bushenkova, N. et al. Tomographic images of magma chambers beneath the Avacha and Koryaksky volcanoes in Kamchatka. J. Geophys. Res. Solid Earth 124(9), 9694–9713 (2019).
- Díaz-Moreno, A. et al. New insights on Mt. Etna's crust and relationship with the regional tectonic framework from joint active and passive P-wave seismic tomography. Surv. Geophys. 39(1), 57–97. https://doi.org/10.1007/s10712-017-9425-3 (2018).
- Castro-Melgar, I., Prudencio, J., Del Pezzo, E., Giampiccolo, E. & Ibáñez, J. M. Shallow magma storage beneath Mt. Etna: Evidence from new attenuation tomography and existing velocity models. J. Geophys. Res. Solid Earth 126, 7. https://doi.org/10.1029/2021J B022094 (2021).
- García-Yeguas, A., Koulakov, I., Ibáñez, J. M. & Rietbrock, A. High resolution 3D P wave velocity structure beneath Tenerife Island (Canary Islands, Spain) based on tomographic inversion of active-source data. J. Geophys. Res. 117, B09309. https://doi.org/10. 1029/2011/B008970 (2012).
- 18. Prudencio, J. et al. 3D attenuation tomography of the volcanic island of Tenerife (Canary Islands). Surv. Geophys. 36(5), 693–716. https://doi.org/10.1007/s10712-015-9333-3 (2015).
- 19. Di Paolo, F. et al. La Palma island (Spain) geothermal system revealed by 3D magnetotelluric data inversion. Sci. Rep. 10(1), 1-8 (2020).
- Koulakov, I. LOTOS code for local earthquake tomographic inversion: Benchmarks for testing tomographic algorithms. Bull. Seismol. Soc. Am. 99(1), 194–214 (2009).
- Koulakov, I., Komzeleva, V., Smirnov, S. Z. & Bortnikova, S. B. Magma-fluid interactions beneath Akutan Volcano in the Aleutian Arc based on the results of local earthquake tomography. *J. Geophys. Res. Solid Earth* 126(3), e2020JB021192 (2021).
- 22. Koulakov, I. *et al*. Anatomy of the Bezymianny volcano merely before an explosive eruption on 20.12.2017. *Sci. Rep.* **11**(1), 1–12
- Kuznetsov, P. Y. et al. Structure of volatile conduits beneath Gorely Volcano (Kamchatka) revealed by local earthquake tomography. Geosciences 7(4), 111 (2017).
- 24. Paige, C. C. & Saunders, M. A. LSQR: An algorithm for sparse linear equations and sparse least squares. *ACM Trans. Math. Soft.*
- (TOMS) 8(1), 43–71 (1982).
 25. Nolet, G. Seismic wave propagation and seismic tomography. In Seismic tomography (ed. Nolet, G.) 1–23 (Springer, Dordrecht,
- 1987). 26. Fernández, J., Gonzalez, P. J., Camacho, A. G., Rodriguez-Velasco, G., Arjona, A., Pallero, J. L. G., et al. in 2008 Second Workshop
- on Use of Remote Sensing Techniques for Monitoring Volcanoes and Seismogenic Areas 1–5. (IEEE, 2008, November).

 27. González, P. J., Tiampo, K. F., Camacho, A. G. & Fernández, J. Shallow flank deformation at Cumbre Vieja volcano (Canary Islands):
- Implications on the stability of steep-sided volcano flanks at oceanic islands. *Earth Planet Sci. Lett.* **297**(3–4), 545–557 (2010). 28. Prieto, J. F. *et al.* Geodetic and structural research in La Palma, Canary Islands, Spain: 1992–2007 results. *Pure Appl. Geophys.* **166**(8), 1461–1484 (2009).
- Benioff, H. Earthquakes and rock creep:(Part I: Creep characteristics of rocks and the origin of aftershocks). Bull. Seismol. Soc. Am. 41(1), 31-62 (1951).
- van der Meijde, M., van der Lee, S. & Giardini, D. Giardini Crustal structure beneath broad-band seismic stations in the Mediterranean region. *Geophys. J. Int.* 152, 729–739 (2003).
- 31. Klügel, A., Hansteen, T. H. & Schmincke, H. U. Rates of magma ascent and depths of magma reservoirs beneath La Palma (Canary Islands). *Terra Nova* 9(3), 117–121 (1997).
- Waite, G. P. & Moran, S. C. VP Structure of Mount St. Helens, Washington, USA, imaged with local earthquake tomography. J. Volcanol. Geotherm. Res. 182(1–2), 113–122 (2009).
- 33. Koulakov, I. et al. Three different types of plumbing system beneath the neighboring active volcanoes of Tolbachik, Bezymianny, and Klyuchevskoy in Kamchatka. J. Geophys. Res. Solid Earth 122, 3852–3874. https://doi.org/10.1002/2017JB014082 (2017).
- Sychev, I. V. et al. Fault-associated magma conduits beneath the Colima Volcanic Complex revealed by seismic velocity and attenuation tomography studies. J. Geophys. Res. Solid Earth 124, 8908–8923. https://doi.org/10.1029/2019JB017449 (2019).
- 35. Klügel, A., Schmincke, H.-U., White, J. & Hoernle, K. A. Chronology and volcanology of the 1949 multi-vent rift-zone eruption on La Palma (Canary islands). *J. Volcanol. Geotherm. Res.* **94**(1–4), 267–282 (1999).
- 36. Klügel, A., Hansteen, T. H. & Galipp, K. Magma storage and underplating beneath Cumbre Vieja volcano, la Palma (Canary Islands). Earth Planet. Sci. Lett. 236(1-2), 211-226 (2005).
- Eichelberger, J. C. & Izbekov, P. E. Eruption of andesite triggered by dyke injection: contrasting cases at Karymsky Volcano, Kamchatka and Mt Katmai, Alaska. Philos. Trans. R. Soc. Lond. Ser. A Math. Phys. Eng. Sci. 358(1770), 1465–1485 (2000).
- Díaz-Moreno, A. et al. Seismic hydraulic fracture migration originated by successive deep magma pulses: The 2011–2013 seismic series associated to the volcanic activity of El Hierro Island. J. Geophys. Res. Solid Earth 120(11), 7749–7770. https://doi.org/10.1002/2015JB012249 (2015).

Acknowledgements

JP and JMI were partially supported by the FEMALE project of the Spanish Government (Grant No. PID2019-106260GB-I00). IK was supported by the Russian Science Foundation (Grant No. 20-17-00075). The INVOLCAN team was supported by the projects VOLRISKMAC II (MAC2/3.5b/328), co-financed by the EC Cooperation Transnational Program MAC 2014-2020, and "Cumbre Vieja Emergencia", financed by the Spanish Ministry of Science and Innovation. English language editing was performed by Tornillo Scientific, UK.

Author contributions

L.D. Compilation of seismic databases; seismic data acquisition; figure and map creation; discussion of final models; manuscript writing. I.K. Seismic tomography; figure creation; discussion of final models; manuscript writing. J.P. Figure creation; discussion of final models; manuscript writing. I.C.-P. Compilation of seismic databases; seismic data acquisition; figure creation; manuscript writing. J.M.I. Coordinator of the research team; discussion of final models; manuscript writing. J.B. Seismic data acquisition. R.G.-H. Seismic data acquisition. D.M.V.D. Seismic data acquisition. G.D.P. Seismic data acquisition. M.P. Seismic data acquisition. V.O. Seismic data acquisition. P.H. Coordination of funds to acquire seismic databases; coordinators of the INVOLCAN working team.

Competing interests

The authors declare no competing interests.

Additional information

Supplementary Information The online version contains supplementary material available at https://doi.org/10.1038/s41598-022-21818-9.

Correspondence and requests for materials should be addressed to J.M.I.

Reprints and permissions information is available at www.nature.com/reprints.

Publisher's note Springer Nature remains neutral with regard to jurisdictional claims in published maps and institutional affiliations.

Open Access This article is licensed under a Creative Commons Attribution 4.0 International License, which permits use, sharing, adaptation, distribution and reproduction in any medium or format, as long as you give appropriate credit to the original author(s) and the source, provide a link to the Creative Commons licence, and indicate if changes were made. The images or other third party material in this article are included in the article's Creative Commons licence, unless indicated otherwise in a credit line to the material. If material is not included in the article's Creative Commons licence and your intended use is not permitted by statutory regulation or exceeds the permitted use, you will need to obtain permission directly from the copyright holder. To view a copy of this licence, visit http://creativecommons.org/licenses/by/4.0/.

© The Author(s) 2022

scientific reports



OPEN Spatio-temporal velocity variations observed during the pre-eruptive episode of La Palma 2021 eruption inferred from ambient noise interferometry

Iván Cabrera-Pérez^{1⊠}, Luca D'Auria^{1,2}, Jean Soubestre^{3,4}, Monika Przeor¹, José Barrancos², Rubén García-Hernández¹, Jesús M. Ibáñez^{8,9}, Ivan Koulakov^{5,6,7}, David Martínez van Dorth¹, Víctor Ortega¹, Germán D. Padilla², Takeshi Sagiya¹⁰ & Nemesio Pérez^{1,2}

On Sept. 19th, 2021, a volcanic eruption began on the island of La Palma (Canary Islands, Spain). The pre-eruptive episode was characterized by seismicity and ground deformation that started only 9.5 days before the eruption. In this study, we applied seismic interferometry to the data recorded by six broadband seismic stations, allowing us to estimate velocity variations during the weeks preceding the eruption. About 9.5 days before the eruption, we observed a reduction in the seismic velocities is registered next to the eruptive centers that opened later. Furthermore, this zone overlaps with the epicenters of a cluster of volcano-tectonic earthquakes located at shallow depth (< 4 km) and detached from the main cluster of deeper seismicity. We interpret the decrease in seismic velocities and the occurrence of such a shallow earthquake cluster as the effect of hydrothermal fluid released by the ascending magma batch and reaching the surface faster than the magma itself.

La Palma is one of the youngest islands among the volcanic archipelago of Canary Islands (Spain). On Sept. 19th, 2021, a volcanic eruption began on the island, which had a significant social and scientific impact. This eruption also had a catastrophic economic impact generating significant economic losses. The eruptive dynamics were mainly characterized by effusive phases interspersed with more explosive activity, during which eruptive columns dispersed ashes up to tens of kilometers away from the volcano.

The precursory phase of this eruption was characterized by intense volcano-tectonic seismicity, with magnitudes exceeding 4 M_1 and hypocenters located at a depth of less than 10 km, together with ground deformation up to 16 cm on the vertical component of GPS stations. This phase lasted about a week and caught by surprise the scientific community for its short duration. However, given the large amount of scientific instrumentation (seismometers, GPS, etc.) operated by the Instituto Volcanológico de Canarias (INVOLCAN) and other scientific institutions, the entire pre-eruptive episode was accurately monitored and the civil protection authorities were notified in near real-time about the development of the volcanic unrest.

This work aims to detect seismic velocity variations during the pre-eruptive phase through seismic ambient noise interferometry and to compare these changes with the local seismicity detected before the eruption (D'Auria et al.1) and ground deformation. Seismic interferometry has been applied satisfactorily in different fields such as groundwater level^{2,3}, fault zones⁴, the lunar environment⁵, geothermal exploration⁶, landslides monitoring⁷

¹Instituto Volcanológico de Canarias (INVOLCAN), Granadilla de Abona, 38600 Tenerife, Canary Islands, Spain. ²Instituto Tecnológico y de Energías Renovables (ITER), Granadilla de Abona, 38600 Tenerife, Canary Islands, Spain. ³Univ. Grenoble Alpes, Univ. Savoie Mont Blanc, CNRS, IRD, Univ. Gustave Eiffel, ISTerre, 38000 Grenoble, France. 4Icelandic Meteorological Office, Reykjavík, Iceland. 5Trofimuk Institute of Petroleum Geology and Geophysics SB RAS, Prospekt Koptyuga, 3, 630090 Novosibirsk, Russia. ⁶Novosibirsk State University, Pirogova 2, 630090 Novosibirsk, Russia. ⁷Institute of the Earth's Crust SB RAS, Lermontova 128, Irkutsk, Russia. ⁸Department of Theoretical Physics and Cosmos, Science Faculty, University of Granada, Avd. Fuenteneuevas/n, 18071 Granada, Spain. ⁹Andalusian Institute of Geophysiscs, University of Granada, Campus de Cartuja, C/Profesor Clavera 12, 18071 Granada, Spain. ¹¹Disaster Mitigation Research Center, Nagoya University, Nagoya, Japan. [™]email: ivan.cabrera.perez1@gmail.com

and volcano monitoring. The first application of ambient noise interferometry to a volcano was realized by Sens-Schönfelder and Wegler⁵, who observed velocity variations in Merapi volcano produced by changes in hydrological conditions. After this study, several investigations highlighted the effectiveness of the ambient noise interferometry method to monitor volcanoes⁸⁻¹⁴. The velocity variations observed before the eruptions generally consist of a reduction in the seismic velocity caused by the effect of the dilatation or compression of a part of the edifice resulting from the dynamics of the magma chamber^{8,9}, pressurization of a magma pocket^{10,14}, intrusion of magma^{11,15}, topographic changes produced by a caldera collapse¹² or to the effect of hydrothermal fluids^{13,16}.

Geological settings and the recent eruption

La Palma is located in the extreme NW of the Canary Islands. It is the third smallest island of the archipelago and one of the most active from a volcanological point of view, with eight historical eruptions in less than 600 years¹⁷. It is composed of two main geological domains: the Taburiente Domain and the Dorsal Domain (Fig. 1).

The Taburiente Domain is the oldest domain. It is located in the northern part of the island and it is composed of the superposition of stratovolcanoes with a semicircular base and a large depression in the central part (Caldera de Taburiente) (Fig. 1). This domain consisted of a submarine phase (4 Ma), represented by the Bassal

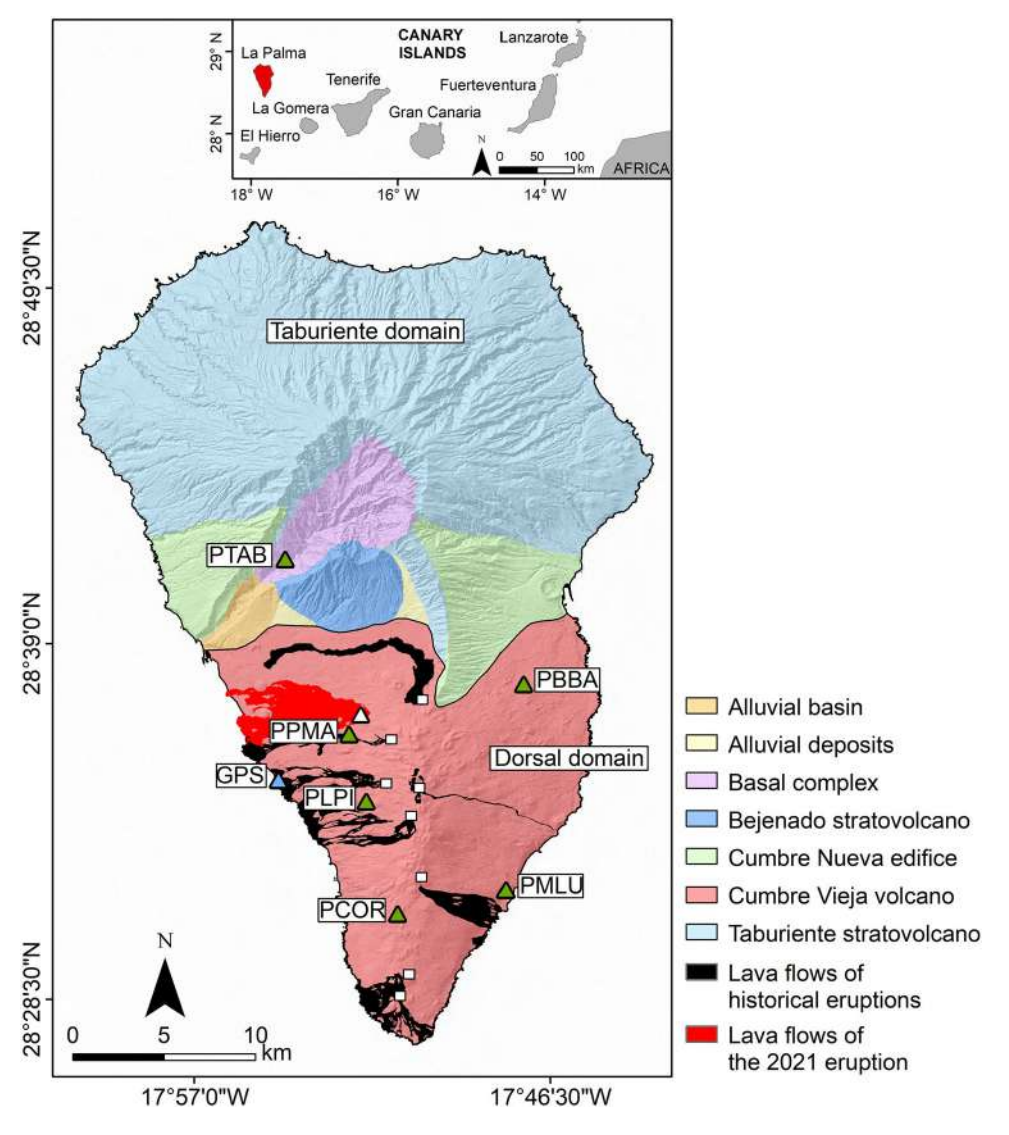


Figure 1. Geological map of La Palma island (modified from Padrón et al.⁴³). The white triangle represents the location of the 2021 eruptive vent and white squares represent the location of historical eruptive vents. The blue and green triangles represent the location of the GPS ARID and seismic stations, respectively. The digital elevation model and historical lava flows were downloaded from the public graphic repository of GrafCan (http://www.grafcan.es). The 2021 lava flow was downloaded from the European agency Copernicus Emergency Management Service (https://emergency.copernicus.eu/mapping/list-of-components/EMSR546). The software used to generate this figure was QGIS 3.22 (https://www.qgis.org).

complex, and a subaerial phase, which originated the big insular edifices conformed by Taburiente (from 1.77 to 1.20 Ma) and Bejenado (from 0.56 to 0.49 Ma) stratovolcanoes¹⁸.

The Dorsal Domain is more recent and currently volcanically active. It is located in the southern part of the island, south of the Taburiente Domain. This volcanic ridge has a North–South orientation and an elongated shape. It is divided into two sectors: in the northern sector is the Cumbre Nueva with an arched shape, while in the southern sector is the Cumbre Vieja with a North–South direction and an extension of 21.5 km. Its formation began 0.123 Ma ago and continues with a high volcanic activity until today¹⁸. This domain hosted seven historical eruptions, including the most recent 2021 eruption (Fig. 1).

The last 2021 eruption of La Palma was announced in 2017, by the first appearance of seismicity¹⁹. The background seismicity of the island was practically non-existent during the last decades, as reflected in the seismic catalogues of the Instituto Geográfico Nacional (IGN). Conversely, between 2017 and 2021, nine seismic swarms took place on the island, with approximately 700 earthquakes located beneath Cumbre Vieja sector at depths between 10 and 20 km. This seismicity was located under the Cumbre Vieja volcano. The 2021 pre-eruptive unrest started on Sept. 11st, only 9.5 days before the eruption (Fig. 3C). During this episode, seismicity quickly migrated from a depth of 10 km to the surface, following the ascending path of the magma¹. On Sept. 15th, we observed earthquakes located at very shallow depth (<4 km) and detached from the main seismicity cluster which was located at depths of 6–8 km (Fig. 3C). A very energetic co-eruptive volcanic tremor also began with the eruption onset on Sept. 19th.

Methodology and data processing

The seismic data used in this work come from the Red Sísmica Canaria (C7) operated by INVOLCAN (Instituto Volcanológico de Canarias, 2016). We used recordings from six broadband seismic stations (Nanometrics © Trillium Compact 120 s and Güralp ©, 3ESPC Series) with a sampling rate of 100 Hz (Fig. 1). The time range used for the analysis covers the interval from Aug. 1st to Sept. 25th, 2021. We analysed the data using the MSNoise python package to estimate relative velocity variations. This software has been applied successfully in different studies of ambient noise interferometry $^{14,20-23}$.

Estimation of the relative velocity variations. The procedure to estimate relative velocity variations (dv/v) has been carried out using the following workflow. Recorded data were downsampled to 20 Hz, bandpass filtered in the 0.1–1.0 Hz frequency range, and pre-processed applying spectral whitening followed by one-bit temporal normalization²⁴. Then, we computed the cross-correlation of ambient noise recordings among pairs of stations to obtain the empirical seismic Green's Functions (GFs), using the vertical–vertical (ZZ) components. To estimate dv/v it is necessary to compare the coda of the obtained GFs with a Reference Green's Function (RGF), which has been computed stacking over the first twenty days of the data in our case (from Aug. 1st to 20th). Assuming a relative velocity variation dv/v in a homogeneous space, one can prove that²⁵:

$$\frac{dv}{v} = -\frac{d\tau}{\tau},\tag{1}$$

where $d\tau$ represents the measured time delay and τ the traveltime. Actually, there are two methods to extract dv/v from the empirical GFs: the stretching technique (Sens-Schönfelder and Wegler²⁵) and the moving window cross-spectral analysis (MWCSA)^{26–28}. In both methods, the dv/v is estimated using the GFs part corresponding to the scattered wavefield at different time lags. Duputel et al.⁹ showed that both methods provide similar results and therefore concluded that both approaches are equivalent. However, Clarke et al.²⁹ demonstrated that the MWCSA method is more efficient to detect very small dv/v. For this reason, in this study, we use the MWCSA method. The error of this estimation can be determined using the squared misfit of the modeled slope of the linear regression of the time-delay ($d\tau$) measurements²⁹.

For each day, we computed cross-correlations on two minute-long windows, which were subsequently stacked over the previous 5 days. The use of shorter stacking windows led to excessive uncertainty over the retrieved dv/v values. Then, we compared GFs with the RGF using the aforementioned MWCSA method on five-second-long windows and a step of two-second-long over the whole 240 s ($-120 \text{ s} \div 120 \text{ s}$) of the cross-correlation functions to estimate a value of dv/v. This window length was selected as being the best compromise between resolution and uncertainty. Figure S1 in the supplementary materials shows three examples of interferograms for station pairs PLPI-PPMA, PLPI-PCOR and PPMA-PCOR (Fig. 1) within the 0.1-1.0 Hz range. We can observe that after the start of the eruption, the GFs show an erratic shape, where the causal and acausal parts are not correctly defined. This is a consequence of the volcanic tremor, which started just at the beginning of the eruption. The tremor acts as a source of contamination due to a persistent coherent signal with a localized source in the 0.3-4.0 Hz frequency range, which encompasses the frequency range of our study (see Fig. S2 in the supplementary materials). For this reason, we decided to limit our interpretation of dv/v values until the start of the eruption. All the daily dv/v for all the pairs of stations are shown in Fig. S3 in the supplementary materials.

Spatial distribution of dv/v. In order to determine the spatial distributions of dv/v we applied a linear inversion technique. We used the analytical approach of Del Pezzo and Ibáñez³⁰ to calculate the sensitivity kernels for the propagation of scattered waves between each station pair:

$$K_{num}(x, y, x_i, y_i, x_j, y_j) = \frac{1}{6\pi (D\delta)^2} exp \left(-\left(\frac{\left(x - \frac{x_i + x_j}{2}\right)^2}{2(\delta D)^2} + \frac{\left(y - \frac{y_i + y_j}{2}\right)^2}{2(\delta D)^2} \right) \right)$$

$$+ \frac{1}{2\pi (\delta D)^2} exp \left(-\left(\frac{(x - x_i)^2}{2(\delta D)^2} + \frac{(y - y_i)^2}{2(\delta D)^2} \right) \right)$$

$$+ \frac{1}{2\pi (\delta D)^2} exp \left(-\left(\frac{(x - x_j)^2}{2(\delta D)^2} + \frac{(y - y_j)^2}{2(\delta D)^2} \right) \right),$$
(2)

where (x_i, y_i) and (x_j, y_j) represent the coordinates of the (virtual) sources and receivers, δ represents the spatial aperture of the weighting function and D represents the source-receiver distance. Figure S4 in the supplementary materials shows an example of sensitivity kernel for the station pair PCOR-PLPI (Fig. 1). Del Pezzo and Ibáñez³⁰ used this kind of kernel for imaging the spatial distribution of the intrinsic attenuation parameter Q. However, this formulation can be useful for imaging dv/v as well, being both quantities related to the scattered wavefield. The kernel of Del Pezzo and Ibáñez³⁰ assumes diffusion as a scattering regime. Since we computed the dv/v overtime windows of 120 s, which is many times the ballistic travel-time for our network, we conclude that this assumption is correct in our case. The authors suggested using a value of 0.2 for the parameter δ . Using this kernel we can express the observed dv/v for a station pair (s_i, s_i) as:

$$\frac{dv}{v}(s_i, s_j) = n^{-1} \int \int K_{num}(x, y, x_i, y_i, x_j, y_j) \frac{dv}{v}(x, y) dxdy$$
(3)

with n being a normalization factor:

$$n = \int \int K_{num}(x, y, x_i, y_i, x_j, y_j) dx dy$$
 (4)

We discretize this forward problem by representing the continuous function dv/v as a mesh of 19×27 km regular tiles having a size of 1.4×1.8 km³¹. The supplementary materials show the ray path and the 2D kernel density map in Figs. S5 and S6, respectively. The resulting discrete inverse linear problem was solved using the Truncated Singular Value Decomposition, selecting the appropriate number of eigenvalues with the L-curve approach³².

Results

Figure 2A shows the daily seismic velocity variations corresponding to the median of all the station pairs (Fig. 2A, black line) and specific station pairs (Fig. 2A, coloured lines) from Aug. 1st to Sept. 25th. The median time series does not show significant velocity variations at the beginning, with mean values generally remaining within \pm 0.01% until Sept. 10th (Fig. 2A, black line). Since Sept. 10th, dv/v started decreasing evidently in the PCOR_PLPI pair, reaching a minimum of - 0.4% on Sept. 18th (Figs. 2A and 3A). Between Sept. 18th and 19th, the average dv/v attains a minimum with an average value of - 0.21% (Figs. 2A and 3A). We note that the days in which significant variations on the average dv/v are observed the error values are generally lower than 0.075% (color-coded in Figs. 2A and 3A).

Figure 4 shows the results of the spatial mapping of daily dv/v from Sept. 8th to 19th. The spatial distribution of dv/v between Sept. 8th and 9th shows low dv/v values in the eruption zone and in the eastern part of Cumbre Vieja (Fig. 4A and B). We consider these low dv/v values as artifacts produced during the inversion process because we don't have enough resolution to observe such minor anomalies. Similar anomalies considered as artifacts are observed in the month prior to the eruption (see Fig. S8 of supplementary materials). On Sept. 10th, we observe low dv/v values located in the southern part of the eruption site, with an average value of -0.059% (Fig. 4C). During this day, no seismicity was recorded and no deformation was observed (Figs. 2B and 3B). Between Sept. 11th and 14th, the dv/v values observed in this zone with the station pair PLPI-PCOR (Fig. 1) decreased, reaching -0.38% in Sept. 14th (Fig. 3A). During this period, a deep seismic swarm (> 4 km) was recorded and deformation began to occur (Figs. 2B and 3B). Between Sept. 15th and 16th, the average dv/v started to decrease, reaching -0.41% in some station pairs (Fig. 3A). We started recording shallow earthquakes (< 4 km) during these days, and the deformation continued increasing. On Sept. 17th, there was a generalized decrease of the dv/v values in most of the station pairs (Fig. 4J), with an average dv/v value of -0.148%. This generated a much larger anomaly distribution, encompassing most of the Cumbre Vieja volcanic complex. Between Sept. 18th and 19th, the dv/v values continued decreasing, reaching -0.43% in some station pairs (Fig. 3B).

Discussion and conclusion

The most important result of this work is the relevant decrease of dv/v observed 9.5 days before the eruption onset. This decrease started on Sept. 10th, the day before the onset of the seismicity. Between Sept. 10th and 14th, the dv/v continued decreasing. During this period, the deep seismicity (> 4 km) continued increasing and ground deformation started to be recorded on Sept. 14th. Then, on the 15th of September, the values of dv/v were still decreasing and a shallow seismicity (< 4 km) was observed (Fig. 3C). This seismicity was distributed between 1 and 5 km south of the eruptive center (Fig. 4). Between the 12th and 15th of September, we observed a velocity increase in the southeastern part of the island. The most likely explanation is that this increase in velocity is related to negative volumetric strain (compression) due to the ground deformation.

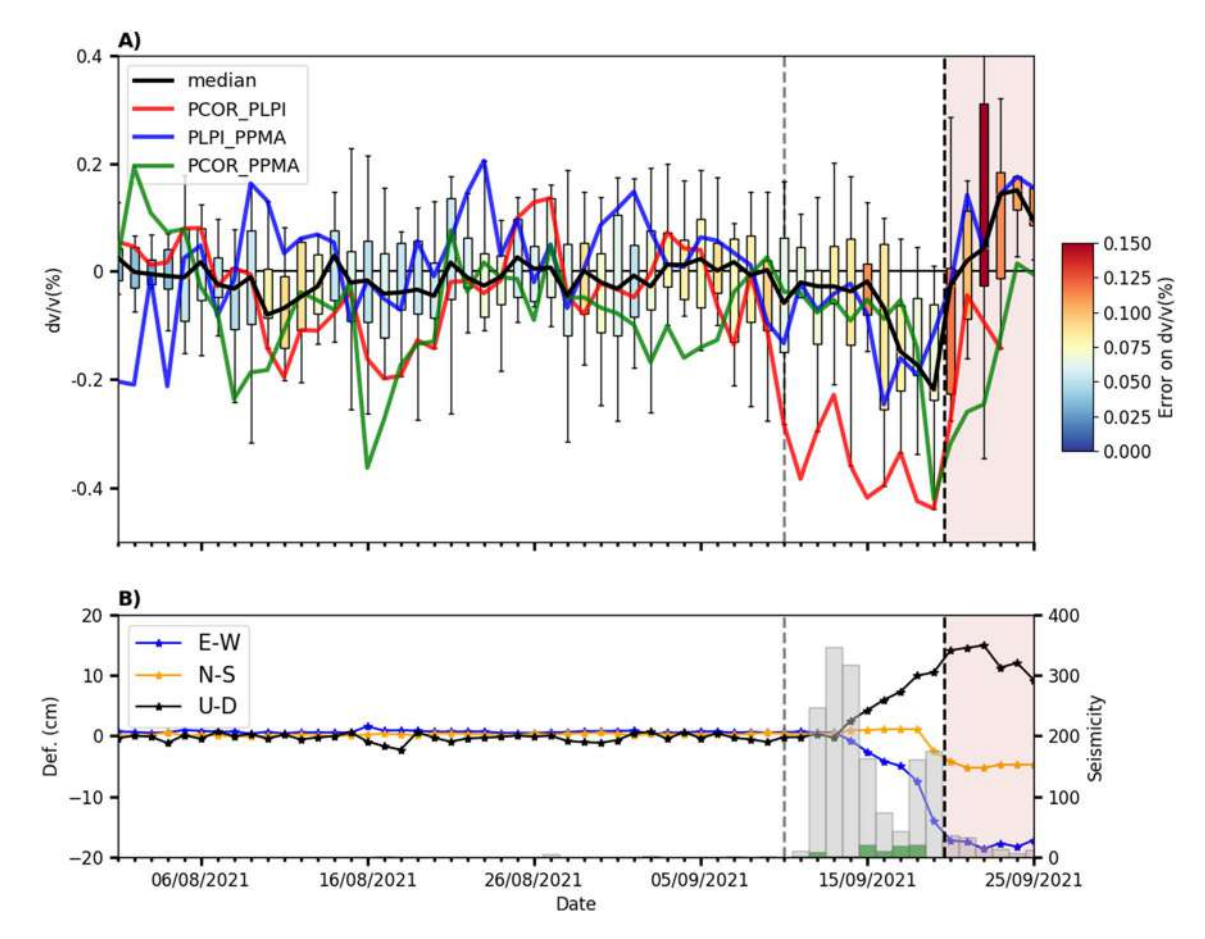


Figure 2. Comparison of daily dv/v with the seismicity and deformation produced during the pre-eruptive and eruptive periods (vertical black dashed line showing the eruption onset). The vertical gray dashed line represents Sept. 10th. (**A**) Statistical analysis of daily dv/v for all the station pairs (median, black line), together with some dv/v for specific station pairs (PCOR_PLPI: red line, PLPI_PPMA: blue line, PCOR_PPMA: green line). Each boxplot represents the minimum and maximum values of dv/v (lower and upper horizontal lines), its lower and upper quartiles (lower and upper box limits), and its median. The color of the boxplots represents the estimated error on dv/v. (**B**) Time series of GPS ARID deformation appear as blue, orange and black lines for the E-W, N-S and U-D components, respectively. The histogram bars indicate the seismicity possibly related to the fluid injection (green dots) and magmatic intrusion (black dots). The relative velocity variation curves were obtained using MSNoise software ¹⁹ (http://www.msnoise.org).

We exclude the stress/strain field variation in the volcanic edifice as a dominant mechanism to explain the observed decrease in dv/v, due to the lack of significant ground deformation between Sept. 10th and 14th. Actually, we observe that the station pair showing the most evident decrease (PCOR_PLPI) is located to the south of the area of the eruptive vent, where the highest ground deformation was observed³³ (Fig. 4). Furthermore, we discard the effect of ground shaking produced by earthquakes as a causative mechanism for the velocity drop, as the earthquakes that occurred during this period had a magnitude generally lower than $2.5\,\mathrm{M}_\mathrm{L}$ (see Fig. S7 of supplementary materials), their hypocenters were deeper than 5 km (Fig. 3C) and their frequency content was above the higher limit of 1 Hz considered for dv/v estimations (Fig. S2). Moreover, the most important velocity drop occurs a few kilometers to the south of the area of most intense seismicity (Fig. 4C-I). Another possible mechanism which can be invoked to justify the velocity drop is the magmatic intrusion itself, with the associated fracturing process. Again, we consider this mechanism unlikely before Sept. 19th since the hypocenter depths (Fig. 3C) clearly show that the magma reached shallow depths (<4 km) only the day before the eruption. Considering the velocity model of D'Auria et al. for the given range periods used in the analyses (1.0–10.0 s), the penetration depth of the Rayleigh waves is just a few kilometers (see Fig. S9 of supplementary materials). Therefore, we can exclude the direct involvement of magma in the process since, as also testified by the hypocenter depths (Fig. 3C), the magma reached the surface only on the day of the eruption (19th of Sept.). Moreover, this explanation is also not compatible with the fact that the most relevant velocity variations are located a few kilometers to the south of the eruptive vents (Fig. 4). However, the marked drop of dv/v observed on the day before the eruption could be related to the magmatic intrusion reaching the surface.

Thus, we consider that the observed velocity drop can be explained by the ascent of hydrothermal fluids towards the surface through areas of weakness, such as those imaged in the Vs model obtained by D'Auria et al. (Fig. 5) and the resistivity model of Di Paolo et al. (see Fig. 2C of Di Paolo et al. (34)). Both models show

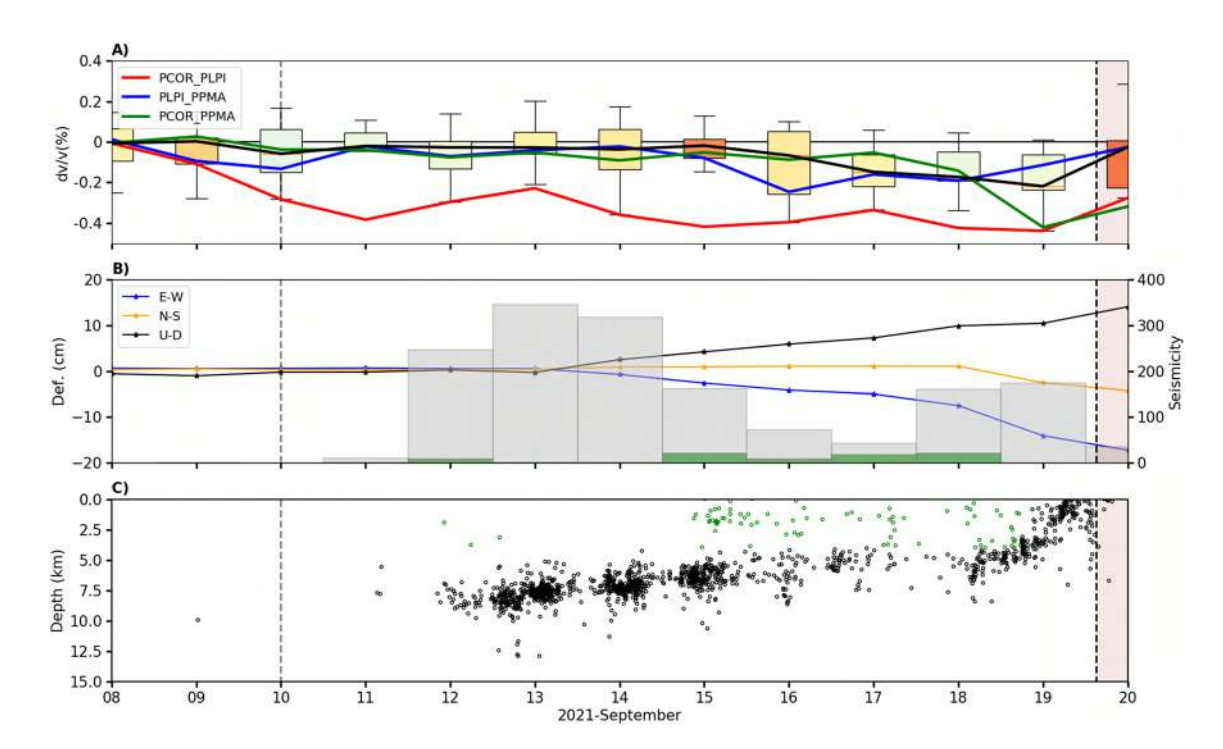


Figure 3. The temporal window of Fig. 2 has been zoomed in to highlight the comparison of dv/v with seismicity and deformation between Sept. 8th and 19th. This time window encompasses the pre-eruptive period. (**A**) Daily dv/v for all station pairs (median, black line) and specific station pairs (red, blue and green lines). (**B**) Deformation times series (GPS ARID) and seismicity histograms. (**C**) Depth distribution of the seismicity related to the fluid injection (green dots) and magmatic intrusion (black dots).

that this area could have hosted a hydrothermal reservoir prior to the eruption, at a depth of about 2 km b.s.l. The area affected by the decrease in dv/v is mostly located between the station PLPI and PCOR, and extends approximately between 2 and 12 km south of the eruptive center (Fig. 4), coinciding with the previously identified hydrothermal reservoir.

The source of these hydrothermal fluids can be ascribed to the ascending magma batch itself. The upward migration of hypocenters and the increase in the ground deformation clearly suggest that the magma was rising at least since Sept. 13th. The consequent depressurization of the magma must have produced the exsolution and the release of the dissolved gases, which migrated upward through fracture systems faster than the magma itself. Recent petrological observations realized by Pankhurst et al. 35 determined that the magmas emitted during the initial phase of the eruption were more hydrated, as evidenced by the presence of amphibolo³⁶. This mineral disappeared from the emitted products during the later phases of the eruption, testifying a lower water content. This supports our hypothesis about the pressurization of a shallow hydrothermal system by the injection of gases released by the ascending magma at depth. Note that a decrease in the average seismic velocities due to the input of hydrothermal fluids is already documented in the scientific literature 13,16,37. The same holds for the triggering of earthquakes caused by the injection of hydrothermal fluids³⁸. In Fig. 5 we represent a north–south cross-section of the S-wave tomographic velocity model from D'Auria et al. 1. It can be observed that the horizontal extent of a low-velocity anomaly (map on the left side of Fig. 5), which has been interpreted as a hydrothermal reservoir, coincides with the area of greater velocity decrease before the eruption (Fig. 4). From this figure, it is also clear that the hypocenters, which we attribute to the injection of hydrothermal fluids, are located on the northernmost side of this reservoir. Therefore we conclude that fluid-induced earthquakes are located only within the zone where hydrothermal fluids, exolving from the magma, are injected into the reservoir. This possibly occurs because of the stronger fluid pressure gradients associated with this area.

From Fig. 3C, we observe that the earthquakes (an therefore the magma) approach quickly the surface between 18 and 19th of Sept. Therefore, as we mentioned before, the mechanism that caused the decrease of dv/v the day before the eruption can be strongly affected by the magmatic intrusion. The intrusion of magma at shallow depth generates structural damage and elastic strain changes in the crust which could explain the rapid drop of dv/v. The decrease in the average seismic velocities due to magmatic intrusion is already documented in the scientific literature^{15,39}.

The results of our analysis demonstrate once again the usefulness of ambient noise interferometry as a volcano monitoring tool. The sensitivity of this method in detecting velocity variations related to volcanic processes and, in particular, to magmatic or hydrothermal fluid injections, makes it a valuable tool for better understanding the volcano dynamics. In our case, it was fundamental to correctly interpret the swallow seismicity observed, 9.5 days before the eruption onset. A major drawback of this technique is that it is negatively affected by coherent sources like a volcanic tremor. For this reason, this method was not applied for the syn-eruptive monitoring of La Palma 2021 eruption.

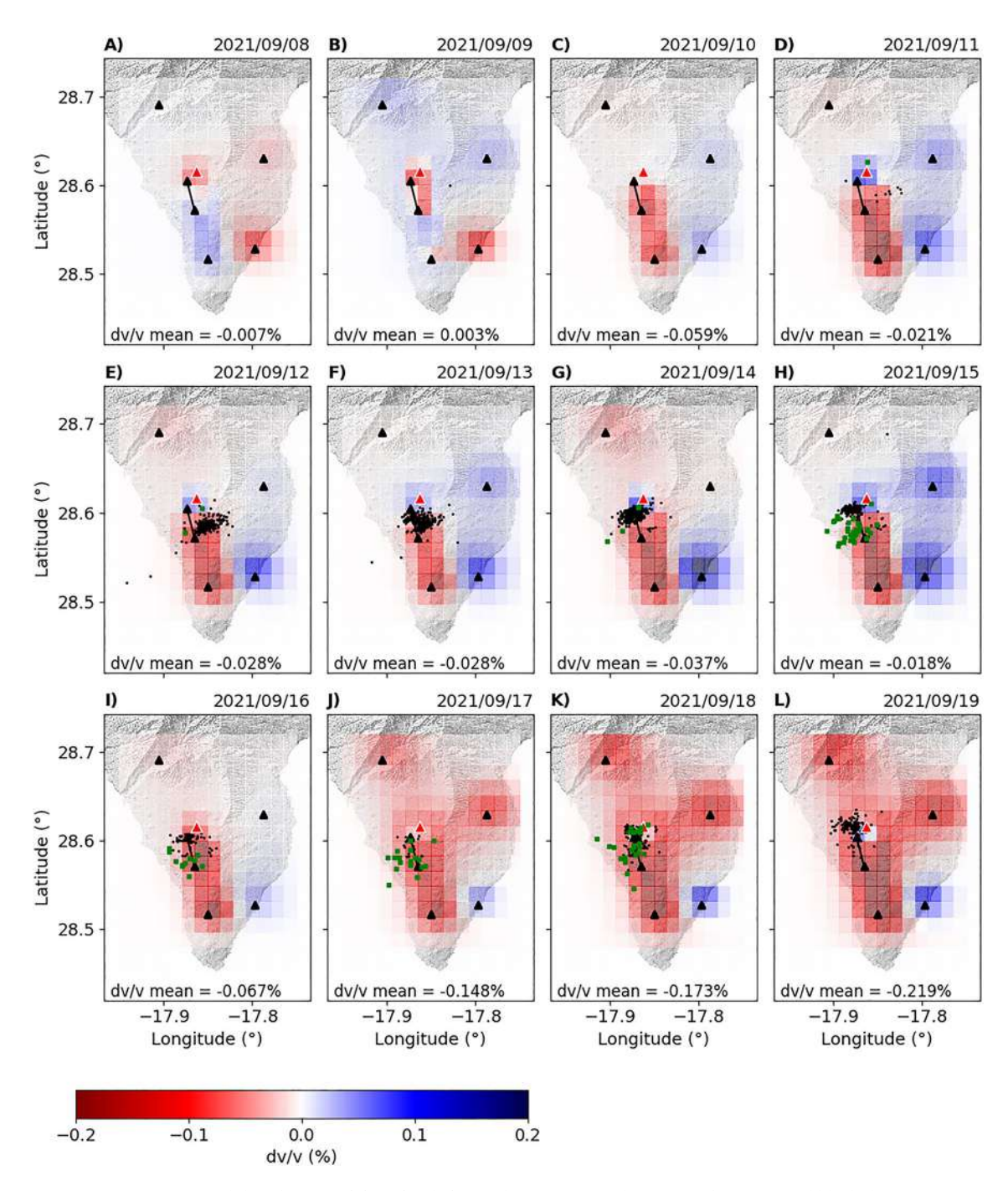


Figure 4. Spatial distribution of dv/v for different dates in September 2021. The green and black dots represent the seismicity related to the fluid injection and magmatic intrusion, respectively. Seismic stations appear like black triangles, and a red triangle shows the 2021 eruptive vent. The black line represents the approximate raypath of the station pair PLPI-PPMA, which is the closest to the eruption site. The digital elevation model was downloaded from the public graphic repository of GrafCan (http://www.grafcan.es).

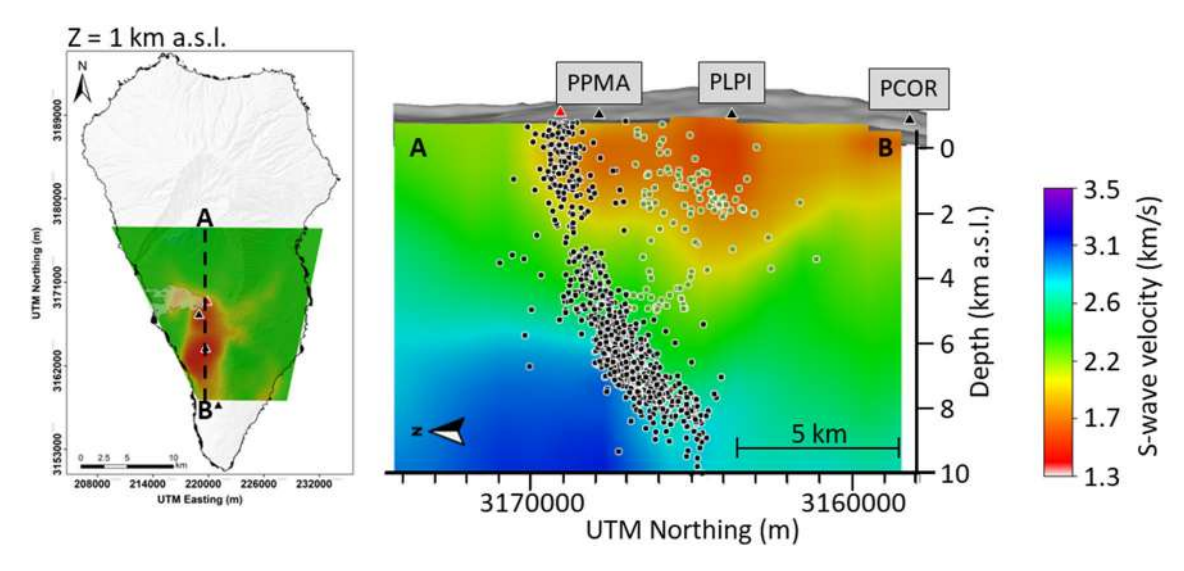


Figure 5. Horizontal (left) and Vertical N-S cross-sections (cf. A-B in left figure) of the 3D S-wave velocity model obtained by D'Auria et al. ¹. The green and black dots represent the seismicity related to the fluid injection and magmatic intrusion, respectively.

Data availability

All data generated or analysed during this study are included in this published article are in the Zenodo repository, https://doi.org/10.5281/zenodo.6678861.

Received: 7 October 2022; Accepted: 21 July 2023

Published online: 25 July 2023

References

- 1. D'Auria, L. et al. Rapid magma ascent beneath La Palma revealed by seismic tomography. Sci. Rep. 2022(12), 17654 (2022).
- 2. Lecocq, T., Longuevergne, L., Pedersen, H. A., Brenguier, F. & Stammler, K. Monitoring ground water storage at mesoscale using seismic noise: 30 years of continuous observation and thermo-elastic and hydrological modeling. Sci. Rep. 7(1), 1–16 (2017).
- 3. Clements, T. & Denolle, M. A. Tracking groundwater levels using the ambient seismic field. *Geophys. Res. Lett.* **45**(13), 6459–6465 (2018).
- 4. Brenguier, F. et al. Postseismic relaxation along the San Andreas fault at Parkfield from continuous seismological observations. *Science* 321(5895), 1478–1481 (2008).
- 5. Sens-Schönfelder, C. & Wegler, U. Passive image interferometry and seasonal variations of seismic velocities at Merapi Volcano, Indonesia. *Geophys. Res. Lett.* **33**(21), 1–5 (2006).
- Stehly, L., Campillo, M. & Shapiro, N. M. Traveltime measurements from noise correlation: Stability and detection of instrumental time-shifts. *Geophys. J. Int.* 171(1), 223–230 (2007).
- 7. Whiteley, J. S., Chambers, J. E., Uhlemann, S., Wilkinson, P. B. & Kendall, J. M. Geophysical monitoring of moisture-induced landslides: A review. *Rev. Geophys.* 57(1), 106–145 (2019).
- 8. Brenguier, F. et al. Towards forecasting volcanic eruptions using seismic noise. Nat. Geosci. 1(2), 126–130 (2008).
- 9. Duputel, Z. et al. Real time monitoring of relative velocity changes using ambient seismic noise at the Piton de la Fournaise volcano (La Réunion) from January 2006 to June 2007. J. Volcanol. Geotherm. Res. 184(1–2), 164–173 (2009).
- Mordret, A., Jolly, A. D., Duputel, Z. & Fournier, N. Monitoring of phreatic cruptions using interferometry on retrieved crosscorrelation function from ambient seismic noise: Results from Mt. Ruapehu, New Zealand. J. Volcanol. Geotherm. Res. 191(1-2), 46-59 (2010).
- 11. Brenguier, F. et al. Monitoring volcanoes using seismic noise correlations. C.R. Geosci. 343(8-9), 633-638 (2011).
- Anggono, T., Nishimura, T., Sato, H., Ueda, H. & Ukawa, M. Spatio-temporal changes in seismic velocity associated with the 2000 activity of Miyakejima volcano as inferred from cross-correlation analyses of ambient noise. J. Volcanol. Geotherm. Res. 247, 93–107 (2012).
- 13. Taira, T. A. & Brenguier, F. Response of hydrothermal system to stress transients at Lassen Volcanic Center, California, inferred from seismic interferometry with ambient noise. *Earth Planets Space* **68**(1), 1–13 (2016).
- 14. Donaldson, C., Caudron, C., Green, R. G., Thelen, W. A. & White, R. S. Relative seismic velocity variations correlate with deformation at Kilauea volcano. *Sci. Adv.* **3**(6), e1700219 (2017).
- 15. Ueno, T. et al. Fractional seismic velocity change related to magma intrusions during earthquake swarms in the eastern Izu peninsula, central Japan. J. Geophys. Res. Solid Earth. 117(B12), 1–11 (2012).
- 16. Yukutake, Y., Ueno, T. & Miyaoka, K. Determination of temporal changes in seismic velocity caused by volcanic activity in and around Hakone volcano, central Japan, using ambient seismic noise records. *Prog. Earth Planet Sci.* 3(1), 1–14 (2016).
- 17. Carracedo, J. C., Day, S. J., Guillou, H., Rodríguez Badiola, E., Canas, J. A. & Pérez Torrado, F. J. Origen y evolución del volcanismo de las Islas Canarias (1998).
- 18. Barrera Morate, J. L. & García Moral, R. Mapa Geológico de Canarias. GRAFCAN, Santa Cruz de Tenerife (2011).
- Lecocq, T., Caudron, C. & Brenguier, F. MSNoise, a python package for monitoring seismic velocity changes using ambient seismic noise. Seismol. Res. Lett. 85(3), 715–726 (2014).
- Lamb, O. D. et al. Seismic and experimental insights into eruption precursors at Volcán de Colima. Geophys. Res. Lett. 44(12), 6092–6100 (2017).
- 21. James, S. R., Knox, H. A., Abbott, R. E., Panning, M. P. & Screaton, E. J. Insights into permafrost and seasonal active-layer dynamics from ambient seismic noise monitoring. *J. Geophys. Res. Earth Surf.* 124(7), 1798–1816 (2019).

- 22. Liu, C., Yang, H., Wang, B. & Yang, J. Impacts of reservoir water level fluctuation on measuring seasonal seismic travel time changes in the Binchuan Basin, Yunnan, China. *Remote Sens.* 13(12), 2421 (2021).
- 23. Calò, M., Mazariegos, E. A. L., Tramelli, A. & Orazi, M. Hydrothermal systems characterization of the Stromboli volcano using spatial and temporal changes of the seismic velocities. *J. Volcanol. Geoth. Res.* 411, 107177 (2021).
- 24. Bensen, G. D. et al. Processing seismic ambient noise data to obtain reliable broad-band surface wave dispersion measurements. *Geophys. J. Int.* **169**(3), 1239–1260 (2007).
- 25. Poupinet, G., Ellsworth, W. L. & Frechet, J. Monitoring velocity variations in the crust using earthquake doublets: An application to the Calaveras Fault, California. *J. Geophys. Res. Solid Earth* **89**(B7), 5719–5731 (1984).
- Sens-Schönfelder, C. & Wegler, U. Passive image interferometry for monitoring crustal changes with ambient seismic noise. C.R. Geosci. 343(8–9), 639–651 (2011).
- 27. Ratdomopurbo, A. & Poupinet, G. Monitoring a temporal change of seismic velocity in a volcano: Application to the 1992 eruption of Mt. Merapi (Indonesia). *Geophys. Res. Lett.* 22(7), 775–778 (1995).
- 28. Snieder, R., Grêt, A., Douma, H. & Scales, J. Coda wave interferometry for estimating nonlinear behavior in seismic velocity. Science 295(5563), 2253–2255 (2002).
- 29. Clarke, D., Zaccarelli, L., Shapiro, N. M. & Brenguier, F. Assessment of resolution and accuracy of the Moving Window Cross Spectral technique for monitoring crustal temporal variations using ambient seismic noise. *Geophys. J. Int.* 186(2), 867–882 (2011).
- 30. Del Pezzo, E. & Ibáñez, J. M. Seismic coda-waves imaging based on sensitivity kernels calculated using an heuristic approach. *Geosciences* 10(8), 304 (2020).
- 31. Aster, R. C., Borchers, B. & Thurber, C. H. Parameter Estimation and Inverse Problems (Elsevier, 2018).
- 32. Hansen, P. C. The L-curve and its use in the numerical treatment of inverse problems (1999).
- 33. De Luca, C. et al. Pre-and co-eruptive analysis of the September 2021 eruption at Cumbre Vieja volcano (La Palma, Canary Islands) through DInSAR measurements and analytical modeling. *Geophys. Res. Lett.* 49(7), e2021GL097293 (2022).
- 34. Di Paolo, F. et al. La Palma island (Spain) geothermal system revealed by 3D magnetotelluric data inversion. Sci. Rep. 10(1), 1-8 (2020).
- 35. Pankhurst, M. J. et al. Rapid response petrology for the opening eruptive phase of the 2021 Cumbre Vieja eruption, La Palma, Canary Islands. Volcanica 5(1), 1–10 (2022).
- 36. Simakin, A. G., Salova, T. P. & Kovalenko, V. I. Fluid-magmatic interactions at oceanic islands as a possible source for the sodic agpaitic trend. *Petrology* 19, 641–652. https://doi.org/10.1134/S0869591111070046 (2011).
- 37. Caudron, C. *et al.* Hidden pressurized fluids prior to the 2014 phreatic eruption at Mt Ontake. *Nat. Commun.* **13**(1), 6145 (2022).
- 38. D'Auria, L. *et al.* Repeated fluid-transfer episodes as a mechanism for the recent dynamics of Campi Flegrei caldera (1989–2010). *J. Geophys. Res. Solid Earth* **116**(B4), 1–24 (2011).
- 39. Donaldson, C., Winder, T., Caudron, C. & White, R. S. Crustal seismic velocity responds to a magmatic intrusion and seasonal loading in Iceland's Northern Volcanic Zone. Sci. Adv. 5(11), eaax6642 (2019).
- 40. Hunter, J. D. Matplotlib: A 2D graphics environment. Comput. Sci. Eng. 9(3), 90-95 (2007)
- 41. Beyreuther, M. et al. ObsPy: A Python toolbox for seismology. Seismol. Res. Lett. 81(3), 530–533 (2010).
- 42. Krischer, L. et al. ObsPy: A bridge for seismology into the scientific Python ecosystem. Comput. Sci. Discov. 8(1), 014003. https://doi.org/10.1088/1749-4699/8/1/014003 (2015).
- 43. Padrón, E. et al. Helium emission at Cumbre Vieja volcano, La Palma, Canary Islands. Chem. Geol. 312, 138-147 (2012).

Acknowledgements

This paper benefited from various Python packages including Matplotlib⁴⁰, Obspy^{41,42} and MSNoise¹⁹. The INVOLCAN team was supported by the projects VOLRISKMAC II (MAC2/3.5b/328) co-financed by the EC Cooperation Transnational Program MAC 2014-2020 and Cumbre Vieja Emergencia, financed by Ministerio de Ciencia e Innovación of the Spanish Government. J.M.I and I.K. were supported by the project FEMALE of the Spanish Government (Grant No. PID2019-106260GB-I00). J.M.I. is founded by the Spanish PROOF-FOREVER (EUR2022.134044) project.

Author contributions

I.C.-P. processed the data and elaborated the figures. I.C.-P. and L.D. developed the inversion method. L.D., J.M.I. and I.K. provided the seismic catalogue and T.S. the GPS data used in this study. All the authors contributed to the interpretation of the data, discussion of the results, and manuscript preparation.

Competing interests

The authors declare no competing interests.

Additional information

Supplementary Information The online version contains supplementary material available at https://doi.org/10.1038/s41598-023-39237-9.

Correspondence and requests for materials should be addressed to I.C.-P.

Reprints and permissions information is available at www.nature.com/reprints.

Publisher's note Springer Nature remains neutral with regard to jurisdictional claims in published maps and institutional affiliations.

Open Access This article is licensed under a Creative Commons Attribution 4.0 International License, which permits use, sharing, adaptation, distribution and reproduction in any medium or format, as long as you give appropriate credit to the original author(s) and the source, provide a link to the Creative Commons licence, and indicate if changes were made. The images or other third party material in this article are included in the article's Creative Commons licence, unless indicated otherwise in a credit line to the material. If material is not included in the article's Creative Commons licence and your intended use is not permitted by statutory regulation or exceeds the permitted use, you will need to obtain permission directly from the copyright holder. To view a copy of this licence, visit http://creativecommons.org/licenses/by/4.0/.

© The Author(s) 2023



RESEARCH ARTICLE

Ambient Noise Tomography studies for geothermal exploration in the Canary Islands

Estudios de tomografía de ruido sísmico para la exploración geotérmica en Canarias

Iván Cabrera-Pérez¹, Luca D'Auria^{1,2}, Jean Soubestre^{3,4}, David Martínez van Dorth², Germán Cervigón-Tomico¹, Alba Martín-Lorenzo¹, Monika Przeor², Rubén García-Hernández¹, Víctor Ortega¹, Germán D. Padilla^{1,2}, José Barrancos^{1,2}, Eleazar Padrón^{1,2}, Nemesio M. Pérez^{1,2}

- ¹ Instituto Volcanológico de Canarias (INVOLCAN), 38600 Granadilla de Abona, Tenerife, Islas Canarias, España.
- ² Instituto Tecnológico y de Energías Renovables (ITER), 38600 Granadilla de Abona, Tenerife, Islas Canarias, España.
- ³ Univ. Grenoble Alpes, Univ. Savoie Mont Blanc, CNRS, IRD, Univ. Gustave Eiffel, ISTerre, 38000 Grenoble, France.
- ⁴ Icelandic Meteorological Office, Reykjavik, Iceland.

Corresponding author: icabrera@involcan.org (Iván Cabrera-Pérez)

Key points

Imaged velocity anomalies are related to the main geological structures of the Gran Canaria island.

Low-velocity zones observed in Tenerife could be associated to a shallow clay cap.

Two low-velocity zones observed in the southern part La Palma island can be related to hydrothermalized clays.

ABSTRACT

Ambient Noise Tomography is a geophysical exploration technique that has proven to be highly efficient for studies at different scales and for multiple purposes, such as geothermal exploration. In this article, we introduce this technique by reviewing its various steps. Additionally, we present some examples of applications from studies conducted in the Canary Islands (specifically in Tenerife, Gran Canaria, and La Palma) for geothermal exploration purposes. The study realized in Gran Canaria reveals a series of low-velocity zones in the southern and eastern parts of the island, which could be linked to convective cells. In Tenerife, a low-velocity zone has been observed, potentially associated with a superficial clay cap that could facilitate the ascent of gases to the surface. Finally, the study carried out in La Palma highlights the existence of two low-velocity zones in the southern part of the island, possibly related to hydrothermally altered clay zones, indicating a circulation of hydrothermal fluids.

Keywords: Ambient Noise Tomography; Geothermal Exploration; Gran Canaria; Tenerife; La Palma.

Article History:

Received: 16/01/2023 Accepted: 31/07/2023

Puntos clave

Las anomalías de velocidad observadas en Gran Canaria están relacionadas con las principales estructuras geológicas de la isla.

Las zonas de baja velocidad observadas en Tenerife podrían estar asociadas a una clay cap superficial.

Las dos zonas de baja velocidad observadas en la parte sur de la isla de La Palma podrían estar relacionadas con arcillas hidrotermalizadas.

RESUMEN

La tomografía de ruido sísmico es una técnica de exploración geofísica que ha mostrado ser muy eficiente para estudios a diferentes escalas y para múltiples propósitos, como la exploración geotérmica. En este artículo hacemos una introducción de esta técnica repasando sus diferentes pasos. También, se muestran algunos ejemplos de aplicaciones de estudios realizados en las Islas Canarias (concretamente en Tenerife, Gran Canaria y La Palma) con fines de exploración geotérmica. El estudio realizado en Gran Canaria muestra una serie de zonas de baja velocidad en la parte sur y este de la isla que podrían estar vinculadas a células convectivas. En Tenerife se ha observado una zona de baja velocidad que podría estar relacionada con un *clay cap* superficial que podría permitir el ascenso de gases a la superficie. Por último, el estudio realizado en La Palma muestra la existencia de dos zonas de baja velocidad en la parte sur de la isla que podrían estar vinculadas con zonas de arcillas hidrotermalizadas, lo que podría indicar una circulación de fluidos hidrotermales.

Palabras clave: Tomografía de ruido sísmico; Exploración geotérmica; Gran Canaria; Tenerife; La Palma.

Historial del artículo: Recibido: 16/01/2023 Aceptado: 31/07/2023

Copyright: ©2023 CSIC. This is an open-access article distributed under the terms of the Creative Commons Attribution 4.0 International (CC BY 4.0) License

1. Introducción

La tomografía sísmica es un método de exploración geofísica que reconstruye las velocidades de las ondas sísmicas que viajan a través de la Tierra para inferir las propiedades mecánicas del subsuelo. Para realizar la tomografía sísmica se pueden utilizar fuentes artificiales, cuya localización y características son bien conocidas. La utilización de fuentes artificiales (explosiones, camiones vibroseis...) permiten simplificar el problema inverso relacionado, pero a menudo conlleva costes altos y campañas de medida con una logística complicada. Por otro lado, la utilización de terremotos como fuentes sísmicas permite la realización de tomografía sísmica con costes muy reducidos. Sin embargo, la utilización de la sismicidad natural es imposible en entornos geológicos donde dicha sismicidad sea escasa o ausente. Además, el problema inverso relacionado es más complicado, siendo las fuentes mismas parte del problema inverso.

Sin embargo, la vibración ambiente del suelo de la Tierra, llamado ruido sísmico (seismic ambient noise en inglés), representa un tipo diferente de señal sísmica disponible en cualquier lugar del planeta y sin costes. El ruido sísmico puede ser utilizado para construir modelos de velocidad de la Tierra mediante una técnica denominada tomografía de ruido sísmico o ANT, de sus siglas en inglés (Ambient Noise Tomography). La técnica ANT ha demostrado ser eficaz para obtener modelos de velocidad de estructuras a escala continental (Yang et al., 2007; Saygin and Kennett, 2010), escala regional (Shapiro et al., 2005; Sabra et al., 2005; Lin et al., 2007) y escala local como volcanes (Brenguier et al., 2007; Masterlark et al., 2010; Stankiewicz et al., 2010; Cabrera-Pérez et al., 2022) o sistemas geotérmicos (Yang et al., 2011; Planès et al., 2020).

El primer trabajo de ANT aplicado para la exploración geotérmica fue realizado por Yang et al. (2011) y obtuvo un modelo de Vs superficial del campo geotérmico de Coso (California). Este estudio reveló la existencia de anomalías de baja velocidad relacionadas con alteración geotérmica. A este trabajo le siguieron otros estudios que permitieron descubrir la presencia de nuevos reservorios geotérmicos (Caló et al., 2013), anomalías de temperatura relacionadas con la circulación de fluidos hidrotermales (Lehujeur et al., 2018; Cabrera-Pérez et al., 2023), reservorios de agua (Wahida et al., 2018), zonas de fusión par-

cial (Martins et al., 2020) y el espesor de un depósito sedimentario relacionado con un sistema geotérmico (Planès et al., 2020). Estos estudios muestran el gran potencial de la ANT como método geofísico para la exploración geotérmica.

El objetivo de este artículo es introducir la ANT, explicando la metodología que constituye esta técnica y que consta de los siguientes pasos: (i) el preprocesamiento de datos de ruido sísmico, (ii) la correlación cruzada de señales de diferentes parejas de estaciones, (iii) la extracción de las curvas de dispersión, (iv) la obtención de los mapas de velocidad de grupo o fase de ondas superficiales para diferentes periodos y (v) la inversión en profundidad (Shapiro et al., 2005). Además, se muestran algunas aplicaciones de esta técnica en Canarias con fines de exploración geotérmica, centrándose en estudios realizados en La Palma, Tenerife y Gran Canaria.

2. Tomografía de ruido sísmico

2.1. Ruido sísmico

El ruido sísmico es la vibración ambiente del suelo compuesta principalmente por ondas superficiales. Esta señal puede estar generada por múltiples fuentes como pueden ser el ruido de origen antropogénico, atmosférico y el microsismo oceánico. La principal característica que diferencia las señales generadas por las diferentes fuentes es su rango de periodos característicos. En la Figura 1 mostramos la densidad espectral de energía o Power Spectral Density (PSD) para las señales de ruido sísmico registradas durante el 2020 por la estación GSNT. A periodos cortos (0,1 - 1 s), se observa principalmente el ruido sísmico relacionado con fuentes antropogénicas como vehículos o maquinarias (Figura 1A). La distribución de amplitud de esta fuente de ruido es bimodal debido a las variaciones diurnas de la actividad humana. En este rango de periodos también se puede generar ruido sísmico como consecuencia de fuentes atmosféricas, que es producido por la interacción del viento con árboles o estructuras que pueden causar vibraciones del suelo (Nakata et al., 2019).

Por otro lado, para periodos más largos (1 - 30 s) el ruido es producido principalmente por el oleaje océanico y se suele nombrar como microsismo oceánico. El microsismo oceánico de mayor amplitud se genera como consecuencia de los enérgicos sistemas ciclónicos que poseen grandes

gradientes de presión provocando fuertes vientos en la superficie, lo que genera una transferencia de energía desde la atmósfera al oleaje oceánico (swell en inglés), que posteriormente se convierte en ondas sísmicas (Kedar et al., 2008). El microsismo oceánico posee dos picos dominantes a 7 y 14 s, denominados respectivamente pico primario (Figura 1B) y secundario (Figura 1C). El pico primario es generado cerca de la costa en aguas poco profundas como consecuencia de la interacción de ondas de gravedad con la corteza, produciendo ondas sísmicas con el mismo contenido espectral que las olas oceánicas originales. Al contrario, el pico secundario puede producirse en

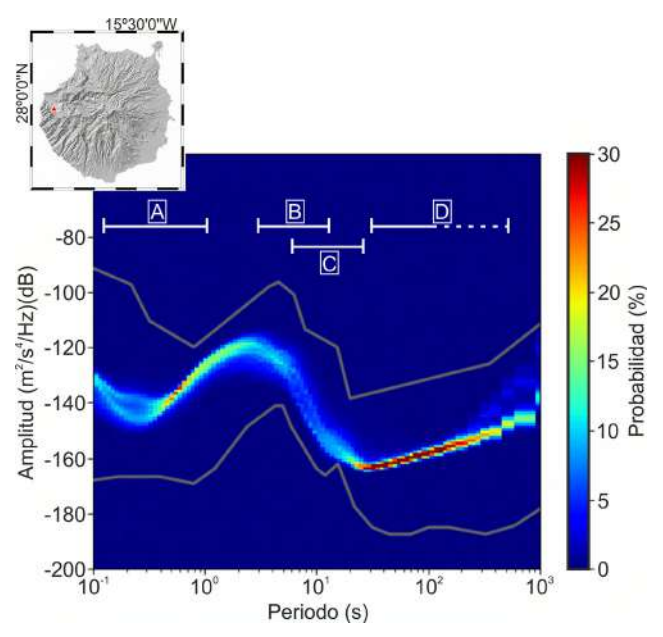


Figura 1. El mapa muestra la localización de la estación sísmica GSNT (triángulo rojo) en la isla de Gran Canaria. La gráfica muestra la distribución de probabilidad de la PSD para un año de datos de esta estación. Las líneas grises muestran los valores mínimos y máximos del modelo probabilístico de ruido de fondo de Peterson (1993). Las marcas blancas representan el rango de periodos para el ruido sísmico generado por fuentes antropogénicas y atmosféricas (A), segundo microsismo (B), primer microsismo (C) y el hum de la Tierra (D). La línea discontinua blanca indica el límite a 120 s, que es el periodo máximo de respuesta del sensor.

Figure 1. The map shows the location of the seismic station GSNT (red triangle) on the island of Gran Canaria. The graph shows the probability distribution of the Power Spectral Density (PSD) for one year of data from this station. The gray lines represent the minimum and maximum values of the background noise probabilistic model by Peterson (1993). The white markers represent the range of periods for seismic noise generated by anthropogenic and atmospheric sources (A), the second microseism (B), the first microseism (C), and the Earth's hum (D). The white dashed line indicates the limit at 120 seconds, which is the maximum period response of the sensor.

aguas tanto profundas como poco profundas va que resulta de la interacción no lineal entre olas oceánicas propagándose en sentidos contrarios, generando ondas de presión que se propagan verticalmente hasta el fondo marino con una frecuencia doble a la de las olas oceánicas originales. Por último, a periodos más altos (> 50 s) la fuente de ruido está relacionado con el "hum" de la Tierra (Figura 1D), que son las oscilaciones libres del planeta generadas de manera aleatoria por importantes perturbaciones oceánicas y/o atmosféricas. Para la ANT, la principal fuente de ruido que se utiliza es el microsismo oceánico, dado su rango de periodos y la buena distribución temporal y espacial de las fuentes. No obstante, la fuente de ruido utilizada dependerá de la escala de estudio y el rango de frecuencias que se quiera utilizar.

2.2. Pre-procesamiento de los datos

Para obtener información de la velocidad de propagación del ruido sísmico, es necesario que las fuentes se encuentren distribuidas homogéneamente de forma espacial y temporal, habiendo unas condiciones de isotropía del campo difuso para reconstruir correctamente las funciones empíricas de Green. Estas funciones empíricas de Green se obtienen apilando durante un periodo de tiempo suficientemente largo las correlaciones cruzadas de la señal de ruido sísmico para las diferentes parejas de estaciones que componen una red sísmica. Sin embargo, previamente es necesario normalizar la señal en el dominio del tiempo y la frecuencia (Bensen et al., 2007).

La normalización en el dominio del tiempo se aplica con el fin de reducir el efecto de las señales como terremotos que se encuentran geográficamente localizadas y que son excepcionalmente fuertes. Tradicionalmente, se han utilizado dos normalizaciones en el dominio del tiempo W (t): running absolute mean normalization and one-bit normalization. La normalización running absolute mean en el dominio del tiempo es definida como:

$$W(t_n) = \frac{1}{N+1} \sum_{j=n-N/2}^{n+N/2} \left| u(t_j) \right|, \tag{1}$$

donde el tiempo se representa a través de una secuencia discreta. Por lo tanto, para un punto en esta secuencia t_j , la normalización se realiza dividiendo la señal por la media absoluta del sismograma en una ventana de tiempo de longitud N.

Por otro lado, la *one-bit normalization* consiste en reemplazar cada muestra de un registro sísmico por su signo, en el cual la amplitud de la señal se convierte en ±1.

La normalización en el dominio de la frecuencia es aplicada por dos razones: para ampliar el ancho de banda de las funciones de Green y para disminuir el efecto de las fuentes con frecuencias dominantes. Uno de los métodos más utilizados es el *spectral whitening*, que es aplicado para normalizar la amplitud del espectro de Fourier de la señal. Para realizar esta normalización se utiliza una versión suavizada de la amplitud espectral de la señal de ruido. En este caso en espectro normalizado de la señal resulta ser:

$$N(w) = S(w) / |S^{sm}(w)|$$
 (2)

donde $S^{sm}(w)$ es la amplitud espectral suavizada a través de diferentes tipos de filtros. La amplitud espectral suavizada corresponde a la envolvente del espectro de la señal.

La última etapa del pre-procesamiento consiste en eliminar las ventanas de tiempo que todavía contienen fuentes sísmicas impulsivas (ej. terremotos). Esto se puede hacer de forma manual o automática.

2.3. Correlaciones cruzadas

Después de que los datos hayan sido pre-procesados, el siguiente paso es calcular la correlación cruzada del ruido sísmico para múltiples ventanas de tiempo que son posteriormente apiladas.

Varios estudios teóricos y experimentales han demostrado que, en un sistema lineal con una atenuación débil, la derivada temporal de la correlación cruzada de un campo de onda aleatorio o ruido sísmico registrado por dos estaciones converge en la función empírica de Green (Weaver y Lobkis, 2001; Gouédard *et al.*, 2008). Esto puede ser escrito como:

$$\lim_{T \to \infty} \frac{\partial}{\partial t} C_{AB}(t) = F(t)^* \left[G_{AB}(t) + G_{AB}(-t) \right]$$
 (3)

donde C_{AB} (t) es la correlación cruzada entre las señales registradas por dos estaciones A y B, calculadas para una ventana de tiempo de longitud T. G_{AB} (t) es la función de Green entre ambas estaciones y G_{AB} (-t) es su recíproco. F (t) es una

función en el dominio del tiempo que tiene en cuenta las características del espectro del ruido sísmico (Weaver and Lobkis, 2001; Snieder, 2004; Wapenaar, 2004). Este procedimiento puede ser aplicado para cada pareja de estaciones de una red sísmica. La correlación cruzada puede ser calculada en ventanas de tiempo un poco más largas que el tiempo de propagación de ondas superficiales entre las estaciones A y B (típicamente unos minutos en una red local), usando las componentes vertical (Z), transversal (T) y radial (R) en todas sus posibles combinaciones (ej. ZZ, ZR, TT, TZ, etc..). Para ondas de Rayleigh se puede obtener la función de Green utilizando las componentes ZZ, mientras que para la ondas de Love es conveniente utilizar las componentes TT.

En la Figura 2A se muestra la función empírica de Green para la componente ZZ para todas las parejas de estaciones que fueron instaladas de forma temporal en el 2020 en Gran Canaria. Están ordenadas en función de la distancia entre las estaciones con respecto a la diferencia de tiempo (lag de tiempo). La parte negativa (lag de tiempo < 0 s) de esta señal es la parte anticausal, mientras que la parte positiva (lag de tiempo > 0 s) es la causal. Estas correlaciones muestran señales coherentes constituidas por trenes de ondas de Rayleigh. Estos trenes de ondas están bien definidos en ambas partes causales y anticausales, lo que valida la homogeneidad de la distribución espacial y temporal de las fuentes de ruido, como es requerido por la teoría del campo difuso para que las correlaciones cruzadas converjan en las funciones de Green (Weaver and Lobkis, 2001; Snider, 2004; Wapenaar, 2004).

2.4. Curvas de dispersión

Después del cálculo de las correlaciones cruzadas y su apilamiento, el siguiente paso es obtener la curva de dispersión para cada pareja de estaciones. Esta curva de dispersión expresa la velocidad de grupo o fase en función del periodo. Hay diversos métodos para extraer la curva de dispersión, sin embargo, aquí describimos el método más utilizado, el cual es un análisis en frecuencia-tiempo llamado FTAN, de sus siglas en inglés (*Frequency-Time ANalysis*) (Levshin *et al.*, 1992). El primer paso para calcular la FTAN es cambiar la función de Green del dominio del tiempo al dominio de la frecuencia a través de la transformada de Fourier: $s(t) \rightarrow S(\omega)$. El segundo paso es la aplicación de una serie de filtros gaus-

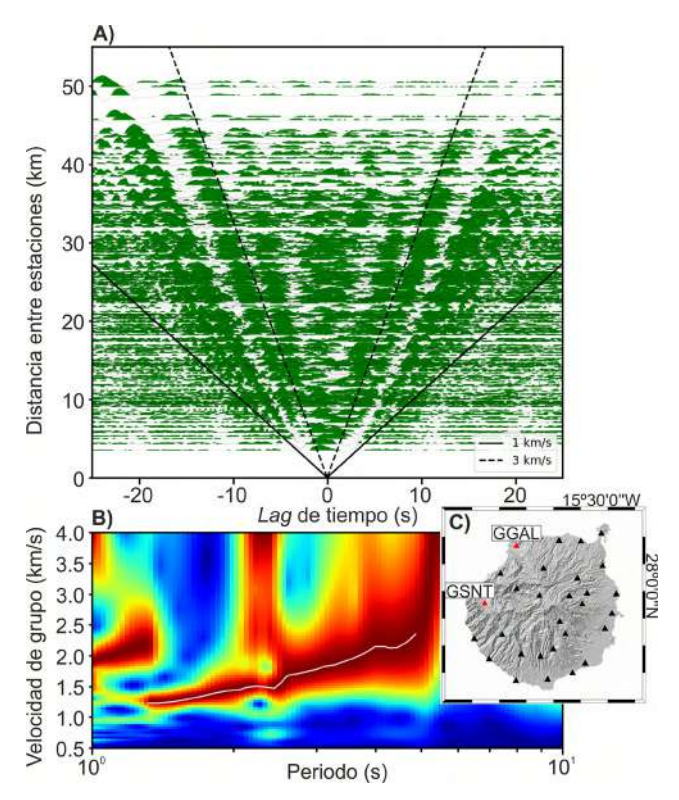


Figura 2. A) Correlaciones cruzadas de todas las parejas de estaciones sísmicas ordenadas de acuerdo con la distancia entre las estaciones. Las velocidades de 1,0 y 3,0 km/s están marcadas con líneas continuas y discontinuas, respectivamente. B) Gráfica FTAN obtenida de la correlación cruzada extraída de la pareja de estaciones sísmicas de GGAL y GSNT. La línea blanca representa la curva de dispersión para esta pareja de estaciones. C) Los triángulos negros representan la distribución de la red sísmica temporal utilizada para obtener la Figura 2A. Los triángulos rojos representan la localización de las estaciones sísmicas permanentes de GGAL y GSNT.

Figure 2. A) Cross-correlations of all pairs of seismic stations sorted according to the distance between the pairs of stations. Velocities of 1.0 km/s and 3.0 km/s are marked with solid and dashed lines, respectively. B) FTAN graph obtained from the cross-correlation of seismic stations GGAL and GSNT. The white line represents the dispersion curve for this pair of stations. C) The black triangles represent the distribution of the temporary seismic network used to obtain Figure 2A. The red triangles represent the location of the permanent seismic stations GGAL and GSNT.

sianos de banda estrecha con una frecuencia central ω_0 :

$$S_a(\omega,\omega_0) = S(\omega)(1 + sgn(\omega))G(\omega - \omega_0),$$
 (4)

donde

$$G(\omega - \omega_0) = \exp\left(-\alpha \left(\frac{\omega - \omega_0}{\omega_0}\right)^2\right), \quad (5)$$

α es un parámetro relacionado con el ancho del filtro y sgn es la función signo. Posteriormente, se aplica la inversa de la transformada de Fourier para convertir cada función $S_a(\omega, \omega_0)$ al dominio del tiempo y se calcula la envolvente por cada una de estas señales. Este proceso se repite para diferentes frecuencias centrales obteniendo una amplitud en función de la frecuencia y el tiempo. A través de la representación gráfica de esta función se puede determinar de forma manual o automática el tiempo de viaje, t_q , de las ondas entre la pareja de estaciones, seleccionando la posición de los valores máximos por cada frecuencia $t_a(\omega)$. Eso permite obtener la curva de dispersión de la velocidad de grupo que se define como $U(\omega) = r / t_{\alpha}(\omega)$, siendo r la distancia entre las estaciones. Un ejemplo de aplicación de la FTAN está representado en la Figura 2B para la función de Green obtenida entre la pareja de estaciones GSNT y GGAL (Figura 2A).

2.5. Mapas 2-D de velocidad de grupo o fase de ondas superficiales

El siguiente paso en ANT consiste en realizar la inversión utilizando las curvas de dispersión con la finalidad de obtener mapas de velocidad de grupo para diferentes periodos (Shapiro et al., 2005). Este procedimiento es similar a la tomografía de tiempo de viaje con terremotos, aunque en este caso el problema, siendo bidimensional, es más sencillo. El método de inversión estándar consiste en una aproximación con una línea recta de la trayectoria superficial del rayo sísmico entre la fuente y el receptor, lo que en el caso de la ANT equivale a una pareja de estaciones. El problema directo de la tomografía de ondas superficiales se basa en predecir el tiempo de viaje, que es dependiente de la frecuencia, para un modelo de velocidad de fase o de grupo:

$$t(\omega) = \int_{p} \frac{ds}{v(\omega, x, y)},$$
(6)

donde ω es la frecuencia, x e y son las coordenadas de la posición en la superficie, $t(\omega)$ es el tiempo de viaje de fase o grupo de las ondas superficiales, $v(\omega,x,y)$ es el mapa de velocidad, p es la trayectoria del rayo y s es la distancia a lo largo del rayo sísmico (Wang and Dahlen, 1995; Woodhouse, 1974; Nakata et al., 2019). Discretizando la distribución de velocidad $v(\omega,x,y)$ con un núme-

ro finito M de funciones elementales, se obtiene un sistema de M ecuaciones, que puede ser invertido para encontrar el modelo de velocidad de grupo para una frecuencia específica ω basándose en N medidas de tiempo de viaje (Aster *et al.*, 2018; Nakata *et al.*, 2019).

Los primeros estudios de ANT se basaron en la utilización de una inversión lineal, o también llamado regionalización. La validez de la utilización de una inversión lineal se basa en el supuesto de que existen pequeñas perturbaciones o variaciones de velocidad con respecto a un modelo de referencia (Nolet, 2008). Una aproximación lineal puede ser suficiente para un estudio a escala global o regional debido a las limitadas variaciones relativas de velocidad. Sin embargo, a escala local, en entornos geológicos muy complejos como los volcanes o zonas geotérmicas, las perturbaciones de velocidad de grupo o fase pueden exceder el 30%, por lo que una inversión lineal no es adecuada para realizar la inversión (Mordret et al., 2015; Spica et al., 2015).

El primer estudio de ANT en el cual se usó una inversión no lineal fue el de Stankiewicz et al. (2010) sobre el lago Toba, donde se usó el método Fast Marching Method (FMM), desarrollado por Sethian (1996) para calcular el tiempo de travecto de las ondas sísmicas, teniendo en cuenta las heterogeneidades del modelo de velocidad. Este método está basado en la solución por diferencias finitas de la ecuación eikonal. que describe el tiempo de trayecto de las ondas sísmicas y que se ha utilizado para estudiar estructuras volcánicas (Shomali and Shirzad 2015: Spica et al., 2015; Li et al., 2016; De Siena et al., 2018). Por otro lado, Fang et al. (2015) propuso un método donde no es necesario realizar el paso de la inversión para obtener los mapas de velocidad de grupo. El método consiste en invertir los datos de dispersión de ondas superficiales directamente para las variaciones tridimensionales de la velocidad de onda de corte. Este método fue aplicado, entre otros, por Li et al. (2016) para invertir el modelo 3-D de velocidad de onda en el área urbana de Hefei, en China.

Otro enfoque para la inversión de las curvas de dispersión es el propuesto por Cabrera-Pérez et al. (2021), que es el esquema de inversión utilizado en las zonas de aplicación que se exponen más adelante. Este enfoque consiste en una inversión no lineal multiescala que permite obte-

ner mapas de velocidad de grupo fiables, incluso para modelos de velocidad con variaciones de velocidad muy fuertes al mejorar progresivamente el modelo. El modelo inicial consiste en un modelo de velocidad homogéneo. La parametrización del modelo se mejora en los pasos posteriores de inversión no lineal agregando nodos de control sobre una cuadrícula regular. El resultado de cada paso se utiliza como modelo inicial para el siguiente paso de inversión.

2.6. Inversión en profundidad

El último paso es el proceso de inversión en profundidad, que consiste en invertir las curvas de dispersión de velocidades de grupo o fase, extraídas de los mapas por cada punto, para obtener perfiles 1-D de velocidad de onda P (Vp) y onda S (Vs) en profundidad. Las velocidades de grupo o de fase de las ondas superficiales están vinculadas con las velocidades Vp y Vs, así como con la densidad (ρ) del medio, $U = f(Vp, Vs, \rho)$, y se puede extraer la información de las velocidades de las curvas de dispersión.

El procedimiento para realizar la inversión en profundidad consiste en buscar el modelo 1-D de Vs, cuya curva de dispersión sintética se ajuste mejor a la obtenida para cada punto. Existen varios métodos para calcular las curvas de dispersión sintéticas para modelos 1-D, cada uno con un coste computacional diferente frente a una mejor precisión y fiabilidad del cálculo. En este trabajo se utiliza el método de Ke *et al.* (2011) que utiliza una modificación del método tradicional de Thompson-Haskell, con una mayor estabilidad numérica y un tiempo de cálculo inferior a otros métodos.

Existen múltiples métodos para la inversión en profundidad del modelo 1-D. En este artículo nos centraremos en la inversión transdimensional bayesiana (Bodin et al., 2012), que es la que se ha utilizado para la inversión en profundidad de los modelos de Gran Canaria, que se muestran más adelante. Este enfoque permite obtener una distribución de probabilidad a posteriori, que es en gran medida independiente de una parametrización específica. De hecho, el enfoque transdimensional incluye la propia parametrización en el problema inverso (Sambridge et al., 2006). Los resultados de la inversión transdimensional consisten en una distribución de probabilidad para la velocidad a cada profundidad (Zheng et al., 2017; Kim et al., 2016).

3. Aplicaciones en Canarias

3.1. Gran Canaria

Gran Canaria es la tercera isla del archipiélago en extensión y altitud, alcanzando su cota máxima a 1956 m sobre el nivel del mar y cubriendo un área de 1560,1 km². La isla de Gran Canaria presenta dos dominios geológicos muy bien diferenciados: el dominio suroeste o Paleocanarias, que es la parte geológicamente más antigua; y el dominio Noreste o Neocanarias, donde se localizan las erupciones holocénicas de los ciclos más recientes (Figura 3). La historia volcánica subaérea de Gran Canaria se agrupa en tres grandes ciclos constructivos: el primer ciclo incluye emisiones del Mioceno superior (14,5 - 8,28 Ma) y se caracterizó por la emisión de un gran volumen de flujos basálticos que constituyeron un escudo volcánico; el segundo ciclo o ciclo del Roque Nublo, consistió en emisiones producidas en el Plioceno (5 - 4,5 a 3,5 - 3 Ma) y destacó por ser un período volcánico

explosivo y por la generación de múltiples deslizamientos gravitacionales (Schmincke and Sumita, 2010); y por último, el tercer ciclo comprende emisiones de edad de <3,2 Ma, emitidas después del Ciclo Roque Nublo y ciclo reciente. Este ciclo se caracteriza por la ocurrencia de todas las erupciones holocénicas que tuvieron lugar en la isla. Este vulcanismo se concentra en la parte Noreste de la isla o Neocanarias (Figura 3).

3.1.1. Campañas de medida y procesamiento de los datos

Los datos utilizados en este trabajo derivan de una campaña de exploración geotérmica realizada por el Instituto Volcanológico de Canarias (IN-VOLCAN) en el año 2019 y 2020 en Gran Canaria. En esta campaña se instalaron 28 estaciones sísmicas de banda ancha (Nanometrics © Trillium Compact 120s y Güralp ©, Serie 3ESPC) en dos fases (Figura 3). En la primera fase, se instalaron

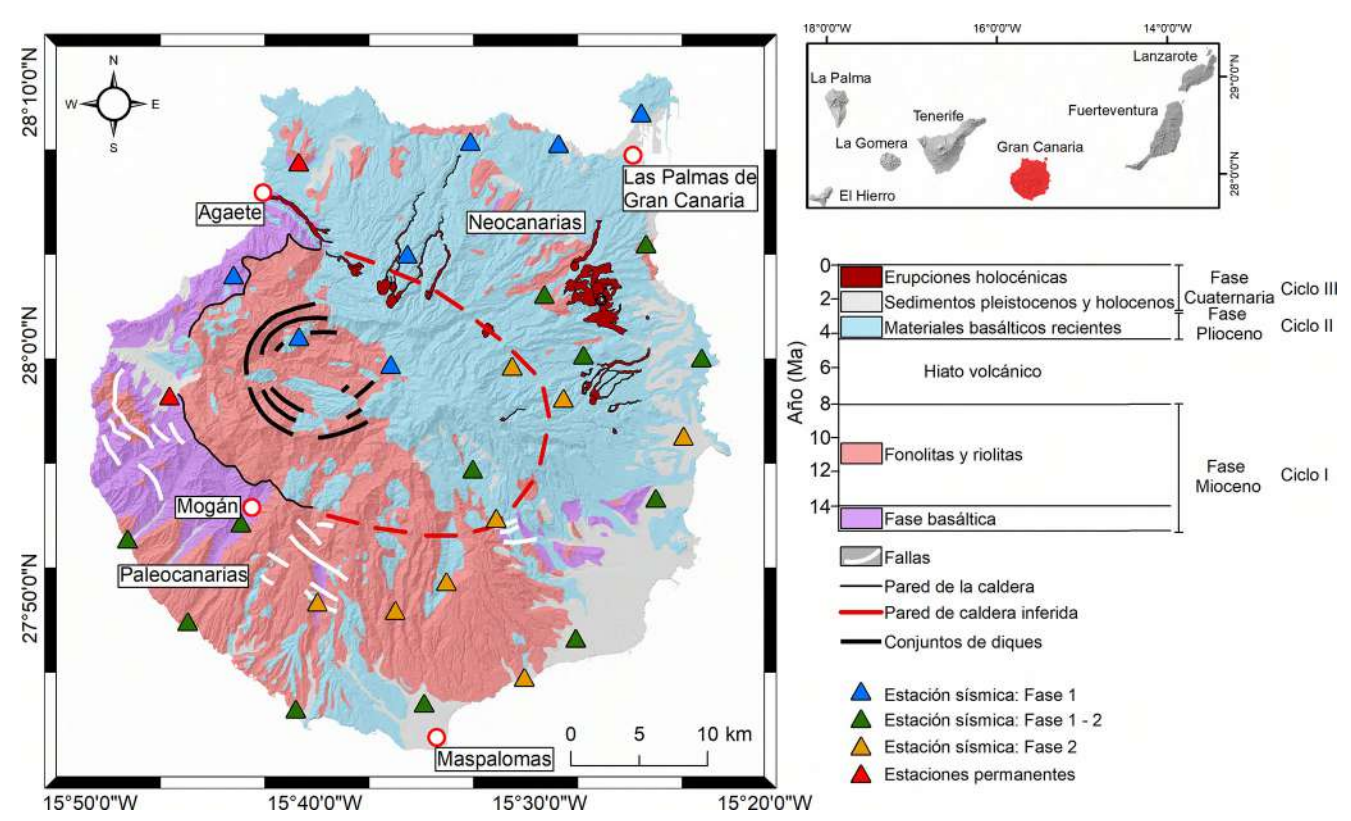


Figura 3. Mapa geológico de Gran Canaria modificado de Bacells *et al.* (1990). Las edades de las principales unidades volcano estratigráficas fueron obtenidos de Schmincke *and* Sumita (2010). Los triángulos azules, verdes y naranjas representan la localización de la red sísmica temporal desplegada en diferentes fases durante la campaña de exploración geotérmica. Los triángulos rojos representan la ubicación de la red sísmica permanente operada por INVOLCAN para la monitorización volcánica del archipiélago.

Figure 3. Geological map of Gran Canaria modified from Bacells *et al.* (1990). The ages of the main volcano-stratigraphic units were obtained from Schmincke and Sumita (2010). The blue, green, and orange triangles represent the location of the temporary seismic network deployed in different phases during the geothermal exploration campaign. The red triangles represent the location of the permanent seismic network operated by INVOLCAN for volcanic monitoring of the archipelago.

20 estaciones que cubrían toda la isla. Después de dos meses de registrar datos, se trasladaron 8 estaciones a la parte Este y sureste de la isla para aumentar la densidad de los rayos sísmicos en estas zonas de interés. El motivo de esta decisión es la existencia de anomalías geofísicas y geoquímicas observadas en estudios previos de exploración geotérmica (Ledo et al., 2021; Rodríguez et al., 2021). Además, se usaron dos estaciones permanentes operadas por INVOLCAN que se utilizan para la monitorización volcánica del archipiélago (Figura 3). Los datos se adquirieron a una frecuencia de muestreo de 100 Hz.

Seguidamente, los datos registrados fueron preprocesados para quitar las ventanas con terremotos de manera automática. Los datos se analizaron sobre un rango de frecuencias entre 5-10 Hz y 0,02-0,05 Hz para detectar terremotos volcano-tectónicos y telesismos, respectivamente. En total, se detectaron y eliminaron automáticamente un total de 97 terremotos locales y 106 telesismos.

Posteriormente, se aplicó un filtro para un rango de frecuencia de 0.01 a 2.0 Hz y se normalizó la señal aplicando los métodos one-bit normalization y spectral whitening (Bensen et al., 2007). Seguidamente, se calcularon las correlaciones cruzadas de los datos preprocesados para todas las parejas de estaciones en ventanas de 5 minutos y se apilaron durante dos meses para la fase 1 y un mes de duración para la fase 2. Algunas estaciones estuvieron registrando durante ambas fases (estaciones temporales: Fase 1-2 en la Figura 3), por lo que para estas estaciones se realizó un apilamiento durante tres meses. Este análisis se realizó sobre componentes ZZ para 325 parejas de estaciones (Figura 2A). Luego se obtuvieron 279 curvas de dispersión mediante la técnica FTAN (Levshin et al., 1992) para la componente ZZ. La inversión para obtener los mapas de velocidad de grupo se ha realizado para periodos entre 0,7 y 3,2 s. Nuestro análisis se limitó a rangos de periodos con al menos 50 mediciones fiables.

3.1.2. Mapas 2-D de velocidad de grupo de ondas de Rayleigh

Después, se aplicó una inversión no lineal multiescala (Cabrera-Pérez *et al.*, 2021) para obtener los modelos 2-D de velocidad de grupo para diferentes periodos. La Figura 4 muestra los mapas 2-D de velocidad de grupo de ondas de Rayleigh

obtenidos con la componente ZZ para periodos de T = 0.70 s, T = 1.00 s, T = 2.00 s y T = 3.00 s. Los mapas muestran una anomalía de baja velocidad ubicada en la Caldera de Tejeda. Se observa muy bien a periodos cortos de T = 0,70 s y T = 1,00 s (ver Figuras 4A y B). Esta zona de baja velocidad cambia a zona de alta velocidad a periodos más altos, correspondiendo a profundidades más importantes. También existe la presencia de zonas de baja velocidad en la parte norte y sur de la isla, aunque solo a periodos menores. Sin embargo, en la parte Noreste (donde se ubica la capital de Las Palmas de Gran Canaria), se observa una zona de baia velocidad en todos los periodos. Además, a un periodo de T = 3,00 s observamos la presencia de una zona de alta velocidad ubicada en la parte central y sureste de la isla (Figura 4D).

3.1.3. Modelo 3-D de velocidad de onda S

El último paso que se ha realizado es la inversión en profundidad utilizando los mapas de velocidades de grupo obtenidos para diferentes periodos. Para ello, se extrajo la curva de dispersión de los mapas de velocidad del grupo 2-D para 120 puntos, que se utilizaron para la inversión 1-D en profundidad. Cada curva de dispersión se invirtió utilizando un método transdimensional bayesiano (Bodin *et al.*, 2012).

Las Figuras 5A y 5B muestran un corte horizontal y vertical del modelo 3-D de Vs, respectivamente. Como se puede observar, existe un alto contraste de velocidad en la isla donde se alcanzan en algunas áreas anomalías negativas de velocidad con un valor del 40% inferior al promedio (2,96 km/s). La Figura 5A muestra también la presencia de una zona de alta velocidad en la parte central de la isla, siguiendo una dirección NO-SE, en la que el área de anomalía aumenta en profundidad (H1). Otra zona de alta velocidad (H2) se observa en la parte central de la isla, siguiendo una dirección SO-NE (Figuras 5A y B). A poca profundidad estas dos anomalías están bien diferenciadas, sin embargo, a mayores profundidades se unen en una sola. Por otro lado. se observa una anomalía de baja velocidad que se encuentra en la parte occidental de la isla, situada en la Caldera de Tejeda (L1). La velocidad aumenta considerablemente en profundidad. pasando de anomalías negativas del 30% a valores positivos con 30% de variación relativa de velocidad de Vs. Además, existe otra anomalía

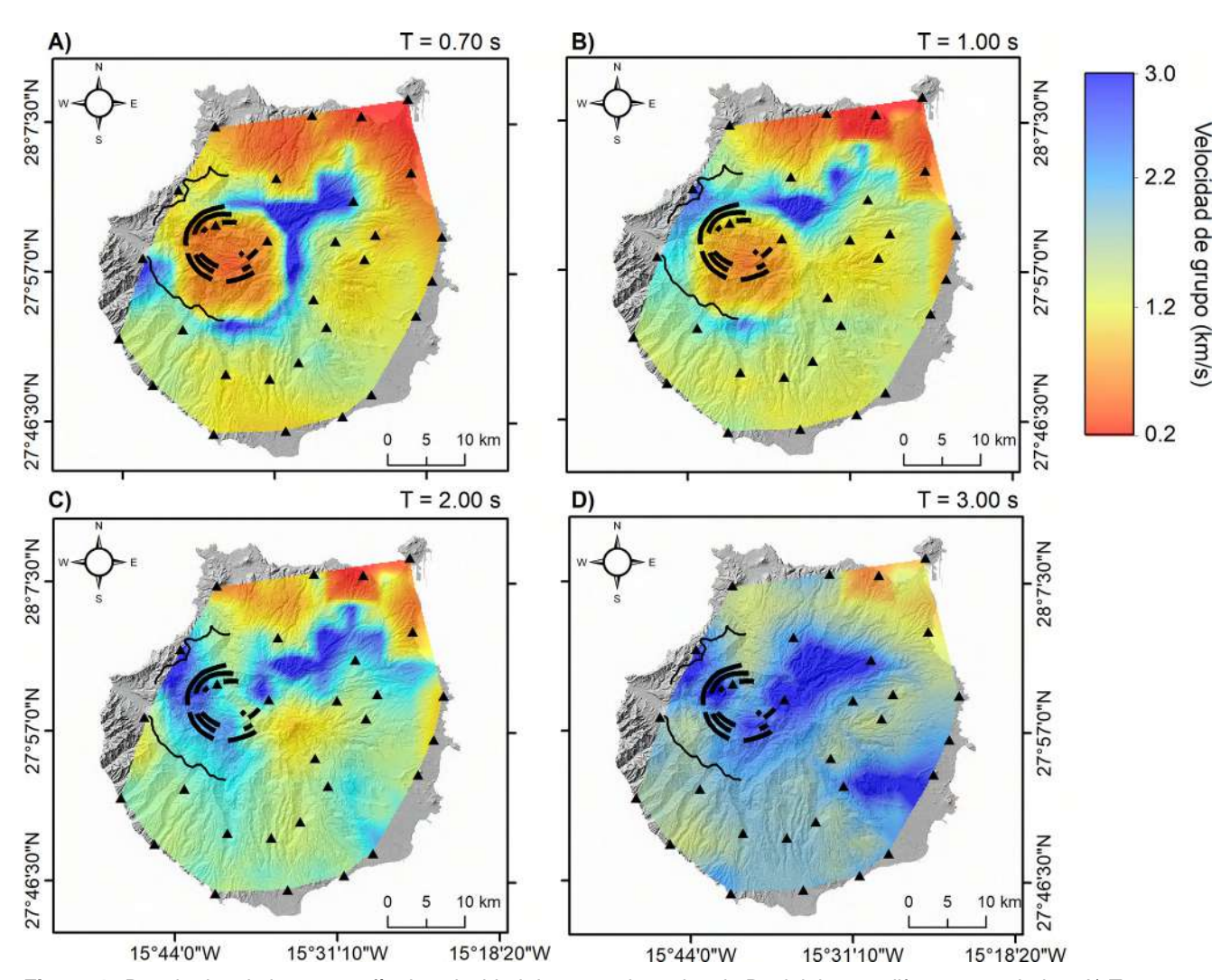


Figura 4. Resultados de la tomografía de velocidad de grupo de ondas de Rayleigh para diferentes periodos: A) T = 0.70 s, B) T = 1.00 s, C) T = 2.00 s y D) T = 3.00 s. Los triángulos negros representan la localización de las estaciones sísmicas. Las líneas negras indican la localización del conjunto de diques y la pared de la caldera de Tejeda.

Figure 4. Results of Rayleigh wave group velocity tomography for different periods: A) T = 0.70 s, B) T = 1.00 s, C) T = 2.00 s, and D) T = 3.00 s. The black triangles represent the location of seismic stations. The black lines indicate the location of the dike set and the wall of the Tejeda Caldera.

de baja velocidad en la parte norte y este (L3) de la isla con -20% de variación relativa de Vs en algunas áreas, a una profundidad de 0 m.a.s.l. Se puede observar la existencia de una anomalía de baja velocidad en la parte suroeste de la isla (L2) que aparece a diferentes profundidades (Figura 5).

El modelo de Vs obtenido de la ANT se correlaciona muy bien con estudios geofísicos previos de gravimetría (Camacho et al., 2000), tomografía sísmica (Krastel et al., 2002), aeromagnetismo (Blanco-Montenegro et al., 2003) y magnetotelúrica (Ledo et al., 2021). Al igual que el modelo de ANT, estos estudios observan la existencia de una anomalía (H1 y H2) que divide la isla en dos: Paleocanarias y Neocanarias, y que se vincula con antiguas intrusiones fisurales compuestas por densos materiales basálticos. Por otro lado, la zona de baja velocidad L1 podría estar relacionada con una zona de fracturación provocada por el colapso de la Caldera de Tejeda. Las otras dos zonas de baja velocidad L2 y L3 podrían estar vinculadas con zonas fracturadas generadas por la actividad volcánica reciente (Camacho et al., 2000), con lava subaérea más débil o porosa (Krastel et al., 2002), o bien con la presencia de fluidos hidrotermales (Ledo et al., 2021). Ledo et al. (2021) observaron algunas estructuras de baja resistividad casi verticales en la parte sur y este de la isla (<10 ohm m). Los autores afirman que estas estructuras verticales podrían estar asociadas a alteraciones hidrotermales y arcillas gene-

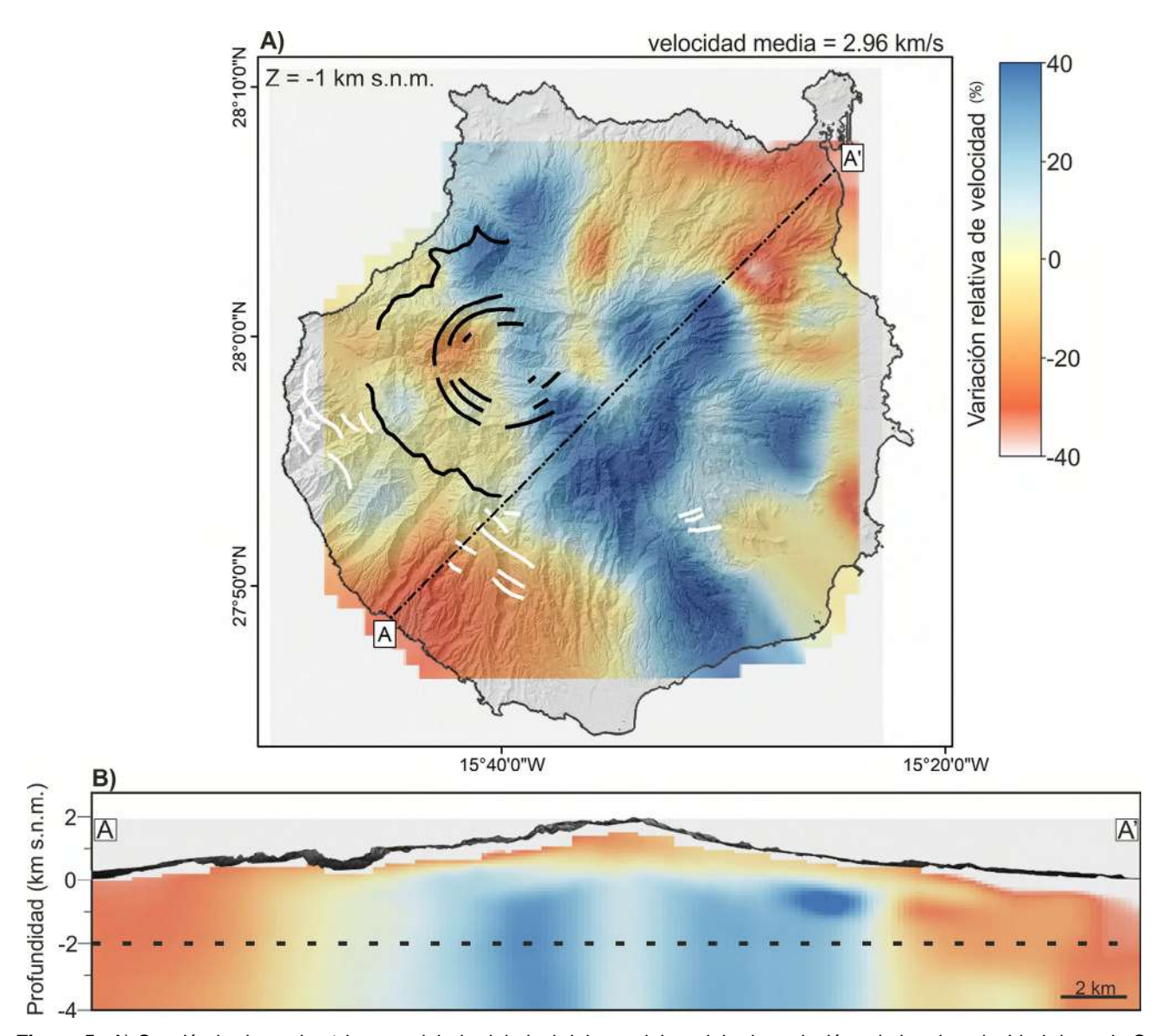


Figura 5. A) Sección horizontal a 1 km por debajo del nivel del mar del modelo de variación relativa de velocidad de onda S. Las líneas negras continuas representan la pared de la caldera y el complejo de diques. Las líneas blancas representan las fallas. La línea discontinua negra representa el trazado de la sección vertical mostrado en la Figura B. B) La línea discontinua representa el límite de mayor resolución del modelo que se encuentra a 2 km por debajo del nivel del mar. A mayor profundidad la resolución del modelo es menor.

Figure 5. A) Horizontal section at 1 km below sea level of the model showing relative variation of S-wave velocity. The continuous black lines represent the caldera wall and the dike complex. The white lines represent faults. The black dashed line represents the trace of the vertical section shown in Figure B. B) The dashed line represents the limit of higher resolution of the model, which is located at 2 km below sea level. At greater depths, the resolution of the model decreases.

radas por pequeñas células convectivas aisladas. Además, Cabrera-Pérez et al. (2023) observaron una correlación espacial entre las anomalías conductivas observadas en el modelo de resistividad de Ledo et al. (2021) y fuertes gradientes laterales en el modelo de velocidad de onda S. Estas anomalías conductivas podrían representar evidencias de circulación hidrotermal y anomalías térmicas, asociadas a contactos laterales entre diferentes unidades geológicas y/o fallas. Es por

ello que este estudio ha permitido corroborar la existencia de zonas de anomalías que podrían estar relacionadas con estructuras de posible interés para la explotación geotérmica.

3.2. Tenerife - Dorsal Norte-Sur

Tenerife es la isla más grande del archipiélago con una extensión de 2036 km². En esta isla se pueden distinguir varios dominios geológicos, te-

niendo en cuenta su evolución temporal y su historia geológica. El dominio de los edificios antiquos está relacionado con la primera fase volcánica subaérea que formaron los macizos de Anaga, Teno y Rogue del Conde (Figura 6). El dominio Cañadas corresponde a todo el material generado por las erupciones volcánicas del edificio Cañadas, que conforman el complejo volcánico central de la isla, y comenzó a crecer hace 3,5 Ma (Ancochea et al., 1990). Este complejo volcánico posee una gran depresión volcánica de 16 km x 9 km, que se produjo como resultado de múltiples colapsos verticales, que posteriormente fue rellenado por materiales durante el dominio de las erupciones post caldera. Durante esta actividad se formaron, en la parte norte de la Caldera de Las Cañadas, los estratovolcanes Teide y Pico Viejo (Ablay and Martí, 2000). El último dominio lo conforman los ejes de rift que constituyen todas las erupciones volcánicas ocurridas a través de los principales ejes estructurales de la isla. Los tres ejes estructurales son el rift NE o Dorsal de Pedro Gil, rift NO y rift NS, donde se localiza la zona de estudio (Figura 6). En estos ejes es donde se han concentrado todas las erupciones

históricas ocurridas en la isla, siendo la última la del volcán Chinyero, en 1909.

La isla de Tenerife ha sido estudiada ampliamente utilizando múltiples métodos de exploración geofísica. Con respecto a la tomografía sísmica, durante la última década se han realizado una serie de estudios sísmicos basados en datos de fuentes activas (Canales et al., 2000; Ibáñez et al., 2008; García-Yeguas et al., 2012). El primer estudio fue realizado por Canales et al. (2000) que reveló la presencia de un complejo plutónico debajo del complejo volcánico Teide-Pico Viejo. Posteriormente, García-Yeguas et al. (2012), utilizando los datos obtenidos durante el experimento de fuentes activas TOM-TEIDEVS (Ibáñez et al., 2008), descubrieron la presencia de un cuerpo de alta velocidad debajo del centro de Tenerife que es consistente con estudios previos de gravimetría y magnetotelúrica. La existencia de este cuerpo de alta velocidad fue corroborada por un estudio de tomografía de terremotos locales realizado por Koulakov et al. (2023), que permitió, además, desvelar la existencia de un reservorio de magma fonolítico a una profundidad de ~5 km. Además, Prudencia et al. (2015) realizaron una tomografía

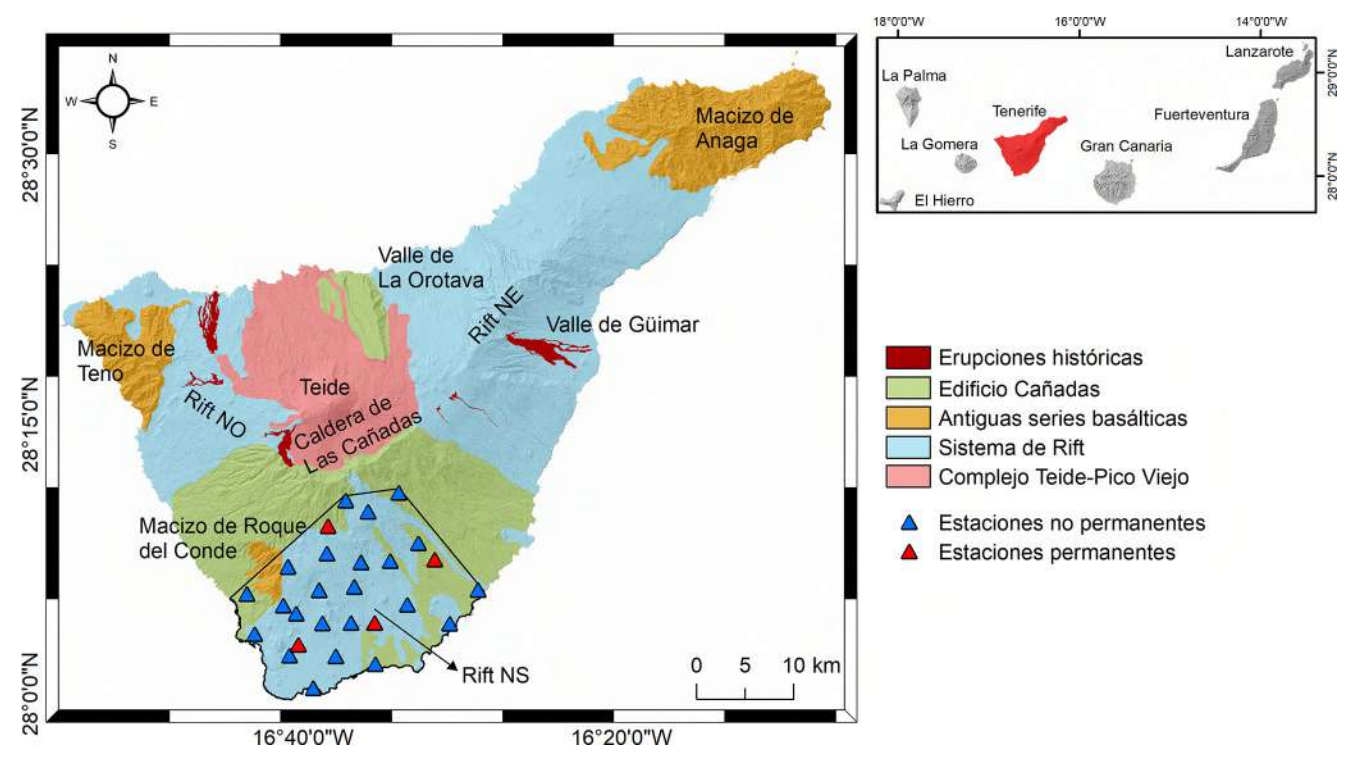


Figura 6. Mapa geológico de Tenerife modificado de Ablay *and* Martí (2000). Los triángulos azules representan la localización de la red sísmica temporal desplegada durante la campaña de exploración geotérmica. Los triángulos rojos representan la localización de la red sísmica permanente operada por INVOLCAN.

Figure 6. Geological map of Tenerife modified from Ablay and Martí (2000). The blue triangles represent the location of the temporary seismic network deployed during the geothermal exploration campaign. The red triangles represent the location of the permanent seismic network operated by INVOLCAN.

de atenuación utilizando los datos obtenidos en el experimento TOM-TEIDEVS permitieron revelar que la corteza superior hasta ~5 km de profundidad se caracteriza por una baja atenuación, mientras que la corteza más profunda está compuesta principalmente por rocas altamente atenuadas. Todos estos estudios han mostrado que la geología de Tenerife es muy compleja, caracterizada por unos contrastes de velocidad muy fuertes.

3.2.1. Campaña de medida y procesamiento de los datos

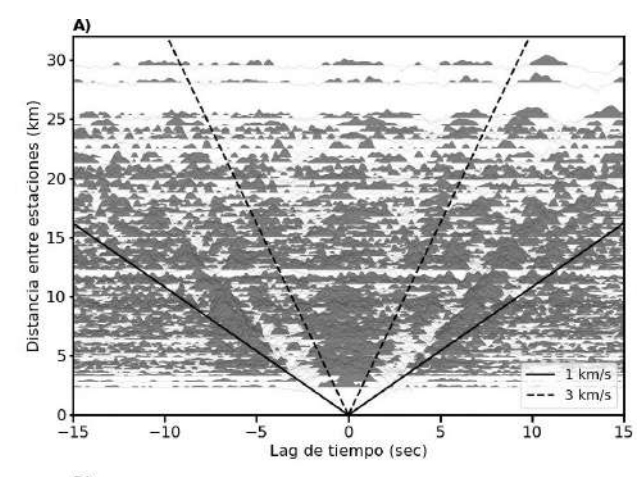
En este estudio se han utilizado los datos de una campaña de exploración geotérmica realizada por el INVOLCAN en el 2018 y en el 2019 en Tenerife. En esta campaña se instalaron 23 estaciones sísmicas de banda ancha (Nanometrics © Trillium Compact 120s) que estuvieron adquiriendo datos durante tres meses a una frecuencia de muestreo de 100 Hz. Además, usamos cuatro estaciones permanentes operadas por INVOLCAN que se utilizan para la monitorización volcánica (Figura 6).

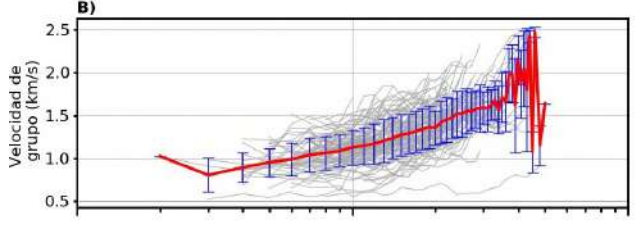
El procesamiento de los datos aplicados a los datos de Tenerife es similar al realizado en Gran Canaria. En este caso, se aplicó un filtro para un rango de frecuencia de 0,01 a 5,0 Hz y se extrajeron 133 curvas de dispersión. Además, se realizó la inversión para obtener los mapas de velocidad de grupo para un rango de periodos de 0,5 - 2,5 s (Figura 7).

3.2.2. Mapas 2-D de velocidad de grupo de ondas de Rayleigh

La Figura 8 muestra los mapas de velocidad de grupo para diferentes periodos T = 0,50 s, T = 1,00 s, T = 1,50 s y T = 2,00 s. Las velocidadesde grupo de ondas de Rayleigh oscilan entre 0,5 km/s y 2,0 km/s. A periodos cortos (Figura 8A), el modelo es casi homogéneo y no se observa ninguna anomalía. A periodos más altos, se incrementan las variaciones de velocidad de los modelos. La Figura 8B muestra una anomalía de baja velocidad en la parte norte, casi en el límite del modelo. Esta zona de anomalía se mantiene casi constante para los diferentes modelos. Por otro lado, en la zona costera se observa una anomalía de alta velocidad que, a periodos altos (Figura 8D), se extiende por toda la parte central de la zona de estudio.

El estudio de magnetotelúrica de Piña-Varas et al. (2014) realizado en la isla muestra una es-





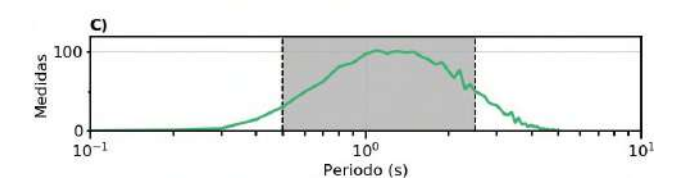


Figura 7. A) Correlaciones cruzadas de todas las parejas de estaciones instaladas en la Dorsal Norte-Sur (Tenerife) ordenadas según la distancia entre estaciones. Las líneas continuas y discontinuas negras marcan velocidades de 1,0 y 3,0 km/s, respectivamente. B) Las líneas grises marcan las curvas de dispersión de ondas de Rayleigh utilizadas en este estudio. La línea roja y las barras azules representan la curva de dispersión promedio y desviación estándar, respectivamente. C) La línea verde representa el número de medidas en función del periodo y el cuadrado gris representa el rango de períodos utilizado en la inversión (0,5-2,5 s).

Figure 7. A) Cross-correlations of all station pairs installed in the North-South Ridge (Tenerife) sorted by pair-station distance. The solid and dashed black lines mark velocities of 1.0 and 3.0 km/s, respectively. B) The gray lines represent Rayleigh wave dispersion curves used in this study. The red line and blue bars represent the average and standard deviation of the dispersion curve, respectively. C) The green line represents the number of measurements as a function of period, and the gray square represents the period range used in the inversion (0.5-2.5 s).

tructura de baja resistividad en la zona de estudio interpretada como una capa de arcilla (*clay cap*) producida por alteración hidrotermal. Esta capa de arcilla no es continua y en algunas zonas de la Dorsal Norte-Sur llega a localizarse de forma muy somera, llegando a encontrarse solo a 0,9 km de profundidad. Rodríguez *et al.* (2015) observaron que la continuidad y extensión de esta capa

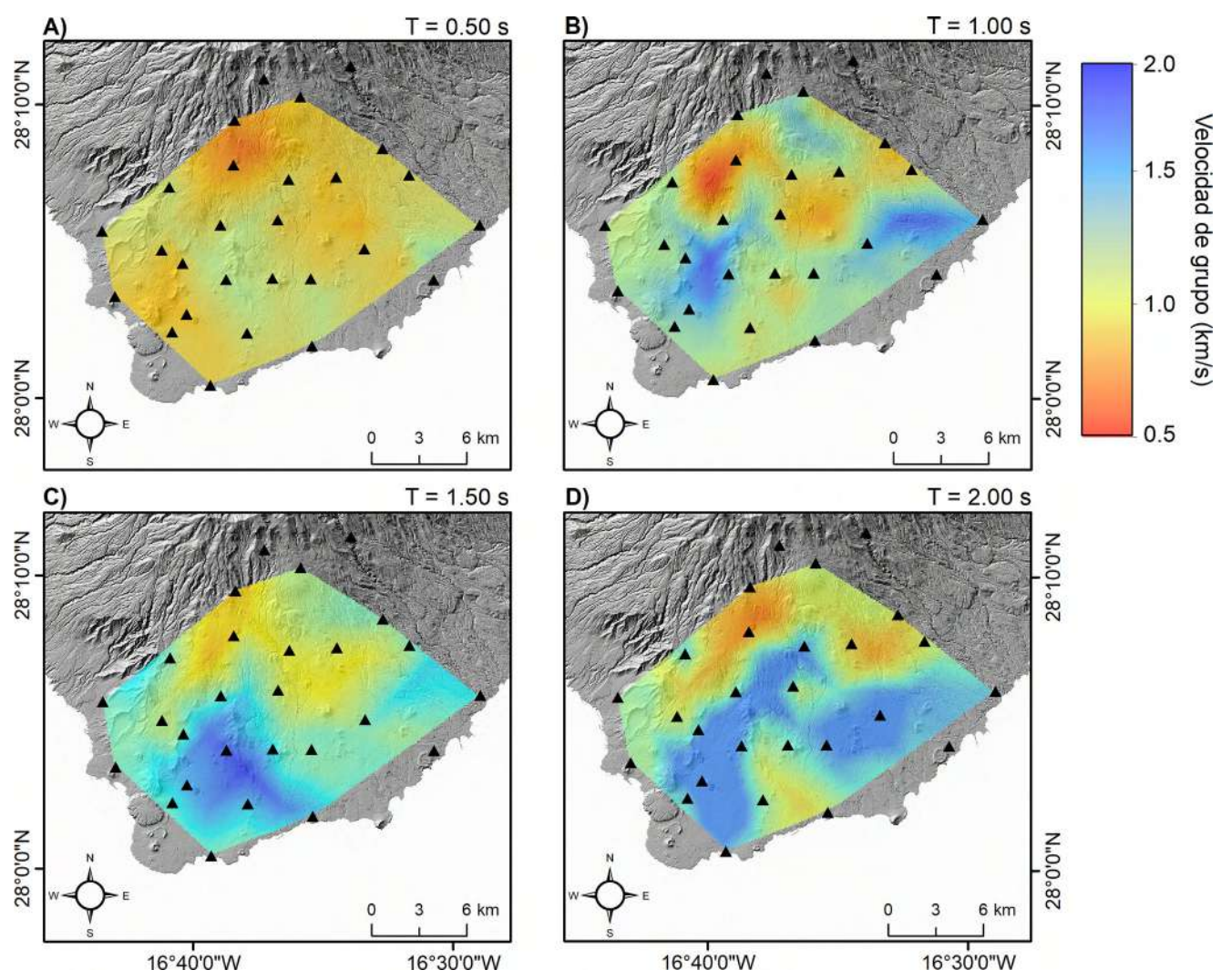


Figura 8. Mapas de velocidades de grupo de ondas de Rayleigh en la Dorsal Norte-Sur para diferentes periodos: A) T = 0.50 s, B) T = 1.00 s, C) T = 1.50 s y D) T = 2.00 s. Los triángulos negros representan la localización de las estaciones sísmicas. **Figure 8.** Rayleigh wave group velocities maps in the North-South Ridge for different periods: A) T = 0.50 s, B) T = 1.00 s, C) T = 1.50 s, and D) T = 2.00 s. The black triangles represent the location of seismic stations.

de arcillas influye en la manifestación superficial de las emisiones de algunos gases como el helio en la Dorsal Norte-Sur de la isla. Las anomalías de baja velocidad de onda de Rayleigh observadas en los modelos obtenidos de la ANT podrían estar asociados con una capa de arcilla más somera. Este *clay cap* más superficial podría ser de gran interés desde el punto de vista geotérmico.

3.3. La Palma

La Palma es una de las islas más jóvenes y la tercera isla más pequeña del archipiélago canario con un área de 706 km² y una altura máxima de 2426 metros sobre el nivel del mar. En esta isla se pueden distinguir dos dominios geológicos: Dominio Taburiente o parte septentrional de la

isla y Dominio Dorsal o parte meridional (Barrera Morate and García Moral, 2011). La evolución geológica de la isla comenzó hace 4 Ma, con la emisión submarina de materiales que constituyeron el complejo basal de la isla (Figura 9). Posteriormente, hace 2-3 Ma, los materiales submarinos ascendieron por encima del nivel del mar y empezaron a ser erosionados. Entre 0,77 - 0,56 Ma apareció un nuevo centro de emisión que se trasladó hacia el sur y que acabaría conformando el edificio Cumbre Nueva. Tras la formación de este edificio se produjo un deslizamiento de la parte occidental, creando una gran depresión en la parte central de la isla. La última parte de la formación de la isla se produjo hace 0,12 Ma cuando se comenzó a formar el edificio Cumbre Vieja, siguiendo una dirección N-S (Barrera Mo-

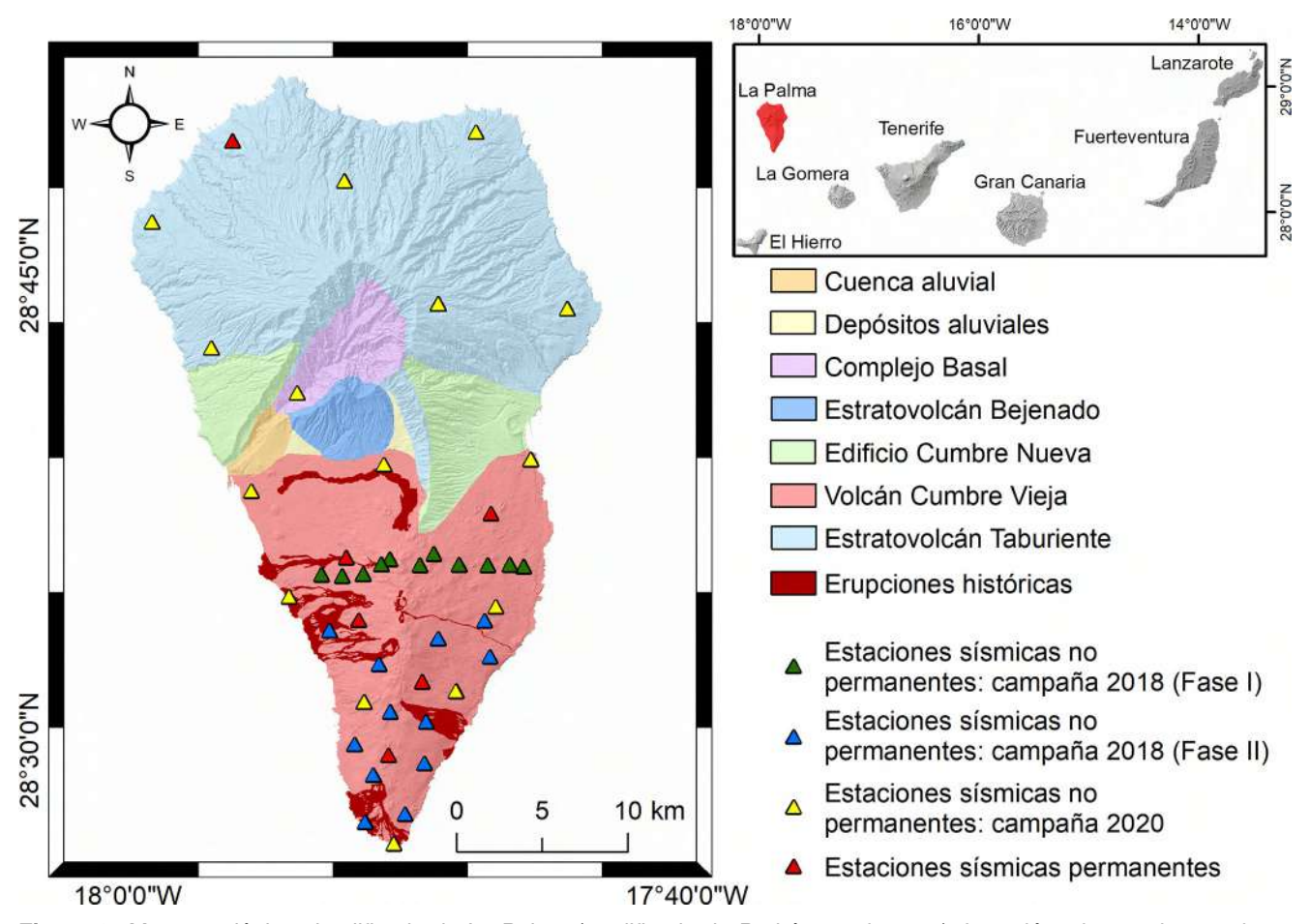


Figura 9. Mapa geológico simplificado de La Palma (modificado de Padrón *et al.*, 2012). Los triángulos verdes, azules y amarillos representan la localización de las estaciones sísmicas temporales instaladas en las diferentes campañas. Los triángulos rojos representan la ubicación de las estaciones permanentes.

Figure 9. Simplified geological map of La Palma (modified from Padrón *et al.*, 2012). The green, blue, and yellow triangles represent the location of temporary seismic stations installed during different campaigns. The red triangles represent the location of permanent stations.

rate and García Moral, 2011). Este periodo se caracterizó por la emisión de un gran volumen de material y un crecimiento muy rápido de la parte sur de la isla. El edificio Cumbre Vieja está formado por una cresta montañosa de 21,5 km de longitud donde se localizan todas las erupciones históricas ocurridas en la isla, incluida la última erupción de la isla que comenzó el 19 de septiembre y terminó el 13 de diciembre de 2021.

Campañas de medida y procesamiento de los datos

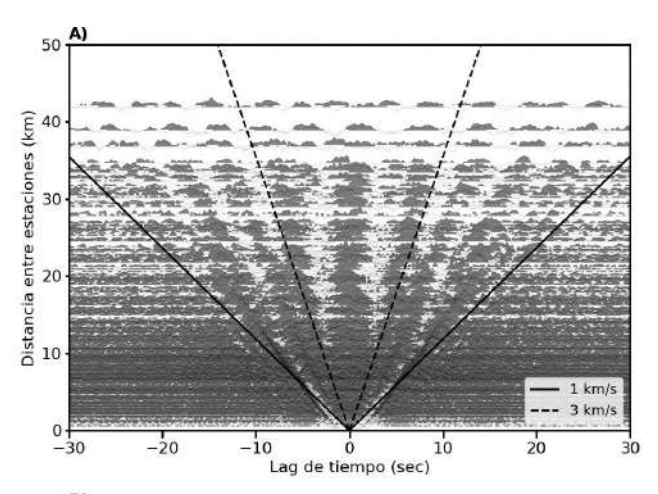
Los datos utilizados en este trabajo provienen de dos campañas de exploración geotérmica realizadas por INVOLCAN en el 2018 y en el 2020 (Figura 9). En 2018 se instalaron 22 estaciones sísmicas de banda ancha (Nanometrics © Trillium Compact 120s) en el volcán Cumbre Vieja en dos

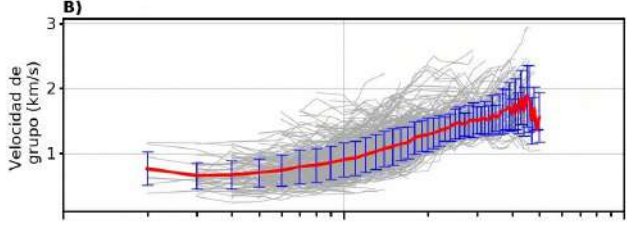
fases (Figura 9). En una primera fase se instalaron 11 estaciones en un perfil en la parte norte de Cumbre Vieja y una estación de referencia en el sur que se mantuvo durante toda la campaña. Transcurrido un mes, se inició la segunda fase donde se trasladaron las estaciones del perfil a la parte central de Cumbre Vieja durante dos meses (Figura 9). En el año 2020 se instalaron 15 estaciones sísmicas repartidas por diferentes partes de la isla y se mantuvieron durante dos meses. Además, se utilizaron las seis estaciones permanentes operadas por INVOLCAN, que tenían en aquel momento, para la monitorización volcánica. En ambas campañas se registraron datos a una frecuencia de muestreo de 100 Hz.

El procesamiento de los datos aplicados a los datos obtenidos en La Palma es similar al aplicado en las islas de Gran Canaria y Tenerife (Figura 10). Se realizó la inversión para obtener los mapas de velocidad de grupo para un rango de periodos de 0,4 - 3,2 s (Figura 10).

3.3.2. Mapas 2-D de velocidad de grupo de ondas de Rayleigh

La Figura 11 muestra los mapas de velocidad de grupo de ondas de Rayleigh para diferentes rangos de periodos, de T = 1,20 s, T = 2,00 s, T = 2,50 s y T = 3,00 s. A periodos cortos (Figuras 11A y B), se observa una zona de baja velocidad





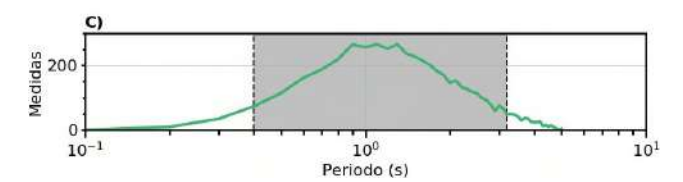


Figura 10. A) Correlaciones cruzadas de todas las parejas de estaciones de La Palma ordenadas según la distancia entre estaciones. Están marcadas velocidades de 1,0 y 3,0 km/s. B) Curvas de dispersión de ondas de Rayleigh (líneas grises) utilizadas en este estudio. La línea roja representa la curva de dispersión promedio y las barras azules representan la desviación estándar. C) Número de medidas en función del periodo (línea verde). El cuadrado gris representa el rango de períodos utilizado en la inversión (0,4-3,2 s).

Figure 10. A) Cross-correlations of all station pairs in La Palma sorted by pair station distance. Velocities of 1.0 and 3.0 km/s are marked. B) Rayleigh wave dispersion curves (gray lines) used in this study. The red line represents the average dispersion curve and the blue bars represent the standard deviation. C) Number of measurements as a function of period (green line). The gray square represents the period range used in the inversion (0.4-3.2 s).

en la zona sur de la isla, abarcando el complejo volcánico de Cumbre Vieja. A periodos más largos (Figuras 11C y D), las bajas velocidades se concentran en los flancos este y oeste del complejo (L1). Esta zona de baja velocidad coincide con zonas conductivas del modelo de resistividad obtenido por Di Paolo et al. (2020), zonas de baja velocidad (D'Auria et al., 2022) y también con las anomalías de baja densidad observadas en Camacho et al. (2009). Tales estructuras de baja resistividad se vinculan con capas de arcillas y pueden estar relacionadas con procesos de alteración hidrotermal, que podrían indicar un movimiento de fluidos hidrotermales que sería de gran interés desde el punto de vista geotérmico. Por otro lado, se observa una zona de alta velocidad (H1) en el norte de la isla, localizada bajo el estratovolcán Taburiente. Esta anomalía corresponde con un cuerpo resistivo (Di Paolo et al., 2020) y una zona de alta densidad (Camacho et al.. 2009), el cual se extiende hasta una profundidad de ~10 km. Esta anomalía ha sido interpretada como un cuerpo intrusivo del Plioceno relacionado con el antiguo vulcanismo de la isla.

4. Conclusiones

La tomografía de ruido sísmico ha demostrado ser una excelente herramienta de exploración geofísica para el estudio a diferentes escalas y para múltiples finalidades. Desde el punto de vista de la exploración geotérmica, la ANT ha probado ser una técnica complementaria a otras técnicas geofísicas como la magnetotelúrica, la tomografía sísmica convencional, la gravimetría, etc. En Canarias, la ANT ha sido utilizada con éxito en las tres zonas de estudio: Gran Canaria. Tenerife y La Palma. El estudio realizado en Gran Canaria ha desvelado la existencia de zonas de baja velocidad en las partes sur y este de la isla, que corresponden con zonas de baja resistividad observadas en los modelos obtenidos por Ledo et al. (2021), que podrían estar asociadas con células convectivas. Por otro lado, el modelo obtenido en la Dorsal Norte-Sur de Tenerife muestra una zona de baja velocidad que podría estar vinculada con un clay cap más superficial, lo que sugiere la presencia de discontinuidades de permeabilidad en esa área donde los gases y fluidos hidrotermales podrían migrar más fácilmente hacia la superficie. Por último, el modelo de La Palma muestra una zona de baja velocidad localizada en los flancos este y oeste del complejo

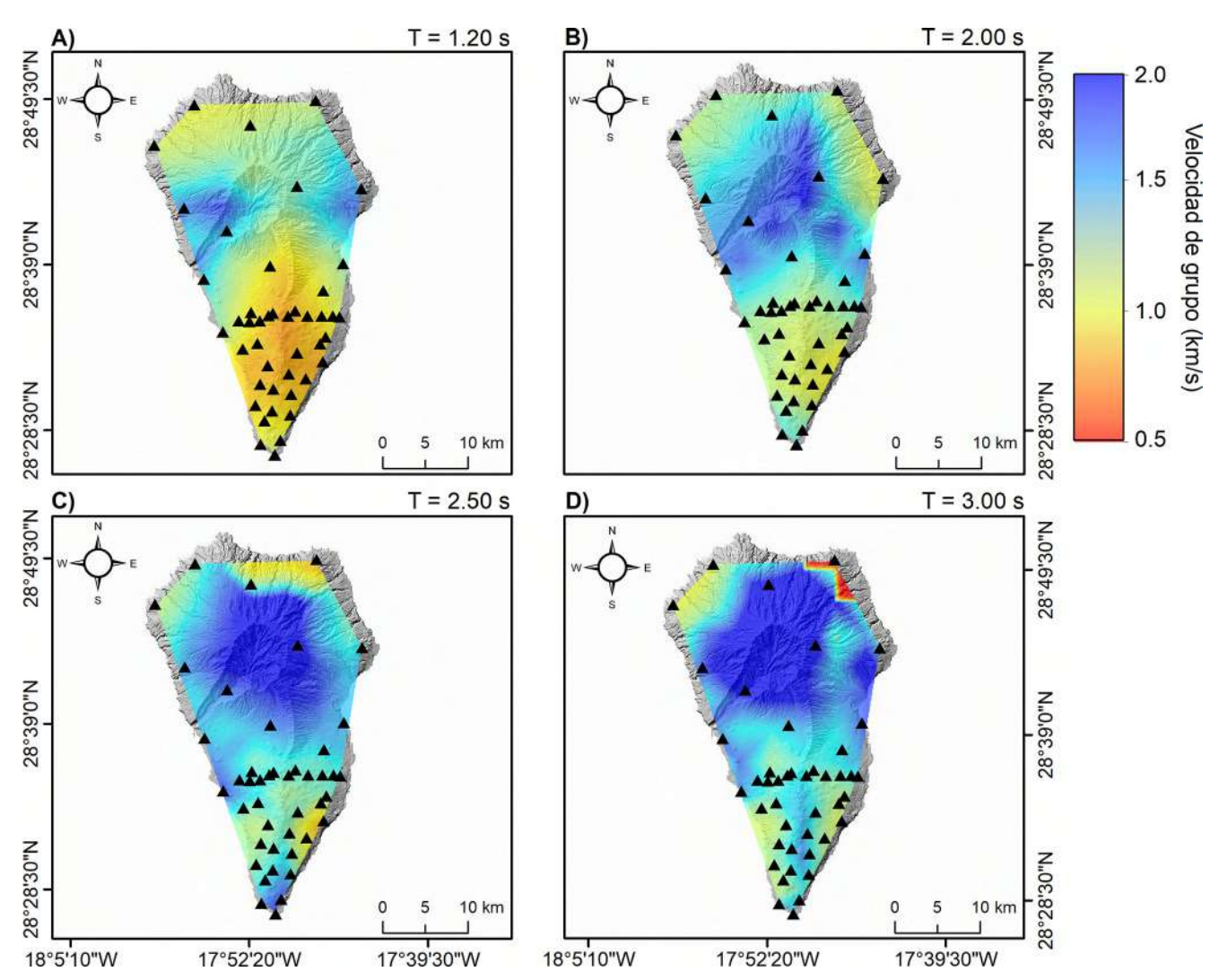


Figura 11. Mapas de velocidad de grupo de ondas de Rayleigh en La Palma para diferentes períodos: A) T = 1,20 s, B) T = 2,00 s, C) T = 2,50 s y D) T = 3,00 s. Los triángulos negros representan la localización de las estaciones sísmicas.

Figure 11. Rayleigh wave group velocities maps of La Palma for different periods: A) T = 1.20 s, B) T = 2.00 s, C) T = 2.50 s, and D) T = 3.00 s. The black triangles represent the location of seismic stations.

volcánico Cumbre Vieja que podrían estar relacionadas con arcillas hidrotermalizadas. Esto podría estar vinculado con una circulación de fluidos hidrotermales, lo cual podría ser de gran interés desde el punto de vista geotérmico.

El método de ANT proporciona información muy útil y relativamente económica para la localización de recursos geotérmicos. Los resultados obtenidos pueden ayudar a definir las áreas más apropiadas que son susceptibles de más investigación detallada para minimizar la incertidumbre sobre la ubicación de una futura perforación exploratoria.

Contribución de los autores

I. C.-P. ha realizado el análisis de los datos. Todos los autores han contribuido a la recopilación de los datos y su interpretación, además de la discusión de los resultados y a la preparación del artículo.

Agradecimientos

La realización de este trabajo ha sido posible gracias al proyecto TERMOVOLCAN (RTC-2017–6627-3), co-financiado por el Plan Nacional de Investigación 2017-2020.

Referencias

Ablay, G. J., and Martí, J. (2000). Stratigraphy, structure, and volcanic evolution of the Pico Teide—Pico Viejo formation, Tenerife, Canary Islands. Journal of Volcanology and Geothermal research, 103(1-4), 175-208.

- Ancochea, E., Fuster, J., Ibarrola, E., Cendrero, A., Coello, J., Hernan, F., ... and Jamond, C. (1990). Volcanic evolution of the island of Tenerife (Canary Islands) in the light of new K-Ar data. Journal of Volcanology and Geothermal Research, 44(3-4), 231-249.
- Aster, R. C., Borchers, B., and Thurber, C. H. (2018). Parameter estimation and inverse problems. Elsevier.
- Bacells, R., Barrera, J. L., and Gómez Sainz de Ajam, J. A. (1990). Mapa geológico digital continuo e. 1:25.000, zona canarias-gran canaria. (zona-2912).
- Barrera Morate, J. L., and García Moral, R. (2011). Mapa Geológico de Canarias. GRAFCAN, Santa Cruz de Tenerife.
- Bensen, G. D., Ritzwoller, M. H., Barmin, M. P., Levshin, A. L., Lin, F., Moschetti, M. P., ... and Yang, Y. (2007). Processing seismic ambient noise data to obtain reliable broad-band surface wave dispersion measurements. Geophysical Journal International, 169(3), 1239-1260.
- Blanco-Montenegro, I., Torta, J. M., García, A., and Araña, V. (2003). Analysis and modelling of the aeromagnetic anomalies of Gran Canaria (Canary Islands). Earth and Planetary Science Letters, 206(3-4), 601-616.
- Bodin, T., Sambridge, M., Rawlinson, N., and Arroucau, P. (2012). Transdimensional tomography with unknown data noise. Geophysical Journal International, 189(3), 1536-1556.
- Brenguier, F., Shapiro, N. M., Campillo, M., Nercessian, A., and Ferrazzini, V. (2007). 3-D surface wave tomography of the Piton de la Fournaise volcano using seismic noise correlations. Geophysical research letters, 34(2), L02305.
- Cabrera-Pérez, I., D'Auria, L., Soubestre, J., Barrancos, J., Padilla, G. D., and Pérez, N. M. (2021). A nonlinear multiscale inversion approach for ambient noise tomography. Geophysical Journal International, 225(2), 1158-1173.
- Cabrera-Pérez, I., Centeno, R., Soubestre, J., D'Auria, L., Rivera, M., and Machacca, R. (2022). Ambient noise tomography of Misti volcano, Peru. Journal of Volcanology and Geothermal Research, 426, 107538.
- Cabrera-Pérez, I., Soubestre, J., D'Auria, L., van Dorth, D. M., Ledo, J., Piña-Varas, P., ... and Pérez, N. M. (2023). Ambient noise tomography of Gran Canaria island (Canary Islands) for geothermal exploration. Geothermics, 108, 102609.
- Calò, M., Kinnaert, X., and Dorbath, C. (2013). Procedure to construct three-dimensional models of geothermal areas using seismic noise cross-correlations: application to the Soultz-sous-Forêts enhanced geothermal site. Geophysical Journal International, 194(3), 1893-1899.

- Camacho, A. G., Montesinos, F. G., and Vieira, R. (2000). Gravity inversion by means of growing bodies. Geophysics, 65(1), 95-101.
- Camacho, A. G., Fernández, J., González, P. J., Rundle, J. B., Prieto, J. F., and Arjona, A. (2009). Structural results for La Palma island using 3-D gravity inversion. Journal of Geophysical Research: Solid Earth, 114(B5), B05411.
- Canales, J. P., Dañobeitia, J. J., and Watts, A. B. (2000). Wide-angle seismic constraints on the internal structure of Tenerife, Canary Islands. Journal of volcanology and geothermal research, 103(1-4), 65-81.
- D'Auria, L., Koulakov, I., Prudencio, J., Cabrera-Pérez, I., Ibáñez, J. M., Barrancos, J., ... and Peréz, N. M. (2022). Rapid magma ascent beneath La Palma revealed by seismic tomography. Scientific Reports, 12(1), 17654.
- De Siena, L., Sammarco, C., Cornwell, D. G., La Rocca, M., Bianco, F., Zaccarelli, L., and Nakahara, H. (2018). Ambient seismic noise image of the structurally controlled heat and fluid feeder pathway at Campi Flegrei caldera. Geophysical Research Letters, 45(13), 6428-6436.
- Di Paolo, F., Ledo, J., Ślęzak, K., van Dorth, D. M., Cabrera-Pérez, I., and Pérez, N. M. (2020). La Palma island (Spain) geothermal system revealed by 3D magnetotelluric data inversion. Scientific reports, 10(1), 1-8.
- Fang, H., Yao, H., Zhang, H., Huang, Y. C., and van der Hilst, R. D. (2015). Direct inversion of surface wave dispersion for three-dimensional shallow crustal structure based on ray tracing: methodology and application. Geophysical Journal International, 201(3), 1251-1263.
- García-Yeguas, A., Koulakov, I., Ibanez, J. M., and Rietbrock, A. (2012). High resolution 3D P wave velocity structure beneath Tenerife Island (Canary Islands, Spain) based on tomographic inversion of active-source data. Journal of Geophysical Research: Solid Earth, 117(B9), B09309.
- Gouédard, P., Stehly, L., Brenguier, F., Campillo, M.,
 De Verdière, Y. C., Larose, E., ... and Weaver, R.
 L. (2008). Cross-correlation of random fields: Mathematical approach and applications. Geophysical prospecting, 56(3), 375-393.
- Ibáñez, J. M., Rietbock, A., and García-Yeguas, A. (2008). Imaging an active volcano edifice at Tenerife Island, Spain. Eos, Transactions American Geophysical Union, 89(32), 289-290.
- Ke, G., Dong, H., Kristensen, Å., and Thompson, M. (2011). Modified Thomson–Haskell matrix methods for surface-wave dispersion-curve calculation and their accelerated root-searching schemes. Bulletin of the Seismological Society of America, 101(4), 1692-1703.

- Kedar, S., Longuet-Higgins, M., Webb, F., Graham, N., Clayton, R., and Jones, C. (2008). The origin of deep ocean microseisms in the North Atlantic Ocean. Proceedings of the Royal Society A: Mathematical, Physical and Engineering Sciences, 464(2091), 777-793.
- Kim, S., Tkalčić, H., Rhie, J., and Chen, Y. (2016). Intraplate volcanism controlled by back-arc and continental structures in NE Asia inferred from transdimensional Bayesian ambient noise tomography. Geophysical Research Letters, 43(16), 8390-8398.
- Koulakov, I., D'Auria, L., Prudencio, J., Cabrera-Pérez, I., Barrancos, J., Padilla, G. D., ... and Ibáñez, J. M. (2023). Local earthquake seismic tomography reveals the link between crustal structure and volcanism in Tenerife (Canary Islands). Journal of Geophysical Research: Solid Earth, 128(3), e2022JB025798.
- Krastel, S., and Schmincke, H. U. (2002). Crustal structure of northern Gran Canaria, Canary Islands, deduced from active seismic tomography. Journal of Volcanology and Geothermal Research, 115(1-2), 153-177.
- Ledo, J., Garcia-Merino, M., Larnier, H., Slezak, K., Pina-Varas, P., Marcuello, A., ... and Sumita, M. (2021). 3D electrical resistivity of Gran Canaria island using magnetotelluric data. Geothermics, 89, 101945.
- Lehujeur, M., Vergne, J., Schmittbuhl, J., Zigone, D., Le Chenadec, A., and EstOF Team. (2018). Reservoir imaging using ambient noise correlation from a dense seismic network. Journal of Geophysical Research: Solid Earth, 123(8), 6671-6686.
- Levshin, A., Ratnikova, L., and Berger, J. O. N. (1992). Peculiarities of surface-wave propagation across central Eurasia. Bulletin of the Seismological Society of America, 82(6), 2464-2493.
- Li, C., Yao, H., Fang, H., Huang, X., Wan, K., Zhang, H., and Wang, K. (2016a). 3D near-surface shearwave velocity structure from ambient-noise tomography and borehole data in the Hefei urban area, China. Seismological Research Letters, 87(4), 882-892.
- Li, Z., Ni, S., Zhang, B., Bao, F., Zhang, S., Deng, Y., and Yuen, D. A. (2016b). Shallow magma chamber under the Wudalianchi Volcanic Field unveiled by seismic imaging with dense array. Geophysical Research Letters, 43(10), 4954-4961.
- Lin, F. C., Ritzwoller, M. H., Townend, J., Bannister, S., and Savage, M. K. (2007). Ambient noise Rayleigh wave tomography of New Zealand. Geophysical Journal International, 170(2), 649-666.
- Martins, J. E., Weemstra, C., Ruigrok, E., Verdel, A., Jousset, P., and Hersir, G. P. (2020). 3D S-wave velocity imaging of Reykjanes Peninsula high-enthalpy geothermal fields with ambient-noise tomo-

- graphy. Journal of Volcanology and Geothermal Research, 391, 106685.
- Masterlark, T., Haney, M., Dickinson, H., Fournier, T., and Searcy, C. (2010). Rheologic and structural controls on the deformation of Okmok volcano, Alaska: FEMs, InSAR, and ambient noise tomography. Journal of Geophysical Research: Solid Earth, 115(B2), B02409.
- Mordret, A., Rivet, D., Landès, M., and Shapiro, N. M. (2015). Three-dimensional shear velocity anisotropic model of Piton de la Fournaise Volcano (La Réunion Island) from ambient seismic noise. Journal of Geophysical Research: Solid Earth, 120(1), 406-427.
- Nakata, N., Gualtieri, L., and Fichtner, A. (Eds.). (2019). Seismic ambient noise. Cambridge University Press.
- Nolet, G. (2008). A Breviary of Seismic Tomography Cambridge Univ. Press, Cambridge, UK, 324.
- Padrón, E., Pérez, N. M., Hernández, P. A., Sumino, H., Melián, G., Barrancos, J., ... and Padilla, G. (2012). Helium emission at Cumbre Vieja volcano, La Palma, Canary Islands. Chemical Geology, 312, 138-147.
- Peterson, J. (1993). Observation and Modeling of Seismic Background Noise. USGS Technical Report 93-322, 95 pp.
- Piña-Varas, P., Ledo, J., Queralt, P., Marcuello, A.,
 Bellmunt, F., Hidalgo, R., and Messeiller, M. (2014).
 3-D magnetotelluric exploration of Tenerife geothermal system (Canary Islands, Spain). Surveys in Geophysics, 35(4), 1045-1064.
- Planès, T., Obermann, A., Antunes, V., and Lupi, M. (2020). Ambient-noise tomography of the Greater Geneva Basin in a geothermal exploration context. Geophysical Journal International, 220(1), 370-383.
- Prudencio, J., Ibáñez, J. M., Del Pezzo, E., Martí, J., García-Yeguas, A., and De Siena, L. (2015). 3D attenuation tomography of the volcanic island of Tenerife (Canary Islands). Surveys in Geophysics, 36, 693-716.
- Rodríguez, F., Pérez, N. M., Padrón, E., Melián, G., Pina-Varas, P., Dionis, S., ... and Hidalgo, R. (2015). Surface geochemical and geophysical studies for geothermal exploration at the southern volcanic rift zone of Tenerife, Canary Islands, Spain. Geothermics, 55, 195-206.
- Rodríguez, F., Pérez, N. M., Melián, G. V., Padrón, E., Hernández, P. A., Asensio-Ramos, M., ... and D'Auria, L. (2021). Exploration of deep-seated geothermal reservoirs in the Canary Islands by means of soil CO2 degassing surveys. Renewable Energy, 164, 1017-1028.
- Sabra, K. G., Gerstoft, P., Roux, P., Kuperman, W. A., and Fehler, M. C. (2005). Surface wave tomography from microseisms in Southern California. Geophysical Research Letters, 32(14), L14311.

- Sambridge, M., Gallagher, K., Jackson, A., and Rickwood, P. (2006). Trans-dimensional inverse problems, model comparison and the evidence. Geophysical Journal International, 167(2), 528-542.
- Saygin, E., and Kennett, B. L. (2010). Ambient seismic noise tomography of Australian continent. Tectonophysics, 481(1-4), 116-125.
- Schmincke, H. U., and Sumita, M. (2010). Geological evolution of the Canary Islands: a young volcanic archipelago adjacent to the old African Continent. Goerres-Druckerei und Verlag, 196 p. ISBN: 978-3-86972-005-0.
- Sethian, J. A. (1996). A fast marching level set method for monotonically advancing fronts. Proceedings of the National Academy of Sciences, 93(4), 1591-1595.
- Shapiro, N. M., Campillo, M., Stehly, L., and Ritzwoller, M. H. (2005). High-resolution surface-wave tomography from ambient seismic noise. Science, 307(5715), 1615-1618.
- Shomali, Z. H., and Shirzad, T. (2015). Crustal structure of Damavand volcano, Iran, from ambient noise and earthquake tomography. Journal of Seismology, 19(1), 191-200.
- Snieder, R. (2004). Extracting the Green's function from the correlation of coda waves: A derivation based on stationary phase. Physical Review E, 69(4), 046610.
- Spica, Z., Legrand, D., Iglesias, A., Walter, T. R., Heimann, S., Dahm, T., ... and Pardo, M. (2015). Hydrothermal and magmatic reservoirs at Lazufre volcanic area, revealed by a high-resolution seismic noise tomography. Earth and Planetary Science Letters, 421, 27-38.
- Stankiewicz, J., Ryberg, T., Haberland, C., and Natawidjaja, D. (2010). Lake Toba volcano magma chamber imaged by ambient seismic noise tomo-

- graphy. Geophysical Research Letters, 37(17), L17306.
- Wahida, A., Wijaya, H., Yudistira, T., and Sule, M. R. (2018, July). Ambient noise tomography for geothermal exploration, a case study of WWs geothermal field. In AIP Conference Proceedings (Vol. 1987, No. 1, p. 020101). AIP Publishing LLC.
- Wang, Z., and Dahlen, F. A. (1995). Validity of surface-wave ray theory on a laterally heterogeneous earth. Geophysical Journal International, 123(3), 757-773.
- Wapenaar, K. (2004). Retrieving the elastodynamic Green's function of an arbitrary inhomogeneous medium by cross correlation. Physical review letters, 93(25), 254301.
- Weaver, R. L., and Lobkis, O. I. (2001). Ultrasonics without a source: Thermal fluctuation correlations at MHz frequencies. Physical Review Letters, 87(13), 134301.
- Woodhouse, J. H. (1974). Surface waves in a laterally varying layered structure. Geophysical Journal International, 37(3), 461-490.
- Yang, Y., Ritzwoller, M. H., Levshin, A. L., and Shapiro, N. M. (2007). Ambient noise Rayleigh wave tomography across Europe. Geophysical Journal International, 168(1), 259-274.
- Yang, Y., Ritzwoller, M. H., and Jones, C. H. (2011). Crustal structure determined from ambient noise tomography near the magmatic centers of the Coso region, southeastern California. Geochemistry, Geophysics, Geosystems, 12(2), Q02009.
- Zheng, D., Saygin, E., Cummins, P., Ge, Z., Min, Z., Cipta, A., and Yang, R. (2017). Transdimensional Bayesian seismic ambient noise tomography across SE Tibet. Journal of Asian Earth Sciences, 134, 86-93.

scientific reports



OPEN Geothermal and structural features of La Palma island (Canary Islands) imaged by ambient noise tomography

Iván Cabrera-Pérez^{1⊠}, Jean Soubestre^{2,3}, Luca D'Auria^{1,4}, José Barrancos⁴, Alba Martín-Lorenzo⁴, David Martínez van Dorth⁴, Germán D. Padilla⁴, Monika Przeor⁴ & Nemesio M. Pérez^{1,4}

La Palma island is located in the NW of the Canary Islands and is one of the most volcanically active of the archipelago, therefore the existence of geothermal resources on the island is highly probable. The main objective of this work is to detect velocity anomalies potentially related to active geothermal reservoirs on La Palma island, by achieving a high-resolution seismic velocity model of the first few kilometres of the crust using Ambient Noise Tomography (ANT). The obtained ANT model is merged with a recent local earthquake tomography model. Our findings reveal two high-velocity zones in the island's northern and southern parts, that could be related to a plutonic intrusion and old oceanic crust materials. Conversely, four low-velocity zones are imaged in the southern part of the island. Two of them can be related to hydrothermal alteration zones located beneath the Cumbre Vieja volcanic complex. This hypothesis is reinforced by comparing the S-wave velocity model with the seismicity recorded during the pre-eruptive phase of the 2021 Tajogaite eruption, which revealed an aseismic volume coinciding with these low-velocity zones. Another low-velocity zone is observed in the southern part of the island, which we interpret as highly fractured rocks which could favour the ascent of hot fluids. A last low-velocity zone is observed in the central part of the island and associated with loose deposits generated by the Aridane valley mega landslide.

The Canary Islands archipelago comprises seven islands located close to the northwest coast of Africa, between latitudes 27°38'N and 29°25'N, and longitudes 13°20'W and 18°90'W (Fig. 1). All these islands have a volcanic origin. Volcanism in the Canary Islands began during the Oligocene and is still active¹. La Palma island is located in the western part of the archipelago and is one of the youngest islands. The island has an elongated shape following a North-South direction with a maximum height of 2426 m a.s.l. (above the sea level). Two very well differentiated geological domains can be distinguished on La Palma island: the Taburiente Domain, which is the oldest domain located in the northern part of the island, and the Cumbre Vieja volcanic complex, which is constituted by the most recent volcanic materials in the southern part of the island (Fig. 1). The island's formation began with submarine lava emissions 4 My ago. The first subaerial material was emitted 1.77 My ago, forming the Taburiente stratovolcano. Between 0.77 and 0.56 My, the Cumbre Nueva volcanic complex formed to the South of the Taburiente stratovolcano. During this period, a landslide occurred on the western flank of Cumbre Nueva, creating the large Aridane valley in the central part of the island². Between 0.56 and 0.49 My, the Bejenado stratovolcano was formed on top of the Cumbre Nueva edifice. Finally, the Cumbre Vieja volcanic complex started its formation 0.12 My ago. It is currently the only volcanically active zone of the island, where all the historical eruptions took place.

The last volcanic eruption on La Palma island started on September 19th, 2021, and lasted approximately three months up to December 13th. This eruption, named Tajogaite eruption, resulted in significant social, economic and scientific impacts. Pre-eruptive unrest started on September 11st, 2021, eight days before the eruption³. During this unrest, the seismicity quickly migrated from 10 km depth to the surface, following the ascending

¹Instituto Volcanológico de Canarias (INVOLCAN), 38600 Granadilla de Abona, Tenerife, Canary Islands, Spain. ²Univ. Grenoble Alpes, Univ. Savoie Mont Blanc, CNRS, IRD, Univ. Gustave Eiffel, ISTerre, 38000 Grenoble, France. ³Icelandic Meteorological Office, Reykjavik, Iceland. ⁴Instituto Tecnológico y de Energías Renovables (ITER), 38600 Granadilla de Abona, Tenerife, Canary Islands, Spain. [™]email: icabrera@involcan.org

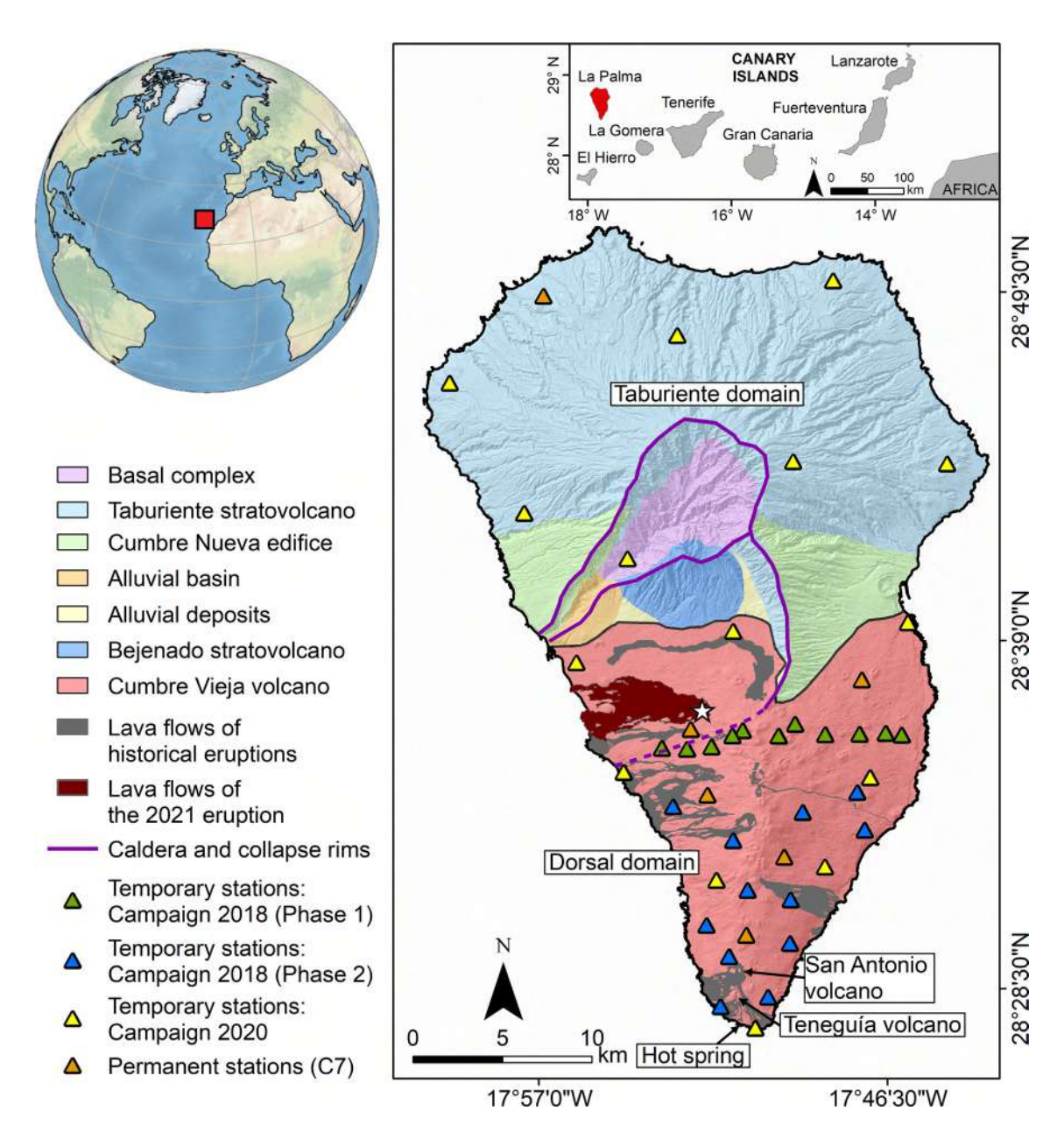


Figure 1. Geological map of La Palma island (modified from Padrón et al.⁴⁶). The white star represents the location of the Tajogaite eruption, the last eruption which took place on the island between September 19th and December 13th, 2021. The triangles represent the location of temporal and permanent seismic stations, with colors corresponding to different phases as described in the caption.

path of the magma. Finally, a fissural eruption began on September 19th at about 14:00 UTC, with a dominantly strombolian activity and episodic phreatomagmatic pulses^{4,5}. This latest eruption has reminded the potential of this island to host geothermal resources. By the way, the interest for geothermal exploration had recently been renewed in the Canary Islands, as testified by several geophysical and geochemical studies realized on Gran Canaria island⁶⁻⁸, Tenerife island^{7,9-12} and La Palma island¹³.

The present study aims at determining the geological structure of La Palma island through seismic ambient noise tomography (ANT), focusing on velocity anomalies possibly related to geothermal reservoirs. The ANT has proven to be an efficient method to image structures at different scales e.g., ^{14–25}. The first ANT dedicated to geothermal exploration was realized by Yang et al. ²⁶ at the Coso geothermal field (California) and revealed the existence of shallow low-velocity zones related to geothermal alteration. Other studies of ANT inferred the presence of temperature anomalies related to deep hydrothermal circulation e.g., ^{8,27,28}, water reservoirs e.g., ²⁹, new geothermal reservoirs e.g., ³⁰, pockets of partial melt e.g., ³¹ or deep heat sources e.g., ³². These studies evidenced the potential of ANT as a complementary geophysical method for geothermal exploration.

Data acquisition was realized between 2018 and 2020, by deploying 38 broadband seismic stations during different campaigns (Fig. 1). The methodology used for the ANT is detailed in the "Methods" section. The ANT first comprises a non-linear multiscale inversion taking the topography into account³³ to retrieve the 2-D group

velocity maps at different periods. Those group velocity maps are then inverted at depth using a transdimensional approach³⁴. The obtained 3-D S-wave velocity model of the island is exposed and discussed in the following sections. It is compared with previous geophysical studies^{3,13,35} to determine common features. Furthermore, the ANT model is combined with a recent local earthquake tomography (LET) model³, having ANT a higher resolution at shallow depth but a limited penetration depth compensated by the LET.

Results

This section illustrates the results of the ambient noise tomography. Figure 2 shows the obtained maps of S-wave relative velocity variation at different depths. The relative velocity variation at each depth is calculated with respect to the mean velocity at the corresponding depth. The main anomalies observed in the S-wave velocity model are marked in Figure 2C, distinguishing between high (H) and low (L) velocity anomalies. It can be seen

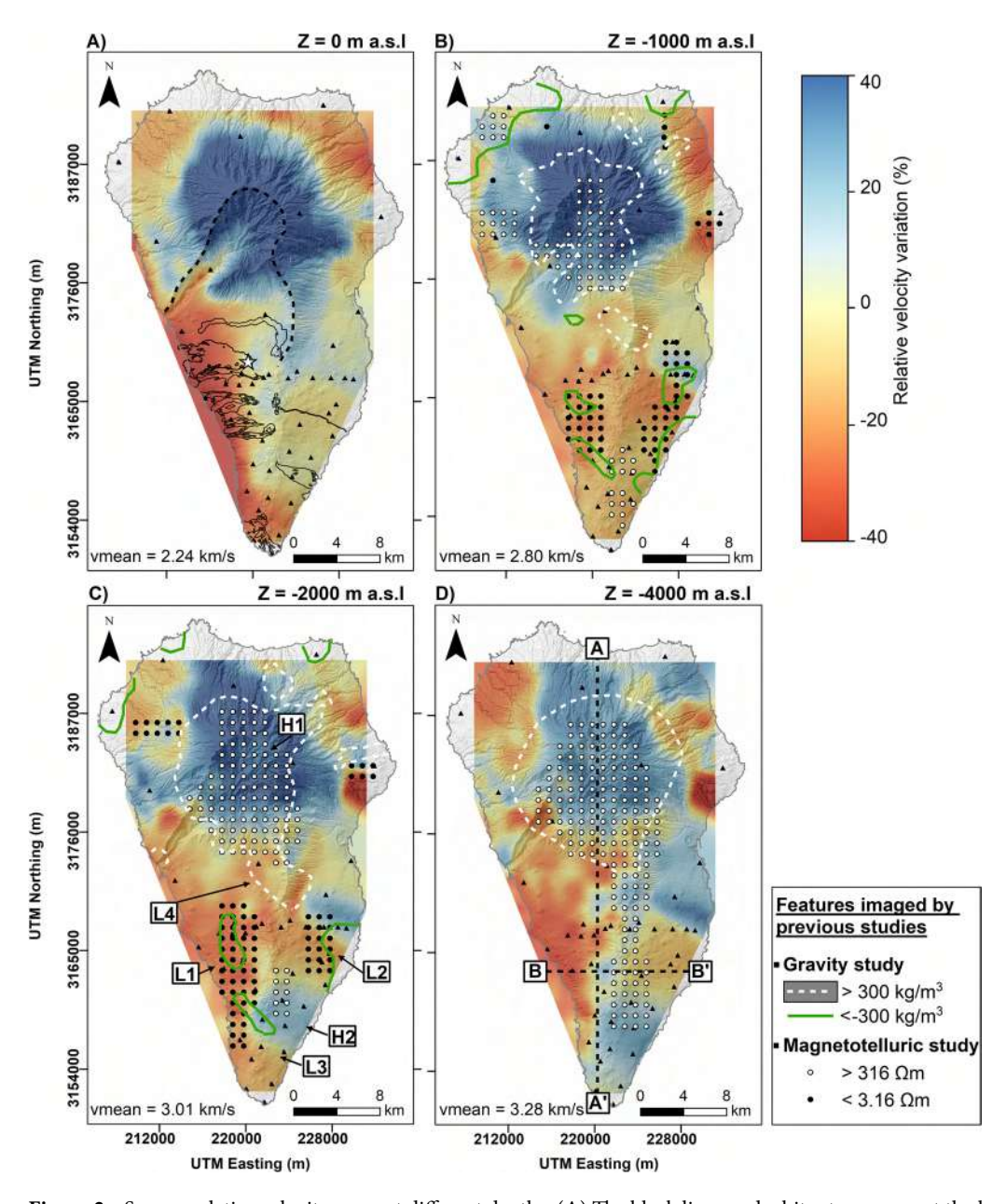


Figure 2. S-wave relative velocity maps at different depths. (**A**) The black lines and white star represent the lava flows of the historical eruptions and the location of the Tajogaite volcano, respectively. The black triangles show the location of seismic stations. The white and green lines in subplots (**B-D**) represent the high and low-density anomalies from a previous density study³⁵, respectively. The white and black points in subplots (**B-D**) represent the high and low resistivity zones from a previous magnetotelluric study¹³, respectively. The different seismic velocity anomalies obtained from this study and discussed in the text are shown in subplot (**C**). Vertical cross-sections corresponding to Figs. 3 and 4 are shown in subplot (**D**).

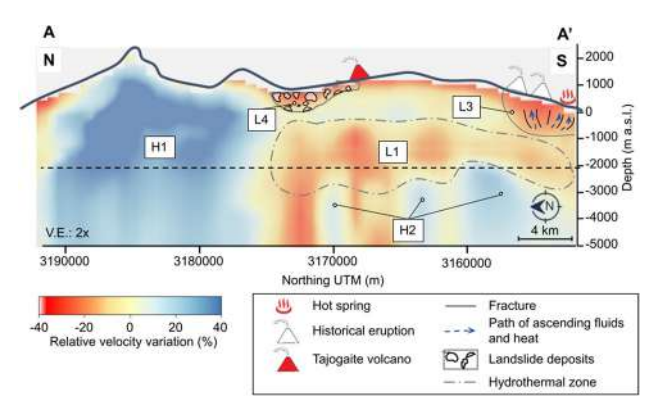


Figure 3. Vertical N–S cross-section (cf. A–A' in Fig. 2D) of the S-wave relative velocity model. The black dashed line represents the depth at which the model resolution is maximum and below which it starts to decrease. White and red triangles represent the historical and Tajogaite eruption sites, respectively.

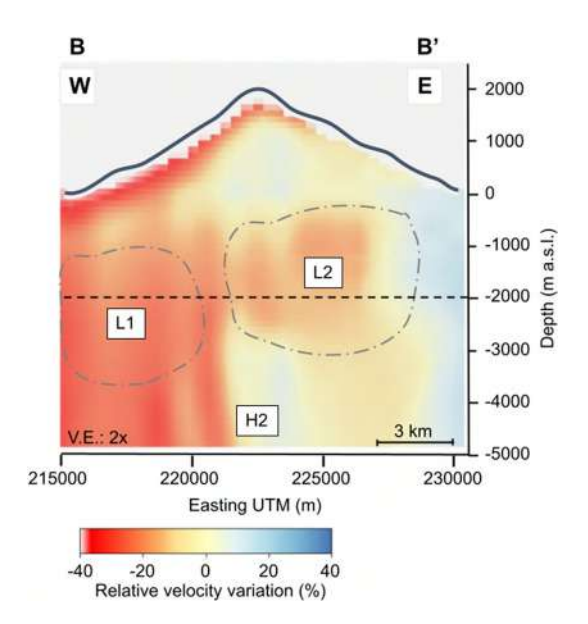


Figure 4. Vertical E-W cross-sections (cf. B-B' in Figure 2D) of the S-wave relative velocity model. The black dashed line represents the depth at which the model resolution is maximum and below which it starts to decrease.

on Figure 2 that the island shows very strong velocity variations, reaching 40% in some areas. The mean S-wave velocity is 2.24 km/s in superficial zones (Fig. 2A), while it reaches 3.28 km/s for deeper zones (Fig. 2D).

Figures 3 and 4 show two vertical cross-sections of the 3-D S-wave velocity model, which positions are indicated in Fig. 2D. A high-velocity zone (H1) extends from the surface to a depth of 5000 m b.s.l. (below sea level) in the island's northern part, with relative velocities that vary between 20% and 40% (Fig. 3). Another high-velocity zone (H2) is present between 2000 m b.s.l. and 5000 m b.s.l. in the island's southern part (Fig. 3). On the other hand, two low-velocity zones (L1 and L2) can be observed in the southern part of the island, located on the western (L1) and eastern (L2) flanks of the Cumbre Vieja volcanic complex (Fig. 2C). These velocity anomalies are found at a depth ranging from 0 down to 3000 m b.s.l. (Fig. 4) with relative velocity variations ranging between -20% and -40%. A third low-velocity anomaly (L3) is located in the southern part of the Cumbre Vieja volcanic complex at a depth between 0 and 1000 m b.s.l., with relative velocities of less than -20% (Fig. 3). Finally, a fourth low-velocity anomaly (L4) can be observed in the central part of the island, with a depth not exceeding the sea level and relative velocity variations of -20% (Fig. 3). As detailed in the "Methods" section, some resolution tests confirmed the capacity of the used network configuration to image all the previously mentioned anomalies (Figs. S4, S5 and S6 from the supplementary materials).

Figure 5 shows a vertical cross-section of the unified ANT+LET S-wave velocity model together with the hypocenters of the earthquakes recorded during the Tajogaite eruption pre-eruptive unrest (11-19 Sept. 2021). This seismicity was relocated by D'Auria et al.³ using a tridimensional velocity model obtained from LET. This allowed determining the path of the ascending magma to the surface. The unified S-wave velocity model (Fig. 5)

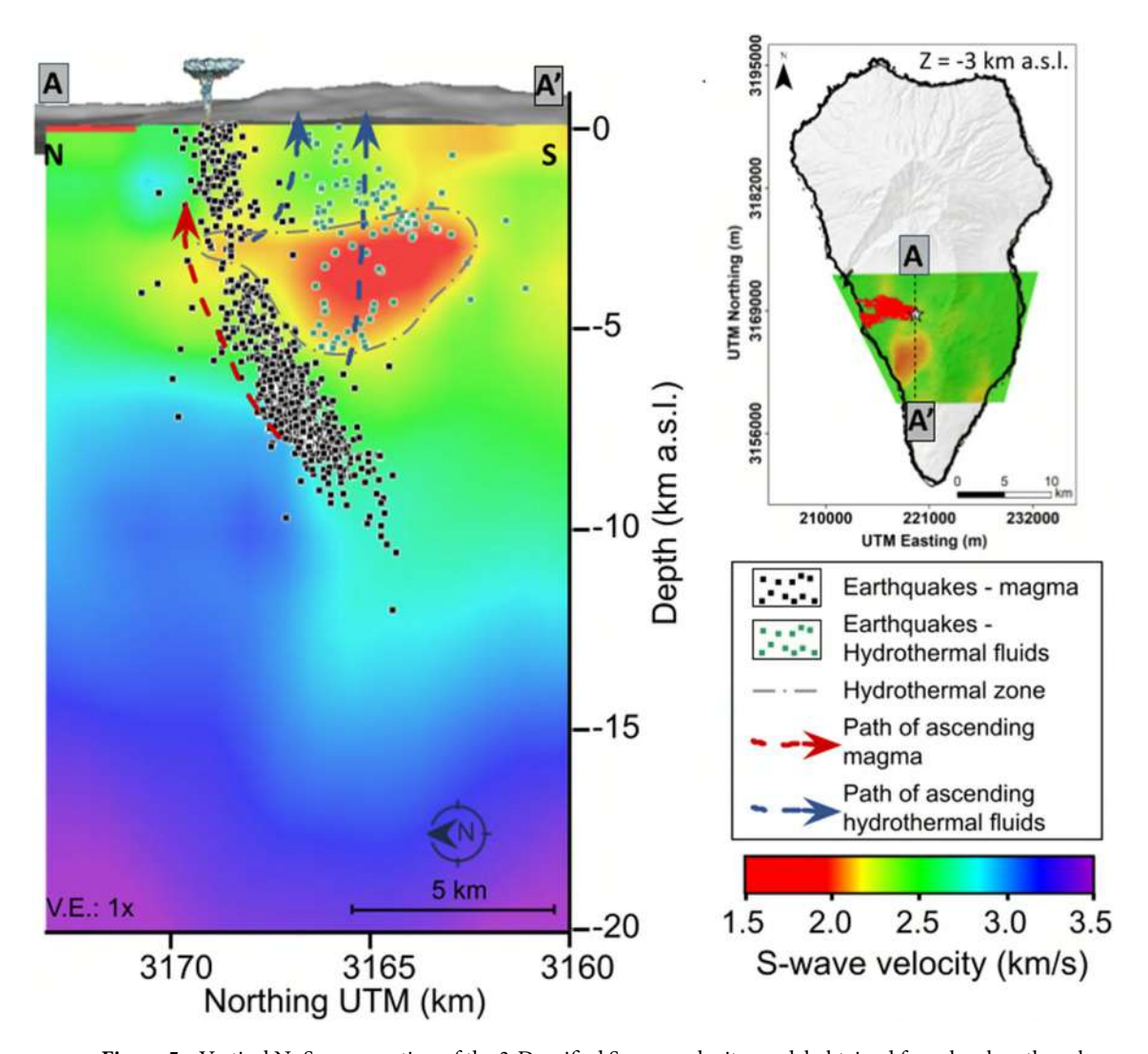


Figure 5. Vertical N–S cross-section of the 3-D unified S-wave velocity model obtained from local earthquake tomography (LET, previous study) and ambient noise tomography (ANT, this study). The black and green dots represent earthquakes related to magma and hydrothermal fluid ascent, respectively.

shows some relevant velocity anomalies. A high-velocity zone is observed below 5 km b.s.l., whose depth increases in the southern part of the island. D'Auria et al. 3 related this feature to the geometry of the Moho beneath the island. In addition, a low-velocity anomaly is clearly observed at shallow depth (< 5 km b.s.l.) and coincides with anomalies detected by other geophysical studies in the same area 13,35 , as discussed in the next section.

Discussion

The 3-D S-wave velocity model of La Palma island reveals a great complexity of the geological structure with six principal velocity anomalies: two high-velocity anomalies located in the northern and southern parts of the island, and four low-velocity anomalies associated with the Cumbre Vieja volcanic complex in the southern part of the island. The approach we used for the tomographic inversion takes into account the topography of the island. Furthermore, the use of a transdimensional approach for depth inversion does not require establishing an "a priori" parametrization and provides velocity profiles in a Bayesian fashion, which allows a quantitative non-linear estimation of the uncertainties. In the following, we discuss the volcanological and geothermal relevance of such anomalies, making a comparison with the resistivity model of Di Paolo et al. ¹³ and the density model of Camacho et al. ³⁵.

The anomaly H1 is one of the most relevant due to its giant size. It has already been observed by other geophysical studies. Camacho et al. 35 observed a high-density body in this zone, with values above 300 kg/m^3 . In the same zone, Di Paolo et al. 13 imaged a high-resistivity anomaly, with peak values exceeding $316 \Omega m$ (Fig. 2). Considering these studies and our S-wave velocity model, this anomaly is interpreted as linked to the plutonic intrusion related to the ancient volcanism of the island during its basal complex formation (ca. 4.0 to 3.0 Ma) $^{1.36}$.

Another group of significant high-velocity anomalies (H2) coincides with a high-resistivity zone (Figs. 2C and D) with values higher than $316\,\Omega m$ (Di Paolo et al. 13). We note that the density model of Camacho et al. 35 doesn't show any anomaly in this zone. Di Paolo et al. 13 suggest that this anomaly could be related to the upper part of

a shallow intrusive magmatic complex. This hypothesis is compatible with our velocity model. Such intrusive bodies were observed in other ANT studies realized in Snæfellsjökull volcano³⁷, Eyjafjallajökull volcano³⁸, Misti volcano²⁵, and other volcanic and geothermal environments.

From a geothermal point of view, the most relevant features are the low-velocity anomalies L1 and L2 (Fig. 2). Both anomalies coincide with zones of low resistivity and low density. Camacho et al. 35 associated these anomalies with zones of shallow fractures following the direction of the N-S rift structure of Cumbre Vieja. On the other hand, Di Paolo et al. 13 interpreted these anomalies as clay alteration caps (illite and illite-smectite). Because of the geophysical characteristics detailed hereafter, we consider that these low-velocity anomalies are related to a hydrothermal alteration zone which could indicate the presence of an active or fossil hydrothermal system in the Cumbre Vieja volcanic complex. Previous studies demonstrated that hydrothermal fluids could decrease the S-wave velocity 39,40. This hypothesis matches observations from our unified S-wave velocity model and its comparison with the hypocenters of the pre-eruptive seismicity (Fig. 5). The seismicity recorded during the preeruptive episode of the Tajogaite eruption indicates a nearly vertical ascent of the magma to the surface (Fig. 5, black dots), which rose through a network of interconnected sills and dykes⁴¹. However, the seismicity south of the eruption site (Fig. 5, green dots) was associated with the ascent of hydrothermal fluids^{3,42}. Cabrera-Pérez et al. 42 indirectly confirmed the existence of a possible geothermal reservoir in the western flank of the Cumbre Vieja volcanic complex through ambient noise interferometry by computing relative velocity variations (dv/v) during the pre-eruptive phase of Tajogaite eruption. The authors observed a decrease of dv/v in this zone prior to the eruption, which they interpreted as the ascent of hydrothermal fluids exsolved from the magma, which reached the surface only a few days later. Furthermore, recent petrological observations realized by Pankhurst et al.⁴³ determined that the magmas emitted during the initial phase of the Tajogaite eruption were more hydrated, which could indicate that this hydrothermal alteration zone is still active, with the current presence of fluids. These fluids would travel faster through zones of high permeability caused by intense fracturing, such as the lowvelocity anomaly L1 imaged by our S-wave velocity model. Moreover, the number of earthquakes is considerably reduced in this low-velocity zone (Fig. 5, green dots). This could be a consequence of the presence of hydrothermally altered material characterized by a lower rigidity, which could explain the reduced seismogenic capability of this zone. Conversely, the microseismic activity is higher and more important outside of this zone (Fig. 5, black dots), indicating a more fragile behaviour. Those different geophysical and petrological observations sustain our hypothesis of the existence of an active hydrothermal system beneath the Cumbre Vieja volcanic complex.

Another low-velocity anomaly is L3, located in the southern part of the island (Fig. 2C), beneath the two historical eruptions of San Antonio (1677) and Teneguía (1971) volcanoes (Fig. 3). This zone of low velocity does not coincide with any resistivity or density anomaly observed in the studies of Di Paolo et al. ¹³ and Camacho et al. ³⁵. However, subsidence was detected by InSAR beneath Teneguía volcano by Prieto et al. ⁴⁴, which they related to a thermal source. In addition, Padrón et al. ⁴⁵ measured an anomaly of diffuse CO_2 emission ($>800 \ g \ m^{-2} day^{-1}$) in the area of Teneguía volcano prior to the Tajogaite eruption (2001-2013). Moreover, they sampled anomalous temperatures varying between 90° C and 130° C at 40 cm depth in this zone. It should be noted that a hot spring (Fuente Santa) is present in the southern part of the Teneguía volcano (Figs. 1 and 3), where water temperatures reaching 40° C and concentration levels of HCO_3^- and $SO_4^{-2}^-$ exceeding 2000 mg/L were measured ⁴⁶, which could indicate the circulation of underground water through high-temperature rocks. Our hypothesis to explain the low-velocity anomaly L3 is that high-temperature rocks and a series of fractures through which hydrothermal fluids and gases are rising to the surface are present under the Teneguía and San Antonio volcanoes, which would explain the observed geochemical anomalies ^{45,46} and subsidence ⁴⁴.

Finally, the low-velocity anomaly L4 is located in a valley zone of the island's central part (Fig. 2C). This valley was produced by at least two destructive episodes related to huge landslides that formed the arc of Cumbre Nueva and the Taburiente caldera, partially destroying the existing volcanic edifices². This anomaly could be related to landslide deposits mostly composed of conglomerate materials.

Considering the previous geophysical models^{3,13,35} and the S-wave velocity model obtained from ANT in this study, we argue for the highest geothermal potential of La Palma island to be located on both the western and eastern flanks of the active Cumbre Vieja volcanic complex at a depth of 2000 m b.s.l., approximately. In addition, the southern part of this volcanic system also seems to host some shallow geothermal resources, as evidenced by this study and additional geophysical⁴⁴ and geochemical^{45,46} observations.

Conclusions

A 3-D S-wave velocity model of La Palma island was obtained by unifying results from a new ANT model obtained in this study and a LET model obtained by D'Auria et al.³. We applied ANT on data recorded by 38 broadband seismic stations to extract the dispersion curves of all the station pairs. Subsequently, we obtained the 2-D group velocity maps through a non-linear multiscale inversion taking the topography into account³³. Finally, we derived some S-wave 1-D profiles using a Bayesian tridimensional inversion. The final 3-D S-wave velocity model shows the presence of two high-velocity zones (H1 and H2) and four low-velocity zones (L1, L2, L3 and L4).

The high-velocity anomalies H1 and H2 are interpreted as related to a plutonic intrusion related to the island's ancient volcanism and more recent solidified intrusive dyke complexes, respectively. From the point of view of geothermal exploration, the most interesting imaged features are the low-velocity anomalies L1, L2, and L3. The low-velocity zones L1 and L2 are interpreted as hydrothermal alteration zones associated with the presence of an active or fossil hydrothermal system in the Cumbre Vieja volcanic complex. Velocity variations estimated before the Tajogaite eruption seem to favour the hypothesis of an active hydrothermal reservoir. The anomaly L3 is interpreted as associated with fractured rocks favouring the ascent of hot fluids toward the surface in the island's southern part. This hypothesis could also explain the geochemical and geophysical anomalies observed

in previous studies^{44–46}. Finally, the low-velocity anomaly L4 could be related to landslide deposits produced during destructive episodes of the island's geological history.

It would be necessary to carry out more detailed geophysical and geochemical exploration surveys at the scale of the Cumbre Vieja volcanic complex in order to further advance in the characterization of the geothermal potential of La Palma island. This is especially true in the southern part of the island, where S-wave low-velocity anomalies are shallower. Furthermore, it would be necessary to apply clustering and machine learning techniques to realize a quantitative comparison of the resistivity, density and S-wave velocity models, in order to better interpret the geological context.

Methods

Data acquisition. In 2018 we installed 23 seismic stations in the southern part of the island, in two phases of one month each, focusing on the Cumbre Vieja volcano. In 2020 we installed 15 stations distributed throughout the whole island which were recording during two months. The goal was to characterize the zones that were not sampled during the first two campaigns. Considering the distribution of the seismic stations, the highest density of stations and ray path anisotropy is in the Cumbre Vieja volcano (Fig. S1 in the supplementary materials), which is the most active part of the island from a volcanological point of view. Furthermore, we used six permanent stations operated by Instituto Volcanológico de Canarias for volcano monitoring (Fig. 1).

Ambient noise data processing. In order to realize the ambient noise data processing we pre-processed the data, cross-correlated all the station pairs and extracted the dispersion curves¹⁴, as detailed hereafter. We used an automatic network-based method^{47,48} to remove time windows containing earthquakes (Fig. S2 in the supplementary materials). Subsequently, a bandpass filter was applied in the 0.01–5.00Hz frequency range and a standard ambient noise pre-processing composed of temporal one-bit normalization and spectral whitening was applied to the remaining data to reduce its non-stationarity⁴⁹.

Afterwards, the cross-correlations of pre-processed data were computed for all station pairs on five-minute-long windows and stacked over one month for the 2018 campaigns and two months for the 2020 campaign. We performed this analysis on vertical-vertical components for 578 station pairs. The obtained cross-correlations appear in Figure S3.A, evidencing coherent wavetrains of dispersive Rayleigh waves. In order to verify that the noise sources distribution was close to isotropy, which is a fundamental assumption when doing ANT^{50,51}, we calculated the amplitude ratio of the causal and acausal parts of cross-correlations as a function of the azimuthal distribution of station pairs (Fig. S3B). Figure S3B shows an excellent azimuthal distribution for all orientations of station pairs. Furthermore, it seems that there is no specific dominating noise source, as the amplitude ratio is mostly close to 1 for all the station pairs (Fig. S3B).

Then, the Rayleigh wave group velocity dispersion curves were determined through frequency-time analysis (FTAN)⁵². We extracted 415 dispersion curves shown in Figure S3.C. The red curve represents the mean dispersion curve with its standard deviation at each period (blue line). Figure S3.D shows the number of measurements as a function of the period. We limit our analysis to reasonably covered period ranges with at least 50 measurements, restricting us to periods between 0.35 s and 3.2 s for the tomographic inversion.

2-D group velocity maps. We applied a non-linear multiscale inversion taking the topography into account³³ to obtain the 2-D group velocity maps at different periods. The starting model consists of a homogeneous velocity model. The model parametrization is refined at subsequent non-linear inversion steps by adding control nodes over a regular grid. In other words, at each step, we refine the model by increasing the scale, which means increasing the number of parameters used to define the model. The result of each scale is used as a starting model for the following inversion scale. This inversion method was applied satisfactorily in different studies of volcanic areas^{8,25}.

We performed different tests on synthetic models to determine the spatial resolution of the tomographic images. First, checkerboard tests (Fig. S4 in the supplementary materials) and a test on a synthetic model composed of a pattern of low and high-velocity diamond-shaped anomalies (Fig. S5 in the supplementary materials) were performed. We used three different linear sizes for both tests, namely 0.05° x 0.05° , 0.1° × 0.1° and 0.2° x 0.2° , corresponding approximately to sizes of 5.5 km x 5.5 km, 11.1 km x 11.1 km and 22.2 km x 22.2 km, respectively, with a maximum velocity of 2.1 km/s and a minimum of 1.9 km/s (Figs. S4 and S5 in the supplementary materials). Both models with a resolution of 0.1° x 0.1° and 0.2° x 0.2° were correctly retrieved (Figs. S4.D, S4.F, S5.D and S5.F in the supplementary materials). Conversely, the checkerboard test with a resolution of 0.05° x 0.05° was not correctly retrieved in the island's northern part (Figs. S4.B and S5.B) due to a lower ray path density in this zone (Fig. S1), but it was correctly retrieved in the southern part of the island where the ray path density is higher (Figs. S4B, S5B and S1 in the supplementary materials). Furthermore, a resolution test was realized on a synthetic model composed of anomalies similar to anomalies H1, L1, and L2 imaged from real data (Fig. S6A in the supplementary materials). Figure S6.B shows that the three anomalies were correctly retrieved.

Figure S7 of the supplementary materials shows the results of the 2-D mapping of the Rayleigh wave group velocity obtained using a checkerboard test at different scales of 4, 5 and 6. Maps of scales 4 and 5 are pretty similar and correctly retrieve both the geometry and velocity. Conversely, the map of scale 6 shows artefacts, and the velocity pattern cannot be retrieved correctly. Therefore, we limit our inversion process on real data to a scale of 5.

Figure S8 shows four Rayleigh wave 2-D group velocity maps obtained from real data for periods between $T=1.2 \, s$ and $T=3.0 \, s$. The variance reduction(VarRed) and mean velocity are indicated on each panel of Figure S8. For all the considered periods, the VarRed is higher than 50%. On the other hand, the mean velocity increases with the period, from 1.22 km/s to 1.81 km/s, consistently with the global trend of the average dispersion curve shown in Figure S3.C.

Regarding the spatial patterns in the 2-D group velocity maps (Fig. S8 in the supplementary materials), we observe important velocity contrasts at different periods. At short period corresponding to shallow depth, the T=1.2~s map does not show significant anomalies, predominating the low-velocity zone in the great majority of the island with a mean velocity of 1.2~km/s. At higher period, the T=2.00~s map shows a velocity increase in the island's northern part, which increases again at higher periods. Between the periods of T=2.5~s and T=3.0~s, we can observe the presence of two low-velocity zones on both flanks of the Cumbre Vieja volcanic complex, with a velocity lower than 1.25~km/s.

Depth inversion. The last step in the inversion process involves inverting the group velocity maps to obtain S-wave 1-D profiles in depth. We extracted a dispersion curve corresponding to each of the 347 control points of the 2-D group velocity maps to perform the inversion using a transdimensional approach³⁴. This approach allows obtaining an "a posteriori" probability distribution of the seismic velocities, largely independent of a specific parametrization, namely the number of layers. The transdimensional approach includes the parametrization itself among the inverse problem parameters⁵³. In this work, we explored models having a number of uniform horizontal layers ranging between one and five. The calculation of the forward model used for the computation of dispersion curves was performed using a modified Thomson-Haskell matrix method⁵⁴, which allows for improving the numerical stability of the computation and accelerating the calculation of the dispersion curves. Figures S9 and S10 in the supplementary materials show some examples of the transdimensional inversion result, which consists of a probability distribution and the position of discontinuities for the S-wave velocity at each depth. The selected 1-D S-wave velocity model corresponds to the median probability value at each depth.

Figures S9A-B and C-D in the supplementary materials show the transdimensional inversion results corresponding to high-velocity anomalies H1 and H2, respectively. Figure S9A shows a rapid increase in S-wave velocity, starting from 1 km/s at the surface and reaching 4 km/s at 2 km depth. Three main discontinuities can be observed between the depths of 0 and 2 km (Fig. S9.B). Conversely, Figure S9.D shows a greater number of discontinuities in the superficial part above 1 km depth. At a depth of 1 km, the velocity begins to increase reaching approximately 3.0 km/s (Fig. S9.C).

Figure S10 shows four examples of transdimensional inversion results corresponding to low-velocity anomalies L1, L2, L3, and L4. Figures S10.A-B show the 1-D S-wave velocity profiles in depth for anomaly L1. A shallow discontinuity appears between 0 and 1 km depth, where the velocity increases rapidly, starting at 1 km/s and increasing until 2 km/s. Between 1 km and 3 km depth, the velocity is almost constant. At depths greater than 3 km, there is a velocity increase related to anomaly H2. Conversely, Figures S10.C-D show the 1-D S-wave velocity profiles in depth for anomaly L2. At shallow depths less than 1 km, there are multiple discontinuities with velocity increasing from 1 km/s to 2 km/s. At greater depths, the velocity remains almost constant. Figures S10.E-F and G-H show the 1-D S-wave velocity profiles in depth for anomalies L3 and L4, respectively. In both profiles, the velocity increases rapidly at shallow depths and does not vary significantly at greater depths.

In order to determine the depth resolution of our S-wave velocity model, we computed the group velocity sensitivity kernels for the fundamental mode of Rayleigh wave at different periods using the software senskernel-1.0⁵⁵ (Fig. S11 of the supplementary materials). We note that the kernels have a sufficient resolution down to 3 km depth and no resolution below 5 km.

Unification of S-wave velocity models. The S-wave velocity models obtained by ANT (this study) and LET³ have different resolutions as a function of depth. The ANT model has a higher resolution at a shallow depth of less than 4 km, while the LET model has a higher resolution at greater depths. The two models are therefore unified following the procedure described by D'Auria et al.⁵⁶, where the two models are joined into a single one through a weighted averaging:

$$v(x_i, y_j, z_k) = \frac{\sum_{m=1}^{M} v_m(x_i, y_j, z_k) w_m(x_i, y_j, z_k)}{\sum_{m=1}^{M} w_m(x_i, y_j, z_k)}$$
(1)

where M is the number of models at the point (x_i, y_j, z_k) , $v_m(x_i, y_j, z_k)$ is the S-wave velocity and $w_m(x_i, y_j, z_k)$ is the weight of the m-th model. Figure S12 in the supplementary materials shows the weight as a function of depth for both S-wave velocity models. The S-wave velocity model unification was performed down to 5 km depth with weights varying between 0 and 1 (Fig. S12 in the supplementary materials). The unified S-wave velocity model has therefore a good resolution at both shallow and great depth, revealing the geometry of various low-velocity anomalies (Fig. S13 in the supplementary materials).

Data availability

All the results obtained in this study are shared at https://doi.org/10.5281/zenodo.7113144.

Received: 15 December 2022; Accepted: 2 August 2023 Published online: 09 August 2023

References

- 1. Staudigel, H. & Schmincke, H.-U. The Pliocene seamount series of La Palma/Canary Islands. J. Geophys. Res. Solid Earth 89, 11195–11215. https://doi.org/10.1029/JB089iB13p11195 (1984).
- 2. Ancochea, E. et al. Constructive and destructive episodes in the building of a young oceanic island, La Palma, Canary Islands, and genesis of the Caldera de Taburiente. J. Volcanol. Geoth. Res. 60, 243–262. https://doi.org/10.1016/0377-0273(94)90054-X (1994).

- 3. D'Auria, L. et al. Rapid magma ascent beneath La Palma revealed by seismic tomography. Sci. Rep.https://doi.org/10.1038/s41598-022-21818-9 (2022).
- 4. Carracedo, J. C. et al. The 2021 eruption of the Cumbre Vieja volcanic ridge on La Palma, Canary Islands. Geol. Today 38, 94-107. https://doi.org/10.1111/gto.12388 (2022).
- 5. Romero, J. E. et al. The initial phase of the 2021 Cumbre Vieja ridge eruption (Canary Islands): Products and dynamics controlling edifice growth and collapse. J. Volcanol. Geoth. Res. 431, 107642. https://doi.org/10.1016/j.jvolgeores.2022.107642 (2022).
- Ledo, J. et al. 3D electrical resistivity of Gran Canaria island using magnetotelluric data. Geothermics 89, 101945. https://doi.org/ 10.1016/j.geothermics.2020.101945 (2021).
- 7. Rodríguez, F. et al. Exploration of deep-seated geothermal reservoirs in the Canary Islands by means of soil CO2 degassing surveys. Renew. Energy 164, 1017-1028. https://doi.org/10.1016/j.renene.2020.09.065 (2021).
- 8. Cabrera-Pérez, I. et al. Ambient noise tomography of Gran Canaria island (Canary Islands) for geothermal exploration. Geothermics 108, 102609. https://doi.org/10.1016/j.geothermics.2022.102609 (2023).
- 9. Piña-Varas, P. et al. 3-D magnetotelluric exploration of Tenerife geothermal system (Canary Islands, Spain). Surv. Geophys. 35, 1045-1064 (2014).
- 10. Rodríguez, F. et al. Surface geochemical and geophysical studies for geothermal exploration at the southern volcanic rift zone of Tenerife, Canary Islands, Spain. Geothermics 55, 195-206. https://doi.org/10.1016/j.geothermics.2015.02.007 (2015).
- 11. Rodríguez, F. et al. Diffuse helium and hydrogen degassing to reveal hidden geothermal resources in oceanic volcanic islands: The Canarian archipelago case study. Surv. Geophys. 36, 351-369. https://doi.org/10.1007/s10712-015-9320-8 (2015).
- 12. Alonso, M. et al. Heat and Helium-3 fluxes from Teide volcano, Canary Islands, Spain. Geofluidshttps://doi.org/10.1155/2019/ 3983864 (2019).
- 13. Di Paolo, F. et al. La Palma island (Spain) geothermal system revealed by 3D magnetotelluric data inversion. Sci. Rep. 10, 1-8. https://doi.org/10.1038/s41598-020-75001-z (2020).
- 14. Shapiro, N. M., Campillo, M., Stehly, L. & Ritzwoller, M. H. High-resolution surface-wave tomography from ambient seismic noise. Science 307, 1615-1618. https://doi.org/10.1126/science.1108339 (2005).
- Sabra, K. G., Gerstoft, P., Roux, P., Kuperman, W. A. & Fehler, M. C. Surface wave tomography from microseisms in Southern California. *Geophys. Res. Lett.* 32, 1–4. https://doi.org/10.1029/2005GL023155 (2005).
- 16. Lin, F.-C., Ritzwoller, M. H., Townend, J., Bannister, S. & Savage, M. K. Ambient noise Rayleigh wave tomography of New Zealand.
- Geophys. J. Int. 170, 649-666. https://doi.org/10.1111/j.1365-246X.2007.03414.x (2007). Yang, Y., Ritzwoller, M. H., Levshin, A. L. & Shapiro, N. M. Ambient noise Rayleigh wave tomography across Europe. Geophys. J.
- Int. 168, 259-274. https://doi.org/10.1111/j.1365-246X.2006.03203.x (2007). 18. Brenguier, F., Shapiro, N. M., Campillo, M., Nercessian, A. & Ferrazzini, V. 3-D surface wave tomography of the Piton de la Four-
- naise volcano using seismic noise correlations. Geophys. Res. Lett.https://doi.org/10.1029/2006GL028586 (2007) 19. Moschetti, M., Ritzwoller, M. & Shapiro, N. Surface wave tomography of the western United States from ambient seismic noise:
- Rayleigh wave group velocity maps. Geochem. Geophys. Geosyst.https://doi.org/10.1111/j.1365-246X.2008.03720.x (2007).
- Saygin, E. & Kennett, B. L. Ambient seismic noise tomography of Australian continent. Tectonophysics 481, 116-125. https://doi. org/10.1016/j.tecto.2008.11.013 (2010).
- Masterlark, T., Haney, M., Dickinson, H., Fournier, T. & Searcy, C. Rheologic and structural controls on the deformation of Okmok volcano, alaska: FEMs, Insar, and ambient noise tomography. J. Geophys. Res. Solid Earthhttps://doi.org/10.1029/2009JB006324 (2010).
- Stankiewicz, J. et al. Lake Toba volcano magma chamber imaged by ambient seismic noise tomography. Geophys. Res. Lett. https:// doi.org/10.1029/2010GL044211 (2010).
- 23. Jin, G. & Gaherty, J. B. Surface wave phase-velocity tomography based on multichannel cross-correlation. Geophys. J. Int. 201, 1383-1398. https://doi.org/10.1093/gji/ggv079 (2015).
- Obermann, A. et al. Structure of Masaya and Momotombo volcano, Nicaragua, investigated with a temporary seismic network. J. Volcanol. Geoth. Res. 379, 1-11. https://doi.org/10.1016/j.jvolgeores.2019.04.013 (2019).
- 25. Cabrera-Pérez, I. et al. Ambient noise tomography of Misti volcano, Peru. J. Volcanol. Geotherm. Res. https://doi.org/10.1016/j. jvolgeores.2022.107538 (2022).
- 26. Yang, Y., Ritzwoller, M. H. & Jones, C. H. Crustal structure determined from ambient noise tomography near the magmatic centers of the Coso region, southeastern California. Geochem. Geophys. Geosyst. https://doi.org/10.1029/2010GC003362 (2011).
- 27. Lehujeur, M., Vergne, J., Schmittbuhl, J. & Maggi, A. Characterization of ambient seismic noise near a deep geothermal reservoir and implications for interferometric methods: A case study in northern Alsace, France. Geotherm. Energy 3, 3. https://doi.org/10. 1186/s40517-014-0020-2 (2016).
- 28. Lehujeur, M., Vergne, J., Schmittbuhl, J., Zigone, D. & Le Chenadec, A. Reservoir imaging using ambient noise correlation from a dense seismic network. J. Geophys. Res. Solid Earthhttps://doi.org/10.1029/2018JB015440 (2018).
- 29. Wahida, A., Wijaya, H., Yudistira, T. & Sule, M. R. Ambient noise tomography for geothermal exploration, a case study of WWs geothermal field. *AIP Conf. Proc.* **1987**, 020101. https://doi.org/10.1063/1.5047386 (2018).

 30. Calò, M., Kinnaert, X. & Dorbath, C. Procedure to construct three-dimensional models of geothermal areas using seismic noise
- cross-correlations: Application to the Soultz-sous-Forêts enhanced geothermal site. Geophys. J. Int. 194, 1893–1899. https://doi. org/10.1093/gji/ggt205 (2013).
- 31. Martins, J. E. et al. 3D S-wave velocity imaging of Reykjanes Peninsula high-enthalpy geothermal fields with ambient-noise tomography. J. Volcanol. Geoth. Res.https://doi.org/10.1016/j.jvolgeores.2019.106685 (2019).
- 32. Ars, J.-M. et al. Joint inversion of gravity and surface wave data constrained by magnetotelluric: Application to deep geothermal exploration of crustal fault zone in felsic basement. Geothermics 80, 56-68. https://doi.org/10.1016/j.geothermics.2019.02.006 (2019).
- 33. Cabrera-Pérez, I. et al. A nonlinear multiscale inversion approach for ambient noise tomography. Geophys. J. Int. 225, 1158-1173.
- https://doi.org/10.1093/gji/ggaa574 (2021).

 34. Bodin, T. *et al.* Transdimensional inversion of receiver functions and surface wave dispersion. *J. Geophys. Res. Solid Earth*https:// doi.org/10.1029/2011JB008560 (2012).
- Camacho, A. G. et al. Structural results for La Palma island using 3-D gravity inversion. J. Geophys. Res. Solid Earthhttps://doi. org/10.1029/2008JB005628 (2009).
- Galipp, K., Klügel, A. & Hansteen, T. H. Changing depths of magma fractionation and stagnation during the evolution of an oceanic island volcano: La Palma (Canary Islands). J. Volcanol. Geoth. Res. 155, 285-306. https://doi.org/10.1016/j.jvolgeores.2006.04.002 (2006).
- 37. Obermann, A., Lupi, M., Mordret, A., Jakobsdóttir, S. S. & Miller, S. A. 3D-ambient noise Rayleigh wave tomography of Snæfellsjökull volcano, Iceland. J. Volcanol. Geoth. Res. 317, 42-52. https://doi.org/10.1016/j.jvolgeores.2016.02.013 (2016)
- 38. Benediktsdóttir, Á., Gudmundsson, Ó., Brandsdóttir, B. & Tryggvason, A. Ambient noise tomography of Eyjafjallajökull volcano, Iceland. J. Volcanol. Geoth. Res. 347, 250-263. https://doi.org/10.1016/j.jvolgeores.2017.09.017 (2017)
- Spica, Z. et al. Hydrothermal and magmatic reservoirs at Lazufre volcanic area, revealed by a high-resolution seismic noise tomography. Earth Planet. Sci. Lett. **421**, 27–38. https://doi.org/10.1016/j.epsl.2015.03.042 (2015). Fallahi, M. J., Obermann, A., Lupi, M., Karyono, K. & Mazzini, A. The plumbing system feeding the Lusi eruption revealed by
- ambient noise tomography. J. Geophys. Res. Solid Earth 122, 8200-8213. https://doi.org/10.1002/2017JB014592 (2017).

- 41. De Luca, C. et al. Pre-and co-eruptive analysis of the September 2021 Eruption at Cumbre Vieja Volcano (La Palma, Canary Islands) through DInSAR measurements and analytical modeling. Geophys. Res. Lett. https://doi.org/10.1029/2021GL097293 (2022).
- 42. Cabrera-Pérez, I. et al. Spatio-temporal velocity variations observed during the pre-eruptive episode of La Palma 2021 eruption inferred from ambient noise interferometry. Sci. Rep. 13, 12039 (2023).
- 43. Pankhurst, M. J. et al. Rapid response petrology for the opening eruptive phase of the 2021 Cumbre Vieja eruption, La Palma, Canary Islands. Volcanica 5, 1–10. https://doi.org/10.30909/vol.05.01.0110 (2022).
- 44. Prieto, J. F. et al. Geodetic and structural research in La Palma, Canary Islands, Spain: 1992–2007 results. Pure Appl. Geophys. 166, 1461–1484. https://doi.org/10.1007/s00024-009-0505-2 (2009).
- 45. Padrón, E. et al. Dynamics of diffuse carbon dioxide emissions from Cumbre Vieja volcano, La Palma, Canary Islands. Bull. Volcanol. 77, 1–15. https://doi.org/10.1007/s00445-015-0914-2 (2015).
- Padrón, E. et al. Helium emission at Cumbre Vieja volcano, La Palma, Canary Islands. Chem. Geol. 312, 138–147. https://doi.org/ 10.1016/j.chemgeo.2012.04.018 (2012).
- Seydoux, L., Shapiro, N. M., De Rosny, J., Brenguier, F. & Landès, M. Detecting seismic activity with a covariance matrix analysis
 of data recorded on seismic arrays. Geophys. J. Int. 204, 1430–1442. https://doi.org/10.1093/gji/ggv531 (2016).
- 48. Soubestre, J. et al. Network-based detection and classification of seismovolcanic tremors: Example From the Klyuchevskoy volcanic group in Kamchatka. J. Geophys. Res. Solid Earth 123, 564–582. https://doi.org/10.1002/2017JB014726 (2018).
- 49. Bensen, G. et al. Processing seismic ambient noise data to obtain reliable broad-band surface wave dispersion measurements. *Geophys. J. Int.* 169, 1239–1260 (2007).
- Lobkis, O. I. & Weaver, R. L. On the emergence of the Green's function in the correlations of a diffuse field. J. Acoust. Soc. Am. 110, 3011–3017. https://doi.org/10.1121/1.1417528 (2001).
- 51. Derode, A. et al. Recovering the Green's function from field-field correlations in an open scattering medium (l). J. Acoust. Soc. Am. 113, 2973–2976. https://doi.org/10.1121/1.1570436 (2003).
- Levshin, A., Ratnikova, L. & Berger, J. Peculiarities of surface-wave propagation across central Eurasia. Bull. Seismol. Soc. Am. 82, 2464–2493. https://doi.org/10.1785/BSSA0820062464 (1992).
- 2464–2493. https://doi.org/10.1/85/BSSA0820002464 (1992).
 53. Sambridge, M., Gallagher, K., Jackson, A. & Rickwood, P. Trans-dimensional inverse problems, model comparison and the evidence.
- Geophys. J. Int. 167, 528–542 (2006).
 54. Ke, G., Dong, H., Kristensen, Å. & Thompson, M. Modified Thomson-Haskell matrix methods for surface-wave dispersion-curve calculation and their accelerated root-searching schemes. Bull. Seismol. Soc. Am. 101, 1692–1703. https://doi.org/10.1785/01201
- 00187 (2011). 55. Zhang, S. Senskernel-1.0. (2018).
- 56. D'Auria, L., Martini, M., Esposito, A., Ricciolino, P. & Giudicepietro, F. A unified 3D velocity model for the Neapolitan volcanic areas. ISBN: 978-88-89972-09-0.
- $57. \ \ Hunter, J.\ D.\ Matplotlib:\ A\ 2D\ graphics\ environment.\ \textit{Comput. Sci. Eng. 9},\ 90-95.\ \ https://doi.org/10.1109/MCSE.2007.55\ (2007).$
- 58. Beyreuther, M. et al. Obspy: A Python toolbox for seismology. Seismol. Res. Lett. 81, 530–533. https://doi.org/10.1785/gssrl.81.3. 530 (2010).
- Krischer, L. et al. Obspy: A bridge for seismology into the scientific python ecosystem. Comput. Sci. Discov. 8, 014003. https://doi. org/10.1088/1749-4699/8/1/014003 (2015).

Acknowledgements

The INVOLCAN team was supported by the project VOLRISKMAC II (MAC2/3.5b/328) co-financed by the EC Cooperation Transnational Program MAC 2014-2020, "Impulso a la energía geotérmica de alta entalpía en Canarias" (187G0132), financed by Gobierno de Canarias, and "Desarrollo de la geotermia en La Palma" (425/226613), financed by Cabildo Insular de La Palma. This paper benefited from various Python packages including Matplotlib⁵⁷ and Obspy^{58,59}.

Author contributions

I.C.-P. performed the data analysis. L.D., J.S. and I.C.-P. developed the Python package used to realize the Multiscale Ambient NOiSe TomogrAphy (MANgOSTA). I.C.-P., L.D., J.S., A.M.-L, D.M.D. and M.P. worked on data collection and campaign organization. All the authors contributed to the interpretation of the data, discussion of the results, and manuscript preparation.

Competing interests

The authors declare no competing interests.

Additional information

Supplementary Information The online version contains supplementary material available at https://doi.org/10.1038/s41598-023-39910-z.

Correspondence and requests for materials should be addressed to I.C.-P.

Reprints and permissions information is available at www.nature.com/reprints.

Publisher's note Springer Nature remains neutral with regard to jurisdictional claims in published maps and institutional affiliations.

Open Access This article is licensed under a Creative Commons Attribution 4.0 International License, which permits use, sharing, adaptation, distribution and reproduction in any medium or format, as long as you give appropriate credit to the original author(s) and the source, provide a link to the Creative Commons licence, and indicate if changes were made. The images or other third party material in this article are included in the article's Creative Commons licence, unless indicated otherwise in a credit line to the material. If material is not included in the article's Creative Commons licence and your intended use is not permitted by statutory regulation or exceeds the permitted use, you will need to obtain permission directly from the copyright holder. To view a copy of this licence, visit http://creativecommons.org/licenses/by/4.0/.

© The Author(s) 2023

TYPE Original Research
PUBLISHED 09 January 2024
DOI 10.3389/feart.2023.1326634



OPEN ACCESS

EDITED BY Yosuke Aoki, The University of Tokyo, Japan

REVIEWED BY

Simona Petrosino, Istituto Nazionale di Geofisica e Vulcanologia, Sezione di Napoli - Osservatorio Vesuviano, Italy Francesca Di Luccio, National Institute of Geophysics and Volcanology (INGV), Italy

*CORRESPONDENCE

Iván Cabrera-Pérez,

ivan.cabrera.perez1@gmail.com

RECEIVED 23 October 2023 ACCEPTED 21 December 2023 PUBLISHED 09 January 2024

CITATION

Cabrera-Pérez I, Soubestre J, D'Auria L, Przeor M, García R, Barrancos J, Padilla GD, Pérez NM and Prudencio J (2024), Ambient noise tomography of El Hierro island (Canary Islands).

Front. Earth Sci. 11:1326634. doi: 10.3389/feart.2023.1326634

COPYRIGHT

© 2024 Cabrera-Pérez, Soubestre, D'Auria, Przeor, García, Barrancos, Padilla, Pérez and Prudencio. This is an open-access article distributed under the terms of the Creative Commons Attribution License (CC BY). The use, distribution or reproduction in other forums is permitted, provided the original author(s) and the copyright owner(s) are credited and that the original publication in this journal is cited, in accordance with accepted academic practice. No use, distribution or reproduction is permitted which does not comply with these terms.

Ambient noise tomography of El Hierro island (Canary Islands)

Iván Cabrera-Pérez^{1*}, Jean Soubestre^{2,3}, Luca D'Auria⁴, Monika Przeor⁴, Rubén García¹, José Barrancos⁴, Germán D. Padilla⁴, Nemesio M. Pérez^{1,4} and Janire Prudencio^{5,6}

¹Instituto Volcanológico de Canarias (INVOLCAN), Tenerife, Canary Islands, Spain, ²University Grenoble Alpes, University Savoie Mont Blanc, CNRS, IRD, University Gustave Eiffel, Grenoble, France, ³Icelandic Meteorological Office, Reykjavik, Iceland, ⁴Instituto Tecnológico y de Energías Renovables (ITER), Tenerife, Canary Islands, Spain, ⁵Department of Theoretical Physics and Cosmos, Science Faculty, University of Granada, Granada, Spain, ⁴Andalusian Institute of Geophysiscs, Campus de Cartuja, University of Granada, Granada, Spain

El Hierro island is one of the most active islands in the Canary Islands from a volcanological point of view. This is the reason why the imaging of the internal crustal structure is of huge importance. The geophysical exploration methods employed on El Hierro Island, such as gravimetry and seismic tomography, allowed obtaining the high-resolution characterization of the crust's deep part. However, these methods did not yield significant information about the surface and the shallower part of the crust. To gain a deeper insight into the shallow geological structure of El Hierro island, we employed Ambient Noise Tomography to construct a 3D S-wave velocity model. Our investigation revealed the presence of seven significant seismic velocity anomalies, partly identified by previous studies. We identified two high-velocity anomalies located in the eastern and western parts of the island at a depth between 0 and 3 km below sea level (b.s.l.). We interpreted these anomalies as dense intrusive complexes of dikes, possibly linked to the Tanganasoga volcano and the formation of the Tiñor edifice. Additionally, we observed two high-velocity anomalies in the northern and southern parts of the island at a depth between 3 and 4 km b.s.l., which we related to the accumulation of solidified igneous rocks. On the other hand, a low-velocity anomaly was observed in the Golfo valley, between 0 and 0.5 km b.s.l., and we interpreted it as megalandslide deposits. This anomaly was evidenced for the first time in the present study. Finally, two lowvelocity anomalies were observed in the southern part of the island at different depths, between 0-0.5 km b.s.l. and 0-2 km b.s.l. These were interpreted as fractures generated by Quaternary volcanism along the SSE Rift. Also, one of them was evidenced for the first time in this study, corresponding to the zone of the fractures produced during the Quaternary volcanism. This study has allowed us to gain a more detailed understanding of the shallow geological structure of the island. Even if most of the anomalies had been evidenced previously, we could observe the existence of two low-velocity zones in the shallow crust that have not been observed before

KEYWORDS

ambient noise tomography, El Hierro island, intrusive bodies, fractures zones, megalandslide

1 Introduction

The first instance of Ambient Noise Tomography (ANT) applied to a volcano was conducted by Brenguier et al. (2008). In this study, they successfully imaged a high-velocity intrusive body beneath the Piton de la Fournaise volcano on La Réunion Island, France. Subsequent ANT investigations have been carried out on numerous other volcanoes to identify anomalies in shear wave velocity. Typically, high-velocity anomalies observed in ANT are commonly interpreted as cooled igneous intrusions (Brenguier et al., 2008; Mordret et al., 2015; Wang et al., 2017), consolidated dike complexes (Mordret et al., 2015; Cabrera-Pérez et al., 2022), or solidified magma chambers (Mordret et al., 2015). On the other hand, low-velocity anomalies detected in ANT are associated with various volcanic features, including hydrothermal systems, e.g., (Spica et al., 2015; Wang et al., 2017; Cabrera-Pérez et al., 2022; Cabrera-Pérez et al., 2023a), calderarelated structures, e.g., (Masterlark et al., 2010; Koulakov et al., 2014; Benediktsdóttir et al., 2017), porous and highly fractured materials, e.g., (Cabrera-Pérez et al., 2023b), shallow crustal magma reservoirs, e.g., (Masterlark et al., 2010; Stankiewicz et al., 2010; Spica et al., 2015; Fallahi et al., 2017; Obermann et al., 2019), or fractures, e.g., (Cabrera-Pérez et al., 2023a). The Ambient Noise Tomography was applied to El Hierro island (Canary Islands) in order to shed light on the internal structure of the shallow crust, up to 5 km b.s.l.

The Canary Islands, situated around 100 km from the African coast, exhibit characteristics typical of an active oceanic island

chain. Their formation is associated with a hot spot or plume, leading to the intrusion of unusually hot mantle material into the African plate. The islands are predominantly composed of mafic rocks and encompass elevated submarine volcanic structures, above-water shield volcanoes, and remnants of substantial lateral collapses (Troll and Carracedo, 2016). El Hierro island (27°43.6'N, 18°1.0'W) is located in the western part of the Canary Islands (Figure 1) and is the youngest island of the archipelago and has a "Y" shape with a maximum height of 1,501 m a.s.l. (above sea level), (Figure 1). El Hierro island can be categorized into three distinct and differentiated geological domains: i) Tiñor edifice (1.12-0.88 Myr), ii) El Golfo-Las Playas edifice (545-176 kyr), and iii) Rift volcanism (158 kyr to the present) (Figure 1). The island's formation began in the lower and middle Pleistocene with the construction of the Tiñor volcanic edifice. Subsequently, the El Golfo and Las Playas volcanic edifices were formed during the middle Pleistocene. Finally, the dorsal volcanism started during the middle and upper Pleistocene in the three principal rifts of the island (NE, WNW and SSE rift), where all the recent eruptions have been located (Figure 1). During this period (21-133 kyr), a megalandslide occurred as a consequence of the rapid growth of the El Golfo volcano and generated a great depression in the northern part of the island (Golfo Valley). The Holocene volcanism on El Hierro island is limited to just a few eruptions: Tanganasoga volcano and the Montaña Chamuscada volcano (Figure 1), 4,000 and 2,500 years before present, respectively (Guillou et al., 1996). No historical subaerial eruptions were observed.

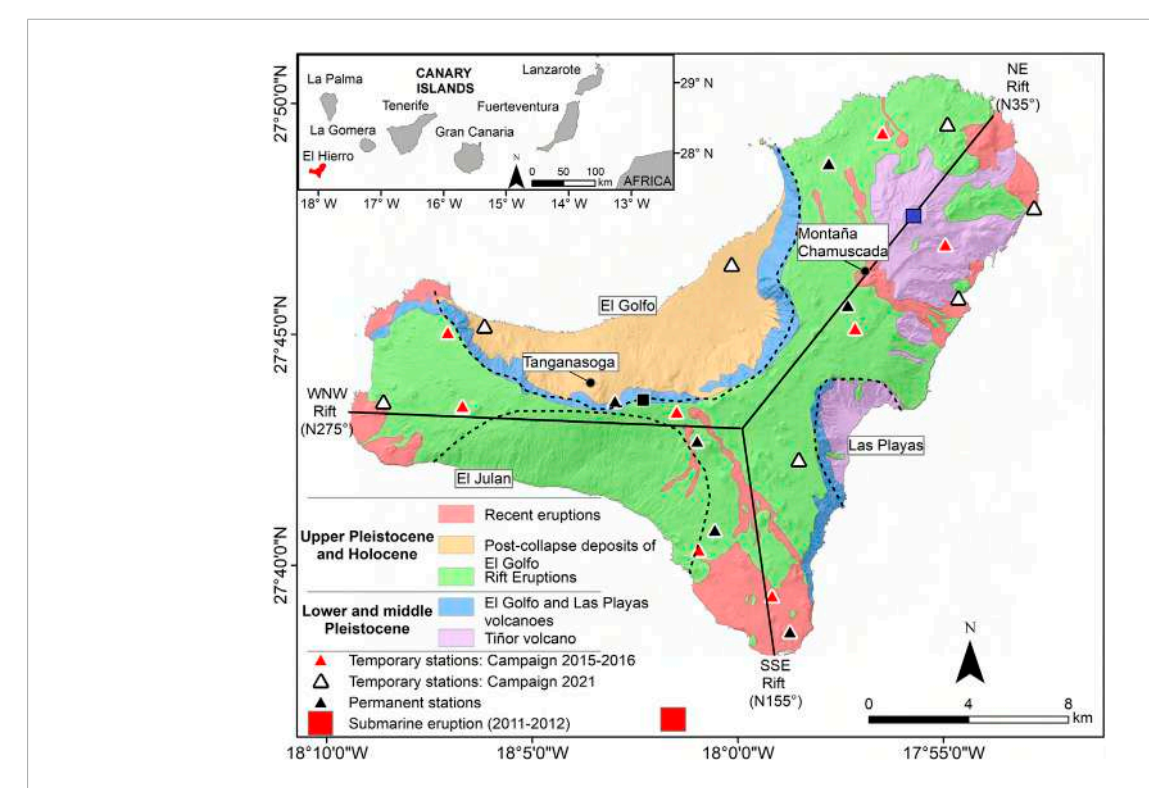


FIGURE 1
Geological map of El Hierro island. The black dashed and solid lines represent the collapse rims and the direction of the principal rifts, respectively. The red square on the top-right globe shows the position of the Canary Islands archipelago and the island of El Hierro appears in red in the top-left inset. The black and blue square represents the location of the maximum height of the island and the Tiño volcano, respectively.

The last eruption in El Hierro was the Tagoro volcano submarine eruption which took place 4 km away from the island's southern extremity (Figure 1). The pre-eruptive episode lasted 83 days, starting on 17 July 2011, with more than 11,000 earthquakes (Ibáñez et al., 2012). The seismicity migrated from the north (El Golfo) to the southern part of the island following the movement of magma at depth (Ibáñez et al., 2012). Furthermore, the Instituto Geográfico Nacional (IGN) registered an uplift of ~2-4 cm motion toward the northeast (González et al., 2013), and the Instituto Volcanológico de Canarias (INVOLCAN) observed an increase in endogenous gas emissions (Melián et al., 2014; Pérez et al., 2014) during this pre-eruptive period. The eruptive process began on 12 October 2011, and lasted about 5 months until 5 March 2012. During the eruptive process, floating pyroclasts emerged on the sea surface near the place of eruption. These volcanic bombs and slags were named Restingolites (Pérez et al., 2012). In addition to the volcanic materials emitted, the huge emissions of volcanic gases produced a change in the color of the seawater (Somoza et al., 2017). The Tagoro volcano formed alternating between constructive and destructive episodes produced by effusive and explosive stages, respectively. During the final effusive stage of the eruption, a principal cone formed underwater, reaching a maximum height of 89-120 m above the sea floor (Somoza et al., 2017).

Many of the studies of El Hierro island focused on the Tagoro eruption process, analyzing the seismicity, e.g., (Ibáñez et al., 2012; López et al., 2012), deformation patterns, e.g., (González et al., 2013; Cerdeña et al., 2018), and geochemical anomalies, e.g., (Pérez et al., 2012; Padilla et al., 2013; Padrón et al., 2013; Melián et al., 2014; Rodriguez-Losada et al., 2015). Only a few studies applied geophysical methods to study the geological structure of El Hierro. The first one was carried out by Montesinos et al. (2006), who obtained a 3-D density model through the inversion of gravity data. Subsequently, Gorbatikov et al. (2013) studied the deep structure of the island using a microseismic-sounding method. Finally, García-Yeguas et al. (2014) and Martí et al. (2017) applied local seismic tomography (LET) to reveal the deeper geological structures of the island. However, all of these methods have poor resolution at shallow depths. In this study, we carried out the first Ambient Noise Tomography (ANT) of El Hierro Island to gain a more detailed understanding of the surface structure and geology of the island.

2 Methods

2.1 Data collection and pre-processing

In this study, we used a dataset obtained from permanent broadband stations completed by temporary stations installed in two campaigns. We used eight temporary stations (Güralp® 3ESPC Series) installed on the island by the Helmholtz Center for Ocean Research Kiel Germany (GEOMAR) and the Instituto de Productos Naturales y Agrobiología (CSIC) (Dietrich and Vicente, 2019) that were recording between 1 January 2015 and 30 December 2016 (Figure 1, campaign 2015–2016). Moreover, seven temporary seismic stations (Nanometrics® Trillium Compact 120s) were installed by the INVOLCAN and recorded between March and June 2021 (Figure 1, campaign 2021). Additionally, during the

4 months of the 2021 campaign, six permanent stations managed by INVOLCAN for volcanic monitoring (Figure 1), remained in active operation. Those data were used in this study. Data were collected at a sampling rate of 100 Hz.

We carried out data pre-processing, conducted cross-correlations between all station pairs, and extracted the dispersion curves, as outlined by (Shapiro et al., 2005). First, we downsampled the data from 100 to 25 Hz to reduce the computational time. Then, we used a network-based method (Seydoux et al., 2016; Soubestre et al., 2018) to remove time windows containing earthquakes automatically. Subsequently, we applied a bandpass filter within the 0.1–5.0 Hz frequency range, covering the frequency range of the microseism ambient noise (Gutenberg, 1958). We implemented a standard ambient noise pre-processing procedure. This pre-processing included temporal one-bit normalization and spectral whitening to mitigate non-stationarity in the remaining

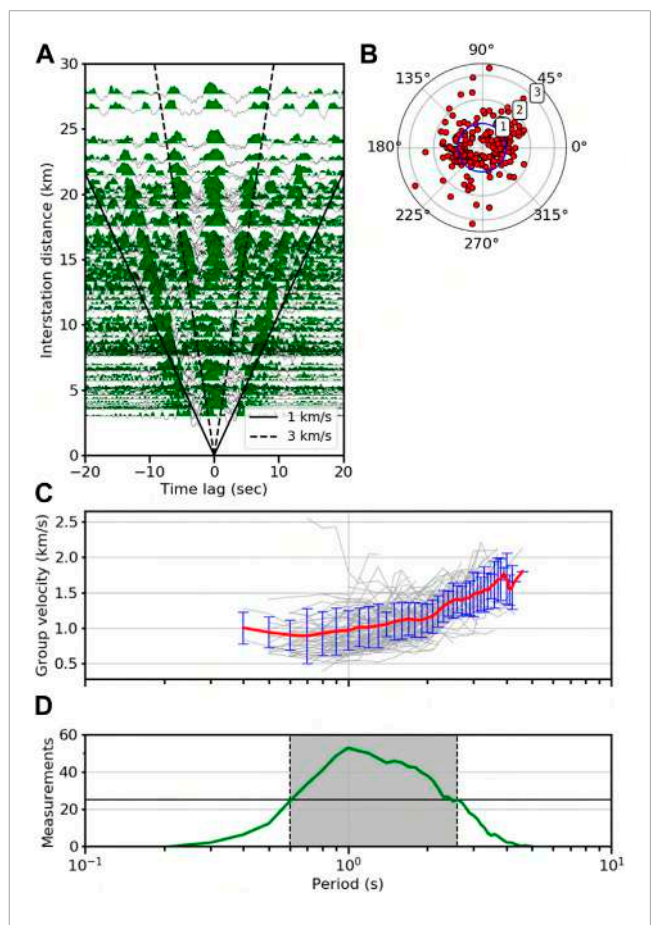


FIGURE 2
Processing of ambient noise data. (A) Vertical empirical Green's functions sorted according to the distance between stations. The black solid and dashed lines represent the velocities of 1.0 and 3.0 km/s, respectively. (B) Amplitude ratios of causal and acausal parts of vertical cross-correlations as a function of azimuthal distribution of station pairs. The white circle represents the unitary value of the amplitude ratio. (C) Rayleigh wave dispersion curves (grey lines), together with their mean (red line) and standard deviation at each period (blue vertical bars). (D) Number of measured dispersion curves as a function of the period (green line). The grey area represents the range of periods with at least 25 measurements were used in the inversion (0.6–2.7s).

data, as discussed by Bensen et al. (2007). Following these steps, we computed cross-correlations for all station pairs on 5-minlong windows, stacking over 1 year for the 2015–2016 campaign and 4 months for the 2021 campaign. This analysis was conducted specifically on the vertical-vertical components of 112 station pairs. The resulting cross-correlations are illustrated in Figure 2A, clearly displaying coherent dispersive Rayleigh waveforms.

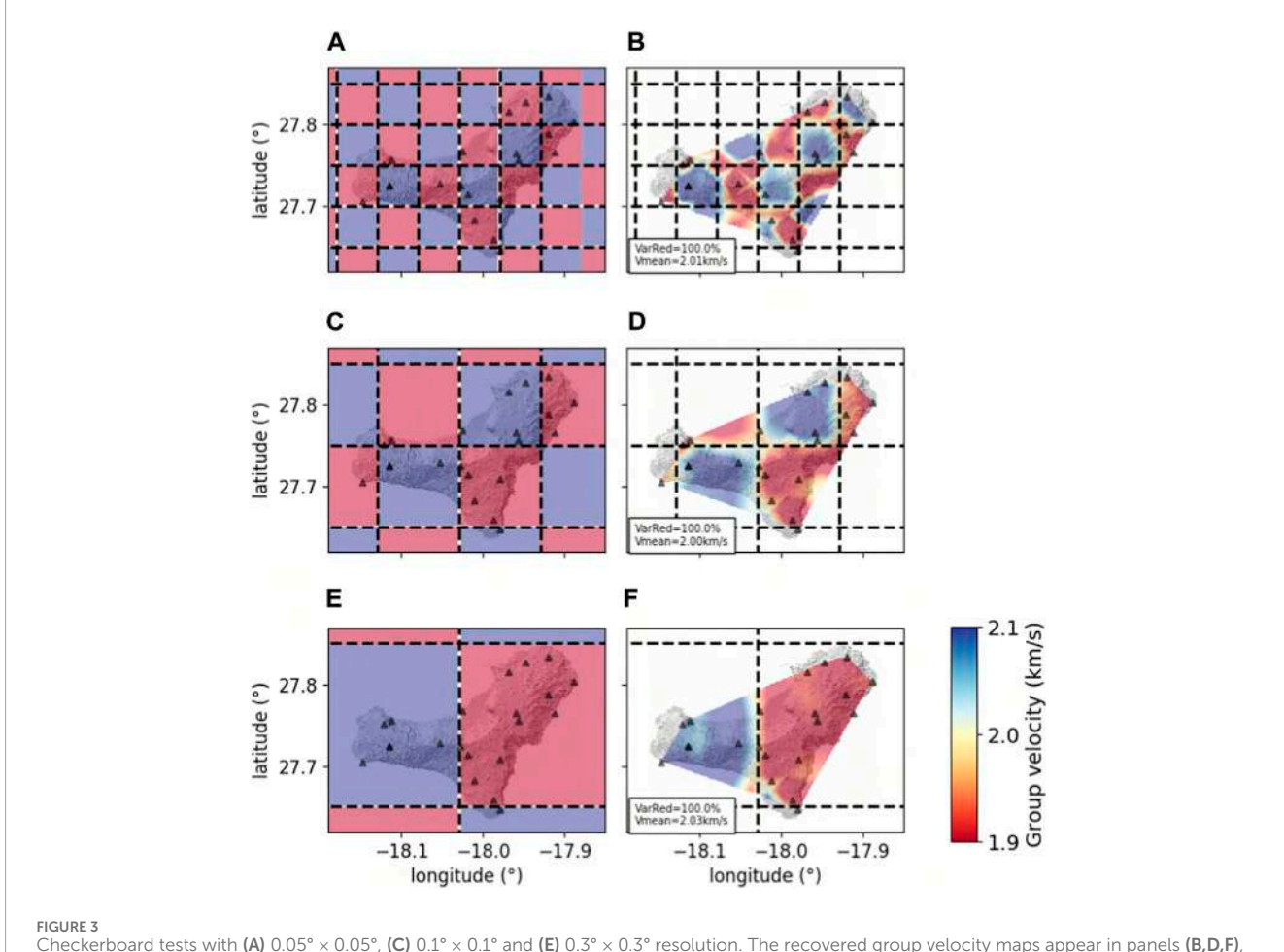
Moreover, we computed the amplitude ratio between the causal and acausal segments of the cross-correlations, examining its dependence on the azimuthal arrangement of station pairs (Figure 2B). This analysis was conducted to confirm that the distribution of noise sources closely approximated isotropy, a critical prerequisite for performing ANT (Lobkis and Weaver, 2001; Derode et al., 2003). Figure 2B shows an acceptable azimuthal distribution of station pairs with a slightly dominant northeast-southwest orientation. Nonetheless, there is no discernible predominant noise source, as all station pairs' amplitude ratio remains consistently near 1 (Figure 2B).

Subsequently, we employed the Frequency-Time Analysis (FTAN) method, as outlined by Levshin et al. (1992), to determine the Rayleigh wave group velocity dispersion curves. A total of 105 dispersion curves were extracted (Figure 2C). Among these, the red curve represents the average dispersion curve, with its

associated standard deviation indicated by the blue line at each period (Figure 2C). In Figure 2D, the number of measurements is illustrated in relation to the period. To ensure the reliability of our analysis, we considered periods within a reasonably covered range, requiring a minimum of 25 measurements. As a result, our tomographic inversion was limited to periods spanning from 0.6 s to 2.7 s.

2.2 2-D group velocity maps

We applied a non-linear multiscale inversion methodology, which considers the topography, as Cabrera-Pérez et al. (2021) detailed, to generate 2-D group velocity maps at various periods. Initially, our model assumed a uniform velocity structure. We refined the model parameters in successive iterations of the non-linear inversion process by introducing control nodes distributed across a regular grid. We improved the model at each stage by increasing the scale, which entailed augmenting the number of parameters employed for model characterization. The result obtained at each scale served as the initial model for the subsequent inversion scale. This inversion approach has demonstrated its efficacy in numerous investigations of volcanic



Checkerboard tests with (A) $0.05^{\circ} \times 0.05^{\circ}$, (C) $0.1^{\circ} \times 0.1^{\circ}$ and (E) $0.3^{\circ} \times 0.3^{\circ}$ resolution. The recovered group velocity maps appear in panels (B,D,F), respectively.

regions (Cabrera-Pérez et al., 2022; Cabrera-Pérez et al., 2023a; Cabrera-Pérez et al., 2023b).

Initially, we conducted synthetic checkerboard tests to evaluate the spatial resolution of the tomographic images. Three distinct sizes of checkerboards were employed, measuring $0.05^{\circ} \times 0.05^{\circ}$, $0.1^{\circ} \times$ 0.1° , and $0.3^{\circ} \times 0.3^{\circ}$. These dimensions approximately correspond to areas of 5.5 km \times 5.5 km, 11.1 km \times 11.1 km, and 33.3 km \times 33.3 km, respectively. In these tests, the checkerboards featured a maximum velocity of 2.1 km/s and a minimum of 1.9 km/s, as depicted in Figure 3. The checkerboard experiments conducted at resolutions of $0.1^{\circ} \times 0.1^{\circ}$ and $0.3^{\circ} \times 0.3^{\circ}$, as shown in Figures 3D, F, respectively, yielded accurate results. In contrast, the checkerboard test at a resolution of $0.05^{\circ} \times 0.05^{\circ}$ failed to correctly retrieve the outer areas due to lower ray path density in those regions (Figure 3B and refer to Supplementary Figure S1). However, it is worth noting that the checkerboard was accurately retrieved in the central part of the island (Figure 3B), where the ray path density was higher (see Supplementary Figure S1).

In Supplementary Figure S2, you can observe the results of our 2-D mapping of Rayleigh wave group velocities derived from a checkerboard test conducted at different scales, 4, 5, and 6. The maps produced at scales 4 and 5 show significant similarity and effectively represent the geometric structure and the velocity distribution. In contrast, the map generated at scale 6 displays noticeable artifacts, and has difficulty determining the velocity pattern accurately. Consequently, we have decided to confine our inversion process for actual data to a scale of 5.

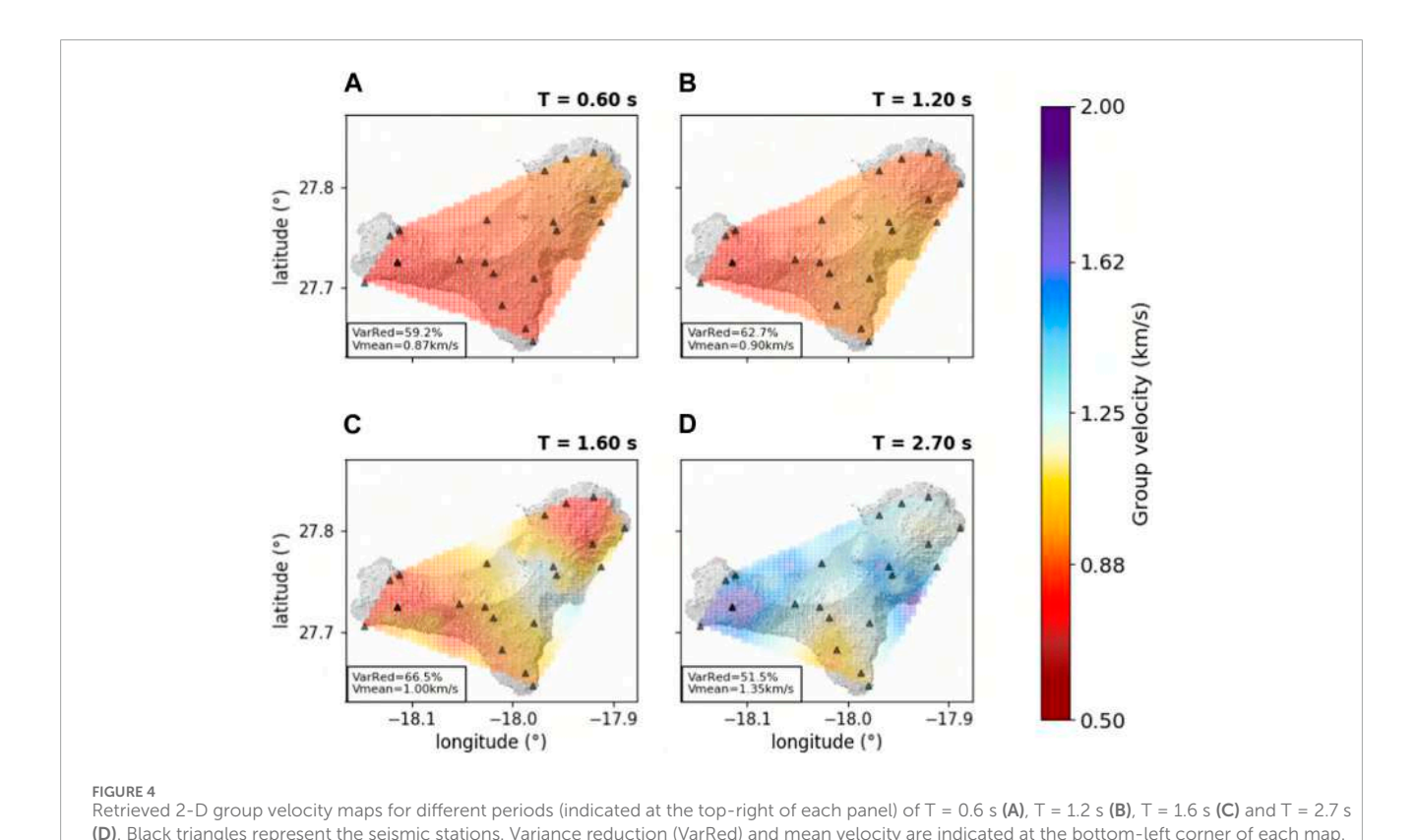
Figure 4 displays four 2-D group velocity maps of Rayleigh waves, each corresponding to periods ranging from $T=0.6\,\mathrm{s}$ to

T=2.7~s. In each panel of Figure 4, you can find information about the variance reduction (VarRed) and the mean velocity. It is worth noting that, for all the investigated periods, the variance reduction exceeds 50%. However, the mean velocity exhibits an upward trend as the period increases, ranging from 0.87 to 1.35 km/s. This pattern aligns with the overall trend in the average dispersion curve presented in Figure 2C.

Regarding the spatial anomalies observed in the 2-D group velocity maps (Figure 4), we discern noteworthy variations in velocity, particularly at longer periods. At the shorter periods, corresponding to shallower depths, the maps for $T=0.6\,\mathrm{s}$ and $T=1.20\,\mathrm{s}$ do not exhibit substantial anomalies (Figures 4A, B). Instead, a prevalent low-velocity region dominates most of the island, with mean velocities of 0.87 and 0.90 km/s, respectively. At longer periods, the T=2.7 map reveals an increase in velocity in the western and eastern parts of the island (refer to Figure 4D).

2.3 1-D depth inversion

The final stage of the inversion process entails deriving 1-D S-wave profiles in depth from the group velocity maps. To perform this task, we extracted a dispersion curve associated with each of the 449 control points on the 2-D group velocity maps and carried out the inversion using a transdimensional approach, as outlined by Bodin et al. (2012). The transdimensional approach allows us to derive a "posterior" probability distribution for seismic velocities, and this distribution remains largely uninfluenced by particular parameterization choices, such as the number of layers. Notably,



parametrization becomes one of the parameters within the inverse problem (Sambridge et al., 2006). In this study, we explored models featuring uniform horizontal layers ranging from one to five.

The forward model used for computing dispersion curves was based on a modified Thomson–Haskell matrix method (Ke et al., 2011), which not only enhances numerical stability but also expedites the calculation of dispersion curves. An example of the transdimensional inversion outcome is presented in Supplementary Figure S3. It illustrates a probability distribution for S-wave velocity at various depths.

To gauge the depth resolution of our S-wave velocity model, we computed the group velocity sensitivity kernel using the disba software developed by Luu (2021). Supplementary Figure S4 depicts this sensitivity kernel, highlighting that it provides adequate resolution down to 4 km depth, with the highest resolution observed

at 2 km depth. Finally, the 3-D S-wave velocity model is constructed by interpolating the 1-D S-wave velocity profiles within a 3-D mesh.

3 Results

This section presents the findings from the ambient noise tomography. Figure 5 shows the maps of S-wave velocity acquired at various depths. Figures 5C, E highlight the primary anomalies in the S-wave velocity model, categorizing them as either high (H) or low (L) velocity anomalies. As depicted in Figure 5, the island exhibits significant variations in velocity, with fluctuations of up to 25% in certain regions (refer to Supplementary Figure S5). In the surface areas, the average S-wave velocity stands at 2.10 km/s (Figure 5A), whereas it escalates to 3.0 km/s in the deeper regions (Figure 5E).

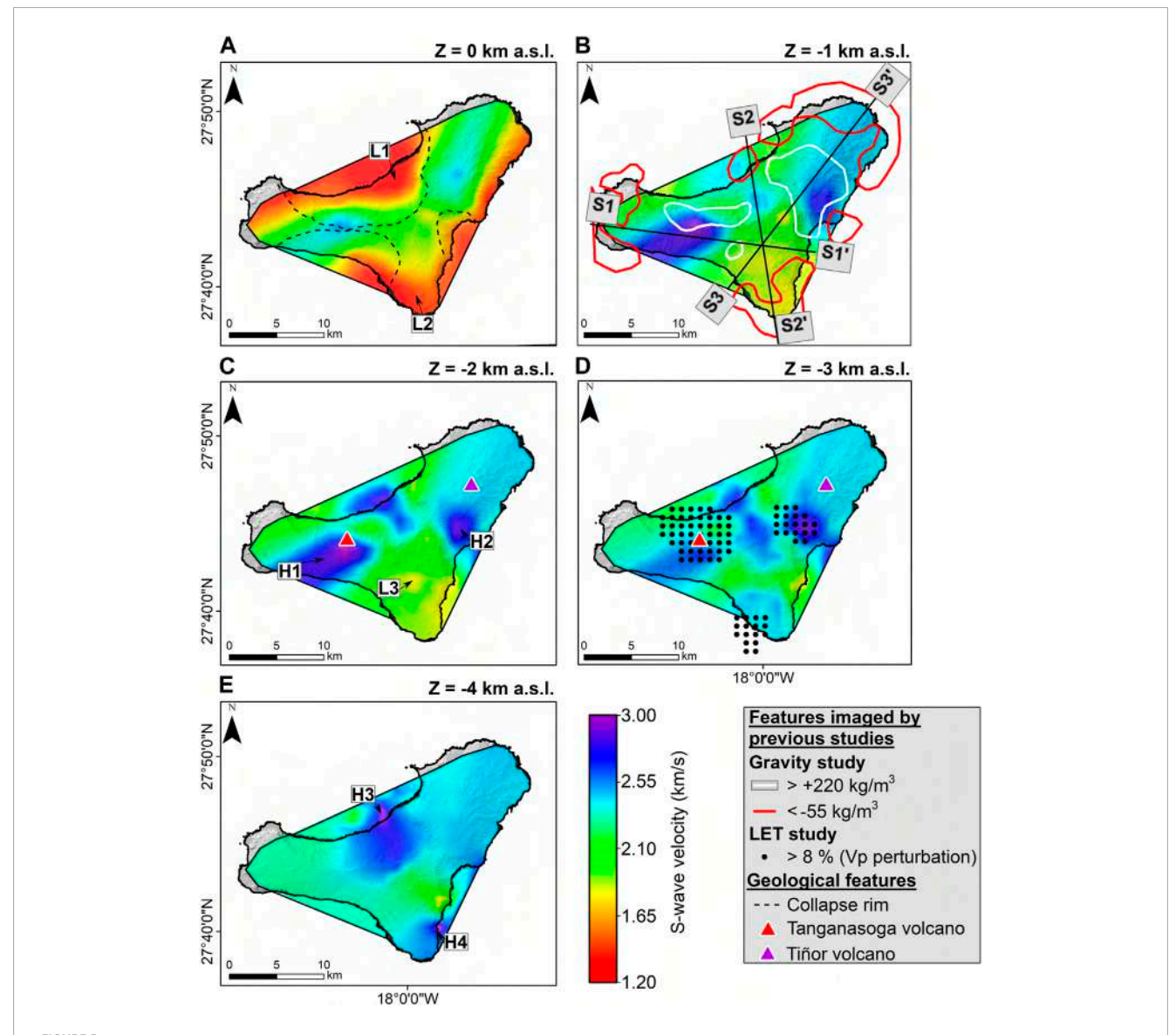


FIGURE 5
Maps of the S-wave velocities (A-E). (A) The black dashed line and red triangle represent the collapse rim delimitation and Tanganasoga volcano location, respectively. (B) White and red lines represent the high- and low-density anomalies obtained by Montesinos et al. (2006), respectively. (D) Black points represent high-velocity anomalies obtained from LET by Martí et al. (2017).

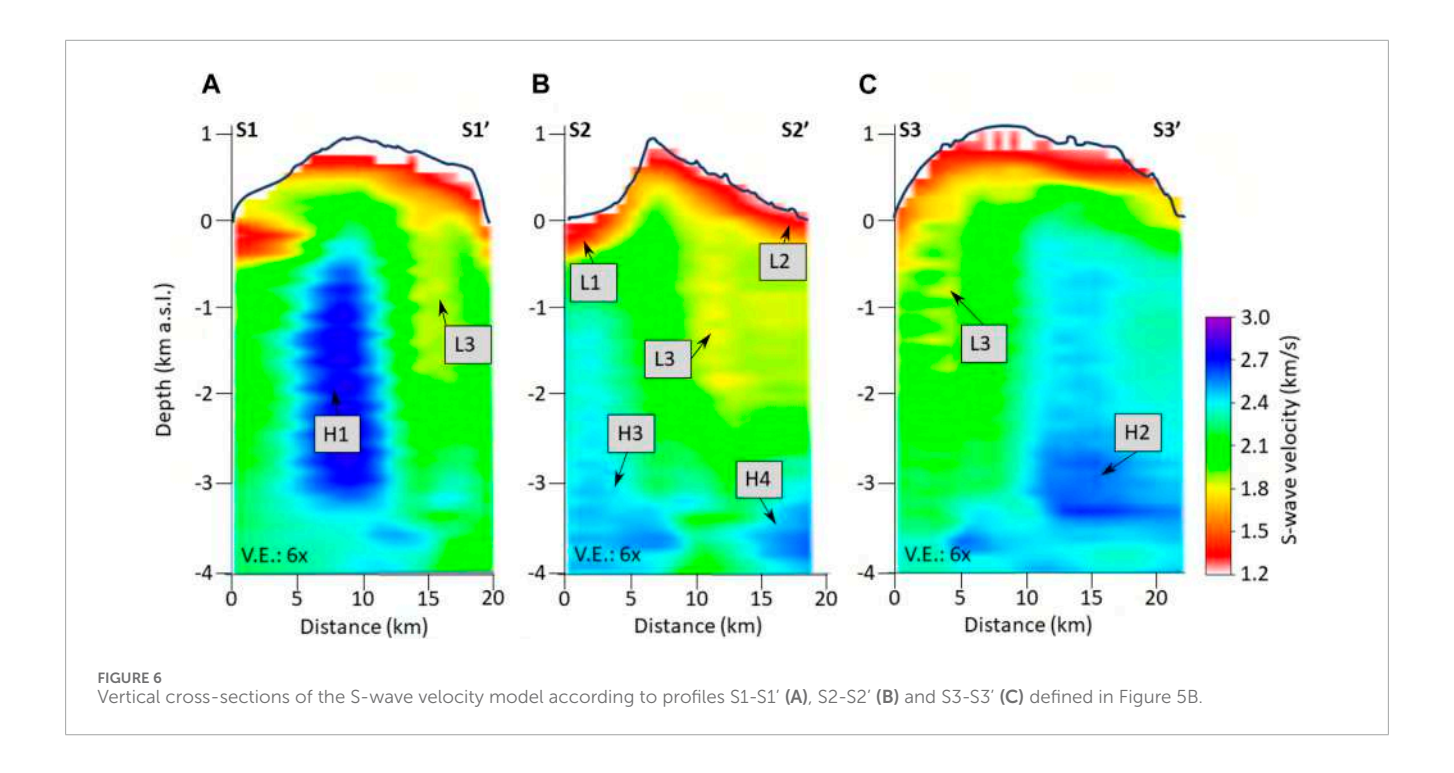


Figure 6 depicts three vertical slices of the 3-D S-wave velocity model, with their positions referenced in Figure 5B. The island features two elevated-velocity regions (H1 and H2) on its western and eastern flanks (Figure 5C) spanning from 0 to 3 km below sea level (b.s.l.) as shown in Figures 6A, C. These regions exhibit an S-wave velocity fluctuation of 25%. Furthermore, two additional high-velocity regions (H3 and H4) were found on the island's northern and southern sectors, found between 3 and 4 km b.s.l. (Figure 6B). Conversely, a low-velocity zone (L1) is situated in the Golfo Valley at the island's center (Figure 5A), ranging from 0 to 0.5 km b.s.l. in depth (Figure 6B). Two more areas with low-velocity (L2 and L3) lie in the island's southern region, spanning depths of 0–0.5 km b.s.l. and 0–2 km b.s.l., respectively (Figure 6B).

4 Discussion

El Hierro island's 3-D S-wave velocity model unveils the complex geological structure, characterized by the presence of seven prominent velocity anomalies with high-velocity variation reaching to $\pm 25\%$ (see Supplementary Figure S5): four high-velocity and three low-velocity anomalies. We discuss the volcanological relevance of such anomalies hereafter, comparing our results with geophysical models from previous studies.

The anomalies H1 (~2.7 km/s) and H2 (~2.6 km/s) found in the present study are located on the western and eastern sides of the island (Figure 5C) between 0 and 3 km b.s.l. (Figures 6A, C) with an S-wave relative velocity variation of 25% (Supplementary Figure S5). These high-velocity anomalies were already observed by other geophysical studies such as Montesinos et al. (2006), García-Yeguas et al. (2014) and Martí et al. (2017). García-Yeguas et al. (2014) and Martí et al. (2017) imaged these high-velocity anomalies by LET (Figure 5D), between 1 and 5 km b.s.l., that they interpreted as intrusive magmatic bodies. Furthermore, Montesinos et al. (2006)

observed high-density anomalies (> +220 kg/m³, Figure 5B) in the same zone interpreted as basaltic dikes. Taking into account the previous studies, the imaged high-velocity anomalies H1 and H2 are interpreted as dense intrusive complexes of dikes possibly linked to the Tanganasoga volcano (Figure 5B) and the formation of the Tiñor edifice formed between 1.20 and 0.88 Myr (Figure 5B).

Our study observes another group of significant high-velocity anomalies, denoted as H3 (~2.4 km/s) and H4 (~2.4 km/s), located in the northern and southern part of the island, at a depth between 3 and 4 km b.s.l. (Figure 6B). These are also imaged by the LETs from García-Yeguas et al. (2014) and Martí et al. (2017). García-Yeguas et al. (2014) related these high-velocity zones to the accumulation of solidified igneous rocks. Moreover, Martí et al. (2017) linked them to deep zones of solidified magma. Consequently, we interpret these anomalies as plutonic intrusions associated with the island's early volcanic activity during the formation of its basal complex. Note that similar high-velocity anomalies imaged in ambient noise tomography studies of La Palma and Gran Canaria islands were also interpreted as plutonic intrusions (Cabrera-Pérez et al., 2023a; Cabrera-Pérez et al., 2023b).

On the other hand, we imaged three low-velocity zones. The L1 anomaly (\sim 1.3 km/s) is located in the Golfo Valley, in the central part of the island (Figure 5A), at a shallow depth between 0 and 0.5 km b.s.l. (Figure 6B). This anomaly was not observed in other geophysical studies, and we consider that it may be associated with mega-landslide deposits, predominantly composed of conglomerate materials. These deposits can extend up to 500 m in thickness.

The second low-velocity anomaly L2 (\sim 1.3 km/s) is located in the southern part of the island (Figure 5A), at a shallow depth between 0 and 0.5 km b.s.l. (Figure 6B). Montesinos et al. (2006) observed a low-density anomaly in the same zone (< –55 kg/m³, Figure 5B), which they related to the concentration of fractures produced by Quaternary eruptive vents. We also relate this anomaly

to fractures generated by the Quaternary volcanism in the southern part of the SSE Rift (Figure 1). This interpretation is supported by a recent study documenting 69 volcano-tectonic features such as dikes and eruptive fissures in the SSE Rift (Abis et al., 2023). Alternatively, this L2 anomaly could also be partly due to fractures generated during the El Julan and Las Playas megalandslides (Figure 1). Finally, the L3 anomaly (\sim 1.8 km/s) located in the southern part of the island (Figure 5C) at a depth between 0 and 2 km b.s.l. (Figure 6B), which was not observed in previous geophysical studies. We consider that this anomaly is possibly associated with deeper fissures and fractures produced during the Quaternary volcanic activity.

5 Conclusion

Our ANT of El Hierro island provides a high-resolution S-wave velocity model for the first 5 km below the island's surface. Our dataset incorporated 21 seismic stations equipped with broadband sensors. We employed a non-linear multiscale inversion technique to generate the 2D group velocity maps, and a transdimensional approach was applied for the depth inversion process.

Our 3-D S-wave velocity model reveals the presence of seven velocity anomalies. We detected two high-velocity anomalies in the island's eastern and western regions, ranging in depth from 0 to 3 km below sea level (b.s.l.). Our interpretation suggests that these anomalies represent dense intrusive complexes of dikes, potentially associated with the Tanganasoga volcano and the formation of the Tiñor edifice. Furthermore, we noted two high-velocity anomalies in the northern and southern sections of the island at a depth between 3 and 4 km b.s.l., which we attributed to the accumulation of solidified igneous rocks.

On the other hand, a low-velocity anomaly was observed in the Golfo valley, within the depth range of 0–0.5 km b.s.l., and we construed it as megalandslide deposits. Lastly, two low-velocity anomalies were identified in the southern part of the island at varying depths, spanning from 0–0.5 km b.s.l. to 0–2 km b.s.l. These were interpreted as fractures generated by Quaternary volcanism along the SSE Rift.

The anomalies observed in various previous geophysical studies were also evidenced in the present work, demonstrating the effectiveness of ambient noise tomography in imaging crustal features. Moreover, the increased sensitivity of ANT in the shallower crust enabled the identification of two previously unseen low-velocity anomalies.

Data availability statement

The original contributions presented in the study are included in the article/Supplementary Material; further inquiries can be directed to the corresponding author.

References

Abis, C., Dajma, F., Di Capua, A., Marti Molist, J., Meletlidis, S., Norini, G., et al. (2023). Geology of el hierro southern rift, canary islands, Spain. *J. Maps* 1. doi:10.1080/17445647.2023.2214173

Author contributions

IC-P: Conceptualization, Data curation, Formal Analysis, Investigation, Visualization, Writing-original draft, Writing-review and editing. JS: Data curation, Investigation, Software, Supervision, Writing-review and editing. LD'A: Conceptualization, Investigation, Methodology, Software, Supervision, Writing-review and editing. MP: Data curation, Writing-review and editing. RG: Data curation, Writing-review and editing. JB: Data curation, Resources, Writing-review and editing. GP: Data curation, Resources, Writing-review and editing. NP: Resources, Writing-review and editing. JP: Methodology, Resources, Writing-review and editing.

Funding

The author(s) declare that no financial support was received for the research, authorship, and/or publication of this article.

Acknowledgments

The INVOLCAN team was supported by the project VOLRISKMAC II (MAC2/3.5b/328) and co-financed by the Cabildo Insular de Tenerife (TFassistance).

Conflict of interest

The authors declare that the research was conducted in the absence of any commercial or financial relationships that could be construed as a potential conflict of interest.

Publisher's note

All claims expressed in this article are solely those of the authors and do not necessarily represent those of their affiliated organizations, or those of the publisher, the editors and the reviewers. Any product that may be evaluated in this article, or claim that may be made by its manufacturer, is not guaranteed or endorsed by the publisher.

Supplementary material

The Supplementary Material for this article can be found online at: https://www.frontiersin.org/articles/10.3389/feart.2023. 1326634/full#supplementary-material

Benediktsdóttir, Á., Gudmundsson, Ó., Brandsdóttir, B., and Tryggvason, A. (2017). Ambient noise tomography of Eyjafjallajökull volcano, Iceland. *J. Volcanol. Geotherm. Res.* 347, 250–263. doi:10.1016/j.jvolgeores.2017.09.017

Bensen, G., Ritzwoller, M., Barmin, M., Levshin, A. L., Lin, F., Moschetti, M., et al. (2007). Processing seismic ambient noise data to obtain reliable broad-band surface wave dispersion measurements. *Geophys. J. Int.* 169, 1239–1260. doi:10.1111/j.1365-246x.2007.03374.x

Bodin, T., Sambridge, M., Tkalčić, H., Arroucau, P., Gallagher, K., and Rawlinson, N. (2012). Transdimensional inversion of receiver functions and surface wave dispersion. *J. Geophys. Res. Solid Earth* 117. doi:10.1029/2011JB008560

Brenguier, F., Shapiro, N. M., Campillo, M., Ferrazzini, V., Duputel, Z., Coutant, O., et al. (2008). Towards forecasting volcanic eruptions using seismic noise. *Nat. Geosci.* 1, 126–130. doi:10.1038/ngeo104

Cabrera-Pérez, I., Centeno, R., Soubestre, J., D'Auria, L., Rivera, M., and Machacca, R. (2022). Ambient noise tomography of Misti volcano, Peru. *J. Volcanol. Geotherm. Res.* 107538, 107538. doi:10.1016/j.jvolgeores.2022.107538

Cabrera-Pérez, I., D'Auria, L., Soubestre, J., Barrancos, J., Padilla, G. D., and Pérez, N. M. (2021). A nonlinear multiscale inversion approach for ambient noise tomography. *Geophys. J. Int.* 225, 1158–1173. doi:10.1093/gji/ggaa574

Cabrera-Pérez, I., Soubestre, J., D'Auria, L., Barrancos, J., Martín-Lorenzo, A., van Dorth, D. M., et al. (2023a). Geothermal and structural features of La Palma island (Canary Islands) imaged by ambient noise tomography. *Sci. Rep.* 13, 12892. doi:10.1038/s41598-023-39910-z

Cabrera-Pérez, I., Soubestre, J., D'Auria, L., van Dorth, D. M., Ledo, J., Piña-Varas, P., et al. (2023b). Ambient noise tomography of Gran Canaria island (Canary Islands) for geothermal exploration. *Geothermics* 108, 102609. doi:10.1016/j.geothermics.2022.102609

Cerdeña, I. D., García-Cañada, L., Benito-Saz, M., Del Fresno, C., Lamolda, H., de Pablo, J. P., et al. (2018). On the relation between ground surface deformation and seismicity during the 2012–2014 successive magmatic intrusions at el hierro island. *Tectonophysics* 744, 422–437. doi:10.1016/j.tecto.2018.07.019

Derode, A., Larose, E., Tanter, M., De Rosny, J., Tourin, A., Campillo, M., et al. (2003). Recovering the Green's function from field-field correlations in an open scattering medium (l). *J. Acoust. Soc. Am.* 113, 2973–2976. doi:10.1121/1.1570436

Dietrich, L., and Vicente, S. (2019). Monitoring the unrest of El Hierro island with seismic observations. doi:10.14470/7Y7560573304

Fallahi, M. J., Obermann, A., Lupi, M., Karyono, K., and Mazzini, A. (2017). The plumbing system feeding the Lusi eruption revealed by ambient noise tomography. *J. Geophys. Res. Solid Earth* 122, 8200–8213. doi:10.1002/2017JB014592

García-Yeguas, A., Ibánez, J. M., Koulakov, I., Jakovlev, A., Romero-Ruiz, M. C., and Prudencio, J. (2014). Seismic tomography model reveals mantle magma sources of recent volcanic activity at El Hierro Island (Canary Islands, Spain). *Geophys. J. Int.* 199, 1739–1750. doi:10.1093/gji/ggu339

González, P. J., Samsonov, S. V., Pepe, S., Tiampo, K. F., Tizzani, P., Casu, F., et al. (2013). Magma storage and migration associated with the 2011–2012 El Hierro eruption: implications for crustal magmatic systems at oceanic island volcanoes. *J. Geophys. Res. Solid Earth* 118, 4361–4377. doi:10.1002/jgrb.50289

Gorbatikov, A., Montesinos, F., Arnoso, J., Stepanova, M. Y., Benavent, M., and Tsukanov, A. (2013). New features in the subsurface structure model of El Hierro Island (Canaries) from low-frequency microseismic sounding: an insight into the 2011 seismo-volcanic crisis. *Surv. Geophys.* 34, 463–489. doi:10.1007/s10712-013-9240-4

Guillou, H., Carracedo, J. C., Torrado, F. P., and Badiola, E. R. (1996). K-ar ages and magnetic stratigraphy of a hotspot-induced, fast grown oceanic island: el hierro, canary islands. *J. Volcanol. Geotherm. Res.* 73, 141–155. doi:10.1016/0377-0273(96)00021-2

Gutenberg, B. (1958). "Microseisms," in Advances in geophysics (Amsterdam, Netherlands: Elsevier), 53–92.

Ibáñez, J., De Angelis, S., Díaz-Moreno, A., Hernández, P., Alguacil, G., Posadas, A., et al. (2012). Insights into the 2011–2012 submarine eruption off the coast of El Hierro (Canary Islands, Spain) from statistical analyses of earthquake activity. *Geophys. J. Int.* 191, 659–670. doi:10.1111/j.1365-246X.2012.05629.x

Ke, G., Dong, H., Kristensen, Å., and Thompson, M. (2011). Modified Thomson–Haskell matrix methods for surface-wave dispersion-curve calculation and their accelerated root-searching schemes. *Bull. Seismol. Soc. Am.* 101, 1692–1703. doi:10.1785/0120100187

Koulakov, I., Jaxybulatov, K., Shapiro, N. M., Abkadyrov, I., Deev, E., Jakovlev, A., et al. (2014). Asymmetric caldera-related structures in the area of the Avacha group of volcanoes in Kamchatka as revealed by ambient noise tomography and deep seismic sounding. *J. Volcanol. Geotherm. Res.* 285, 36–46. doi:10.1016/j.jvolgeores.2014.08.012

Levshin, A., Ratnikova, L., and Berger, J. (1992). Peculiarities of surfacewave propagation across central Eurasia. *Bull. Seismol. Soc. Am.* 82, 2464–2493. doi:10.1785/BSSA0820062464

Lobkis, O. I., and Weaver, R. L. (2001). On the emergence of the Green's function in the correlations of a diffuse field. *J. Acoust. Soc. Am.* 110, 3011–3017. doi:10.1121/1.1417528

López, C., Blanco, M., Abella, R., Brenes, B., Cabrera Rodríguez, V., Casas, B., et al. (2012). Monitoring the volcanic unrest of El Hierro (Canary Islands) before the onset of the 2011–2012 submarine eruption. *Geophys. Res. Lett.* 39. doi:10.1029/2012GL051846

Luu, K. (2021). disba: numba-accelerated computation of surface wave dispersion. Zenodo. doi:10.5281/zenodo.3987395

Martí, J., Villaseñor, A., Geyer, A., López, C., and Tryggvason, A. (2017). Stress barriers controlling lateral migration of magma revealed by seismic tomography. *Sci. Rep.* 7, 40757–40810. doi:10.1038/srep40757

Masterlark, T., Haney, M., Dickinson, H., Fournier, T., and Searcy, C. (2010). Rheologic and structural controls on the deformation of Okmok volcano, Alaska: FEMs, Insar, and ambient noise tomography. *J. Geophys. Res. Solid Earth* 115. doi:10.1029/2009]B006324

Melián, G., Hernández, P. A., Padrón, E., Pérez, N. M., Barrancos, J., Padilla, G., et al. (2014). Spatial and temporal variations of diffuse co2 degassing at el hierro volcanic system: relation to the 2011–2012 submarine eruption. *J. Geophys. Res. Solid Earth* 119, 6976–6991. doi:10.1002/2014JB011013

Montesinos, F., Arnoso, J., Benavent, M., and Vieira, R. (2006). The crustal structure of El Hierro (Canary Islands) from 3-d gravity inversion. *J. Volcanol. Geotherm. Res.* 150, 283–299. doi:10.1016/j.jvolgeores.2005.07.018

Mordret, A., Rivet, D., Landès, M., and Shapiro, N. M. (2015). Three-dimensional shear velocity anisotropic model of Piton de la Fournaise Volcano (La Réunion Island) from ambient seismic noise. *J. Geophys. Res. Solid Earth* 120, 406–427. doi:10.1002/2014JB011654

Obermann, A., Molinari, I., Métaxian, J.-P., Grigoli, F., Strauch, W., and Wiemer, S. (2019). Structure of Masaya and Momotombo volcano, Nicaragua, investigated with a temporary seismic network. *J. Volcanol. Geotherm. Res.* 379, 1–11. doi:10.1016/j.jvolgeores.2019.04.013

Padilla, G. D., Hernández, P. A., Padrón, E., Barrancos, J., Pérez, N. M., Melián, G., et al. (2013). Soil gas radon emissions and volcanic activity at El Hierro (Canary Islands): the 2011-2012 submarine eruption. *Geochem. Geophys. Geosystems* 14, 432–447. doi:10.1029/2012GC004375

Padrón, E., Pérez, N. M., Hernández, P. A., Sumino, H., Melián, G. V., Barrancos, J., et al. (2013). Diffusive helium emissions as a precursory sign of volcanic unrest. *Geology* 41, 539–542. doi:10.1130/G34027.1

Pérez, N. M., Padilla, G. D., Padrón, E., Hernández, P. A., Melián, G. V., Barrancos, J., et al. (2012). Precursory diffuse co2 and h2s emission signatures of the 2011–2012 El Hierro submarine eruption, Canary Islands. *Geophys. Res. Lett.* 39. doi:10.1029/2012GL052410

Pérez, N. M., Somoza, L., Hernández, P. A., de Vallejo, L. G., León, R., Sagiya, T., et al. (2014). Evidence from acoustic imaging for submarine volcanic activity in 2012 off the west coast of el hierro (canary islands, Spain). *Bull. Volcanol.* 76, 882–915. doi:10.1007/s00445-014-0882-y

Rodriguez-Losada, J. A., Eff-Darwich, A., Hernandez, L. E., Viñas, R., Pérez, N., Hernandez, P., et al. (2015). Petrological and geochemical highlights in the floating fragments of the October 2011 submarine eruption offshore El Hierro (Canary Islands): relevance of submarine hydrothermal processes. *J. Afr. Earth Sci.* 102, 41–49. doi:10.1016/j.jafrearsci.2014.11.005

Sambridge, M., Gallagher, K., Jackson, A., and Rickwood, P. (2006). Transdimensional inverse problems, model comparison and the evidence. *Geophys. J. Int.* 167, 528–542. doi:10.1111/j.1365-246x.2006.03155.x

Seydoux, L., Shapiro, N. M., De Rosny, J., Brenguier, F., and Landès, M. (2016). Detecting seismic activity with a covariance matrix analysis of data recorded on seismic arrays. *Geophys. J. Int.* 204, 1430–1442. doi:10.1093/gji/ggv531

Shapiro, N. M., Campillo, M., Stehly, L., and Ritzwoller, M. H. (2005). High-resolution surface-wave tomography from ambient seismic noise. *Science* 307, 1615–1618. doi:10.1126/science.1108339

Somoza, L., González, F. J., Barker, S., Madureira, P., Medialdea, T., De Ignacio, C., et al. (2017). Evolution of submarine eruptive activity during the 2011–2012 El Hierro event as documented by hydroacoustic images and remotely operated vehicle observations. *Geochem. Geophys. Geosystems* 18, 3109–3137. doi:10.1002/2016GC006733

Soubestre, J., Shapiro, N. M., Seydoux, L., de Rosny, J., Droznin, D. V., Droznina, S. Y., et al. (2018). Network-based detection and classification of seismovolcanic tremors: example from the klyuchevskoy volcanic group in kamchatka. *J. Geophys. Res. Solid Earth* 123, 564–582. doi:10.1002/2017JB014726

Spica, Z., Legrand, D., Iglesias, A., Walter, T. R., Heimann, S., Dahm, T., et al. (2015). Hydrothermal and magmatic reservoirs at Lazufre volcanic area, revealed by a high-resolution seismic noise tomography. *Earth Planet. Sci. Lett.* 421, 27–38. doi:10.1016/j.epsl.2015.03.042

Stankiewicz, J., Ryberg, T., Haberland, C., and Natawidjaja, D. (2010). Lake Toba volcano magma chamber imaged by ambient seismic noise tomography. *Geophys. Res. Lett.* 37. doi:10.1029/2010GL044211

Troll, V. R., and Carracedo, J. C. (2016). *The geology of the canary islands*. Amsterdam, Netherlands: Elsevier.

Wang, Y., Lin, F. C., Schmandt, B., and Farrell, J. (2017). Ambient noise tomography across Mount St. Helens using a dense seismic array. *J. Geophys. Res. Solid Earth* 122, 4492–4508. doi:10.1002/2016/B013769